Discovery and Characterization of Fungal Secondary Metabolites with Antibacterial and Antibiofilm Activities

Inaugural Dissertation

for the attainment of the title of doctor
in the Faculty of Mathematics and Natural Sciences
at the Heinrich Heine University Düsseldorf

Presented by

Di He
from Kunming

Düsseldorf, August 2026

from the Institute of Pharmaceutical Biology and Biotechnology
at Heinrich Heine University Düsseldorf

Published with the permission of the
Faculty of Mathematics and Natural Sciences at
Heinrich Heine University Düsseldorf

Supervisor: Prof. Dr. Rainer Kalscheuer

Co-Supervisor: Prof. Dr. Julia Frunzke

The date of the oral examination: 26.10.2026

Contents

Abbreviations ..... **III**

Abstract ..... **IX**

1. Introduction **1**

1.1 Infectious diseases and the challenge of antimicrobial resistance 2
1.1.1 Mechanisms of AMR *2*
1.1.2 Strategies to mitigate AMR *3*
1.2 Overview of antibiotics and their mechanisms of action 5
1.2.1 Antibiotics inhibiting cell wall synthesis *5*
1.2.2 Antibiotics inhibiting nucleic acid replication and transcription *5*
1.2.3 Antibiotics inhibiting protein synthesis *5*
1.2.4 Antibiotics disrupting cell membrane function *6*
1.2.5 Antibiotics inhibiting folate metabolism *6*
1.2.6 Novel or recently developed antibiotic classes *6*
1.3 *S. aureus* as a clinically important pathogen 7
1.3.1 MRSA *8*
1.3.2 hVISA and VISA *9*
1.3.3 VRSA *10*
1.4 Biofilm-associated infections and anti-biofilm strategies 10
1.4.1 Biofilm formation and its clinical significance *11*
1.4.2 Biofilm-mediated antibiotic tolerance and resistance *11*
1.4.3 Anti-biofilm strategies *12*
1.5 Application of natural products in anti-infective drug discovery 13
1.6 Application of fungal secondary metabolites in antibacterial and anti-biofilm activities 15
1.7 Co-cultivation strategies and the activation of cryptic fungal metabolic pathways 16

2. Aim of this thesis **18**

3. Manuscript 1 ..... **19**

4. Manuscript 2 ..... **78**

5. Manuscript 3 ..... **165**

6. General Discussion **280**

6.1 Fungal secondary metabolites in anti-infective research 280
6.2 OSMAC and co-culture strategies for activating fungal cryptic metabolism 281
6.3 Selective antibacterial activity of PAA against VISA and its significance 281
6.4 Mode of action of PAA 282
6.5 GraRS-associated cell envelope homeostasis in the activity of PAA 283
6.6 Possible significance of *cysK* mutations and current limitations 286
6.7 Complementation limitations and GraRS regulatory complexity 287
6.8 Proteomic evidence for PAA-induced cell envelope remodeling in VISA 288
6.9 Inhibition of VISA biofilm formation by PAA 292
6.10 Fusapurpurins as mature biofilm-disrupting molecules 292

6.11 PAA and fusapurpurins represent two distinct antibiofilm modes 293
6.12 Biosynthetic hypothesis of fusapurpurins 294
6.13 Computational support for the fusapurpurin biosynthetic hypothesis 296
6.14 Future perspectives and limitations 299
7. Other structural identification work 301
8. Contribution to the three manuscripts 301
Reference 303
Acknowledgements 316

Abbreviations

%	percent
°C	degree Celsius
°C/min	degrees Celsius per minute
°C/s	degrees Celsius per second
× MIC	fold of the minimum inhibitory concentration
1D	one-dimensional
2D	two-dimensional
A. baylyi	*Acinetobacter baylyi*
ABC	ATP-binding cassette
ADS	albumin-dextrose-saline
AMR	antimicrobial resistance
ANI	average nucleotide identity
antiSMASH	antibiotics and Secondary Metabolite Analysis Shell
ATCC	American Type Culture Collection
ATCC 25922	*Escherichia coli* ATCC 25922
ATCC 25923	*Staphylococcus aureus* ATCC 25923
ATCC 29212	*Enterococcus faecalis* ATCC 29212
ATCC 29213	*Staphylococcus aureus* ATCC 29213
ATCC 43300	methicillin-resistant *Staphylococcus aureus* ATCC 43300
ATCC 51299	vancomycin-resistant *Enterococcus faecium* ATCC 51299
ATCC 700699	vancomycin-intermediate *Staphylococcus aureus* ATCC 700699
A. terreus	*Aspergillus terreus*
AWaRe	Access, Watch, and Reserve
B. amyloliquefaciens	*Bacillus amyloliquefaciens*
BGC	biosynthetic gene cluster
BGCs	biosynthetic gene clusters
BL21(DE3)	*Escherichia coli* BL21(DE3) expression strain
BLAST	Basic Local Alignment Search Tool
bp	base pair
BSA	bovine serum albumin
BSTFA	*N*,*O*-bis(trimethylsilyl)trifluoroacetamide
Ca^{2+}	calcium ion
C. albicans	*Candida albicans*
CA-MRSA	community-associated methicillin-resistant *Staphylococcus aureus*
CCCP	carbonyl cyanide *m*-chlorophenyl hydrazone
CD_3OD	deuterated methanol
$CDCl_3$	deuterated chloroform
cDNA	complementary DNA
cells/mL	cells per milliliter
cells/well	cells per well
CFU	colony forming unit
CFU/mL	colony forming units per milliliter
CFU/well	colony forming units per well
$CHCl_3$	chloroform
CLSI	Clinical and Laboratory Standards Institute
cm^{-1}	reciprocal centimeter; wavenumber

CO_2	carbon dioxide
CoA	coenzyme A
COSY	correlation spectroscopy
CRISPR-Cas	clustered regularly interspaced short palindromic repeats-CRISPR-associated proteins
C. rosea	*Clonostachys rosea*
CT	cycle threshold
C. violaceum	*Chromobacterium violaceum*
CysK	cysteine synthase / O-acetylserine sulfhydrylase
cysK	cysteine synthase / O-acetylserine sulfhydrylase gene
DAD	diode array detector
DAIR	debridement, antibiotics, and implant retention
DC10B	*Escherichia coli* DC10B methylation-deficient cloning strain
DE3	lysogen carrying T7 RNA polymerase under lacUV5 control
DFT	density functional theory
DHFR	dihydrofolate reductase
DHPS	dihydropteroate synthase
DiOC2(3)	3,3′-diethyloxacarbocyanine iodide
DltA	D-alanine-D-alanyl carrier protein ligase
dltA	D-alanine-D-alanyl carrier protein ligase gene
DMEM	Dulbecco's modified Eagle medium
DMSO	dimethyl sulfoxide
DMSO-d_6	deuterated dimethyl sulfoxide
DNA	deoxyribonucleic acid
DNase	deoxyribonuclease
DTT	dithiothreitol
ECD	electronic circular dichroism
E. coli	*Escherichia coli*
eDNA	extracellular DNA
E. faecalis	*Enterococcus faecalis*
E. faecium	*Enterococcus faecium*
EMEM	Eagle's minimum essential medium
EPS	extracellular polymeric substances
ESI-MS	electrospray ionization mass spectrometry
ESIMS	electrospray ionization mass spectrometry
EtOAc	ethyl acetate
FBS	fetal bovine serum
FCS	fetal calf serum
FDA	Food and Drug Administration
F. fujikuroi	*Fusarium fujikuroi*
FIC	fractional inhibitory concentration
FICI	fractional inhibitory concentration index
FmtC	phosphatidylglycerol lysyltransferase; synonym of MprF
fmtC	phosphatidylglycerol lysyltransferase gene; synonym of *mprF*
FO-LovD-like	*Fusarium oxysporum* LovD-like protein
F. oxysporum	*Fusarium oxysporum*
FTIR	Fourier-transform infrared spectroscopy
g	gram
g/L	grams per liter
GAPDH	glyceraldehyde-3-phosphate dehydrogenase

GBD	Global Burden of Disease
GC	gas chromatography
GLASS	Global Antimicrobial Resistance and Use Surveillance System
GraR	glycopeptide resistance-associated response regulator
graR	glycopeptide resistance-associated response regulator gene
GraRS	GraR/GraS two-component regulatory system
GraS	glycopeptide resistance-associated sensor histidine kinase
graS	glycopeptide resistance-associated sensor histidine kinase gene
gyrA	DNA gyrase subunit A gene
h	hour
H37Rv	*Mycobacterium tuberculosis* H37Rv strain
HA-MRSA	hospital-associated methicillin-resistant *Staphylococcus aureus*
HEK293	human embryonic kidney 293 cells
HIV	human immunodeficiency virus
HIV-1	human immunodeficiency virus type 1
HMBC	heteronuclear multiple bond correlation
HPLC	high-performance liquid chromatography
HRESIMS	high-resolution electrospray ionization mass spectrometry
HSQC	heteronuclear single quantum correlation
HUH-7	human hepatocellular carcinoma cell line
hVISA	heterogeneous vancomycin-intermediate *Staphylococcus aureus*
Hz	hertz
IC_{50}	half-maximal inhibitory concentration
IC_{90}	90% inhibitory concentration
IcaA	*N*-acetylglucosaminyltransferase involved in PIA/PNAG synthesis
icaA	*N*-acetylglucosaminyltransferase gene involved in PIA/PNAG synthesis
IcaB	deacetylase involved in PIA/PNAG modification
icaB	deacetylase gene involved in PIA/PNAG modification
IcaC	membrane protein involved in PIA/PNAG export or elongation
icaC	membrane protein gene involved in PIA/PNAG export or elongation
ICU	intensive care unit
INH	isoniazid
IPTG	isopropyl β-D-1-thiogalactopyranoside
IsaA	immunodominant staphylococcal antigen A
ITS	internal transcribed spacer
K17*	nonsense mutation resulting in a stop codon at amino acid position 17
kJ/mol	kilojoule per mole
K. pneumoniae	*Klebsiella pneumoniae*
L	liter
LAGI	Leu-Ala-Gly-Ile amino acid motif deleted in CysK
LA-MRSA	livestock-associated methicillin-resistant *Staphylococcus aureus*
LB	lysogeny broth
LC-MS	liquid chromatography-mass spectrometry
LH-20	Sephadex LH-20
LovD	lovastatin diketide synthase
LrgB	antiholin-like murein hydrolase regulator protein B
LtaS	lipoteichoic acid synthase
LytM	peptidoglycan hydrolase / glycyl-glycine endopeptidase
M	molar

m/z	mass-to-charge ratio
MALDI-TOF-MS	matrix-assisted laser desorption/ionization time-of-flight mass spectrometry
MATE	multidrug and toxic compound extrusion
mAU	milli-absorbance unit
MaxQuant	software platform for mass spectrometry-based proteomics analysis
MDR	multidrug resistance
MecA	penicillin-binding protein 2a
mecA	methicillin resistance gene encoding PBP2a
MecI	methicillin resistance regulatory repressor protein
MeCN	acetonitrile
MeOH	methanol
MFS	major facilitator superfamily
Mg^{2+}	magnesium ion
mg	milligram
mg/L	milligrams per liter
mg/mL	milligrams per milliliter
MH	Mueller-Hinton
MHB	Mueller-Hinton broth
MHz	megahertz
MIC	minimum inhibitory concentration
MIC_{90}	minimum concentration inhibiting 90% of growth
min	minute
mL	milliliter
mL/min	milliliters per minute
mM	millimolar
mm	millimeter
MMFF	Merck molecular force field
MOI	multiplicity of infection
MOPS	3-(*N*-morpholino)propanesulfonic acid
MprF	multiple peptide resistance factor / phosphatidylglycerol lysyltransferase
mprF	multiple peptide resistance factor; phosphatidylglycerol lysyltransferase
MRSA	methicillin-resistant *Staphylococcus aureus*
MS	mass spectrometry
MS/MS	tandem mass spectrometry
MSD	mass selective detector
MSSA	methicillin-sensitive *Staphylococcus aureus*
Mtb	*Mycobacterium tuberculosis*
M. tuberculosis	*Mycobacterium tuberculosis*
Mu1	pestalotic acid A-resistant mutant 1 derived from vancomycin-intermediate *Staphylococcus aureus*
Mu2	pestalotic acid A-resistant mutant 2 derived from vancomycin-intermediate *Staphylococcus aureus*
Mu3	pestalotic acid A-resistant mutant 3 derived from vancomycin-intermediate *Staphylococcus aureus*
Mu50	vancomycin-intermediate *Staphylococcus aureus* Mu50 strain
NaPPA	sodium phenylpyruvate
NCBI	National Center for Biotechnology Information
NEB	New England Biolabs
ng	nanogram

Ni-NTA	nickel-nitrilotriacetic acid
nm	nanometer
NMR	nuclear magnetic resonance
NOE	nuclear Overhauser effect
OD600	optical density at 600 nm
ODS	octadecylsilyl
OR	optical rotation
OSMAC	one strain many compounds
P200*	nonsense mutation resulting in a stop codon at amino acid position 200
PAA	pestalotic acid A
P. aeruginosa	*Pseudomonas aeruginosa*
PAO1	*Pseudomonas aeruginosa* PAO1 strain
parC	DNA topoisomerase IV subunit A gene
PBP	penicillin-binding protein
PBP2a	penicillin-binding protein 2a
PBPs	penicillin-binding proteins
PBS	phosphate-buffered saline
P. chamaeropis	*Pestalotiopsis chamaeropis*
PCR	polymerase chain reaction
P. ehimensis	*Paenibacillus ehimensis*
pET28a	pET28a expression vector
PI	propidium iodide
PIA	polysaccharide intercellular adhesin
PKS	polyketide synthase
pLA02	*Staphylococcus aureus*/*E. coli* shuttle vector
PNAG	poly-*N*-acetylglucosamine
PPA	phenylpyruvic acid
ppm	parts per million
qPCR	quantitative polymerase chain reaction
RBC	red blood cell
RIF	rifampicin
RNA	ribonucleic acid
RND	resistance-nodulation-division
ROESY	rotating-frame nuclear Overhauser effect spectroscopy
rpm	revolutions per minute
RPMI	Roswell Park Memorial Institute medium
rpoB	DNA-directed RNA polymerase beta subunit gene
RT-qPCR	reverse transcription quantitative polymerase chain reaction
s	second
SARS-CoV-2	severe acute respiratory syndrome coronavirus 2
S. aureus	*Staphylococcus aureus*
SAV0513	*Staphylococcus aureus* Mu50 locus tag for *cysK*
SAV0659	*Staphylococcus aureus* Mu50 locus tag for *graR*
SCCmec	staphylococcal cassette chromosome mec
SceD	lytic transglycosylase-like cell wall hydrolase
SDS-PAGE	sodium dodecyl sulfate-polyacrylamide gel electrophoresis
S. epidermidis	*Staphylococcus epidermidis*
SI	selectivity index
SMR	small multidrug resistance

SNAC	*N*-acetylcysteamine thioester
S. pneumoniae	*Streptococcus pneumoniae*
T7	bacteriophage T7 promoter/RNA polymerase system
T77P	threonine-to-proline substitution at amino acid position 77
TDDFT	time-dependent density functional theory
THP-1	human monocytic leukemia cell line
TLC	thin-layer chromatography
TMCS	trimethylchlorosilane
TMS	tetramethylsilane
U/mL	units per milliliter
USA300	community-associated methicillin-resistant *Staphylococcus aureus* USA300 strain
UV	ultraviolet
vanA	vancomycin resistance gene / gene cluster
VISA	vancomycin-intermediate *Staphylococcus aureus*
VLC	vacuum liquid chromatography
VraF	cell envelope stress-associated ABC transporter ATP-binding protein
VraFG	VraF/VraG ABC transporter system
VraG	cell envelope stress-associated ABC transporter permease
vraG	cell envelope stress-associated ABC transporter permease gene
VraS	sensor histidine kinase of the VraSR system
vraS	sensor histidine kinase gene of the VraSR system
VraSR	VraS/VraR two-component regulatory system
VraX	cell wall stress-associated protein
VRE	vancomycin-resistant Enterococcus
VRSA	vancomycin-resistant *Staphylococcus aureus*
VSSA	vancomycin-susceptible *Staphylococcus aureus*
WHO	World Health Organization
Xcalibur	software for mass spectrometry data acquisition and analysis
µg	microgram
µg/mL	micrograms per milliliter
µL	microliter
µL/well	microliters per well
µM	micromolar
Å	angstrom

Abstract

Antimicrobial resistance and biofilm-associated infections severely limit the effectiveness of conventional anti-infective therapy, creating an urgent need to discover anti-infective lead compounds with new structures and novel modes of action. Fungal secondary metabolites possess rich structural diversity and broad biological activities and represent an important source of antibacterial and antibiofilm natural products. This dissertation mainly focuses on two projects concerning fungus-derived anti-infective natural products: first, the antibacterial activity of pestalotic acid A (PAA) derived from *Pestalotiopsis chamaeropis* against vancomycin-intermediate *Staphylococcus aureus* (VISA) and its mechanism of action; and second, the mature biofilm-disrupting activity and possible biosynthetic pathway of fusapurpurins A and B induced by co-cultivation of *Fusarium oxysporum* with *Paenibacillus ehimensis*.

The first part of this dissertation investigated the secondary metabolism of *P. chamaeropis* induced by the OSMAC strategy, leading to the isolation of a series of pestalotic acid-related natural products, including pestalotic acids A–H and pestaloside A. Among them, pestalotic acid H and pestaloside A were identified as new natural products, and the absolute configuration of pestalotic acid C was determined by single-crystal X-ray diffraction. Bioactivity evaluation showed that pestalotic acid A exhibited strong inhibitory activity against VISA, together with low cytotoxicity and low hemolytic activity.

Mechanistic studies indicated that the activity of PAA against VISA was closely associated with cell envelope homeostasis. PAA mutants with reduced susceptibility obtained by continuous liquid-pressure selection all carried disruptive mutations in *graR* and showed increased susceptibility to vancomycin, daptomycin, polymyxin B, and colistin. Antibiotic synergy assays, cytochrome c binding assays, RT-qPCR, and proteomic results collectively suggested that PAA may interfere with GraRS-related cell envelope regulation, cell surface charge modification, and cell envelope stress adaptation. The action of PAA showed concentration-dependent characteristics: at low concentrations, it tended to interfere with the VISA-specific cell envelope adaptive state, whereas at high concentrations, it produced broader membrane-related or cell envelope-damaging effects. In addition, proteomic results showed that PAA downregulated proteins related to biofilm matrix synthesis, and experimental validation demonstrated that PAA inhibited VISA biofilm formation at sub-MIC concentrations, indicating that its anti-infective potential is reflected not only in the inhibition of planktonic cell growth, but also in the weakening of early biofilm establishment.

The second part of this dissertation used a co-cultivation strategy to activate cryptic metabolic pathways in *F. oxysporum*, leading to the isolation of new compounds such as fusachinon, fusapurpurin A, and fusapurpurin B. Among them, fusapurpurins A and B are structurally unique bridged fusarubin derivatives and were confirmed by single-crystal X-ray diffraction to be racemates. Bioactivity studies

showed that fusapurpurins A and B exhibited obvious disruptive effects on mature biofilms of *S. aureus* Mu50 and *Pseudomonas aeruginosa* PAO1, whereas their direct antibacterial activity was relatively weak. This suggests that their main value lies in interfering with mature biofilms rather than acting as conventional bactericidal agents. This result complements the biofilm formation-inhibitory activity of PAA, indicating that fungal natural products can act at different stages of the biofilm life cycle.

To investigate the biosynthetic mechanism of fusapurpurins, this study combined genome sequencing, antiSMASH analysis, AlphaFold structure prediction, US-align structural comparison, and Chai-1 protein–ligand complex prediction, and proposed that the FO-LovD-like protein may participate in the coupling reaction between 9-*O*-methylfusarubin and an activated phenylpyruvate-derived acyl donor. According to the current model, subsequent oxidative dehydrogenation may generate a reactive intermediate, which may further undergo non-stereoselective Diels–Alder-like cyclization to form fusapurpurins A and B. The fact that both products are racemates supports the possibility that the final cyclization process lacks clear chiral control. Since phenylpyruvic acid or defined reaction intermediates could not be detected in the extracts, this biosynthetic hypothesis still requires further validation through in vitro enzymatic reactions, substrate feeding, targeted LC-MS/MS, and genetic experiments.

In addition, this dissertation also includes the determination of the sugar configuration in glycosylated asperphenalenone derivatives derived from *Clonostachys rosea*.

In summary, this dissertation demonstrates the multiple values of fungal secondary metabolites in research on drug-resistant bacteria, antibiofilm activity, and natural product biosynthesis. PAA revealed a potential vulnerability in the cell envelope adaptive state of VISA, while fusapurpurins A and B demonstrated the application potential of co-culture-induced metabolites in disrupting mature biofilms. These results provide an important basis for the discovery of new anti-infective natural product lead structures, the exploration of antibiofilm strategies, and the understanding of late-stage biosynthetic processes in fungal natural products.

1. Introduction

While antibiotics have significantly improved clinical outcomes for infectious diseases over the past few decades, the effective control of bacterial infections still faces severe challenges. On one hand, the global spread of antimicrobial resistance (AMR) has compromised the efficacy of traditional antibiotics and is associated with substantial mortality [1]. On the other hand, bacteria can evade drug-induced killing independent of classical resistance mutations by forming biofilms or entering a low-metabolic, tolerant physiological state [2]. Concurrently, the discovery of entirely new antibiotic classes has markedly declined since the 1980s, resulting in limited novel therapeutic options in the clinic [1]. Therefore, it is of great significance to discover antimicrobial natural products with novel mechanisms of action and to develop alternative therapeutic strategies targeting resistant bacteria, biofilms, and tolerant cells.

Among bacterial pathogens, *Staphylococcus aureus* is of particular clinical significance. This bacterium causes a wide range of diseases, ranging from superficial skin and soft tissue infections to bacteremia, infective endocarditis, pneumonia, osteomyelitis, and medical device-associated infections. Due to its capacity to acquire antibiotic resistance, evade host immune clearance, survive in a tolerant state, and form biofilms, *S. aureus* infections are often difficult to treat and prone to recurrence. Therefore, *S. aureus* serves as a crucial model pathogen for the development of novel antimicrobial agents and anti-biofilm strategies, as well as for investigating the mechanisms of bacterial resistance and tolerance [2].

Natural products have historically played a central role in antibiotic discovery and continue to provide structurally diverse scaffolds with antibacterial, anti-biofilm, and anti-virulence potential. A recent comprehensive analysis of approved natural product-inspired antibiotics indicates that a total of 217 such agents were approved for human therapy between 1943 and 2025. These agents comprise the natural products themselves alongside their semi-synthetic or synthetic derivatives, thereby underscoring the enduring value of natural products in anti-infective drug discovery [3].

Fungi are prolific producers of secondary metabolites among eukaryotic microorganisms, capable of producing a diverse array of structurally divers compounds such as polyketides, terpenoids, alkaloids, and peptides, many of which possess biological activities relevant to infection control [4–6]. However, under standard laboratory culture conditions, a substantial portion of their biosynthetic gene clusters (BGCs) remains silent or is expressed only at basal levels. Strategies such as microbial co-cultivation can effectively simulate microbial ecological interactions, activate cryptic biosynthetic pathways, and induce the production of metabolites that are otherwise difficult to detect under conventional conditions [7]. Accordingly, this general introduction will focus on the paradigms of AMR, mechanisms of antibiotic action, the physiology and pathogenesis of *S. aureus*, biofilm dynamics, natural products, fungal secondary metabolites, and co-cultivation strategies, thereby establishing the

theoretical foundation for the research presented in this study.

1.1 Infectious diseases and the challenge of antimicrobial resistance

Infectious diseases remain a significant burden on global public health, and the continuous rise of AMR further undermines the effectiveness of traditional anti-infective therapies [8]. In 2019, bacterial AMR was directly responsible for approximately 1.27 million deaths and was associated with an estimated 4.95 million deaths, highlighting its emergence as a major global source of mortality and disease burden [8]. The World Health Organization (WHO) considers AMR to be one of the foremost global public health and development threats, driven primarily by the misuse and overuse of antimicrobials in human medicine, animal care, and agriculture [9].

The clinical threat of AMR is predominantly driven by several high-risk bacterial pathogens, including *Escherichia coli*, *S. aureus*, *Klebsiella pneumoniae*, *Acinetobacter baumannii*, and *Pseudomonas aeruginosa* [8]. These pathogens are frequently associated with hospital-acquired infections, bloodstream infections, pulmonary infections, urinary tract infections, and medical device-associated infections, evading antibiotic action through a variety of intrinsic or acquired mechanisms [10]. The WHO 2024 Bacterial Priority Pathogens List designates multiple drug-resistant Gram-negative bacteria, drug-resistant *Mycobacterium tuberculosis*, *S. aureus*, and some other high-burden pathogens as priority targets for antimicrobial research and development and for public health interventions [11].

Beyond genetic resistance, bacteria can also reduce their susceptibility to antimicrobial agents by forming biofilms or entering a low-metabolic, tolerant physiological state. These non-classical forms of resistance can lead to persistent and recurrent infections, increasing the risk of clinical treatment failure. Therefore, addressing infectious diseases and AMR requires not only the rational use of existing antibiotics and enhanced resistance surveillance, but also the urgent development of novel antimicrobial agents with unprecedented mechanisms of action, alongside alternative or adjunctive therapeutic strategies targeting biofilms and tolerant cells [10].

1.1.1 Mechanisms of AMR

The development of bacterial AMR typically involves multiple distinct molecular mechanisms, including the enzymatic inactivation of antimicrobial agents, alteration of drug targets, decreased cell envelope permeability, and enhanced active efflux systems. These mechanisms can arise from chromosomal mutations or be transmitted horizontally between bacteria via plasmids, transposons, or other mobile genetic elements. Their accumulation within a single strain drives the emergence of multidrug resistance (MDR) [1, 12].

Enzymatic inactivation represents one of the most prevalent resistance mechanisms. Bacteria produce specialized enzymes such as β-lactamases, aminoglycoside-modifying enzymes, or chloramphenicol acetyltransferases that hydrolyze or chemically modify antibiotics before they reach their target sites, thereby resulting in the loss of their antibacterial activity. For example, β-lactamases

hydrolytically cleave the core β-lactam ring, whereas aminoglycoside-modifying enzymes decrease the binding affinity of the drug to the ribosome through acetylation, adenylylation, or phosphorylation [1, 13].

Alteration of drug targets decreases the affinity of antibiotics for their cognate binding sites, representing a crucial mechanism of resistance to β-lactams, quinolones, glycopeptides, and ribosome-targeting antibiotics. For example, the low-affinity penicillin-binding protein PBP2a encoded by *mecA* in methicillin-resistant *S. aureus* (MRSA) sustains cell wall synthesis even in the presence of β-lactam antibiotics. Similarly, target-site mutations in genes such as *gyrA* and *parC* diminish the inhibitory effects of quinolone drugs on DNA gyrase or topoisomerase IV [1, 14].

Decreased cell envelope permeability and enhanced active efflux systems primarily confer resistance by reducing the effective intracellular drug concentration. In Gram-negative bacteria, the loss or downregulated expression of outer membrane porins restrict the entry of hydrophilic antibiotics into the cell. Concurrently, efflux pump families such as the RND, MFS, MATE, SMR, and ABC superfamilies actively extrude multiple classes of drugs out of the cell, further decreasing drug accumulation [1, 15]. Because many efflux systems exhibit broad-spectrum substrate profiles and frequently act synergistically with low permeability and enzymatic inactivation, these mechanisms are critical drivers of the MDR phenotype in Gram-negative bacteria [15].

In addition to classical genetic resistance mechanisms, bacteria can also reduce their susceptibility to antibiotics through biofilm formation, the generation of persister cells, and transient alterations in metabolic states. These states are not necessarily accompanied by a significant increase in the minimum inhibitory concentration (MIC), but they enable bacteria to temporarily survive prolonged antibiotic exposure and are closely associated with chronic, recurrent, and medical device-associated infections [1]. Therefore, AMR should be understood as the consequence of the combined effects of genetic resistance, permeability barriers, active efflux systems, and physiological adaptation, rather than a simple phenotype driven by single resistance genes.

1.1.2 Strategies to mitigate AMR

Addressing AMR requires a multi-tiered, comprehensive strategy, rather than relying solely on the discovery of new antibiotics. Infection prevention and control, vaccination, rational drug use, resistance surveillance, rapid diagnostics, and the development of novel anti-infective therapies collectively constitute the core framework for AMR mitigation [1]. Among these, infection prevention and vaccination alleviate antibiotic selection pressure at the source by reducing the overall incidence of bacterial infections, decreasing the demand for antibiotic use, and minimizing the transmission of resistant bacteria [16, 17]. The GBD 2021 Antimicrobial Resistance Collaborators study further emphasizes that mitigating the future burden of AMR necessitates a combination of infection prevention, vaccination, the reduction of inappropriate antibiotic use in humans and agriculture, and the research and development of new antimicrobial agents [17].

Antimicrobial stewardship and improving drug accessibility are equally vital components of global AMR control. The Access–Watch–Reserve (AWaRe) framework introduced by the WHO categorizes antibiotics into three groups—Access, Watch, and Reserve—to promote the rational accessibility of common first-line antibiotics while restricting the unnecessary use of "last-resort" antibiotics or those with a high risk of resistance [18]. In conjunction with this stewardship, AMR surveillance and rapid diagnostics can assist clinicians in selecting more effective, narrow-spectrum therapeutic regimens wherever possible, thereby reducing the empirical use of broad-spectrum antibiotics and safeguarding last-resort options [1]. For instance, the Global Antimicrobial Resistance and Use Surveillance System (GLASS) established by the WHO provides a standardized framework for collecting global data on AMR and antimicrobial use. Meanwhile, advanced technologies such as molecular diagnostics and whole-genome sequencing can be utilized for pathogen identification, resistance gene detection, and tracking hospital transmission [1, 19]. Timely and accurate diagnosis is also crucial for reducing unnecessary antibiotic prescriptions in cases of self-limiting or viral infections [1].

Beyond traditional small-molecule antibiotic therapy, non-traditional anti-infective strategies are emerging as a crucial direction in AMR research. The current clinical research and development pipeline includes not only structurally modified traditional antibiotics but also non-traditional therapeutics such as antibody therapies, antibody-antibiotic drug conjugates, antimicrobial peptides, bacteriophage therapies, and CRISPR-Cas antimicrobial technologies [1]. Antibody therapies can target specific pathogens via toxin neutralization, opsonophagocytosis, complement deposition, or anti-virulence mechanisms, with minimal disruption to the normal microbiota. Similarly, antibody-antibiotic conjugates harness the specificity of antibodies to deliver antimicrobial molecules directly to specific pathogens or sites of infection [20, 21]. Antimicrobial peptides and anti-biofilm peptides, characterized by their rapid, multi-target, and membrane-active properties, are considered to possess significant potential for combating MDR pathogens and biofilm-associated infections [22, 23]. Bacteriophage therapy, which leverages the highly specific infective and lytic capabilities of phages against bacteria, can serve as an adjunctive or alternative treatment strategy for refractory drug-resistant infections. However, it still faces challenges concerning host range, bacterial anti-phage mechanisms, immune responses, and regulatory standardization [24, 25].

In recent years, CRISPR-Cas-based programmable antimicrobial strategies have also gained attention. By designing guide RNAs that target resistance genes or essential bacterial genes, the CRISPR-Cas system can induce sequence-specific DNA damage within specific bacterial populations, thereby achieving selective bacterial killing or the clearance of resistance plasmids [26, 27]. However, such strategies are currently still primarily in the experimental or preclinical stages, and their practical application must still overcome challenges such as delivery efficiency, host range, safety, and scalable production [1]. Therefore, AMR mitigation should be viewed as a continuous system encompassing prevention, diagnosis, rational drug use, and the development of new therapies, rather than relying solely

on a single technology or a specific class of new drugs.

1.2 Overview of antibiotics and their mechanisms of action

Antibiotics exert their anti-infective effects by either inhibiting bacterial growth (bacteriostatic) or directly killing bacteria (bactericidal), serving as an essential foundation for modern infection treatment, surgical procedures, organ transplantation, cancer chemotherapy, and intensive care medicine [28]. Based on their primary targets of action, antibiotics can generally be classified into those that inhibit cell wall synthesis, disrupt cell membrane integrity, inhibit nucleic acid replication or transcription, inhibit protein synthesis, and interfere with metabolic pathways [28]. Categorizing antibiotics according to their mechanisms of action facilitates a better understanding of their antimicrobial spectra and bactericidal modes, as well as their corresponding resistance mechanisms, such as target alteration, drug efflux, decreased permeability, and enzymatic inactivation [28]. The cited literature explicitly classifies antibiotics based on molecular targets including cell wall synthesis, membrane integrity, nucleic acid replication, protein synthesis, and folate metabolism, while simultaneously discussing the corresponding resistance mechanisms [28].

1.2.1 Antibiotics inhibiting cell wall synthesis

The bacterial cell wall is primarily composed of peptidoglycan, whose structure is essential for maintaining cell shape, mechanical strength, and osmotic stability [28]. Because mammalian cells lack peptidoglycan, the cell wall biosynthesis pathway serves as a crucial target for selective antibiotic action [28]. β-lactam antibiotics bind to penicillin-binding proteins (PBPs), inhibiting the peptidoglycan cross-linking reaction, thereby disrupting cell wall integrity and causing bacterial lysis [29, 30]. Glycopeptide antibiotics, such as vancomycin, bind sterically to the terminal D-Ala-D-Ala motif of lipid II peptidoglycan precursors, simultaneously blocking transglycosylation and transpeptidation reactions, and are primarily used for Gram-positive bacterial infections [28, 31].

1.2.2 Antibiotics inhibiting nucleic acid replication and transcription

Bacterial DNA replication and transcription depend on key enzymes such as DNA gyrase, topoisomerase IV, and RNA polymerase, making these enzymes important antimicrobial targets [32]. Fluoroquinolone antibiotics inhibit DNA gyrase and topoisomerase IV by stabilizing the enzyme-DNA cleavage complex, causing DNA fragmentation and ultimately leading to bacterial death [33, 34]. In most Gram-negative bacteria, DNA gyrase is typically the primary target for fluoroquinolones, whereas in most Gram-positive bacteria, topoisomerase IV is often the primary target [35]. A review by Halawa similarly summarized the inhibition of DNA gyrase and topoisomerase IV by fluoroquinolones, as well as the differences in primary targets between Gram-negative and Gram-positive bacteria [32]. Additionally, rifamycin antibiotics inhibit transcription initiation by binding to the β subunit of bacterial DNA-dependent RNA polymerase, holding significant importance in the treatment of tuberculosis [28].

1.2.3 Antibiotics inhibiting protein synthesis

Bacterial protein synthesis is carried out by the 70S ribosome, which consists of 30S and 50S subunits and serves as a major target for multiple classes of antibiotics [28, 36]. The 30S subunit is primarily involved in mRNA decoding and translational accuracy control, while the 50S subunit contains the peptidyl transferase center and participates in peptide bond formation and peptide chain elongation [36]. Aminoglycosides mainly bind to the 16S rRNA within the 30S subunit, leading to mRNA misreading, the production of aberrant proteins, and the blockade of protein synthesis [37, 38]. Tetracycline antibiotics inhibit peptide chain elongation by preventing aminoacyl-tRNA from entering the ribosomal A site [39]. Macrolides, chloramphenicols, lincosamides, and oxazolidinones primarily act on the 50S subunit, inhibiting protein synthesis by blocking the nascent peptide exit tunnel, peptide bond formation, or translation initiation [40–42].

1.2.4 Antibiotics disrupting cell membrane function

The cell membrane is vital for bacteria to maintain energy metabolism, ion homeostasis, and substance transport. Thus, membrane structure and function are also viable antibiotic targets [28]. Polymyxin antibiotics primarily disrupt membrane integrity by interacting with the lipopolysaccharides of the Gram-negative bacterial outer membrane, thereby increasing membrane permeability and causing cell damage [28]. Daptomycin is a representative cyclic lipopeptide antibiotic that, in the presence of Ca^{2+}, interacts with the cell membrane of Gram-positive bacteria, causing membrane potential alteration, disruption of ion homeostasis, and cell death [43]. Because its mode of action differs from that of cell wall or protein synthesis inhibitors, daptomycin is of great clinical value in treating infections caused by resistant Gram-positive bacteria such as MRSA and vancomycin-resistant *Enterococcus* (VRE) [43].

1.2.5 Antibiotics inhibiting folate metabolism

Folate metabolism provides essential one-carbon units for the de novo synthesis of bacterial purines, pyrimidiness and certain amino acids [44]. Sulfonamide antibiotics, acting as structural analogs of *p*-aminobenzoic acid, primarily inhibit dihydropteroate synthase (DHPS) [44]. Trimethoprim inhibits dihydrofolate reductase (DHFR), blocking the conversion of dihydrofolate to tetrahydrofolate [44]. Because these two drugs act on different steps of the same metabolic pathway, the combination of sulfonamides and trimethoprim can produce a sequential blockade effect [44].

1.2.6 Novel or recently developed antibiotic classes

Among the antimicrobial agents approved or entering clinical development in recent years, those with genuinely unprecedented mechanisms of action remain limited. Most candidates involve structural optimizations of existing antibiotic classes, combinations with β-lactamase inhibitors, improvements in cellular entry mechanisms, or altered target-binding modes [45, 46].

The WHO 2025 antibacterial pipeline report reveals that, as of February 2025, there are 90 antibacterial agents or combinations in the global clinical pipeline containing at least one new therapeutic entity. Of these, 50 are traditional antibacterial agents and 40 are non-traditional antibacterial

strategies [45]. This WHO report also notes that these candidates include new chemical entities, traditional small-molecule antibiotics, new biological entities, and non-traditional strategies such as bacteriophages, antibodies, anti-virulence agents, oligonucleotides, and microbiome modulators [45].

β-Lactam / β-lactamase inhibitor combinations: This represents an important direction in recent traditional antibiotic research. The core strategy is to use inhibitors to protect β-lactam antibiotics from hydrolysis by β-lactamases, thereby restoring their activity against certain resistant Gram-negative bacteria [47]. Examples include meropenem–vaborbactam, imipenem–relebactam, and sulbactam–durlobactam [47].

"Trojan horse" strategies: Cefiderocol is a siderophore cephalosporin that exploits the bacterial iron uptake system to enter the periplasmic space [47, 48]. Upon entry, it still exerts its bactericidal effect by binding to PBPs and inhibiting peptidoglycan synthesis [48].

Next-generation classical inhibitors: The new generation of protein synthesis inhibitors reflects the trend of developing novel chemical scaffolds based on classical targets. For instance, lefamulin belongs to the pleuromutilin class, which binds to the peptidyl transferase center of the 50S subunit [47, 49]. Omadacycline and eravacycline are next-generation tetracyclines, while plazomicin is a structurally optimized aminoglycoside; a key developmental goal for these drugs is to mitigate the impact of traditional resistance mechanisms [47].

Novel DNA topoisomerase inhibitors: Gepotidacin belongs to the triazaacenaphthylene class and targets both DNA gyrase and topoisomerase IV, but its binding mode differs from that of traditional fluoroquinolones [47]. The WHO 2025 report noted that gepotidacin had entered the U.S. regulatory approval process, and a post-report update indicated it was approved by the FDA in March 2025 for uncomplicated urinary tract infections in female adults and adolescents aged 12 and older [45].

Overall, the primary focus of current antibiotic research and development is not to completely replace classical antibiotic classes, but rather to improve drug stability, enhance cellular penetration, evade existing resistance mechanisms, or establish new binding modes based on established targets. In parallel, bacteria still rapidly develop resistance to new drugs through mechanisms such as enzymatic inactivation, target mutation, enhanced efflux, and decreased permeability [47]. Therefore, researching the mechanisms of antibiotic action not only aids in understanding the antimicrobial activity of existing drugs but also provides a foundation for new drug design, combination therapies, and resistance surveillance.

1.3 *S. aureus* as a clinically important pathogen

S. aureus is one of the most clinically significant Gram-positive bacterial pathogens, acting as both a commensal organism and an opportunistic pathogen. This bacterium colonizes the anterior nares, skin, and other mucosal surfaces, with approximately 20–30% of the healthy human population carrying *S. aureus* persistently or intermittently. When the host barrier is compromised, immune function declines,

or medical implants are present, colonizing strains can serve as a source of endogenous infection [2, 50]. Clinically, *S. aureus* causes a wide spectrum of diseases, ranging from skin and soft tissue infections to pneumonia, bacteremia, infective endocarditis, osteomyelitis, septic arthritis, and medical device-associated infections [2, 51]. Once *S. aureus* enters the bloodstream, it can infect virtually any organ system, leading to endocarditis, osteomyelitis, implant infections, and other metastatic infections [2].

The clinical importance of *S. aureus* stems not only from its broad spectrum of infections but also from its robust adaptability. The bacterium can persist within the host via surface adhesins, toxins, immune evasion factors, and biofilm formation, and it can rapidly accumulate antibiotic resistance through mutations or the acquisition of mobile genetic elements [51, 52]. From the perspective of antibiotic susceptibility, *S. aureus* is clinically categorized into methicillin-susceptible *S. aureus* (MSSA) and MRSA. Based on vancomycin susceptibility, it can be further classified into vancomycin-susceptible *S. aureus* (VSSA), heterogeneous vancomycin-intermediate *S. aureus* (hVISA), vancomycin-intermediate *S. aureus* (VISA), and vancomycin-resistant *S. aureus* (VRSA). These phenotypes reflect the divergent adaptive trajectories of *S. aureus* to β-lactam and glycopeptide antibiotics, providing critical insights into clinical treatment failures and resistance evolution [51, 53].

1.3.1 MRSA

MRSA is one of the most prevalent phenotypes in the antibiotic resistance evolution of *S. aureus*. Although penicillin initially dramatically improved the treatment of staphylococcal infections, penicillin resistance mediated by the β-lactamase gene *blaZ* rapidly emerged in the 1940s. Following the clinical introduction of semi-synthetic anti-staphylococcal penicillins in the 1960s, MRSA was also quickly observed [51, 54]. Genomic studies further suggest that the emergence of methicillin resistance may have predated the widespread clinical use of methicillin and related semi-synthetic penicillins [55].

The core resistance mechanism of MRSA is the acquisition of *mecA* (or its homolog *mecC*), a gene located on a mobile genetic element known as the staphylococcal cassette chromosome mec (SCCmec) that encodes the low-affinity penicillin-binding protein PBP2a [56, 57]. PBP2a can continue to catalyze peptidoglycan cross-linking even when endogenous PBPs are inhibited by β-lactam antibiotics; consequently, MRSA is generally resistant to the majority of β-lactam agents [51]. The *mecA* gene is frequently acquired horizontally via transfer of SCCmec [51].

The epidemiology of MRSA is not driven by a single global clone, but rather by the episodic expansion of diverse clonal lineages across different geographic regions and ecological niches. Traditionally, MRSA has been classified into hospital-associated (HA-MRSA), community-associated (CA-MRSA), and livestock-associated (LA-MRSA) types. However, as strains disseminate among hospital, community, and animal-associated environments, the genetic and epidemiological boundaries between these types have increasingly blurred [51, 58]. Furthermore, the accessory genome of MRSA can harbor a variety of resistance and virulence-associated mobile genetic elements—including plasmids, transposons, bacteriophages, and pathogenicity islands— that encode elements related to virulence,

immune evasion, and antibiotic resistance such as *blaZ*, *dfrA*/*dfrK*, *ermC*, *tetK*, and *tetL*, enabling continuous adaptation to antibiotic pressure and the host environment [51, 59].

1.3.2 hVISA and VISA

Vancomycin has long been a critical drug for the treatment of MRSA infections; thus, declining vancomycin susceptibility in *S. aureus* is of major clinical significance. Unlike VRSA, which is mediated by the exogenous *vanA* gene cluster, hVISA and VISA typically do not harbor *van* genes. Instead, they evolve gradually through multi-step mutations in the core genome and by the remodeling of cell wall metabolism [51, 60]. hVISA is a heterogeneous intermediate resistance phenotype where the routine minimum inhibitory concentration (MIC) may remain within the susceptible range, but a small subpopulation capable of surviving at higher vancomycin concentrations exists within the culture. Under continuous selection pressure, these subpopulations can further evolve into VISA [53, 60]. Mu50 and Mu3, isolated in 1996, represent clinical VISA and hVISA isolates, respectively, corroborating that hVISA represents the evolutionary precursor of VISA [60].

The hallmark physiological features of VISA include a thickened cell wall, enhanced cell wall metabolism, and decreased autolytic activity. Because vancomycin must bind to the terminal D-Ala-D-Ala of the lipid II peptidoglycan precursors and needs to traverse the cell wall to reach the nascent peptidoglycan synthesis site, a thickened cell wall rich in uncross-linked D-Ala-D-Ala residues acts as a "drug trap" or diffusion barrier, thereby reducing the amount of effective drug that reaches its target site [61, 62]. The review by Hiramatsu conceptualized the VISA mechanisms as "false targets affinity trapping" and "thickened peptidoglycan mesh clogging," meaning the thickened peptidoglycan layer both adsorbs vancomycin and retards its transit to the true target site near the cell membrane [60].

The genetic basis of VISA is notably diverse. Various mutations related to cell wall synthesis, cell envelope stress, autolysis, and membrane charge regulation can promote the hVISA/VISA phenotype, involving pathways associated with *vraUTSR*/*vraSR*, *walKR*, *graRS*, *rpoB*, *mprF*, and *dlt* [60, 63, 64]. Among these, VraSR is a crucial two-component system for the cell wall stress response, upregulating cell wall biosynthesis-related genes such as *murZ*, *pbp2*, *sgtB*, *tarA*, *fmtA*, and *lcpC*. In the hallmark strains Mu3 and Mu50, the *vraS*(I5N) mutation activates VraSR and enhances the expression of the mentioned cell wall biosynthesis genes [60, 65].

Mutations related to GraRS are similarly linked to hVISA/VISA evolution. Together with GraX and VraFG, GraRS constitutes a system that senses cationic antimicrobial peptides and regulates cell surface charge, influencing the expression of genes in the *mprF* and *dlt* pathways as well as VraFG [66, 67]. In Mu50, the *graR*(N197S) mutation is implicated in the transition from Mu3 to the VISA phenotype; however, a single *graR* mutation is generally insufficient to fully account for high-level VISA and requires synergistic interactions with other mutations, such as those in *rpoB*[67–68]. While the *graR*(N197S) mutation elevates Mu3 to a low-level VISA, the subsequent introduction of the *rpoB*(H481Y) mutation converts it to a high-level VISA [60].

1.3.3 VRSA

The mechanism of developing VRSA differs from that of VISA. High-level VRSA is typically mediated by the *vanA* gene cluster, which largely originates from VRE and can be transferred to MRSA via plasmid- or transposon-associated mechanisms [53, 69]. Since the first isolation of VRSA in Michigan, USA, in 2002, 52 VRSA strains have been reported globally [53].

The core mechanism of VanA-type resistance is the alteration of the lipid II peptidoglycan precursor terminus from D-Ala-D-Ala to D-Ala-D-Lac. VanH, VanA, and VanX within the *vanA* gene cluster are responsible for D-Lac generation, D-Ala-D-Lac ligation, and D-Ala-D-Ala hydrolysis, respectively, thereby depleting the normal vancomycin targets and generating a low-affinity substitute structure [53, 70]. Because the binding affinity of vancomycin for D-Ala-D-Lac is significantly lower than that for D-Ala-D-Ala, *S. aureus* carrying *vanA* exhibits high-level vancomycin resistance [53, 71]. VanS/VanR regulates the expression of the *vanA* gene cluster, while VanH/VanA/VanX change the precursor from D-Ala-D-Ala to D-Ala-D-Lac, culminating in an approximate 1,000-fold reduction in vancomycin affinity [53].

Despite the high efficacy of the *vanA*-mediated resistance mechanism, VRSA remains relatively rare. This rarity may be attributed to the lack of natural competence in *S. aureus*, restrictions on conjugative plasmid transfer, the instability of the *vanA* plasmid, and fitness costs [51, 72]. Clinically, the emergence of VRSA is frequently associated with MRSA and VRE co-infections or co-colonization, particularly in the contexts of intensive care units (ICUs), long-term care facilities, diabetes, chronic wounds, indwelling catheters, and recent antibiotic exposure [53, 73]. A review summarized common characteristics of VRSA cases, which include VRE/MRSA co-colonization, recent vancomycin use, underlying diseases or wound/catheter-associated biofilms, and the fact that most U.S. isolates belong to the CC5 lineage [53].

In summary, MRSA, VISA/hVISA, and VRSA represent distinct strategies employed by *S. aureus* in response to antibiotic pressure: MRSA circumvents β-lactam action by acquiring SCCmec and PBP2a; VISA/hVISA diminish the effective action of vancomycin through core genome mutations and cell wall remodeling; and VRSA alters the drug target by acquiring the *vanA* gene cluster. Together, these resistance phenotypes illustrate that the clinical threat of *S. aureus* arises from the synergistic integration of its infectivity, resistance evolution, immune evasion, and persistence.

1.4 Biofilm-associated infections and anti-biofilm strategies

A biofilm is a structured community of microorganisms formed after attachment to biotic or abiotic surfaces, with its cells encased in a self-produced matrix of extracellular polymeric substances (EPS) [74, 75]. The EPS matrix is typically composed of polysaccharides, proteins, extracellular DNA (eDNA), lipids, and other polymers, which maintain the structural stability of the biofilm, promote intercellular adhesion, and establish local oxygen, nutrient, and pH gradients [75, 76]. Compared to

planktonic cells, biofilm cells exhibit distinct gene expression profiles, metabolic states, and spatial organization. Consequently, they hold significant clinical importance in chronic wounds, cystic fibrosis airway infections, urinary tract infections, osteomyelitis, and implant- or catheter-associated infections [75, 77]. Clinical biofilm infections are categorized in surface-associated biofilm infections and in microbial aggregates formed within tissues or secretions, noting that their common hallmark is a high degree of recalcitrance to antimicrobial agents and host immune clearance [75].

1.4.1 Biofilm formation and its clinical significance

Biofilm formation generally undergoes a dynamic process progressing from initial attachment, microcolony formation, and EPS production, to biofilm maturation and dispersion [74, 75]. During this process, bacteria transition from a planktonic state to a sessile growth state, coordinating adhesion, matrix production, maturation, and dispersion through cyclic-di-GMP, quorum sensing, and various stress regulatory networks [75, 76].

A mature biofilm is not a homogeneous mass of bacteria; rather, it contains distinct subpopulations, including metabolically active cells at the surface, low-metabolic or dormant cells in the deeper layers, persister cells, and potentially emergent mutant cells [75, 78]. This spatial and physiological heterogeneity enables biofilms to survive long-term under nutrient limitation, oxygen deprivation, immune attacks, and antibiotic exposure [76, 78]. The dynamic biofilm process is divided into different phases, including attachment/aggregation, EPS production, maturation/differentiation, and detachment/dispersion, emphasizing that cells in deeper layers frequently exhibit a slow-growing or tolerant state [75].

Clinically, biofilms are particularly common in infection environments characterized by the presence of foreign body surfaces or local tissue damage, such as vascular catheters, artificial joints, heart valves, orthopedic implants, chronic wounds, and cystic fibrosis airway infections [75, 79]. In these infections, even if the isolated bacteria display susceptibility in conventional planktonic antimicrobial susceptibility testing, actual treatment may still fail because standard MIC assays do not adequately reflect the tolerance and persistence capacities of the bacteria within a biofilm [75, 76]. Therefore, the recalcitrance of biofilm-associated infections is not merely a problem of "resistant bacterial infections" but also involves antibiotic failure jointly caused by bacterial population structure, metabolic heterogeneity, and the localized infection environment.

1.4.2 Biofilm-mediated antibiotic tolerance and resistance

One of the core reasons biofilm-associated infections are difficult to eradicate is antibiotic tolerance and persistence. Resistance typically refers to the ability of bacteria to grow at drug concentrations higher than the MIC of susceptible strains due to stable genetic alterations or acquired resistance genes. Tolerance refers to the phenomenon where a bacterial population, without a significant increase in MIC, requires a longer time to be eradicated due to a reduced killing rate. Persistence involves persister cells—a small subpopulation within the community that temporarily enter a dormant

or low-metabolic state, allowing them to survive under lethal concentrations of antibiotics [80, 81]. Restricted drug penetration, nutrient/oxygen limitation, stress responses, and metabolic heterogeneity within biofilms can all promote tolerance and persistence [76].

The biofilm matrix itself can restrict or alter the penetration of antimicrobial agents to inner cells. The eDNA, polysaccharides, and proteins in the EPS can reduce the effective drug concentration through physical barriers, electrostatic interactions, or drug adsorption, while matrix-associated enzymes, such as β-lactamases, can inactivate drugs before they reach the deeper cells [76, 82]. Simultaneously, oxygen and nutrient gradients exist within the biofilm. Surface cells are generally more active, whereas deeper cells are more prone to a slow-growing, low-energy, or dormant state [78, 83]. Because many antibiotics depend on active cell wall synthesis, protein synthesis, or DNA replication processes to exert their effects, the low-metabolic cells in the deeper layers are often insensitive to these drugs [75, 84].

Biofilms can also facilitate the emergence and dissemination of genetic resistance. Due to high cell density, close intercellular proximity, abundant eDNA, and prolonged exposure to sub-inhibitory concentrations of antibiotics, mutation accumulation and horizontal gene transfer occur more readily within biofilms [75, 85]. For example, the rate of conjugative plasmid transfer in *S. aureus* biofilms can be significantly higher than under planktonic culture conditions, suggesting that biofilms may serve as a crucial microenvironment for the dissemination of resistance genes [86]. Therefore, biofilms not only cause treatment failure through non-genetic tolerance but may also provide conditions for the evolution of resistance during long-term infections.

1.4.3 Anti-biofilm strategies

Because biofilm-associated infections simultaneously involve matrix protection, metabolic heterogeneity, persister cells, and localized infection sources, monotherapy with a single antibiotic is usually insufficient to completely eradicate the infection [75, 79]. Current clinical and investigational anti-biofilm strategies primarily include infection source control, optimizing antibiotic combinations, disrupting the EPS matrix, inhibiting quorum sensing, bacteriophage therapy, antimicrobial peptides, and nanodelivery systems [76, 87]. The effective management of biofilm infections generally requires combining accurate detection with multimodal therapies, including antibiotics, matrix-degrading enzymes, quorum sensing inhibitors, bacteriophages, metabolic reactivators, and nanodelivery systems [76].

Infection source control is fundamental to treating biofilm infections. For catheter-, artificial joint-, heart valve-, or other implant-associated infections, antibiotic therapy alone is frequently inadequate to clear biofilms attached to foreign surfaces. Therefore, procedures such as device removal, replacement, debridement, drainage, or DAIR (debridement, antibiotics, and implant retention) are required, depending on the infection site and the patient's condition [79, 88]. Antibiotics remain the core of the treatment, but they typically require combination therapies, extended courses, or enhanced local

drug exposure to cover bacteria in various physiological states within the biofilm [79, 89]. For instance, rifampicin, due to its excellent tissue and biofilm penetration capabilities, is often combined with other antimicrobial agents for staphylococcal implant-associated infections, though it should not be used as a monotherapy to avoid rapid resistance emergence [79, 89].

Directly disrupting the EPS matrix is a vital adjunctive strategy to enhance antibiotic penetration into the biofilm interior. DNase can degrade eDNA, Dispersin B can hydrolyze PNAG-type polysaccharides, and alginate lyase can target the alginate enriched in *P. aeruginosa* biofilms. These enzymes generally do not exert direct bactericidal effects; instead, they weaken the matrix structure, promote biofilm dispersion, and enhance the efficacy of antibiotics or immune factors [90–92]. Quorum sensing inhibitors interfere with bacterial signaling, affecting adhesion, EPS production, virulence factor expression, and dispersion processes. This strategy leans more towards anti-virulence or anti-colonization rather than direct bactericidal action and is therefore believed to potentially reduce the selective pressure characteristic of traditional antibiotics [93, 94]. Crucial multimodal anti-biofilm strategies in recent years comprised enzymatic degradation, natural compounds, chelating agents, nanoparticles, photodynamic therapy, and combination therapies [93].

Bacteriophages and some of their hydrolytic enzymes are also being explored for the treatment of biofilm infections. Phages can specifically infect and lyse bacteria, and some phages can also produce depolymerases to degrade EPS, thereby improving their diffusion and bactericidal efficacy within biofilms [24, 25]. However, phage therapy still faces challenges such as narrow host ranges, bacterial anti-phage mechanisms, immune clearance, formulation standardization, and unclear regulatory pathways. Hence, it is more likely to serve as a component of personalized or combination treatment strategies [25, 95]. Nanoparticles, liposomes, and polymeric delivery systems can enhance anti-biofilm activity by increasing local drug concentrations, improving penetrability, enabling sustained release, or combining with photothermal/photodynamic effects. Nevertheless, their *in vivo* safety, stability, and clinical translation still require further validation [76, 93].

Overall, anti-biofilm therapy is shifting from purely bactericidal approaches to a comprehensive paradigm of "structural disruption + drug delivery + metabolic or signaling regulation + infection source control." For chronic, recurrent, and implant-associated infections, an ideal strategy generally requires first weakening or removing the biofilm barrier, followed by the combined use of antimicrobial agents capable of killing bacteria in various physiological states, while simultaneously reducing the risks of recolonization and the spread of resistance. This rationale also illustrates that the discovery of natural products or adjunctive compounds with anti-biofilm activity holds great significance for improving the efficacy of existing anti-infective therapies.

1.5 Application of natural products in anti-infective drug discovery

Natural products have historically been an important source for anti-infective drug discovery. Compared to conventional synthetic compounds, natural products typically possess more complex

scaffolds, diverse stereochemistry, and evolutionary optimized pharmacophores, allowing them to cover a broader chemical space and provide a foundation for the discovery of antibacterial lead compounds with novel mechanisms of action [96, 97]. Against the backdrop of increasing multidrug-resistant bacteria and the slowdown in traditional antibiotic research and development, natural products are still considered a crucial resource for developing novel anti-infective drugs and anti-resistance strategies [98].

From the perspective of antibiotic history, natural products have made decisive contributions to modern anti-infective therapies. Penicillin inaugurated the modern antibiotic era, and multiple important classes—such as cephalosporins, macrolides, tetracyclines, aminoglycosides, and glycopeptides—also originated from, or were inspired by, natural products [3, 99]. Between 1943 and 2025, 217 natural product-inspired antibiotics have been approved for human therapy, of which 52 are genuine natural products and 165 are semi-synthetic or synthetic derivatives [3]. This indicates that natural products frequently provide the core scaffold, while structural modifications can improve the antimicrobial spectrum, stability, pharmacokinetics, and adaptability to resistance mechanisms, as exemplified by semi-synthetic penicillins, cephalosporins, and pleuromutilin derivatives such as retapamulin and lefamulin [100, 101].

The anti-infective value of natural products is also reflected by their diverse mechanisms of action. Many natural products can interfere with cell wall synthesis, disrupt cell membranes, inhibit protein synthesis, affect DNA replication and transcription, interfere with folate metabolism, or disrupt bacterial metabolic homeostasis [102, 103]. These inherent multi-target or multi-mechanism characteristics help mitigate the risk of rapid resistance development caused by mutations of a single target. Moreover, some natural products also exhibit anti-biofilm, anti-virulence, or anti-inflammatory activities, serving as important complements to traditional antibiotics [104].

In recent years, natural products have garnered renewed attention in research targeting the WHO priority resistant pathogens. The WHO priority pathogens list includes carbapenem-resistant *A. baumannii*, drug-resistant Enterobacterales, carbapenem-resistant *P. aeruginosa*, vancomycin-resistant *Enterococcus faecium*, MRSA, and drug-resistant *M. tuberculosis* [105]. A relevant systematic review indicates that plant-derived natural products exhibit potential activity against multiple classes of resistant pathogens, among which *P. aeruginosa*, *E. coli*, *Klebsiella pneumoniae*, *Salmonella typhi*, and *S. aureus* are the most frequently studied. The primary classes of active components include alkaloids, flavonoids, phenolics, saponins, tannins, and terpenoids [106]. These findings suggest that natural products can serve not only as direct antibacterial molecules but may also participate in anti-infective therapy by enhancing the efficacy of existing antibiotics or interfering with resistance-related processes [107].

Modern natural product drug discovery is no longer limited to the traditional "extraction–isolation–activity screening" paradigm. Instead, it has gradually evolved into a comprehensive research

and development system that integrates bioassay-guided fractionation, structural modification, semi-synthesis, total synthesis, fermentation optimization, genome mining, and mechanistic studies. Between 2000 and 2025, 119 natural product-derived drugs were approved for the first time, of which 34 were anti-infective drugs and 34 were oncological drugs, representing the two primary therapeutic areas [108]. Their sources include plants, bacteria, fungi, marine organisms, and their symbiotic microorganisms, indicating that natural product drug discovery has expanded from traditional plant resources to more diverse biological origins [108].

Despite this, the development of natural products into anti-infective drugs still faces challenges such as low yields, difficulties in isolation and purification, structural complexity, the rediscovery of known compounds (dereplication issues), poor solubility and stability, and the difficulty of translating *in vitro* activity into *in vivo* efficacy [97]. Therefore, future research on natural product-derived anti-infective drugs needs to place greater emphasis on dereplication strategies, the elucidation of mechanisms of action, structural optimization, pharmacokinetic improvements, and the establishment of clinically relevant infection models. The integration of technologies such as genomics, metabolomics, synthetic biology, and artificial intelligence-based screening holds promise for activating silent biosynthetic gene clusters, discovering novel antibacterial chemical scaffolds, and increasing the success rate of translating natural product leads into clinical drug candidates [108].

Overall, natural products have not only laid the foundation for modern antibiotic therapy but also remain a vital, innovative resource for combatting AMR and MDR pathogens. Their structural diversity, multi-target mechanisms of action, anti-biofilm potential, and possibilities for combined use with existing antibiotics ensure their enduring value in future anti-infective drug discovery.

1.6 Application of fungal secondary metabolites in antibacterial and anti-biofilm activities

Fungi are an important yet underutilized resource in natural product research, capable of producing a diverse array of secondary metabolites—including polyketides, terpenoids, alkaloids, peptides, glycosides, steroids, polysaccharides, and phenolics—exhibiting antibacterial, antifungal, anti-inflammatory, antioxidant, immunomodulatory, and antitumor activities [109–111]. Since the discovery of penicillin, fungus-derived natural products have consistently served as a vital foundation for anti-infective drug discovery, offering novel research directions for combating AMR [112].

In the study of drug-resistant infections, endophytic fungi have garnered particular attention. Residing within plant tissues, endophytic fungi can produce metabolites with antibacterial potential, such as alkaloids, polyketides, terpenoids, peptides, flavonoids, and quinones [6]. Research focusing on MRSA has shown that certain endophytic fungal metabolites can exert their effects by disrupting cell membranes, inhibiting cell wall synthesis, interfering with nucleic acid or protein synthesis, and inhibiting biofilm formation [6]. For example, 2,4-di-*tert*-butylphenol derived from *Pestalotiopsis*

microspora can inhibit MRSA, and endophytic fungi such as *Alternaria alternata* have also been reported to produce anti-MRSA active compounds [113, 114].

In addition to their direct antibacterial effects, fungal metabolites also possess significant potential for anti-biofilm applications. Because the antibiotic tolerance of biofilm-associated bacteria can be 10 to 1,000 times higher than that of planktonic bacteria [82], compounds capable of inhibiting biofilm formation, interfering with quorum sensing, or promoting biofilm dispersion hold potential therapeutic value. Marine fungi are an important source of anti-biofilm active compounds; certain crude extracts or purified metabolites can inhibit the biofilm formation of *P. aeruginosa*, *S. aureus*, *Staphylococcus epidermidis*, and *Candida albicans* [5, 115, 116].

The anti-biofilm effects of fungal metabolites do not necessarily rely on direct bactericidal activity. Some compounds can attenuate pathogenicity by interfering with quorum sensing, downregulating virulence factor expression, or targeting biofilm regulatory proteins. For instance, apicidin, a fungus-derived cyclic peptide, can inhibit the *agr* quorum sensing system and the AgrA regulator in MRSA, thereby reducing toxin production and biofilm formation [117]. Compounds such as epifiscalin C, fiscalin C, aspernolide B, and butyrolactone I have also demonstrated anti-staphylococcal biofilm potential [118].

In recent years, the discovery rate of new fungal metabolites has accelerated significantly. A total of 907 new fungus-derived natural products were reported in 2024, encompassing terpenoids, polyketides, alkaloids, peptides, glycosides, and steroids, representing a 64.01% increase compared to 2023 [119]. Concurrently, strategies such as metabolomics-guided discovery, genome mining, co-cultivation, epigenetic regulation, transcription factor engineering, and fermentation condition optimization are enhancing the discovery efficiency of cryptic metabolites [120].

Despite broad prospects, the clinical translation of fungal secondary metabolites still faces challenges such as low yields, structural complexity, the rediscovery of known compounds, insufficient *in vivo* validation, and limited toxicological and pharmacokinetic data. In the future, integrating standardized extraction and isolation, activity evaluation, multi-omics technologies, *in vivo* infection models, and mechanistic studies is necessary to increase the likelihood of translating these compounds into anti-infective drug candidates [4]. In summary, fungal secondary metabolites can serve not only as direct antibacterial molecules but also as anti-biofilm agents, anti-virulence agents, or antibiotic adjuvants, providing a novel chemical foundation for the treatment of resistant infections such as MRSA.

1.7 Co-cultivation strategies and the activation of cryptic fungal metabolic pathways

Fungi possess robust secondary metabolic capabilities, and many clinically important drugs—such as penicillin, cephalosporin, lovastatin, and ergot alkaloids—are derived from filamentous fungi [121–123]. However, genome sequencing has revealed that fungal genomes harbor a vast number of BGCs. Many of these BGCs remain silent or are expressed only at low levels under standard laboratory

conditions, meaning their full metabolic potential has yet to be fully exploited [124, 125].

To activate silent BGCs, researchers have developed various strategies, including OSMAC (One Strain Many Compounds), co-cultivation, chemical induction, epigenetic regulation, transcription factor regulation, heterologous expression, genome mining, and metabolomics-guided discovery [126, 127]. Among these, the OSMAC approach induces a single strain to produce different metabolites by systematically altering culture medium composition, carbon and nitrogen sources, pH, temperature, oxygen levels, or fermentation methods [128]. This strategy is relatively simple to execute and has been widely utilized to expand fungal metabolite diversity [129–131].

Co-cultivation is one of the most frequently used methods for activating cryptic fungal metabolic pathways. In natural environments, fungi constantly compete with other fungi, bacteria, or host microorganisms for space and nutritional resources. This competition, antagonism, or chemical communication can trigger the production of defensive secondary metabolites [132, 133]. Therefore, simulating ecological interactions in the laboratory can activate BGCs that remain silent in mono-cultures, leading to the production of new or significantly upregulated metabolites [134]. Compared to genetic editing or complex fermentation optimization, co-cultivation is a relatively straightforward approach that can be achieved through various combinations, such as fungus–fungus, fungus–bacterium, or fungus–host-associated microbe interactions [135, 136].

The design of a co-cultivation experiment requires careful consideration of strain pairing, cultivation methods, and metabolite screening. Strain pairing can be based on sharing the same ecological niche or known antagonistic activities [137]. Cultivation methods may include direct mixed cultures, spatial separation, semi-permeable membranes, volatile signal communication, or utilizing the culture supernatant/extract of one strain to stimulate the other [135]. Metabolite screening frequently combines LC-MS, MALDI-TOF-MS, Nano-DESI-IMS, NMR, molecular networking, and bioassay-guided isolation to distinguish induced products from background metabolites [138, 139].

Despite the advantages of co-cultivation and other silent BGC activation strategies, their application still faces limitations. First, the mechanisms of induction are often unclear, requiring further investigation to distinguish among triggers such as nutrient competition, contact-dependent signaling, volatile organic compounds, or antibiotic-like small molecules. Second, in complex co-cultivation systems, it is necessary to identify which strain is the true producer of the newly detected metabolite. This can be determined through mono-culture comparisons, spatial localization, medium supplementation, genomic information, or isotope labeling [137]. Finally, the yield of co-culture-induced products is sometimes very low, necessitating subsequent fermentation optimization, genetic regulation, or heterologous expression to meet the requirements for structural identification and bioactivity evaluation.

Overall, by simulating microbial competition and chemical communication, co-cultivation provides an ecologically inspired approach to activating cryptic fungal metabolic pathways. In the future,

integrating co-cultivation with OSMAC, chemical induction, epigenetic regulation, genome mining, metabolomics, and heterologous expression holds the promise of further unleashing the untapped chemical potential within fungal genomes, thereby providing new directions for the discovery of anti-infective, anti-biofilm, and other therapeutic lead compounds.

2. Aim of this thesis

Based on the aforementioned background, this thesis focuses on the discovery of natural product-derived anti-infective agents, the investigation of their mechanisms of action, and related biosynthetic aspects. The general introduction initially outlines AMR, mechanisms of antibiotic action, and resistance phenotypes associated with *S. aureus*. It subsequently discusses biofilm-associated infections and anti-biofilm strategies, further highlighting the value of natural products, fungal secondary metabolites, and co-cultivation strategies in the discovery of novel anti-infective or anti-biofilm lead compounds. This structure aims to establish a theoretical foundation for the evaluation of compound activities, the elucidation of mechanisms of action, and the exploration of fungal metabolite biosynthesis presented in the subsequent research chapters.

The experimental chapters are organized around two main research directions. The first part focuses on pestalotic acid A and investigates its antibacterial activity against VISA, with particular emphasis on resistance development, cell envelope-associated mechanisms, and interactions with clinically relevant antibiotics. The second part examines metabolites obtained from fungal–bacterial co-cultivation of *Fusarium oxysporum* and *Paenibacillus ehimensis*, including the discovery of fusarubin-derived compounds, their biofilm-disrupting activity, and a proposed biosynthetic route. In this way, the thesis connects the chemical diversity of fungal natural products with their biological activities and mechanistic relevance in anti-infective research.

3. Manuscript 1

Studies on the Antibacterial Activity of the Natural Product Pestalotic acid A against Vancomycin-Intermediate *Staphylococcus aureus*

Di He [a¶], Lin Wang [a¶], Kristin Schwechel [a], Tobias Heinen [b], Lasse van Geelen [a], Christoph Janiak [b], Zhen Liu [c], Rainer Kalscheuer [a*]

[a] Institute of Pharmaceutical Biology and Biotechnology, Heinrich Heine University, Universitätsstr. 1, 40225 Düsseldorf, Germany

[b] Institute of Inorganic and Structural Chemistry, Heinrich Heine University, Universitätsstr. 1, 40225 Düsseldorf, Germany

[c] Key Laboratory of Study and Discovery of Small Targeted Molecules of Hunan Province, School of Medicine, Hunan Normal University, Changsha 410013, China

¶ These authors contributed equally

*Corresponding author.

rainer.kalscheuer@hhu.de; ORCID ID orcid.org/0000-0002-3378-2067

Abstract

Bacterial infections, particularly those caused by drug-resistant *Staphylococcus aureus*, remain a major global public health challenge. In this study, the OSMAC strategy was used to induce secondary metabolite production in the endophytic fungus *Pestalotiopsis chamaeropis*, leading to the isolation of nine pestalotic acid-related natural products from the fermentation extracts, including pestalotic acids A–H (**1**–**8**) and pestaloside A (**9**). Among them, pestalotic acid H (**8**) and pestaloside A (**9**) were identified as new natural products, and their structures were elucidated by 1D/2D NMR and HRESIMS. In addition, the absolute configuration of the known compound pestalotic acid C (3) was determined by high-quality crystals and X-ray diffraction. Antibacterial activity evaluation showed that pestalotic acid A (**1**) and pestalotic acid G (**7**) exhibited the strongest inhibitory activity against vancomycin-intermediate *S. aureus* (VISA), with MIC_{90} values of 6.25 μM, whereas their activities against MSSA and MRSA were weaker. Compared with compound **7**, compound **1** showed lower cytotoxicity and lower hemolytic activity and was therefore selected as the main candidate for subsequent mechanistic studies. Compound **1** did not act on VISA through typical rapid membrane lysis, but mainly displayed bacteriostatic activity, while inducing membrane depolarization and increased membrane permeability only at high concentrations. Resistant mutant screening and whole-genome sequencing revealed that VISA mutants with reduced susceptibility to compound **1** all carried disruptive mutations in *graR* and showed markedly increased susceptibility to vancomycin, daptomycin, polymyxin B, and colistin. Cytochrome c binding assays and RT-qPCR further indicated that compound 1 affected the cell surface charge state of VISA and downregulated the expression of GraRS-related cell envelope regulatory genes, including *fmtC*, *dltA*, and *vraG*. In addition, compound **1** showed synergistic effects with vancomycin, polymyxin B, and colistin and significantly inhibited VISA biofilm formation at sub-MIC concentrations. Taken together, pestalotic acid A is a natural product lead compound with anti-VISA activity, good selectivity, antibiofilm activity, and potential value for combination therapy. Its action is closely associated with disturbance of GraRS-related cell envelope homeostasis and cell surface charge regulation.

Keywords: *Pestalotiopsis chamaeropis*; pestalotic acid A; vancomycin-intermediate *Staphylococcus aureus*; GraRS; cell envelope homeostasis; surface charge; antibiofilm activity; antibiotic synergy

Introduction

Since Alexander Fleming discovered penicillin in 1928, antibiotics have greatly changed the treatment of bacterial infections and initiated the “antibiotic era” of modern anti-infective therapy. However, antibiotic resistance emerged almost in parallel with the clinical use of antibiotics. Taking *Staphylococcus aureus* as an example, penicillin resistance, methicillin resistance, and reduced susceptibility to glycopeptide antibiotics appeared successively, placing *S. aureus* at the center of antibiotic resistance research and clinical infection control [1]. Methicillin-resistant *S. aureus* (MRSA) remains an important global public health threat [2], while vancomycin has long been one of the key drugs for the treatment of severe MRSA infections. The emergence of vancomycin-intermediate *S. aureus* (VISA) has further increased the difficulty of clinical treatment, suggesting that *S. aureus* can reduce its susceptibility to vancomycin through adaptive changes such as cell wall thickening, cell envelope remodeling, alterations in cell surface charge, and stress regulation [3]. Therefore, the discovery of new antibacterial lead compounds that can inhibit VISA or interfere with its adaptive cell envelope regulation is of great significance.

Antibiotic resistance not only reduces the success rate of infection treatment, but also significantly increases hospitalization time, medical costs, and mortality risk, imposing a heavy burden on public health systems and the economy [4, 5]. Despite this urgent clinical need, the pipeline for new antibacterial agents remains limited, especially for antibiotic candidates with new structural scaffolds or novel modes of action [6, 7]. Therefore, the development of antibacterial natural products with novel sources, structural diversity, and distinct modes of action remains an important direction for addressing drug-resistant bacterial infections.

Natural products have always been an important source for anti-infective drug discovery. Fungi are able to produce structurally diverse and biologically active secondary metabolites and have provided several representative molecules for drug discovery, such as penicillin, cyclosporine, and lovastatin [8, 9]. However, under conventional laboratory culture conditions, many fungal biosynthetic gene clusters remain silent or weakly expressed, leaving their secondary metabolic potential insufficiently explored. The OSMAC (“one strain many compounds”) strategy induces microorganisms to produce different secondary metabolites by altering culture conditions, thereby expanding natural product chemical diversity and serving as an important approach for discovering new structures and bioactive compounds [10, 11].

In this study, the endophytic fungus *Pestalotiopsis chamaeropis*, isolated from the plant *Aster subulatus* Michx., was investigated using the OSMAC strategy to induce the production of secondary metabolites, leading to the isolation of a series of pestalotic acid-related natural products from the fermentation products. The antibacterial activity of these compounds against drug-resistant *S. aureus* was evaluated, and pestalotic acid A, which showed strong inhibitory activity against VISA as well as good selectivity and low hemolytic activity, was selected as the main candidate compound for

mechanistic studies. By analyzing its effects on VISA growth, survival, membrane function, resistance development, antibiotic synergy, cell surface charge state, and biofilm formation, this study aimed to clarify the anti-VISA action characteristics of pestalotic acid A and to evaluate its potential value as a natural product lead compound against drug-resistant *S. aureus*.

Results and discussion

Secondary metabolites from fungi play an indispensable role in drug discovery. Following this line, we have isolated from the plant *Aster subulatus* (Michx.) an endophytic fungus, which was identified as *Pestalotiopsis chamaeropis* with 100% identity by BLAST search of the internal transcribed spacer (ITS) sequence in comparison with the nucleotide database of the National Center for Biotechnology Information (NCBI). Next, we fermented *P. chamaeropis* at a large-scale on solid rice medium and extracted the obtained biomass using ethyl acetate to study the profile of the produced secondary metabolites. From the ethyl acetate extract, pestalotic acid A (compound **1**) and pestaloside A (compound **9**) were isolated using different chromatographic steps as described in detail in the Material & Methods section. Since we observed antibacterial activity of pestalotic acid A during preliminary explorative screenings, a modification of the culture conditions was implemented to potentially expand the diversity of compounds. For this, 3.5% sodium iodide was supplemented to standard rice medium. This approach was first described by Zeeck and co-workers [10] and was referred to as "one strain many compounds" (OSMAC), which triggers expression of silent biosynthetic gene clusters and results in unlocking of the fungal chemical diversity. This might allow the discovery of novel molecules of both medical and biotechnological interest [11]. In the present study, the described OSMAC approach yielded compounds **2**–**8** (**Fig. 1**), which were not found in the extract obtained from the non-supplemented rice medium. Notably, from the secondary metabolites we isolated from *P. chamaeropis*, compounds **8** and **9** were identified as new natural products as described in detail below, while all other isolated molecules were identified as known natural compounds based on comparison of their spectroscopic data with the literature.

Compound **8** was obtained as colorless oil, with a molecular formula of $C_{23}H_{32}O_8$ as suggested by high-resolution electrospray ionization mass spectrometry (HRESIMS). The ^{13}C NMR δC: 195.8, 179.2 (179.9), 172.3, 171.9, 160.4 (160.5), 123.5 (123.6), 101.9 (102.5), 37.9, 35.6 indicated compound **8** had good agreement with known compound **6** in position 1-6'. The difference was the terminal residue. HMBC suggested correlations of H-16' related to 13'-C (δ_C 195.5) and 14'-C (δ_C 31.6), while H-17' related to H-16'. Thus, the structure of **8** was elucidated as drawn in **Fig. 1** and the ^1H NMR and ^{13}C NMR data are given at **Table 1**.

Compound **9** was obtained as colorless oil with a molecular formula of $C_{20}H_{30}O_7$ as determined by HRESIMS. HMBC suggested that 3-H, 15-H had correlation to 2-C (δ_C 150.4), 4-H had correlation to 5-C (δ_C 150.0) and 6-C (δ_C 128.4). Furthermore, 14-H related to 1-C (δ_C 129.2) as well to 5-C and 6-C, which is consistent with presence of an aromatic ring. Furthermore, H-7 and H-8 of alkenes could be

assigned to 1-C (δ_C 129.2) and 9-C (δ_C 34.8), respectively. While 9-H was related to 10-C (δ_C 29.8) and 11-C (δ_C 32.6), the terminal methyl related to 11-C (δ_C 32.6) and 12-C (δ_C 23.6). Moreover, the signals in COSY for 9-H related to 8-H and 10-H while 12-H related to 11-H and 13-H, which verified presence of an oct-2-ene side chain linked at position 1. In HMBC, 15-H related to 16-C (δ_C 71.4), 17-C (δ_C 72.6) was related to 16-H and 18-H, 20-H related to 18-C (δ_C 73.8) and 19-C (δ_C 70.2). Together with chemical shift of 15-C (δ_C 100.8), the structure of the sugar moiety was confirmed and linked with the benzene ring. Combined with the structure of fragments, compound **9** was elucidated as pestaloside A with the structure as shown in **Fig. 1**, and the corresponding ^{1}H NMR and ^{13}C NMR data are given in **Table 1**.

Compound **3** was obtained as colorless powder with the molecular formula of $C_{21}H_{30}O_7$ as determined by HRESIMS. The ^{1}H NMR δH (*J* Hz): 7.56 (7.49), 7.45 (7.39), 4.88 (4.80), 3.79, 3.02, 2.94 (2.82), 2.05 (1.99), 1.89, 1.61, 1.41, 1.17 and ^{13}C NMR δC: 194.7, 179.7 (179.3), 170.1, 167.8, 160.3 (159.8), 123.2, 102.4 (101.5), 93.5, 78.4 (78.3), 68.5 (68.2), 39.1, 38.8, 37.8 (37.7), (29.4, 29.2, 29.0, 28.9, 28.7), 25.6 (25.3), 23.4 (23.3), 23.2 (23.1) suggested a structure of the known compound pestalotic acid C. However, the absolute configuration has not previously been described. In the present study, high-quality crystals of compound **3** were obtained in methanol by slow solvent evaporation, enabling us to corroborate the structure and to demonstrate that the absolute configuration is 4 (S), 4' (R), 13' (R) employing X-ray diffraction. Furthermore, due to presence of a double bond between the furan-dione ring and the dihydrofuran ring, the NMR spectra revealed interconversion of *E*- and *Z*-isomers of compounds **1**–**8** occurred at the ratio of approximately 1:1.

Minimum inhibitory concentration (MIC) determination

The minimum inhibitory concentrations (MICs) of compounds **1**–**9** against multiple microorganisms were determined in this study. The results (**Table 2**) showed that the antibacterial activity of this series of pestalotic acid derivatives was mainly concentrated in compounds **1** and **7**, and both compounds showed the most pronounced inhibitory activity against the VISA strain *S. aureus* ATCC 700699, with MIC values of 6.25 μM. In contrast, the MICs of compounds **1** and **7** against the MSSA strain *S. aureus* ATCC 29213 were both 25 μM, and the MIC of compound **1** against the MRSA strain *S. aureus* USA300 was also 25 μM, indicating that VISA showed higher sensitivity to these two compounds.

Structurally, compounds **1** and **7** share a similar core scaffold and retain a long-chain fatty acyl side chain without any obvious polar modification. The two compounds showed the strongest antibacterial activity in this series, suggesting that this type of hydrophobic long-chain side-chain structure may play an important role in maintaining anti-VISA activity. In contrast, the overall activities of compounds **2**–**6** and **8**–**9** were markedly reduced or showed no obvious inhibitory activity. After side-chain hydroxylation, esterification, acetylation, or other polar/substituent modifications, antibacterial activity generally decreased, suggesting that the structural integrity and hydrophobicity of the long-chain side chain may be closely related to the antibacterial activity of this class of compounds.

Cytotoxicity and selectivity index evaluation

The cytotoxicity of compound **1** and compound **7** was evaluated using HEK293, HUH-7, THP-1, CLS-54, and H4 cell lines, and the selectivity index (SI) was calculated based on IC_{50} and MIC_{90}. The results (Table 3) showed that the overall cytotoxicity of compound **1** was lower than that of compound **7**. The IC_{50} values of compound **1** against HUH-7 and H4 cells were both higher than 100 μM, and its IC_{50} values against HEK293, THP-1, and CLS-54 cells were 45.5, 42.0, and 45.6 μM, respectively, corresponding to SI values mainly distributed between 6.72 and >10. Compound **7** showed stronger cytotoxicity against multiple cell lines, especially THP-1 and CLS-54 cells, with IC_{50} values of 7.8 and 0.71 μM, respectively, corresponding to SI values of only 1.3 and 0.1.

The MIC_{90} values of compound **1** and compound **7** against VISA were both 6.25 μM, but their cytotoxicity and selectivity index differed markedly. Structurally, both compounds possess a long-chain fatty acyl side chain and a similar pestalotic acid scaffold. Compound **1** retains a free carboxylic acid moiety, whereas the corresponding carboxylic acid group in compound **7** is methyl-esterified, accompanied by differences in the cyclic scaffold configuration or lactone structure. Carboxylic acid methyl esterification reduces the ionization capacity of the molecule and may increase molecular hydrophobicity and cell membrane permeability, thereby increasing the possibility of nonspecific interactions with mammalian cell membranes or intracellular components. This structural difference may explain why compound **7** maintains anti-VISA activity while showing stronger cytotoxicity against multiple human-derived cell lines.

The hemolysis assay showed that compound **1** did not induce obvious hemolysis in the range of 6.25–100 μM (**Fig. 4**). The absorbance values at 540 nm in all treatment groups were close to the PBS negative control and markedly lower than the Triton X-1% positive control. This result indicates that compound **1** did not show obvious erythrocyte membrane-disrupting activity even at concentrations higher than the anti-VISA MIC_{90}.

Taken together, based on the cytotoxicity, selectivity index, and hemolysis assay results, compound **1** showed better cellular selectivity and blood compatibility while retaining strong anti-VISA activity. Therefore, compound **1** is more suitable as the main candidate compound for subsequent mechanistic studies.

Growth kinetics and time-kill kinetics analysis

Growth kinetics assays and time-kill kinetics analysis were used to evaluate the effects of compound **1** on VISA growth and survival. The growth curve results (**Fig. S1**) showed that compound **1** inhibited VISA growth in a concentration-dependent manner. Under 12.5 μM and 6.25 μM conditions, VISA showed almost no obvious growth within 22 h, and $OD_{600\ nm}$ remained at a low level. Among these concentrations, 6.25 μM corresponded to the MIC_{90} of compound **1** against VISA, consistent with the MIC determination results. Under 3.13 μM, early VISA growth was clearly inhibited, the growth curve was delayed, and then the bacteria gradually resumed growth. Under 1.56 μM, the inhibitory effect

was further weakened, and the growth trend was close to that of the DMSO control group. The moxifloxacin positive control continuously inhibited VISA growth during the detection period. These results indicate that compound **1** effectively inhibited VISA growth, and the inhibitory effect increased with increasing concentration.

The time-kill kinetics results (**Fig. 5**) showed that the viable cell counts of VISA in the DMSO control group increased rapidly with incubation time. After treatment with 25 μM compound **1**, namely 4× MIC, the CFU counts of VISA decreased markedly over time and remained at a low level within 24 h, indicating that high-concentration compound **1** reduced the number of viable VISA cells. The CFU counts in the 25 μM moxifloxacin treatment group decreased more markedly, and the viable cell count after 24 h was lower than that in the compound **1**-treated group. Taken together, the growth kinetics and time-kill kinetics results show that compound **1** has a clear growth-inhibitory effect on VISA and can reduce viable cell counts at higher concentrations; its overall mode of action is closer to being mainly bacteriostatic rather than strongly and completely bactericidal.

Effect on VISA cell membrane potential

The DMSO-treated group maintained a high red/green fluorescence ratio at both 0.5 h and 1 h, whereas the ratio was markedly reduced after treatment with the CCCP positive control. The effect of compound **1** on VISA membrane potential was concentration-dependent (**Fig. 6**). After treatment with 100 μM and 50 μM, the red/green fluorescence ratio decreased markedly, suggesting that high concentrations of compound **1** can induce membrane depolarization. The red/green fluorescence ratio in the 25 μM treatment group was also lower than that of the DMSO control, but the decrease was smaller than that in the 50 μM and 100 μM treatment groups, indicating a weaker effect on membrane potential at this concentration. The red/green fluorescence ratios in the 12.5 μM and 6.25 μM treatment groups were close to those of the DMSO control and the moxifloxacin negative control, and no obvious membrane depolarization was observed. These results indicate that the effect of compound **1** on VISA cell membrane potential increased with increasing concentration, and obvious membrane depolarization mainly occurred at concentrations above the MIC.

Effect on cell membrane permeability

The PI fluorescence signals of the DMSO and moxifloxacin negative controls remained near baseline throughout the detection period, indicating that VISA cell membrane integrity did not change markedly. After treatment with the lysostaphin positive control, the PI fluorescence signal increased rapidly and reached a high level during subsequent detection, consistent with increased PI uptake after disruption of the cell wall/cell membrane structure.

The effect of compound **1** on PI uptake differed by concentration (**Fig. 7**). After treatment with 100 μM compound **1**, the PI fluorescence signal showed no obvious change at early time points, began to increase gradually after approximately 50–60 min, and reached approximately 900 arbitrary units at 120 min, suggesting that high-concentration compound **1** can increase VISA cell membrane

permeability. The PI fluorescence signal in the 50 μM compound **1** treatment group remained near baseline during the detection period, and no obvious increase in PI uptake was observed. This result indicates that compound **1**-induced membrane permeability increase mainly occurred under higher concentration conditions, and its onset occurred later than that induced by lysostaphin, suggesting that compound **1** does not act through rapid lytic membrane disruption.

Together, the membrane potential and PI uptake assay results indicate that compound **1** can cause decreased VISA membrane potential and increased cell membrane permeability under high-concentration conditions, whereas it does not show obvious membrane disruption at concentrations close to the MIC. This result suggests that the anti-VISA activity of compound **1** at low concentrations may not mainly depend on direct membrane disruption; the membrane functional disturbance and permeability increase observed at high concentrations may represent additional membrane-related effects under higher drug pressure.

Screening of resistant mutants and analysis of resistance levels

After liquid serial drug-pressure cultivation, a total of six VISA mutants with reduced susceptibility to compound **1** were obtained. MIC determination showed (**Fig. 8**) that mutants obtained at the 0.5×, 1×, and 2× MIC pressure stages had a compound **1** MIC of 12.5 μM; mutants obtained at the 3×, 4×, and 5× MIC pressure stages had a MIC of 25 μM. This result indicates that continuous liquid drug pressure can gradually reduce the susceptibility of VISA to compound **1**, and the MICs of mutants increased with increasing selection pressure. But no spontaneous resistant mutants were isolated on solid medium containing 5× MIC compound **1** (**Fig. S2**).

Whole-genome sequencing analysis of resistant mutants

The three compound **1**-resistant mutants all carried multiple genetic variants, and the complete mutation information is listed in **Table S1**. Comparison of commonly mutated genes showed that all three mutants carried mutations in SAV0513/*cysK* and SAV0659/*graR*. SAV0513 encodes cysteine synthase / O-acetylserine sulfhydrylase homologue (CysK), and SAV0659 encodes the response regulator GraR of the GraRS two-component system.

Mutant 1 (Mu1) contained a deletion mutation in *cysK*, resulting in deletion of the four amino acids LAGI at positions 264–267 of the CysK protein; its *graR* contained a nonsense mutation, resulting in premature termination of the GraR protein at amino acid position 200. Mutant 2 (Mu2) contained a missense mutation in *cysK*, resulting in substitution of threonine by proline at position 77 of the CysK protein (T77P); its *graR* contained a nonsense mutation, resulting in premature termination of the GraR protein at amino acid position 17 (K17*). Mutant 3 (Mu3) had the same *cysK* mutation as mutant 1, showing deletion of LAGI at positions 264–267 of the CysK protein; its *graR* contained a frameshift mutation, resulting in a reading-frame change after amino acid position 168 of the GraR protein and premature termination at amino acid position 183.

GraRS is an important two-component regulatory system in *S. aureus*, consisting of the histidine kinase GraS and the response regulator GraR, and is mainly involved in bacterial responses to cationic antimicrobial peptides and cell envelope stress. This system can regulate the expression of genes related to cell surface charge and cell envelope homeostasis, such as the *dlt* operon, *mprF*/*fmtC*, and vraFG, thereby affecting bacterial susceptibility to multiple membrane/cell wall-related antimicrobial stresses [12–14]. In the VISA background, all three independent resistant mutants carried *graR* mutations, suggesting that the antibacterial activity of compound **1** or the formation of resistance may be closely related to GraRS-mediated regulation of cell envelope homeostasis.

In addition to *graR*, all three mutants also carried *cysK* mutations. Because CysK is involved in cysteine biosynthesis and related sulfur metabolism processes [15], this result suggests that changes in sulfur metabolism may be one of the adaptive features under continuous compound **1** pressure. However, based on sequencing results alone, the causal relationship between *cysK* mutations and the compound **1**-resistant phenotype cannot yet be determined.

Changes in antibiotic susceptibility of resistant mutants

Mu2 showed markedly increased susceptibility to multiple cell envelope-targeting antibiotics (**Table 4**). Compared with the VISA wild-type, the MIC of daptomycin against the resistant mutants decreased from 0.78 μM to 0.05 μM, an approximately 16-fold decrease; the MIC of polymyxin B decreased from 50 μM to 1.56 μM, an approximately 32-fold decrease; the MIC of colistin decreased from 200 μM to 6.25 μM, an approximately 32-fold decrease; and the MIC of vancomycin decreased from 25 μM to 1.56 μM, an approximately 16-fold decrease. This result indicates that while Mu2 showed reduced susceptibility to compound **1**, it showed higher susceptibility to daptomycin, polymyxin B, colistin, and vancomycin, suggesting that the formation of compound **1** resistance was accompanied by altered susceptibility to cell envelope-related antibiotics. Combined with the whole-genome sequencing results, the recurrent disruptive mutations in *graR* in the resistant mutants may be related to this phenotype.

Combined effects of compound 1 with antibiotics

Compound **1** enhanced the inhibitory activity against VISA when combined with polymyxin B, colistin, and vancomycin, with FICI values all below 0.5, indicating synergistic effects (**Table 5**). Polymyxin B and colistin both belong to polymyxin cationic peptide antibiotics, and their antibacterial activity is closely related to interactions with the bacterial cell envelope [16, 17]. Vancomycin is a glycopeptide antibiotic that inhibits cell wall synthesis by binding to the D-Ala-D-Ala terminus of peptidoglycan precursors [18]. These results show an obvious combined enhancement effect between compound 1 and cell envelope-related antibiotics.

When compound **1** was combined with moxifloxacin, the FICI was 1, and no obvious synergistic effect was observed. Moxifloxacin is a fluoroquinolone antibiotic that mainly targets DNA gyrase and topoisomerase IV, thereby inhibiting bacterial DNA replication [19]. This result indicates

that the combined enhancement effect of compound **1** does not generally occur in all antibiotic combinations but mainly appears in combinations with cell envelope-related drugs such as polymyxin B, colistin, and vancomycin.

Analysis of cell surface charge state (cytochrome c binding assay)

DMSO-treated VISA showed a low cytochrome c binding rate, approximately 10%, markedly lower than the basal binding rate of MSSA. Under DMSO treatment, the cytochrome c binding rate of MSSA was approximately 55%, consistent with its characteristics as a high cytochrome c-binding reference strain. After compound **1** treatment, the cytochrome c binding rate of VISA increased to approximately 30%, suggesting that compound **1** can alter the cell surface charge state of VISA, increasing the negative charge of the surface or reducing the level of positive charge modification on the cell surface (**Fig. 9**).

Under DMSO treatment, the cytochrome c binding rate of Mu2 was approximately 45%, markedly higher than that of VISA and close to the basal binding level of MSSA. This result indicates that even under untreated conditions, the resistant mutants already showed cell surface charge characteristics different from those of the parental VISA strain and closer to those of MSSA, suggesting increased cell surface negative charge or reduced positive charge modification.

Polymyxin B treatment was used to further evaluate the surface charge response of resistant mutants to cationic antimicrobial peptide-related pressure (**Fig. S3**). After polymyxin B treatment, the cytochrome c binding rate of MSSA decreased slightly compared with the DMSO control, whereas the binding rate of the resistant mutants further increased to approximately 70%. This change indicates that the resistant mutants showed stronger cytochrome c binding capacity under polymyxin B pressure, different from the response trend of MSSA. Combined with the above MIC results showing markedly increased susceptibility of resistant mutants to polymyxin B, colistin, and daptomycin, this result suggests that the cell surface charge state of the resistant mutants was altered, which may make them more susceptible to cationic or membrane-related antibiotics.

Overall, compound **1** increased the cytochrome c binding rate of VISA, indicating that it can affect the cell surface charge state of the parental strain. Mu2 themselves had higher cytochrome c binding rates, which further increased after polymyxin B treatment, suggesting enhanced surface negative charge or weakened positive charge modification. Combined with the recurrent *graR* mutations in resistant mutants, this phenotype is consistent with impaired GraRS-related cell surface charge regulation and can also explain the increased susceptibility to antibiotics such as polymyxin B, colistin, and daptomycin.

Global proteomic stress response analysis

Proteomic results (**Table S3**) showed that the protein expression profile of VISA changed markedly after compound **1** treatment, and the differentially expressed proteins were mainly involved

in cell wall remodeling, cell envelope homeostasis, biofilm formation, cell surface polysaccharide synthesis, and metabolic regulation.

Among the upregulated proteins, multiple proteins related to cell wall remodeling and cell envelope homeostasis were increased, including SceD, IsaA, LytM, LrgB, LtaS, and VraG. Among them, SceD, IsaA, and LytM are associated with peptidoglycan hydrolysis, cell wall remodeling, or autolysis-related processes, LtaS participates in lipoteichoic acid synthesis [20], and VraG is related to cell envelope stress defense [12]. The upregulation of these proteins suggests that VISA may activate adaptive responses related to cell wall repair, peptidoglycan remodeling, and maintenance of cell envelope homeostasis after compound **1** treatment.

Among the downregulated proteins, multiple proteins related to biofilm matrix formation and cell surface polysaccharide synthesis showed decreased expression. IcaA, IcaB, and IcaC, which are involved in PIA/PNAG biofilm matrix synthesis, modification, or transport, all showed a downward trend [21], suggesting that compound **1** treatment may weaken the biofilm matrix-forming capacity of VISA. At the same time, multiple capsular polysaccharide synthesis-related proteins decreased, including CapE, CapI, CapG, CapN, CapD, CapM, CapJ, and CapK [22], indicating that compound **1** treatment may also affect the formation of VISA cell surface polysaccharide structures.

In addition to the above cell envelope- and biofilm-related proteins, compound **1** treatment was also accompanied by changes in multiple classes of metabolism- and stress-related proteins. Upregulated proteins mainly included proteins related to protein folding and protein homeostasis maintenance, urea metabolism-related proteins, iron uptake/heme transport-related proteins, redox regulation-related proteins, and some virulence- and cell surface adhesion-related proteins. Downregulated proteins mainly included nitrogen metabolism-related proteins, amino acid metabolism-related proteins, vitamin/cofactor biosynthesis-related proteins, some transporters, and some transcriptional regulators. The complete information on differentially expressed proteins is listed in **Tables S2 and S3**.

In summary, the proteomic changes in VISA after compound **1** treatment were mainly characterized by upregulation of proteins related to cell wall/cell envelope remodeling and downregulation of proteins related to biofilm matrix and cell surface polysaccharide synthesis. This result suggests that long-term low-dose exposure to compound **1** can affect VISA cell envelope homeostasis and may weaken its biofilm- and surface polysaccharide-related phenotypes.

Inhibition of VISA biofilm formation

Compound **1** showed obvious inhibitory activity against VISA biofilm formation (**Fig. 11**). Under 25, 12.5, and 6.25 μM conditions, VISA biofilm formation was almost completely inhibited; under sub-MIC conditions of 3.13 and 1.56 μM, compound **1** still significantly reduced the level of biofilm formation. When the concentration decreased to 0.78 μM, biofilm formation in the compound **1**-treated group was close to that in the DMSO control. As a negative control, moxifloxacin inhibited biofilm formation at 25, 12.5, and 6.25 μM, but under sub-MIC conditions of 3.13 and 1.56 μM, biofilm

formation was close to that in the DMSO control. Compared with moxifloxacin, compound **1** still showed obvious inhibition of biofilm formation at sub-MIC concentrations, indicating that this effect does not completely depend on inhibition of planktonic cell growth and may be related to the affected processes involved in biofilm formation. This result is also consistent with the downregulation of biofilm formation-related proteins in the proteomic results.

Expression verification of GraRS downstream-related genes

RT-qPCR results (**Fig. 10**) showed that after compound **1** treatment, the expression of *fmtC*, *dltA*, and *vraG* in VISA was markedly downregulated. Compared with the DMSO control, after treatment with 8× MIC compound **1** for 1 h, the expression levels of *fmtC*, *dltA*, and *vraG* decreased by approximately 2-fold, 3-fold, and 3-fold, respectively. This result indicates that short-term high-concentration compound **1** stress can rapidly suppress the expression of genes related to cell surface charge modification and cell envelope stress defense.

Mu2 also showed similar low-expression features under DMSO treatment. Compared with VISA, the expression levels of *fmtC*, *dltA*, and *vraG* in the resistant mutants were all markedly decreased, with *vraG* showing the most obvious downregulation. This result indicates that the resistant mutants exhibited a cell envelope regulatory state different from that of the parental strain.

Compound **1** can induce downregulation of *fmtC*, *dltA*, and *vraG* in VISA, and the resistant mutants themselves also showed low expression of these genes. Combined with the *graR* mutations in resistant mutants and the surface charge changes observed in the cytochrome c binding assay, this result further supports that both the action of compound **1** and the formation of the resistant phenotype are related to altered GraRS-associated cell envelope regulation.

Genetic complementation analysis

The MIC of compound **1** against the *cysK* complemented strain remained 25 μM and did not recover to the VISA wild-type level (**Fig. S6**). This result indicates that complementation of *cysK* alone failed to restore the susceptibility of the compound **1**-resistant mutant to compound **1**, suggesting that the *cysK* mutation may not be the main factor that independently determines the compound **1**-resistant phenotype.

The MIC of compound **1** against the *graR* complemented strain also remained 25 μM, and no recovery of susceptibility to compound **1** was observed (**Fig. S7**). Further susceptibility results showed that the susceptibility of the *graR* complemented strain to vancomycin and polymyxin B also did not recover to the VISA wild-type level but remained close to the phenotype of the compound **1**-resistant mutant. Because susceptibility to vancomycin and polymyxin B is closely related to GraRS-associated cell envelope defense and surface charge regulation, this result indicates that the current *graR* complemented strain did not effectively restore the GraRS-related functional phenotype.

Overall, complementation of *cysK* or *graR* alone did not restore the susceptibility of Mu2 to compound **1**. In particular, the *graR* complemented strain did not restore the tolerance phenotype toward vancomycin and polymyxin B, suggesting that the current complementation system may have limitations in expression level, regulatory background, or plasmid burden and is not yet sufficient to reconstruct the original GraRS regulatory state. Therefore, the relationship between *graR* and *cysK* and the compound **1**-resistant phenotype still requires further confirmation through expression validation and more suitable genetic functional experiments.

CONCLUSIONS

This study used the endophytic fungus *Pestalotiopsis chamaeropis* and induced the production of its secondary metabolites through the OSMAC strategy. Nine pestalotic acid-related natural products were isolated from the fermentation products. Among them, pestalotic acid H and pestaloside A were new compounds reported for the first time. In addition, the absolute configuration of the reported compound pestalotic acid C was determined by high-quality crystals and X-ray diffraction. Although the addition of sodium iodide to the culture medium promoted secondary metabolite production, none of the isolated compounds showed halogen substitution, indicating that sodium iodide more likely acted as a metabolic elicitor in this system rather than directly serving as a halogen precursor incorporated into secondary metabolite structures.

Antibacterial activity evaluation showed that the activity of this series of pestalotic acid derivatives was mainly concentrated in compounds **1** and **7**. Both compounds showed the strongest inhibitory activity against VISA, whereas their activity against other Gram-positive bacteria was relatively weak, and no obvious activity was observed against Gram-negative bacteria, fungi, or Mycobacterium tuberculosis. Based on structural comparison, compounds **1** and **7** both retained the long-chain hydrophobic side chain and the basic pestalotic acid scaffold that were relatively important for activity, whereas the activity of other derivatives with side-chain modification or structural alteration was markedly reduced, suggesting that these structural features contributed importantly to antibacterial activity. Compared with compound **7**, compound **1** showed better cellular selectivity and blood compatibility; therefore, it was selected as the main candidate compound for subsequent mechanistic studies.

The action of compound **1** against VISA did not conform to the characteristics of a typical nonspecific membrane-lytic agent. Growth kinetics and time-kill kinetics showed that compound **1** markedly inhibited VISA growth, but its overall action was closer to bacteriostatic activity rather than rapid and complete bactericidal activity. Membrane potential and PI uptake assays showed that the effect of compound **1** on the cell membrane was concentration-dependent: it induced a decrease in membrane potential and an increase in membrane permeability at high concentrations, whereas no obvious rapid membrane disruption was observed at concentrations close to the MIC against VISA. Therefore, the low-MIC inhibitory effect of compound **1** against VISA may not mainly depend on direct membrane

lysis. Compound **1** also showed activity against other Gram-positive bacteria, including MSSA and MRSA, but the MICs were higher than that against VISA. The membrane dysfunction and increased membrane permeability observed at high concentrations may contribute to the inhibitory effect of compound **1** against these Gram-positive bacteria.

Resistant mutant analysis further indicated a clear link between compound **1** and GraRS-related cell envelope regulation in VISA. The compound **1**-resistant mutants all carried disruptive *graR* mutations, including nonsense mutations and frameshift mutations, suggesting that altered GraR function was closely associated with reduced compound **1** susceptibility. Although the resistant mutants showed reduced susceptibility to compound **1**, their susceptibility to cell envelope-related antibiotics, including daptomycin, polymyxin B, colistin, and vancomycin, was markedly increased. Cytochrome c binding assays and RT-qPCR results further showed that both compound **1** treatment and the resistant mutants were accompanied by changes in cell surface charge status and decreased expression of GraRS-related downstream genes, including *fmtC*, *dltA*, and *vraG*. Together, these results support that compound **1** can weaken positive charge modification on the VISA cell surface or enhance its surface electronegativity, and interfere with GraRS-related cell envelope homeostasis regulation.

Antibiotic synergy assays further strengthened this mechanistic interpretation. Compound **1** showed synergistic effects with polymyxin B, colistin, and vancomycin, whereas no obvious synergy was observed with the DNA replication inhibitor moxifloxacin. This result indicates that the potentiating effect of compound **1** mainly occurred with cell envelope-related antibiotics, suggesting that its action is associated with cell membrane/cell wall status, surface charge regulation, or cell envelope stress adaptation. This feature also suggests that compound **1** has potential for combination therapy, especially for enhancing the susceptibility of VISA to antibiotics acting on the cell envelope.

In addition to *graR*, the compound **1**-resistant mutants all carried *cysK* mutations, suggesting that changes related to cysteine biosynthesis or sulfur metabolism may participate in the adaptive process under long-term compound **1** pressure. However, the current evidence cannot prove the role of *cysK* in resistance.

Compound **1** also showed obvious antibiofilm formation activity. Proteomics results showed that, after compound **1** treatment, proteins related to cell wall remodeling and cell envelope homeostasis were upregulated in VISA, whereas proteins related to PIA/PNAG biofilm matrix synthesis and multiple capsular polysaccharide synthesis-related proteins were downregulated. Crystal violet staining confirmed that compound **1** still significantly inhibited VISA biofilm formation at sub-MIC concentrations. This result indicates that compound **1** can not only inhibit VISA planktonic cell growth but may also weaken its biofilm-forming ability by affecting processes related to the biofilm matrix and cell surface polysaccharides.

In summary, compound **1** is a natural product lead compound with anti-VISA activity, good selectivity, antibiofilm formation activity, and potential value for combination therapy. The current

results support that compound **1** has concentration-dependent multilayered effects: in VISA, lower concentrations can interfere with cell envelope homeostasis, surface charge regulation, and GraRS-related adaptive networks; at higher concentrations, compound **1** can also produce membrane-related effects, which may explain its higher-MIC inhibitory activity against other Gram-positive bacteria. Therefore, compound **1** is not a simple nonspecific membrane-disrupting agent, but is more likely an anti-*S. aureus* natural product lead compound centered on cell envelope regulation and accompanied by membrane functional disturbance at high concentrations. Further studies are still needed to clarify the direct molecular target of compound **1** and to validate the causal role of GraRS-related regulation in compound **1** susceptibility and resistance development.

Materials and methods

General experiments

HPLC analysis was performed with a Dionex UltiMate 3000 system through an UltiMate 3000 pump and a photodiode array UV routine at channel 235, 254, 280 and 340 nm (DAD 3000 RS,) on Eurospher 100-10 C_{18} column (125 × 4 mm, L × ID, Knauer, Germany). Semipreparative HPLC was done with a Merck Hitachi Chromaster HPLC system (UV detector 5410; pump 5110; column Eurospher 100-10C_{18}, 300 8 mm, Knauer, Germany) performed by mixtures of MeCN-H_2O with flow rate at 5 mL/min. Merck MN silica gel 60 M (0.04–0.063 mm) and Sephadex LH-20 were used for column chromatography. Thin-layer chromatography (TLC) analysis was performed on silica gel 60 F254 TLC plates, and visualized under UV detection at 254 and 366 nm or by spraying the plates with anisaldehyde reagent followed by heating (Macherey-Nagel, Germany). 1D and 2D NMR spectra were recorded on a Bruker ARX 600 NMR spectrometer through TMS as an internal standard. ESI and HRESIMS spectra were obtained employing an Agilent Finnigan LCQ Deca and a UHR-QTOF maXis 4G (Bruker Daltonics), respectively. Jasco P-2000 polarimeter was used to measure optical rotations in Methanol solvent.

Fungal material and fermentation

The fungal strain *P. chamaeropis* was isolated from the plant *Aster subulatus* (Michx.) collected in April 2018 in Beijing, P.R. China. Identification was performed by determination of the internal transcribed spacer (ITS) sequence and nucleotide BLAST search in the NCBI database following standard molecular biology protocols for fungi as described previously [23]. The accession number of the internal transcribed spacer (ITS) sequence in GenBank is ON556592. The fungal strain is stored as glycerol-agar aliquots in a -80 °C freezer in our laboratory at the Institute of Pharmaceutical Biology and Biotechnology, Heinrich-Heine University, Duesseldorf, Germany.

Chemical section: “OSMAC” approach and isolation

P. chamaeropis was aerobically grown on solid rice medium in fifteen Erlenmeyer flasks each containing 100 g rice and 110 mL water at 22 °C. After two weeks of fermentation, rice cultures were

extracted with 500 mL EtOAc for each flask and soaked overnight, which was repeated twice until the color of EtOAc extract became light. The combined extracts were dried by rotary evaporation to yield 15.8 g of dried crude EtOAc extract. The crude EtOAc extract was fractionated via vacuum liquid chromatography (VLC) with silica gel using *n*-hexane / EtOAc and dichloroform / methanol (V/V) as mobile phase with mixtures from 100:0, 80:20, 60:40, 40:60, 20:80, 0:100, respectively, and resulted in nine fractions (Fr.1 – Fr.9). Fraction 9 (1.9 g) was further separated by Sephadex LH-20 column eluted with dichloroform / methanol = 1:1 (V/V) to gain six sub-fractions (Fr.9-1 – Fr.9-6). Fraction 9-6 (312 mg) was chromatographed on an ODS RP column and eluted using a gradient elution of methanol / H_2O (V/V) from 40:60, 50:50, 60:40, 70:30, 80:20, 90:10, 100:0 to yield four sub-fractions (Fr.9-6-1 – Fr.9-6-4). Sub-fraction 9-6-3 (103 mg) was separated by semi-preparative HPLC with a mixture of MeOH-H_2O to obtain compound **9** (3.5 mg). Same routine was used to obtain sub-fraction Fr.8-2-4, and semi-preparative HPLC was used to harvest compound **1** (5.2 mg) by a mixture of MeOH-H_2O as mobile phase.

Based on the interesting compound **1**, **'**OSMAC' was carried out using 3.5% sodium chloride, sodium fluoride, sodium bromide, sodium iodide, ammonium nitrate, L-rhamnose, zinc sulfate, magnesium nitrate or ferric sulfate, respectively, which were added to rice medium. Furthermore, we performed a co-culture of *P. chamaeropis* with *Bacillus subtilis* on regular rice medium. All small-scale fermentation conditions were incubated at 22 °C for two weeks. Plain rice medium served as blank control. Interestingly, HPLC spectra showed significant change in the secondary metabolite profile during cultivation on rice medium supplemented with sodium iodide with loss of the main peak and enrichment of pestalotic acid derivatives. Next, large scale fermentation using sodium iodide-supplemented rice medium was carried out to obtain 18.5 g crude extract, which showed inhibitory activity against MRSA at a concentration of 100 μg/ml. Crude extract was fractionated via vacuum liquid chromatography (VLC) as well as with silica gel using *n*-hexane / EtOAc from 100:0, 80:20,70:30, 60:40, 50:50, 40:60, 30: 70, 20:80, 0:100 to obtain four fractions (Fr.1 – Fr4). Fraction 2 (4.1 g) was further chromatographed with ODS column using MeOH / H_2O (V/V) from 30:70, 50:50, 60:40, 70:30, 80:20, 90:10, 100:0 to obtain six sub-fractions (Fr.V2-R1 – Fr.V2-R6). Fraction V2-R2 (189 mg) was separated by semi-preparative HPLC with a mixture of MeCN-H_2O to obtain compound **2** (5.1 mg), compound **3** (3.8 mg), compound **4** (3.2 mg) and compound **5** (7.0 mg). Fraction V2-R4 (125 mg) was separated by semi-preparative HPLC as well using mobile phase MeCN-H_2O mixture to harvest compound **6** (2.3 mg) and compound **7** (4.5 mg). Compound **8** (4.7 mg) was obtained using a similar method by semi- preparative HPLC.

Pestalotic acid A (**1**): colorless powder; $[\alpha]_D^{25}$ -225.736 (CH_3OH); UV (MeOH) λ_{max} (nm): 214.7, 313.3, 322.2; ^1H NMR in $CDCl_3$: 7.83 (7.81), 7.50 (7.40), 4.89, 2.96, 2.84, 1.99, 1.60, 1.28, 0.90; ^{13}C NMR in $CDCl_3$: 198.2 (197.1), 181.7 (181.0), 172.5, 170.8, 163.6 (163.3), 123.4, 104.3 (103.6), 94.9 (94.5), 80.7 (80.3), 38.7 (38.6), 36.7 (36.6), 33.1 (33.0), 30.7(30.6), 25.0 (24.9), 23.7, 23.3 (23.2), 14.4.

Pestalotic acid B (**2**): colorless oil; $[\alpha]_D^{25}$ -234.198 (CH_3OH); UV (MeOH) λ_{max} (nm): 235.2, 301.7, 344.9; ^1H NMR in $CDCl_3$: 7.55 (7.48), 7.45 (7.39), 4.87 (4.79), 3.02, 2.95, 2.82, 2.07, 1.63, 1.29, 0.93; ^{13}C NMR in $CDCl_3$: 196.9 (149.6), 179.5, 170.3, 168.2, 160.5, 123.4, 102.6 (101.7), 93.8, 73.5 (73.4), 38.1, 37.7, 36.4, 30.0, 25.3, 24.1, 23.4, 9.9.

Pestalotic acid C (**3**): colorless powder; $[\alpha]_D^{25}$ -205.878 (CH_3OH); UV (MeOH) λ_{max} (nm): 233.7, 316.5, 342.8; ^1H NMR in $CDCl_3$: 7.56 (7.49), 7.45 (7.39), 4.88 (4.80), 3.79, 3.02, 2.94 (2.82), 2.05 (1.99), 1.89, 1.61, 1.44 (1.41), 1.17; ^{13}C NMR in $CDCl_3$: 196.7 (194.8), 173.0 (172.3), 170.6, 167.6, 160.0, 123.5, 101.8, 78.8, 68.4, 39.3, 38.0, 35.6, 29.0, 23.6, 23.5.

Pestalotic acid D (**4**): colorless oil; $[\alpha]_D^{25}$ -196.631 (CH_3OH); UV (MeOH) λ_{max} (nm): 215.0, 305.7, 318.0; ^1H NMR in $CDCl_3$: 7.53 (7.49), 7.45 (7.41), 4.87, 3.20, 2.90 (2.80), 2.40, 2.13, 2.20, 1.99 (1.90), 1.61, 1.25, 1.04; ^{13}C NMR in $CDCl_3$: 211.6, 196.1(194.3), 179.9, 172.6, 170.4, 160.5, 123.5, 101.9, 90.2, 77.4, 43.0, 37.6, 35.9, 30.0, 28.8, 23.3.

Pestalotic acid E (**5**): colorless oil; $[\alpha]_D^{25}$ -223.639 (CH_3OH); UV (MeOH) λ_{max} (nm): 236.1, 302.1, 347.6; ^1H NMR in $CDCl_3$: 7.55 (7.48), 7.45 (7.41), 4.88, 3.18, 2.98 (2.80), 2.40, 2.13, 2.00 (1.91), 1.60, 1.52, 1.23, 1.14; ^{13}C NMR in $CDCl_3$: 209.6, 194.1(193.0), 179.6, 173.0, 170.1, 160.1, 123.8, 101.4, 93.0, 78.4, 43.7, 38.0, 36.5, 29.9, 28.7, 23.6, 23.3.

Pestalotic acid F (**6**): colorless oil; $[\alpha]_D^{25}$ -191.176 (CH_3OH); UV (MeOH) λ_{max} (nm): 235.1, 302.6, 345.2; ^1H NMR in $CDCl_3$: 7.54 (7.49), 7.45 (7.44), 4.88, 4.04, 3.01, 2.83, 2.02, 1.91, 1.61, 1.40, 1.29, 1.24; ^{13}C NMR in $CDCl_3$: 196.7(194.2), 179.5 (179.2), 170.1, 167.9, 160.2 (159.3), 123.4 (123.2), 102.3 (101.4), 94.0 (93.6), 78.4, 62.9, 37.1, 36.8, 36.5, 29.2, 27.7, 23.6, 23.2, 22.6.

Pestalotic acid G (**7**): colorless oil; $[\alpha]_D^{25}$ -121.416 (CH_3OH); UV (MeOH) λ_{max} (nm): 231.7, 304.9, 344.6; ^1H NMR in $CDCl_3$: 7.55 (7.50), 7.43 (7.42), 4.89, 3.71, 2.99, 2.81, 1.99 (1.91), 1.61, 1.42, 1.23,0.88; ^{13}C NMR in $CDCl_3$: 196.8(194.6), 179.4, 170.5, 170.0, 160.3, 123.7 (123.5), 102.7 (102.2), 94.1, 79.1 (78.4), 52.5, 38.5 (38.3), 36.5 (36.2), 29.8, 29.6, 24.4, 23.0, 14.5.

Pestalotic acid H (**8**): colorless oil; $[\alpha]_D^{25}$ -9.614(CH_3OH); UV (MeOH) λ_{max} (nm): 214.5, 320.7, 307.7; HRESIMS *m/z*: 437.2166 $[M + H]^+$ (calcd for $C_{23}H_{33}O_8$ 436.2170); ^1H NMR and ^{13}C NMR data see **Table 1**.

Pestaloside A (**9**): colorless oil; UV (MeOH) λ_{max} (nm): 238.6, 317.1; HRESIMS *m/z*: 405.1881 $[M + Na]^+$ (calcd for $C_{20}H_{30}NaO_7$, 405.1884); ^1H NMR and ^{13}C NMR data see **Table 2**.

Hydrolysis

Compound **9** (2.0 mg) was hydrolyzed with 2N HCl (2.0 mL) at 90 °C for 4 h as previously described [24]. After cooling, the solution was extracted with chloroform (5 mL) and H_2O twice. The water phase containing the sugar was examined using specific optical rotation analysis with $[\alpha]_D^{25}$ -6.990 (Methanol), which had a good agreement with reference [24] and identified the sugar as α, L-rhamnose.

Biological section: Characterization of active substances

Antibacterial characterization.

Nosocomial bacterial strains were incubated aerobically in a Mueller-Hinton broth at 37 °C including *Staphylococcus aureus* (MSSA strain ATCC 25923, VISA strain ATCC 700699, MRSA strain USA300), *Enterococcus faecalis* (ATCC 29212, ATCC 51299 (gentamycin-resistant)), *Enterococcus faecium* (ATCC 35667, ATCC 700221 (vancomycin-resistant)), and *Escherichia coli* ATCC 25922. *Candida albicans* was steadily growing in YPD medium (yeast extract 10 g/L, peptone 20 g/L, D-glucose 20 g/L) at 37 °C. *Mycobacterium tuberculosis* H37Rv strain was grown aerobically in a Middlebrook 7H9 medium supplemented with 0.05% (v/v) tyloxapol, 0.5% (v/v) glycerol and 10% (v/v) ADS (5% w/v, bovine serum albumin fraction V; 2% w/v, glucose; 0.85% w/v, sodium chloride) at 37 °C, 5% CO_2 in a humidified atmosphere.

Minimum inhibitory concentration determination

The biological activities of compounds **1**–**9** were determined by the broth microdilution method according to the method recommended by the Clinical and Laboratory Standards Institute (CLSI) [26]. The test strains included Gram-positive bacteria, such as Staphylococcus aureus, Enterococcus faecalis and Enterococcus faecium, the Gram-negative bacterium Escherichia coli, and the fungus Candida albicans.

Bacteria were inoculated into Mueller-Hinton (MH) broth and cultured with shaking at 37 °C and 180 rpm. The bacterial suspension was then adjusted to approximately 1×10^6 CFU/mL. The test compounds were subjected to two-fold serial dilution in 96-well round-bottom microtiter plates, with final concentrations ranging from 0.78 to 100 μM. The bacterial suspension was then added to each well to obtain a final inoculum of 5×10^5 CFU/mL and a final volume of 100 μL. 2% DMSO was used as the solvent control, and moxifloxacin was used as the positive control. The plates were then aerobically incubated overnight at 37 °C. MIC values were determined using the resazurin assay, and fluorescence signals were read using a Tecan Infinite F200 Pro microplate reader at an excitation wavelength of 540 nm and an emission wavelength of 590 nm. All experiments were repeated twice.

For *C. albicans*, cells were inoculated into YPD broth and cultured overnight in glass shake flasks at 37 °C and 180 rpm to obtain yeast-form cells. The cells were then inoculated into 96-well round-bottom microtiter plates containing the test compounds, and the cell density was adjusted to 1×10^6 CFU/mL. The final concentrations of the test compounds ranged from 0.78 to 100 μM, with a final volume of 100 μL. The plates were incubated overnight at 37 °C. 2% DMSO was used as the negative control, and hygromycin B was used as the positive control. The readout was also performed using the resazurin assay described above.

For *M. tuberculosis*, cells were inoculated into 7H9 medium and cultured at 37 °C and 80 rpm for 5 days. The cell density was then adjusted to 1×10^6 CFU/mL, and 2×10^5 CFU were inoculated

into 96-well round-bottom microtiter plates containing two-fold serial dilutions of the compounds. The final concentrations of the compounds ranged from 0.78 to 100 μM, with a final volume of 100 μL. Rifampicin was used as the positive control, and DMSO was used as the solvent control, with a maximum final concentration of 2%. The plates were then incubated at 37 °C in a humidified atmosphere containing 5% CO_2 for 5 days. The readout was performed according to the resazurin assay described above.

To determine whether compound **1**-resistant mutants were accompanied by changes in susceptibility to other antibiotics, the MICs of vancomycin, daptomycin, polymyxin B and colistin against VISA wild-type and compound **1**-resistant mutants were further determined using the broth microdilution method described above. Except for daptomycin, the MIC test conditions for all antibiotics were the same as those used for the bacterial MIC assay described above. Because the in vitro antibacterial activity of daptomycin depends on Ca^{2+}, Ca^{2+} was supplemented in the medium to a final concentration of 50 mg/L during the daptomycin MIC assay [27]. By comparing changes in MIC values between the VISA wild-type and resistant mutants, whether compound **1** resistance was accompanied by altered susceptibility to antibiotics targeting the cell membrane or cell wall was evaluated.

To evaluate the effects of *cysK* and *graR* complementation on susceptibility to compound **1** and related antibiotics, the susceptibilities of the VISA wild-type, compound **1**-resistant mutants, pLA02 empty-vector control strains, and pLA02::*cysK* and pLA02::*graR* complemented strains to compound **1**, vancomycin and polymyxin B were further tested using the MIC assay described above. For strains carrying the pLA02 plasmid, chloramphenicol was added during culture and MIC determination to maintain plasmid stability at a final concentration of 5 μg/mL.

Determination of growth kinetics

The VISA strain was inoculated in Mueller-Hinton broth and diluted to an $OD_{600\ nm} = 0.1$. The cells were seeded into 96-well microtiter plates containing different concentrations of testing compound. Mueller-Hinton broth with DMSO was used as growth control, moxifloxacin was used as positive control. Microtiter plates were incubated in a Tecan Infinite F200 Pro microplate reader at 37 °C shaking and $OD_{600\ nm}$ was measured for 24 h every 30 min.

Determination of cytotoxicity and therapeutic index.

Cytotoxicity studies were conducted as described previously [28] to evaluate the therapeutic index of compounds. Human cell lines THP-1 (human monocytic leukemia cell line), CLS-54 (human lung carcinoma cell line) and H4 (human brain neuroglioma cell line) were cultured in RPMI 1640 medium containing 10% fetal bovine serum (FBS), while HEK293 (human embryonic kidney cells) and HUH7 cells (human liver cell line) were cultivated using an EMEM medium supplemented with 2 mM L-glutamine, 1 mM sodium pyruvate, 1% (v/v) non-essential amino acids and 10% (v/v) FBS. All cells were cultured at 37 °C in a humidified atmosphere with 5% CO_2. Afterwards, cells were adjusted to a

density of 2×10^5 cells/mL and seeded into 96-well flat-bottom microtiter plates in a total volume of 100 µL containing two-fold serial dilutions of compounds at a final concentration range from 0.78-100 µM. 2% (v/v) DMSO was used as a solvent control, uninoculated medium was treated as a blank control, and moxifloxacin was employed as a positive control. Subsequently, plates were incubated at 37 °C with 5% CO_2 for 48 hours. Subsequently, fluorescence was evaluated after the addition of 10 µL of resazurin solution (100 µg/mL) and 2-4 hours of further incubation. All tests were duplicated twice.

Determination of time-kill kinetics

Time-killing kinetics was performed for compound **1** against MRSA. An overnight culture was adjusted to a concentration of approx. 2×10^6 CFU/mL and subsequently split into three aliquots. One aliquot was incubated with testing compound **1** at 4-fold MIC, another culture contained 4-fold MIC of moxifloxacin as a positive control, and the third aliquot was cultured with the solvent control. After 0, 3, 6, 9 and 24 h incubation, 100 µL culture aliquots were taken and plated on MH agar plates. CFU were counted after an overnight incubation at 37 °C. In order to avoid the potential degradation of the compound, after 6 hours of incubation, the cultures were centrifuged at 4,000 rpm for 10 min to remove the medium and replace it with an equal volume of fresh medium containing the compound at the initial concentration.

Determination of hemolytic activity

Hemolytic activity was tested following a published standard protocol [29]. Briefly, defibrinated sheep red blood cells (RBC) were washed twice with PBS and centrifuged at 3,000 rpm, 10 min at 4 °C. Afterwards, 100 µL of 8% RBC suspension in PBS was treated with compound **1** at different concentrations ranging from 1.56-100 µM and incubated at 37 °C for 1 hour. The mixtures were collected in 1.5 mL centrifugation tubes and centrifuged at 3,000 rpm for 3 min. The supernatant was transferred to a new 96-well microtiter plate, and hemoglobin release was measured in a Tecan Infinite 200pro plate reader by absorption at 540 nm. 2% Triton X-100 was used as a positive control and PBS was used as a negative control.

Measurement of membrane potential

VISA cells were grown in Mueller-Hinton broth to an $OD_{600\ nm}$ of 0.5. Afterwards, the cells were washed with PBS and centrifuged at 5,000 g for 5 min. Cells were incubated in 30 μM DiOC2(3) for 15 min for dye uptake in the dark. Subsequently, cells were transferred to a 96-well black wall plate and measured for 10 min for baseline determination at excitation wavelength 488 nm, emission wavelength 530 nm for green and excitation wavelength 488 nm, emission wavelength 630 nm for red fluorescence. Cells were treated with different concentrations of the compound and measured for another 30 min. Carbonyl cyanide m-chlorophenyl hydrazine (CCCP) was employed as a positive control, 12.5 µM of moxifloxacin and DMSO served as negative controls. Ratios of red and green fluorescence were calculated to quantify membrane potential.

Propidium iodide internalization assay.

The propidium iodide (PI) internalization assay was performed as previously described [30]. Briefly, pre-cultures of the VISA parental strain and spontaneous resistant mutants in Mueller-Hinton broth were washed and diluted to an OD_{600nm} = 0.4–0.5. The cell suspension was incubated with 7.5 μg/mL PI for 10 min at 37 °C. Afterwards, the suspension was transferred to a black-walled 96-well plate and certain concentrations of testing compounds were added. Lysostaphin was employed as a positive control, while moxifloxacin and DMSO served as negative controls; only PBS was used as a background control. The baseline fluorescence at excitation wavelength 535 nm and emission wavelength 617 nm was established for 10 min before the addition of compounds. Subsequently, the fluorescence intensity of the PI dye was measured for another 2 h by Tecan Infinite F200 Pro microplate reader every 5 min.

Screening of compound 1-resistant mutants

To obtain VISA mutants with reduced susceptibility to compound **1**, solid-medium spontaneous mutant screening and liquid serial drug-pressure selection were used in this study [31, 32]. Solid-medium screening was used to evaluate whether VISA could form spontaneous resistant mutants under high concentrations of compound **1**, and liquid serial drug-pressure selection was used to gradually enrich strains with reduced susceptibility.

For solid-medium spontaneous mutant screening, a single VISA colony was inoculated into MH broth and cultured overnight. The next day, bacterial suspensions containing approximately 1×10^5 CFU and 1×10^6 CFU were prepared according to the bacterial cell density and were spread onto MH agar plates containing 5× MIC compound **1** (50 μM). The plates were incubated at 37 °C, and the formation of visible colonies was observed.

For liquid serial drug-pressure selection, a single VISA colony was first inoculated into MH broth and cultured overnight. The next day, the overnight culture was inoculated into fresh MH broth at 1:100 and cultured at 37 °C until the $OD_{600\,nm}$ reached approximately 0.6. The bacteria were then diluted to approximately 1×10^6 CFU/mL and inoculated into MH broth containing 0.5× MIC compound **1** (3.125 μM) for further cultivation. When bacteria grew to an $OD_{600\,nm}$ of approximately 0.6–0.8 at this drug concentration, part of the culture was streaked onto agar plates for isolation, while the culture was transferred at 1:100 into fresh MH broth containing 1× MIC compound **1**. The selection pressure of compound **1** was then gradually increased in the same manner, with sequential transfer into medium containing 2×, 3×, 4× and 5× MIC compound **1**. At each stage, the next passage was performed after bacterial regrowth, and strains from the corresponding stage were retained for subsequent analysis. Strains obtained under different drug-pressure stages were further confirmed by MIC determination to evaluate whether their susceptibility to compound **1** was reduced.

Whole-genome sequencing analysis

To elucidate the genetic basis of compound **1**-resistant mutant formation, three resistant mutants whose compound **1** MICs were increased fourfold compared with the parental VISA wild-type strain, together with the VISA wild-type strain, were selected for whole-genome sequencing analysis. Bacterial genomic DNA was prepared according to a previously reported method for *Staphylococcus* genomic DNA extraction [33].

After the extracted genomic DNA passed concentration and quality assessment, it was sent to a commercial sequencing company for library construction and paired-end sequencing on an Illumina platform [32]. The obtained raw sequencing data were subjected to quality control and aligned to the *S. aureus* subsp. aureus Mu50 reference genome (GenBank accession no. BA000017.4). The sequencing results of the three resistant mutants were then compared separately with the VISA wild-type strain used in this study to exclude background differences between the parental strain and the public reference genome. Genetic variants specifically present in the resistant mutants, including single-nucleotide mutations, insertions, deletions, frameshift mutations and premature stop mutations, were identified by comparative analysis. Genes recurrently mutated in multiple independent resistant mutants were further analyzed as candidate genes potentially associated with reduced susceptibility to compound **1**.

Checkerboard combination assay

To evaluate the interactions between compound **1** and different antibiotics, the combined antibacterial effects were determined using a checkerboard assay [34, 35]. In this study, the combined antibacterial effects of compound **1** with vancomycin, polymyxin B, colistin and moxifloxacin were tested. Compound **1** and the tested antibiotics were subjected to two-fold serial dilution along the horizontal and vertical axes, respectively, of sterile U-bottom 96-well polystyrene microtiter plates to generate different concentration combinations. The starting concentrations of compound **1** and each antibiotic were set at 4× MIC, and the lowest concentration was 0.125× MIC. Fresh VISA cells grown to the logarithmic phase and diluted to the specified inoculum were then added. After incubation at 37 °C for 18–24 h, bacterial growth in each well was detected using the same resazurin assay as that used for MIC determination, and the MICs under single-drug and combination conditions were determined. Drug interactions were evaluated using the fractional inhibitory concentration index (FICI). The FICI was calculated as follows: FICI = FIC of compound **1** + FIC of antibiotic, where FIC is the MIC of the drug in combination divided by the MIC of the drug used alone. The interactions between the two drugs were interpreted according to FICI values: FICI $\leq$ 0.5 was defined as synergy; 0.5 < FICI $\leq$ 1 was defined as partial synergy or additivity; 1 < FICI $\leq$ 4 was defined as no interaction; and FICI > 4 was defined as antagonism.

Cytochrome c binding assay

To evaluate whether compound **1** affects the cell surface charge state of *S. aureus*, a cytochrome c binding assay was used to detect the binding capacity of bacteria to the cationic protein cytochrome c [14, 36]. VISA wild-type, compound **1**-resistant mutants and the MSSA reference strain *S. aureus* ATCC

29213 were cultured to the logarithmic phase. The bacterial cells were then harvested by centrifugation and washed with MOPS buffer. The washed cells were resuspended in MOPS buffer and adjusted to the same $OD_{600\ nm}$ value. *S. aureus* ATCC 29213 was used as a control strain to compare differences in cytochrome c binding capacity among different S. aureus strains.

For the drug-treatment experiment, VISA wild-type cells were treated with 4× MIC compound **1 (**50 μM) for 1 h, and the DMSO-treated group served as the solvent control. In addition, to further compare the effect of cationic antimicrobial peptide-related drug pressure on cell surface charge, *S. aureus* ATCC 29213 and compound **1**-resistant mutants were treated with 50 μM polymyxin B for 1 h. After treatment, bacterial cells were mixed with the cytochrome c solution and incubated at room temperature. The bacterial cells were then removed by centrifugation, and the supernatant was transferred to sterile U-bottom 96-well polystyrene microtiter plates. Absorbance at 530 nm was measured using a Tecan Infinite F200 Pro microplate reader to detect the amount of cytochrome c not bound to bacteria.

The cytochrome c binding rate was calculated by comparison with a cytochrome c control without bacteria. Because cytochrome c is a positively charged protein, its binding capacity to bacterial cell surfaces can serve as an indirect indicator of changes in the net negative charge of the cell surface. Therefore, an increased cytochrome c binding rate usually indicates increased negative charge on the cell surface or reduced levels of positive charge modification on the cell surface. By comparing the cytochrome c binding capacities of VISA wild-type, compound **1**-resistant mutants and *S. aureus* ATCC 29213 under different treatment conditions, whether compound **1** resistance and polymyxin B treatment were accompanied by changes in cell surface charge state was evaluated.

Proteomic analysis

To investigate the effect of long-term exposure to a low concentration of compound **1** on the global protein expression profile of VISA, VISA cells were treated with 0.5× MIC compound **1** (3,125 μM) for 24 h, and differences in protein abundance between the compound 1-treated group and the DMSO solvent control group were compared by LC-MS/MS-based proteomic analysis [32]. A single VISA colony was inoculated into MH broth and cultured overnight. The next day, the overnight culture was inoculated into fresh MH broth at 1:100 and cultured at 37 °C until the $OD_{600\ nm}$ reached approximately 0.6. The bacterial suspension was then diluted to approximately 1×10^6 CFU/mL and inoculated into fresh MH broth containing 0.5× MIC compound 1 for 24 h of treatment. The DMSO-treated group served as the solvent control.

After treatment, bacterial cells were collected and total proteins were extracted. Protein samples were digested, and peptides were desalted and purified using C_{18} StageTips and dried using a vacuum concentrator. LC-MS/MS analysis was performed using an Orbitrap Elite mass spectrometer coupled to an EASY-nLC 1000 liquid chromatography system. Mass spectrometric data were acquired using Xcalibur software 2.2 SP1.48. Raw mass spectrometry data were processed with MaxQuant 1.5.3.30 for

peptide and protein identification, with label-free quantification enabled for protein quantification. MS/MS data were searched against the *S. aureus* Mu50 reference protein database. Perseus 1.5.5.3 was then used for further filtering and statistical analysis of the MaxQuant output results. Potential contaminants, reverse database matches, proteins identified only by site modification and low-confidence proteins were removed before statistical analysis. Differentially expressed proteins were screened based on changes in protein abundance and statistical significance, and their involved biological processes were further analyzed in combination with functional annotation, with a focus on cell envelope homeostasis, stress response, metabolic remodeling and changes in biofilm-associated proteins.

Biofilm formation inhibition assay

To evaluate the effect of compound **1** on VISA biofilm formation, biofilm biomass was measured using the 96-well plate crystal violet staining method [32]. The culture and inoculum of VISA cells were the same as those used for MIC determination. Briefly, VISA cells were inoculated into Mueller-Hinton broth containing 1% glucose and added to sterile flat-bottom 96-well polystyrene microtiter plates. Compound **1** and moxifloxacin were added to each well according to the two-fold serial dilution method used in MIC determination, and DMSO was used as the solvent control. The plates were statically incubated at 37 °C for 18–24 h to allow biofilm formation.

After incubation, the culture medium and planktonic cells were discarded, and the wells were gently washed three times with 1× PBS. Then, 100 μL of 0.1% crystal violet solution was added to each well, followed by incubation at room temperature for 15 min. After staining, the crystal violet solution was discarded, and the wells were washed three times with 1× PBS to remove unbound dye. Then, 30% acetic acid was added to each well and incubated at room temperature for 30 min to dissolve crystal violet bound to the biofilm. After incubation, the dissolved solution was transferred to sterile U-bottom 96-well polystyrene microtiter plates, and absorbance at 600 nm was measured using a Tecan Infinite F200 Pro microplate reader. Biofilm formation was normalized to the DMSO solvent control group, which was set as 100%.

Quantitative real-time PCR

To verify the effect of compound **1** on the expression of cell envelope-related genes and to compare the basal expression levels of related genes in compound **1**-resistant mutants, quantitative real-time PCR was used to analyze transcriptional changes in target genes [32, 37].

Single colonies of the VISA wild-type and compound **1**-resistant mutants were separately inoculated into liquid medium and cultured overnight. The next day, the overnight cultures were inoculated into fresh medium at 1:100 and cultured at 37 °C until the $OD_{600\ nm}$ reached approximately 0.6. The VISA wild-type cells were then treated with 8× MIC compound **1** (50 μM) or an equal volume of DMSO for 1 h, with the DMSO-treated group serving as the solvent control. Compound 1-resistant

mutants were treated with an equal volume of DMSO under the same conditions for 1 h. After treatment, bacterial cells were rapidly collected for RNA extraction.

Total RNA was extracted using the Monarch Spin RNA Isolation Kit (Mini, NEB, T2110S). Bacterial cells were treated with 150 μg/mL lysostaphin at 37 °C for 15 min to facilitate *S. aureus* cell wall lysis. The extracted RNA was treated with the TURBO DNA-free Kit (Invitrogen, AM1907) to remove residual genomic DNA. Then, 500 ng of total RNA was used for cDNA synthesis using GoScript™ Reverse Transcription Mix, Random Primers.

Quantitative real-time PCR was performed using the synthesized cDNA as the template, with 1 μL cDNA added to each reaction. qPCR reactions were performed using GoTaq® qPCR Master Mix (Promega), and amplification and fluorescence detection were carried out using a Stratagene/Agilent Mx real-time PCR system. Data were analyzed using MxPro software. The target genes included *fmtC*, *dltA* and *vraG*, with *rpoB* used as the reference gene. The relative expression levels of target genes were normalized to the reference gene and calculated using the $2^{-\Delta\Delta Ct}$ method. Each experimental group included biological and technical replicates.

Construction and transformation of *cysK* and *graR* complementation plasmids

To verify the relationship between *cysK* and *graR* and the compound 1-resistant phenotype, *E. coli – S. aureus* shuttle vector pLA02 was used to construct *cysK* and *graR* complementation plasmids [38]. Using genomic DNA from the VISA wild-type strain as the template, DNA fragments containing the coding regions of *cysK* or *graR* were amplified using Q5 high-fidelity DNA polymerase, and BamHI and EcoRI restriction sites were introduced into the amplification primers. The PCR products and the pLA02 plasmid were double-digested with BamHI and EcoRI. After separation of the digested products by agarose gel electrophoresis, DNA fragments of the correct size were excised and purified using the NucleoSpin® Gel and PCR Clean-up Kit (Macherey-Nagel).

The purified target fragments and linearized pLA02 vector were ligated using T4 DNA ligase. The ligation products were transformed into NEB 5-alpha competent *E. coli* cells by heat shock according to the standard protocol for NEB 5-alpha competent *E. coli*. Transformants were selected with ampicillin, and plasmids were extracted and verified by restriction enzyme digestion and Sanger sequencing. The sequence-confirmed pLA02::*cysK* and pLA02::*graR* plasmids were introduced into *E. coli* DC10B by electroporation to obtain plasmid DNA suitable for transformation of *S. aureus* [39].

Plasmids amplified in *E. coli* DC10B and verified to be correct were introduced into the corresponding compound 1-resistant mutants by electroporation [40]. At the same time, the pLA02 empty vector was introduced into the VISA wild-type strain and compound 1-resistant mutants using the same procedure as empty-vector controls. *S. aureus* transformants were selected on chloramphenicol-containing selection plates and used for subsequent MIC determination and phenotypic analysis.

ASSOCIATED CONTENT

Supporting Information

AUTHOR'S INFORMATION

Di He E-mail: di.he@hhu.de

Lin Wang E-mail: liwan103@hhu.de

Kristin Schwechel E-mail: Kristin.Schwechel@hhu.de

Tobias Heinen E-mail: heinent@uni-duesseldorf.de

Lasse van Geelen E-mail: Lasse.Geelen@hhu.de

Christopher Janiak E-mail: Janiak@hhu.de

Zhen Liu E-mail: zhenferizi0@sina.com

Rainer Kalscheuer E-mail: rainer.kalscheuer@hhu.de

Funding

This work was financially supported by the China Scholarship Council, the Ministry of Education of China, for a doctoral scholarship awarded to D.H. The Rigaku X-ray diffractometer was funded by the Deutsche Forschungsgemeinschaft (DFG, German Research Foundation) through project number 440366605. We thank the CeMSA@HHU (Center for Molecular and Structural Analytics@Heinrich Heine University) for recording the mass-spectrometric and the NMR-spectroscopic data.

DECLARATION OF COMPETING INTEREST

The authors declare that there is no conflict of interests regarding the publication of this article.

Reference

[1] Henry F. Chambers, et al. Waves of resistance: Staphylococcus aureus in the antibiotic era. *Nature Reviews Microbiology*, 2009, 7(9): 629–641.

[2] Hajo Grundmann, et al. Emergence and resurgence of meticillin-resistant Staphylococcus aureus as a public-health threat. *The Lancet*, 2006, 368(9538): 874–885.

[3] Benjamin P. Howden, et al. Reduced vancomycin susceptibility in Staphylococcus aureus, including vancomycin-intermediate and heterogeneous vancomycin-intermediate strains: resistance mechanisms, laboratory detection, and clinical implications. *Clinical Microbiology Reviews*, 2010, 23(1): 99–139.

[4] Jim O'Neill, et al. Antimicrobial resistance: tackling a crisis for the health and wealth of nations. *Review on Antimicrobial Resistance*, 2014.

[5] Sara E. Cosgrove, et al. The impact of antimicrobial resistance on health and economic outcomes. *Clinical Infectious Diseases*, 2003, 36(11): 1433–1437.

[6] World Health Organization. Antibacterial agents in clinical development: an analysis of the antibacterial clinical development pipeline, including tuberculosis. *World Health Organization*, 2017.

[7] Ursula Theuretzbacher, et al. Resistance drives antibacterial drug development. *Current Opinion in Pharmacology*, 2011, 11(5): 433–438.

[8] Zhiqiang An. Handbook of Industrial Mycology. *CRC Press*, 2004.

[9] Jan L. F. Kock, et al. Bioprospecting for novel oxylipins in fungi: the presence of 3-hydroxy oxylipins in Pilobolus. *Antonie van Leeuwenhoek*, 2001, 80(1): 93–99.

[10] Helge B. Bode, et al. Big effects from small changes: possible ways to explore nature's chemical diversity. *ChemBioChem*, 2002, 3(7): 619–627.

[11] Stefano Romano, et al. Extending the "one strain many compounds" (OSMAC) principle to marine microorganisms. *Marine Drugs*, 2018, 16(7): 244.

[12] Soo-Jin Yang, et al. The Staphylococcus aureus two-component regulatory system, GraRS, senses and confers resistance to selected cationic antimicrobial peptides. *Infection and Immunity*, 2012, 80(1): 74–81.

[13] Mélanie Falord, et al. Investigation of the Staphylococcus aureus GraSR regulon reveals novel links to virulence, stress response and cell wall signal transduction pathways. *PLoS ONE*, 2011, 6(7): e21323.

[14] Dirk Kraus, et al. The GraRS regulatory system controls Staphylococcus aureus susceptibility to antimicrobial host defenses. *BMC Microbiology*, 2008, 8: 85.

[15] Barbara Campanini, et al. Moonlighting O-acetylserine sulfhydrylase: new functions for an old protein. *Biochimica et Biophysica Acta*, 2015, 1854(9): 1184–1193.

[16] Zhiliang Yu, et al. Antibacterial mechanisms of polymyxin and bacterial resistance. *BioMed Research International*, 2015, 2015: 679109.

[17] Adree Khondker, et al. How do bacterial membranes resist polymyxin antibiotics? *Communications Biology*, 2020, 3: 77.

[18] Feng Wang, et al. Insights into key interactions between vancomycin and bacterial cell wall structures. *ACS Omega*, 2018, 3(1): 37–45.

[19] Holger Schedletzky, et al. The effect of moxifloxacin on its target topoisomerases from Escherichia coli and Staphylococcus aureus. *Journal of Antimicrobial Chemotherapy*, 1999, 43(Suppl. B): 31–37.

[20] Joshua A. F. Sutton, et al. Staphylococcus aureus cell wall structure and dynamics during host-pathogen interaction. *PLoS Pathogens*, 2021, 17(3): e1009468.

[21] David Cue, et al. Genetic regulation of the intercellular adhesion locus in staphylococci. *Frontiers in Cellular and Infection Microbiology*, 2012, 2: 38.

[22] Subrata Sau, et al. Molecular characterization and transcriptional analysis of type 8 capsule genes in Staphylococcus aureus. *Journal of Bacteriology*, 1997, 179(5): 1614–1621.

[23] Julia Kjer, et al. Methods for isolation of marine-derived endophytic fungi and their bioactive secondary products. *Nature Protocols*, 2010, 5(3): 479–490.

[24] Mohamed S. Elnaggar, et al. Hydroquinone derivatives from the marine-derived fungus Gliomastix sp. *RSC Advances*, 2017, 7(49): 30640–30649.

[25] Claude S. Hudson, et al. Indirect measurements of the rotatory powers of some alpha and beta forms of the sugars by means of solubility experiments. *Journal of the American Chemical Society*, 1917, 39(5): 1013–1038.

[26] Clinical and Laboratory Standards Institute. Methods for dilution antimicrobial susceptibility tests for bacteria that grow aerobically. CLSI standard M07. *Clinical and Laboratory Standards Institute*, 2024.

[27] Paul C. Fuchs, et al. Daptomycin susceptibility tests: interpretive criteria, quality control, and effect of calcium on in vitro tests. *Diagnostic Microbiology and Infectious Disease*, 2000, 38(1): 51–58.

[28] Nidja Rehberg, et al. Nature-inspired (di)azine-bridged bisindole alkaloids with potent antibacterial in vitro and in vivo efficacy against methicillin-resistant Staphylococcus aureus. *Journal of Medicinal Chemistry*, 2020, 63(21): 12623–12641.

[29] Dieter Meier, et al. The plant-derived chalcone Xanthoangelol targets the membrane of Gram-positive bacteria. *Bioorganic & Medicinal Chemistry*, 2019, 27(23): 115151.

[30] Yaogang Hu, et al. Lipidated peptidomimetics with improved antimicrobial activity. *ACS Medicinal Chemistry Letters*, 2012, 3(8): 683–686.

[31] Lisa Friedman, et al. Genetic changes that correlate with reduced susceptibility to daptomycin in Staphylococcus aureus. *Antimicrobial Agents and Chemotherapy*, 2006, 50(6): 2137–2145.

[32] Lasse van Geelen, et al. Natural brominated phenoxyphenols kill persistent and biofilm-incorporated cells of MRSA and other pathogenic bacteria. *Applied Microbiology and Biotechnology*, 2020, 104(13): 5985–5998.

[33] Kelsey L. Krausz, et al. Rapid isolation of DNA from Staphylococcus. *Methods in Molecular Biology*, 2016, 1373: 59–62.

[34] Gani Orhan, et al. Synergy tests by E test and checkerboard methods of antimicrobial combinations against Brucella melitensis. *Journal of Clinical Microbiology*, 2005, 43(1): 140–143.

[35] Michael H. Hsieh, et al. Synergy assessed by checkerboard: a critical analysis. *Diagnostic Microbiology and Infectious Disease*, 1993, 16(4): 343–349.

[36] Nilesh N. Mishra, et al. Phenotypic and genotypic characterization of daptomycin-resistant methicillin-resistant Staphylococcus aureus strains: relative roles of mprF and dlt operons. *PLoS ONE*, 2014, 9(9): e107426.

[37] April M. Lewis, et al. Quantitative real-time PCR workflow for analyzing Staphylococcus aureus gene expression. *Methods in Molecular Biology*, 2016, 1373: 143–154.

[38] Emmanuelle Charpentier, et al. Novel cassette-based shuttle vector system for gram-positive bacteria. *Applied and Environmental Microbiology*, 2004, 70(10): 6076–6085.

[39] Ian R. Monk, et al. Transforming the untransformable: application of direct transformation to manipulate genetically Staphylococcus aureus and Staphylococcus epidermidis. *mBio*, 2012, 3(2): e00277-11.

[40] Steve Schenk, et al. Improved method for electroporation of Staphylococcus aureus. *FEMS Microbiology Letters*, 1992, 94(1–2): 133–138.

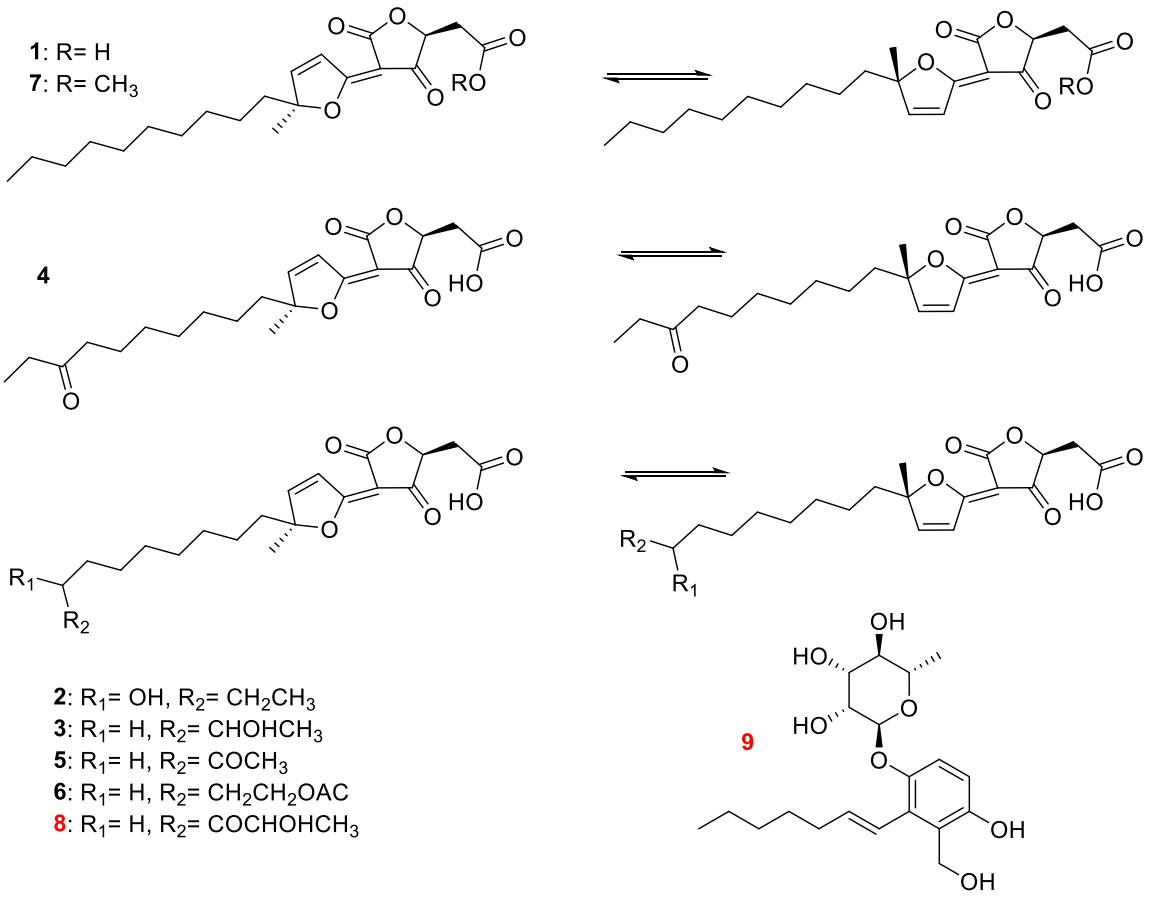


Figure 1. Structure of compounds **1**–**9**

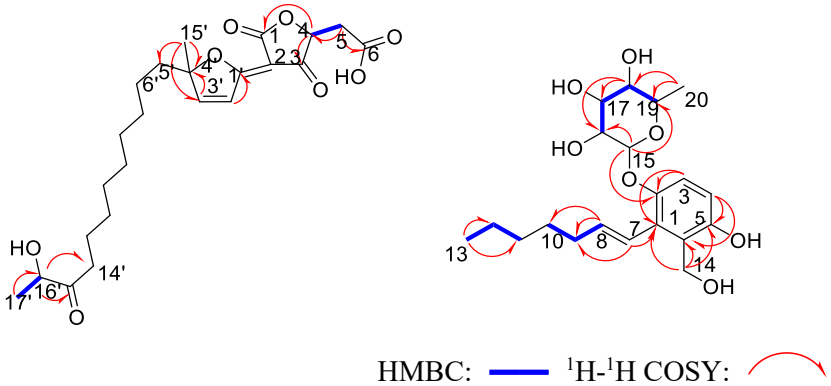


Figure 2. Key correlations of new compounds **8** and **9**

Table 1. ^{1}H and ^{13}C NMR data for **8** and **9** (600 and 125 MHz, TMS, δ in ppm, J in Hz).

Compound 8 ($CDCl_3$)			Compound 9 (MeOH-d_4)		
Position	**δC**	**δH (mult., J in Hz)**	**Position**	**δC**	**δH (mult., J in Hz)**
1	171.9		1	129.2	
2			2	150.4	
3	195.8		3	115.7	6.91, d (8.59)
4	78.4	4.87, m	4	116.2	6.71, d (10.07)
5	35.6	2.83	5	150.0	
6	172.3		6	128.4	
1'	179.4		7	124.5	6.51, dt
	180.0		8	138.3	6.24, dt
2'	123.5	7.55, d (6.82)	9	34.8	2.26, m
	123.6	7.50, d (5.61)	10	29.8	1.51
3'	160.4	7.45, d (5.61)	11	32.6	1.39
	160.5	7.41, dd (1.22, 1.25)	12	23.6	1.36
4'	101.9		13	14.3	0.94
	102.5		14	57.5	4.65
5'	37.9	1.92, td	15	100.8	5.27, d (1.80)
		2.02, s	16	71.4	4.08, dd (1.96, 1.84)
6'	23.8	1.24, m	17	72.6	3.91, dd (4.50, 5.10)
7'–11'	23–29		18	73.8	3.46, d (8.97)
12'	35.1		19	70.2	3.75, d (5.56)
13'	71.1		20	17.8	1.26, d (4.85)
14'	171.8				
15'	23.2	1.61, s			
16'	20.0	1.19, dt			
17'	21.3	2.04, s			

Table 2. Minimum inhibitory concentrations (MICs) of compounds **1**–**9**.

	MIC (μM)								
Strain	**1**	**2**	**3**	**4**	**5**	**6**	**7**	**8**	**9**
S. aureus ATCC 29213	25	n	n	n	n	n	25	n	n
S. aureus USA300	25	-	-	-	-	-	-	-	-
S. aureus ATCC 700699	6.25	n	n	n	n	100	6.25	n	n
E. faecalis ATCC 29212	50	n	n	n	n	n	100	n	n
E. faecalis ATCC 51299	25	n	n	n	n	n	50	n	n
E. faecium ATCC 35667	25	n	n	n	n	100	50	n	n
E. faecium ATCC 700221	25	n	n	n	n	n	12.5	n	n
E. coli ATCC 25922	n	n	n	n	n	n	100	n	n
S. pneumoniae ATCC 49619	n	n	n	n	n	n	n	n	n
C. albicans	n	n	n	n	n	n	n	n	n
M. tuberculosis H37Rv	n	n	n	n	n	n	n	n	n

n, not active (MIC > 100 μM); -, not tested.

Table 3. Selectivity indices of compounds 1 and 7.

Human cell line	**IC_{50} (μM)**		**SI**	
	1	**7**	**1**	**7**
HEK-293	45.5	18.6	7.28	3
HUH-7	>100	41.1	>10	6.6
THP-1	42.0	7.8	6.72	1.3
CLS-54	45.6	0.71	7.29	0.1
H-4	>100	22.5	>10	3.6

MIC_{90} values were 6.25 μM and 6.25 μM for compounds 1 and 7, respectively; SI = IC_{50}/MIC_{90}.

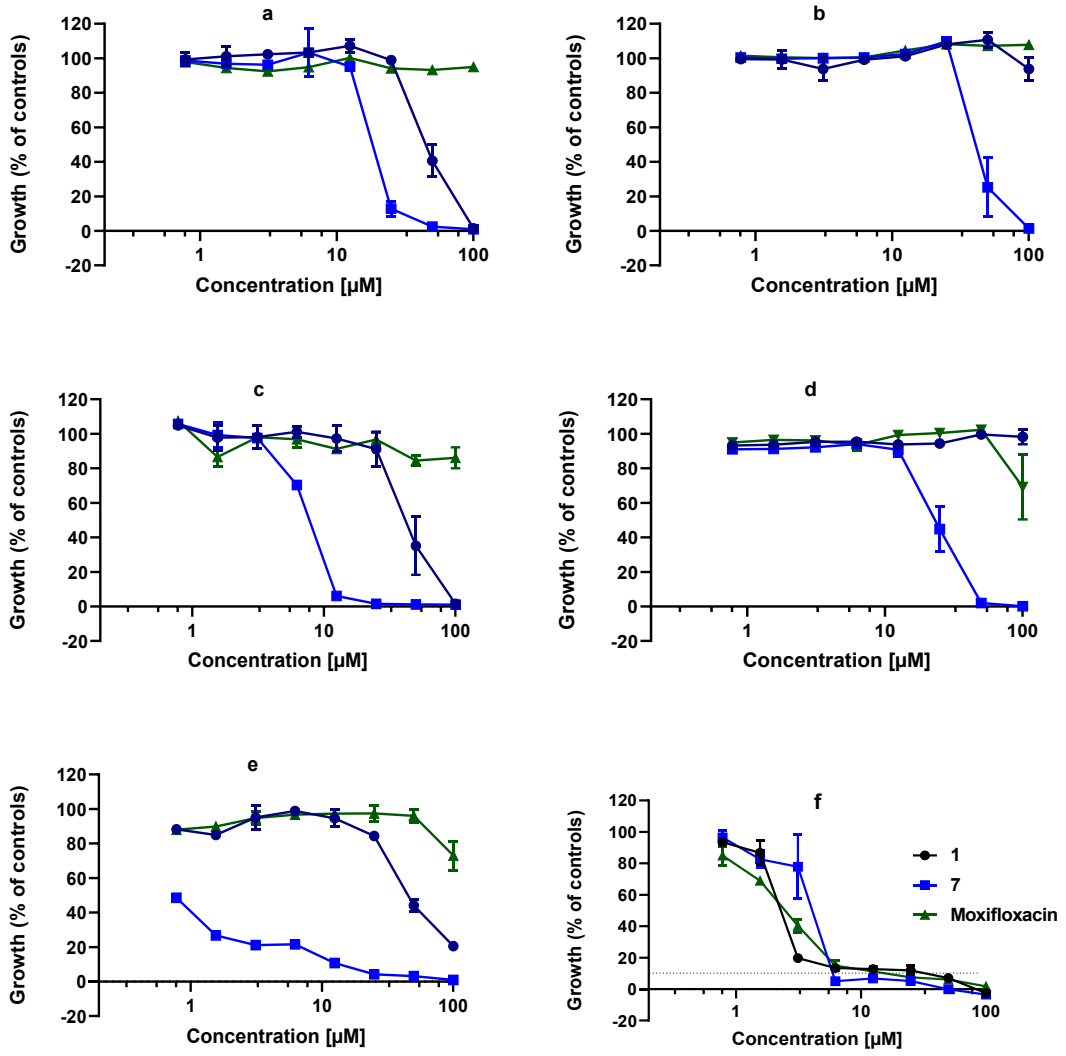


Figure 3: Cytotoxicity of compounds **1** and **7** against different human cell lines. Cell viability after treatment was determined by measuring metabolic activity employing resazurin reduction assay. a: HEK-293; b: HUH-7; c: THP-1; d: H-4; e: CLS-54. f: Antibacterial dose-response of compounds **1** and **7** against to MRSA cells.

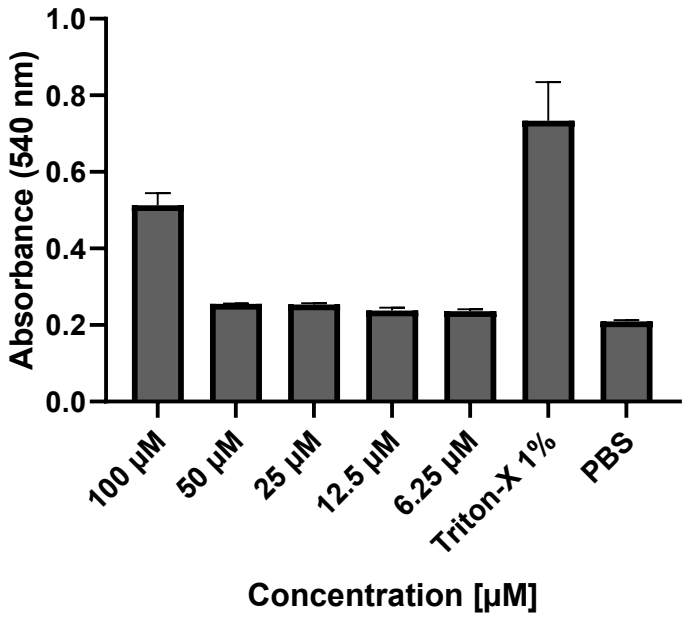


Figure 4: Hemolytic activity of compound **1** (pestalotic acid A). Defibrinated sheep red blood cells were treated at the indicated concentrations. Release of hemoglobin in cell-free supernatatnts was quantified by measuring absorbance at 540 nm. Triton-X (1%) and PBS were used as positive or negative control, respectively.

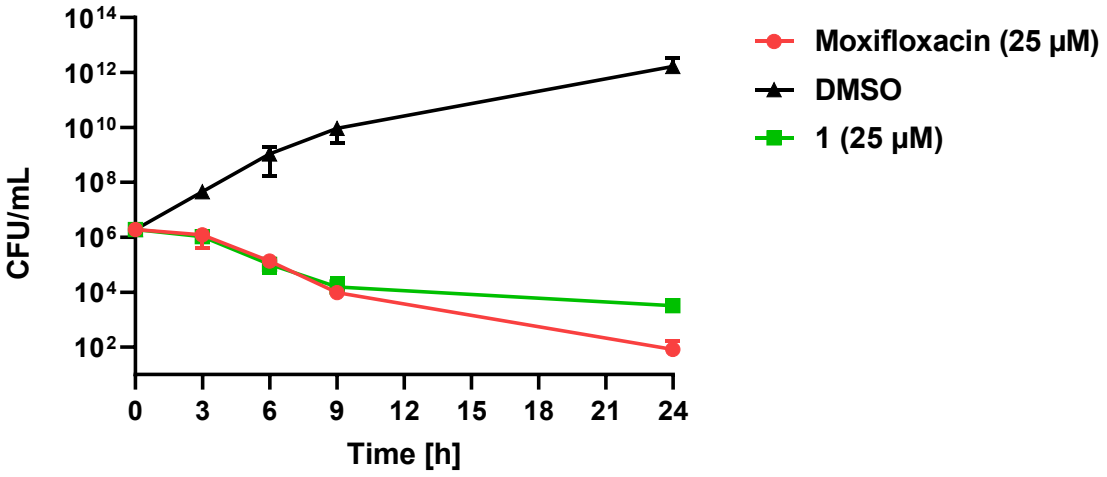


Figure 5: Time-kill kinetics of compound **1** (pestalotic acid A). Initial cell density was 10^6 CFU/mL. Cells were treated with compounds at the indicated concentrations for 24 hours. Aliquots taken at different time points after addition of compounds were serially diluted and plated on solid media for colony forming unit (CFU) counting.

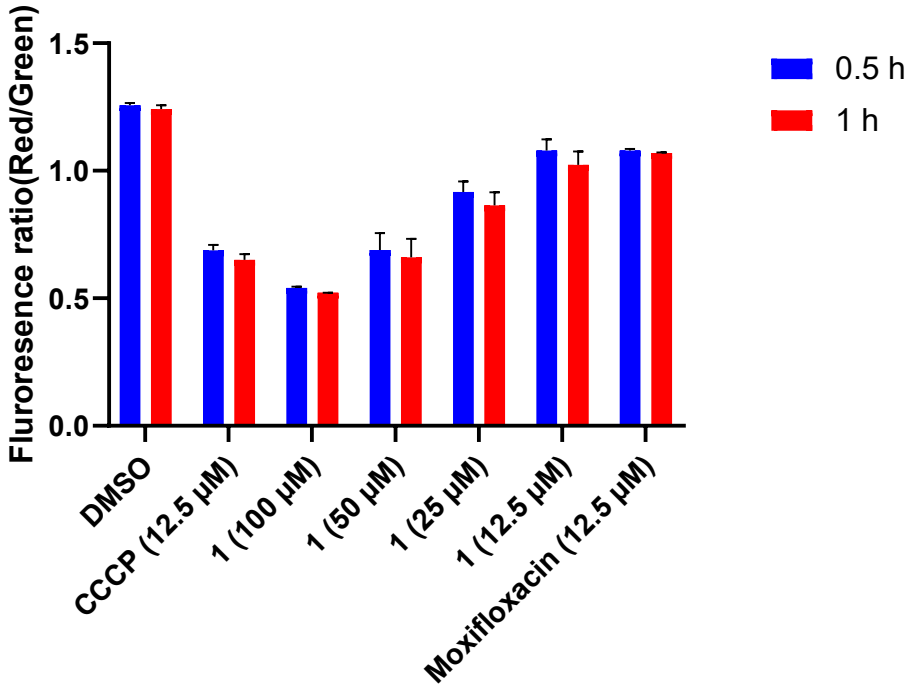


Figure 6. Effect of compound 1 on the membrane potential of VISA. The effect of compound **1** on the membrane potential of VISA was concentration-dependent. Treatment with 100 μM and 50 μM of compound **1** resulted in a significant decrease in the red/green fluorescence ratio, indicating cell membrane depolarization; treatment with 25 μM caused only a slight decrease, while the 12.5 μM treatment groups were similar to the DMSO and moxifloxacin controls, with no obvious membrane depolarization observed. These results indicate that the significant effect of compound **1** on membrane potential primarily occurs at concentrations above the MIC.

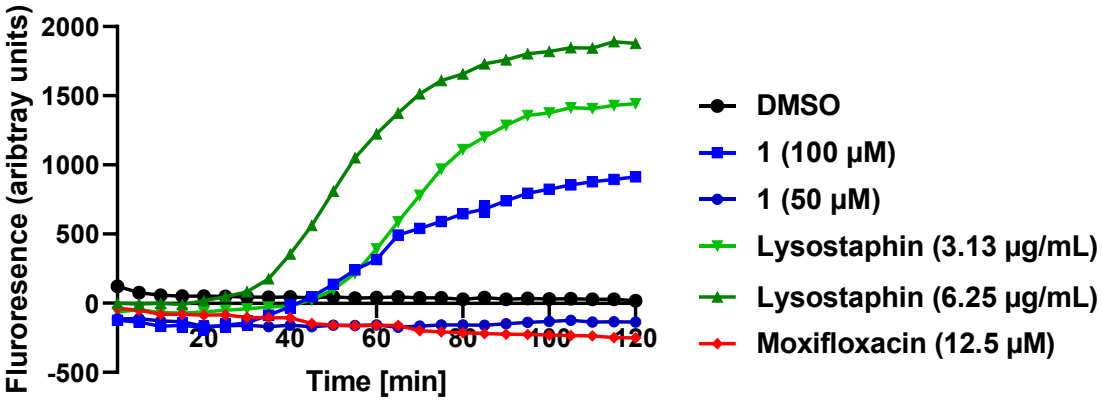


Figure 7. Effect of compound 1 on the membrane permeability of VISA. The effect of compound **1** on the membrane permeability of VISA primarily occurs under high-concentration conditions. After treatment with 100 μM of compound **1**, the PI fluorescence signal gradually increased after approximately 50–60 min and reached a relatively high level at 120 min, indicating an increase in cell membrane permeability. In contrast, the PI fluorescence signal of the 50 μM compound **1** treatment group essentially remained near the baseline. These results demonstrate that compound **1** does not exert a rapid, lytic membrane-disrupting effect, but rather induces increased membrane permeability at higher concentrations and prolonged treatment times.

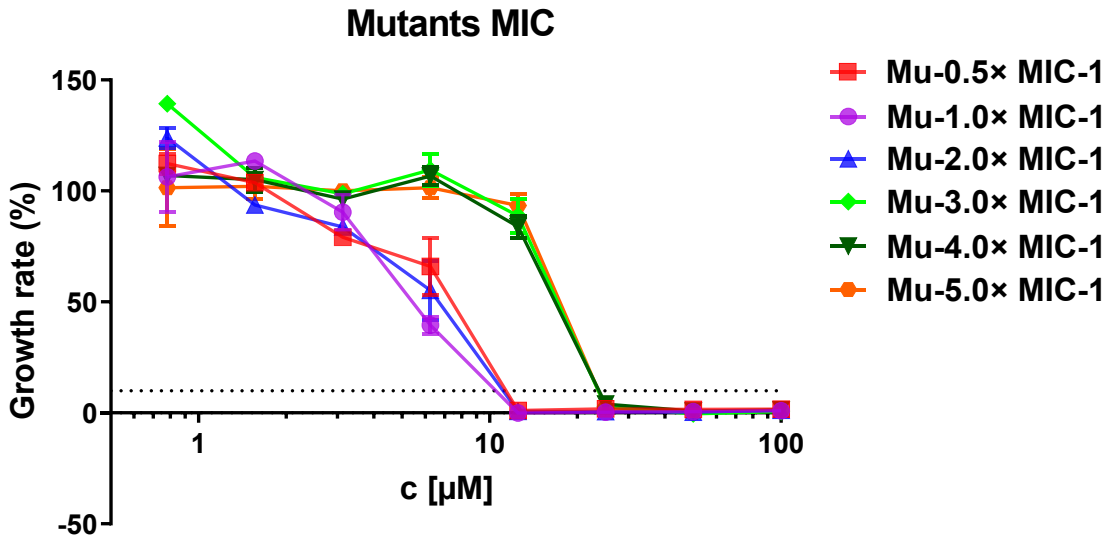


Figure 8. Reduced susceptibility of VISA mutants to compound 1 after serial drug-pressure selection. After serial drug-pressure selection in liquid media, VISA mutants with reduced susceptibility to compound **1** were obtained. The MIC of compound **1** against mutants obtained from the 0.5×, 1×, and 2× MIC pressure stages was 12.5 μM; the MIC of mutants obtained from the 3×, 4×, and 5× MIC pressure stages increased to 25 μM. These results indicate that continuous drug pressure can gradually reduce the susceptibility of VISA to compound **1**, and the MIC of the mutants increases as the selection pressure intensifies.

Table 4. MIC comparison of antibiotics against VISA and the Mu2

Antibiotic	MIC		MIC change (fold)
	VISA (μM)	Mu2 (μM)	
Daptomycin	0.78	0.05	16
Polymyxin B	50	1.56	32
Colistin	200	6.25	32
Vancomycin	25	1.56	16

Table 5. Checkerboard assay of 1 in combination with antibiotics against VISA

Test compound	Antibiotic	FICI	Interaction
1	Polymyxin B	0.25	Synergy
1	Colistin	0.25	Synergy
1	Vancomycin	0.38	Synergy
1	Moxifloxacin	1	No interaction

Note: FICI, fractional inhibitory concentration index; FICI ≤ 0.5 indicates synergy; 0.5 < FICI ≤ 1 indicates partial synergy or additivity; 1 < FICI ≤ 4 indicates no interaction; FICI > 4 indicates antagonism.

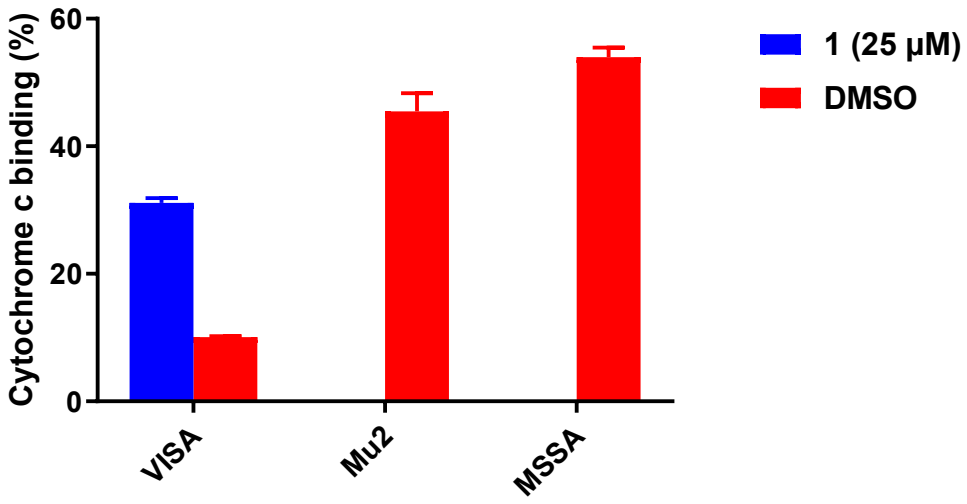


Figure 9. Changes in cytochrome c binding capacity of VISA, Mu2, and MSSA. DMSO-treated VISA showed a low cytochrome c binding rate, whereas MSSA exhibited a higher basal binding rate. After treatment with compound **1**, the cytochrome c binding rate of VISA increased, suggesting an alteration in its cell surface charge state. The Mu2 exhibited a high cytochrome c binding rate even under untreated conditions. These results indicate that the cell surface charge state of Mu2 differs from that of the parental VISA, potentially manifesting as enhanced surface electronegativity or reduced levels of positive charge modifications. Cytochrome c binding capacity is commonly used to reflect changes in the net negative surface charge of *S. aureus*; therefore, these results support that the compound **1** resistance phenotype is associated with altered cell surface charge regulation [13,35].

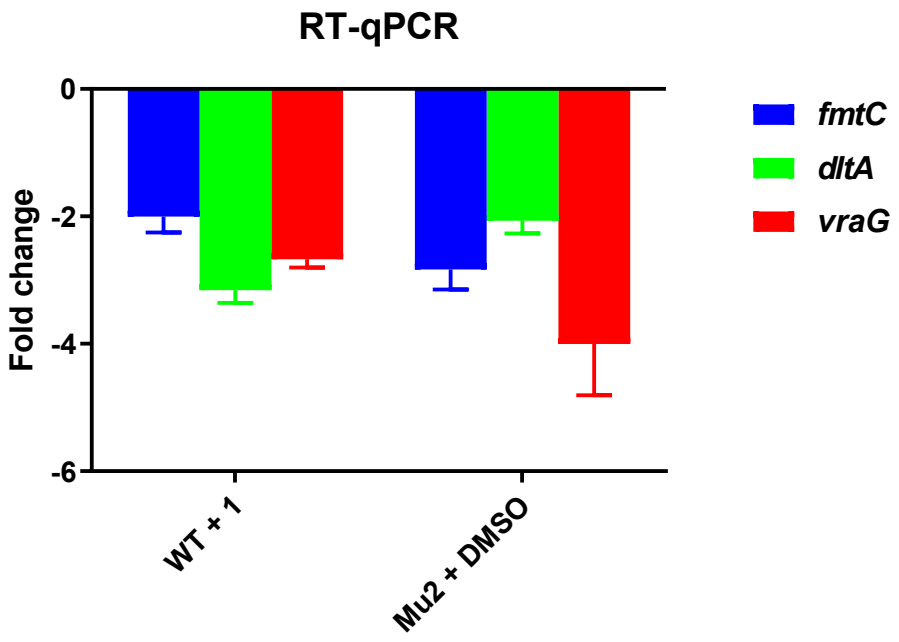


Figure 10. Expression changes of GraRS downstream-related genes after compound 1 treatment and in Mu2. After compound **1** treatment, the expression of *fmtC*, *dltA*, and *vraG* in VISA was significantly downregulated. Mu2 also exhibited low expression profiles for these genes under DMSO treatment conditions, among which *vraG* showed the most significant downregulation. These results indicate that both the action of compound **1** and the resistance phenotype are accompanied by a decreased expression of GraRS downstream-related cell envelope regulatory genes. Because *fmtC/mprF*, *dltA*, and *vraG* are all associated with *S. aureus* cell surface charge modification and cell envelope defense, these results further support the connection between compound **1** and GraRS-related cell envelope homeostasis regulation [11–13].

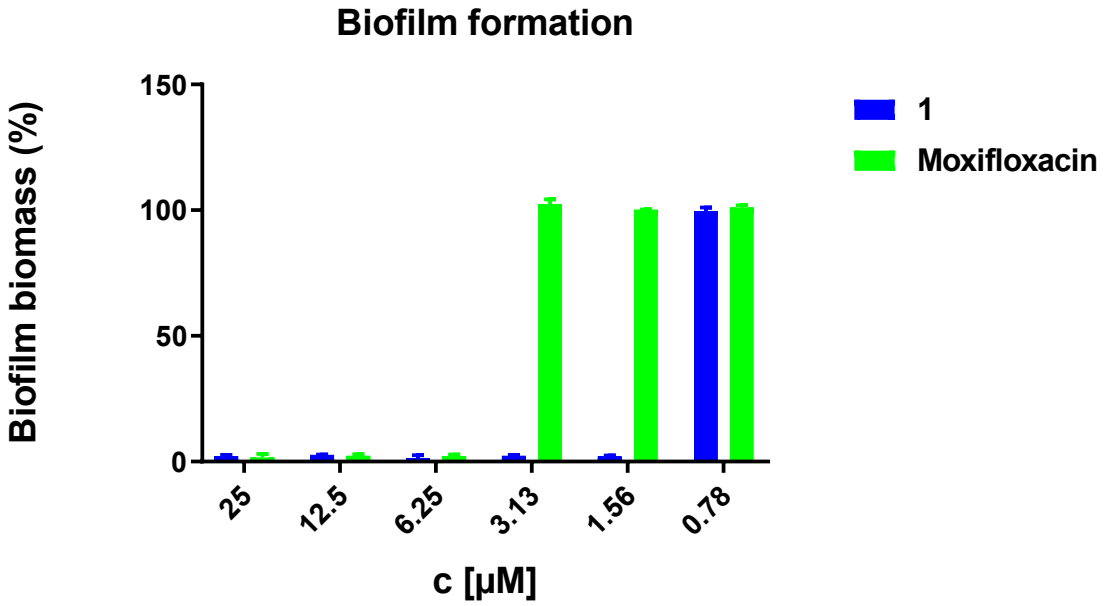


Figure 11. Inhibition of VISA biofilm formation by compound 1. Compound **1** exhibited a significant inhibitory effect on the biofilm formation of VISA. Under conditions of 25, 12.5, and 6.25 µM, VISA biofilm formation was almost completely inhibited; at the sub-MIC concentrations of 3.13 and 1.56 µM, compound **1** still significantly reduced the level of biofilm formation. In contrast, the inhibitory effect of moxifloxacin on biofilm formation was noticeably diminished at sub-MIC concentrations. These results indicate that the anti-biofilm effect of compound **1** is not completely dependent on the inhibition of planktonic cell growth.

Supporting information

Studies on the Antibacterial Activity of the Natural Product Pestalotic acid A against vancomycin-intermediate *Staphylococcus aureus*

Di He [a¶], Lin Wang [a¶], Kristin Schwechel [a], Tobias Heinen [b], Lasse van Geelen [a], Christoph Janiak [b], Zheng Liu [c], Rainer Kalscheuer [a *]

a. Institute of Pharmaceutical Biology and Biotechnology, Heinrich Heine University Universitätsstrasse 1, 40225 Düsseldorf, Germany

b. Institute of Inorganic and Structural Chemistry, Heinrich Heine University Düsseldorf, Universitätsstrasse 1, 40225 Düsseldorf, Germany

c. Key Laboratory of Study and Discovery of Small Targeted Molecules of Hunan Province, School of Medicine, Hunan Normal University, Changsha 410013, China

¶ These authors contributed equally

*Corresponding author.

CONTENT

Table S1. Mutations identified in compound **1**-resistant VISA mutants. 62
Table S2. Upregulated proteins in VISA after compound **1** treatment. 62
Table S3. Downregulated proteins in VISA after compound **1** treatment. 64
Table S4. Primers list 66
Figure S1. Growth kinetics of compound **1** 67
Figure S2. MICs of clones obtained from single-step mutant selection 67
Figure S3. Result of polymyxin B binding cytochrome c 67
Figure S4. MICs of compound 1 and moxifloxacin against the VISA WT+pLA02. 68
Figure S5. MICs of **1**, vancomycin, polymyxin B and moxifloxacin against the Mu2 + pLA02. 68
Figure S6. MICs of **1**, vancomycin, polymyxin B and moxifloxacin against the Mu2 + pLA02::*cysK*. 68
Figure S7. MICs of **1**, vancomycin, polymyxin B and moxifloxacin against the Mu2 + pLA02::*graR*. 68
Figure S8. HREISMS of compound **8** 69
Figure S9. ^{1}H NMR of compound **8** 70
Figure S10. ^{13}C NMR of compound **8** 70
Figure S11. HSQC of compound **8** 71
Figure S12. HMBC of compound **8** 71
Figure S13. ^{1}H-^{1}H COSY of compound **8** 72
Figure S14. ROESY of compound **8** 72
Figure S15. HREISMS of compound **9** 73
Figure S16. ^{1}H NMR of compound **9** 74
Figure S17. ^{13}C NMR of compound **9** 74
Figure S18. HSQC of compound **9** 75
Figure S19. HMBC of compound **9** 75
Figure S20. ^{1}H-^{1}H COSY of compound **9** 76
Figure S21. ROESY of compound **9** 76
Figure S22. UV absorption of compound **8** 77
Figure S23. UV absorption of compound **9** 77

Table S1. Mutations identified in compound **1**-resistant VISA mutants.

Strain	Mutations
Mu1	SAV0188: A530T, SAV0513: ΔLAGI264–267, SAV0659: R200*, SAV1434: insertion at aa 5169–5178, SAV2041: E14K, SAV2113: Y61D
Mu2	SAV0513: T77P, SAV0659: K17*, SAV0970: E210K, SAV1202: M234I, SAV2019: N50K, SAV2019: L3I
Mu3	SAV0513: ΔLAGI264–267, SAV0659: frameshift after aa 168, stop at aa 183, SAV1156: K123*

Table S2. Upregulated proteins in VISA after compound **1** treatment.

Protein ID	Protein name	Gene	Protein description
P67406	URE2_STAAM	*ureB*	Urease subunit beta
Q99SG2	SCED_STAAM	*sceD*	Probable transglycosylase SceD
A0A0H3JTC8	A0A0H3JTC8	SAV0421	Putative nucleoside-diphosphate-sugar epimerase
A0A0H3JT62	A0A0H3JT62	SAV2287	Similar to urea transporter
P63189	GRPE_STAAM	*grpE*	Protein GrpE
A0A0H3K0M	A0A0H3K0M	SAV2205	MAP domain-containing protein
A0A0H3JQH	A0A0H3JQH	SAV0707	Uncharacterized protein
A0A0H3JWE	A0A0H3JWE	SAV2033	Similar to nitroreductase family protein
Q932F7	SDRE_STAAM	*sdrE*	Serine-aspartate repeat-containing protein E
A0A0H3JY17	A0A0H3JY17	SAV0885	Phage terminase, small subunit
A0A0H3JUF4	A0A0H3JUF4	SAV0898	Phage major tail protein, TP901-1 family
Q99VV3	SARX_STAAM	*sarX*	HTH-type transcriptional regulator SarX
Q99QY4	SRAP_STAAM	*sraP*	Serine-rich adhesin for platelets
P60184	MECA_STAAM	*mecA*	Adapter protein MecA
Q932L5	MECI_STAAM	*mecI*	Methicillin resistance regulatory protein MecI
Q99RX9	UREG_STAAM	*ureG*	Urease accessory protein UreG
A0A0H3JUC4	A0A0H3JUC4	SAV2530	L-serine dehydratase
Q99VQ4	LTAS_STAAM	*ltaS*	Lipoteichoic acid synthase
Q99VB5	CLPB_STAAM	*clpB*	Chaperone protein ClpB
Q99SN8	LUKL1_STAAM	SAV2004	Uncharacterized leukocidin-like protein 1
P68799	FIB_STAAM	*fib*	Fibrinogen-binding protein
A0A0H3JQK	A0A0H3JQK	SAV0789	DUF1474 family protein
P63785	CLPP_STAAM	*clpP*	ATP-dependent Clp protease proteolytic subunit
P67403	URE1_STAAM	*ureC*	Urease subunit alpha
A0A0H3K09	A0A0H3K09	SAV1988	Phi PVL orf 39-like protein
P0A0A9	MECR_STAAM	*mecR1*	Methicillin resistance mecR1 protein
Q932K5	AZOR_STAAM	*azoR*	FMN-dependent NADH:quinone oxidoreductase
A0A0H3JUK	A0A0H3JUK	SAV0981	MAP domain-containing protein
A0A0H3JTM	A0A0H3JTM	SAV2705	HTH cro/C1-type domain-containing protein
A0A0H3JP53	A0A0H3JP53	SAV0171	DUF4242 domain-containing protein
A0A0H3JNR	A0A0H3JNR	SAVP006	Lipoprotein
A0A0H3JSV7	A0A0H3JSV7	*ureD*	Urease accessory protein
P67718	URE3_STAAM	*ureA*	Urease subunit gamma
A0A0H3JTR5	A0A0H3JTR5	SAV2552	Similar to antibiotic transport-associated protein homolog ydfJ
A0A0H3JQP	A0A0H3JQP	SAV0897	Phage protein
A0A0H3JQ0	A0A0H3JQ0	*set14*	Exotoxin 14
Q99UX1	ISDE_STAAM	*isdE*	High-affinity heme uptake system protein IsdE
A0A0H3JP63	A0A0H3JP63	SAVP010	Uncharacterized protein
A0A0H3JTC6	A0A0H3JTC6	tst	Toxic shock syndrome toxin-1
Q99RY0	UREF_STAAM	*ureF*	Urease accessory protein UreF

Protein ID	Protein name	Gene	Protein description
P64407	DNAK_STAAM	*dnaK*	Chaperone protein DnaK
Q931I5	LUKL2_STAAM	SAV2005	Uncharacterized leukocidin-like protein 2
Q99RY1	UREE_STAAM	*ureE*	Urease accessory protein UreE
A0A0H3JSZ2	A0A0H3JSZ2	SAV2353	Similar to multidrug resistance protein A
A0A0H3JXF6	A0A0H3JXF6	SAV2522	VOC domain-containing protein
A0A0H3JSM	A0A0H3JSM	*fmtB#mrp*	FmtB protein
A0A0H3JWT	A0A0H3JWT	SAV2259	DNA repair/chromosome segregation ATPase
A0A0H3JPM	A0A0H3JPM	SAV0229	Staphylococcal complement inhibitor
A0A0H3JP29	A0A0H3JP29	SAV0144	DNA-binding protein
P65645	ISAA_STAAM	*isaA*	Probable transglycosylase IsaA
A0A0H3JR62	A0A0H3JR62	SAV1110	DUF2197 domain-containing protein
A0A0H3JUE3	A0A0H3JUE3	SAV0893	Phi Mu50B-like protein
Q99RX4	SSAA2_STAAM	*ssaA2*	Staphylococcal secretory antigen ssaA2
A0A0H3JR26	A0A0H3JR26	SAV1038	Similar to ferrichrome ABC transporter
A0A0H3K14	A0A0H3K14	SAV2531	L-serine deaminase
A0A0H3JQQ	A0A0H3JQQ	SAV0434	FKLRK protein
A0A0H3JUK	A0A0H3JUK	SAV2644	Similar to autolysin
A0A0H3JX6	A0A0H3JX6	*hlgB*	Gamma-hemolysin component B
A0A0H3JUR	A0A0H3JUR	SAV1050	Acyltransferase 3 domain-containing protein
A0A0H3JP68	A0A0H3JP68	SAVP015	Uncharacterized protein
A0A0H3JQP	A0A0H3JQP	SAV0855	Similar to anti-repressor
A0A0H3JUX	A0A0H3JUX	SAV1155	Fibrinogen-binding protein
A0A0H3JQG	A0A0H3JQG	SAV0465	Probable autolysin (N-acetylmuramoyl-L-alanine amidase)
A0A0H3JWZ	A0A0H3JWZ	SAV2332	HTH lysR-type domain-containing protein
A0A0H3JUV	A0A0H3JUV	SAV1003	Globin
Q99W47	SDRD_STAAM	*sdrD*	Serine-aspartate repeat-containing protein D
A0A0H3JUL8	A0A0H3JUL8	*appF*	Oligopeptide transport system ATP-binding protein AppF homologue
P0A071	HLGA_STAAM	*hlgA*	Gamma-hemolysin component A
A0A0H3JQN	A0A0H3JQN	SAV0887	Phage portal protein
A0A0H3JP97	A0A0H3JP97	*uhpT*	Hexose phosphate transport protein
A0A0H3JPK2	A0A0H3JPK2	SAVP018	YolD-like family protein
P60641	LRGB_STAAM	*lrgB*	Antiholin-like protein LrgB
A0A0H3K11	A0A0H3K11	SAV2483	Cytosolic protein
Q99RL1	HLGC_STAAM	*hlgC*	Gamma-hemolysin component C
A0A0H3JZW	A0A0H3JZW	SAV1755	Putative flavoprotein
A0A0H3JTP6	A0A0H3JTP6	SAV2532	Regulatory protein pfoR
A0A0H3JQN	A0A0H3JQN	SAV0835	Toprim domain-containing protein
A0A0H3K1A	A0A0H3K1A	SAV2651	Accessory Sec system protein Asp2
A0A0H3JZ3	A0A0H3JZ3	*ftsL*	Cell division protein FtsL
A0A0H3JQV	A0A0H3JQV	*vraG*	ABC transporter permease
P0A012	CH10_STAAM	*groES*	Co-chaperonin GroES
Q932A8	SSB2_STAAM	*ssb-p*	Single-stranded DNA-binding protein 2
P68811	NRDI_STAAM	*nrdI*	Protein NrdI
A0A0H3JTB0	A0A0H3JTB0	SAV2510	DUF2188 domain-containing protein
Q7A2K8	SSAA1_STAAM	*ssaA1*	Staphylococcal secretory antigen ssaA1
A0A0H3JSF7	A0A0H3JSF7	SAV2032	Membrane anchored protein
A0A0H3JTF5	A0A0H3JTF5	SAV2410	DUF4467 domain-containing protein
Q99WV0	LYTM_STAAM	*lytM*	Glycyl-glycine endopeptidase LytM

Note: Protein IDs, protein names, gene names, and protein descriptions were summarized from the proteomic dataset.

Table S3. Downregulated proteins in VISA after compound **1** treatment.

Protein ID	Protein name	Gene	Protein description
Q932I8	TETM_STAAM	*tetM*	Tetracycline resistance protein TetM
A0A0H3JPH4	A0A0H3JPH4	*capE*	UDP-glucose 4-epimerase
A0A0H3JWY	A0A0H3JWY	*capI*	Capsular polysaccharide synthesis enzyme Cap5I
A0A0H3JT56	A0A0H3JT56	SAV2443	2-dehydropantoate 2-reductase
A0A0H3JSP8	A0A0H3JSP8	*capG*	Capsular polysaccharide synthesis enzyme Cap5G
A0A0H3JXI0	A0A0H3JXI0	SAV0413	DNA 3'-5' helicase
A0A0H3JX43	A0A0H3JX43	*narG*	Nitrate reductase (quinone)
A0A0H3JWX	A0A0H3JWX	SAV2315	Similar to transcription regulator RpiR family
A0A0H3JTN3	A0A0H3JTN3	SAV2514	Probable transport protein
P67343	ADPRH_STAAM	SAV0325	Protein-ADP-ribose hydrolase
A0A0H3JQ9	A0A0H3JQ9	SAV0368	Abi family protein
A0A0H3JTE1	A0A0H3JTE1	SAV2395	Similar to nitrate reductase delta chain
A0A0H3JT16	A0A0H3JT16	*narH*	Nitrate reductase beta chain
A0A0H3JXX3	A0A0H3JXX3	SAV0584	Cationic amino acid transporter
Q99RK7	BIOB_STAAM	*bioB*	Biotin synthase
A0A0H3JW3	A0A0H3JW3	SAV1883	Similar to transporter
Q7A2W7	VRAX_STAAM	*vraX*	Protein VraX
A0A0H3JWY	A0A0H3JWY	*capN*	Capsular polysaccharide synthesis enzyme Cap5N
A0A0H3JSY2	A0A0H3JSY2	SAV2329	Similar to amino acid amidohydrolase
A0A0H3JWX	A0A0H3JWX	*capD*	Capsular polysaccharide synthesis enzyme Cap5D
A0A0H3JU94	A0A0H3JU94	SAV0838	Similar to ABC transporter, permease protein homolog
A0A0H3JNY	A0A0H3JNY	SAV0088	Similar to sulfide-quinone reductase
A0A0H3JVD4	A0A0H3JVD4	SAV1367	Anthranilate synthase component 1
Q99RQ5	FENR_STAAM	SAV2372	Ferredoxin--NADP reductase
A0A0H3JX36	A0A0H3JX36	SAV2390	Putative transcriptional regulator
A0A0H3JTP3	A0A0H3JTP3	SAV2183	DUF2273 domain-containing protein
A0A0H3JT40	A0A0H3JT40	*bioD*	ATP-dependent dethiobiotin synthetase BioD
A0A0H3JPW	A0A0H3JPW	*capM*	Capsular polysaccharide synthesis enzyme Cap5M
A0A0H3JPN	A0A0H3JPN	SAV0250	Sorbitol dehydrogenase homologue
A0A0H3JT87	A0A0H3JT87	SAV0372	PepSY domain-containing protein
A0A0H3JRP3	A0A0H3JRP3	SAV1026	Competence transcription factor
A0A0H3JXR	A0A0H3JXR	SAV2660	peptide-methionine (S)-S-oxide reductase
A0A0H3K0V	A0A0H3K0V	*narI*	Nitrate reductase gamma chain
Q99QV7	Y2684_STAAM	SAV2684	Putative ABC transporter ATP-binding protein SAV2684
P64348	HIS1_STAAM	*hisG*	ATP phosphoribosyltransferase
A0A0H3JTG8	A0A0H3JTG8	*bioA*	Adenosylmethionine-8-amino-7-oxononanoate aminotransferase
A0A0H3JU1	A0A0H3JU1	nasF	uroporphyrinogen-III C-methyltransferase
P64375	ACUC_STAAM	*acuC*	Acetoin utilization protein AcuC
A0A0H3JUG	QUEH_STAAM	*queH*	Epoxyqueuosine reductase QueH
Q99SJ1	ILVA_STAAM	*ilvA*	L-threonine dehydratase biosynthetic IlvA
A0A0H3JPH	A0A0H3JPH	*capJ*	Capsular polysaccharide synthesis enzyme Cap5J
Q99QX2	ICAB_STAAM	*icaB*	Poly-beta-1,6-N-acetyl-D-glucosamine N-deacetylase
A0A0H3JQB	A0A0H3JQB	SAV0402	ATP/GTP-binding protein
A0A0H3JTT1	A0A0H3JTT1	SAV2582	Similar to cobalamin synthesis related protein CobW
A0A0H3JP43	A0A0H3JP43	*capK*	Capsular polysaccharide synthesis enzyme Cap5K
A0A0H3K1B	A0A0H3K1B	SAV2682	N-acetyltransferase domain-containing protein
Q99QX3	ICAA_STAAM	*icaA*	Poly-beta-1,6-N-acetyl-D-glucosamine synthase
A0A0H3JPR8	A0A0H3JPR8	SAV0091	TfoX N-terminal domain-containing protein
A0A0H3JRK	A0A0H3JRK	SAV1377	Hydrolase
Q99UX0	ISDF_STAAM	*isdF*	Probable heme-iron transport system permease protein IsdF
A0A0H3JSY9	A0A0H3JSY9	SAV2348	Thioesterase
A0A0H3JRL8	A0A0H3JRL8	SAV1440	5'-3' exonuclease
A0A0H3JU68	A0A0H3JU68	SAV2460	CPBP family intramembrane metalloprotease
A0A0H3JQG	A0A0H3JQG	SAV0735	Similar to ferrichrome ABC transporter ATP-binding protein
A0A0H3JUS8	A0A0H3JUS8	SAV1079	Uncharacterized protein
P61636	AGRB_STAAM	*agrB*	Accessory gene regulator protein B
A0A0H3JTZ9	A0A0H3JTZ9	SAV2658	DoxX family protein
P63952	HISX_STAAM	*hisD*	Histidinol dehydrogenase
A0A0H3JU12	A0A0H3JU12	SAV2683	Similar to cobalt transport family protein
A0A0H3JPK	A0A0H3JPK	SAV0359	homocysteine desulfhydrase

Protein ID	Protein name	Gene	Protein description
A0A0H3JTD0	A0A0H3JTD0	SAV2533	Uncharacterized protein
A0A0H3JTG4	A0A0H3JTG4	SAV2415	Similar to multidrug resistance protein homolog ycnB
A0A0H3JTB7	A0A0H3JTB7	SAV2358	DUF218 domain-containing protein
A0A0H3K02	A0A0H3K02	SAV1870	Similar to teichoic acid transport protein tagG
A0A0H3K0X	A0A0H3K0X	SAV2424	Similar to 8-amino-7-oxononanoate synthase
A0A0H3JWP	A0A0H3JWP	SAV0010	Amino acid permease
A0A0H3JPR3	A0A0H3JPR3	SAV0085	Persulfide-sensing transcriptional repressor CstR
A0A0H3JPU	A0A0H3JPU	SAV0450	Putative cobalamin synthesis protein
Q931E4	ICAC_STAAM	*icaC*	Probable poly-beta-1,6-N-acetyl-D-glucosamine export protein
Q99VG5	Y840_STAAM	SAV0840	UPF0337 protein SAV0840
A0A0H3JY3	A0A0H3JY3	SAV0670	DUF985 domain-containing protein

Note: Protein IDs, protein names, gene names, and protein descriptions were summarized from the proteomic dataset.

Table S4. Primers list

Primer Name	**Sequence (5′–3′)**	**Purpose**
P1-F	CTGACAGGATCCCTAACTAAAAAGGAGTGTTCTTAATGGCAC	*cysK* complementation
P1-R	CTGACAGAATTCGCAAGTTATCTCAAAAAGATAACTCACTCT	*cysK* complementation
P2-F	GTCAGGATCCAAGGAGTGTTCTTAATGCAAATACTACTAGTAGAAGATGA	*graR* complementation
P2-R	GACTCAGAATTCATCCAGTTCATGCGAGATTT	*graR* complementation
P3-F	GTTTCGGTGAGATGGAGGTATG	*rpoB*, RT-qPCR reference gene
P3-R	CGTCCTACTGTATCATCGGATTTG	*rpoB*, RT-qPCR reference gene
P4-F	AGTGGCGACATTCTTCACTTAC	*fmtC*, RT-qPCR
P4-R	CGTTTCAACCTACGTGCTCTAC	*fmtC*, RT-qPCR
P5-F	TCCCAAGTGCGACGATTTAC	*dltA*, RT-qPCR
P5-R	CTTTCAACGCCAACAGGTAATG	*dltA*, RT-qPCR
P6-F	AGCAAAGCATATCGTCTCTCAA	*vraG*, RT-qPCR
P6-R	TGAGCTTATCGCTTCACTTCTT	*vraG*, RT-qPCR

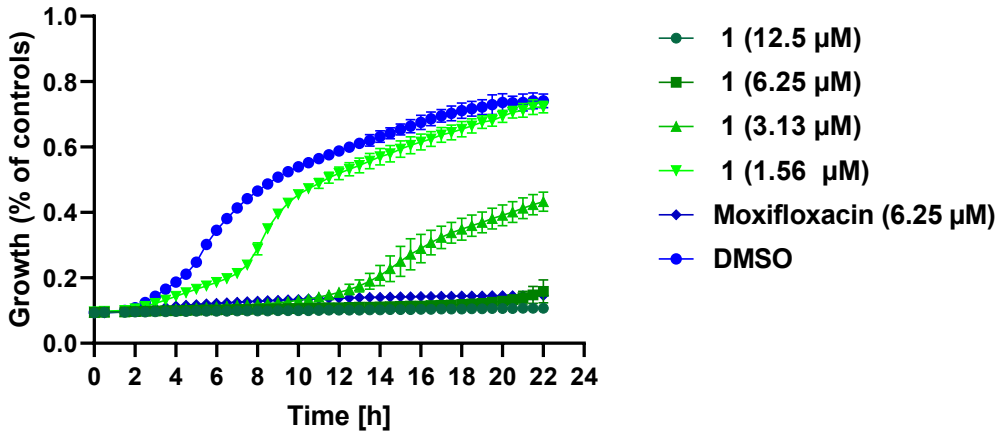


Figure S1. Growth kinetics of compound **1**

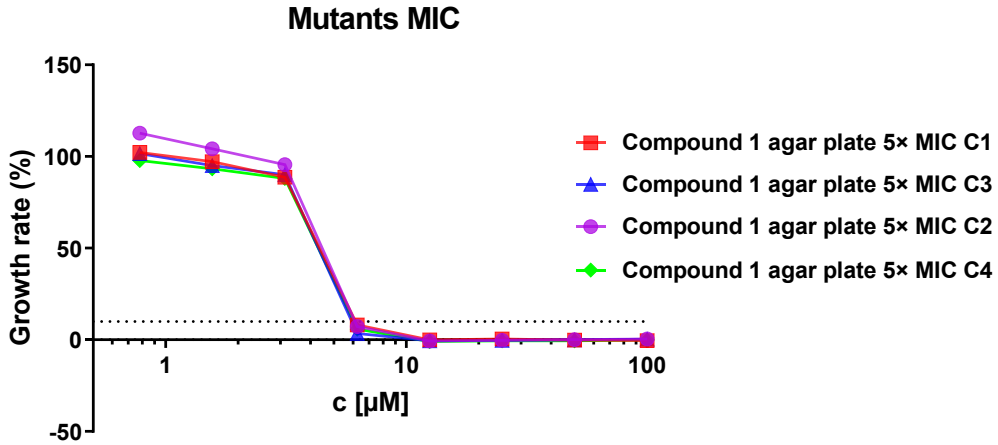


Figure S2. MICs of clones obtained from single-step mutant selection

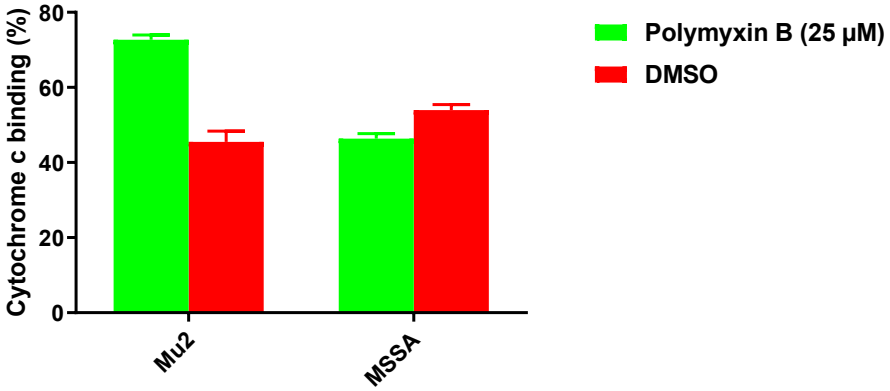


Figure S3. Result of polymyxin B binding cytochrome c

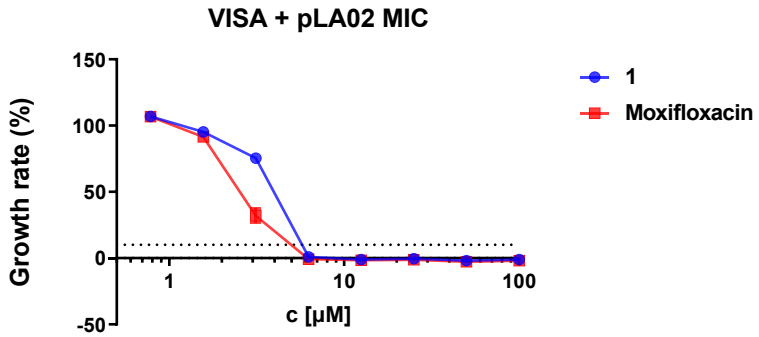


Figure S4. MICs of compound 1 and moxifloxacin against the VISA WT+pLA02.

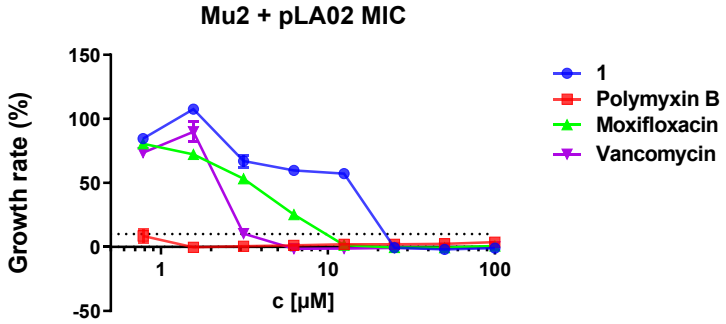


Figure S5. MICs of **1**, vancomycin, polymyxin B and moxifloxacin against the Mu2 + pLA02.

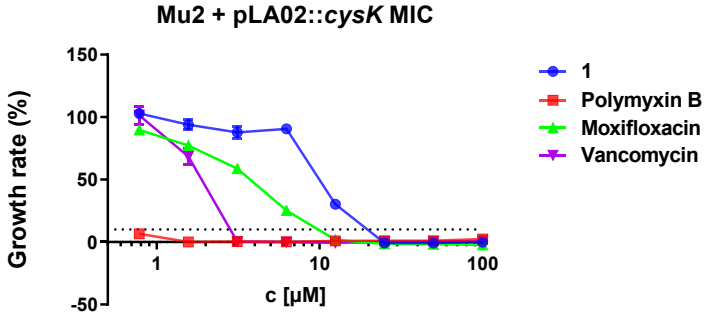


Figure S6. MICs of **1**, vancomycin, polymyxin B and moxifloxacin against the Mu2 + pLA02::*cysK*.

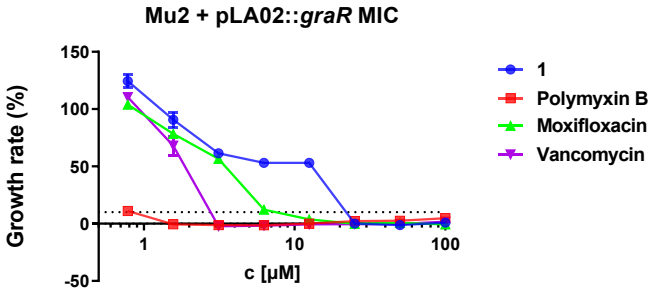
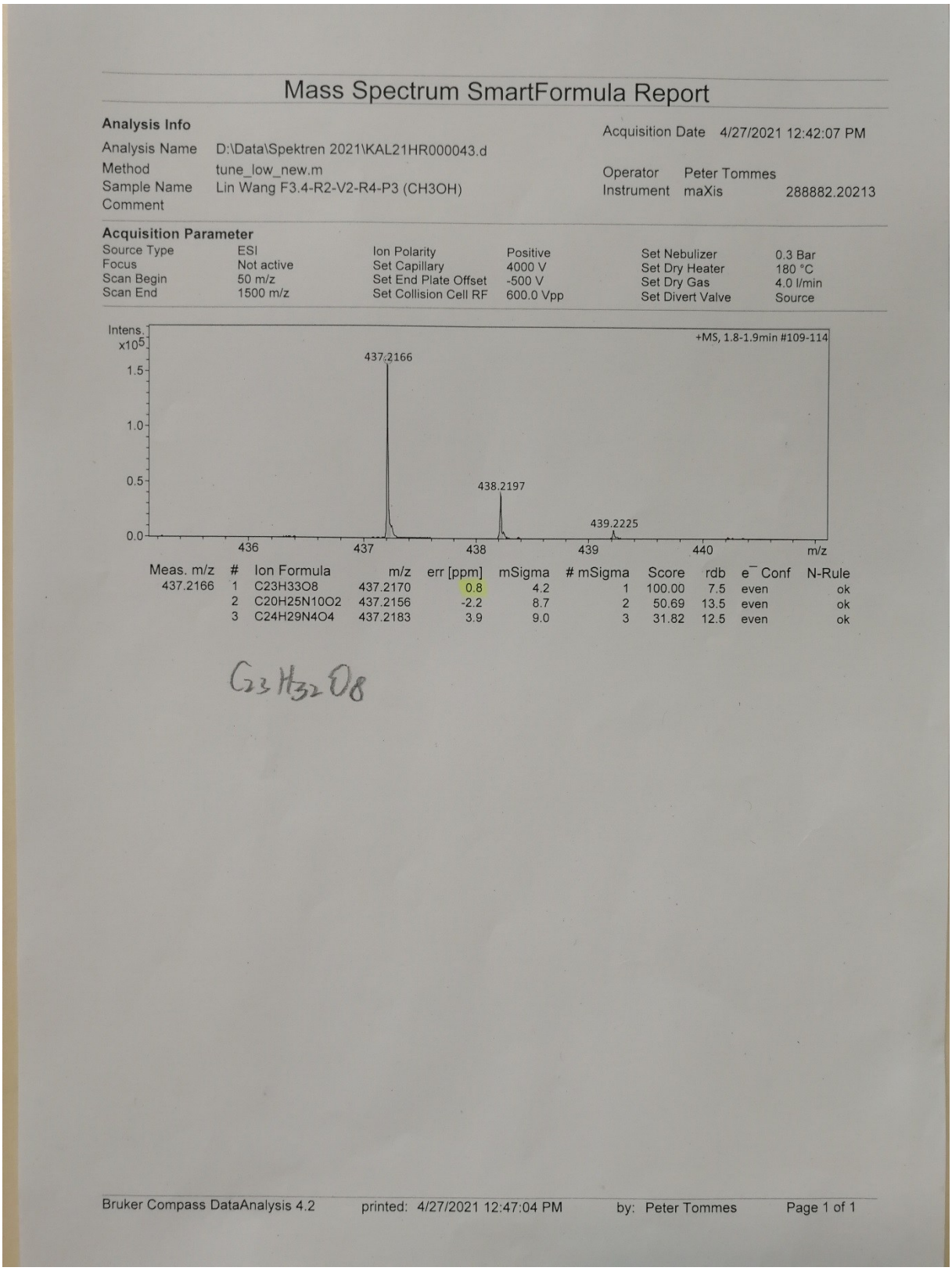


Figure S7. MICs of **1**, vancomycin, polymyxin B and moxifloxacin against the Mu2 + pLA02::*graR*.



Mass Spectrum SmartFormula Report

Analysis Info

Analysis Name	D:\Data\Spektren 2021\KAL21HR000043.d	Acquisition Date	4/27/2021 12:42:07 PM
Method	tune_low_new.m	Operator	Peter Tommes
Sample Name	Lin Wang F3.4-R2-V2-R4-P3 (CH3OH)	Instrument	maXis 288882.20213
Comment			

Acquisition Parameter

Source Type	ESI	Ion Polarity	Positive	Set Nebulizer	0.3 Bar
Focus	Not active	Set Capillary	4000 V	Set Dry Heater	180 °C
Scan Begin	50 m/z	Set End Plate Offset	-500 V	Set Dry Gas	4.0 l/min
Scan End	1500 m/z	Set Collision Cell RF	600.0 Vpp	Set Divert Valve	Source

Meas. m/z	#	Ion Formula	m/z	err [ppm]	mSigma	# mSigma	Score	rdb	e⁻ Conf	N-Rule
437.2166	1	C23H33O8	437.2170	0.8	4.2	1	100.00	7.5	even	ok
	2	C20H25N10O2	437.2156	-2.2	8.7	2	50.69	13.5	even	ok
	3	C24H29N4O4	437.2183	3.9	9.0	3	31.82	12.5	even	ok

$C_{23}H_{32}O_8$

Bruker Compass DataAnalysis 4.2 printed: 4/27/2021 12:47:04 PM by: Peter Tommes Page 1 of 1

Figure S8. HREISMS of compound **8**

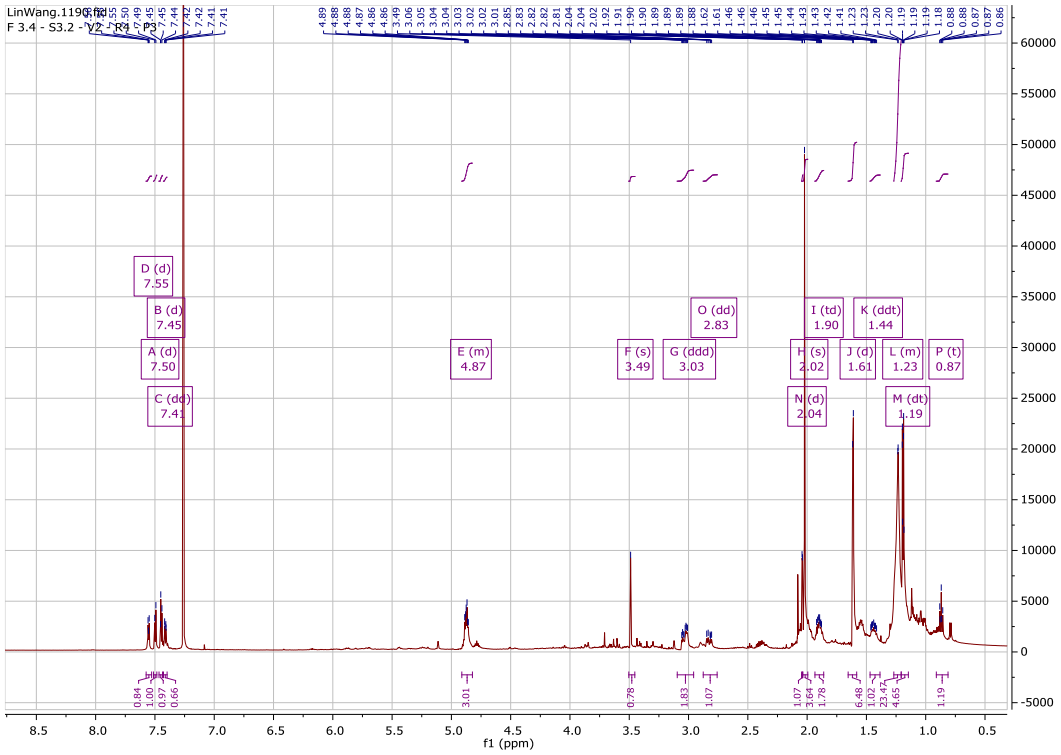


Figure S9. ^{1}H NMR of compound **8**

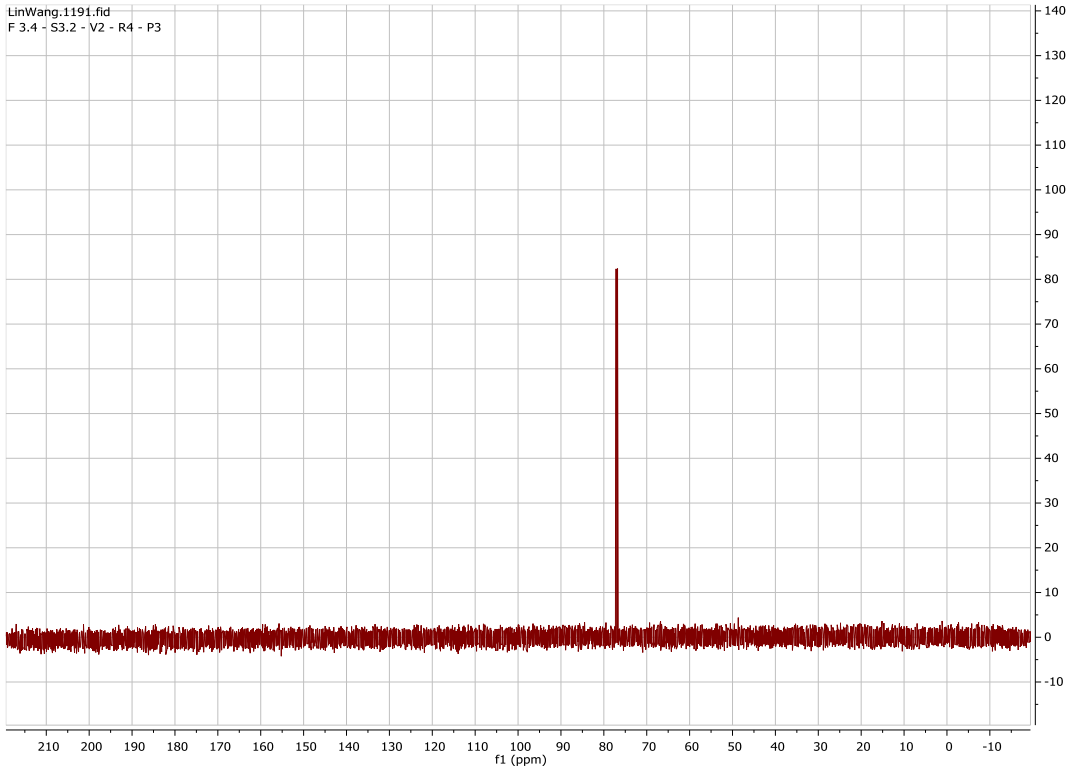


Figure S10. ^{13}C NMR of compound **8**

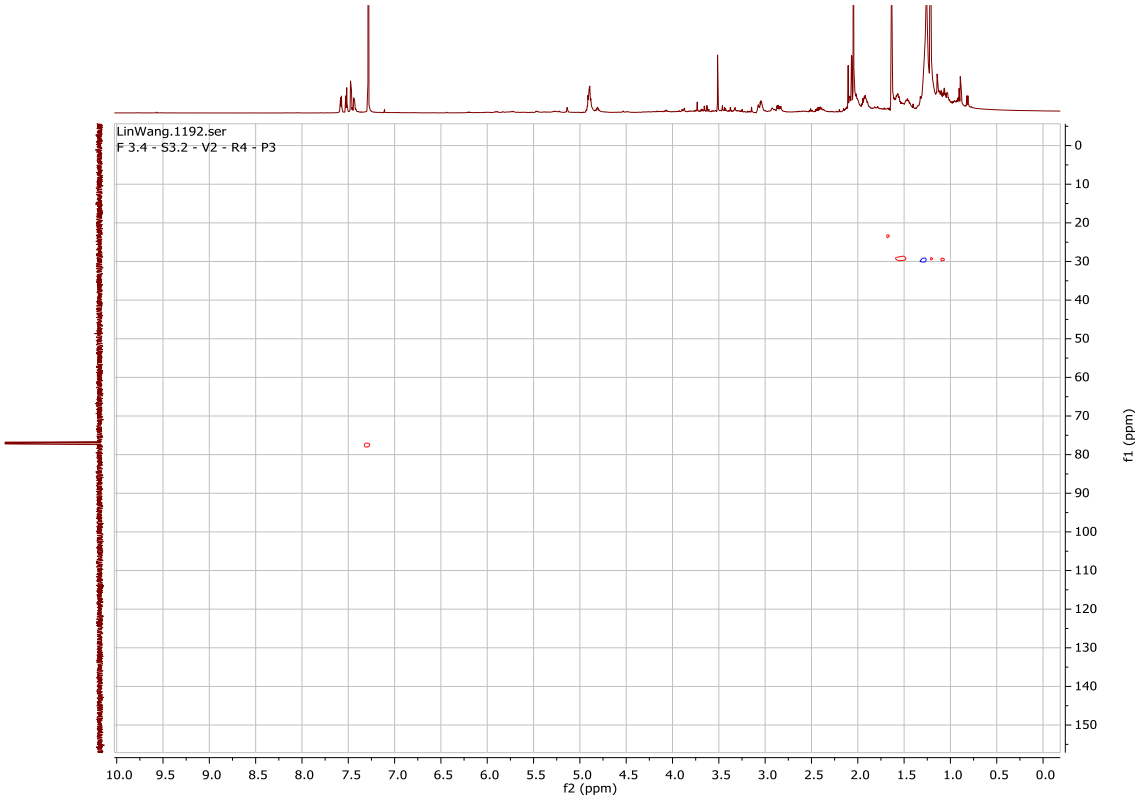


Figure S11. HSQC of compound **8**

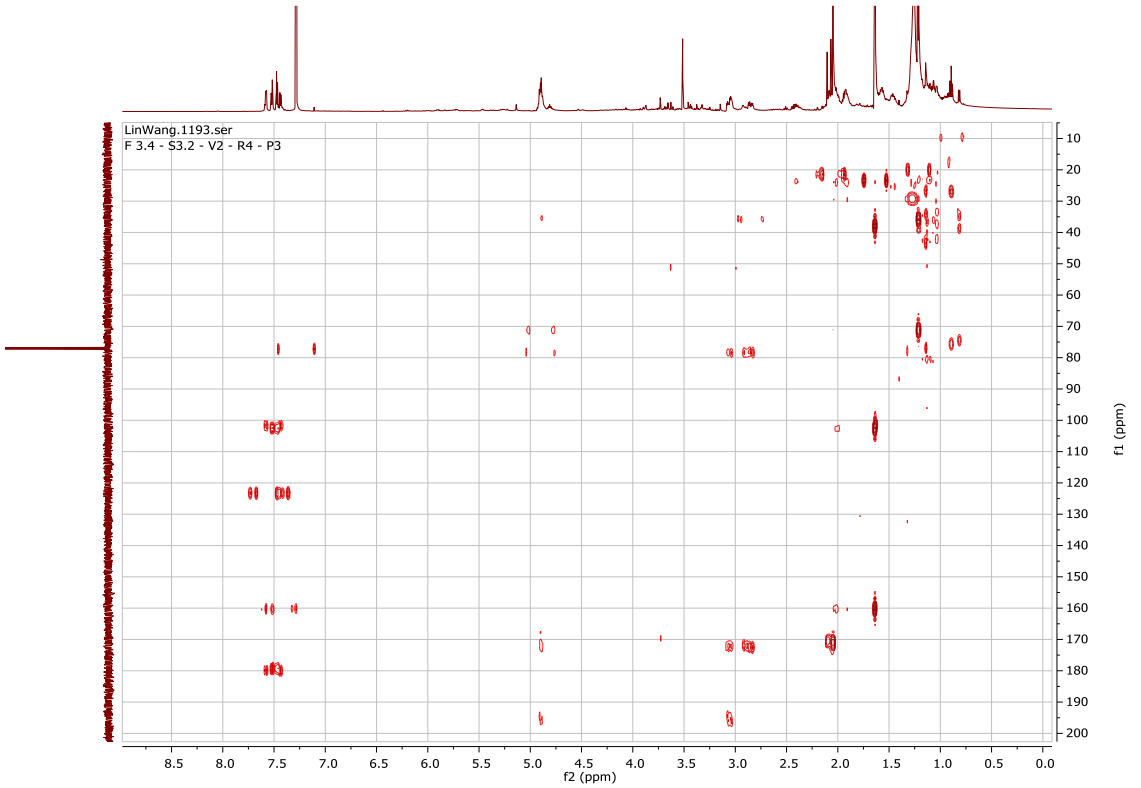


Figure S12. HMBC of compound **8**



Figure S13. ^{1}H-^{1}H COSY of compound **8**

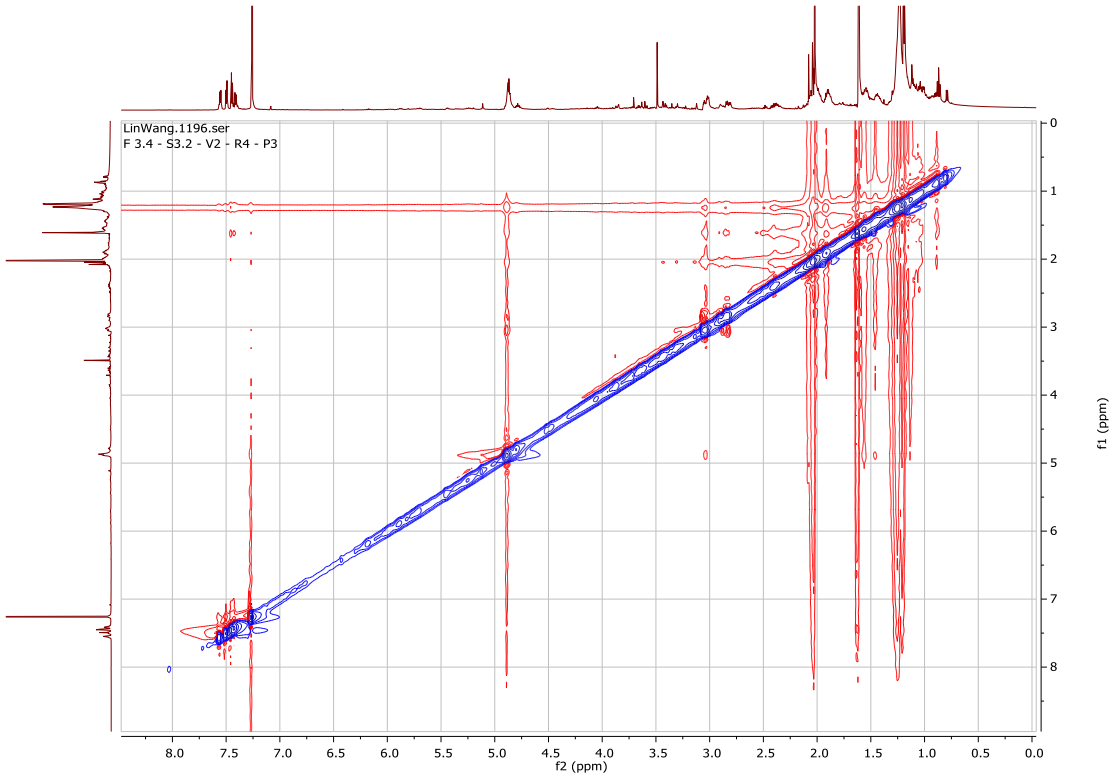


Figure S14. ROESY of compound **8**

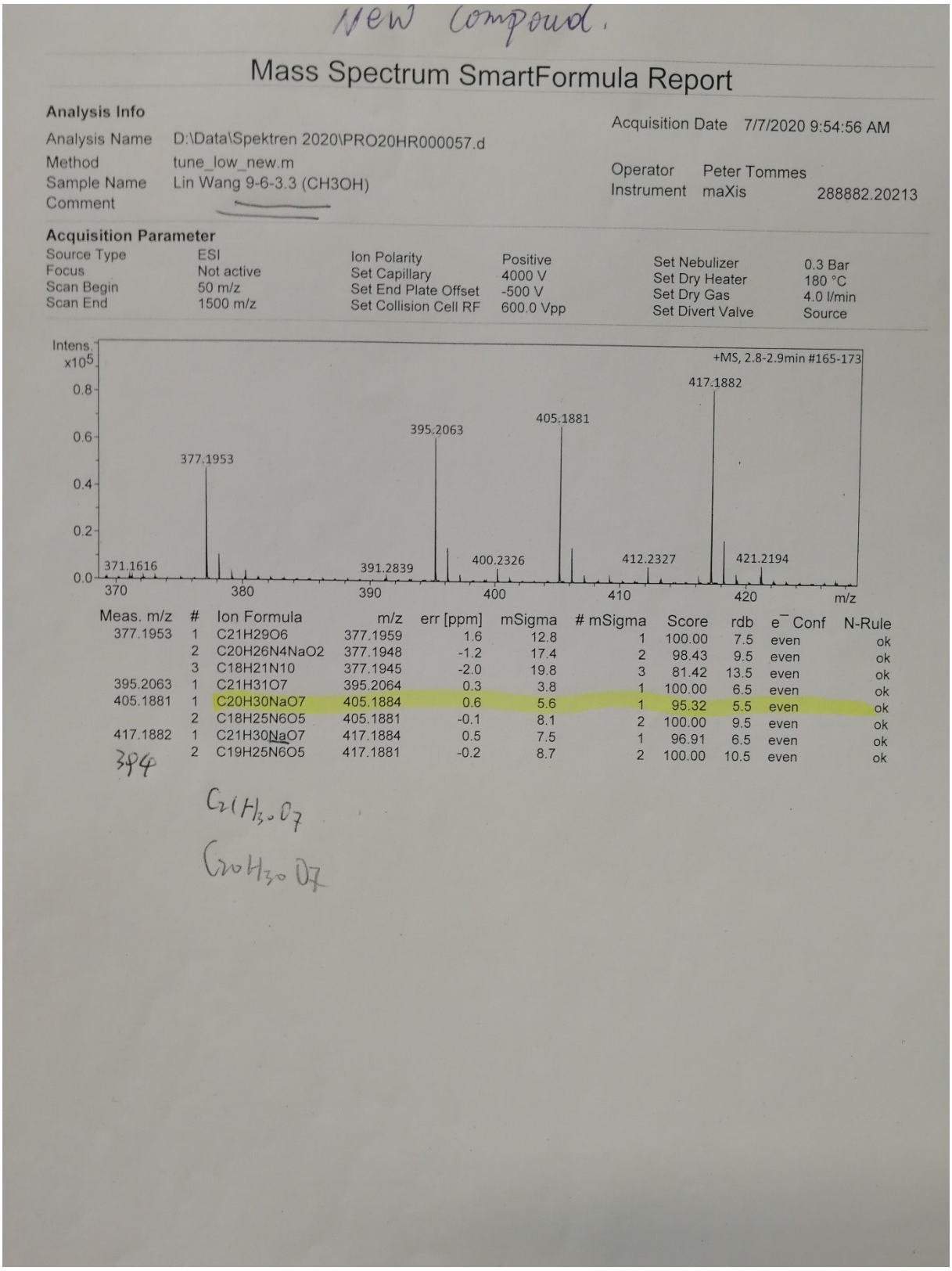


Figure S15. HREISMS of compound **9**

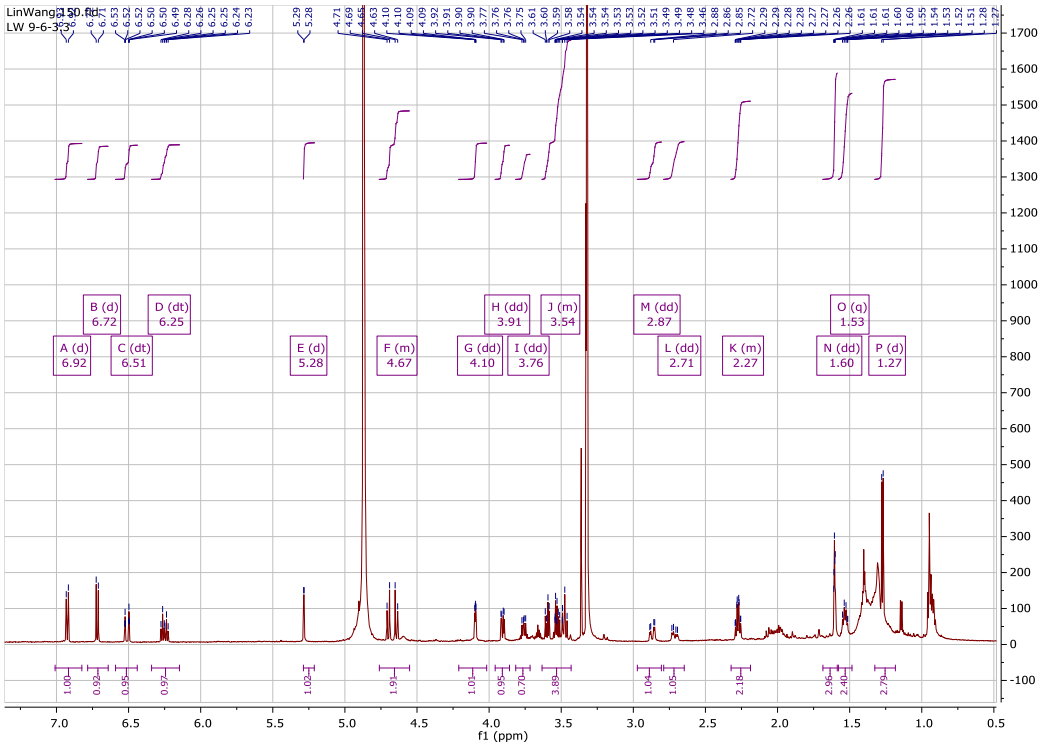


Figure S16. [1]H NMR of compound **9**

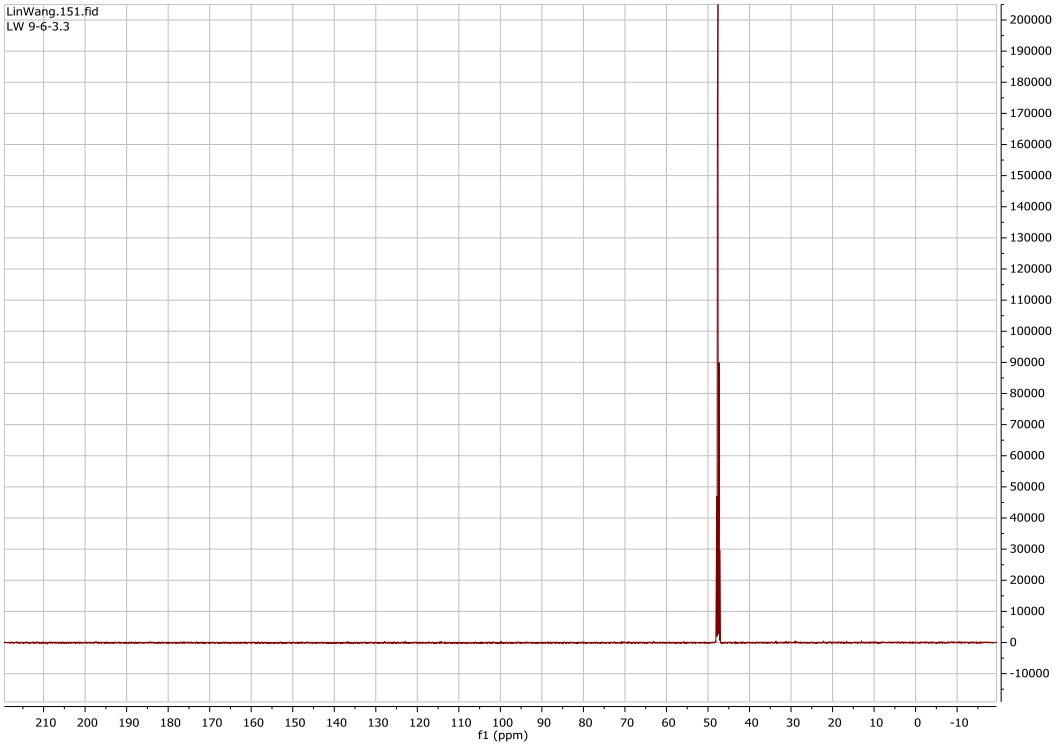


Figure S17. [13]C NMR of compound **9**

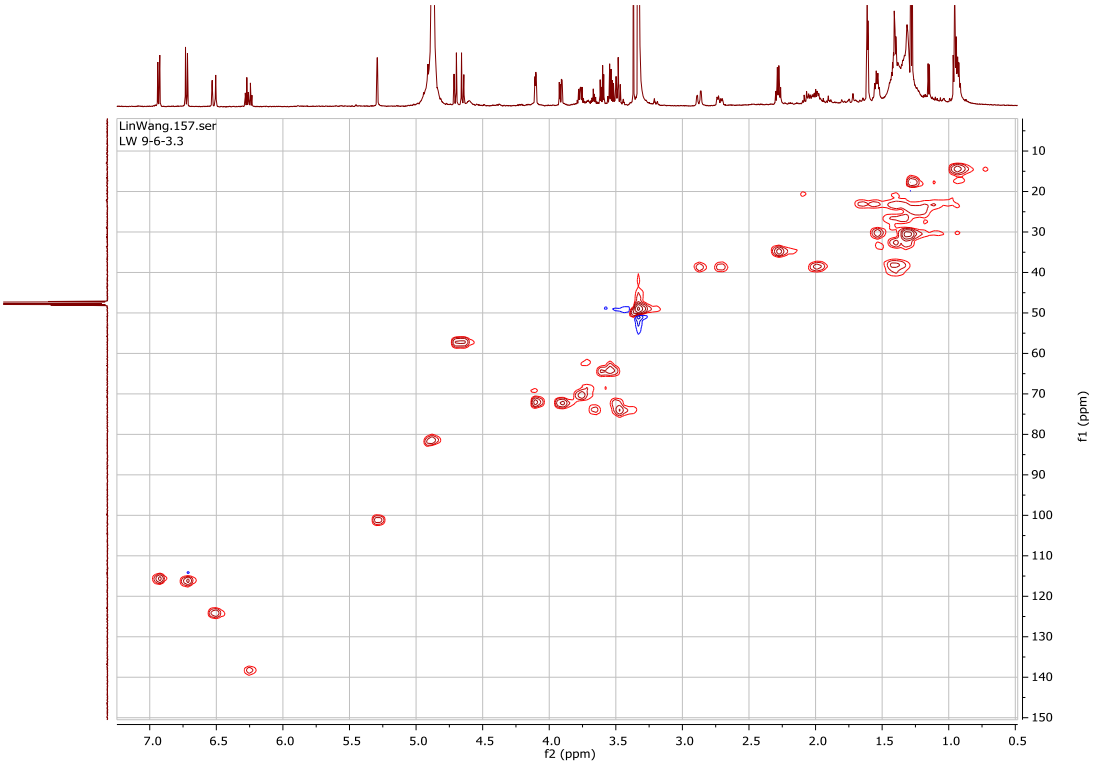


Figure S18. HSQC of compound **9**

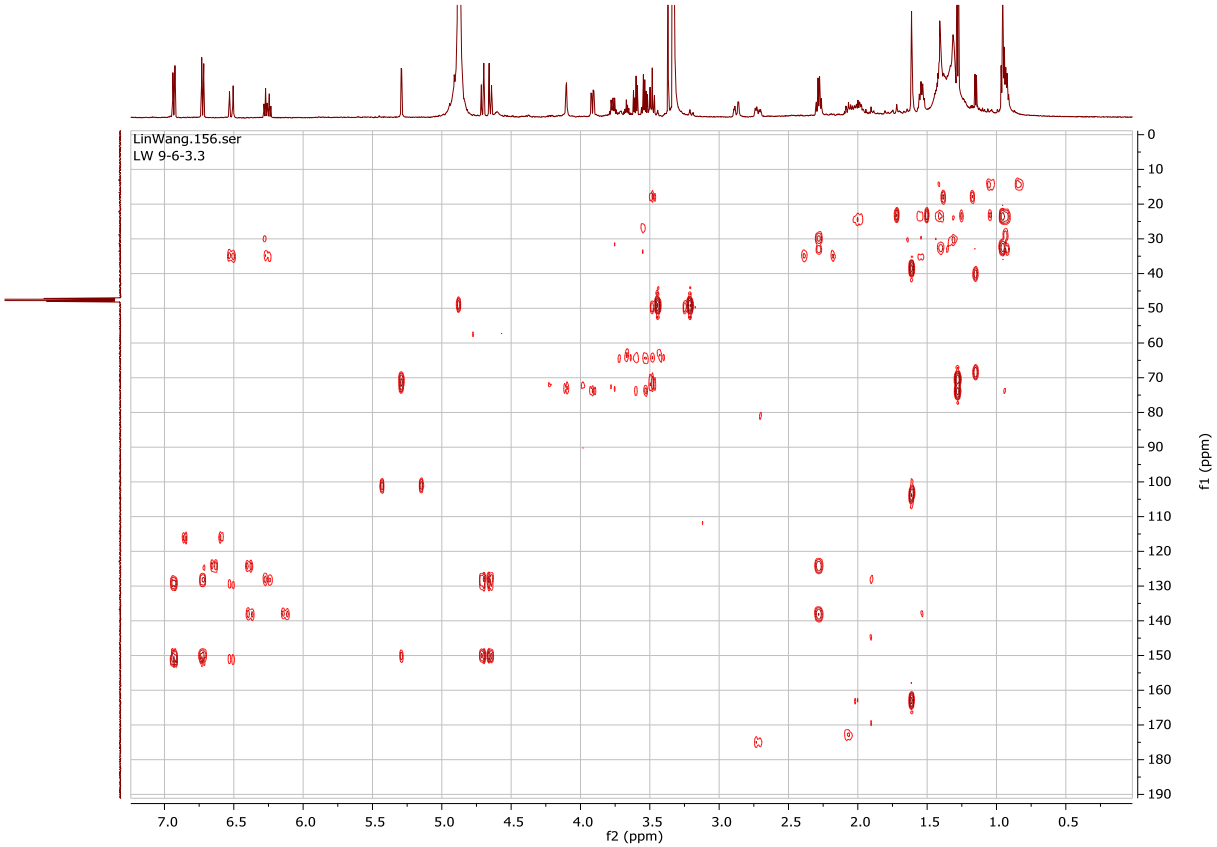


Figure S19. HMBC of compound **9**

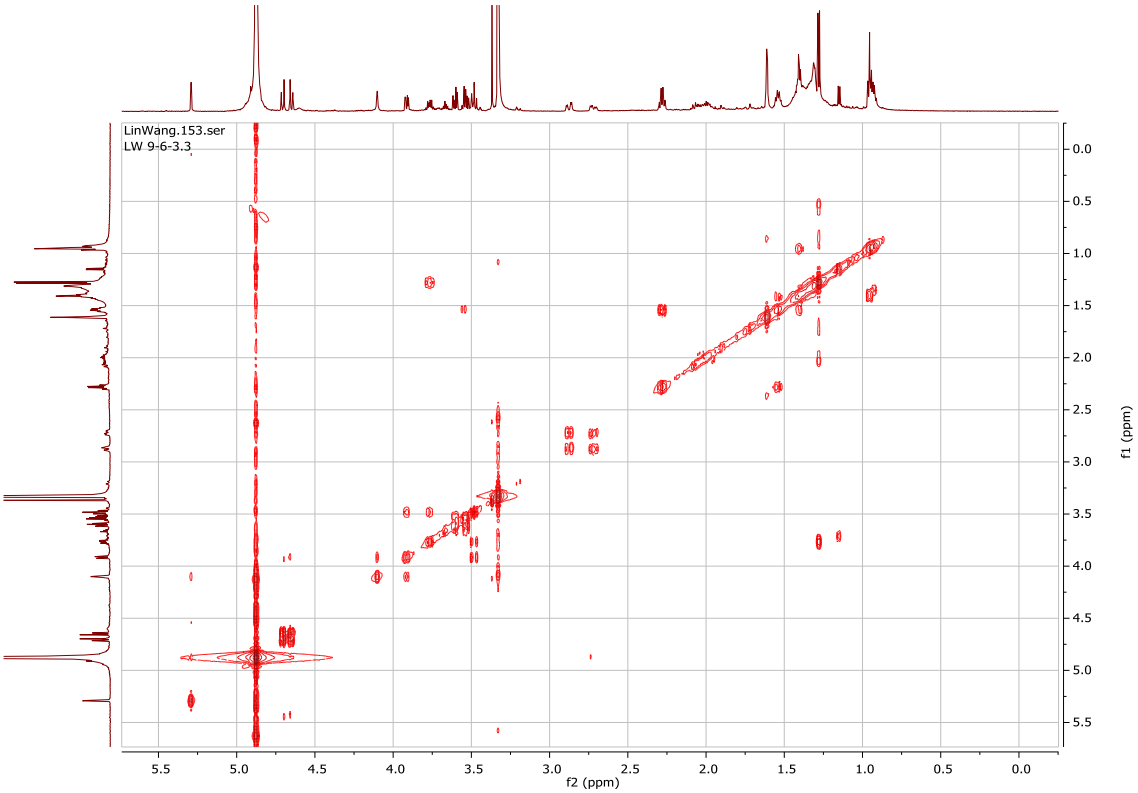


Figure S20. ^{1}H-^{1}H COSY of compound **9**

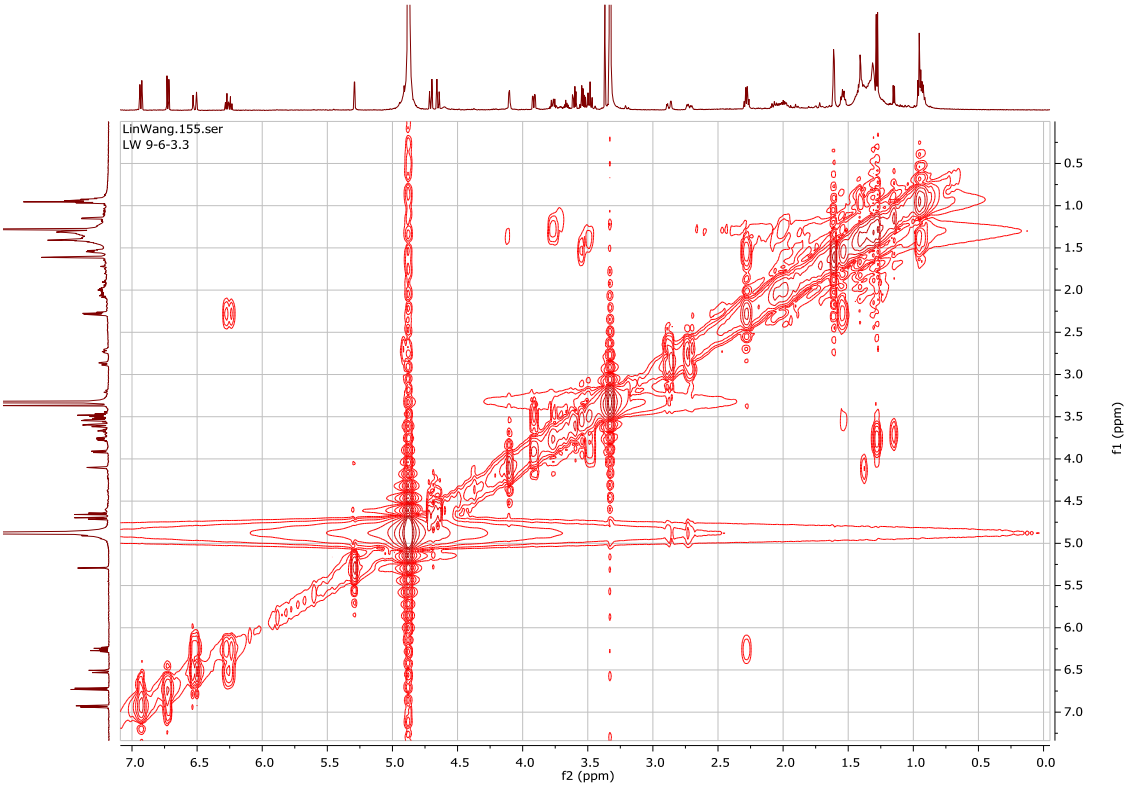


Figure S21. ROESY of compound **9**

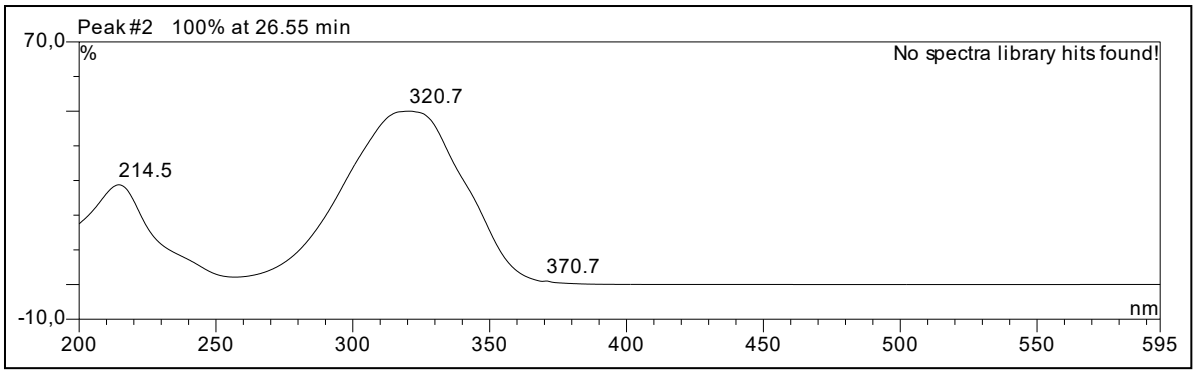


Figure S22. UV absorption of compound **8**

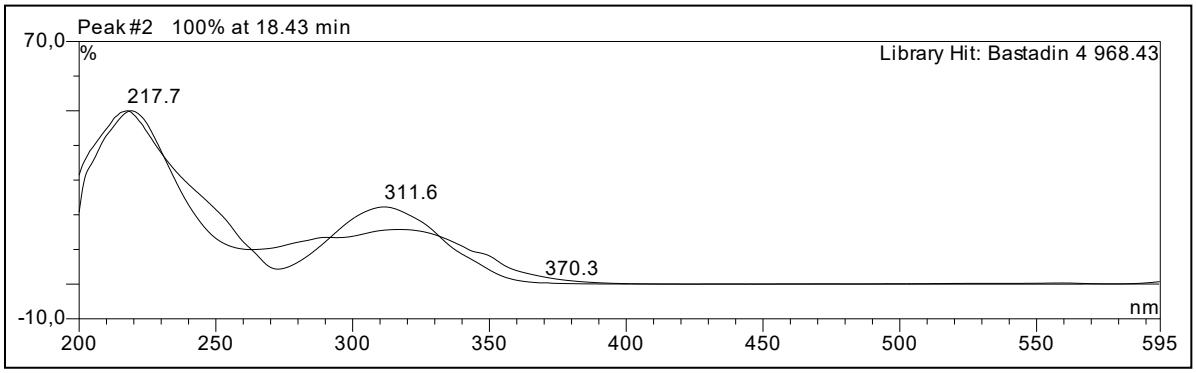


Figure S23. UV absorption of compound **9**

4. Manuscript 2

Fusarubin Derivatives with Biofilm-Disrupting Activities Derived from *Fusarium oxysporum*

Di He[a¶], Viktor E. Simons[a¶], Lasse van Geelen[a], Dennis Woschko[b], Attila Mándi[c], Philipp Spohr[d], Sebastian Scharf[e], Marian Frank[a], Christoph Janiak[b], Tibor Kurtán[c], Gunnar W. Klau[d], Rainer Kalscheuer[a*]

[a]Institute of Pharmaceutical Biology and Biotechnology, Heinrich Heine University, Universitätsstrasse 1, 40225 Düsseldorf, Germany

[b]Institute for Nanoporous and Nanoscale Materials, Heinrich Heine University, Universitätsstrasse 1, 40225 Düsseldorf, Germany

[c]Department of Organic Chemistry, University of Debrecen, P.O. Box 400, 4002 Debrecen, Hungary

[d]Algorithmic Bioinformatics, Heinrich Heine University, Universitätsstrasse 1, 40225 Düsseldorf, Germany

[e]Institute of Medical Microbiology and Hospital Hygiene, Heinrich Heine University, Universitätsstrasse 1, 40225 Düsseldorf, Germany

¶ These authors contributed equally

[*]Corresponding author.

rainer.kalscheuer@hhu.de; ORCID ID orcid.org/0000-0002-3378-2067

Abstract

The genus *Fusarium* is known for its versatility in the production of secondary metabolites. Based on the OSMAC (one strain many compounds) concept, in this study, the co-cultivation of the soil-borne fungus *Fusarium oxysporum* with the soil-borne bacterium *Paenibacillus ehimensis* yielded the three new natural products fusachinon (**2**), fusapurpurin A (**3**) and fusapurpurin B (**4**), together with seven previously described compounds (**1** and **5**-**10**). The structures were elucidated based on comprehensive spectroscopic measurements. The unusually bridged structures of fusapurpurin A and B were confirmed via single crystal X-ray diffraction analysis. Nanopore whole genome sequencing of *F. oxysporum* together with antiSMASH analysis led to the identification of a biosynthetic gene cluster (BGC) likely responsible for the biosynthesis of fusarubin base structures, which are structurally closely related to the novel fusapurpurins. On this basis, a possible biosynthetic route to fusapurpurin A and B is being proposed. Fusapurpurin A and B showed potent biofilm-desintegrating activities against *Staphylococcus aureus* Mu50 with IC_{90} = 6.25 µM and *Pseudomonas aeruginosa* PAO1 with IC_{90} = 12.5 µM. Additionally, fusapurpurin B also showed moderate biofilm-disrupting activity against *Mycobacterium tuberculosis* H37Rv and reduced pre-formed biofilm by more than 50% at 100 µM. Of the three new compounds (2-4), only fusapurpurin B showed a weak direct antibacterial activity against *S. aureus* Mu50 with a minimal inhibitory concentration (MIC) of 100 µM. Compound 9 had weak activity against *S. aureus* Mu50 with a MIC of 50 µM and strong activity against *Mycobacterium tuberculosis* H37Rv with a MIC of 3.125 µM. Fusapurpurin A and B showed weak to moderate cytotoxic effects against the tested human cell lines THP1 (40.66 vs. 11.57 µM), Huh-7 (47.85 vs. 12.67 µM) and HEK 293 (>100 vs. 26.81 µM). Genome annotation and candidate enzyme screening suggested that an FO-LovD-like protein may be involved in the late-stage conjugation reaction between 9-O-methylfusarubin and the phenylpyruvate-derived moiety. AlphaFold-based structural prediction and US-align structural comparison showed that the FO-LovD-like protein shares a similar overall structural fold with *Aspergillus terreus* LovD and retains a potential Ser–Lys–Tyr catalytic core. Protein–ligand complex prediction indicated that the binding pocket of FO-LovD-like can accommodate 9-O-methylfusarubin as well as activated phenylpyruvate-derived thioester donors, such as phenylpyruvate-CoA. Taken together, this study discovered new fusarubin derivatives with biofilm-dispersing activity and proposed a structural hypothesis for the post-modification step in the biosynthesis of fusapurpurins A and B, as well as for the candidate LovD-like enzyme. These findings provide a basis for further elucidating their biosynthetic mechanism and antibiofilm mode of action.

Keywords: *Fusarium oxysporum*; OSMAC; fusarubin; fusapurpurin; co-cultivation; biofilm disruption; antibiofilm activity; antiSMASH; LovD-like acyltransferase; AlphaFold; natural product biosynthesis.

1. Introduction

Antimicrobial resistance has become a steadily increasing threat to human health during the last decades. The golden era between 1950 and 1970, where a lot of new antibiotics have been introduced to the clinic, was followed by decades of underdevelopment of new antibiotic compounds [1]. Environmental microorganisms are still a very fruitful natural source of novel antibiotics since new chemical skeletons derived from these sources have been continuously being identified during the last decades [2]. Even though there is a long history of isolation of bioactive natural products, various approaches for the activation of silent gene clusters have emerged during recent years leading to a substantial expansion of our portfolio of natural compounds, highlighting the huge hidden treasure chest of what is still to be found [3-5]. Especially fungi belonging to the genus *Fusarium* have been shown to be very versatile when it comes to the activation of silent gene clusters for the production of cryptic metabolites [6-10]. In this regard, the so-called OSMAC concept (One Strain Many Compounds) [11] is an easy and valuable tool to manipulate *Fusarium* species under laboratory conditions [12, 13]. One of the possible activating parameters of the OSMAC concept is co-cultivation with other microorganisms since it mimics naturally occurring interactions and competition [14, 15]. Interestingly, co-cultivation with different bacteria can also induce different cryptic metabolites [16, 17].

The ability of many pathogenic bacteria to form biofilms is severely complicating anti-infective treatment and a major factor promoting the development of antimicrobial resistance. Bacterial biofilms are one of the main reasons for the establishment of chronic bacterial infections [18]. Biofilms represent a robust physical barrier that effectively protects the embedded bacteria from being reached by most antibiotics. In addition, the majority of embedded cells are in a metabolically inactive and non-replicating state that causes phenotypic resistance, meaning that the bacteria are tolerant to antibiotics, which typically target processes of active metabolism and cell division. On the flip side, this also promotes the development of genetic resistance because the amount of antibiotics reaching the bacteria is lower than expected and the treatment is therefore at subinhibitory concentrations promoting the occurrence of mutations [19]. A recent study suggests that biofilms can even put mechanical stress on the infected tissues, leading to additional damage [20]. This shows the huge importance of finding new biofilm-inhibiting and disrupting compounds.

In this study, the soil-borne fungus *Fusarium oxysporum* was co-cultivated with the soil-borne bacterium *Paenibacillus ehimensis* resulting in the production and isolation of one new anthrachinone and two new naphthoquinones together with seven known compounds. The two new naphthoquinones, fusapurpurin A and B, inherit a completely new structural subclass of fusarubin derivatives, where the addition of a phenyl pyruvic acid moiety adds a complex bridged element to the 9-O-methylfusarubin base structure. The absolute configurations of novel compounds 3 and 4 were determined via single-crystal X-ray diffraction analysis. A whole genome nanopore sequencing of *F. oxysporum* was accomplished and analysed by the antiSMASH fungi version to identify a possible biosynthetic pathway

for fusapurpurins A and B. Fusapurpurins A and B exhibit dispersing activity against pre-formed biofilms of methicillin-resistant *Staphylococcus aureus* Mu50 and *Pseudomonas aeruginosa* PAO1 and to a lesser extent also against *Mycobacterium tuberculosis* H37Rv.

2. Results and Discussion

Influence of bacterial co-cultivation on the secondary metabolite profile of *F. oxysporum*

In our ongoing search for new antimicrobial compounds derived from microorganisms, we isolated the filamentous fungus *F. oxysporum* from a soil sample collected in Texel, the Netherlands. Since members of the genus *Fusarium* appear to be particularly amenable to the OSMAC concept for the induction of silent biosynthetic gene clusters [11], *F. oxysporum* was grown in co- culture with cells of five different bacterial species on solid rice medium enriched with LB-medium including one lab strain (*Acinetobacter baylyi* ADP1) and four strains that have been isolated from various soil samples in our laboratory (*Bacillus amyloliquefaciens*, *Pseudomonas sp.*, *Lysinibacillus sp.* and *P. ehimensis*). Interestingly, the fungus responded in very distinct ways to the presence of the different bacteria. While *B. amyloliquefaciens* suppressed the growth of *F. oxysporum* almost completely, the presence of *A. baylyi* ADP1, *Lysinibacillus sp.*, *Pseudomonas sp.* and *P. ehimensis* led to the production of red-coloured pigments after four weeks of culturing. However, only during co- cultivation with *P. ehimensis*, the fungus responded by strong production of darker, purple-coloured pigments (**Fig. 1**).

To compare the co-cultures analytically, crude extracts were obtained from small-scale cultivations and measured via High-Performance Liquid Chromatography (HPLC). HPLC-chromatograms of different crude extracts from co-cultivations with *F. oxysporum* and axenic cultures are shown in Fig. 2. Comparison of the HPLC-chromatograms of extracts obtained from co-cultivation with *A. baylyi* ADP1, *Lysinibacillus sp.*and *Pseudomonas sp.* showed only moderate differences to the extract obtained from the axenic *F. oxysporum* culture, while co-cultivation with *B. amyloliquefaciens* strongly repressed overall production of secondary metabolites. In contrast, co-culture with *P. ehimensis* resulted in the elicitation of a very different metabolite profile with strong induction of a peak at retention-time 24.32 minutes that was later identified as 9-*O*-methylfusarubin (compound **1**), among some additional minor peaks (**Fig. 2**). These new peaks were not detactable in the HPLC-chromatograms of extracts from the axenic *F. oxysporum* and *P. ehimensis* controls (**Fig. 2**).

Compound isolation and structure elucidation

The crude ethyl acetate extract of the co-cultivation of *F. oxysporum* with *P. ehimensis* was purified via silica and Sephadex column chromatography and semi-preparative HPLC to yield one new anthrachinone (**2**) and the two new naphthoquinone derivatives **3**-**4** together with seven known compounds including the five naphthoquinones 9-*O*-methylfusarubin (**1**) [21], 9-*O*-methylbostrycoidin (**5**) [21], 2,5-dihydroxy-6,8-dimethoxy-3-(2-oxopropyl)-1,4-naphthalenedione (**6**) [22], 9-*O*-methylanhydrofusarubin (**7**) [22], 9-*O*-methylanhydrofusarubinlactol (**8**) [23], and the two

cyclopeptides beauvericin (**9**) [24] and beauvericin J (**10**) [25]. An overview of the chemical structures of the isolated compounds is provided in Fig. 3. The absolute configuration of compounds 3 and 4 was determined via single crystal X-ray diffraction.

Structure elucidation of compound **2**:

Compound **2** was isolated as an amorphous orange solid. The molecular formula was assigned as $C_{17}H_{14}O_7$ based on the high-resolution quasi-molecular ion peak at 331.0817 m/z (calcd. for $C_{17}H_{15}O_7$ 331.0812 m/z). The UV spectrum exhibited high similarity to other co-isolated fusarubin derivatives. Detailed analysis of the HMBC and HSQC correlations of aromatic methoxy-unit 2- OCH3 (δ 3.96 ppm), aromatic protons H-3 (δ 6.96 ppm), H-5 (δ 8.35 ppm), H-8 (δ 7.62 ppm) and phenolic protons OH-1 (δ 13.17 ppm), OH-4 (δ 13.70 ppm) and OH-7 (δ 11.21 ppm) revealed an anthraquinone core structure. The position of C9 (δ 187.6 ppm) was confirmed through a strong HMBC correlation from H-8 and a weak J4 correlation from H-5. The position of C10 (δ 183.8 ppm) was confirmed the same way mirrored through a strong correlation from H-5 and a weak J4 correlation from H-8. The COSY correlations between H3-12 (δ 1.33 ppm) and H-11 (δ 5.03 ppm), in addition to HMBC correlations from H-12 to C-11 (δ 62.6 ppm) and C-6 (δ 141.6 ppm), a strong HMBC correlation between H-5 and C11 and an NOE correlation between H-5 and H-11 revealed the presence of the hydroxyethyl group at position C-6. The position of OH-1 was confirmed by strong HMBC correlations between OH-1 and C-1 (δ 149.0 ppm), C-2 (δ 156.6 ppm) and C-9a (δ 112.0 ppm). In the same manner, position of OH-4 was revealed by HMBC correlations with C-3 (δ 107.2 ppm), C-4 and C-4a (δ 104.7 ppm). OH-7 was confirmed by correlations with C-6, C-7 (δ 158.9 ppm) and C8 (δ 111.3 ppm).

Structure elucidation of compound **3** and **4**:

Compound **3** was isolated as an amorphous purple solid, which crystallized in form of pink square crystals from a mixture of ethyl acetate and n-heptane. The molecular formula was assigned as $C_{25}H_{20}O_9$ based on the high-resolution quasi-molecular ion peak at 465.1177 m/z (calcd. for $C_{25}H_{21}O_9$ 465.1180 m/z). The UV spectrum exhibited high similarity to other co-isolated fusarubin derivatives, suggesting a shared chromophore, but had a stronger bathochromic shift in the highest maximum at around 520 nm. Detailed analysis of the HMBC and HSQC correlations of aromatic methoxy units 9-OCH_3 (δ 4.02 ppm), 7-OCH_3 (δ 3.88 ppm), isolated aromatic proton H-8 (δ 7.10 ppm) and chelated phenolic proton OH-10 (12.99 ppm) revealed a naphthoquinone core structure identical to 8-O-methylfusarubin. The position of carbonyl C-6 (δ 175.4 ppm) was confirmed based on a weak J_4-HMBC correlation from H-8, while carbonyl C-11 (δ 186.7 ppm) was inferred from the chelated nature of OH-10 as well as the absence of an HMBC correlation from H-8. The remaining ^{1}H-NMR signals revealed a phenyl-moiety expressing the typical overlapping multiplet pattern of protons H-13 to H-17 (δ 7.03 — 7.12 ppm), a strongly deshielded hydroxyl proton 3a-OH (δ 6.71 ppm), three deshielded methine protons H-5 (δ 5.30 ppm), H-11b (δ 4.34 ppm), H-4 (δ 3.97 ppm) and an aliphatic methyl unit H_3-1-CH_3 (δ 1.44 ppm). Detailed analysis of the HMBC and HSQC correlations of signals H-5, H-11b and H_3-1-

CH_3 revealed the presence of a pyrano-unit connected to the formerly established naphthoquinone core via fusing carbons C-5a (δ 148.9 ppm) and C-11a (δ 138.9 ppm). The orientation of the pyrano-unit relative to the naphthoquinone core was established based on the strong J_3-HMBC correlations of H-11b to C-11 & C-5a and H-5 to C-6 & C-11a.

Compound **4** was isolated as an amorphous purple solid, which crystallized in form of purple crystals from MeOH. The molecular formula was assigned as $C_{25}H_{20}O_9$ based on the high-resolution quasi-molecular ion peak at 465.1174 m/z (calcd. for $C_{25}H_{21}O_9$ 465.1180 m/z). The UV spectrum was identical to that of 3. The NMR data (Table 2) for compounds **3** and **4** also showed that they are largely structurally identical. Surprisingly for compound **4**, we could observe a lower chemical shift for position H-4 (δ 2.91 ppm) compared to that of compound **3** and positions H-4 and H-5 (δ 5.41 ppm) both showing singlet signals instead of doublets. Besides these findings, both compounds share the same information with only very low differences in the chemical shifts. The missing COSY signals for H-4 and H-5 also supported the missing doublet signals in the ^{1}H-NMR. This could be caused by a dihedral angle that is close to 90° as described by the Karplus equation [26]. Nevertheless, HMBC signals from H-5 to C-12 (δ 136.8 ppm) and H-4 to C-13/17 (δ 127.7 ppm) showed a close range and connection to the phenyl moiety and also proved H-4 and H-5 being directly adjacent to each other. These findings were independently confirmed through X-ray crystallographic measurements that gave the absolute configurations shown in Fig. 5. The absolute configuration is also congruent to the relative configuration found through the NOE signals from the same NMR measurement finding 3a-OH (δ 6.65 ppm), H-4, H-5 and H-11b (δ 4.30 ppm) all having the same orientation.

The constitutions of compounds **3** and **4** with their absolute configurations were confirmed through single-crystal X-ray structures. Before the X-ray structure measurements, the compounds were assumed to be chiral. During the crystallographic data collection, no restraints were applied with respect to acentric or centrosymmetric space groups. Therefore, measurement parameters were chosen for the highest quality absolute configuration data with the Friedel pairs being non-equivalent. During the data integration and data reduction process the Friedel pairs were also not merged to retain the highest quality absolute configuration data. The resulting reduction statistics suggested centrosymmetric space groups for both compounds **3** and **4** for the later solution and refinement of both compounds, indicating racemic mixtures. Thus, the X-ray structures of both compounds **3** and **4** were solved and refined in centrosymmetric space groups. Upon structure solution no acentric space group was suggested. A centrosymmetric space group contains an inversion centre as a symmetry element. Thus, a chiral molecule in such a space group will be present in both enantiomeric forms in perfectly equal amounts, that is, as a racemate or practically very close to a racemic mixture. For compound **3,** this means that the investigated single crystal contained the enantiomers with configuration 1S,3aR,4R,5R,11bR and 1R,3aS,4S,5S,11bS. For compound **4,** the single crystal had the enantiomers 1R,3aS,4R,5S,11bS and 1S,3aR,4S,5R,11bR, which are the diastereomers and epimers to the content of compound **3**. In the solid state, the -OH groups are engaged in intra- and inter-molecular hydrogen bonding (**Fig. S1**). The

intramolecular packing is further controlled by π-π stacking interactions (**Fig. S2**). The molecular structures of 3 and 4 cannot pack very efficiently in the solid state so that solvent filled voids are formed in the crystal lattice (**Fig. S3**).

Re-induction attempts for fusapurpurins A and B under different fermentation conditions

In this study, co-cultivation of *F. oxysporum* and *P. ehimensis* induced the production of purple-red metabolites. From the co-culture fermentation extract, 9-*O*-methylfusarubin and the new fusarubin derivatives fusapurpurins A and B were isolated. 9-*O*-methylfusarubin has previously been reported as a naphthoquinone pigment produced by several Fusarium species, whereas fusapurpurins A and B contain an additional phenylpyruvate-derived moiety attached to the 9-*O*-methylfusarubin core, representing a new structural type of fusarubin derivatives [21-22].

However, in subsequent repeated fermentation experiments, fusapurpurins A and B could not be stably detected again. To re-induce the production of these two compounds, we applied the OSMAC strategy and performed multiple rounds of fermentation optimization, including changes in medium composition, supplementation with different additives, and adjustment of cultivation temperature and other parameters. Both the OSMAC strategy and microbial co-culture have been widely used to activate silent or lowly expressed fungal secondary metabolic pathways, thereby expanding the chemical diversity of natural products [3, 5, 11].

Nevertheless, fusapurpurins A and B were not redetected in any of the fermentation conditions tested. Under some fermentation conditions, the amount of 9-*O*-methylfusarubin increased markedly, but the formation of fusapurpurins A and B was still not observed. Therefore, we propose that the absence of fusapurpurins A and B may be due to the silencing of a key catalytic enzyme in the biosynthetic pathway.

Genome sequencing and BGC analysis support the biosynthetic capacity for 9-*O*-methylfusarubin production

To investigate the potential biosynthetic basis of fusapurpurins A and B, we performed whole-genome sequencing, genome assembly, and antiSMASH analysis of this *F. oxysporum* strain. FastANI analysis showed that the assembled genome shared an ANI of 97.073% with the NCBI reference genome GCF_000271745.1, supporting the assignment of this strain to *F. oxysporum* [27]. The genome assembly consisted of 537 contigs, with a total length of 53,627,915 bp, an N50 of 3,253,949 bp, and an average sequencing depth of 215×.

Analysis using the fungal version of antiSMASH identified a type I polyketide synthase gene cluster on contig 160. This region showed 87% similarity to BGC0001242, a known biosynthetic gene cluster involved in oxyjavanicin/fusarubin biosynthesis in *Fusarium fujikuroi* IMI 58289 (**Fig. 7**) [23, 28]. This result supports that the *F. oxysporum* strain possesses the genetic basis for producing the naphthoquinone core related to 9-*O*-methylfusarubin.

According to the reported fusarubin biosynthetic pathway, the naphthoquinone core of fusarubin derivatives is mainly formed through a polyketide synthase pathway, in which Fsr1 is involved in core scaffold biosynthesis, while Fsr2 and Fsr3 participate in subsequent oxidative modification and O-methylation, respectively [23]. Therefore, the stable detection of 9-*O*-methylfusarubin in this study is consistent with the presence of a fusarubin-like PKS gene cluster in the genome.

The post-modification coupling step may be the limiting step in fusapurpurin A and B formation

Compared with 9-*O*-methylfusarubin, the key structural difference of fusapurpurins A and B is the attachment of a phenylpyruvate-derived moiety to the 9-*O*-methylfusarubin core. We therefore proposed a biosynthetic pathway for fusapurpurins A and B (**Fig. 8**). The formation of fusapurpurins A and B requires at least two levels of biosynthetic processes: first, the generation of the 9-*O*-methylfusarubin naphthoquinone core; and second, the conjugation of a phenylpyruvate-derived unit to this core.

In the genome analysis, a gene encoding an amino acid transporter and a gene encoding an L-amino acid oxidase were found near the fusarubin-like gene cluster on contig 160. This L-amino acid oxidase showed high sequence similarity to a homologous enzyme from *F. oxysporum* sp. *vasinfectum*. Therefore, we propose that L-phenylalanine may be transported and oxidatively deaminated to generate phenylpyruvic acid, which subsequently participates in the formation of fusapurpurins A and B as a phenylpyruvate-derived moiety. This phenylpyruvate-derived moiety may first need to be activated into a thioester-type acyl donor, such as a CoA thioester or a carrier-tethered thioester, before undergoing acyltransferase-catalyzed conjugation with 9-*O*-methylfusarubin.

Screening of the candidate FO-LovD-like protein and its biosynthetic significance

Based on this hypothesis, we searched for candidate acyltransferases that could catalyse the coupling between 9-*O*-methylfusarubin and an activated phenylpyruvate-derived acyl donor.

LovD is an important acyltransferase known from the biosynthesis and semisynthetic modification of lovastatin/simvastatin in *Aspergillus terreus*. It exhibits broad substrate adaptability and can use CoA thioesters or SNAC thioesters as acyl donors in transacylation reactions [29]. In addition, LovD/PcEST-like enzymes generally possess a conserved Ser–Lys–Tyr catalytic core, in which Ser acts as a key nucleophilic residue involved in acyl-transfer- or ester-hydrolysis-related reactions [30].

Based on genomic information and functional annotation, we identified a candidate LovD-like protein in *F. oxysporum*. The gene encoding this protein is located on contig 160, which contains the 9-*O*-methylfusarubin biosynthetic gene cluster, but it is not located within the core fusarubin-like biosynthetic gene cluster and is genomically distant from this core cluster. Since the formation of fusapurpurins A and B may represent a post-modification or hybrid conjugation step after the production of 9-*O*-methylfusarubin, the enzyme catalyzing this step does not necessarily have to be co-localized with the 9-*O*-methylfusarubin PKS gene cluster. Based on the known functional features of LovD-like

enzymes, this FO-LovD-like protein can be considered a reasonable candidate enzyme involved in the late-stage conjugation step of fusapurpurins A and B biosynthesis.

Structural prediction and comparison of FO-LovD-like protein with *A. terreus* LovD

To evaluate whether this candidate protein possesses the structural basis of a LovD-like acyltransferase, we used AlphaFold to predict the three-dimensional structure of FO-LovD-like (**Fig. 9a**) and compared it with the reported structure of *A. terreus* LovD (**Fig. S6**). AlphaFold has been widely used for protein three-dimensional structure prediction, and metrics such as pLDDT and pTM can be used to assess the local and global reliability of predicted structures [31-32].

Structural superposition showed that although FO-LovD-like shares only approximately 31.7% sequence identity with *A. terreus* LovD, the two proteins still exhibit high overall structural similarity (**Fig. 9b**). USalign analysis gave TM-scores of 0.834 and 0.866, respectively, with an overall Cα RMSD of approximately 2.67 Å. USalign is a tool for unified structural alignment of proteins, nucleic acids, and macromolecular complexes. Its core principle is to evaluate structural similarity by maximizing the TM-score; therefore, the high TM-scores support that FO-LovD-like and LovD possess similar overall folds [33].

Analysis of the catalytic core region showed that Ser76, Lys79, and Tyr188 in *A. terreus* LovD correspond to Ser61, Lys64, and Tyr173 in FO-LovD-like, respectively, and that these residues are located in highly similar spatial positions in the superposed structures (**Fig. 10a**). This indicates that FO-LovD-like retains the key Ser–Lys–Tyr catalytic core of LovD-like acyltransferases.

In contrast, obvious conformational differences were observed in several peripheral loop regions between the two proteins (**Fig. 10b**), especially the FO-LovD-like region 227–249 and the corresponding *A. terreus* LovD region 241–262. Since peripheral loop regions often influence substrate entry, binding-pocket shape, and substrate recognition, this difference suggests that FO-LovD-like may possess substrate-adaptation features distinct from those of the canonical *A. terreus* LovD. This structural difference is also consistent with the hypothesis that FO-LovD-like may recognize 9-*O*-methylfusarubin and a phenylpyruvate-derived thioester donor in this study.

Heterologous expression and purification of FO-LovD-like protein

To verify whether this candidate protein could be used for subsequent in vitro functional experiments, we cloned the FO-LovD-like gene into a heterologous expression vector and expressed it in *Escherichia coli* BL21(DE3). After IPTG induction, SDS-PAGE analysis showed that the target protein could be expressed in *E. coli* (**Fig. S70**). Subsequently, we purified the His-tagged FO-LovD-like protein using Ni-NTA affinity chromatography and obtained purified protein suitable for subsequent in vitro enzymatic reaction assays.

This result provides an experimental basis for further testing whether FO-LovD-like can catalyze the conjugation between 9-*O*-methylfusarubin and an activated phenylpyruvate-derived acyl donor.

Complex prediction of 9-O-methylfusarubin, phenylpyruvate-SNAC and phenylpyruvate-CoA

After obtaining the FO-LovD-like structural model and purified protein, we performed exploratory protein–small molecule complex predictions to evaluate the potential capacity of its active pocket to accommodate relevant substrates or substrate mimics. AlphaFold3-class models can be used to predict complex structures involving proteins, small molecules, nucleic acids, and other components; Chai-1 has also been described as being capable of predicting various types of biomolecular structures, including protein–ligand complexes, from protein sequences and chemical inputs [34-35].

The single-substrate complex prediction of FO-LovD-like with 9-*O*-methylfusarubin showed that 9-*O*-methylfusarubin could be positioned within an internal or semi-open pocket of FO-LovD-like (**Fig. 11a**). This result indicates that the FO-LovD-like pocket may be spatially capable of accommodating the naphthoquinone scaffold of 9-*O*-methylfusarubin, providing a structural basis for its role as a potential acyl acceptor.

To simulate an activated phenylpyruvate-derived acyl donor, we first used phenylpyruvate-SNAC as a simplified thioester donor for complex prediction. Compared with the 9-*O*-methylfusarubin single-substrate model, the phenylpyruvate-SNAC single-substrate model showed a geometry more closely related to catalysis (**Fig. S7**). The distance between the thioester carbonyl carbon C5_1 and Ser61 OG was 3.81 Å, and the distance between sulfur atom S1_1 and Ser61 OG was 4.00 Å. In addition, the distance between the thioester carbonyl oxygen O2_1 and Tyr173 OH was 4.31 Å, whereas the distance to Lys64 NZ was 6.22 Å.

These results suggest that the active pocket of FO-LovD-like can accommodate a phenylpyruvate-derived thioester donor and position its thioester carbonyl group close to the catalytic Ser61, thereby providing a spatial basis for the formation of an acyl-enzyme intermediate. This is consistent with the mechanism of LovD-like enzymes, in which Ser acts as a nucleophilic residue involved in acyl-transfer reactions [29-30].

We also predicted single-substrate complexes of FO-LovD-like with phenylpyruvate-CoA. The results showed that in all five phenylpyruvate-CoA single-substrate models, the thioester carbonyl carbon C1_1 of phenylpyruvate-CoA was located near Ser61, with Ser61 OG–C1_1 distances ranging from 3.56 to 4.57 Å (**Fig. S8**). Among them, CoA-1, CoA-3, and CoA-5 showed distances of 3.64 Å, 3.56 Å, and 4.04 Å, respectively, all of which fall within a relatively reasonable catalysis-related distance range. Meanwhile, the Ser61 OG–S1_1 distance ranged from 3.87 to 4.79 Å, the Tyr173 OH–O1_1 distance ranged from 4.18 to 5.16 Å, and the Lys64 NZ–O1_1 distance ranged from 5.19 to 6.96 Å.

These results indicate that the thioester-reactive end of phenylpyruvate-CoA can be relatively stably positioned near the catalytic region of FO-LovD-like, especially close to Ser61. Together, the phenylpyruvate-SNAC and phenylpyruvate-CoA single-substrate models support the ability of the FO-LovD-like active pocket to accommodate an activated phenylpyruvate-derived thioester donor.

Double-substrate model prediction

After constructing a dual-substrate model of FO-LovD-like, 9-*O*-methylfusarubin, and phenylpyruvate-SNAC, we found that the two molecules could be located simultaneously near the same internal pocket of FO-LovD-like (**Fig. S7**), but their spatial arrangement did not support the proposed acylation reaction of the target alcohol hydroxyl group. In this model, the distance between the thioester carbonyl carbon C5_1 of phenylpyruvate-SNAC and Ser61 OG increased to 6.70 Å, while the distance between the target alcohol hydroxyl O7_1 of 9-*O*-methylfusarubin and C5_1 was 13.23 Å. This distance is clearly too long, indicating that although this model supports the co-localization of the two substrate scaffolds within the FO-LovD-like pocket, it does not represent a catalytic conformation suitable for acyl transfer involving the target alcohol hydroxyl group of 9-*O*-methylfusarubin.

In contrast, the dual-substrate models using phenylpyruvate-CoA as the activated phenylpyruvate-derived acyl donor showed more consistent and catalysis-related conformations (**Fig. 11b**). In all five phenylpyruvate-CoA dual-substrate models, the thioester carbonyl carbon C1_1 of phenylpyruvate-CoA was stably positioned close to Ser61 OG, with distances ranging from 3.58 to 4.00 Å. This is consistent with the trend observed in the phenylpyruvate-CoA single-substrate models, indicating that the reactive end of the CoA thioester donor can be relatively stably positioned in the catalytic region of FO-LovD-like.

Meanwhile, the Tyr173 OH–O1_1 distances were mostly within 3.88–4.70 Å, and the Lys64 NZ–O1_1 distances were approximately 4.73–6.04 Å, suggesting that the Ser61/Lys64/Tyr173 catalytic core may form a relatively reasonable spatial environment around the CoA thioester group in the predicted models. More importantly, in the phenylpyruvate-CoA dual-substrate models, the distance between the target alcohol hydroxyl O7_1 of 9-*O*-methylfusarubin and the thioester carbonyl carbon C1_1 of phenylpyruvate-CoA was markedly shorter than that in the phenylpyruvate-SNAC dual-substrate model. The O7_1–C1_1 distances in the five phenylpyruvate-CoA dual-substrate models were 6.11 Å, 6.39 Å, 9.10 Å, 5.66 Å, and 5.28 Å, respectively. Among them, CoA-4 and CoA-5 were closest to the proposed reaction conformation. In particular, in the CoA-5 model, the Ser61 OG–C1_1 distance was 3.73 Å, the O7_1–C1_1 distance was 5.28 Å, and the Ser61 OG–S1_1 distance was 3.89 Å.

These results suggest that, compared with the SNAC mimic, the CoA thioester form of the phenylpyruvate-derived donor may be more favorable for positioning the phenylpyruvate acyl moiety near the target alcohol hydroxyl group of 9-*O*-methylfusarubin. Therefore, phenylpyruvate-CoA is more suitable than phenylpyruvate-SNAC as the hypothesized activated phenylpyruvate-derived acyl donor in the current structural model.

Model confidence and limitations of the results

Although the phenylpyruvate-CoA dual-substrate models showed spatial relationships closer to the proposed reaction conformation than the phenylpyruvate-SNAC model, these results should still be interpreted cautiously. In the phenylpyruvate-CoA dual-substrate prediction, Model 1 had the highest aggregate score of 0.5561 and a pTM of 0.8787, indicating that the overall protein structure prediction was relatively reliable. However, its ipTM was only 0.4755, suggesting that the relative positioning of the two substrates and their interactions with the protein still contain considerable uncertainty. In addition, the ligand positions were not fully consistent among the different CoA models, indicating that the ternary complex prediction had not fully converged. Therefore, these complex prediction results cannot be regarded as direct evidence for the catalytic function of FO-LovD-like, but they support the structural hypothesis that this enzyme possesses the capacity to accommodate the relevant substrates and may provide a potential catalytic space.

Speculation on racemic product formation

After acyl transfer, the conjugated intermediate may further undergo dehydration and oxidation to generate a conjugated intermediate capable of intramolecular cyclization. In the proposed biosynthetic model, the final cyclization step is hypothesized to be a Diels–Alder-like [4+2] cycloaddition and may be catalyzed by a Diels–Alderase-like enzyme. Genome analysis also identified a putative Diels–Alderase-like gene in contig 44 region 8 (**Fig. S9**), and the region containing this gene showed a certain degree of similarity to the equisetin gene cluster from *Fusarium heterosporum*. Previous studies have reported or discussed the roles of Diels–Alderase-like enzymes in the biosynthesis of fungal natural products such as equisetin, Sch 210972, solanapyrone A, and macrophomic acid [36-39].

However, both fusapurpurins A and B are racemic, and this stereochemical feature provides an important clue regarding the nature of the final cyclization step. Although the two compounds exhibit different relative configurations at the linkage position associated with the phenylpyruvate-derived moiety, neither compound shows obvious enantiomeric enrichment. If the final Diels–Alder-like cyclization were strictly catalyzed by a highly stereoselective enzyme, it would generally be expected to produce a single enantiomer or at least an enantiomerically enriched product. In contrast, the formation of racemic products is more consistent with a model in which enzymatic steps first generate a reactive precursor, followed by spontaneous or weakly stereocontrolled intramolecular cyclization of this precursor. Studies on racemic natural products and scalemic natural products have also pointed out that racemic natural products are often associated with nonenzymatic or spontaneous reaction processes, whereas optically enriched or scalemic cycloaddition products more strongly support enzymatic stereocontrol [40-42].

Biofilm-dispersing activities

Initial explorative bioactivity testings with *Mycobacterium tuberculosis* H37Rv revealed a low biofilm-dispersing activity in addition to a direct antibacterial effect of the crude ethyl acetate extract of

the co-cultivation of *F. oxysporum* with *P. ehimensis*. Thus, the pure compounds derived from the isolation process were submitted to assays assessing their ability to disperse preformed biofilms against three important human pathogenic bacteria known to notoriously form biofilms during chronic infections: the gram-positive methicillin-resistant *Staphylococcus aureus* (MRSA) strain Mu50, the gram-negative *Pseudomonas aeruginosa* strain PAO1, and *M. tuberculosis* strain H37Rv. Interestingly, the racemic mixtures of compounds 3 and 4 showed potent biofilm-dispersing activities against both MRSA Mu50 and *P. aeruginosa* PAO1 with IC90 of 6.25 µM and 12.5 µM, respectively (**Fig. 12 A+B**), while only 4 caused partial dispersion of *M. tuberculosis* H37Rv biofilms at the highest tested concentration of 100 µM (**Fig. 12 E**). Intriguingly, both fusapurpurins were unable to prevent the formation of biofilms (**Fig. 12 C+D**). Furthermore, they also did neither impair viability of cells in biofilms (**Fig. S11**) nor show any direct antimicrobial effect on actively growing submersed microbial cells (**Table 3**). Quorum sensing has been identified as a cell density- dependent mechanism of cell-cell communication that is involved in all steps of biofilm development and maturation [43]. Consistent with the inability to prevent biofilm-formation, the fusapurpurins also did not interfere with quorum sensing-induced violacein production in a bioassay employing *Chromobacterium violaceum* (**Fig. S12**).

Consequently, both fuspurpurins exhibit an unusal, very specific desintegratiung effect at low micromolar concentration only when added to preformed biofilms. This effect appears to be broad spectrum including both gram-positive and gram-negative bacteria and to a lesser extent also mycobacteria.

Bacterial biofilms are virulence factors that are complicating treatment, prolonging infections and increasing mortality of infectious diseases and are therefore a huge health concern [44]. Thus, the discovery of new and potent biofilm-inhibiting compounds is crucial. In addition to compounds that are able to prevent biofilm formation and/or kill bacterial cells embedded in the biofilms, molecules able to disintegrate the biofilm matrix thereby removing biofilms from biotic and abiotic surfaces are also of great clinical relevance [43]. Therefore, our discovery of the specific biofilm-desintegrating properties of fusapurpurin A and B at low micromolar concentrations are of potential medical interest as these compounds in combination with antibiotics targeting the dispersed bacterial cells might be able to eradicate chronic bacterial infections. In this regard, the unusual broad-spectrum activity of these compounds against a gram-positive, a gram-negative and a mycobacterial organism is a highly beneficial attribute as it might suggest potential broad clinical applicability. For future research, it will be of great interest to distinguish, if the activity of **3** and **4** is connected to either one of the two enantiomers of the mixture or if all isolated isomers show a biofilm disrupting activity. If the shown activity is only connected to one enantiomer, the biofilm disrupting activity could be stronger than expected, elucidating an even higher potential.

In order to assess the therapeutic potential of the fusapurpurins, the cytotoxic activity of compound enantiomeric mixtures **3** and **4** was evaluated against the human cell lines THP-1 (human monocytic leukaemia cell line), Huh-7 (Human liver carcinoma cell line), and HEK293 (human

embryonic kidney cell line). Compound 3 showed weak cytotoxicity against THP-1 and Huh-7 cell lines and no cytotoxic effect on the HEK293 cell line, while compound **4** showed moderate cytotoxic activities against all three tested cell lines, showing no to moderate cytotoxic effects (**Table 4**). Although this results in some selectivity particularly for fusapurpurin A (compound **3**) (selectivity index = IC_{50} cytotoxicity / IC_{90} antibiofilm activity against MRSA ranging from 6 to >16 dependent on human cell type), these properties might not be sufficient for direct clinical application. Nevertheless, elucidation of the mode of action of fusapurpurin A and B and identification of their molecular target might allow the development of more potent and more specific broad-spectrum biofilm-desinteragting drugs in future studies.

3. Experimental section

General Experimental Procedures

Optical rotations were measured on a Jasco P-2000 polarimeter. UV spectra were obtained by the use of a Dionex P580 system in combination with a diode array detector (UVD340S) and a Eurosphere 10 C_{18} column (125 × 4 mm). 1D and 2D NMR spectra were recorded on a Bruker Avance III (^{1}H, 600 MHz; ^{13}C 150 MHz) spectrometer. Mass spectra were measured on a Finnigan LCQ Deca (Thermo Quest) mass spectrometer and for HRESIMS on a UHR-QTOF maXis 4G (Bruker Daltonics) mass spectrometer. Semipreperative HPLC was performed on a Lachrom-Merck Hitachi system (pump L7100, UV-detector L7400, Eurospher 100 C_{18} column 300 × 8 mm, Knauer Germany) and a Chromaster-VWR Hitachi system (pump 5110, UV-detector 5410, Eurospher 100 C18 column 300 × 8 mm, Knauer Germany). VLC and non-vacuum-column chromatography were accomplished using Macherey-Nagel silica gel 60M (0.04-0.063 mm). Precoated TLC silica gel 60 F254 plates (Merck) were used for tracking separation using detection under UV light at 254 and 365 nm wavelengths or spraying Anisaldehyde-sulfuric acid reagent. Sephadex LH20 (GE Healthcare Bio. Sciences AB) was used as a stationary phase for column chromatography. The measurement of optical rotations was accomplished by using spectral-grade solvents. The optical density of fungal yeast cultures was measured using a WPA Biowave CO8000 Cell Density Meter.

Fungal Material

The fungus *Fusarium oxysporum* was obtained from a soil sample collected from Texel, the Netherlands (GPS 53.00 N 4.44 E) by using a co-cultivation method. A spatula of the soil was mixed with 100 µL from an overnight culture of the auxotrophic yeast *Saccharomyces cerevisiae* FY1679- 01B with the optical density of 1.0 and 20 mL Lysogeny Broth (LB)-medium in a 100-ml Erlenmeyer flask. The co-cultivation mixture was incubated statically for 14 days at 30 °C, initially aiming at enriching microorganisms that can antagonize yeast growth. 10 µL of the liquid co-culture were spread on an agar plate containing Yeast Nitrogen Base without Amino Acids (BD Difco), enriched with D-glucose and 20 mg/L chloramphenicol, using a spatula and incubated for 3 days at 30 °C. The fungus was growing on top of the agar plate as a white filamentous spot. The isolated strain was identified as *F. oxysporum*

by internal transcribed spacer (ITS) sequences with 100% identity to known *F. oxysporum* (GenBank Accession OP122502). Additionally, the identity was confirmed via whole genome sequencing with a core genome identity (ANI) of 97.073% with the NCBI reference GCF_000271745.1 using FastANI (GenBank Accession PRJNA861985).

Fermentation and Extraction

The fermentation of the fungus was carried out as a co-cultivation approach, first at a small-scale to compare different co-cultivation attempts followed by large-scale cultivation for isolation purposes. For all samples, solid rice medium enriched with Lysogeny Broth (LB) medium was used as

the main nutrient. For the small-scale co-cultivation approaches, 100 g of rice and 100 mL of LB- medium were added to seven Erlenmeyer flasks followed by autoclaving. 10 ml of overnight cultures of five different bacteria respectively, namely *Acinetobacter baylyi* ADP1, *Pseudomonas qingdaonensis*, *Bacillus amyloliquefaciens*, *Lysinibacillus macroides* and *Paenibacillus ehimensis* were then each added to one of these Erlenmeyer flasks and incubated for four days at 22 °C under static conditions. Then 1 × 1 cm^2 fungal material was inserted into each of the Erlenmeyer flasks containing bacterial cultures using a flame-sterilized scalpel and into one of the Erlenmeyer flasks not containing bacterial cultures as a control. One Erlenmeyer flask was used as a background control for the LB medium. All flasks were then incubated for four weeks at 22 °C under static conditions. For the large-scale co-cultivation approach, ten Erlenmeyer flasks were prepared with rice and LB-medium as mentioned above. 10 mL of an overnight culture of *P. ehimensis* was then added to each flask and incubated for 4 days at 22 °C under static conditions followed by the addition of 1 × 1 cm^2 fungal material and incubation for four weeks at 22 °C under static conditions. Each flask of the small-scale and large-scale fermentations was extracted with 250 mL Ethylacetate. The rice medium was cut into small pieces and shaken for eight hours followed by evaporation of the EtOAc.

Re-induction of fusapurpurins A and B under multiple fermentation conditions and metabolite detection

OSMAC fermentation was performed using a co-culture system of *Fusarium* and *P. ehimensis*. *F. oxysporum* and *P. ehimensis* were inoculated onto solid rice medium and statically co-cultivated. Under different fermentation conditions, the rice medium was supplemented with 2.5% L-phenylalanine, 2.5% L-leucine, 2.5% L-cysteine, 2.5% L-tryptophan, 2.5% sodium glutamate, 2.0% glucose, 3.5% NaCl, 3.5% NaBr, 3.5% NaI, 3.5% $(NH_4)_2SO_4$, 3.5% $NaNO_3$, or 3.5% zinc lactate. According to the stability and solubility of each additive, the supplements were either added directly to the medium before sterilization or added by sterile filtration to sterilized and cooled medium.

In another set of OSMAC co-culture experiments, in addition to the original *F. oxysporum* strain, another *Fusarium* sp. strain was also used for parallel co-cultivation with *P. ehimensis*. This set of fermentations included a non-supplemented control, as well as phenylpyruvic acid (PPA)- and sodium phenylpyruvate (NaPPA)-supplemented conditions. PPA was added at 50 mg per fermentation system,

whereas NaPPA was added at 1 g per fermentation system. PPA and NaPPA were added either at the time of inoculation, after 2 days of cultivation, or after 2 weeks of cultivation. These conditions were tested in both the *F. oxysporum–P. ehimensis* and the alternative *Fusarium* sp.–*P. ehimensis* co-culture systems.

For each cultivation condition, corresponding fungal monoculture, bacterial monoculture, and uninoculated medium controls were included. Some co-culture systems were statically incubated at room temperature, 28 °C, or 30 °C. After cultivation, the fermentation substrate was cut into small pieces and thoroughly extracted with ethyl acetate. The ethyl acetate extract was concentrated under reduced pressure to obtain the crude extract. The crude extract was dissolved in an appropriate amount of methanol or acetonitrile and then centrifuged or filtered before HPLC or LC-MS analysis. The production of 9-*O*-methylfusarubin, fusapurpurin A, and fusapurpurin B was examined by comparing chromatograms, target compound retention times, and mass spectrometric signals of crude extracts obtained under different fermentation conditions.

Isolation

The crude extract (3.89 g) obtained from the large-scale co-cultivation with *P. ehimensis* was separated by the use of Vacuum Liquid Chromatography with silica gel as a stationary phase. A step gradient from 100% hexane to 100% EtOAc followed by a step gradient from 100% CH_2Cl_2 to 100% CH_3CN and finished with 100% EtOH, with 500 mL for each eluent, yielded 16 fractions (V1-V16). Fractions V3 (787.9 mg), V4 (901.6 mg) and V5 (328.6 mg) were combined and further separated over a Sephadex LH20 column with Acetone as eluent to give 6 subfractions (V3-5S1-V3-5S6). Subfraction V3-5S5 (35.3 mg) was purified over semi-preparative HPLC using a MeOH-H_2O step gradient from 50-100 % MeOH to give **2** (2.9 mg). Fractions V6 (229.7 mg), V7 (28.0 mg), V8 (2.8 mg), V9 (5.9 mg), V10 (11.0 mg), V11 (13.9 mg), V12 (41.9 mg), V13 (56.8 mg), V14 (72.8 mg) and V15 (38.8 mg) were combined and then separated using a LH20 Sephadex column with 100% Acetone as an eluent to yield 4 subfractions (V6-15S1-V6-15S4). Subfraction V6-15S1 was finally purified over semi-preparative HPLC using a CH_3CN-H_2O step gradient from 30-80% CH_3CN to give **3** (2.4 mg) and **4** (2.9 mg).

Spectral Data of compounds 2-4:

Fusachinon (**2**): orange amorphous solid; $[\alpha]_D^{25}$ -65 (c 0.8, MeOH) λmax 230, 277, 480 nm; ^{1}H NMR (DMSO-d_6) and ^{13}C NMR (DMSO-d_6) see Table 1; HRESIMS m/z 331.0817 $[M + H]^+$ (calcd. for $C_{17}H_{15}O_7$ 331.0812 m/z).

Fusapurpurin A (**3**): pink crystals (Ethylacetate); UV (MeOH) λmax 200, 226, 284, 520 nm; ^{1}H NMR (DMSO-d_6) and ^{13}C NMR (DMSO-d_6) see Table 2; HRESIMS m/z 465.1177 $[M + H]^+$ (calcd. for $C_{25}H_{21}O_9$ 465.1180 m/z).

Fusapurpurin B (**4**): purple crystals (MeOH); UV (MeOH) λmax 201, 226, 283, 520 nm; ^{1}H NMR (DMSO-d_6) and ^{13}C NMR (DMSO-d_6) see Table 2; HRESIMS m/z 465.1174 m/z $[M + H]^+$ (calcd.

for $C_{25}H_{21}O_9$ 465.1180 m/z). The detailed NMR- and other spectral data for compounds 1-10 are provided in the supplementary information **S13-S69**.

X-ray crystallographic data

Suitable crystals were carefully selected under a polarized-light microscope, covered in protective oil and mounted on a cryo-loop. The single crystal diffraction data were collected on a Rigaku XtaLAB Synergy S four circle diffractometer with a Hybrid Pixel Array Detector and a PhotonJet X-ray source for Cu-Kα radiation (» = 1.54184 Å) with a multilayer mirror monochromator. Data was collected at 100.0 ± 0.1 K using ω-scans. Data reduction and absorption correction were performed with CrysAlisPro 1.171.41.105a [45]. Structure analysis and refinement: The structures were solved by direct methods (SHELXT-2015). Full-matrix least-squares refinements on F2 were carried out using the SHELXL-2017/1 program package in OLEX 2.1.3 [46-48]. All hydrogen atoms on C were positioned geometrically (with C–H = 0.95 Å for aromatic and aliphatic CH, C–H = 1.00 Å for ternary CH, C–H = 0.99 Å for CH_2 and C–H = 0.98 Å for CH_3) and refined using riding models (AFIX 43, 13, 23 and 137 with Uiso(H) = 1.2 Ueq (CH, CH2) and 1.5 Ueq (CH_3). The protic hydrogen atom for OH in compounds **3** and **4** was found and refined freely. Strongly disorderd solvent molecules of MeOH for compound **4** have been removed with the solvent mask feature as implemented in OLEX 2.1.3. 176 electrons were found in a volume of 1300 $Å^3$ per unit cell, which may correspond to about 10 methanol molecules (18 electrons each) as the solvent of crystallization per unit cell or about 1.25 methanol per asymmetric unit (Z = 8). Crystal data and details on the structure refinement are given in Table 5. Graphics were drawn with the program DIAMOND [49]. Computations on the supramolecular interactions were carried out with PLATON for Windows [50-52]. The crstallographic data for compounds 3 and 4 reported in this paper have been deposited in the CCDC under the numbers 2232516 and 2232517. This data can be obtained free of charge from the Cambridge Crystallographic Data Centre via www.ccdc.cam.ac.uk/data_request/cif.

Whole genome nanopore sequencing and genome assembly

For long-read nanopore sequencing, the GDE_9141_v112_revE_01Dec2021 protocol for ligation sequencing of genomic DNA was followed, using the SQK-LSK112 ligation kit and a MinION Flow Cell R10 Version. Reads were assembled using Flye [53]. Assembled contigs are available under the SRA accession [PRJNA861985]. The antiSMASH software [28] was used to detect gene clusters and identify potential genes of interest involved in the production of fusarubin and derivatives.

Genome annotation, BGC comparison and candidate enzyme screening

The assembled genome of *F. oxysporum* was used for subsequent biosynthetic gene cluster and candidate enzyme analyses. The taxonomic relationship of the strain was evaluated by average nucleotide identity comparison against reference genomes using FastANI [27]. BGC prediction was performed using the fungal version of antiSMASH, with particular attention paid to the type I polyketide synthase gene cluster related to fusarubin/oxyjavanicin-type naphthoquinone biosynthesis [28].

Candidate tailoring enzymes were screened based on genome annotation, protein function prediction, conserved domain analysis, and their distribution on the same contig as the fusarubin-like BGC. Since the structures of fusapurpurins A and B suggest that their formation may involve a conjugation reaction between 9-*O*-methylfusarubin and a phenylpyruvate-derived moiety, LovD/PcEST-like proteins with potential acyltransferase activity were specifically searched.

Structural prediction and structural comparison of FO-LovD-like protein

The three-dimensional structure of FO-LovD-like was predicted using AlphaFold, and the reliability of the model was assessed based on parameters such as pLDDT and pTM [31-32]. The reported A. terreus LovD structure was used as the reference model for structural comparison. Overall structural superposition of FO-LovD-like protein and LovD was performed using US-align, and TM-score, C-alpha RMSD and the spatial correspondence of catalytic core residues were recorded [33]. Structural comparisons focused on the conserved Ser-Lys-Tyr catalytic core of LovD-like/PcEST-like enzymes and loop regions that may influence substrate entrance and substrate recognition.

Cloning, heterologous expression and Ni-NTA purification of FO-LovD-like protein

The FO-LovD-like coding sequence was designed according to the genome annotation information of *Fusarium oxysporum*. Since this gene was derived from fungal genomic DNA and contained intronic regions, primers were designed according to the predicted exon–intron structure to avoid intron sequences, and the corresponding coding-region fragments were amplified separately from *F. oxysporum* gDNA. PCR amplification was performed using Phusion High-Fidelity DNA Polymerase (New England Biolabs, NEB). The two resulting PCR fragments were joined by overlap PCR to obtain the intron-free FO-LovD-like coding sequence.

The amplified FO-LovD-like coding sequence and the pET28a expression vector were double-digested with BamHI-HF and XhoI (New England Biolabs, NEB), respectively. After purification of the digestion products, ligation was performed using T4 DNA Ligase (New England Biolabs, NEB), allowing insertion of the target gene into the pET28a expression vector with a His-tag for subsequent affinity purification. The ligation product was transformed into competent Escherichia coli cells for plasmid amplification and screening. After the recombinant plasmid was confirmed by sequencing to contain the correct insert sequence and reading frame, it was transformed into E. coli BL21(DE3) competent cells for heterologous expression. The pET/BL21(DE3) system is a commonly used T7 RNA polymerase-dependent recombinant protein expression system suitable for IPTG-inducible expression in E. coli [54, 55].

Positive clones were inoculated into LB medium containing kanamycin and cultured overnight at 37 °C with shaking. On the following day, the overnight culture was inoculated into fresh LB medium containing kanamycin and grown at 37 °C with shaking until the logarithmic growth phase. IPTG was then added to a final concentration of 500 μM, and FO-LovD-like protein expression was induced at 30 °C for 5 h. After induction, cells were collected by centrifugation. The cell pellet was resuspended

in lysis buffer containing 20 mM Tris-HCl, 300 mM NaCl, 20 mM imidazole, and 1% Triton X-100, pH 8.0. Cells were mechanically disrupted by bead beating. After removal of cell debris by centrifugation, the resulting supernatant was used as the soluble protein fraction for subsequent purification. Samples from the pre-induction culture, post-induction culture, lysis supernatant, and pellet fractions were collected and analyzed by SDS-PAGE to evaluate target protein expression and soluble distribution.

SDS-PAGE analysis was performed using 12% Mini-PROTEAN TGX Stain-Free Precast Gels (Bio-Rad). Protein samples were mixed with SDS loading buffer and heat-denatured before electrophoresis. After electrophoresis, the gel was imaged using the laboratory Gel Doc imaging system to examine target protein expression and purification.

His-tagged FO-LovD-like protein was purified by Ni-NTA affinity chromatography. Protino Ni-NTA Agarose (Macherey-Nagel) was equilibrated with lysis buffer before use. The soluble lysate containing the target protein was then incubated with Ni-NTA agarose to allow binding of the His-tagged protein to the resin. After binding, the resin was thoroughly washed with washing buffer containing a low concentration of imidazole to remove nonspecifically bound proteins. The target protein was subsequently eluted using elution buffer containing a higher concentration of imidazole. Ni-NTA affinity purification is based on the interaction between a polyhistidine tag and nickel-chelating resin and is a commonly used method for the purification of recombinant His-tagged proteins [56].

After SDS-PAGE analysis of the elution fractions, fractions containing the target protein were pooled. To remove the high concentration of imidazole and exchange the protein into a buffer suitable for subsequent in vitro reactions, the purified protein was concentrated and buffer-exchanged using a Vivaspin 500 centrifugal concentrator. The final protein was stored in buffer containing 50 mM Tris-HCl, 150 mM NaCl, and 10% glycerol, pH 7.5. Protein concentration was determined using a routine protein quantification method. The purified FO-LovD-like protein was stored in the above buffer and used for subsequent in vitro reaction assays.

Protein-ligand complex prediction and distance analysis

To evaluate the potential capacity of the FO-LovD-like active pocket to accommodate 9-*O*-methylfusarubin and activated phenylpyruvate-derived acyl donors, AlphaFold3-class complex prediction models and Chai-1 were used for protein-small molecule complex prediction [34-35]. 9-*O*-Methylfusarubin was defined as the potential acyl acceptor, while phenylpyruvate-SNAC and phenylpyruvate-CoA were used as a simplified thioester donor and a CoA-thioester-type acyl donor model, respectively. Binary complex models of FO-LovD-like protein with individual substrates and ternary complex models of FO-LovD-like protein, 9-*O*-methylfusarubin and thioester donors were constructed.

The complex models were analysed with respect to whether the substrates were located in the same internal or semi-open pocket, the distance between the thioester carbonyl carbon and catalytic Ser61 OG, the distance between the thioester carbonyl oxygen and Tyr173 OH or Lys64 NZ, and the

distance between the target alcohol hydroxyl O7_1 of 9-*O*-methylfusarubin and the thioester carbonyl carbon. Distances were measured in molecular visualization software and recorded in Å. Because LovD-like enzymes typically involve catalytic Ser in the formation of an acyl-enzyme intermediate, these distance parameters were used to assess whether the predicted models approximate a possible acyl-transfer conformation [29-30]. Complex prediction was used only as a structural hypothesis and substrate-accommodation analysis, not as direct evidence of enzymatic catalytic function.

Biofilm assays

Biofilm assays were performed as previously described [57]. Briefly, biofilm integrity was evaluated using the crystal violet assay. A bacterial cell suspension was prepared in Mueller-Hinton broth supplemented with 10% glucose and adjusted to an OD equal to 10^8 cells per mL. One hundred microlitres of the bacterial cell solution were added to each well and incubated statically for 24 h at 37 °C to allow the formation of biofilms. The wells were washed twice with PBS to remove planktonic cells and compounds were added in a 1:1 serial dilution to the wells. Crystal violet staining was performed 24 h later as follows. The liquids in the wells were aspirated and each well was washed twice with PBS. After air drying for 30 min, 100 µL of a 0.1% crystal violet solution was added and allowed to stain the biofilms for 15 min. Afterwards, the plates were washed twice with PBS and 100 µL 30% acetic acid was added for 30 min to solubilise the dye. Fifty microlitres were transferred to a fresh 96-well round-bottom plate and absorption was measured at 600 nm in a TECAN plate reader. A sterile and vehicle control were used as controls for calculations. For mycobacterial biofilms, 24-well polystyrene flat-bottom cell culture plates and Sauton medium without tyloxapol were used. A saturated Mtb H37Rv culture in Sauton medium (OD_{600} = 1.0) was used to start the growth of the biofilms. 450 µL Sauton medium and 50 µL saturated Mtb H37Rv cell suspension was added to each well of the 24-well plate. The plate was covered with a clear sealing foil and was incubated for five weeks at 37 °C, 5% CO_2, and humified atmosphere to allow the formation of the biofilms. Hereafter, test compounds were injected beneath the pellicle to a final concentration of 100 µM. Rifampicin (RIF, 100 µg/mL = 121.5 µM), isoniazid (INH, 50 µg/mL = 365 µM), and DMSO were used as positive and negative controls, respectively. After five days, the medium was carefully removed from each well without disturbing the pellicle and 1000 µL of a 0.1% crystal violet solution was added to stain the extracellular polymeric substances. After staining for 30 minutes, the staining solution was removed and the wells were washed twice with PBS. The pellicles were allowed to air-dry for 15 minutes and 500 µL methanol was added to each well to extract the colour from the pellicles. Using a polystyrene 96-well round bottom plate, 100 µL of each well was transferred into the 96-well plate and absorbance was measured at 600 nm in a TECAN plate reader.

The quorum sensing assay with *Chromobacterium violaceum* was carried out as follows. 100 µL of an overnight culture of *C. violaceum* in Mueller Hinton broth (MHB) was evenly spread over an agar plate of Mueller Hinton medium. Cotton test discs were put on the surface of the agar medium using forceps. Each disc was soaked with 5 µL of samples or control solutions in DMSO. 125 mg/mL

vanillin was used as a positive control. DMSO was used as a negative control. Samples were added at concentrations of 10 mg/mL and for fusapurpurin A and B at 100 µM. Test plates were incubated at 30 °C overnight.

Cytotoxicity assays

The cytotoxicity assays were performed using THP-1 (human monocytic leukaemia cell line), Huh-7 (Human liver carcinoma cell line) and HEK293 (human embryonic kidney cell line) cell lines as described before [58]. The THP-1 cells were cultured using RPMI 1640 medium containing 2 mM L-glutamine and supplemented with 10% fetal calf serum (FCS) and 1% sodium pyruvate. Huh-7 cells were cultured using a 1:1 mixture of RPMI 1640 medium containing 2 mM L-glutamine and 10% FCS medium and DMEM medium containing 10% FCS and 1% sodium pyruvate. The HEK293 cells were cultured with EMEM medium including 2 mM L-glutamine and supplemented with 1% NE amino acids, 1% 1.0 mM sodium pyruvate and 10% FCS. All three cell lines were then incubated at 37 °C in an atmosphere of 5 % CO_2 at humid conditions for 2 weeks while renewing the medium twice weekly. Subsequently, the cells were suspended and adjusted to a density of 2×10^5 cells/ml. In a 96-well flat-bottom microtiter plate, the cells were adjusted to a total volume of 100 µL containing 2-fold serial dilutions of the tested compounds **2** and **3** ranging from 100 to 0.78 µM. Cycloheximide (4, 2, 1, 0.5, 0.25, 0.13, 0.06, 0.03 µg/ml) was used as a positive control. After an incubation time of 48 h at 37 °C in an atmosphere of 5% CO_2 under humid conditions, 10 µL resazurin solution (100 µg/mL) was added to each well and incubated for another 4 h. The fluorescence was then quantified using a Tecan Infinite 200pro microplate reader (excitation 540 nm, emission 590 nm). The residual growth was calculated relative to non-inoculated (0% growth) and controls treated with DMSO (100% growth), respectively.

Media and Strains

Methicillin-resistant *Staphylococcus aureus* (MRSA) Mu50 (ATCC 700699) and *Pseudomonas aeruginosa* PAO1 (ATCC 47085) were grown in Mueller-Hinton broth (MHB). The yeast *Candida albicans* ATCC 24433 was grown in a standard YPD medium (1% yeast extract, 2% peptone, and 2% glucose). The pathogenic bacterium *Mycobacterium tuberculosis* (Mtb) H37Rv (ATCC 27294) was grown in 7H9 supplemented with ADS (0.85% NaCl, 5% BSA, 2% glucose), 0.5% glycerol, and 0.05% tyloxapol. Nosocomial bacteria and *C. albicans* were grown shaking at 120 rpm and 37 °C, Mtb was grown at 37 °C shaking at 80 rpm.

Determination of the minimal inhibitory concentration

The minimal inhibitory concentration (MIC_{90}) of compounds was determined via microbroth dilution assays. Briefly, a serial 1:1 dilution of compounds was prepared in a 96-well round-bottom polystyrene plate in 50 µL growth medium ranging from 200 µM to 1.56 µM. Pre-grown bacterial cultures were measured for their $OD_{600\ nm}$, and a cell suspension in the growth medium was adjusted to 10^6 CFU/mL. After 50 µL of the cell suspension was added to each well, the compound concentration was changed to a range from 100 µM to 0.78 µM. In the case of MRSA Mu50, P. aeruginosa PAO1 and

C. albicans ATCC 24433, the BacTiter Glo assay (Promega) was used to quantify growth after 24 h of incubation as described in the manufacturer's manual. Briefly, equal volumes of BacTiter Glo reagent and bacterial cell suspensions were mixed in a white flat-bottom 96-well plate. After 5 minutes, luminescence was measured with a TECAN plate reader. The positive control for MRSA Mu50 and P. aeruginosa PAO1 was moxifloxacin and for *C. albicans* hygromycin was used, while DMSO was used as solvent control for all three organisms. The growth of Mtb H37Rv was quantified via the resazurin assay following a protocol as described earlier [59]. Briefly, 10 µL of a 100 µg/mL resazurin solution was added to each well of the 96-well plate after five days of incubation at 37 °C, 5% CO_2, and in a humidified atmosphere. After incubating the plates for another 18 hours at room temperature, the reaction was stopped by the addition of 100 µL 10% formalin solution to each well. The fluorescence was measured at 535 nm excitation and 590 nm emission using a TECAN plate reader. Rifampicin and DMSO were used as positive and vehicle control, respectively. All experiments have been conducted in triplicate.

Impairment of cell viability in biofilms

The impairment of cell viability in biofilms of *S. aureus* (MRSA) Mu50 (ATCC 700699) and *P. aeruginosa* PAO1 (ATCC 47085) by fusapurpurin A and B (**3** and **4**) was tested in a microbroth dilution assay. First, cells were grown to form biofilms as described above. Subsequently, a serial 1:1 dilution of fusapurpurin A and B and moxifloxacin was prepared in a 96-well round-bottom polystyrene plate containing the bacterial biofilms, using 50 µL growth medium ranging from 100 µM to 0.78 µM. The viability of cells in the biofilms was measured using the BacTiter Glo assay (Promega) as described above. DMSO was used as solvent control for both organisms.

Acknowledgements

We thank the CeMSA@HHU (Center for Molecular and Structural Analytics@Heinrich Heine University) for recording the mass-spectrometric and the NMR-spectroscopic data. We thank Heike Goldbach-Gecke for testing the cytotoxic activity against the human monocytic cell-line THP1.

References

1. Ventola, C.L., The antibiotic resistance crisis: part 1: causes and threats. *P T*, 2015. **40(4)**: p. 277-83.
2. Moloney, M.G., Natural Products as a Source for Novel Antibiotics. *Trends Pharmacol Sci*, 2016. **37(8)**: p. 689-701.
3. Rutledge, P.J. and G.L. Challis, Discovery of microbial natural products by activation of silent biosynthetic gene clusters. *Nat Rev Microbiol*, 2015. **13(8)**: p. 509-23.
4. Wang, B., et al., Activation of silent biosynthetic gene clusters using transcription factor decoys. *Nat Chem Biol*, 2019. **15(2)**: p. 111-114.
5. Okada, B.K. and M.R. Seyedsayamdost, Antibiotic dialogues: induction of silent biosynthetic gene clusters by exogenous small molecules. *FEMS Microbiol Rev*, 2017. **41(1)**: p. 19-33.
6. Hoogendoorn, K., et al., Evolution and Diversity of Biosynthetic Gene Clusters in *Fusarium*. *Front Microbiol*, 2018. **9**: p. 1158.
7. Studt, L., et al., Knock-down of the methyltransferase Kmt6 relieves H3K27me3 and results in induction of cryptic and otherwise silent secondary metabolite gene clusters in *Fusarium fujikuroi*. *Environ Microbiol*, 2016. **18(11)**: p. 4037-4054.
8. Niehaus, E.M., et al., Apicidin F: characterization and genetic manipulation of a new secondary metabolite gene cluster in the rice pathogen *Fusarium fujikuroi*. *PLoS One*, 2014. **9(7)**: p. e103336.
9. von Bargen, K.W., et al., Isolation and Structure Elucidation of Fujikurins A-D: Products of the PKS19 Gene Cluster in *Fusarium fujikuroi*. *J Nat Prod*, 2015. **78(8)**: p. 1809-15.
10. Connolly, L.R., K.M. Smith, and M. Freitag, The *Fusarium graminearum* histone H3 K27 methyltransferase KMT6 regulates development and expression of secondary metabolite gene clusters. *PLoS Genet*, 2013. **9(10)**: p. e1003916.
11. Bode, H.B., et al., Big effects from small changes: possible ways to explore nature's chemical diversity. *ChemBioChem*, 2002. **3**: p. 619-627.
12. Pérez Hemphill, C.F., et al., OSMAC approach leads to new fusarielin metabolites from *Fusarium tricinctum*. *J Antibiot (Tokyo)*, 2017. **70(6)**: p. 726-732.
13. Rodriguez-Ortiz, R., et al., Stimulation of bikaverin production by sucrose and by salt starvation in *Fusarium fujikuroi*. *Appl Microbiol Biotechnol*, 2010. **85(6)**: p. 1991-2000.
14. Weikl, F., et al., Sesquiterpene emissions from *Alternaria alternata* and *Fusarium oxysporum*: Effects of age, nutrient availability, and co-cultivation. *Sci Rep*, 2016. **6**: p. 22152.
15. Moussa, M., et al., Co-culture of the fungus *Fusarium tricinctum* with *Streptomyces lividans* induces production of cryptic naphthoquinone dimers. *RSC Adv*, 2019. **9(3)**: p. 1491-1500.
16. Ancheeva, E., et al., Expanding the metabolic profile of the fungus *Chaetomium* sp. through co-culture with autoclaved *Pseudomonas aeruginosa*. *European Journal of Organic Chemistry*, 2017. **2017(22)**: p. 3256-3264.
17. Akone, S.H., et al., Inducing secondary metabolite production by the endophytic fungus *Chaetomium sp.* through fungal–bacterial co-culture and epigenetic modification. *Tetrahedron*, 2016. **72(41)**: p. 6340-6347.
18. Sharma, D., L. Misba, and A.U. Khan, Antibiotics versus biofilm: an emerging battleground in microbial communities. *Antimicrob Resist Infect Control*, 2019. **8**: p. 76.
19. Ciofu, O., et al., Antibiotic treatment of biofilm infections. *APMIS*, 2017. **125(4)**: p. 304-319.

20. Cont, A., et al., Biofilms deform soft surfaces and disrupt epithelia. *Elife*, 2020. **9**: e56533.

21. Steyn, P.S., P.L. Wessels, and W.F.O. Marasas, Pigments from *Fusarium moniliforme* Sheldon: Structure and ^{13}C nuclear magnetic resonance assignments of an azaanthraquinone and three naphthoquinones. *Tetrahedron*, 1979. **35(12)**: p. 1551-1555.

22. Tatum, J.H., R.A. Baker, and R.E. Berry, Naphthoquinones produced by *Fusarium oxysporum* isolated from citrus. *Phytochemistry*, 1985. **24(3)**: p. 457-459.

23. Studt, L., et al., Biosynthesis of fusarubins accounts for pigmentation of *Fusarium fujikuroi* perithecia. *Appl Environ Microbiol*, 2012. **78(12)**: p. 4468-80.

24. Hamill, R.L., et al. The structure of beauvericin, a new depsipeptide antibiotic toxic to *Artemia salina*. *Tetrahedron Letters*, 1969, **10(49)**: 4255–4258.

25. Isaka, M., et al., Cyclohexadepsipeptides from *Acremonium sp.* BCC 28424. *Tetrahedron*, 2011. **67(41)**: p. 7929-7935.

26. Karplus, M., Contact Electron-Spin Coupling of Nuclear Magnetic Moments. *The Journal of Chemical Physics*, 1959. **30(1)**: p. 11-15.

27. Jain, C., et al., High throughput ANI analysis of 90K prokaryotic genomes reveals clear species boundaries. *Nat Commun*, 2018. **9(1)**: p. 5114.

28. Blin, K., et al., antiSMASH 6.0: improving cluster detection and comparison capabilities. *Nucleic Acids Res*, 2021. **49(W1)**: p. W29-W35.

29. Xie, X., et al., Biosynthesis of lovastatin analogs with a broadly specific acyltransferase. *Chem Biol*, 2006. **13(11)**: p. 1161-1169.

30. Liang, Y., et al., Structural insights into the catalytic mechanism of lovastatin hydrolase. *J Biol Chem*, 2020. **295(4)**: p. 1047-1055.

31. Jumper, J., et al., Highly accurate protein structure prediction with AlphaFold. *Nature*, 2021. **596(7873)**: p. 583-589.

32. Tunyasuvunakool, K., et al., Highly accurate protein structure prediction for the human proteome. *Nature*, 2021. **596(7873)**: p. 590-596.

33. Zhang, C., et al., US-align: universal structure alignments of proteins, nucleic acids, and macromolecular complexes. *Nat Methods*, 2022. **19(9)**: p. 1109-1115.

34. Abramson, J., et al., Accurate structure prediction of biomolecular interactions with AlphaFold 3. *Nature*, 2024. **630(8016)**: p. 493-500.

35. Chai Discovery team, Chai-1: Decoding the molecular interactions of life. *bioRxiv*, 2024: p. 2024.10.10.615955.

36. Li, X., et al., Chemo-enzymatic synthesis of equisetin. *Chem Commun (Camb)*, 2017. **53(34)**: p. 4695-4697.

37. Watanabe, K., Discovery and investigation of natural Diels-Alderases. *J Nat Med*, 2021. **75(3)**: p. 434-447.

38. Kasahara, K., et al., Solanapyrone synthase, a possible Diels-Alderase and iterative type I polyketide synthase encoded in a biosynthetic gene cluster from Alternaria solani. *Chembiochem*, 2010. **11(9)**: p. 1245-52.

39. Oikawa, H., et al., Biosynthesis of macrophomic acid: Plausible involvement of intermolecular Diels-Alder reaction. *Chemical Communications*, 1997(1): p. 97-98.

40. Bitchagno, G.T.M., et al., Demystifying racemic natural products in the homochiral world. *Nat Rev Chem*, 2022. **6(11)**: p. 806-822.

41. Mazzotta, S., et al., Scalemic natural products. *Nat Prod Rep*, 2023. **40(10)**: p. 1647-1671.

42. Zask, A. and G. Ellestad, Biomimetic syntheses of racemic natural products. *Chirality*, 2018. **30(2)**: p. 157-164.

43. Rumbaugh, K.P. and K. Sauer, Biofilm dispersion. *Nat Rev Microbiol*, 2020. **18(10)**: p. 571-586.

44. Schulze, A., et al., Biofilms by bacterial human pathogens: Clinical relevance - development, composition and regulation - therapeutical strategies. *Microb Cell*, 2021. **8(2)**: p. 28-56.

45. Rigaku Oxford Diffraction. *CrysAlisPro Software System*. Rigaku Oxford Diffraction, 2021.

46. Sheldrick, G.M., Crystal structure refinement with SHELXL. *Acta Crystallogr C Struct Chem*, 2015. **71(Pt 1)**: p. 3-8.

47. Sheldrick, G.M., A short history of SHELX. *Acta Crystallogr A*, 2008. **64(Pt 1)**: p. 112-22.

48. Dolomanov, O.V., et al., OLEX2: a complete structure solution, refinement and analysis program. *Journal of Applied Crystallography*, 2009. **42(2)**: p. 339-341.

49. Brandenburg, K., Diamond (Version 4.6), Crystal and Molecular Structure Visualization, Crystal Impact. copyright 1997-2022, K. Brandenburg & H. Putz GbR, Bonn, Germany.

50. Spek, A. L. *PLATON: A Multipurpose Crystallographic Tool*. Utrecht University, Utrecht, The Netherlands, 2008.

51. Spek, A.L., Structure validation in chemical crystallography. *Acta Crystallogr D Biol Crystallogr*, 2009. **65(Pt 2)**: p. 148-55.

52. Farrugia, L. J. *Windows Implementation, Version 270519*. University of Glasgow, Glasgow, Scotland, UK, 2019.

53. Kolmogorov, M., et al., metaFlye: scalable long-read metagenome assembly using repeat graphs. *Nat Methods*, 2020. **17(11)**: p. 1103-1110.

54. Wurm, D.J., et al., The *E. coli* pET expression system revisited—mechanistic correlation between glucose and lactose uptake. *Appl Microbiol Biotechnol*, 2016. **100(20)**: p. 8721-8729.

55. Rosano, G.L. and E.A. Ceccarelli, Recombinant protein expression in *Escherichia coli*: advances and challenges. *Front Microbiol*, 2014. **5**: p. 172.

56. Hochuli, E., et al., Genetic Approach to Facilitate Purification of Recombinant Proteins with a Novel Metal Chelate Adsorbent. *Nat Biotechnol*, 1988. **6**: p. 1321-1325.

57. van Geelen, L., et al., Natural brominated phenoxyphenols kill persistent and biofilm-incorporated cells of MRSA and other pathogenic bacteria. *Appl Microbiol Biotechnol*, 2020. **104(13)**: p. 5985-5998.

58. Meier, D., et al., The plant-derived chalcone Xanthoangelol targets the membrane of Gram-positive bacteria. *Bioorg Med Chem*, 2019. **27(23)**: p. 115151.

59. Rehberg, N., et al., 3-O-Methyl-Alkylgallates Inhibit Fatty Acid Desaturation in *Mycobacterium tuberculosis*. *Antimicrob Agents Chemother*, 2019. **63(9)**: e00136-19.

60. Wu, Q., et al., A Review on the Synthesis and Bioactivity Aspects of Beauvericin, a *Fusarium* Mycotoxin. *Front Pharmacol*, 2018. **9**: p. 1338.

Figures and Tables

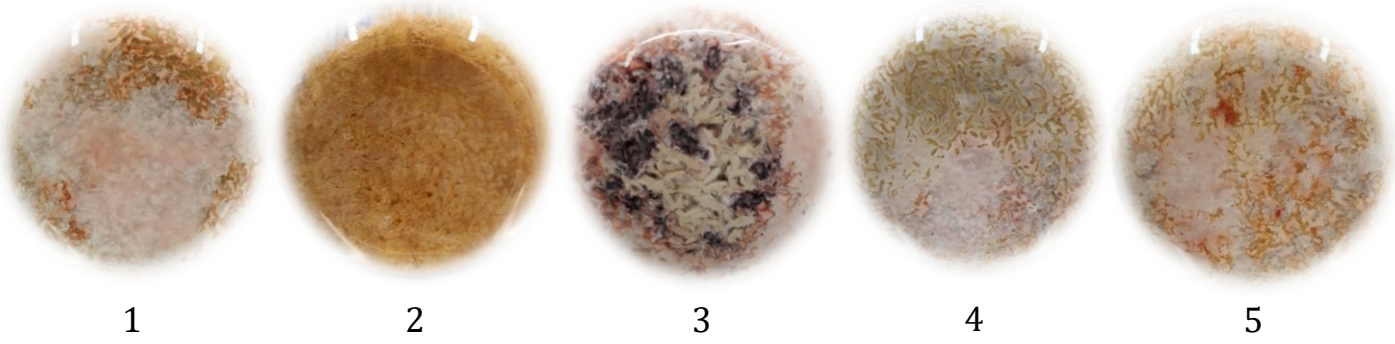


Figure 1. Co-cultivations of different bacteria with *Fusarium oxysporum* on rice medium supplemented with LB medium. Co-cultivation with *Lysinibacillus sp.* (1), *Bacillus amyloliquefaciens* (2), *Paenibacillus ehimensis* (3), *Pseudomonas sp.* (4) and *Acinetobacter baylyi* ADP1 (5) after four weeks of growth at room temperature. Captured is the bottom view of the 1 L Erlenmeyer flasks containing the solidified rice cultures.

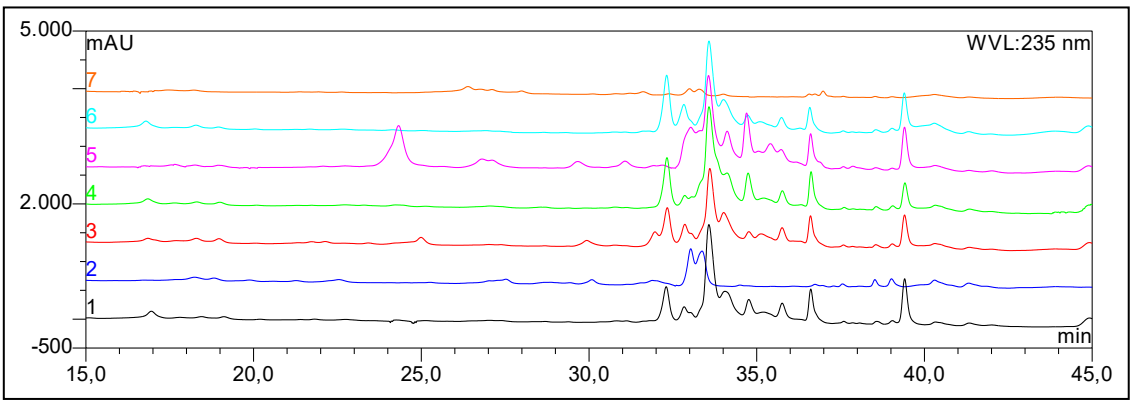


Figure 2. Overlay of HPLC-chromatograms from different axenic and co-culture extracts measured at 235 nm. The chromatograms of crude extracts from *F. oxysporum* axenic (1), *P. ehimensis* axenic (2) and co-cultures of *F. oxysporum* with *Pseudomonas sp.* (3), *Lysinibacillus sp.* (4), *P. ehimensis* (5), *A. baylyi* ADP1 (6) and *B. amyloliquefaciens* (7) are overlayed.

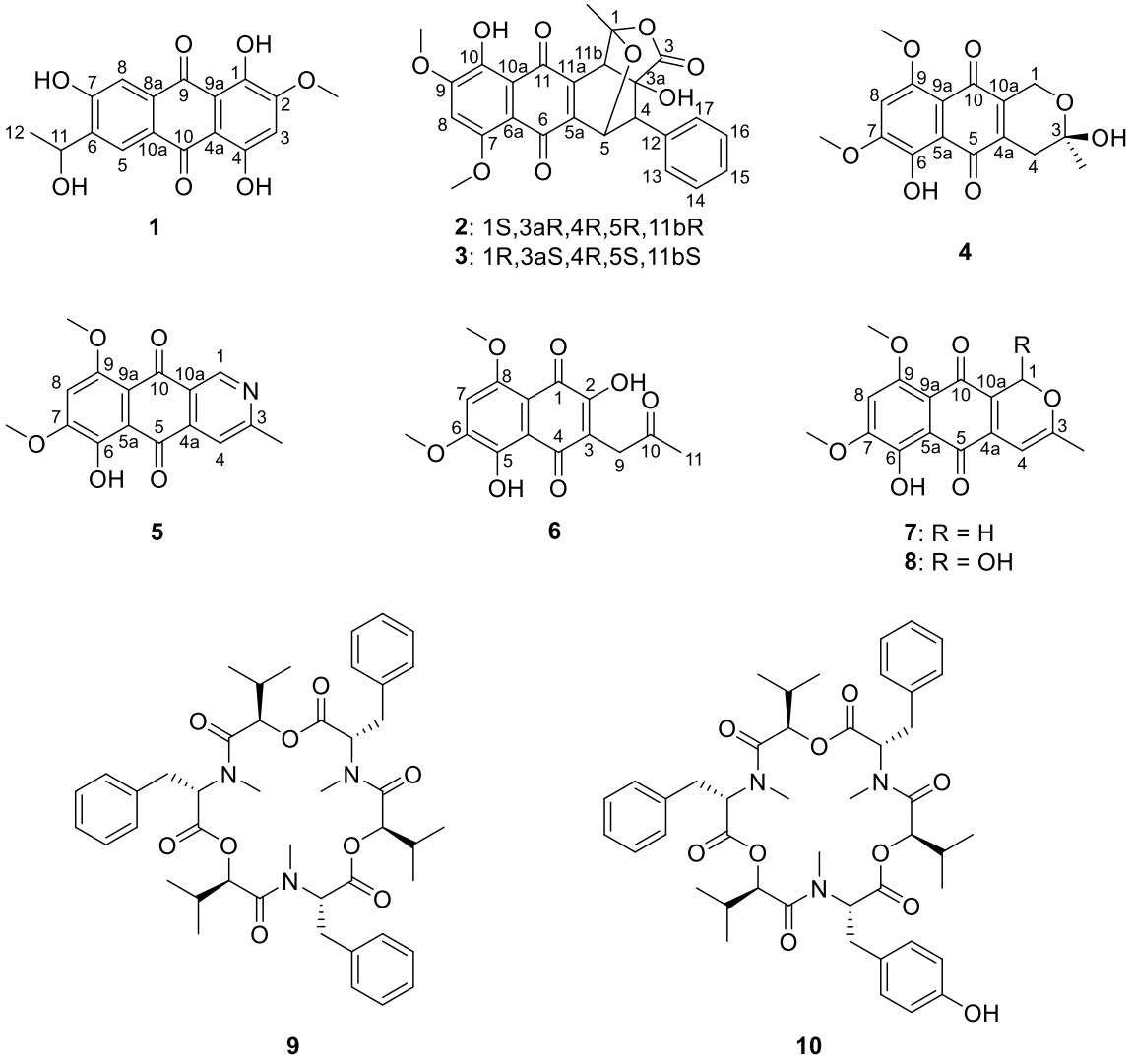


Figure 3. Chemical structures of the isolated compounds from co-culture of *F. oxysporum* with *P. ehimensis*. 9-O-methylfusarubin (**1**), fusachinon (**2**), fusapurpurin A (**3**), fusapurpurin B (**4**), 9-O-methylbostrycoidin (**5**), 2,5-dihydroxy-6,8-dimethoxy-3- (2-oxopropyl)-1,4-naphthalenedione (**6**), 9-O-methylanhydrofusarubin (**7**), 9-O- methylanhydrofusarubinlactol (**8**), beauvericin (**9**), beauvericin J (**10**).

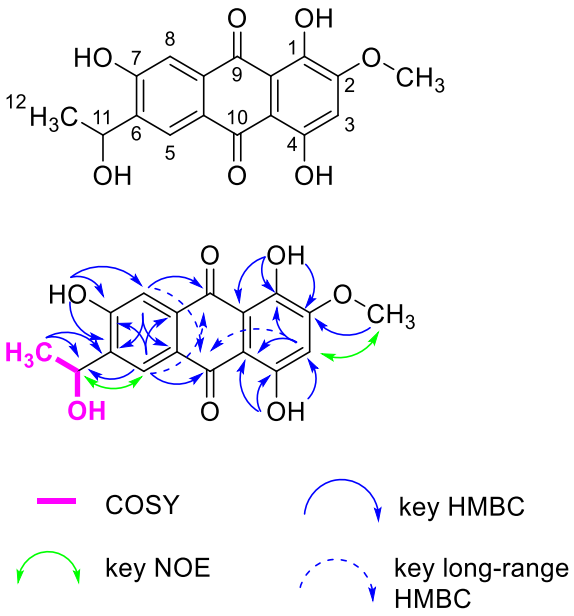


Figure 4. Key NMR correlations for **2** (fusachinon)

Table 1. NMR data for **2** (measured in DMSO-d_6 at 150 MHz for the ^{13}C- and at 600 MHz for the ^{1}H-NMR spectrum)

position	δ_C*	δ_H, m (J in Hz)
1	149.0, C	
2	156.6, C	
3	107.2, CH	6.96, s
4	159.2, C	
4a	104.7, C	
5	124.8, CH	8.35, s
6	141.6, C	
7	158.9, C	
8	111.3, CH	7.62, s
8a	132.9, C	
9	186.7, C	
9a	112.0, C	
10	183.8, C	
10a	125.0, C	
11	62.6, CH	5.03, dq (4.2, 6.4)
12	23.5, CH_3	1.33, d (6.4)
1-OH		13.17, s
2-OCH_3	56.5, CH_3	3.96, s
4-OH		13.70, s
7-OH		11.21, s
11-OH		5.42, d (4.2)

*signals were extracted from HSQC and HMBC spectra.

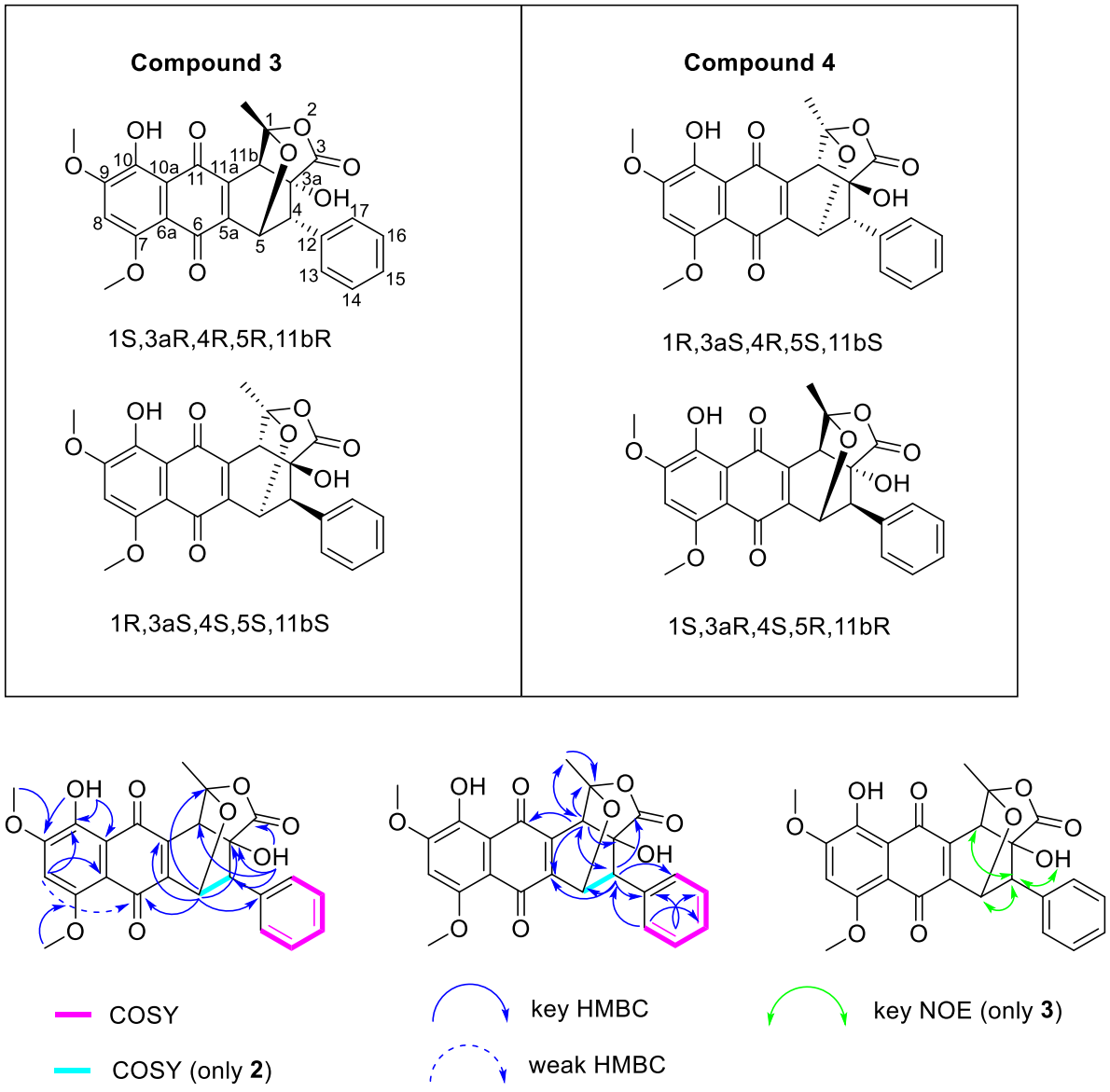


Figure 5. Key NMR correlations for **3** (fusapurpurin A) and 4 (fusapurpurin B)

Table 2. NMR data for **3** and **4** (measured in DMSO-d_6 at 150 MHz for the ^{13}C- and at 600 MHz for the ^{1}H-NMR spectrum)

position	*Compound 2*		*Compound 3*	
	δ_C*	δ_H, m (*J* in Hz)	δ_C*	δ_H, m (*J* in Hz)
1	105.5, C		104.7, C	
3	176.7, CO		173.3, CO	
3a	76.4, C		75.1, C	
4	51.6, CH	3.97, d (4.2)	51.5, CH	2.91, s
5	70.9, CH	5.30, d (4.2)	69.1, CH	5.41, s
5a	148.9, C		149.8, C	
6	175.4, CO		175.5, CO	
6a	109.0, C		109.5, C	
7	157.2, CO		156.4, CO	
8	105.1, CH	7.10, s	104.2, CH	7.14, s
9	156.3, CO		155.9, CO	
10	148.9, C		148.1, C	
10a	114.6, C		114.2, C	
11	186.7, CO		187.2, CO	
11a	138.9, C		135.5, C	
11b	46.9, CH	4.34, s	47.2, CH	4.30, s
12	130.7, C		136.8, C	
13/17	131.3, CH	7.03, m, 2H	127.7, CH	7.37, m, 2H
14/16	127.9, CH	7.12, m, 2H	128.6, CH	7.33, m, 2H
15	127.9, CH	7.08, m	128.1, CH	7.29, m
1-CH_3	22.9, CH_3	1.44, s, 3H	22.4, CH_3	1.47, s, 3H
3a-OH		6.71, s		6.65, s
7-OCH_3	57.1, OCH_3	3,88, s, 3H	56.2, OCH_3	3.97, s, 3H
9-OCH_3	57.1, OCH_3	4.02, s, 3H	56.2, OCH_3	4.03, s, 3H
10-OH		12.99, s		12.94, s

*signals were extracted from HSQC and HMBC spectra

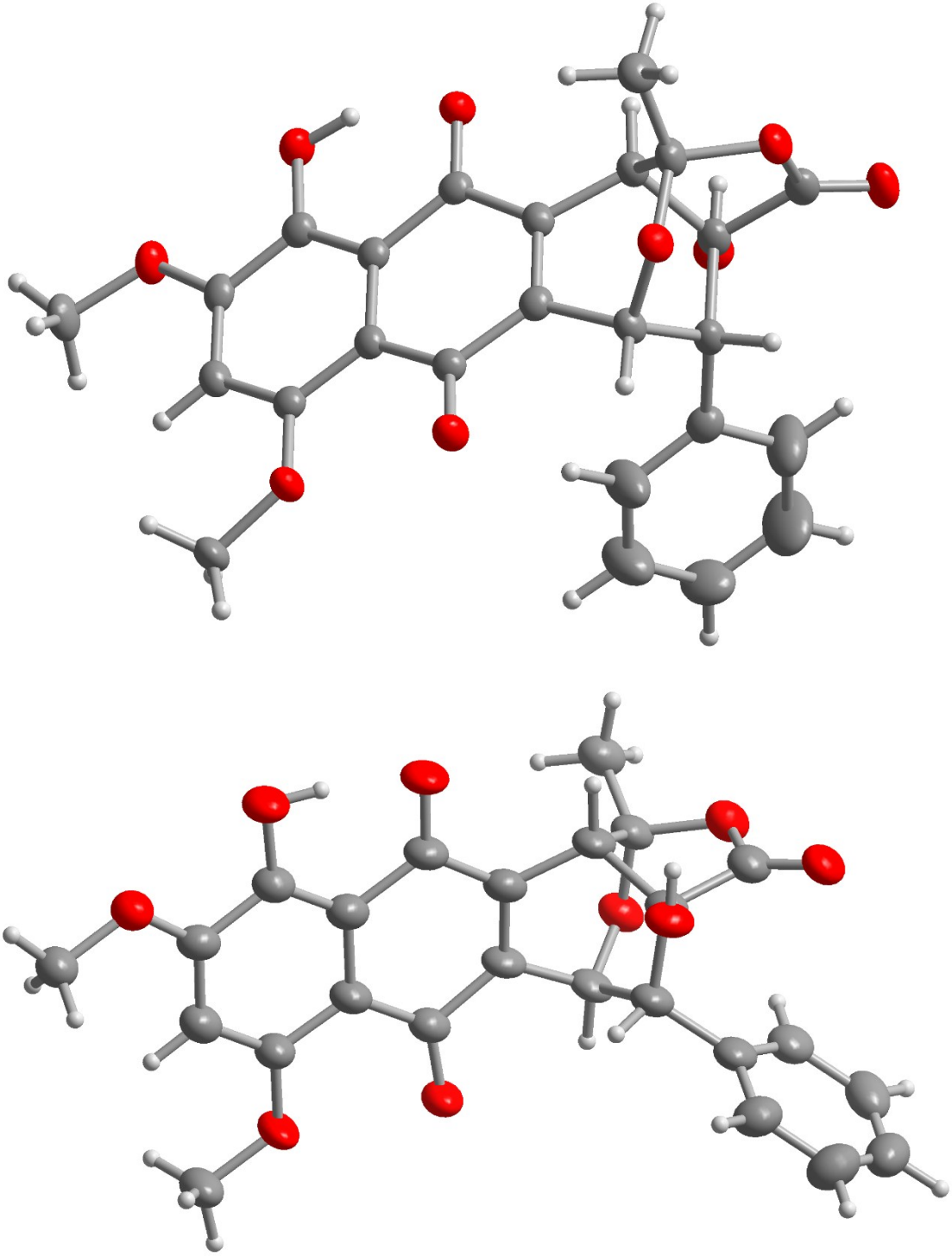


Figure 6. Molecular structures of compounds **3** (a) and **4** (b) from the single crystal X-ray structure (50% thermal ellipsoids, H atoms with arbitrary radii). Compound **3** crystallizes with a partially occupied ethyl acetate molecule (see **Fig. S4**), compound **4** with disordered methanol molecules which were removed by solvent masking during the refinement. (See **Fig. S5**)

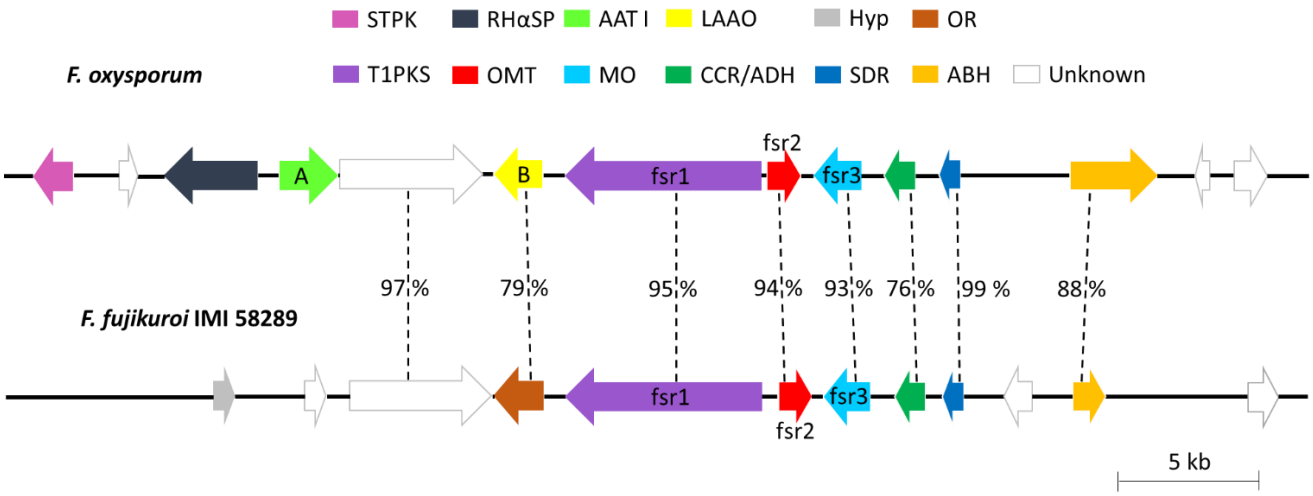


Figure 7. Comparison of the *fsr* cluster in *F. fujikuroi* with the *F. oxysporum* cluster of contig 160 region 1. The sequence identities on the amino acid level are given as percentages. Abbreviations of the enzymes encoded by the genes are as follows: STPK = serine/threonine protein kinase, RH³SP = ring-hydroxylating ³-subunit domain-containing protein, AAT = amino acid transporter, LAAO = L- amino acid oxidase, Hyp = hydrophobin, OR = oxidoreductase, T1PKS = type-1 polyketide synthase, OMT = O-methyltransferase, MO = monooxygenase, CCR/ADH = crotonyl-CoA-reductase/alcohol dehydrogenase, SDR = short-chain dehydrogenase/reductase, ABH = alpha/beta hydrolase

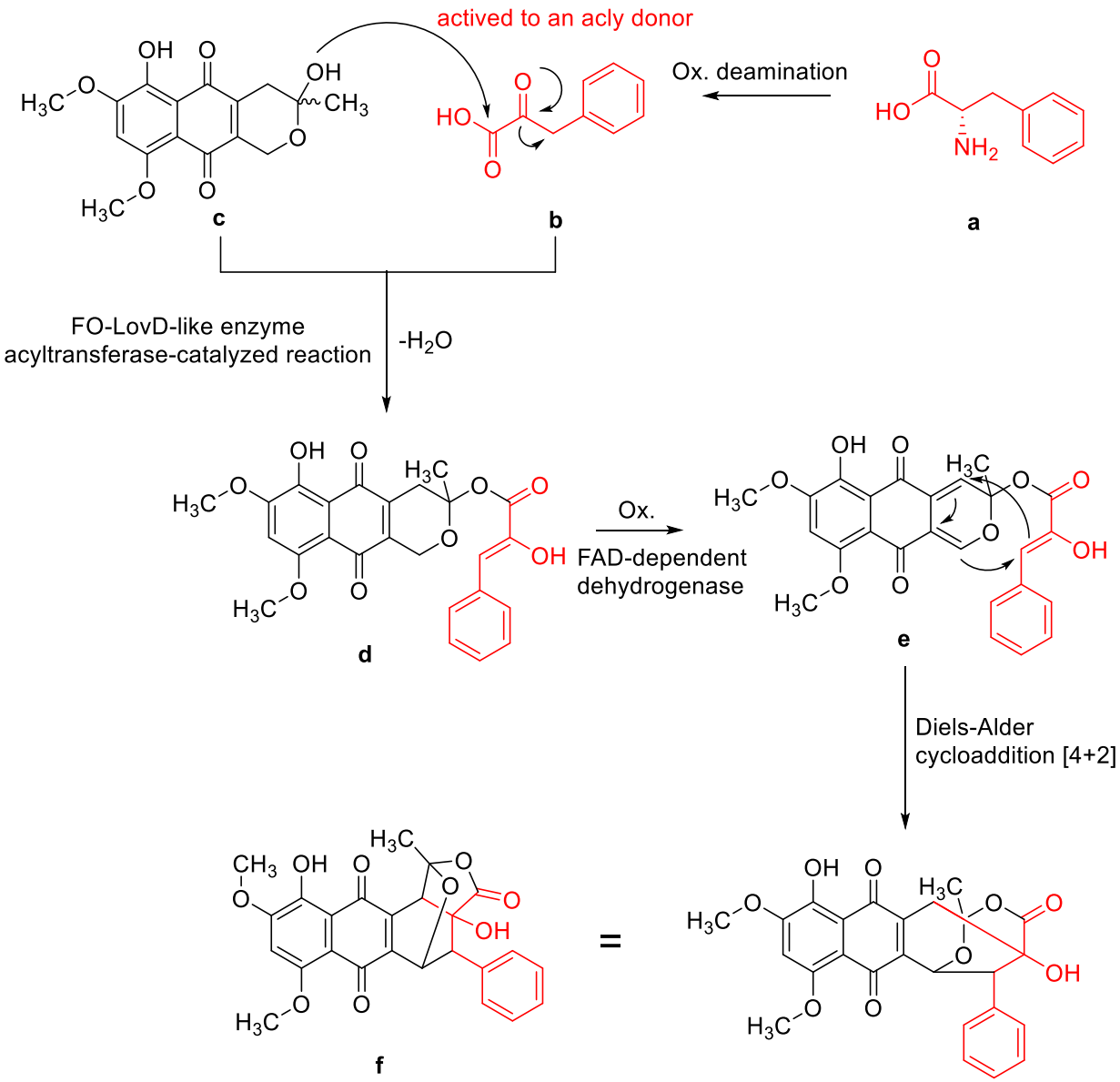
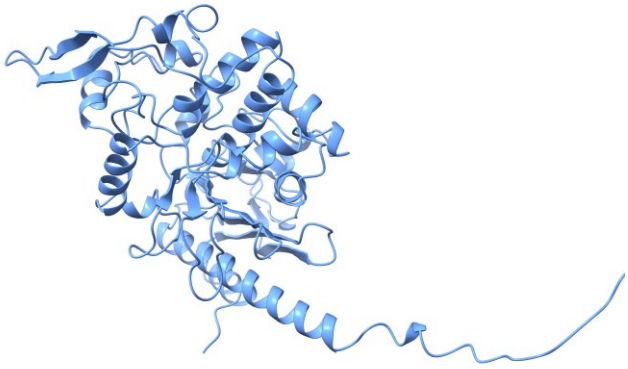
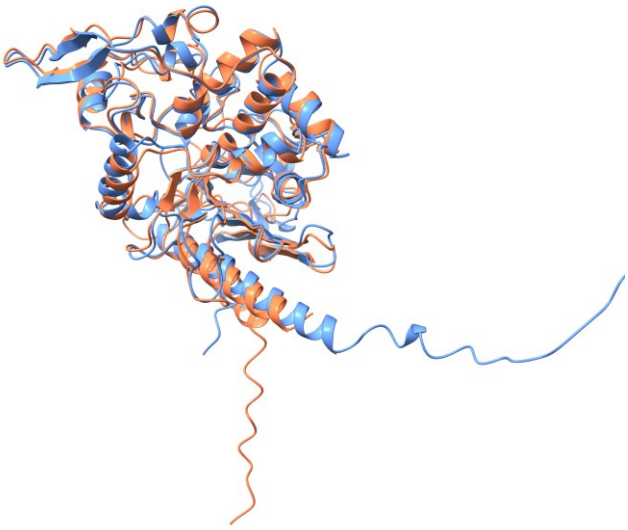


Figure 8. Proposed biosynthetic pathway for formation of compounds **3** and **4**. The amino acid L-phenylalanine (a) is oxidized via oxidative deamination to build phenylpyruvic acid (b). 9-O-Methylfusarubin (c) reacts with phenyl pyruvic acid (b) in a nucleophilic substitution to form intermediate d. After an oxidative step to build intermediate e, structure f (compounds **3** and **4**) is built via a Diels-Alder cycloaddition [4+2] as the final step to build the proposed racemic products.

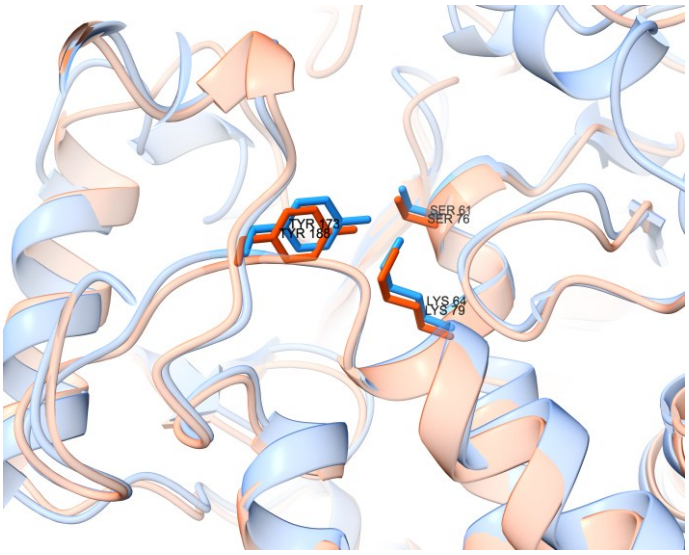


(a)

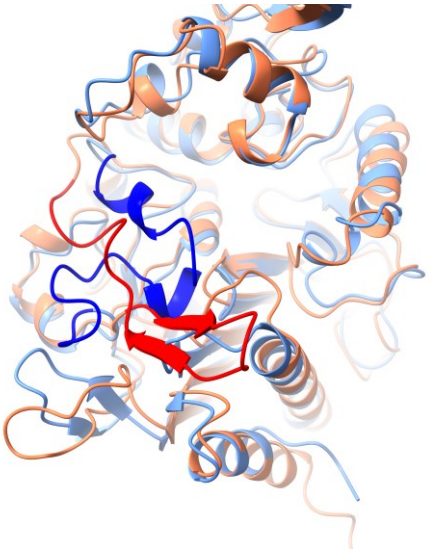


(b)

Figure 9. Predicted structure of FO-LovD-like protein and structural comparison with *A. terreus* LovD. (a) AlphaFold-predicted three-dimensional structure of the candidate FO-LovD-like protein from *F. oxysporum*. The predicted model shows an overall LovD/PcEST-like fold. (b) Structural superposition of FO-LovD-like protein and the reported LovD protein from *A. terreus*. The two proteins show a similar overall fold despite their limited sequence identity, supporting the annotation of FO-LovD-like as a potential LovD-like acyltransferase.

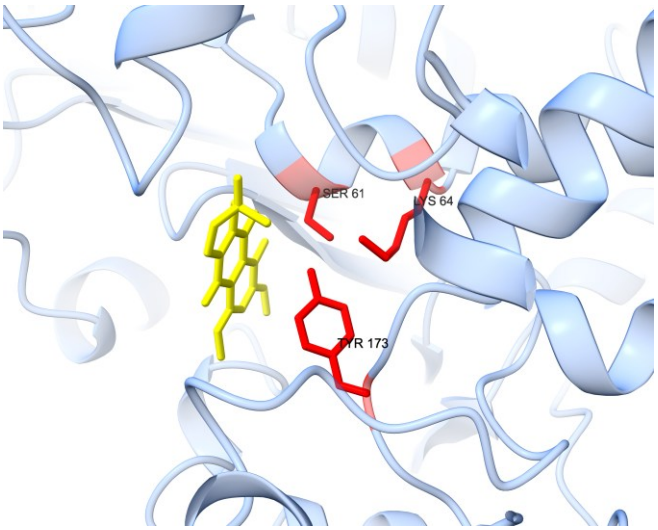


(a)

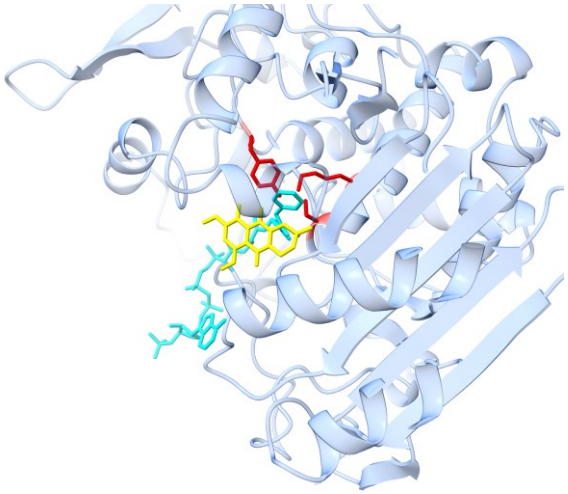


(b)

Figure 10. Comparison of conserved catalytic regions and structural differences between FO-LovD-like protein and *A. terreus* LovD. (a) Superposition of the conserved catalytic regions of FO-LovD-like protein and *A. terreus* LovD. The catalytic residues Ser61, Lys64 and Tyr173 in FO-LovD-like protein spatially correspond to Ser76, Lys79 and Tyr188 in *A. terreus* LovD, indicating conservation of the putative Ser–Lys–Tyr catalytic core. (b) Structural differences between FO-LovD-like protein and *A. terreus* LovD. The major differences are located in peripheral loop regions, especially around residues 227–249 in FO-LovD-like protein and the corresponding region in *A. terreus* LovD, suggesting potential differences in substrate entrance, binding pocket shape and substrate recognition.



(a)



(b)

Figure 11. Predicted binding models of FO-LovD-like protein with 9-O-methylfusarubin and 9-O-methylfusarubin/ phenylpyruvate-CoA. (a) Predicted binary complex model of FO-LovD-like protein with 9-O-methylfusarubin. 9-O-methylfusarubin can be accommodated in an internal or semi-open pocket of FO-LovD-like protein, suggesting that the predicted pocket is spatially compatible with the naphthoquinone scaffold. (b) Predicted ternary complex model of FO-LovD-like protein with 9-O-methylfusarubin and phenylpyruvate-CoA. In this model, the thioester reactive region of phenylpyruvate-CoA is positioned close to the putative catalytic Ser61, while 9-O-methylfusarubin is located in the same binding pocket. This model supports the structural possibility that FO-LovD-like protein may accommodate both the acyl acceptor and the activated phenylpyruvate-derived CoA-thioester donor.

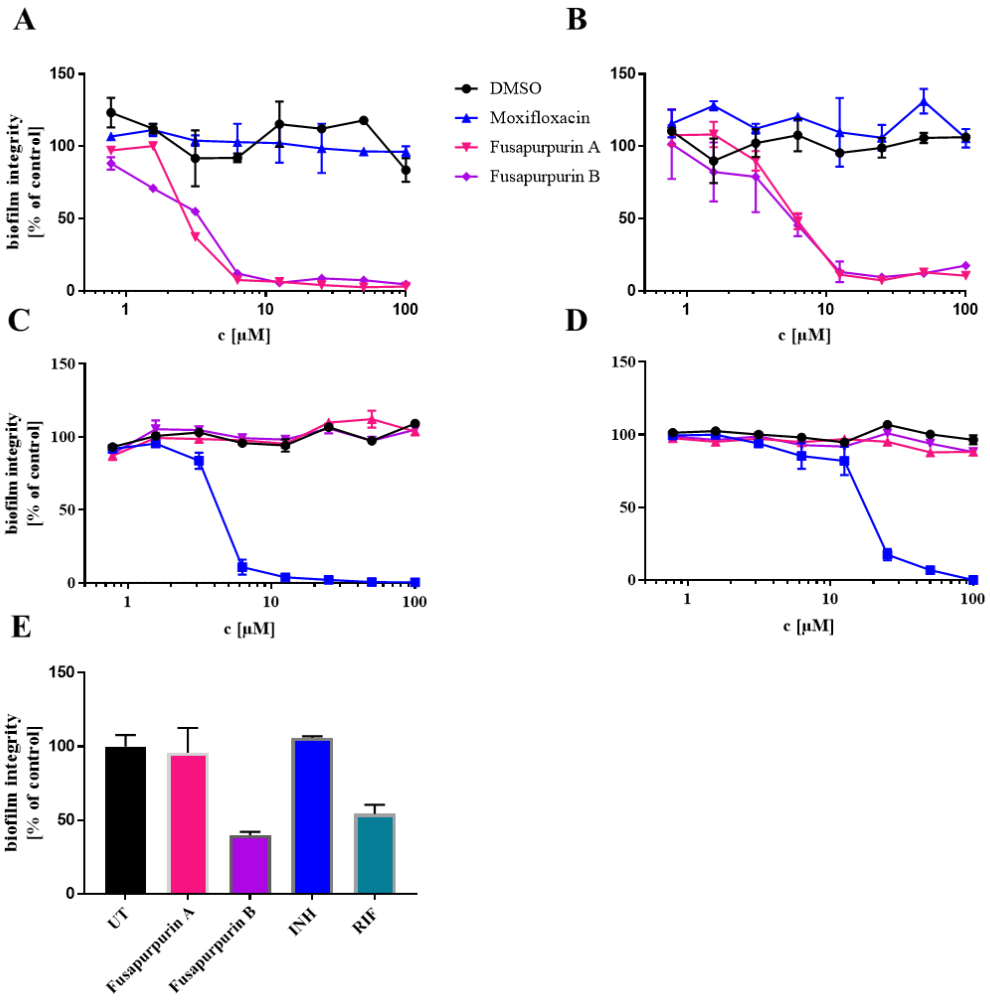


Figure 12. Fusapurpurin A and B (**3** and **4**) mediated dispersion of preformed biofilms in MRSA Mu50 (A) and *P. aeruginosa* PAO1 (B). Moxifloxacin, a bactericidal antibiotic only active gainst replicating bacterial cells, and DMSO were used as negative controls. Fusapurpurin A and B (**3** and **4**) do not prevent biofilm formation when added to suspended cells of MRSA Mu50 (C) and *P. aeruginosa* PAO1 (D). Moxifloxacin, a bactericidal antibiotic active gainst replicating bacterial cells, was used as positive control, and DMSO was used as negative control. The graphs show the biofilm integrity compared to the control in MRSA Mu50 (C) and *P. aeruginosa* PAO1 (D) when fusapurpurin A and B are added during biofilm formation. Disruption of biofilm integrity in *Mycobacterium tuberculosis* H37Rv by fusapurpurin B (E). Fusapurpurin A and B were adjusted at 100 µM to the preformed mycobacterial biofilm. Isoniazide (INH, 200 µM) and rifampicin (RIF, 350 µM) were used as controls. UT = Untreated biofilms. All assays (A-E) were carried out in triplicates and graphs show mean ± SEM.

Table 3. MIC90 of isolated compounds against MRSA Mu50, *P. aeruginosa* PAO1, *Candida albicans* ATCC 24433 and *M. tuberculosis* H37Rv. All concentrations are shown in µM. Concentrations >100 µM indicate no activity in the experimental setup. The experiment was conducted in triplicate. All compounds except **9** were virtually devoid of antimicrobial activity. Compound **9** (beauvericin) showed weak antibacterial activity against MRSA Mu50 with an MIC_{90} of 50 µM and good activity against Mtb H37Rv at 3.125 µM, which is in agreement with the antibacterial and antimycobacterial activity of this mycotoxin reported in the literature [37].

	MIC_{90} [µM]			
Compound	***S. aureus* Mu50**	***P. aeruginosa* PAO1**	***C. albicans* ATCC 24433**	***M. tuberculosis* H37Rv**
1	>100	>100	>100	>100
2	>100	>100	>100	>100
3	>100	>100	>100	>100
4	100	>100	>100	>100
5	>100	>100	>100	>100
6	>100	>100	>100	>100
7	>100	>100	>100	>100
8	>100	>100	>100	>100
9	50	>100	>100	3.125
10	>100	>100	>100	>100

Table 4. Mean IC_{50} values of compounds **3** and **4** against human cell lines THP-1, Huh-7 and Hek293. All concentrations are shown in µM. A concentration >100 µM indicates no activity in the experimental setup. All experiments have been conducted in triplicates. The IC_{50} values were calculated using GraphPad Prism 7. 100% growth control: DMSO. 0% growth control: cycloheximide.

	Mean IC_{50} [µM]		
Compound	**THP-1**	**Huh-7**	**Hek 293**
3	40.66	47.85	>100
4	11.57	12.67	26.81

Table 5. Crystal data and structure refinement for compounds **3** and **4**.

	Compound 3	**Compound 4**
Formula	$C_{25}H_{20}O_9$, 0.401($C_4H_8O_2$)	$C_{25}H_{20}O_9$, 1.25(CH_3OH)
M_r	499.74	464.41
Cryst. size, mm^3	0.18 × 0.15 × 0.02	0.15 × 0.12 × 0.08
Crystal system	orthorhombic	orthorhombic
Temp. (K)	100	100
Space group	*Pnna*	*Pbcn*
a, Å	14.4569 (2)	17.8013 (5)
b, Å	24.5575 (4)	13.8375 (4)
c, Å	12.8869 (2)	20.7494 (6)
V, $Å^3$	4575.18 (12)	5111.1 (3)
Z	8	8
D_{calcd}, g cm^{-3}	1.451	1.207
μ, mm^{-1}	0.940	0.780
F(000)	2090	1936
Trans. (max/min)	0.991/0.991	0.992/0.992
hkl range	±17; ±29 ±15	±21; ±16; ±24
Refl. measured	28841	43551
Refl. unique	4096	4545
R_{int}	0.039	0.061
Param. Refined/Restraints	363/0	316/0
GoF (F^2) [a]	1.162	1.553
R_1/wR_2 [I>2σ (I)] [b]	0.0598/0.1438	0.1095/ 0.3282
R_1/wR_2 (all data) [b]	0.0644/0.1466	0.1182/ 0.3438
Max./min. $\Delta\rho$ (e. $Å^{-3}$) [c]	0.54/–0.42	0.674/–0.556
CCDC number	2232516	2232517

[a] Goodness-of-fit = $[\sum[w(F_o^2 - F_c^2)^2]/(n-p)]^{1/2}$; [b] $R_1=[\sum(||F_o| - |F_c||)/\sum|F_o|]$; $wR_2=[\sum[w(F_o^2 - F_c^2)^2]/\sum[w(F_o^2)^2]]^{1/2}$; [c] Largest difference peak and hole.

Supporting information

Fusarubin derivatives with biofilm-disrupting activities derived from *Fusarium oxysporum*

Di He[a¶], Viktor E. Simons[a¶], Lasse van Geelen[a], Dennis Woschko[b], Attila Mándi[c], Philipp Spohr[d], Sebastian Scharf[e], Marian Frank[a], Christoph Janiak[b], Tibor Kurtán[c], Gunnar W. Klau[d], Rainer Kalscheuer[a*]

[a] Institute of Pharmaceutical Biology and Biotechnology, Heinrich Heine University, Universitätsstrasse 1, 40225 Düsseldorf, Germany

[b] Institute for Nanoporous and Nanoscale Materials, Heinrich Heine University, Universitätsstrasse 1, 40225 Düsseldorf, Germany

[c] Department of Organic Chemistry, University of Debrecen, P.O. Box 400, 4002 Debrecen, Hungary

[d] Algorithmic Bioinformatics, Heinrich Heine University, Universitätsstrasse 1, 40225 Düsseldorf, Germany

[e] Institute of Medical Microbiology and Hospital Hygiene, Heinrich Heine University, Universitätsstrasse 1, 40225 Düsseldorf, Germany

¶ These authors contributed equally

[*]Corresponding author.

rainer.kalscheuer@hhu.de; ORCID ID orcid.org/0000-0002-3378-2067

Supplementary information Page

S1. Hydrogen bonding interactions of compounds **3** and **4** ... 120

Table S1. Hydrogen-bond geometry (Å, º) in the solid-state structures of compounds **3** and **4** ... 121

S2. π-π stacking interactions in **3** and **4** ... 122

S3. Section of the packing diagram in compounds **3** and **4** ... 123

S4. Molecular structure of **3** from the single crystal X-ray structure ... 124

S5. Molecular structures of **3** and **4** with full atom numbering from the single crystal X-ray structure ... 125

S6. Predicted structure of *A. terreus* LovD. ... 126

S7. Predicted binding models of FO-LovD-like protein with phenylpyruvate-SNAC and 9-*O*-methylfusarubin. ... 127

S8. Predicted binding model of FO-LovD-like protein with phenylpyruvate-CoA. ... 128

S9. Comparison of a segment of the eqx gene cluster in F. heterosporum with the F. oxysporum cluster of contig 44 region 8. ... 129

S10. Top 20 assembled contigs and distribution of contigs. ... 130

S11. Effect of fusapurpurin A and B (**3** and **4**) on the cell viability of S. aureus Mu50 and *P. aeruginosa* PAO1 in preformed biofilms. ... 131

S12. Quorum quenching assay of fusapurpurins in *Chromobacterium violaceum.* ... 132

S13. NMR Table of Compound **1** (DMSO-d_6, ^{1}H: 600MHz). ... 133

S14. ^{1}H-NMR Spectrum of Compound **1** (DMSO-d_6, 600 MHz) ... 134

S15. HPLC-DAD UV-Vis Spectrum of Compound **1** (Methanol) ... 134

S16. ESI(+)MS Spectrum of **1** ... 135

S17. ^{1}H-NMR Spectrum of Compound **2** (DMSO-d_6, 600 MHz) ... 135

S18. ^{13}C-NMR Spectrum of Compound **2** (DMSO-d_6, 150 MHz) ... 136

S19. ^{1}H-^{13}C-HSQC Spectrum of Compound **2** (DMSO-d_6, ^{1}H: 600MHz, ^{13}C: 150 MHz) ... 136

S20. ^{1}H-^{13}C-HMBC Spectrum of Compound **2** (DMSO-d_6, ^{1}H: 600MHz, ^{13}C: 150 MHz) ... 137

S21. ^{1}H-^{1}H-COSY Spectrum of Compound **2** (DMSO-d_6, 600MHz) ... 137

S22. ^{1}H-^{1}H-NOESY Spectrum of Compound **2** (DMSO-d_6, 600MHz) ... 138

S23. HPLC-DAD UV-Vis Spectrum of Compound **2** (Methanol) ... 138

S24. High Resolution ESI(+)MS Spectrum of Compound **2** ... 139

S25. ^{1}H-NMR Spectrum of Compound **3** (DMSO-d_6, 600 MHz) ... 139

S26. ^{13}C-NMR Spectrum of Compound **3** (DMSO-d_6, 150 MHz) ... 140

S27. ^{1}H-^{13}C-HSQC Spectrum of Compound **3** (DMSO-d_6, ^{1}H: 600MHz, ^{13}C: 150 MHz) ... 140

S28. ^{1}H-^{13}C-HMBC Spectrum of Compound **3** (DMSO-d_6, ^{1}H: 600MHz, ^{13}C: 150 MHz) ... 141

S29. ^{1}H-^{1}H-COSY Spectrum of Compound **3** (fusapurpurin A) (DMSO-d_6, 600MHz) ... 141

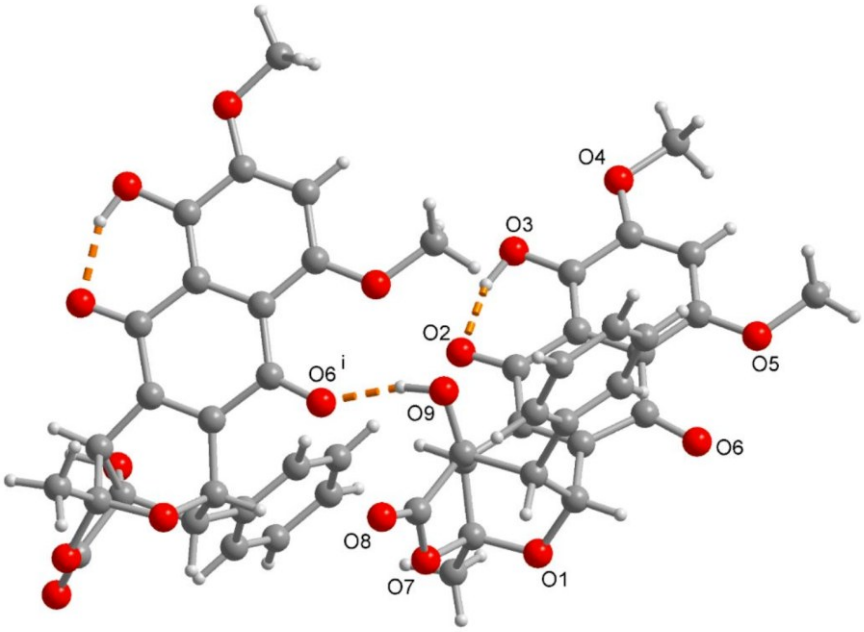
S30. ^{1}H-^{1}H-NOESY Spectrum of Compound **3** (DMSO-d_6, 600MHz) ... 142

S31. HPLC-DAD UV-Vis Spectrum of Compound **3** (Methanol) ... 142

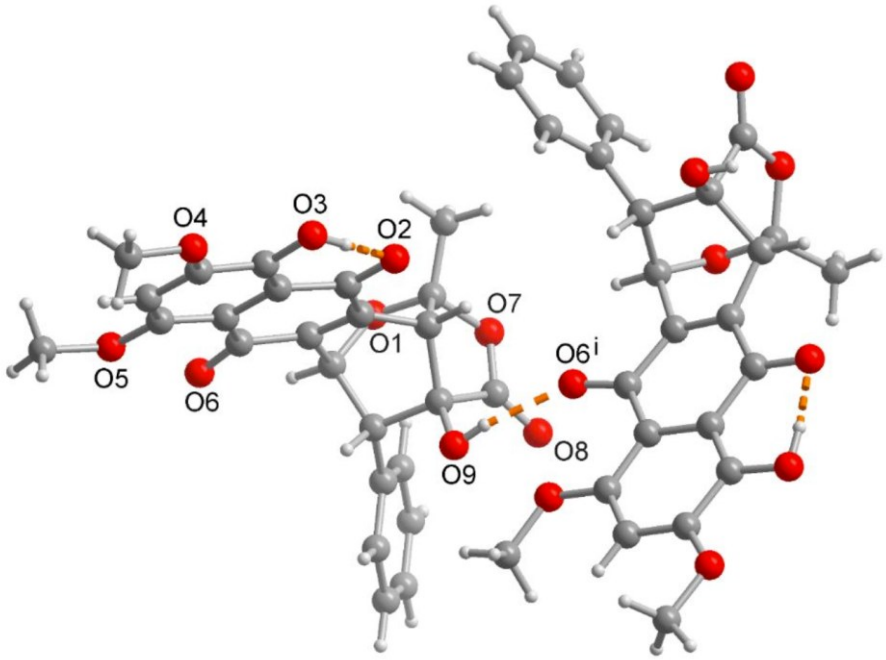
S32. High Resolution ESI(+)MS Spectrum of **3** ... 143

S33. ^{1}H-NMR Spectrum of Compound **4** (DMSO-d_6, 600 MHz) 143
S34. ^{13}C-NMR Spectrum of Compound **4** (DMSO-d_6, 150 MHz) 144
S35. ^{1}H-^{13}C-HSQC Spectrum of Compound **4** (DMSO-d_6, ^{1}H: 600MHz, ^{13}C: 150 MHz) 144
S36. ^{1}H-^{13}C-HMBC Spectrum of Compound **4** (DMSO-d_6, ^{1}H: 600MHz, ^{13}C: 150 MHz) 145
S37. ^{1}H-^{1}H-COSY Spectrum of Compound **4** (DMSO-d_6, 600MHz) 145
S38. ^{1}H-^{1}H-NOESY Spectrum of Compound **4** (DMSO-d_6, 600MHz) 146
S39. HPLC-DAD UV-Vis Spectrum of Compound **4** (Methanol) 146
S40. High Resolution ESI(+)MS Spectrum of **4** 147
S41. NMR Table of Compound **5** (DMSO-d_6, ^{1}H: 600MHz) 147
S42. ^{1}H-NMR Spectrum of Compound **5** (DMSO-d_6, 600 MHz) 148
S43. HPLC-DAD UV-Vis Spectrum of Compound **5** (Methanol) 148
S44. High Resolution ESI(+)MS Spectrum of Compound **5** 149
S45. NMR Table of Compound **6** (DMSO-d_6, 600MHz) 149
S46. 1H-NMR Spectrum of Compound **6** (DMSO-d_6, 600 MHz) 150
S47. UV-Vis Spectrum of Compound **6** (Methanol) 151
S48. High Resolution ESI(+)MS Spectrum of Compound **6** 152
S49. NMR Table of Compound **7** (DMSO-d_6, ^{1}H: 600MHz) 152
S50. ^{1}H-NMR Spectrum of Compound **7** (DMSO-d_6, 600 MHz) 153
S51. UV-Vis Spectrum of Compound **7** (Methanol) 153
S52. High Resolution ESI(+)MS Spectrum of Compound **7** 154
S53. NMR Table of Compound **8** (DMSO-d_6, ^{1}H: 600MHz, ^{13}C: 150 MHz) 154
S54. ^{1}H-NMR Spectrum of Compound **8** (DMSO-d_6, 600 MHz) 155
S55. ^{13}C-NMR Spectrum of Compound **8** (DMSO-d_6, 150 MHz) 155
S56. ^{1}H-^{13}C-HSQC Spectrum of Compound **8** (DMSO-d_6, ^{1}H: 600MHz, ^{13}C: 150 MHz) 156
S57. ^{1}H-^{13}C-HMBC Spectrum of Compound **8** (DMSO-d_6, ^{1}H: 600MHz, ^{13}C: 150 MHz) 156
S58. ^{1}H-^{1}H-COSY Spectrum of Compound **8** (DMSO-d_6, 600MHz) 157
S59. ^{1}H-^{1}H-NOESY Spectrum of Compound **8** (DMSO-d_6, 600MHz) 157
S60. HPLC-DAD UV-Vis Spectrum of Compound **8** (Methanol) 158
S61. High Resolution ESI(+)MS Spectrum of Compound **8** 158
S62. NMR Data of Compound **9** ($CDCl_3$, ^{1}H: 600MHz) 159
S63. ^{1}H-NMR Spectrum of Compound **9** ($CDCl_3$, 600 MHz) 160
S64. HPLC-DAD UV-Vis Spectrum of Compound **9** (Methanol) 160
S65. High Resolution ESI(+)MS Spectrum of Compound **9** 161
S66. NMR Data of Compound **10** (DMSO-d6, ^{1}H: 600MHz) 162
S67. ^{1}H-NMR Spectrum of Compound **10** (DMSO-d_6, 600 MHz) 163
S68. HPLC-DAD UV-Vis Spectrum of Compound **10** (Methanol) 163
S69. High Resolution ESI(+)MS Spectrum of Compound **10** 164
S70. SDS-PAGE analysis of recombinant FO-LovD-like protein expression and purification. 164

S1. Hydrogen bonding interactions of compounds 3 and 4



(a)



(b)

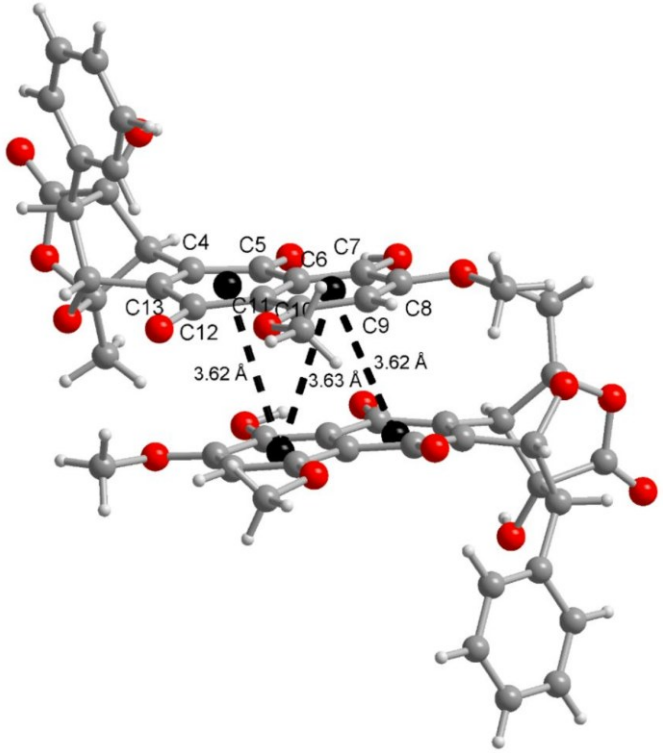
Hydrogen-bonding interaction in the structures of **3** (a) and **4** (b). The hydrogen-bonding parameters are given in Table S1

Table S1. Hydrogen-bond geometry (Å, º) in the solid-state structures of compounds 3 and 4

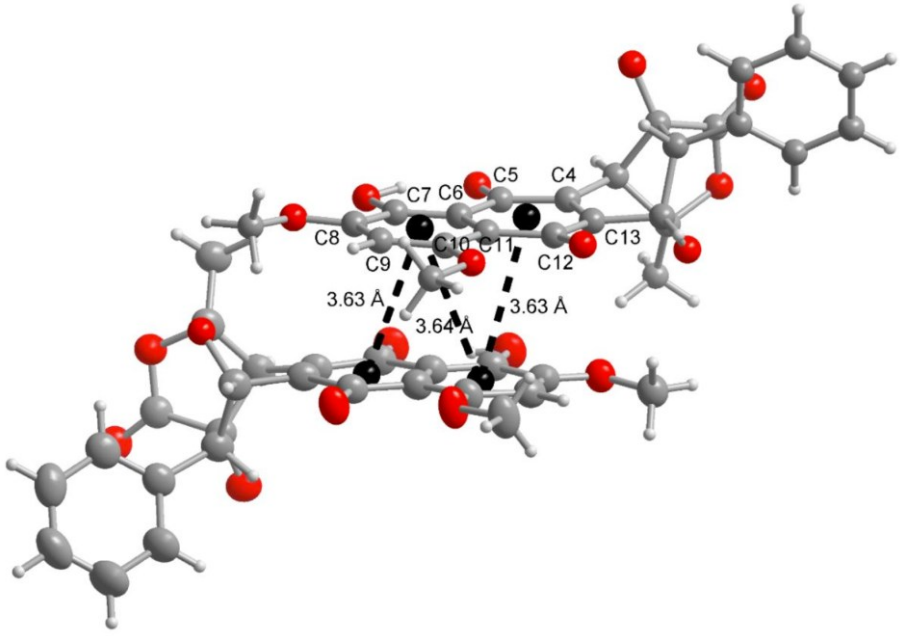
D—*H*···*A*	*D*—*H*	*H*···*A*	*D*···*A*	*D*—*H*···*A*
Compound 3				
O3—H3···O2	0.90 (4)	1.68 (4)	2.534 (2)	156 (4)
O9—H9···O6^{i}	0.96 (4)	1.75 (4)	2.689 (3)	164 (4)
Compound 4				
O3—H3···O2	0.87 (6)	1.72 (6)	2.571 (4)	163 (6)
O9—H9···O6^{i}	0.76 (7)	1.96 (7)	2.680 (4)	160 (6)

Symmetry code: Compound **3** (i) x-1/2, y, -z+1. Compound **4** (i) -x+3/2, y-1/2, z.

S2. π-π stacking interactions in 3 and 4



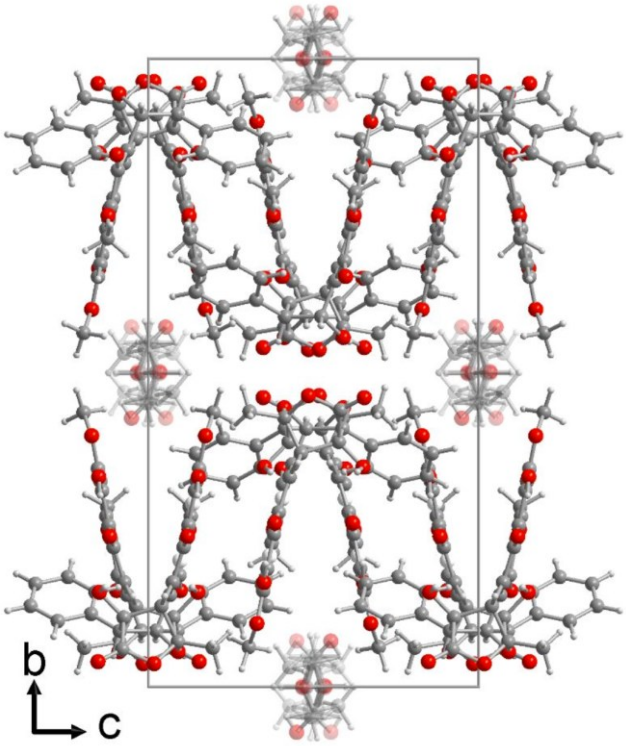
(a)



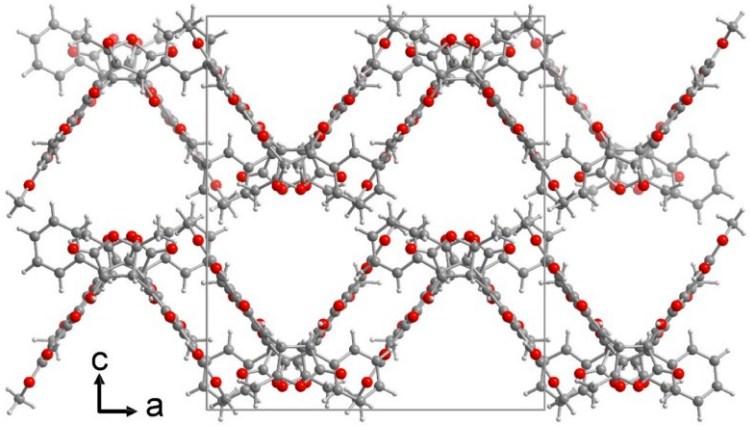
(b)

π-π stacking interactions in compound **3** (a) and **4** (b) with the centroid-centroid distances indicated.

S3. Section of the packing diagram in compounds 3 and 4



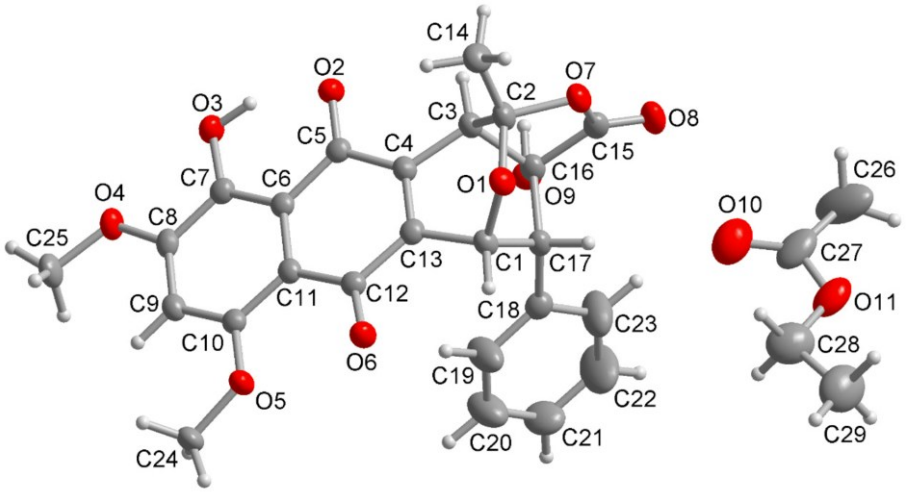
(a)



(b)

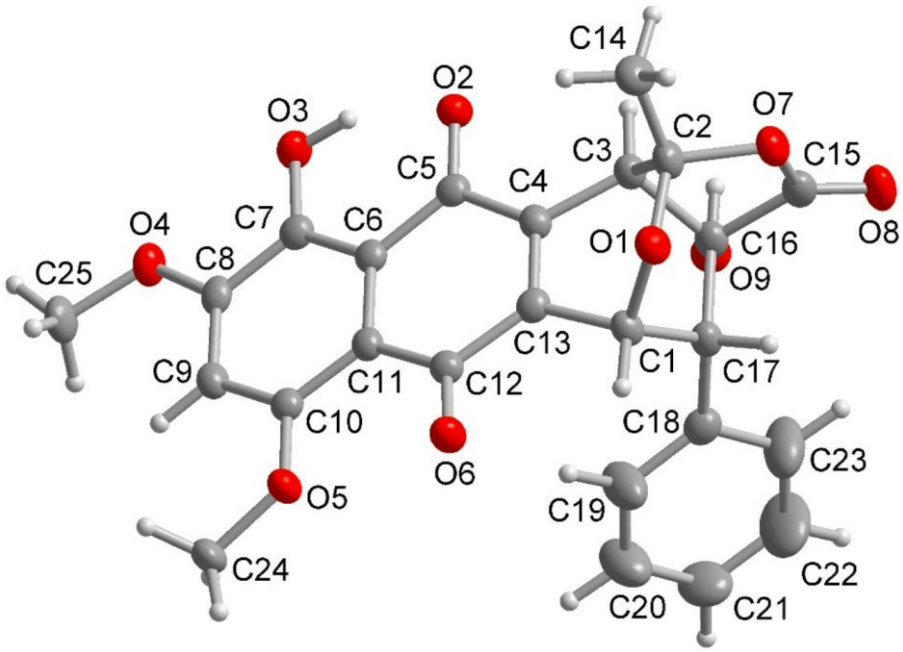
Section of the packing diagram in compound **3** (a) and **4** (b) showing the solvent-filled voids. For compound **3**, the partially occupied ethyl acetate is indicated semi-transparent. In compound **4**, disordered methanol molecules, which were removed by solvent masking during the refinement, hence cannot be shown.

S4. Molecular structure of 3 from the single crystal X-ray structure

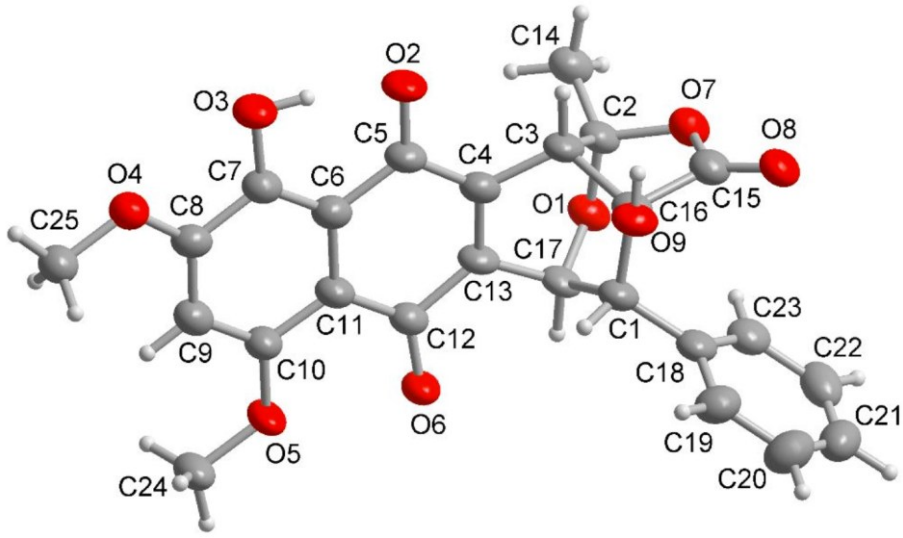


Molecular structure of compound **3** from the single crystal X-ray structure (50% thermal ellipsoids, H atoms with arbitrary radii) with the ethyl acetate solvent molecule of crystallization. The atoms of the ethyl acetate molecule are only partially occupied (sof = 0.4).

S5. Molecular structures of 3 and 4 with full atom numbering from the single crystal X-ray structure



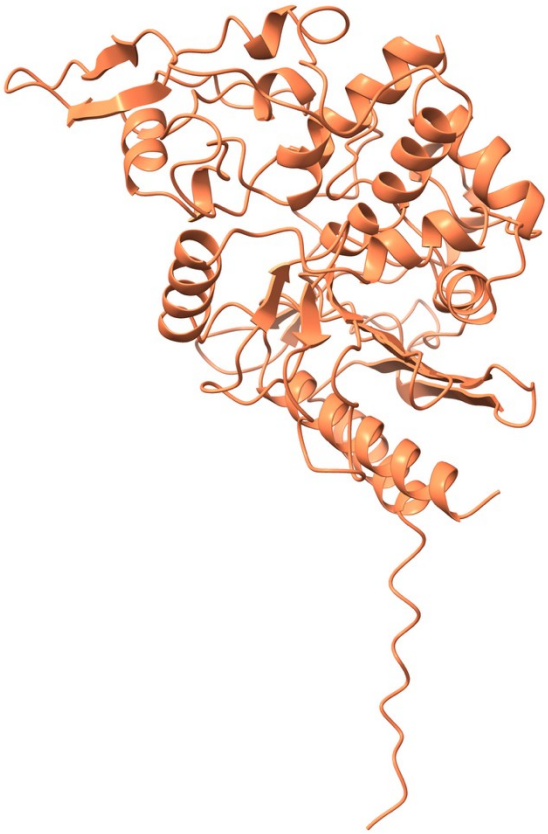
(a)



(b)

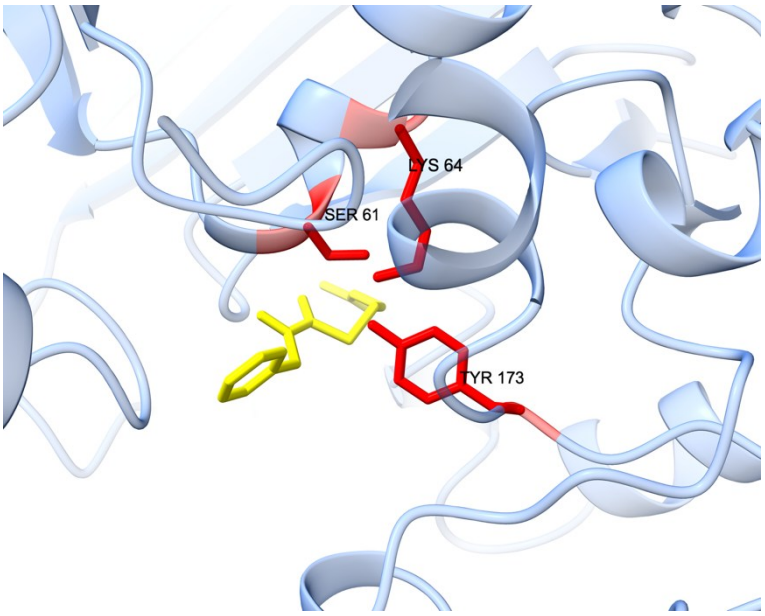
Molecular structures of compounds **3** (a) and **4** (b) with full atom numbering from the single crystal X-ray structure (50% thermal ellipsoids, H atoms with arbitrary radii).

S6. Predicted structure of A. terreus LovD.

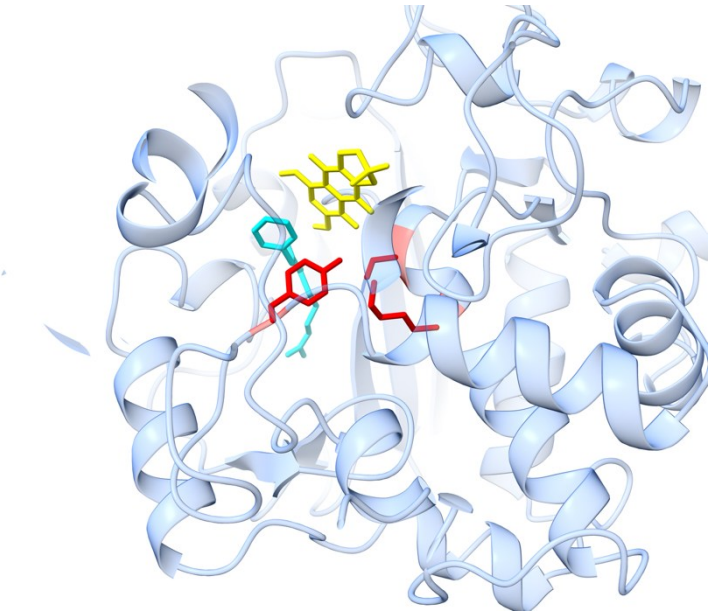


AlphaFold-predicted three-dimensional structure of LovD from *A. terreus*. The structure was used as a reference model for comparison with the candidate FO-LovD-like protein from *F. oxysporum*.

S7. Predicted binding models of FO-LovD-like protein with phenylpyruvate-SNAC and 9-*O*-methylfusarubin.



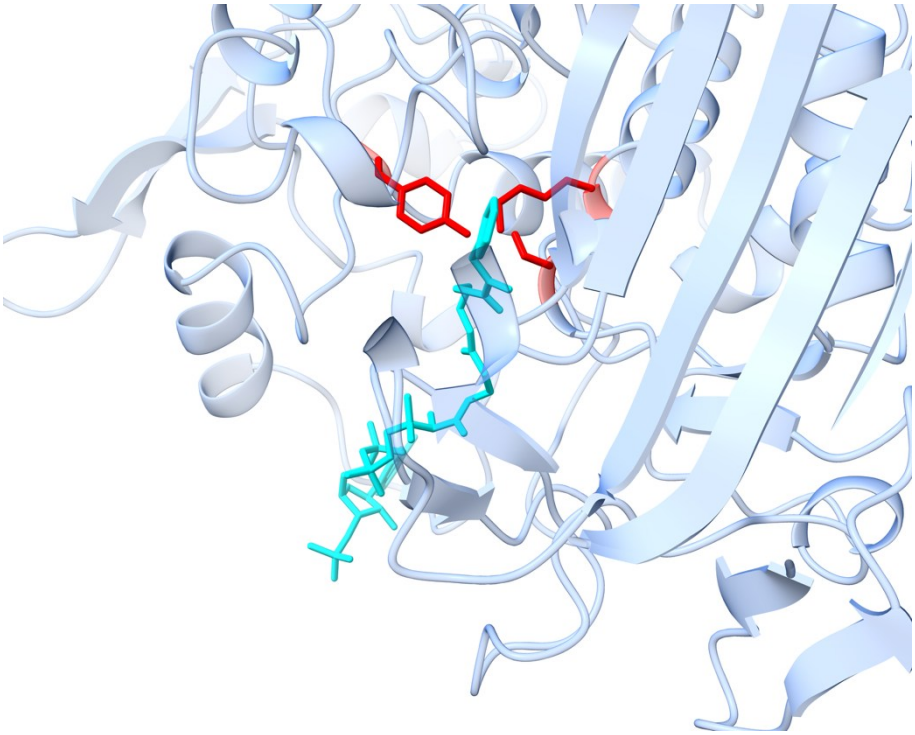
(a)



(b)

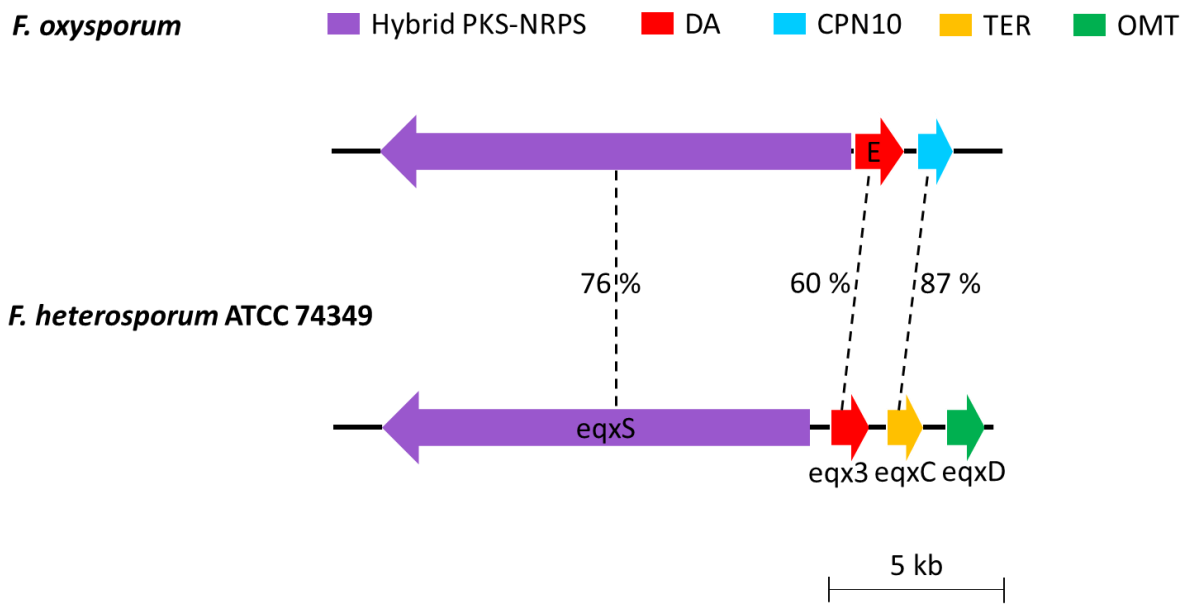
(a) Predicted binary complex model of FO-LovD-like protein with phenylpyruvate-SNAC. The predicted model shows that phenylpyruvate-SNAC can be accommodated in the binding pocket of FO-LovD-like protein, with its thioester region positioned near the putative catalytic site. (b) Predicted ternary complex model of FO-LovD-like protein with 9-O-methylfusarubin and phenylpyruvate-SNAC. Although both ligands can be placed in the same internal pocket of FO-LovD-like protein, the predicted spatial arrangement does not place the 9-O-methylfusarubin hydroxyl group close to the thioester carbonyl carbon of phenylpyruvate-SNAC, suggesting that this model is less compatible with the proposed acyl transfer reaction.

S8. Predicted binding model of FO-LovD-like protein with phenylpyruvate-CoA.



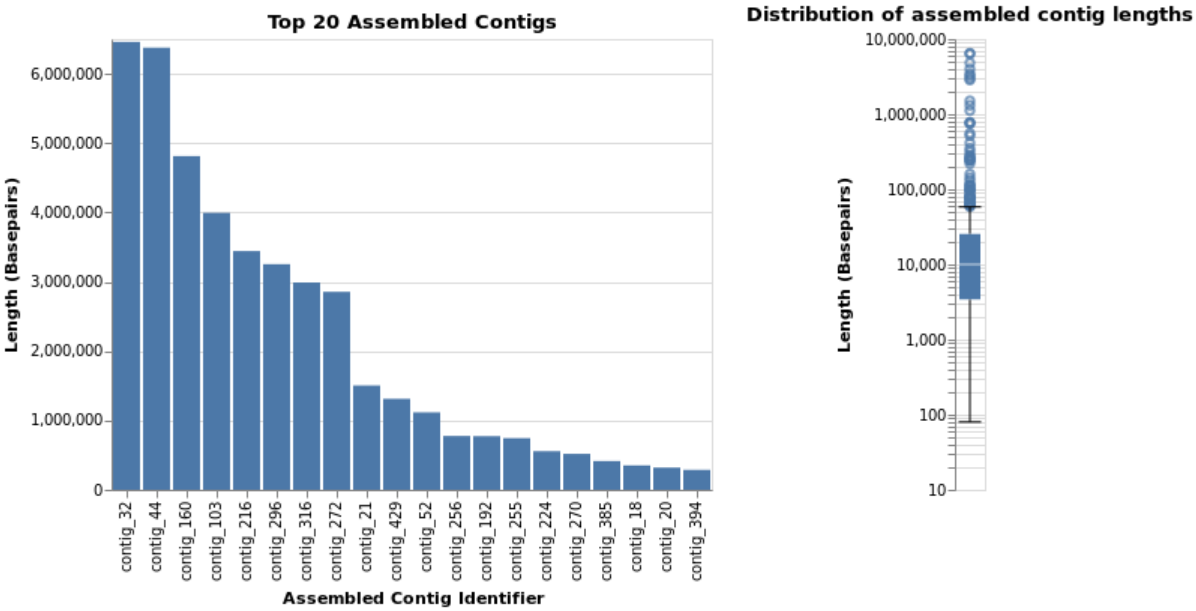
Predicted binary complex model of FO-LovD-like protein with phenylpyruvate-CoA. The predicted model shows that phenylpyruvate-CoA can be accommodated in the binding pocket of FO-LovD-like protein, with its thioester reactive region positioned close to the putative catalytic Ser61. This supports the structural possibility that FO-LovD-like protein may recognize a CoA-thioester form of the phenylpyruvate-derived donor.

S9. Comparison of a segment of the eqx gene cluster in *F. heterosporum* with the *F. oxysporum* cluster of contig 44 region 8.



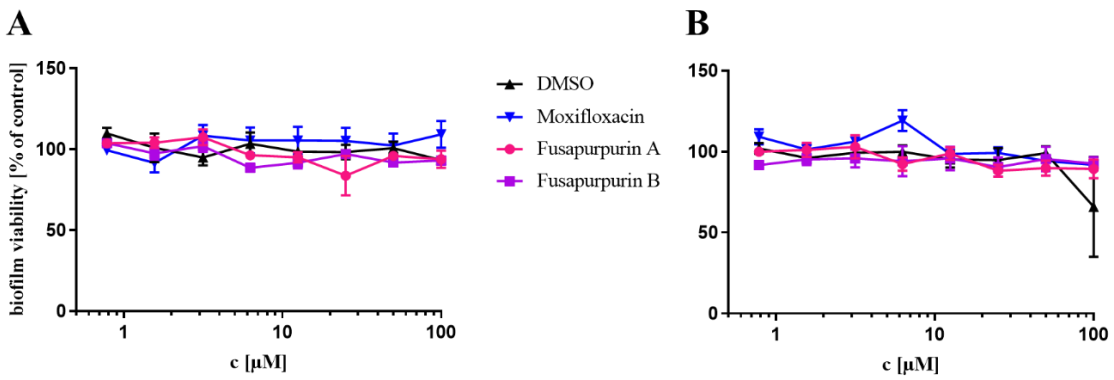
The sequence identities on the amino acid levels are given as percentages. Abbreviations of the enzymes encoded by the genes are as follows: Hybrid PKS-NRPS = hybrid polyketide synthase-nonribosomal peptide synthase, DA = Diels-Alderase, CPN10 = chaperonin 10-like protein, TER = trans-enoyl reductase, OMT = O-methyltransferase.

S10. Top 20 assembled contigs and distribution of contigs.



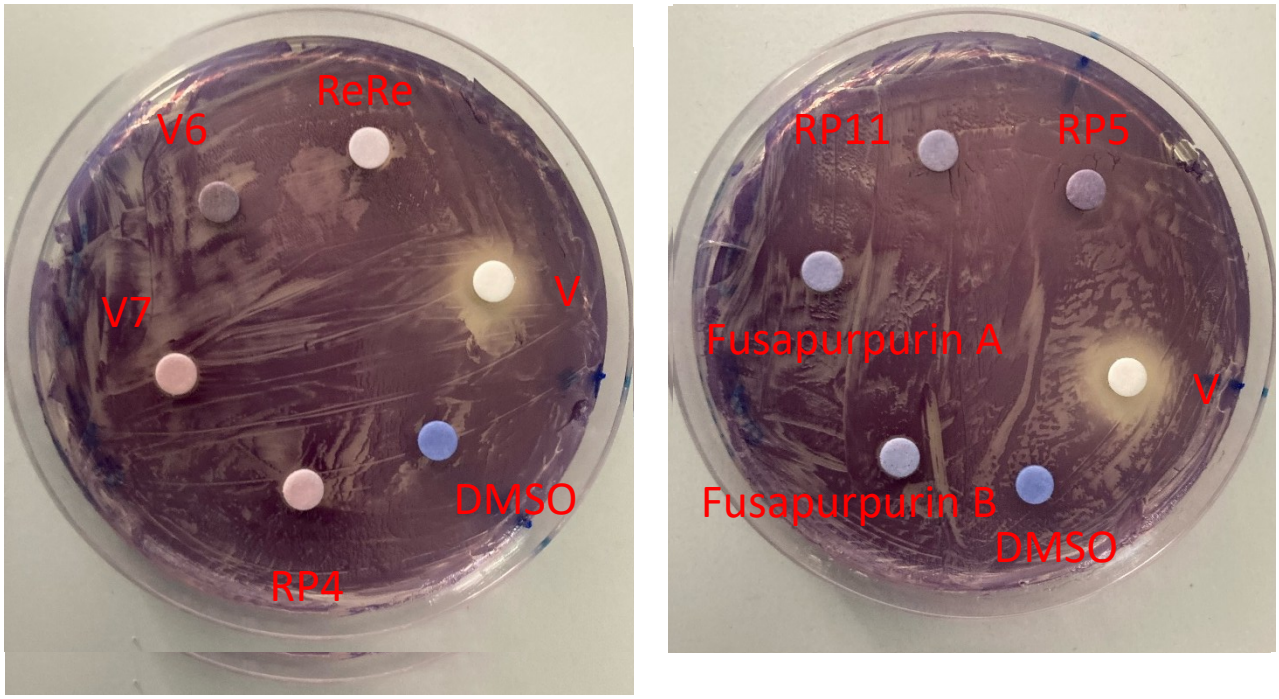
S10 shows the top 20 assembled contigs and the overall distribution of contigs from the nanopore whole genome sequencing, both sorted by lengths

S11. Effect of fusapurpurin A and B (3 and 4) on the cell viability of *S. aureus* Mu50 and *P. aeruginosa* PAO1 in preformed biofilms.



S11 is showing the effect of fusapurpurin A (**3**), fusapurpurin B (**4**) and the antibiotic moxifloxacin on the viability of cells in bacterial biofilms formed by MRSA Mu50 (A) and *P. aeruginosa* PAO1 (B). Fusapurpurin A, fusapurpurin B and moxifloxacin do not impair the viability of cells in biofilms. DMSO was used as solvent control. Both assays were carried out in triplicates. Graphs show mean ± SEM.

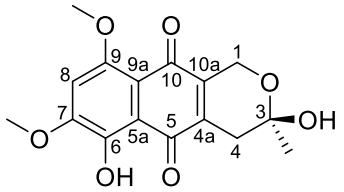
S12. Quorum quenching assay of fusapurpurins in *Chromobacterium violaceum.*



The ability to inhibit quorum sensing (QS) was evaluated using *C. volaceum*. The positive control vanillin (V) inhibits QS, indicated by the colourless circle surrounding the test discs, while negative control DMSO is inactive, indicated by the intensive staining of the test disc and the bacteria around. The different test samples, including fusapurpurin A and B did not inhibit QS.

S13. NMR Table of Compound 1 (DMSO-d_6, ^{1}H: 600MHz).

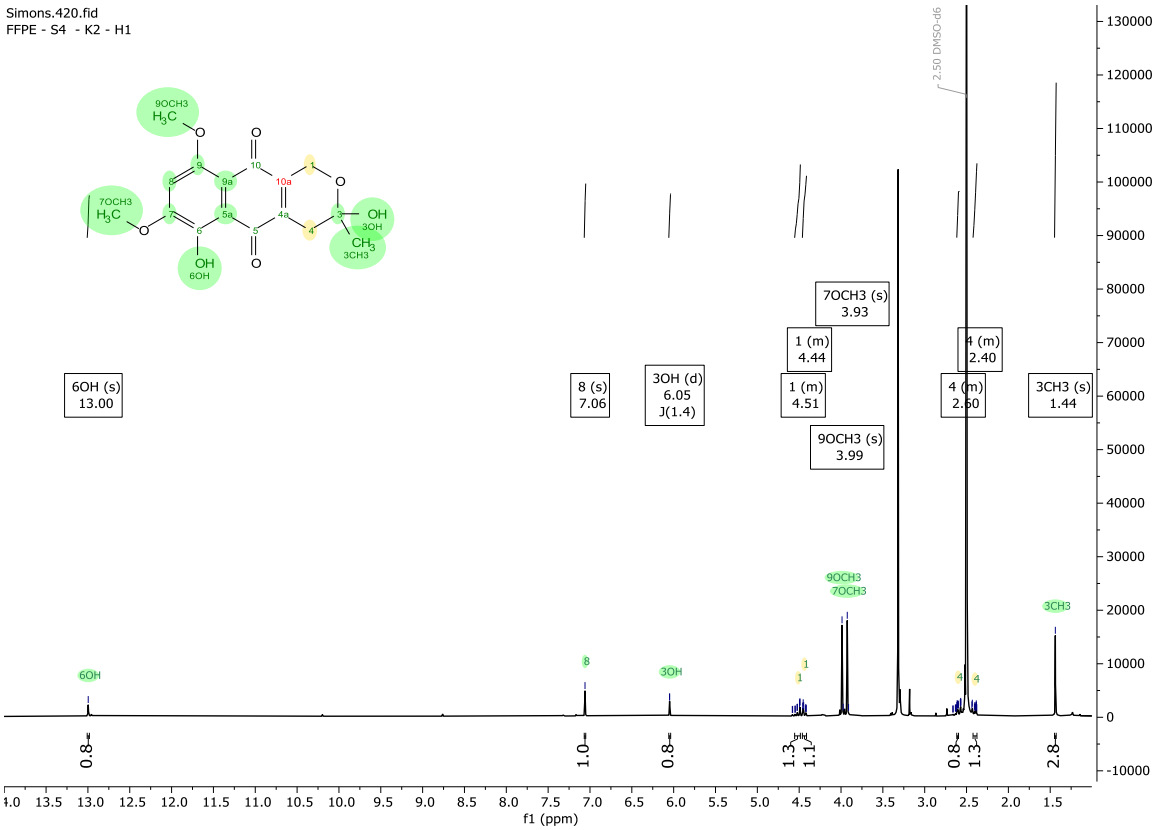
9-O-methylfusarubin



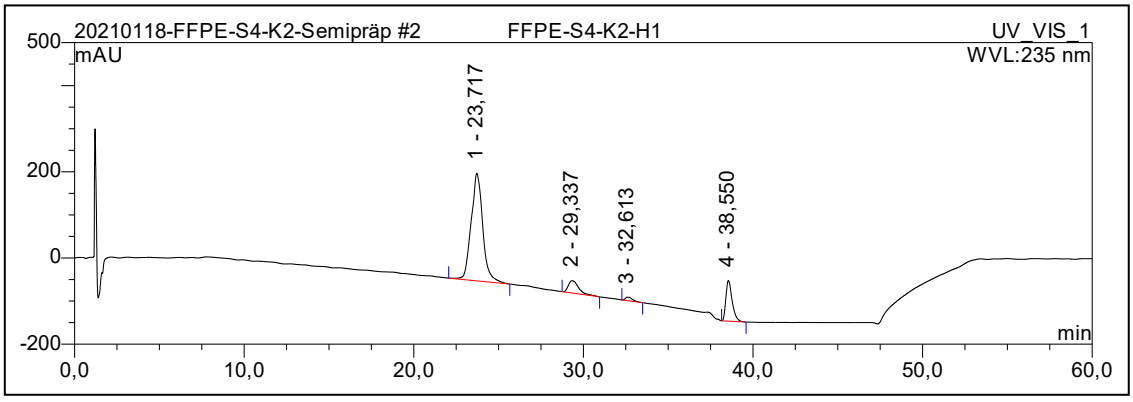
Chemical Formula: $C_{16}H_{16}O_7$
Exact Mass: 320,09
Molecular Weight: 320.30

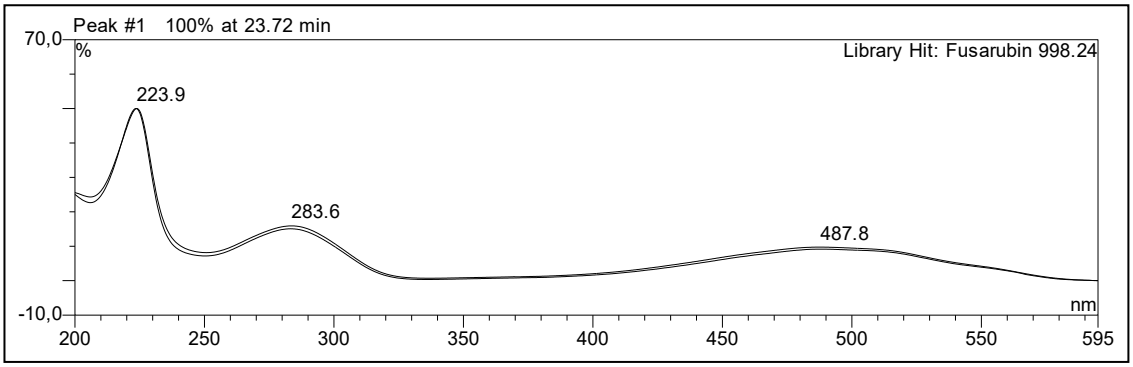
position	δ_H, m (J in Hz)
1	4.44, m
	4.51, m
4	2.40, m
	2.60, m
8	7.06, s
3CH_3	1.44, s, 3H
7OCH_3	3.93, s, 3H
9OCH_3	3.99, s, 3H
3-OH	6.05, d (1.4)
6-OH	13.00, s

S14. [1]H-NMR Spectrum of Compound 1 (DMSO-d_6, 600 MHz)

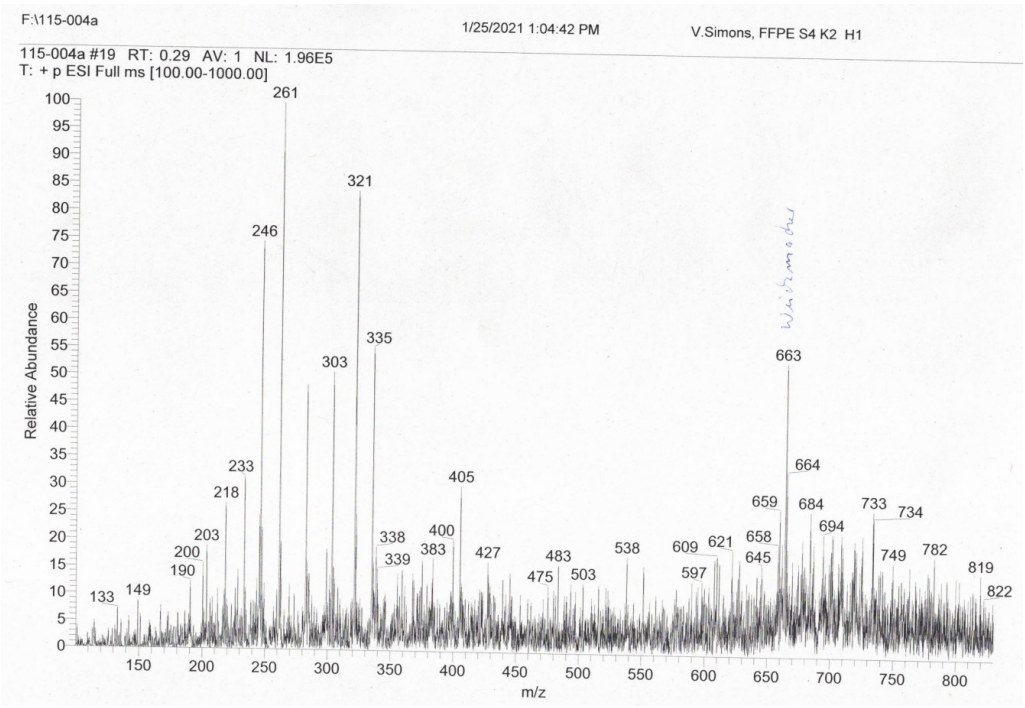


S15. HPLC-DAD UV-Vis Spectrum of Compound 1 (Methanol)

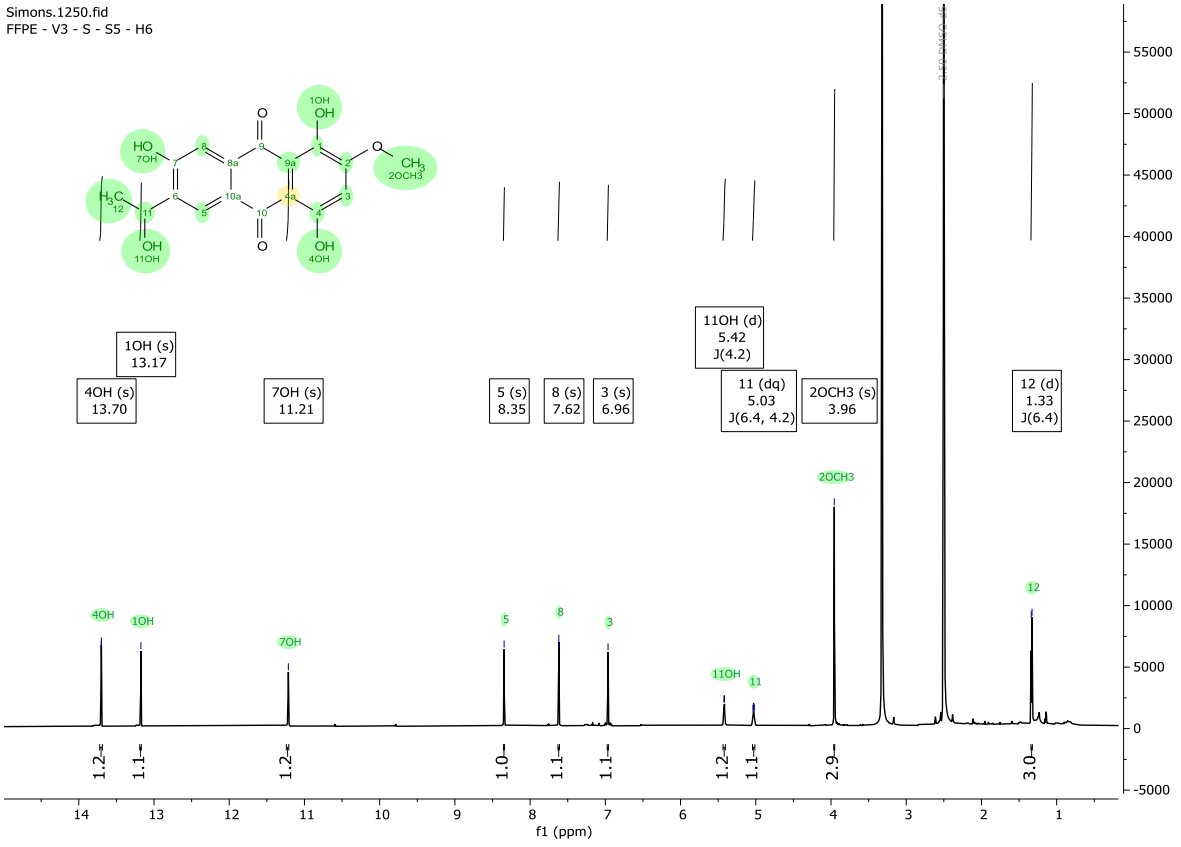




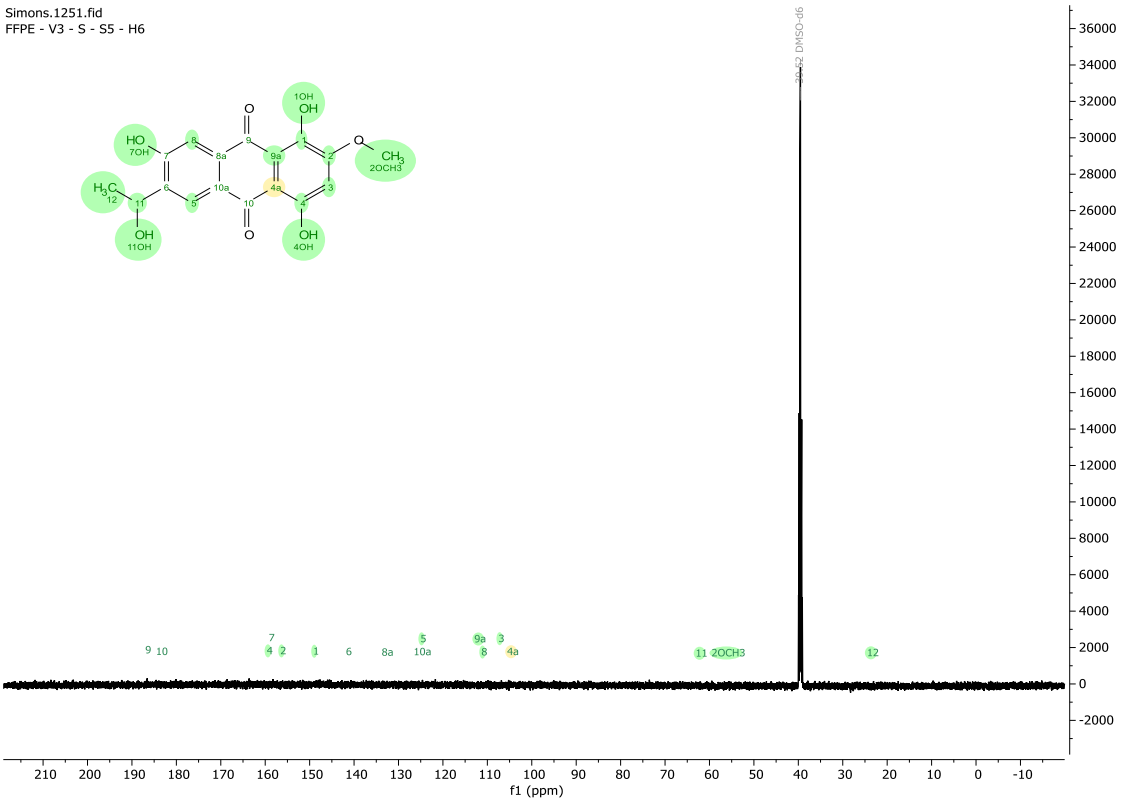
S16. ESI(+)MS Spectrum of 1



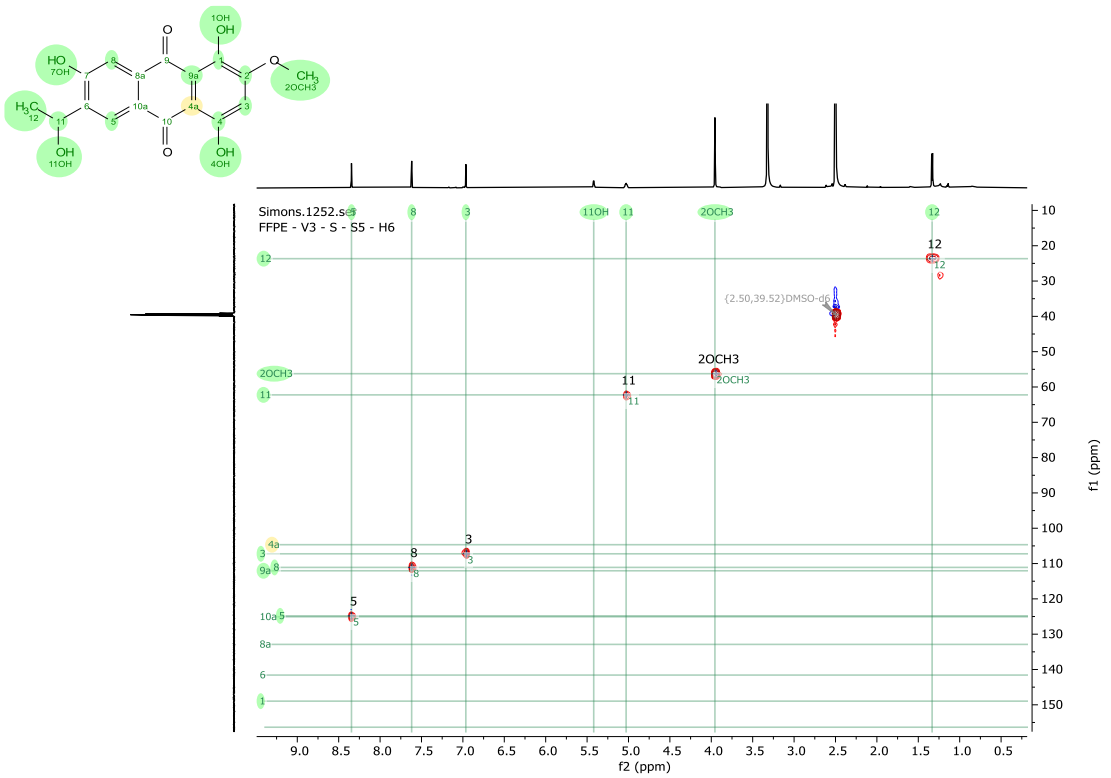
S17. ^{1}H-NMR Spectrum of Compound 2 (DMSO-d_6, 600 MHz)



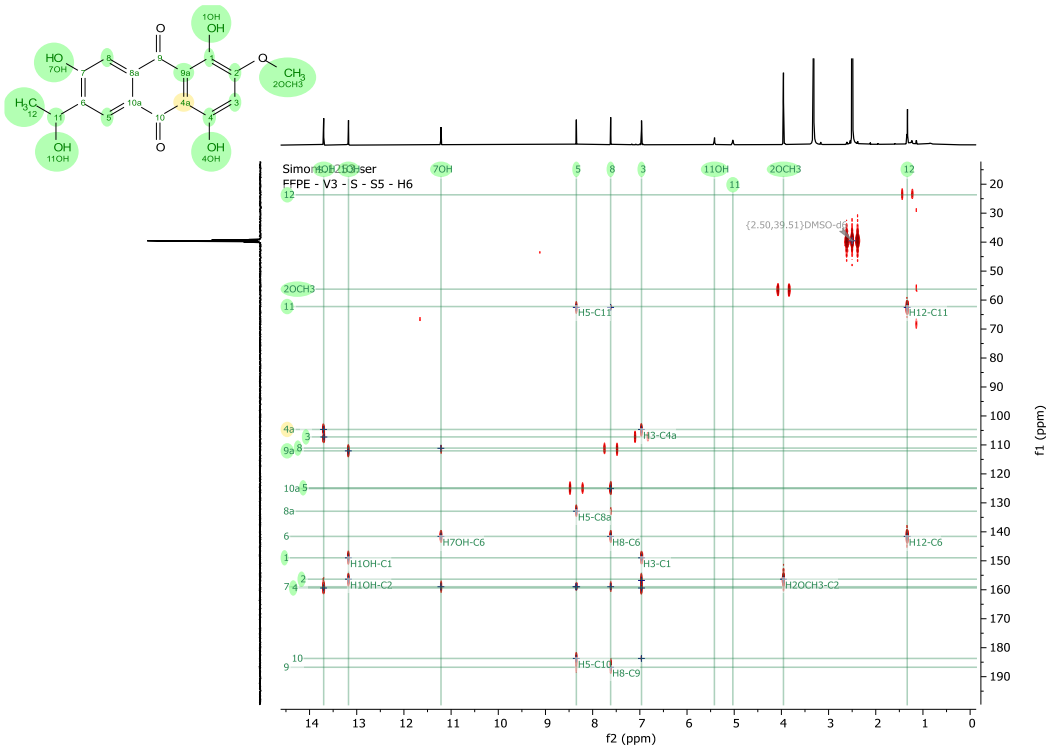
S18. ^{13}C-NMR Spectrum of Compound 2 (DMSO-d_6, 150 MHz)



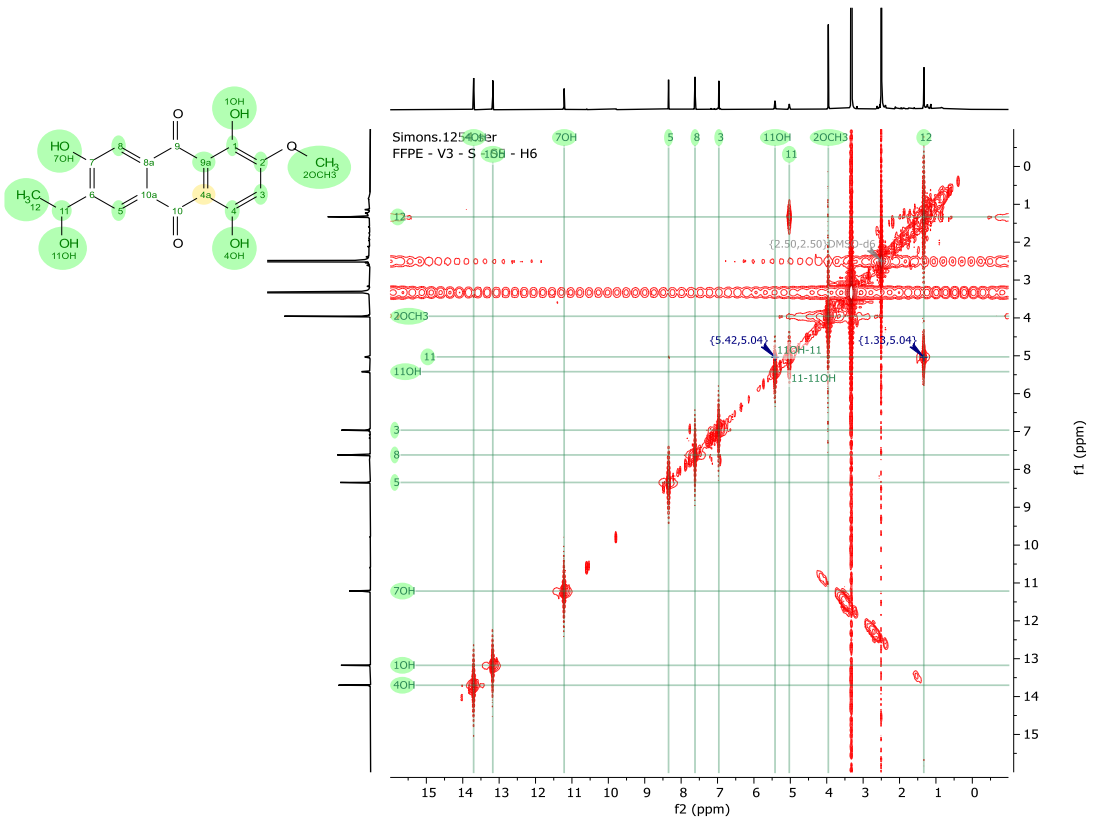
S19. ^{1}H-^{13}C-HSQC Spectrum of Compound 2 (DMSO-d_6, ^{1}H: 600MHz, ^{13}C: 150 MHz)



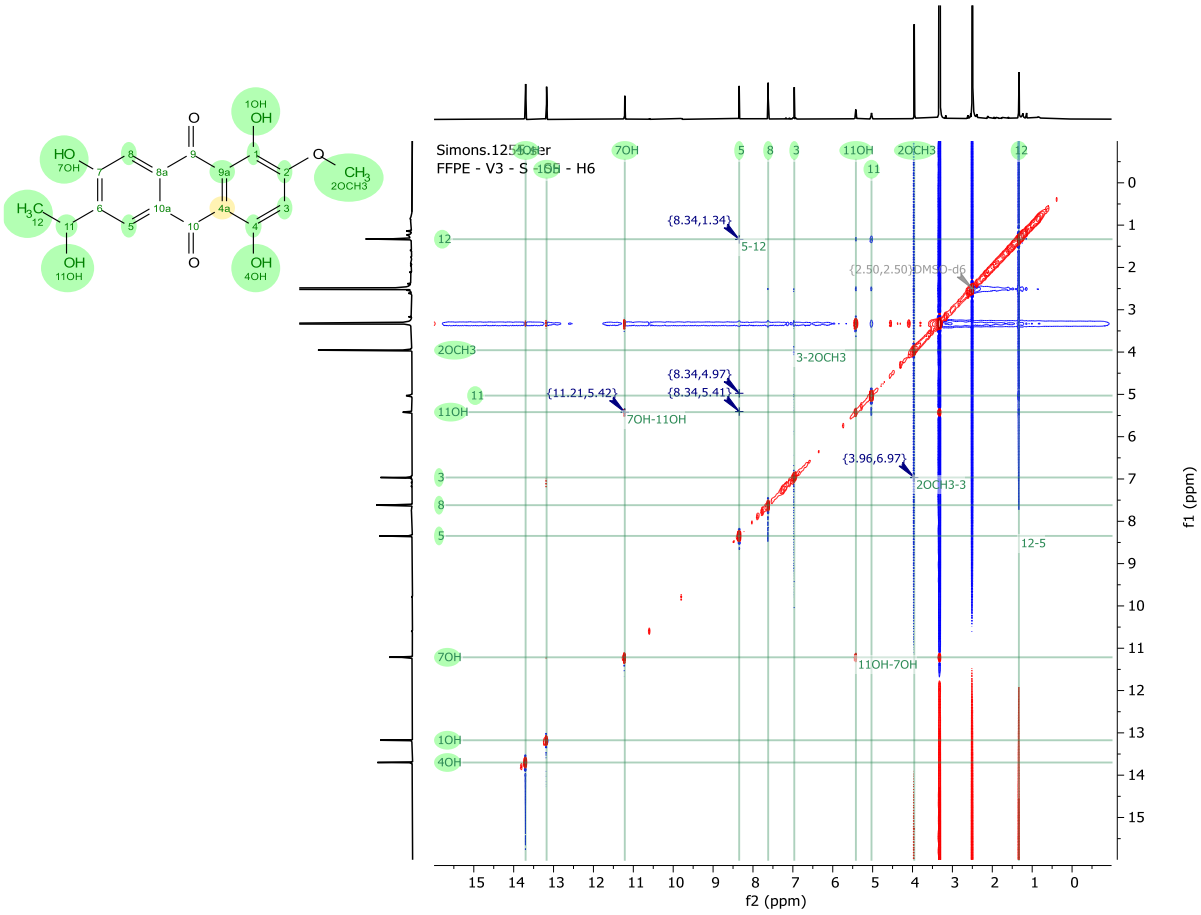
S20. ^{1}H-^{13}C-HMBC Spectrum of Compound 2 (DMSO-d_6, ^{1}H: 600MHz, ^{13}C: 150 MHz)



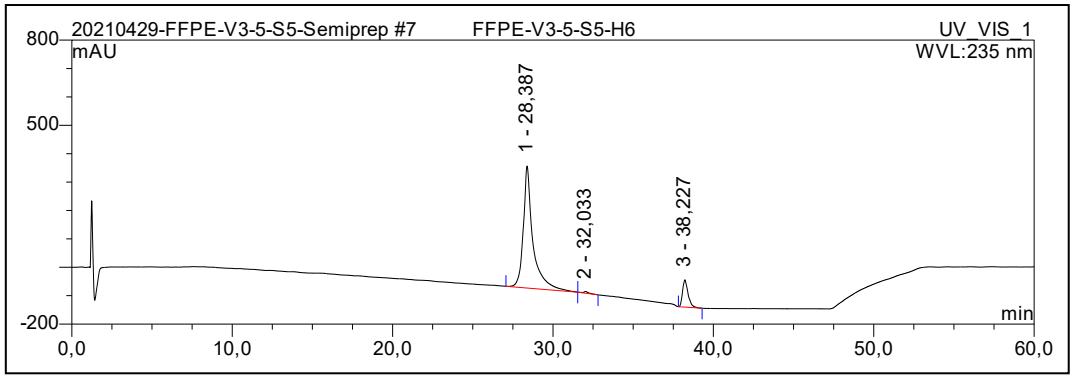
S21. ^{1}H-^{1}H-COSY Spectrum of Compound 2 (DMSO-d_6, 600MHz)

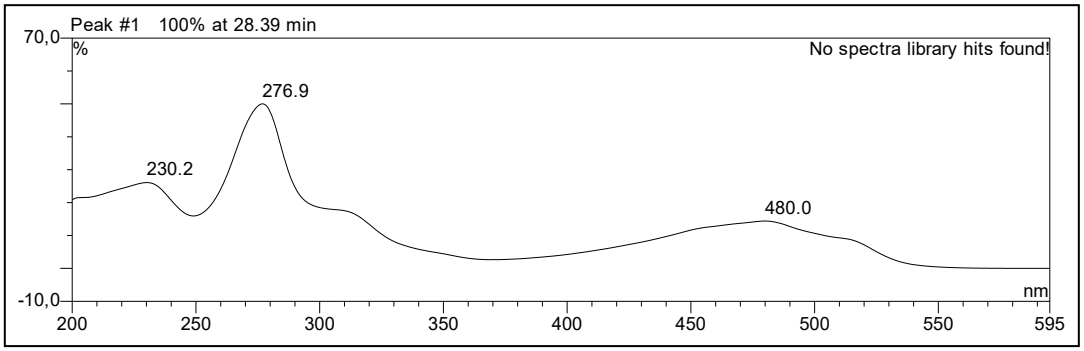


S22. ^{1}H-^{1}H-NOESY Spectrum of Compound 2 (DMSO-d_6, 600MHz)

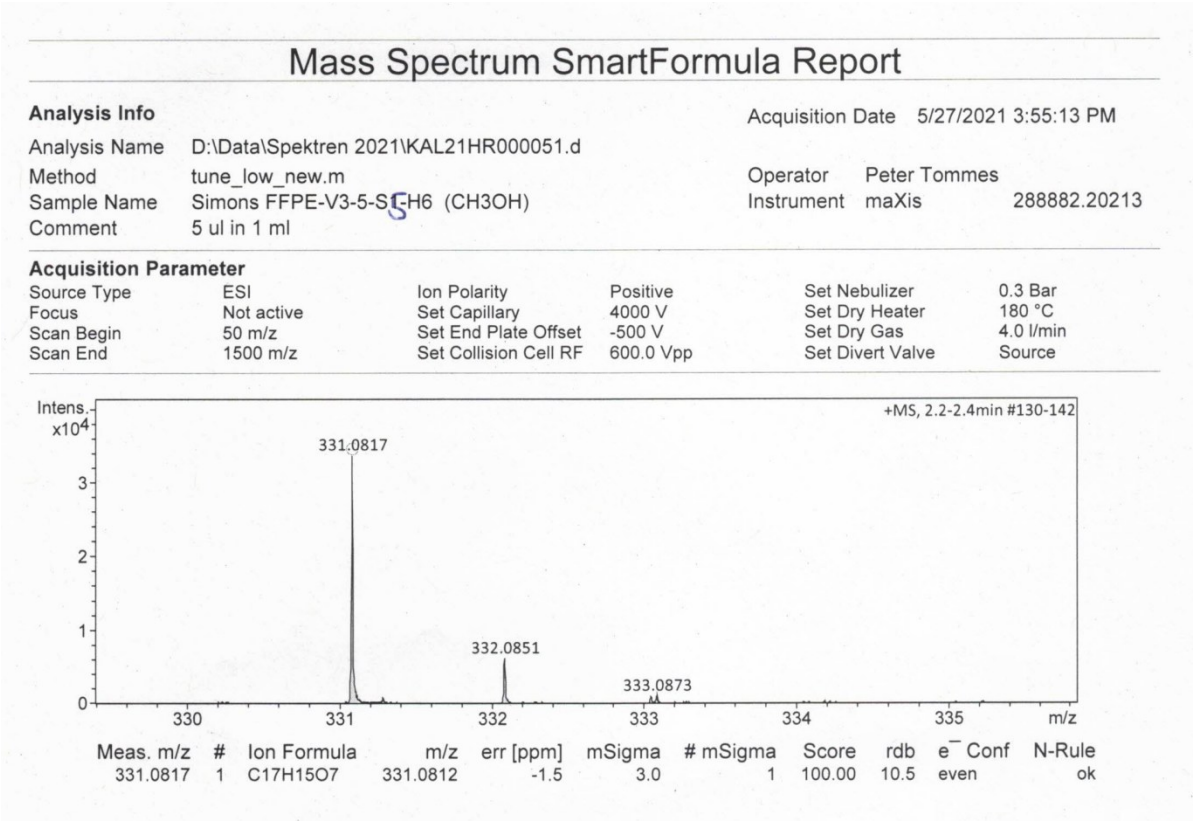


S23. HPLC-DAD UV-Vis Spectrum of Compound 2 (Methanol)





S24. High Resolution ESI(+)MS Spectrum of Compound 2



Mass Spectrum SmartFormula Report

Analysis Info

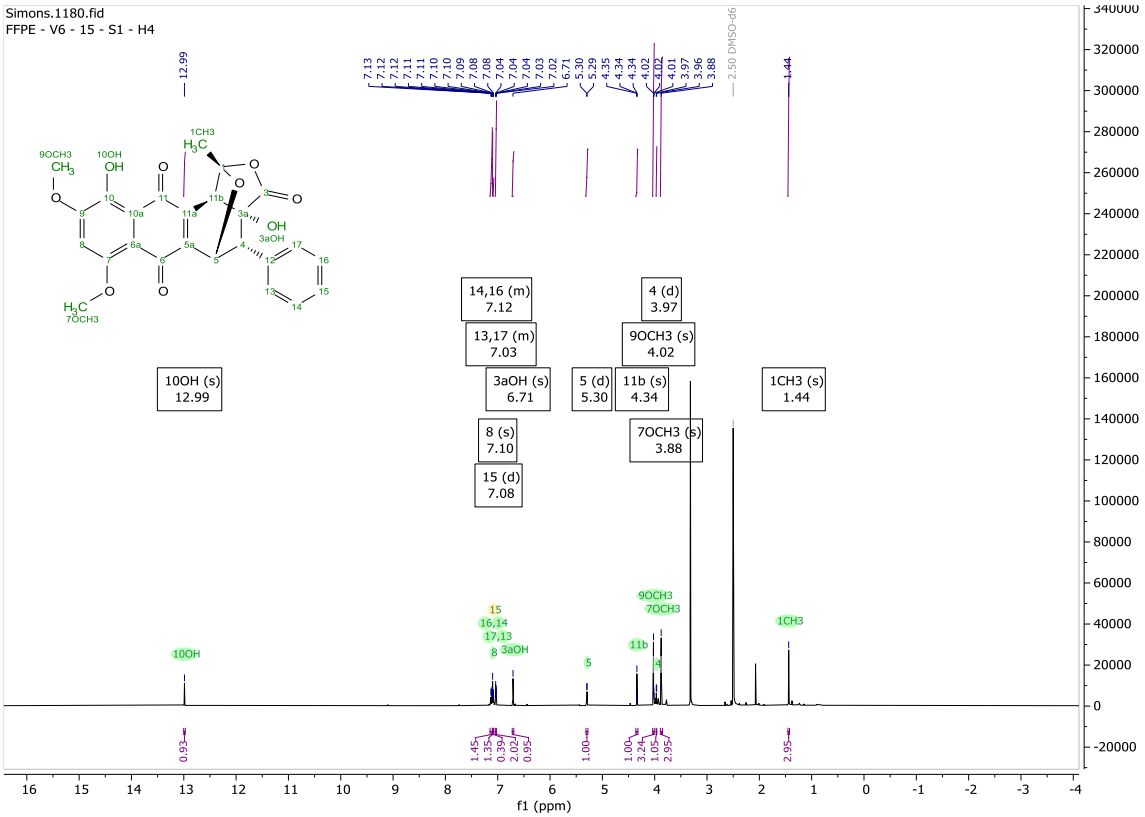
Analysis Name	D:\Data\Spektren 2021\KAL21HR000051.d	Acquisition Date	5/27/2021 3:55:13 PM
Method	tune_low_new.m	Operator	Peter Tommes
Sample Name	Simons FFPE-V3-5-S1-H6 (CH3OH)	Instrument	maXis 288882.20213
Comment	5 ul in 1 ml		

Acquisition Parameter

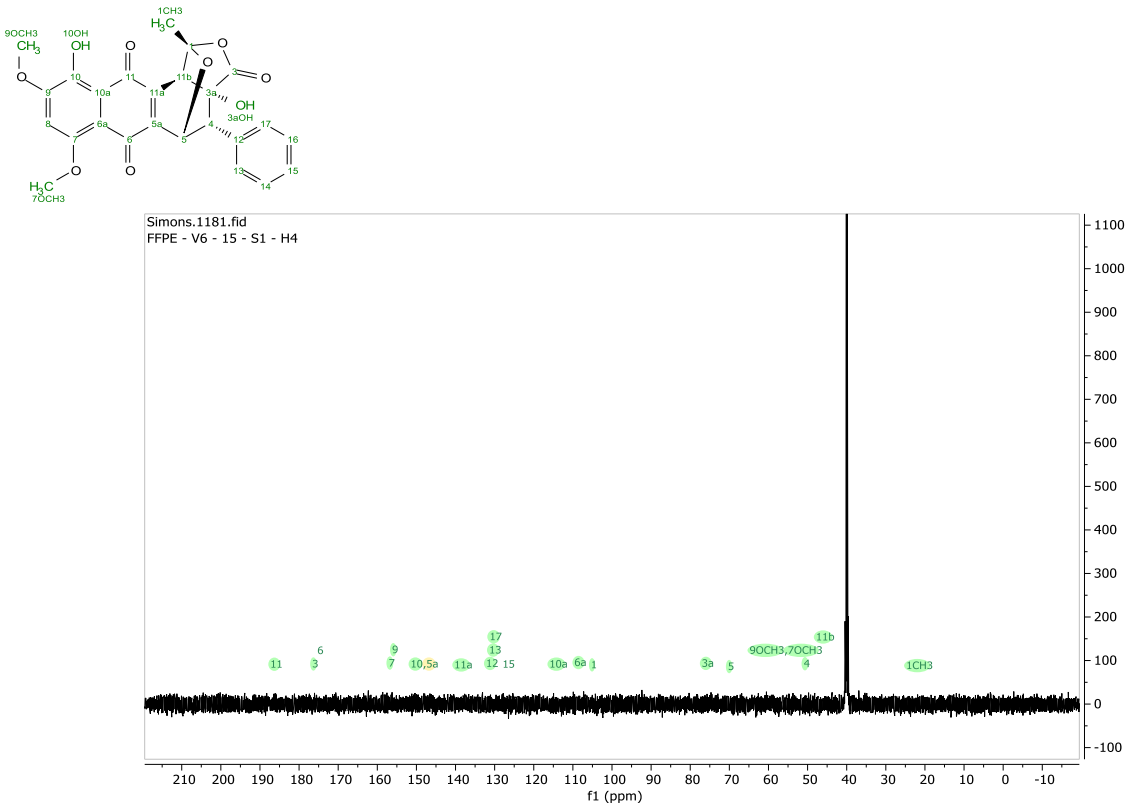
Source Type	ESI	Ion Polarity	Positive	Set Nebulizer	0.3 Bar
Focus	Not active	Set Capillary	4000 V	Set Dry Heater	180 °C
Scan Begin	50 m/z	Set End Plate Offset	-500 V	Set Dry Gas	4.0 l/min
Scan End	1500 m/z	Set Collision Cell RF	600.0 Vpp	Set Divert Valve	Source

Meas. m/z	#	Ion Formula	m/z	err [ppm]	mSigma	# mSigma	Score	rdb	e⁻ Conf	N-Rule
331.0817	1	C17H15O7	331.0812	-1.5	3.0	1	100.00	10.5	even	ok

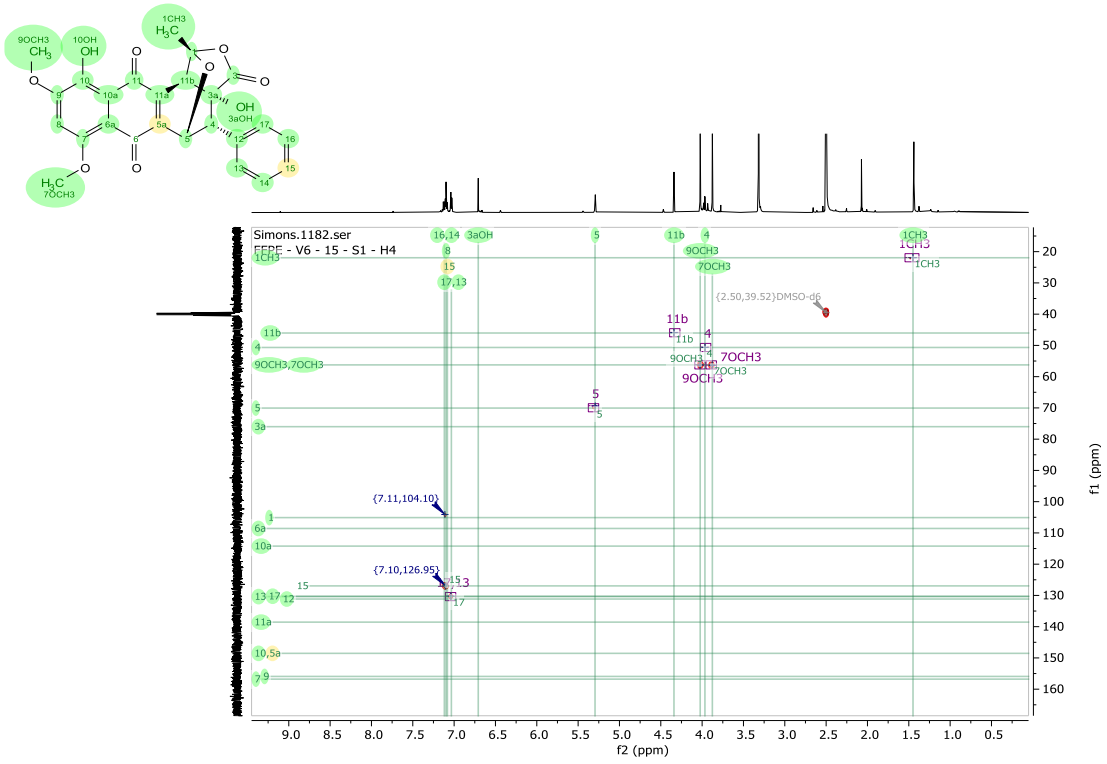
S25. ^{1}H-NMR Spectrum of Compound 3 (DMSO-d_6, 600 MHz)



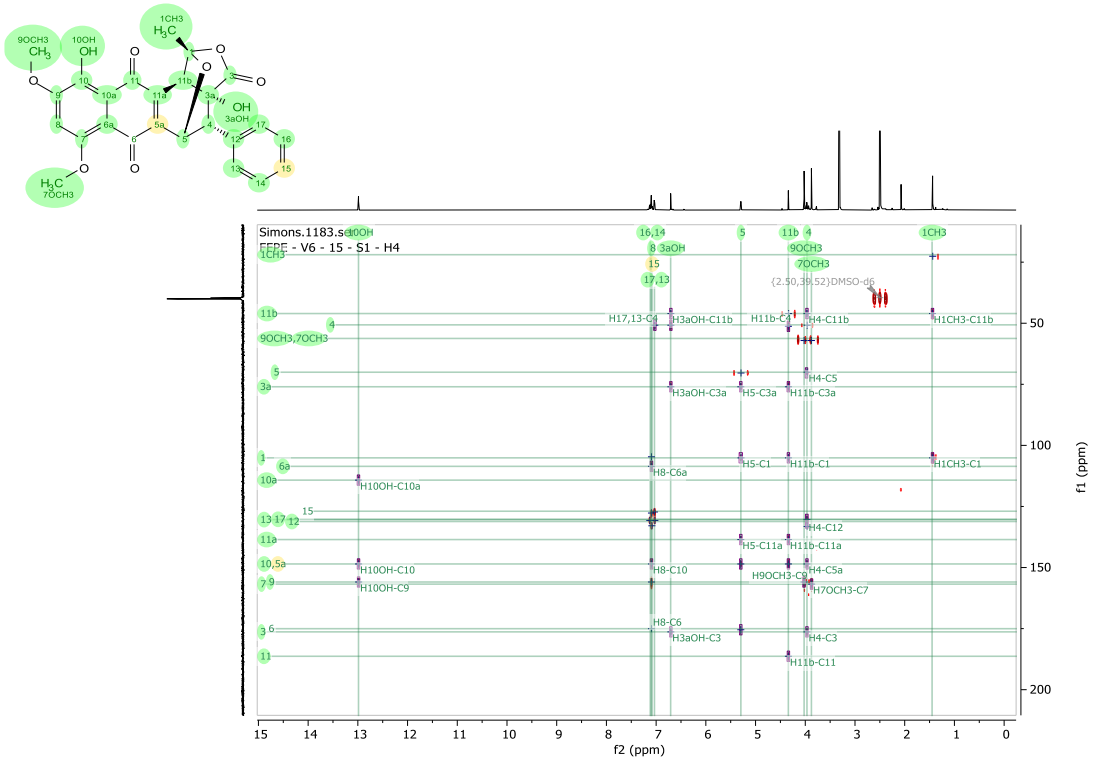
S26. ^{13}C-NMR Spectrum of Compound 3 (DMSO-d_6, 150 MHz)



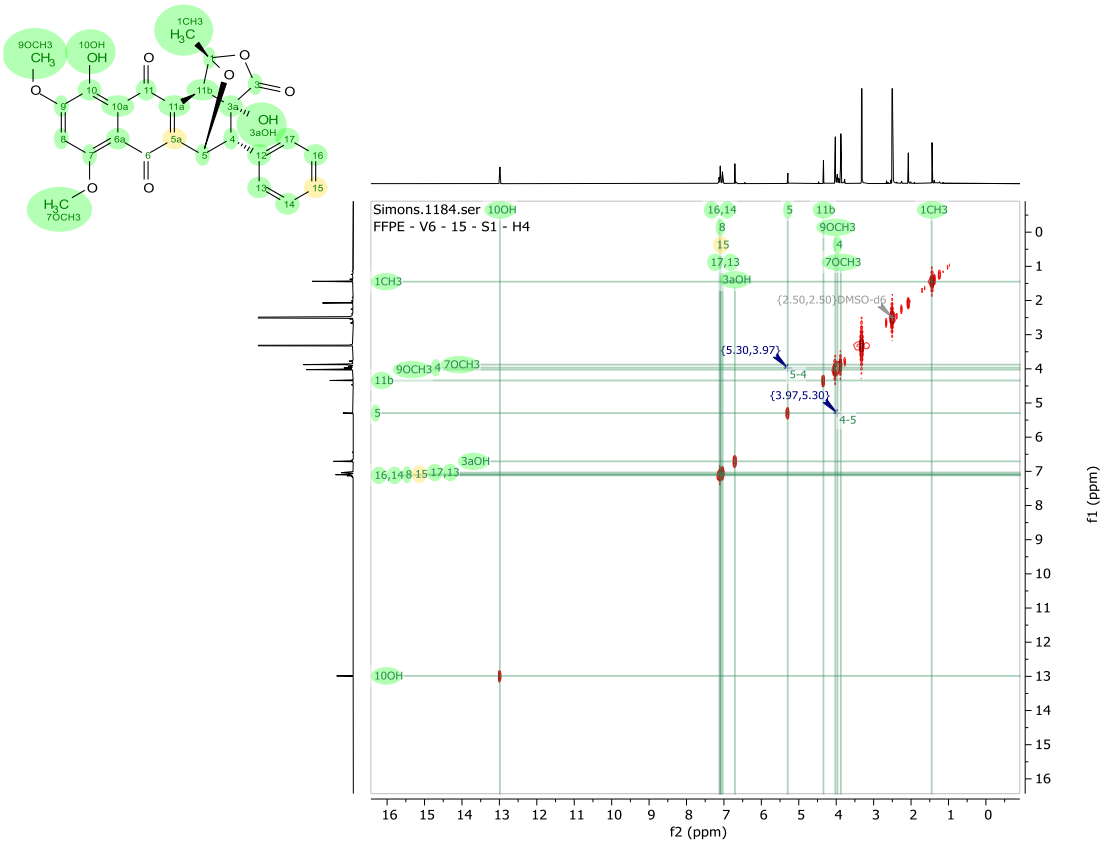
S27. ^{1}H-^{13}C-HSQC Spectrum of Compound 3 (DMSO-d_6, ^{1}H: 600MHz, ^{13}C: 150 MHz)



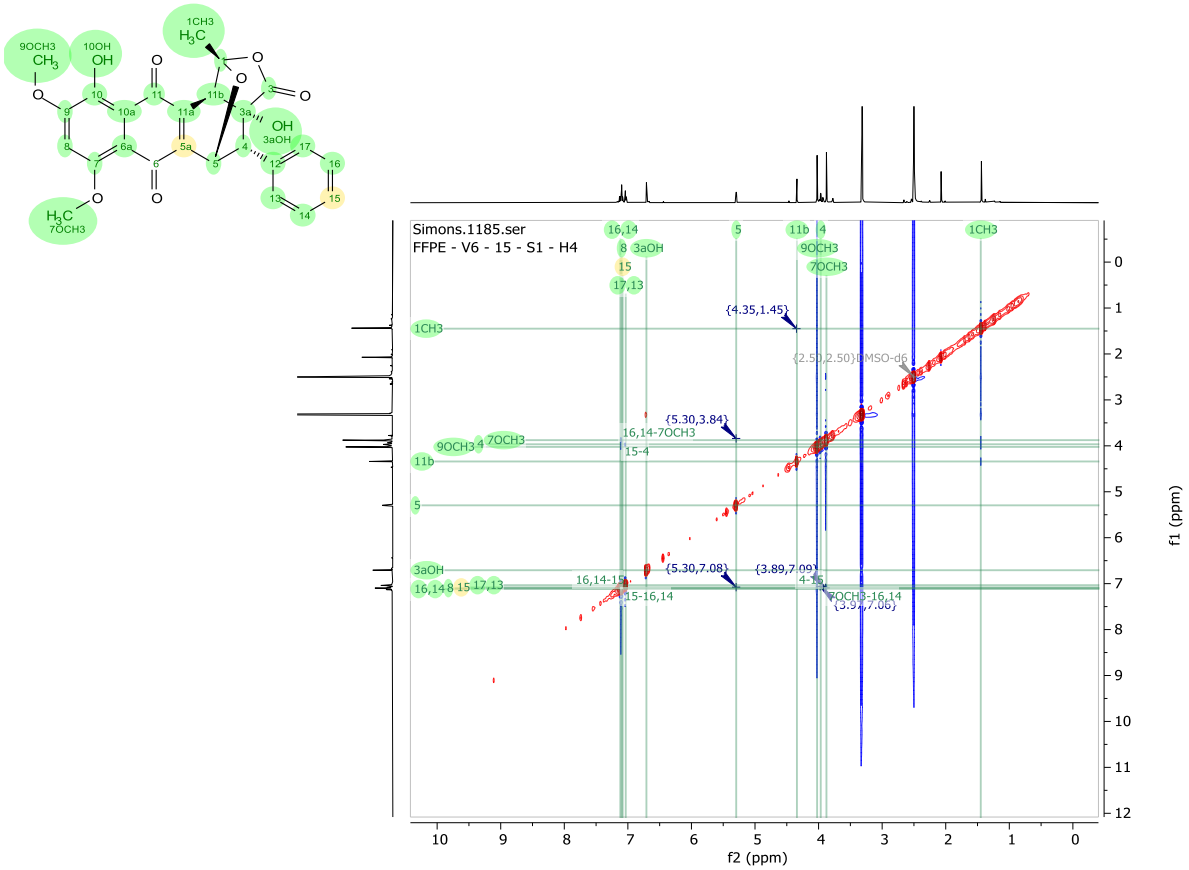
S28. ^{1}H-^{13}C-HMBC Spectrum of Compound 3 (DMSO-*d*$_6$, ^{1}H: 600MHz, ^{13}C: 150 MHz)



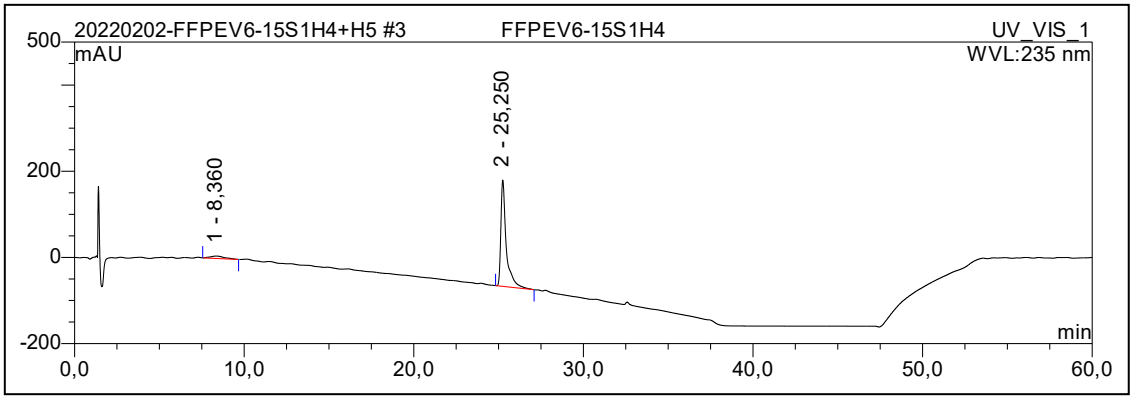
S29. ^{1}H-^{1}H-COSY Spectrum of Compound 3 (fusapurpurin A) (DMSO-*d*$_6$, 600MHz)

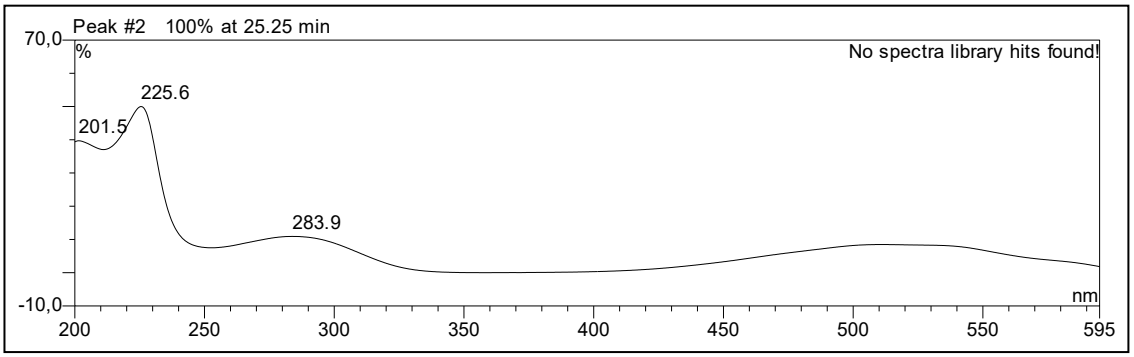


S30. ^{1}H-^{1}H-NOESY Spectrum of Compound 3 (DMSO-d_6, 600MHz)

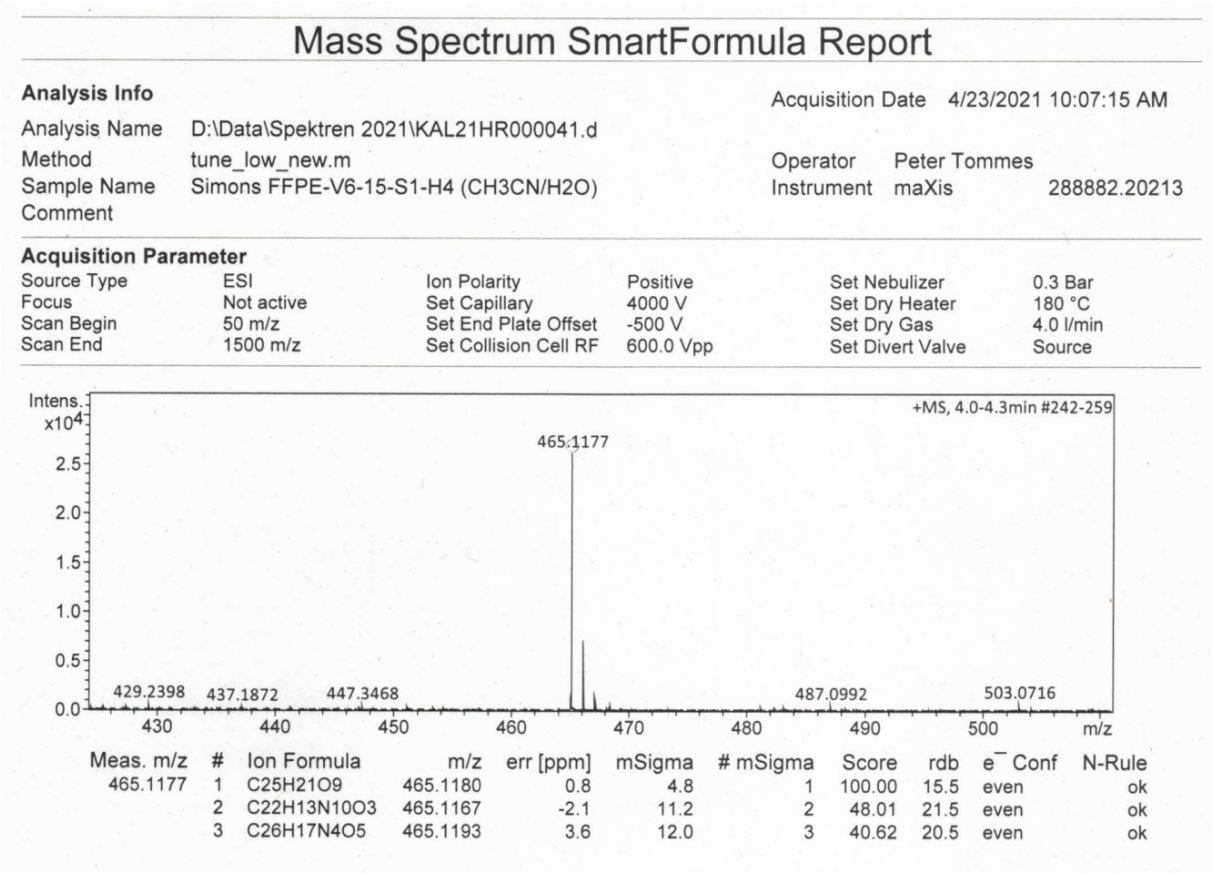


S31. HPLC-DAD UV-Vis Spectrum of Compound 3 (Methanol)





S32. High Resolution ESI(+)MS Spectrum of 3



Mass Spectrum SmartFormula Report

Analysis Info

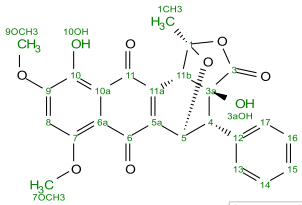
Analysis Name	D:\Data\Spektren 2021\KAL21HR000041.d	Acquisition Date	4/23/2021 10:07:15 AM
Method	tune_low_new.m	Operator	Peter Tommes
Sample Name	Simons FFPE-V6-15-S1-H4 (CH3CN/H2O)	Instrument	maXis 288882.20213
Comment			

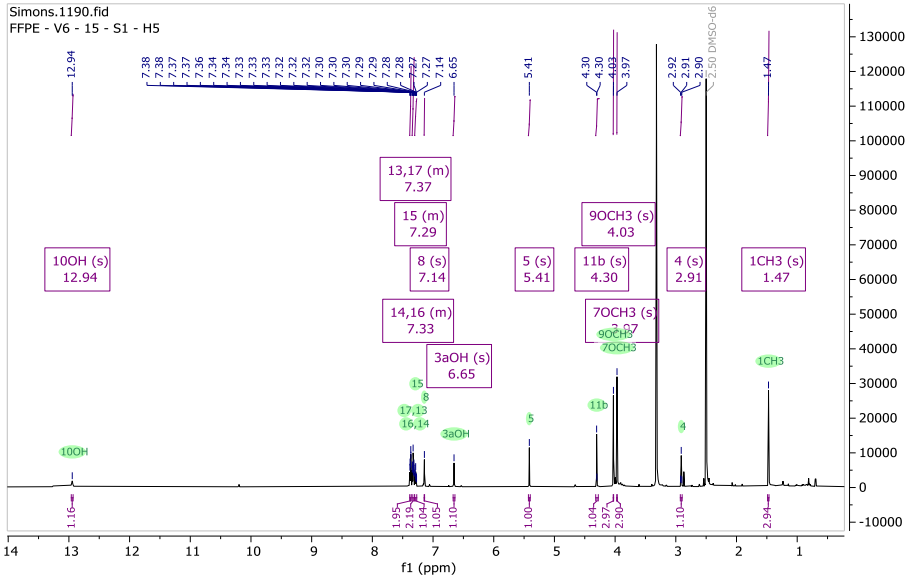
Acquisition Parameter

Source Type	ESI	Ion Polarity	Positive	Set Nebulizer	0.3 Bar
Focus	Not active	Set Capillary	4000 V	Set Dry Heater	180 °C
Scan Begin	50 m/z	Set End Plate Offset	-500 V	Set Dry Gas	4.0 l/min
Scan End	1500 m/z	Set Collision Cell RF	600.0 Vpp	Set Divert Valve	Source

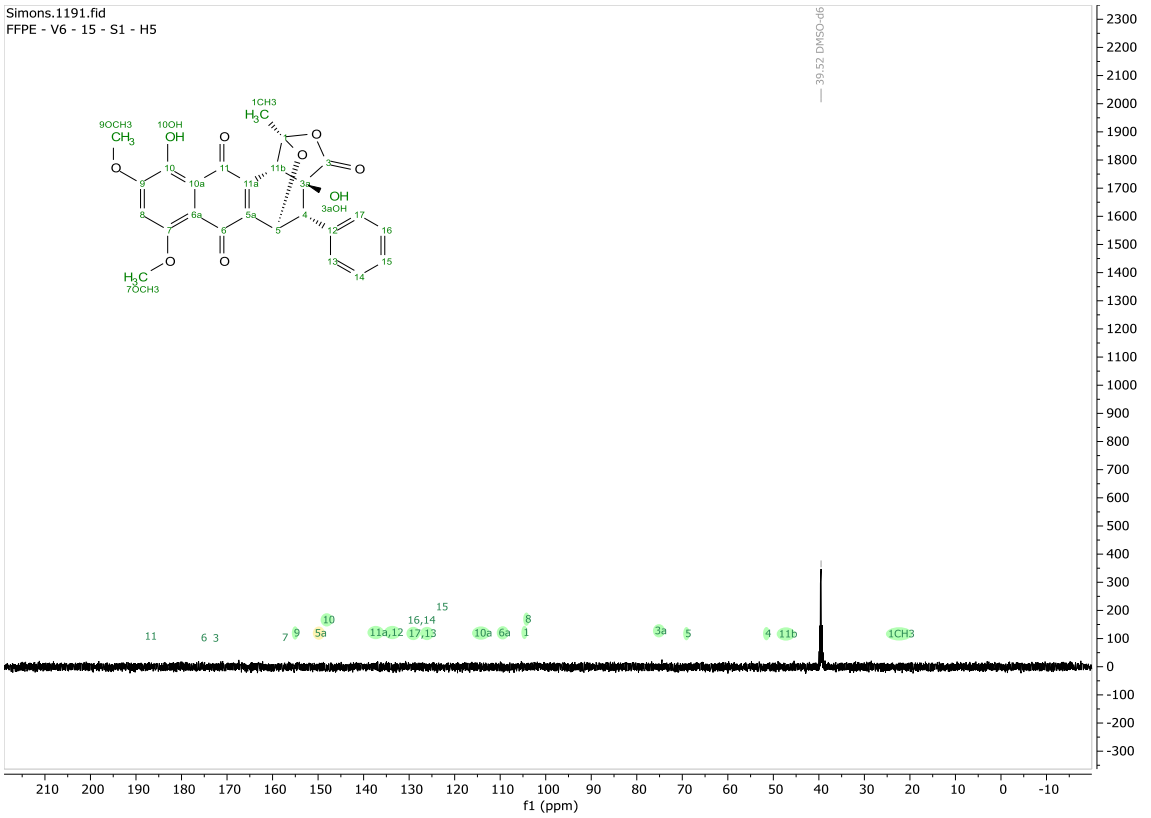
Meas. m/z	#	Ion Formula	m/z	err [ppm]	mSigma	# mSigma	Score	rdb	e⁻ Conf	N-Rule
465.1177	1	C25H21O9	465.1180	0.8	4.8	1	100.00	15.5	even	ok
	2	C22H13N10O3	465.1167	-2.1	11.2	2	48.01	21.5	even	ok
	3	C26H17N4O5	465.1193	3.6	12.0	3	40.62	20.5	even	ok

S33. ^{1}H-NMR Spectrum of Compound 4 (DMSO-d_6, 600 MHz)

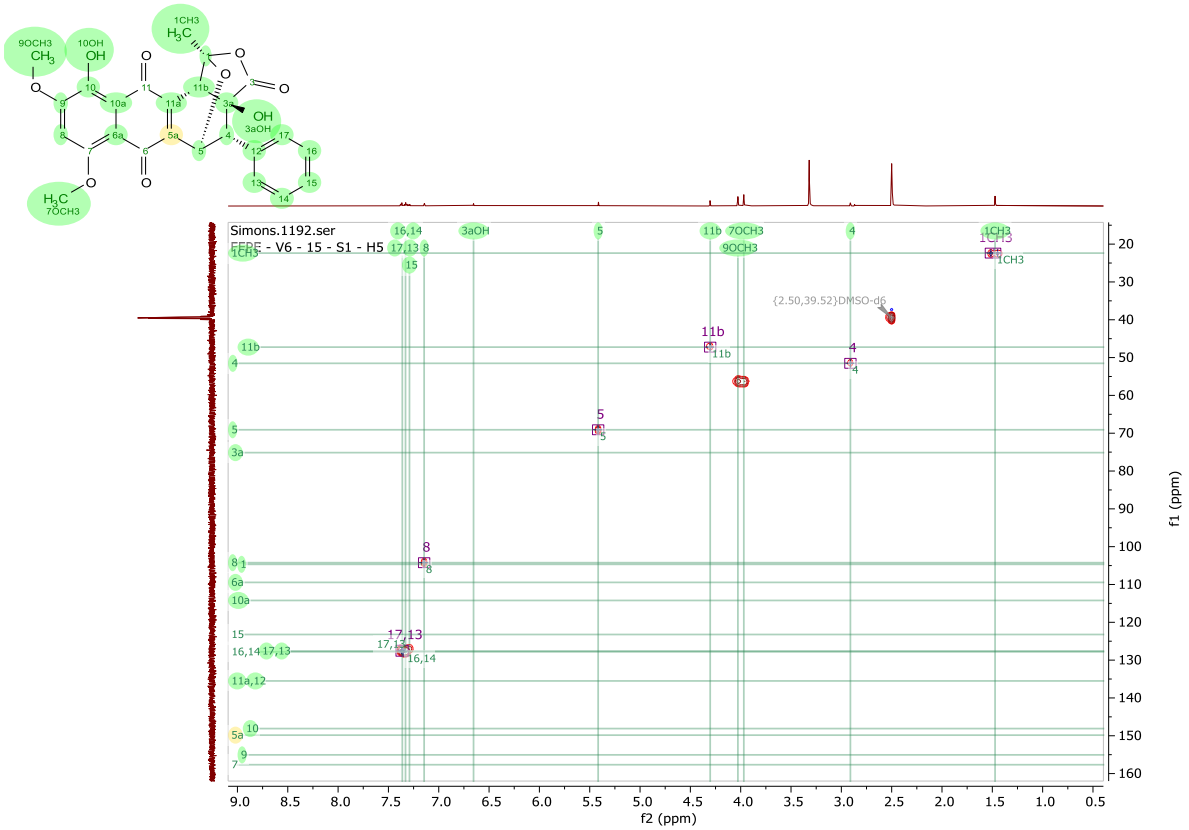




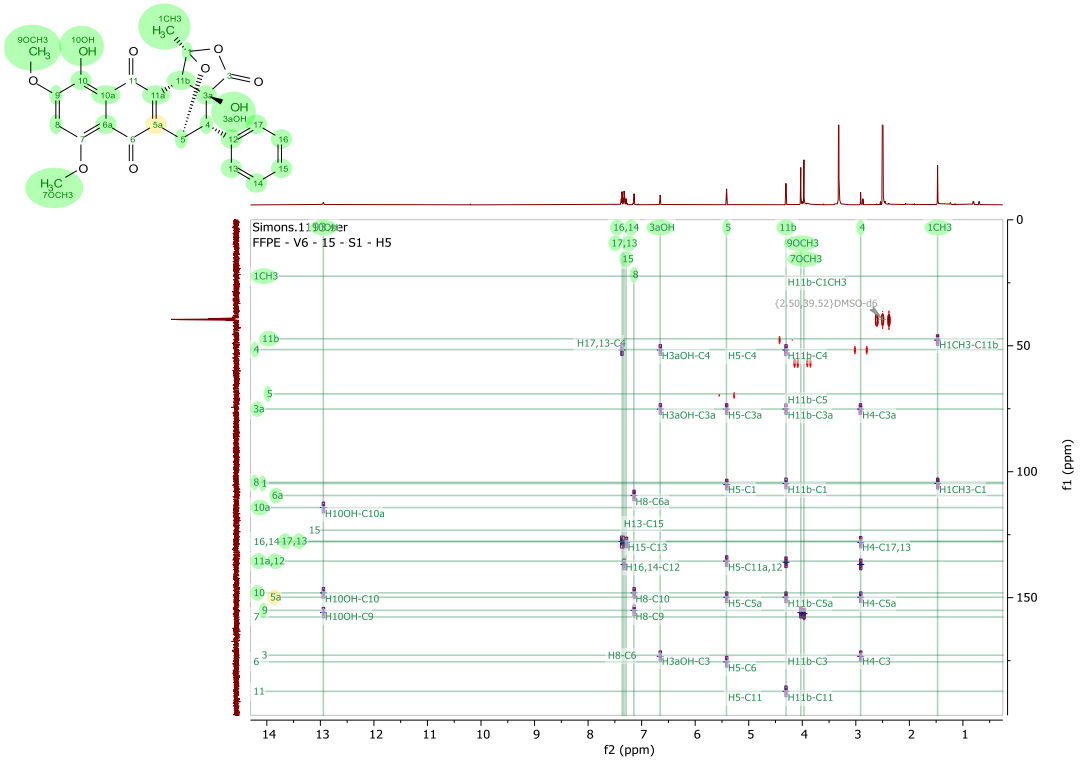
S34. ^{13}C-NMR Spectrum of Compound 4 (DMSO-d_6, 150 MHz)



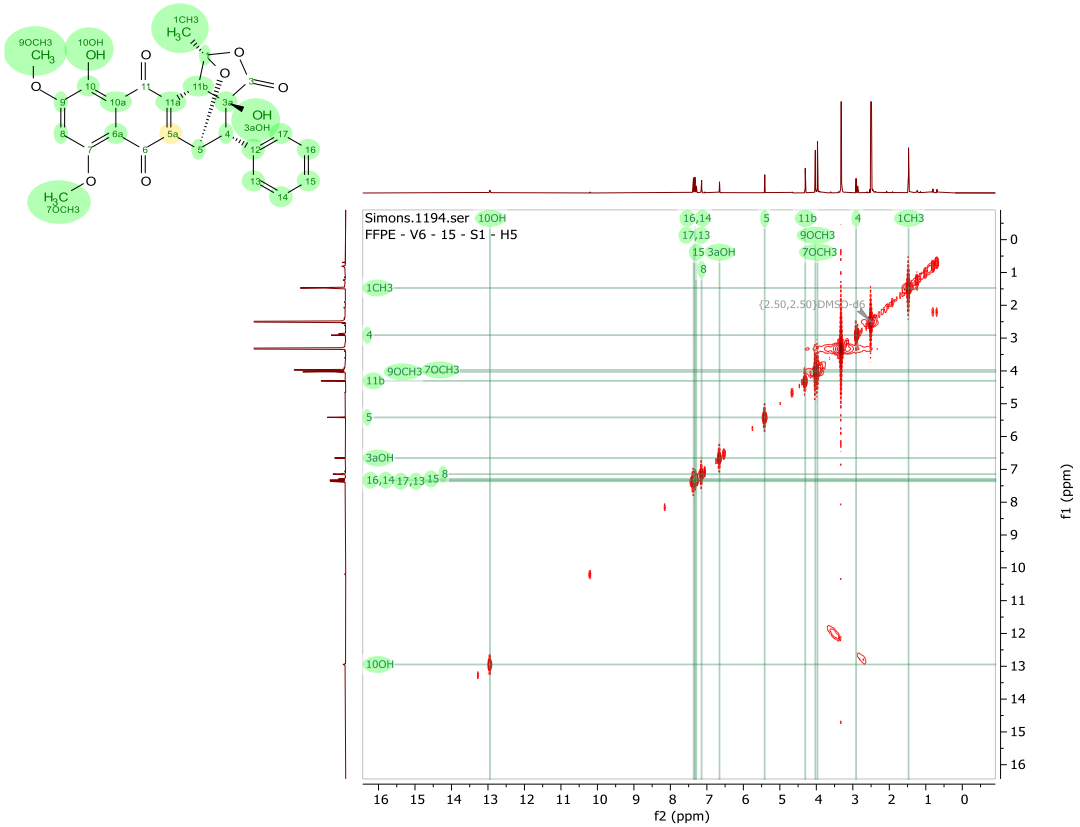
S35. ^{1}H-^{13}C-HSQC Spectrum of Compound 4 (DMSO-d_6, ^{1}H: 600MHz, ^{13}C: 150 MHz)



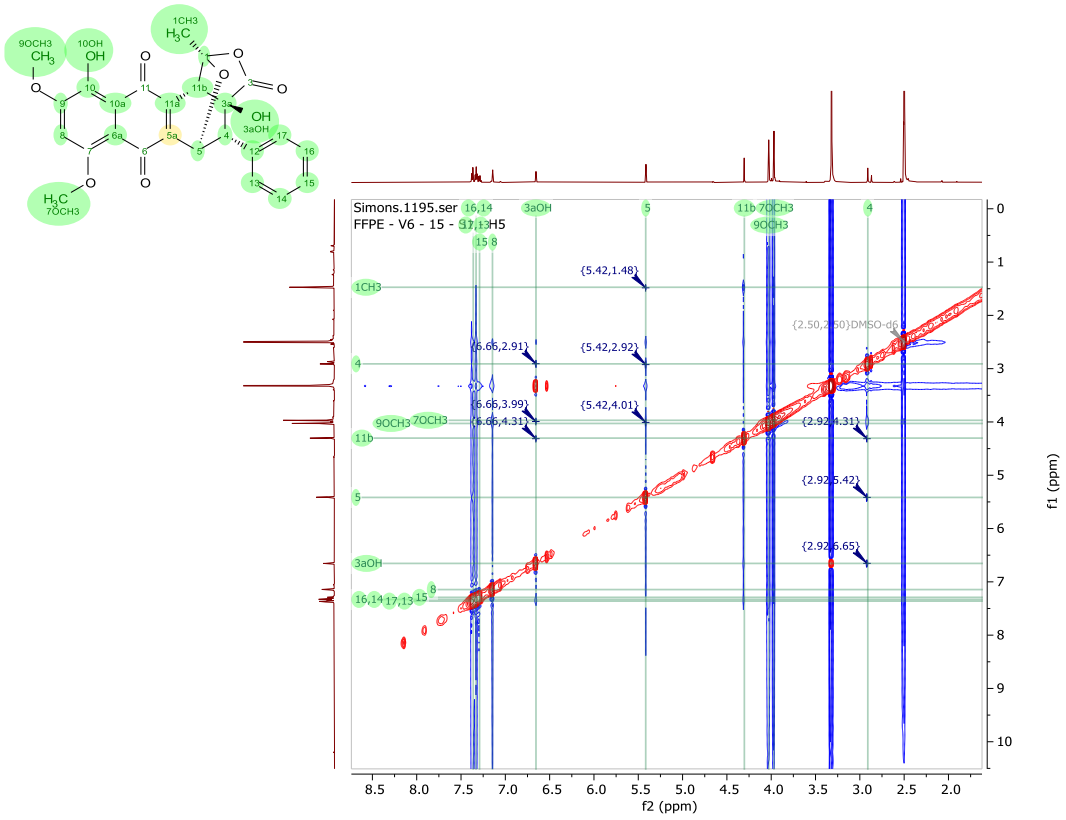
S36. ^{1}H-^{13}C-HMBC Spectrum of Compound 4 (DMSO-*d*$_6$, ^{1}H: 600MHz, ^{13}C: 150 MHz)



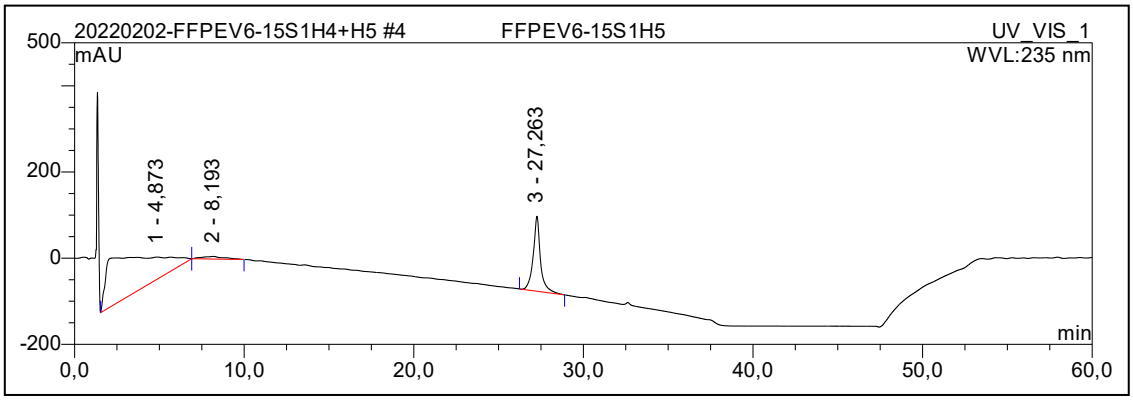
S37. ^{1}H-^{1}H-COSY Spectrum of Compound 4 (DMSO-*d*$_6$, 600MHz)

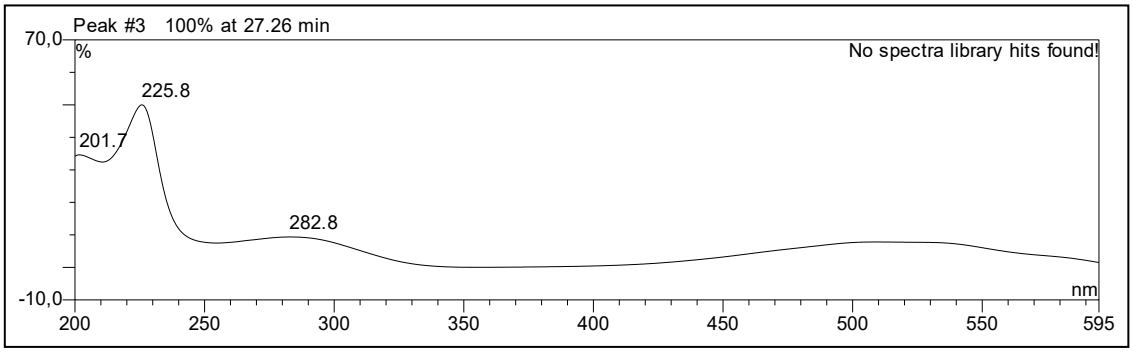


S38. ^{1}H-^{1}H-NOESY Spectrum of Compound 4 (DMSO-d_6, 600MHz)



S39. HPLC-DAD UV-Vis Spectrum of Compound 4 (Methanol)





S40. High Resolution ESI(+)MS Spectrum of 4

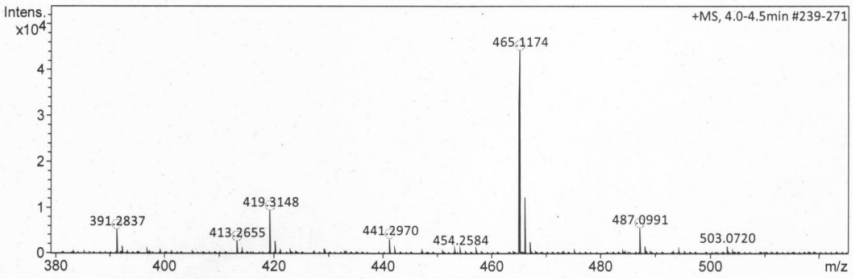
Mass Spectrum SmartFormula Report

Analysis Info

Analysis Name	D:\Data\Spektren 2021\KAL21HR000038.d	Acquisition Date	4/23/2021 8:29:49 AM
Method	tune_low_new.m	Operator	Peter Tommes
Sample Name	Simons FFPE-V6-15-S1-H5 (CH3CN/H2O)	Instrument	maXis 288882.20213
Comment			

Acquisition Parameter

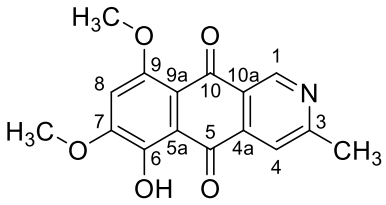
Source Type	ESI	Ion Polarity	Positive	Set Nebulizer	0.3 Bar
Focus	Not active	Set Capillary	4000 V	Set Dry Heater	180 °C
Scan Begin	50 m/z	Set End Plate Offset	-500 V	Set Dry Gas	4.0 l/min
Scan End	1500 m/z	Set Collision Cell RF	600.0 Vpp	Set Divert Valve	Source



Meas. m/z	#	Ion Formula	m/z	err [ppm]	mSigma	# mSigma	Score	rdb	e⁻ Conf	N-Rule
391.2837	1	C24H39O4	391.2843	1.4	22.0	1	100.00	5.5	even	ok
413.2655	1	C22H33N6O2	413.2660	1.0	23.6	1	100.00	9.5	even	ok
419.3148	1	C26H43O4	419.3156	1.9	12.9	1	100.00	5.5	even	ok
441.2970	1	C26H42NaO4	441.2975	1.2	23.0	1	92.64	5.5	even	ok
	2	C24H37N6O2	441.2973	0.6	25.4	2	100.00	9.5	even	ok
465.1174	1	C25H21O9	465.1180	1.4	1.7	1	100.00	15.5	even	ok
	2	C24H18N4NaO5	465.1169	-0.9	4.7	2	78.38	17.5	even	ok
	3	C22H13N10O3	465.1167	-1.5	7.2	3	65.27	21.5	even	ok
	4	C25H14N8NaO	465.1183	1.9	14.3	4	51.78	22.5	even	ok
487.0991	1	C25H20NaO9	487.1000	1.8	11.4	1	89.88	15.5	even	ok
	2	C23H15N6O7	487.0997	1.2	13.4	2	100.00	19.5	even	ok
	3	C22H12N10NaO3	487.0986	-1.0	16.5	3	75.24	21.5	even	ok
	4	C20H7N16O	487.0983	-1.5	19.0	4	62.03	25.5	even	ok
	5	C22H19N2O11	487.0983	-1.5	20.4	5	80.74	14.5	even	ok

S41. NMR Table of Compound 5 (DMSO-d_6, ^{1}H: 600MHz)

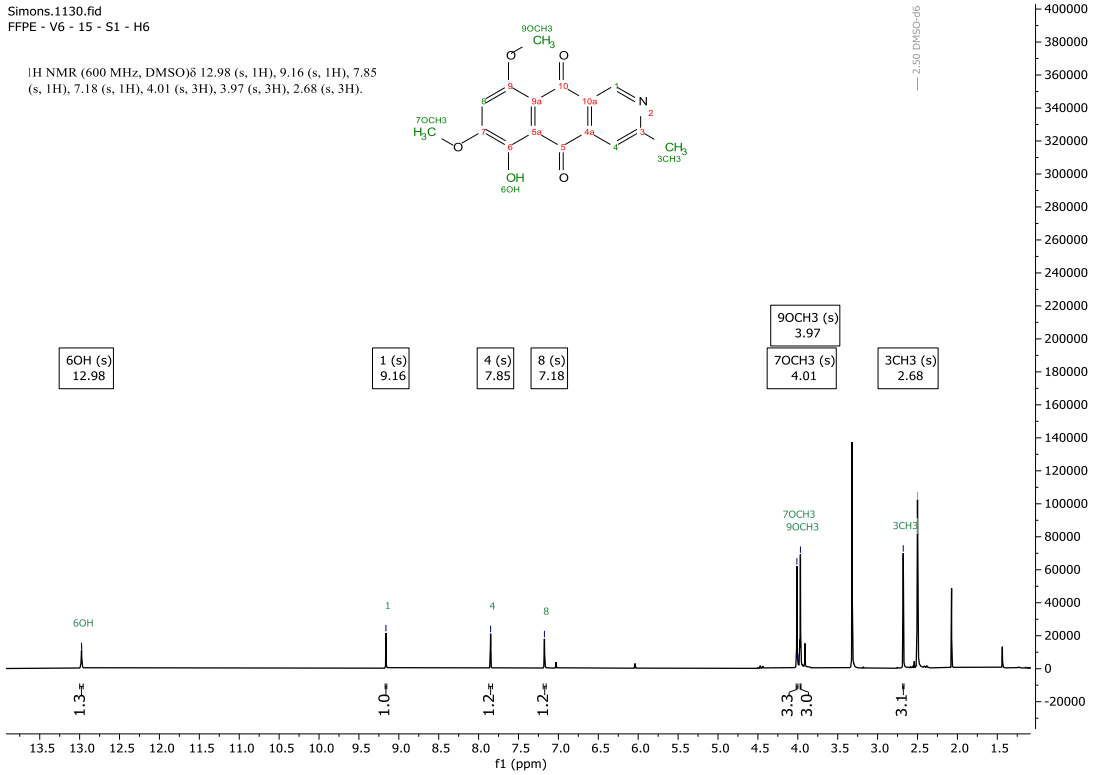
9-*O*-methylbostrycoidin



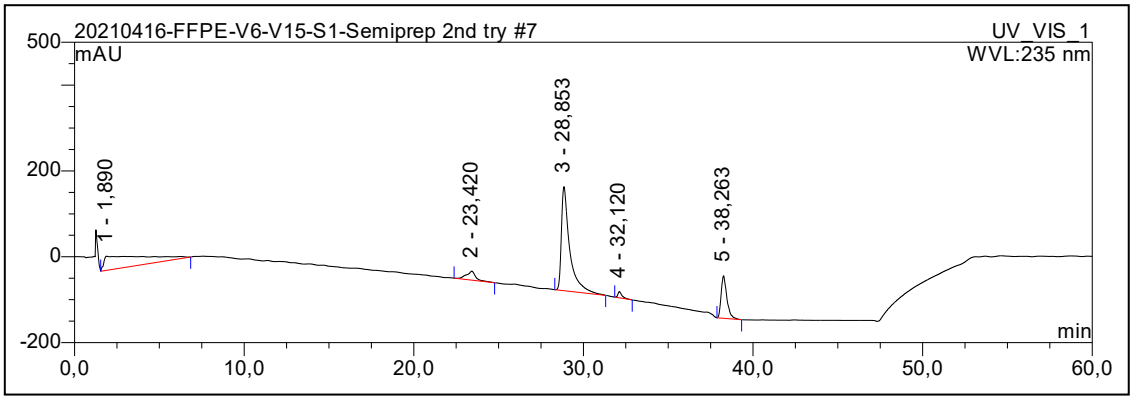
Chemical Formula: $C_{16}H_{13}NO_5$
Molecular Weight: 299,28

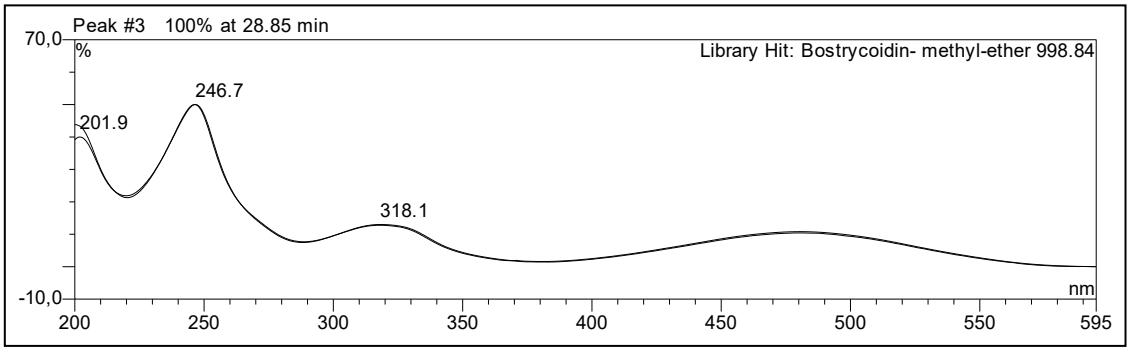
position	δ_H, m (J in Hz)
1	9.16, s
4	7.85, s
8	7.18, s
3-CH_3	2.68, s, 3H
6-OH	12.98, s
7-OCH_3	3.97, s, 3H
9-OCH_3	4.01, s, 3H

S42. [1]H-NMR Spectrum of Compound 5 (DMSO-d_6, 600 MHz)

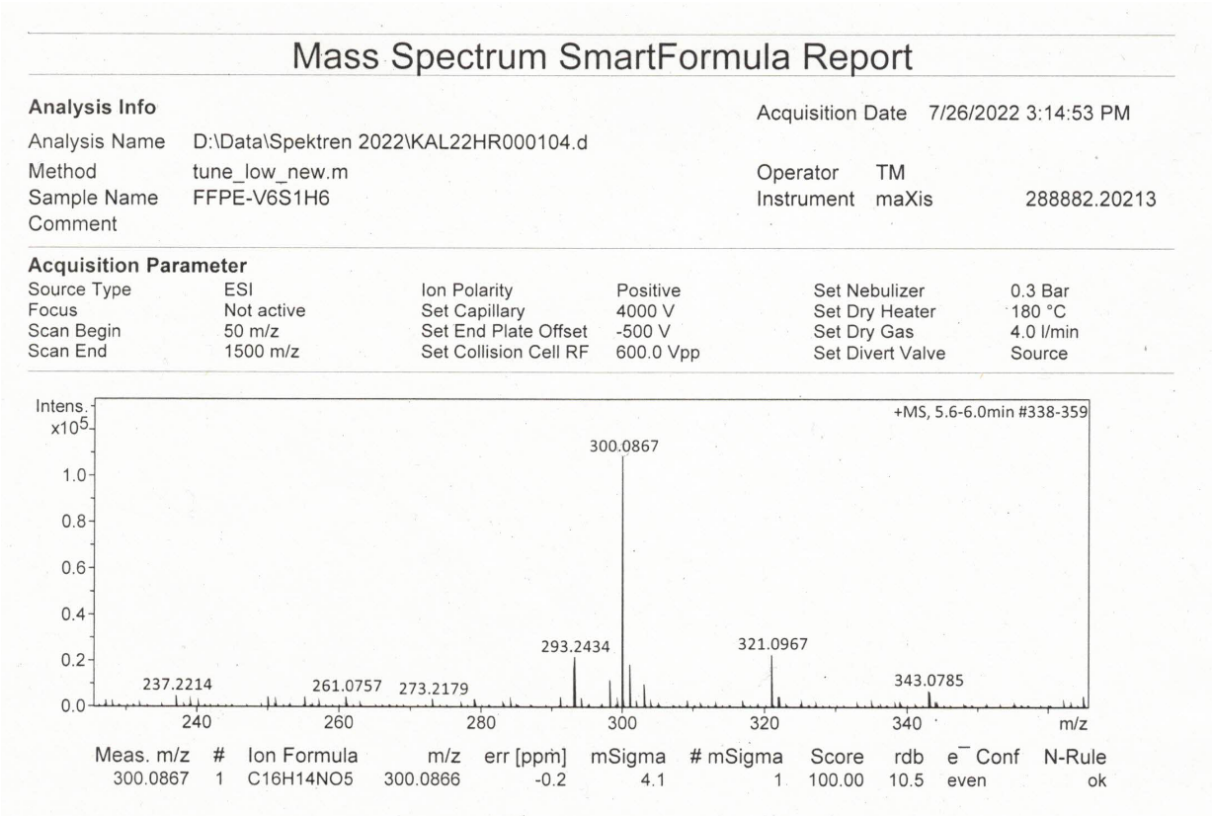


S43. HPLC-DAD UV-Vis Spectrum of Compound 5 (Methanol)



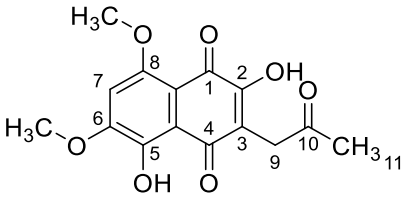


S44. High Resolution ESI(+)MS Spectrum of Compound 5



S45. NMR Table of Compound 6 (DMSO-d_6, 600MHz)

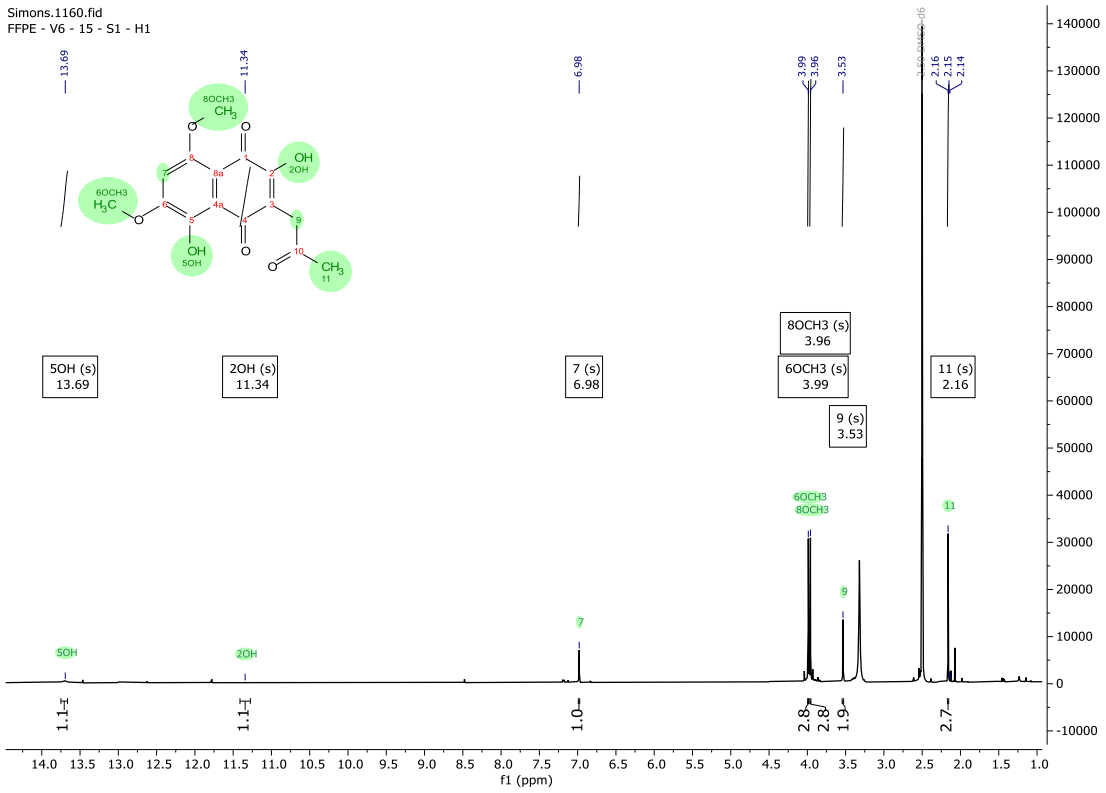
2,5-Dihydroxy-6,8-dimethoxy-3-(2-oxopropyl)-1,4-naphthalenedione



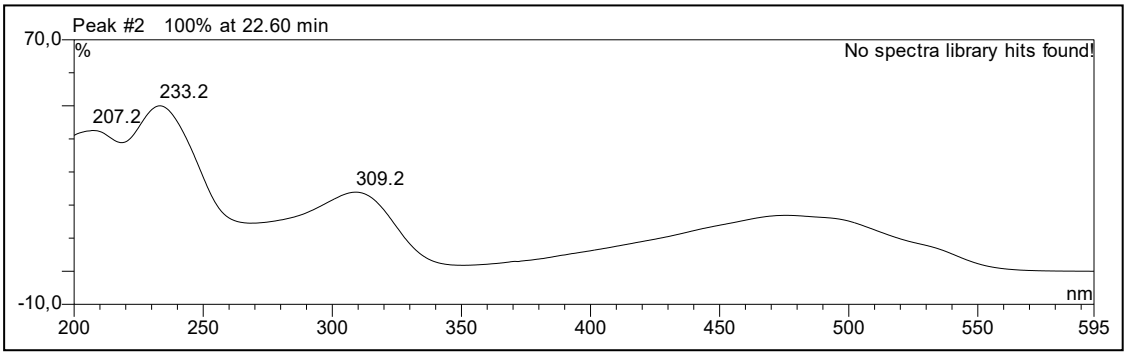
Chemical Formula: $C_{15}H_{14}O_7$
Molecular Weight: 306,27

position	δ_H, m (J in Hz)
7	6.98, s
9	3.53, s 2H
11	2.16, s 3H
2-OH	11.34, br s
5-OH	13.69, s
6-OCH_3	3.99, s 3H
8-OCH_3	3.96, s 3H

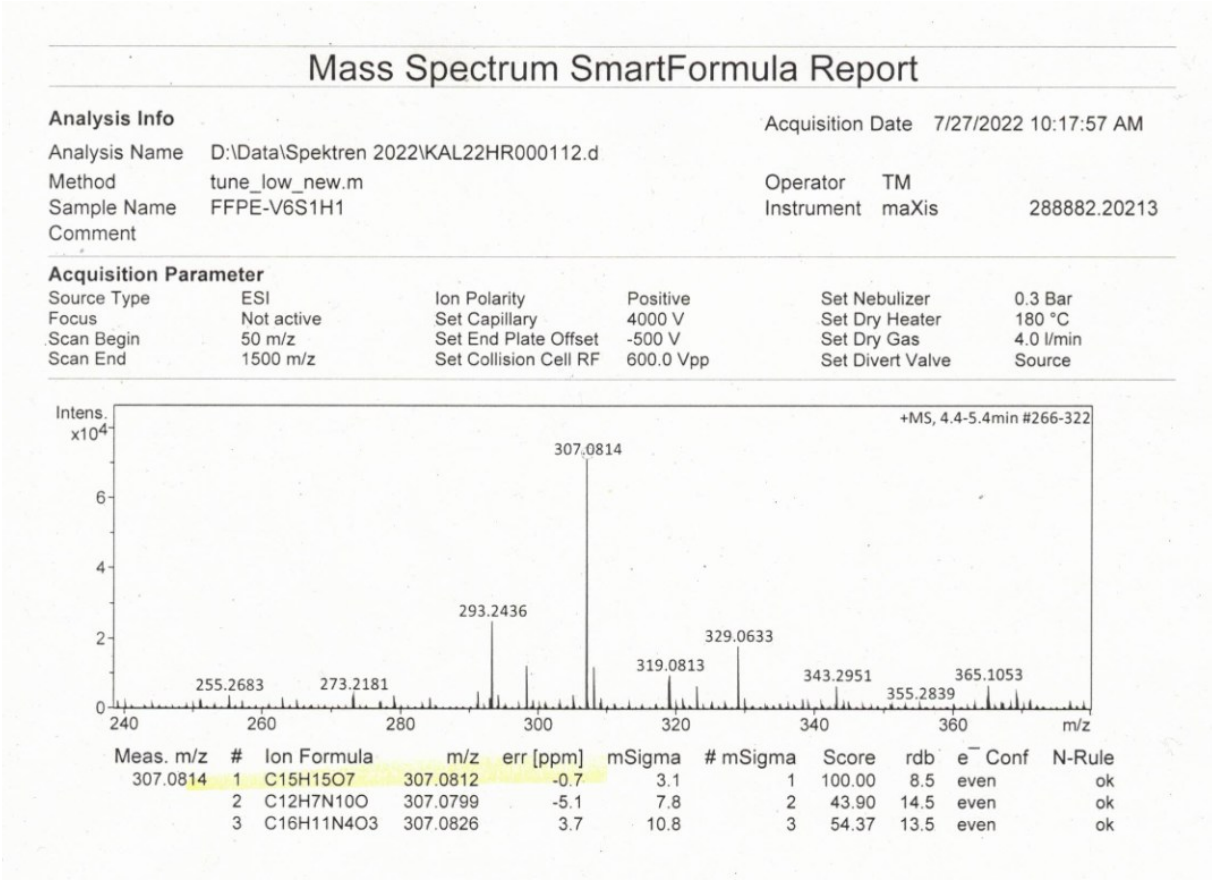
S46. 1H-NMR Spectrum of Compound 6 (DMSO-d_6, 600 MHz)



S47. UV-Vis Spectrum of Compound 6 (Methanol)



S48. High Resolution ESI(+)MS Spectrum of Compound 6



Mass Spectrum SmartFormula Report

Analysis Info

Analysis Name	D:\Data\Spektren 2022\KAL22HR000112.d	Acquisition Date	7/27/2022 10:17:57 AM
Method	tune_low_new.m	Operator	TM
Sample Name	FFPE-V6S1H1	Instrument	maXis 288882.20213
Comment			

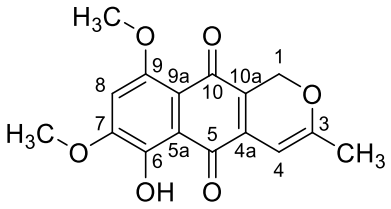
Acquisition Parameter

Source Type	ESI	Ion Polarity	Positive	Set Nebulizer	0.3 Bar
Focus	Not active	Set Capillary	4000 V	Set Dry Heater	180 °C
Scan Begin	50 m/z	Set End Plate Offset	-500 V	Set Dry Gas	4.0 l/min
Scan End	1500 m/z	Set Collision Cell RF	600.0 Vpp	Set Divert Valve	Source

Meas. m/z	#	Ion Formula	m/z	err [ppm]	mSigma	# mSigma	Score	rdb	e⁻ Conf	N-Rule
307.0814	1	C15H15O7	307.0812	-0.7	3.1	1	100.00	8.5	even	ok
	2	C12H7N10O	307.0799	-5.1	7.8	2	43.90	14.5	even	ok
	3	C16H11N4O3	307.0826	3.7	10.8	3	54.37	13.5	even	ok

S49. NMR Table of Compound 7 (DMSO-d_6, ^{1}H: 600MHz)

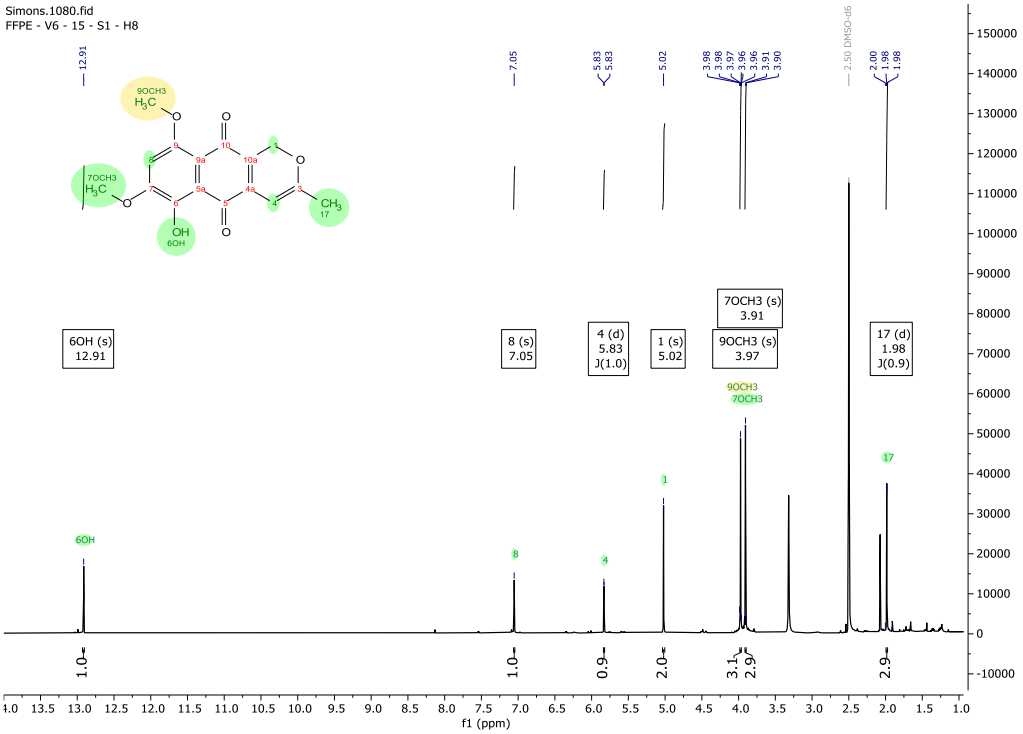
9-*O*-methylanhydrofusarubin



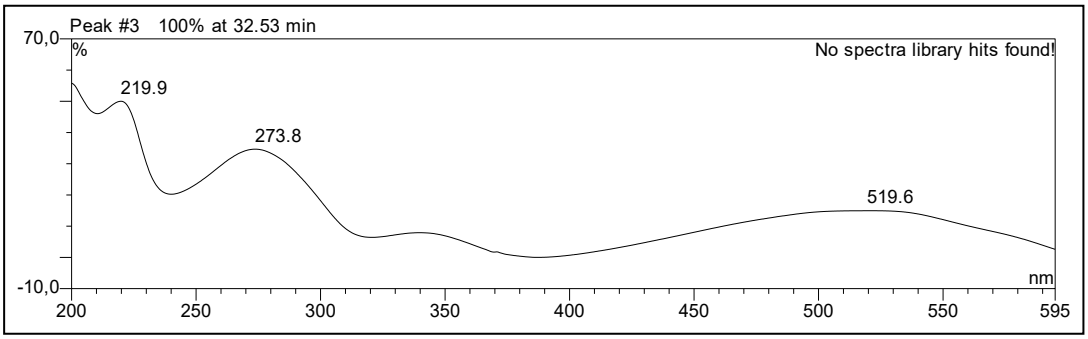
Chemical Formula: $C_{16}H_{14}O_6$
Molecular Weight: 302,28

position	δ_H, m (J in Hz)
1	5.02, s 2H
4	5.83, d (0.9)
8	7.05, s
3-CH_3	1.98, d (0.9)
6-OH	12.91, s
7-OCH_3	3.97, s
9-OCH_3	3.91, s

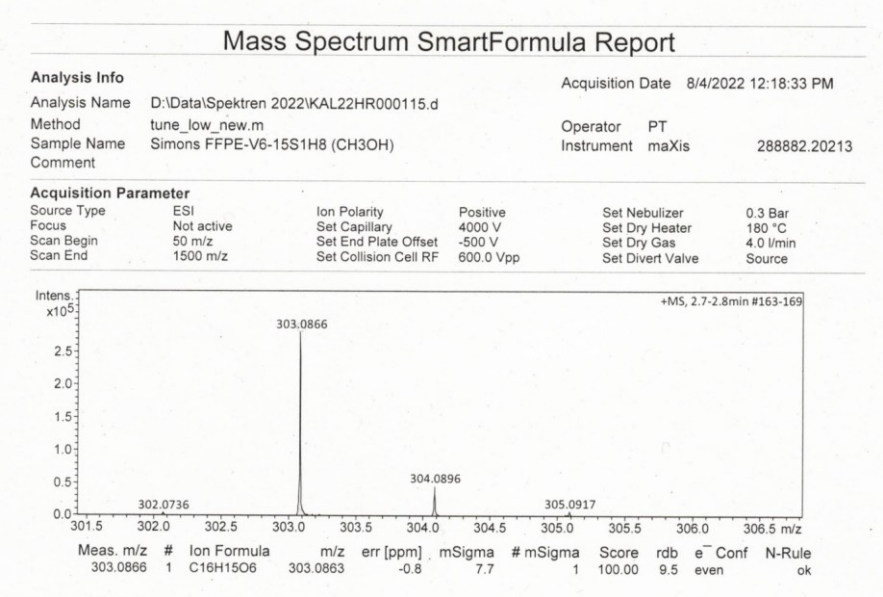
S50. ^{1}H-NMR Spectrum of Compound 7 (DMSO-d_6, 600 MHz)



S51. UV-Vis Spectrum of Compound 7 (Methanol)

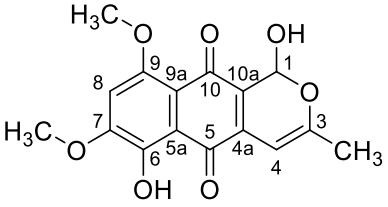


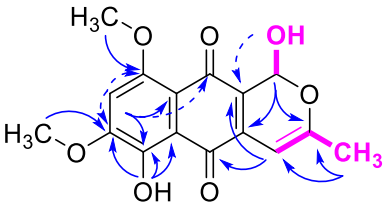
S52. High Resolution ESI(+)MS Spectrum of Compound 7



S53. NMR Table of Compound 8 (DMSO-*d*$_6$, ^{1}H: 600MHz, ^{13}C: 150 MHz)

9-*O*-methylanhydrofusarubinlactol





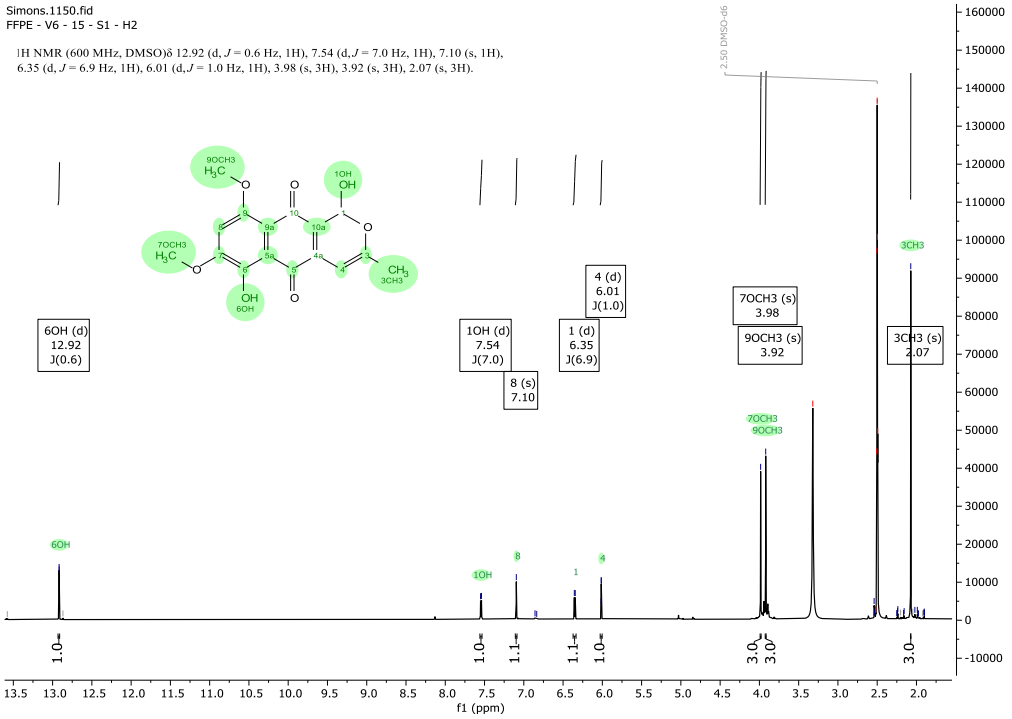
Chemical Formula: $C_{16}H_{14}O_7$
Molecular Weight: 318,28

COSY — weak HMBC
key HMBC

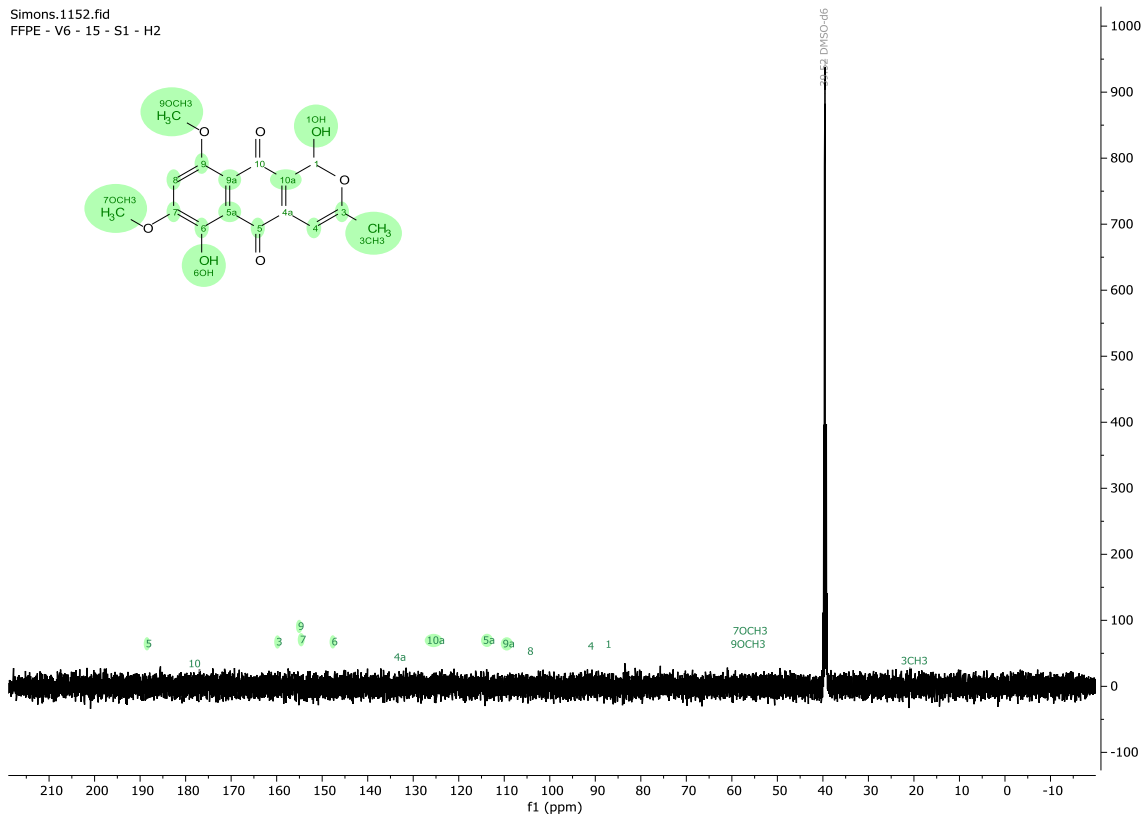
position	δ_C*	δ_H, m (*J* in Hz)
1	87.5, CH	6.35, d (6.9)
3	159.8, C	
4	91.4, CH	6.01, d (0.9)
4a	133.2, C	
5	188.5, C	
5a	113.8, C	
6	147.8, C	
7	154.6, C	
8	104.6, CH	7.10, s
9	155.1, C	
9a	109.5, C	
10	178.5, C	
10a	125.6, C	
1-OH		7.54, d (6.9)
3-CH_3	20.3, CH_3	2.07, d (0.9)
6-OH		12.92, s
7-OCH_3	56.2, CH_3	3.98, s
9-OCH_3	56.2, CH_3	3.92, s

*signals were extracted from HSQC and HMBC spectra.

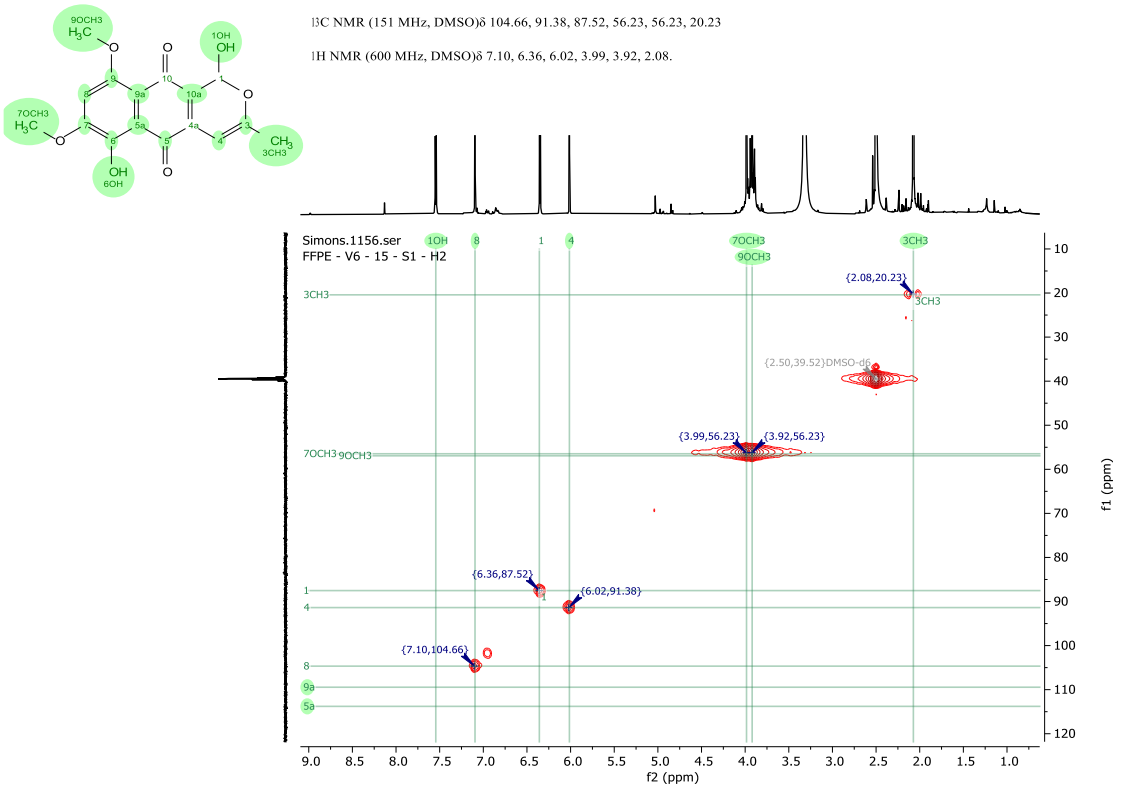
S54. ^{1}H-NMR Spectrum of Compound 8 (DMSO-d_6, 600 MHz)



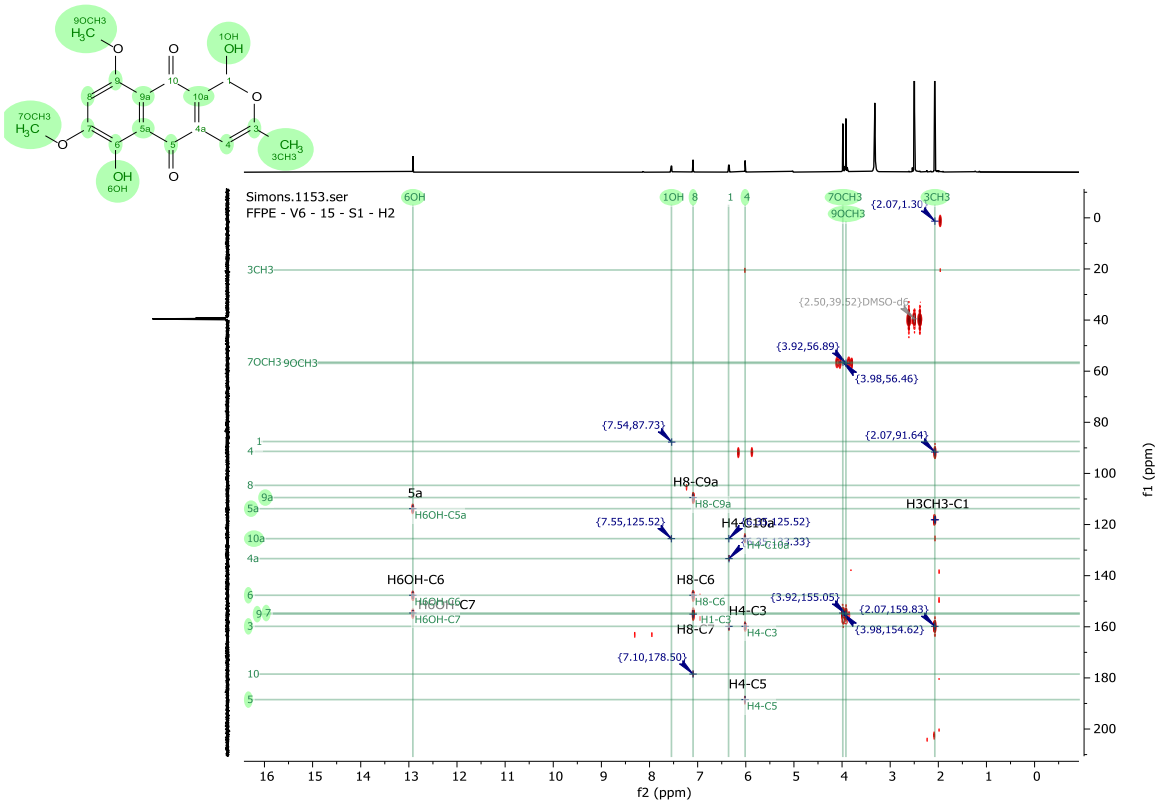
S55. ^{13}C-NMR Spectrum of Compound 8 (DMSO-d_6, 150 MHz)



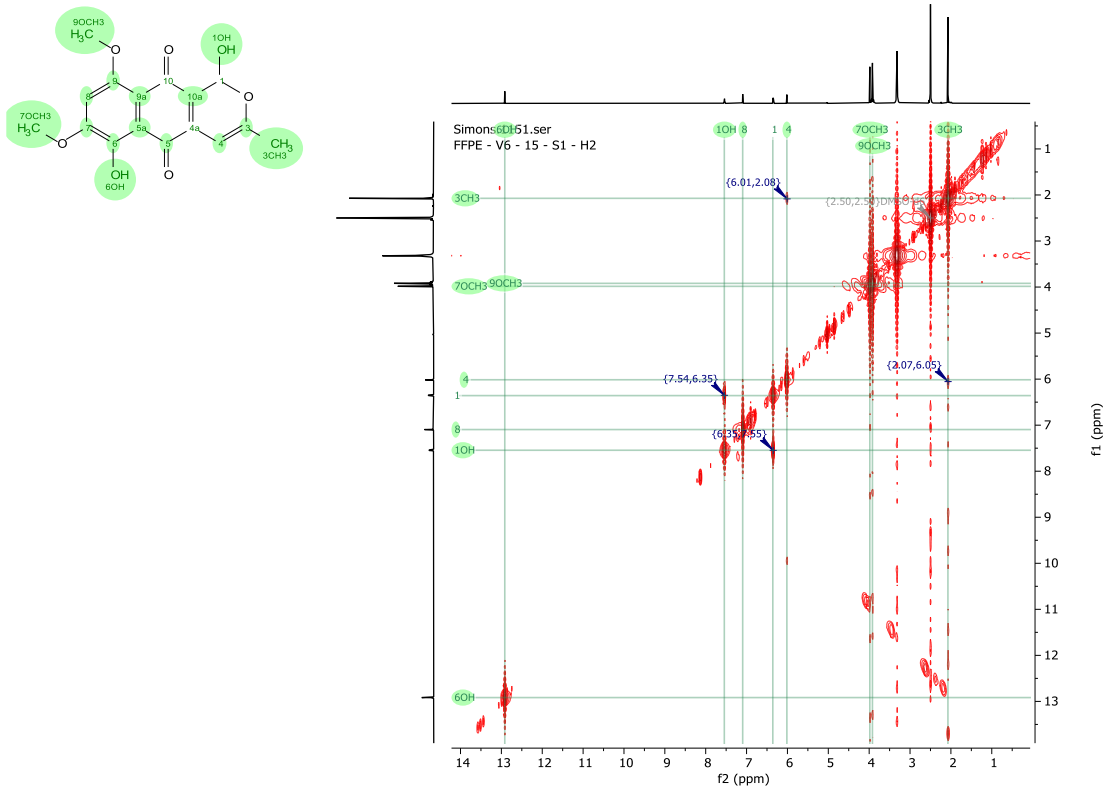
S56. ^{1}H-^{13}C-HSQC Spectrum of Compound 8 (DMSO-d_6, ^{1}H: 600MHz, ^{13}C: 150 MHz)



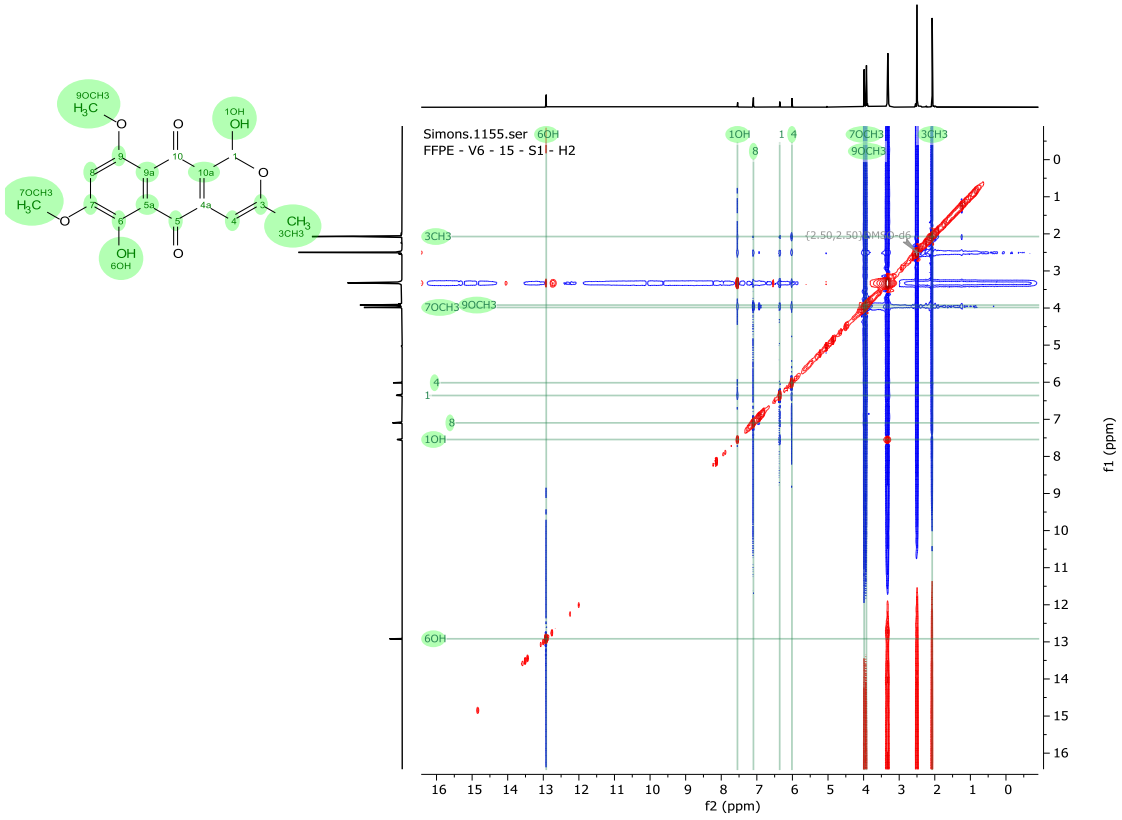
S57. ^{1}H-^{13}C-HMBC Spectrum of Compound 8 (DMSO-d_6, ^{1}H: 600MHz, ^{13}C: 150 MHz)



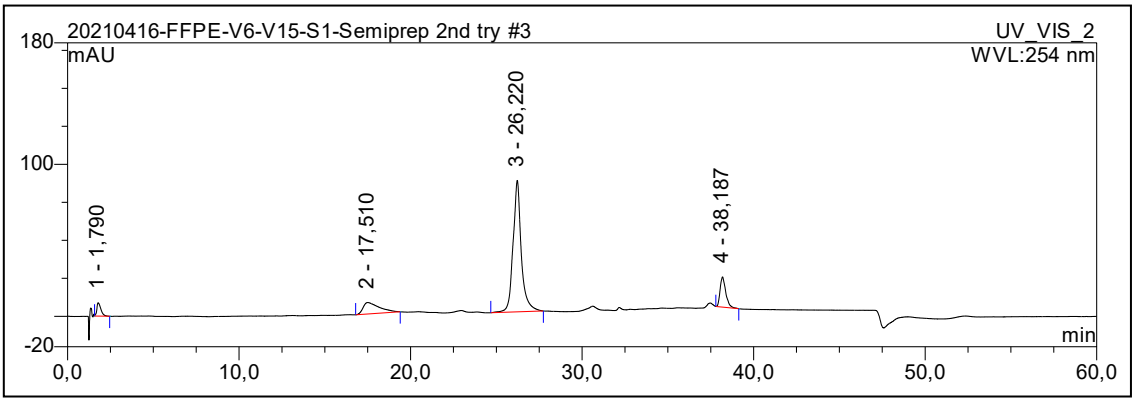
S58. ^{1}H-^{1}H-COSY Spectrum of Compound 8 (DMSO-d_6, 600MHz)

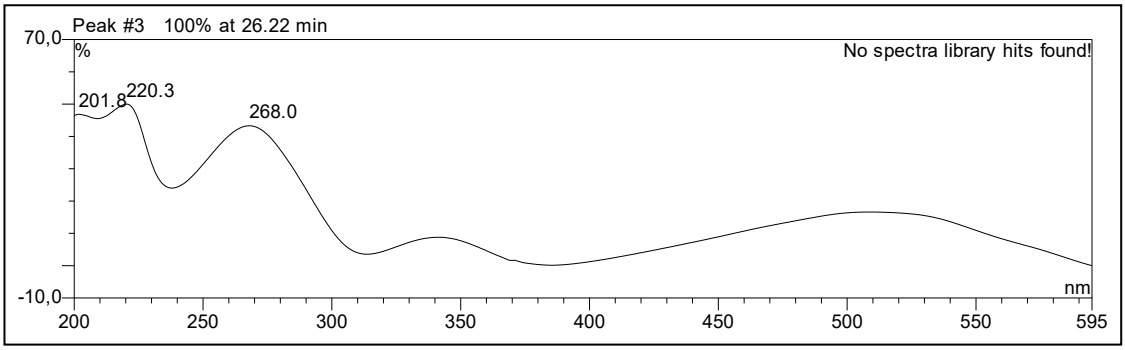


S59. ^{1}H-^{1}H-NOESY Spectrum of Compound 8 (DMSO-d_6, 600MHz)

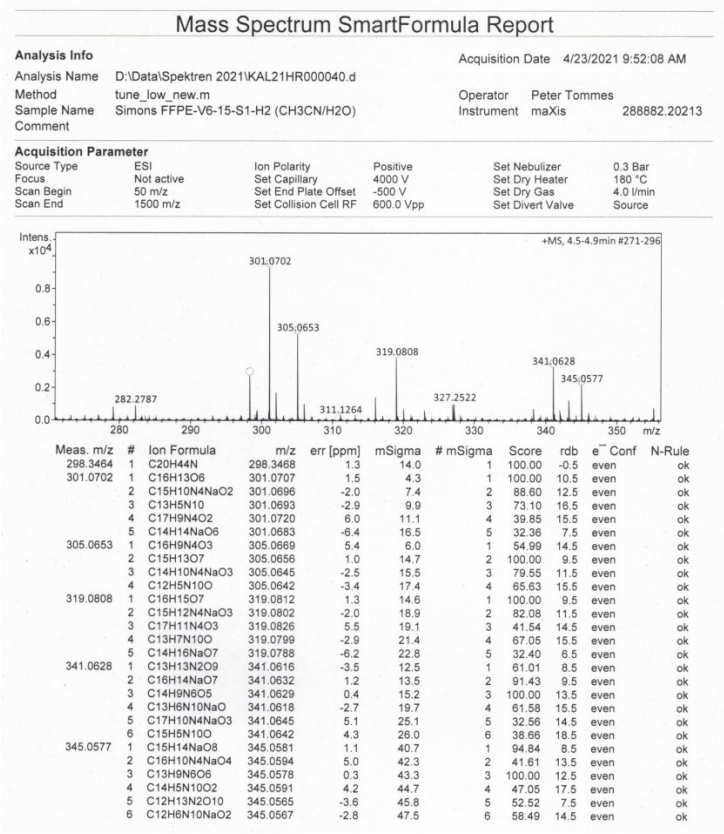


S60. HPLC-DAD UV-Vis Spectrum of Compound 8 (Methanol)





S61. High Resolution ESI(+)MS Spectrum of Compound 8



Mass Spectrum SmartFormula Report

Analysis Info

Analysis Name	D:\Data\Spektren 2021\KAL21HR000040.d	Acquisition Date	4/23/2021 9:52:08 AM
Method	tune_low_new.m	Operator	Peter Tommes
Sample Name	Simons FFPE-V6-15-S1-H2 (CH3CN/H2O)	Instrument	maXis 288882.20213
Comment			

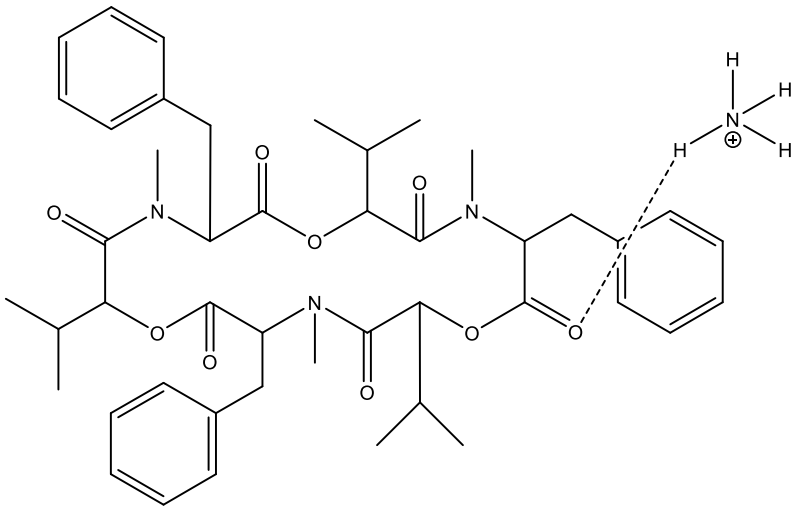
Acquisition Parameter

Source Type	ESI	Ion Polarity	Positive	Set Nebulizer	0.3 Bar
Focus	Not active	Set Capillary	4000 V	Set Dry Heater	180 °C
Scan Begin	50 m/z	Set End Plate Offset	-500 V	Set Dry Gas	4.0 l/min
Scan End	1500 m/z	Set Collision Cell RF	600.0 Vpp	Set Divert Valve	Source

Meas. m/z	#	Ion Formula	m/z	err [ppm]	mSigma	# mSigma	Score	rdb	e⁻ Conf	N-Rule
298.3464	1	C20H44N	298.3468	1.3	14.0	1	100.00	-0.5	even	ok
301.0702	1	C16H13O6	301.0707	1.5	4.3	1	100.00	10.5	even	ok
	2	C15H10N4NaO2	301.0696	-2.0	7.4	2	88.60	12.5	even	ok
	3	C13H5N10	301.0693	-2.9	9.9	3	73.10	16.5	even	ok
	4	C17H9N4O2	301.0720	6.0	11.1	4	39.85	15.5	even	ok
	5	C14H14NaO6	301.0683	-6.4	16.5	5	32.36	7.5	even	ok
305.0653	1	C16H9N4O3	305.0669	5.4	6.0	1	54.99	14.5	even	ok
	2	C15H13O7	305.0656	1.0	14.7	2	100.00	9.5	even	ok
	3	C14H10N4NaO3	305.0645	-2.5	15.5	3	79.55	11.5	even	ok
	4	C12H5N10O	305.0642	-3.4	17.4	4	65.63	15.5	even	ok
319.0808	1	C16H15O7	319.0812	1.3	14.6	1	100.00	9.5	even	ok
	2	C15H12N4NaO3	319.0802	-2.0	18.9	2	82.08	11.5	even	ok
	3	C17H11N4O3	319.0826	5.5	19.1	3	41.54	14.5	even	ok
	4	C13H7N10O	319.0799	-2.9	21.4	4	67.05	15.5	even	ok
	5	C14H16NaO7	319.0788	-6.2	22.8	5	32.40	6.5	even	ok
341.0628	1	C13H13N2O9	341.0616	-3.5	12.5	1	61.01	8.5	even	ok
	2	C16H14NaO7	341.0632	1.2	13.5	2	91.43	9.5	even	ok
	3	C14H9N6O5	341.0629	0.4	15.2	3	100.00	13.5	even	ok
	4	C13H6N10NaO	341.0618	-2.7	19.7	4	61.58	15.5	even	ok
	5	C17H10N4NaO3	341.0645	5.1	25.1	5	32.56	14.5	even	ok
	6	C15H5N10O	341.0642	4.3	26.0	6	38.66	18.5	even	ok
345.0577	1	C15H14NaO8	345.0581	1.1	40.7	1	94.84	8.5	even	ok
	2	C16H10N4NaO4	345.0594	5.0	42.3	2	41.61	13.5	even	ok
	3	C13H9N6O6	345.0578	0.3	43.3	3	100.00	12.5	even	ok
	4	C14H5N10O2	345.0591	4.2	44.7	4	47.05	17.5	even	ok
	5	C12H13N2O10	345.0565	-3.6	45.8	5	52.52	7.5	even	ok
	6	C12H6N10NaO2	345.0567	-2.8	47.5	6	58.49	14.5	even	ok

S62. NMR Data of Compound 9 ($CDCl_3$, ^1H: 600MHz)

Beauvericin

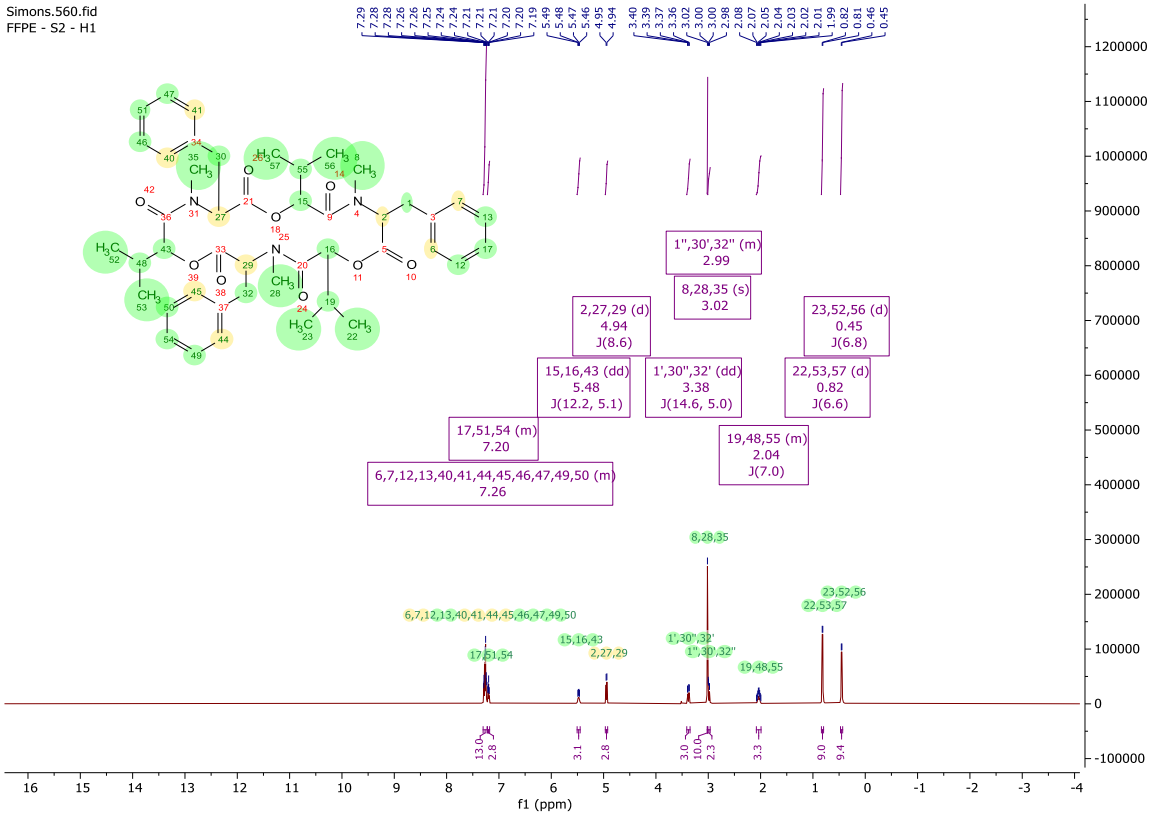


Chemical formula: $C_{45}H_{61}N_4O_9^+$

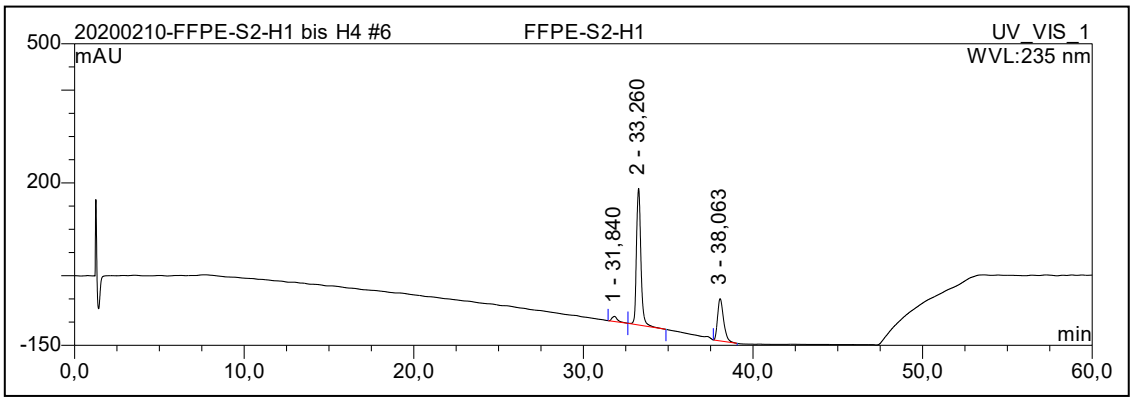
Molecular weight: 801.44 g/mol

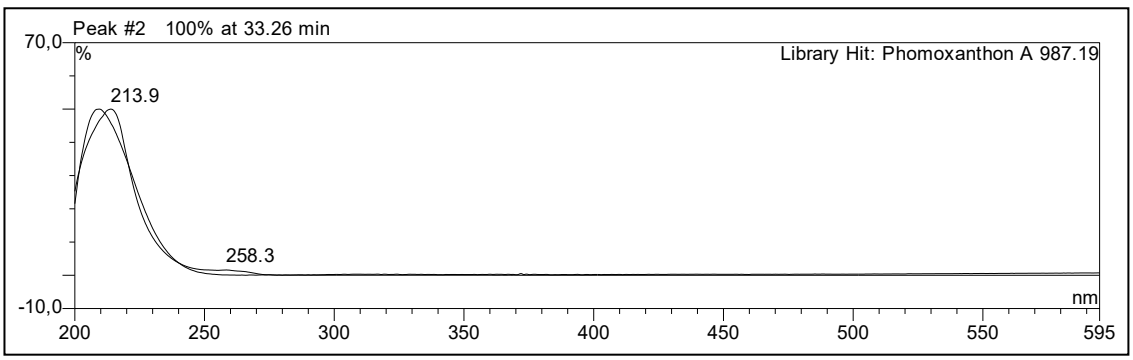
^{1}H-NMR Data: δ 7.29-7.24 (12H, m), 7.21-7.18 (3H, m), 5.48 (3H, dd, *J* = 12.2, 5.1 Hz), 4.94 (3H, d, *J* = 8.6 Hz), 3.38 (3H, dd, *J* = 14.6, 5.0 Hz), 3.02 (9H, s), 2.99 (3H, m), 2.04 (3H, m), 0.82 (9H, d, *J* = 6.6 Hz), 0.45 (9H, d, *J* = 6.8 Hz)

S63. ^{1}H-NMR Spectrum of Compound 9 ($CDCl_3$, 600 MHz)

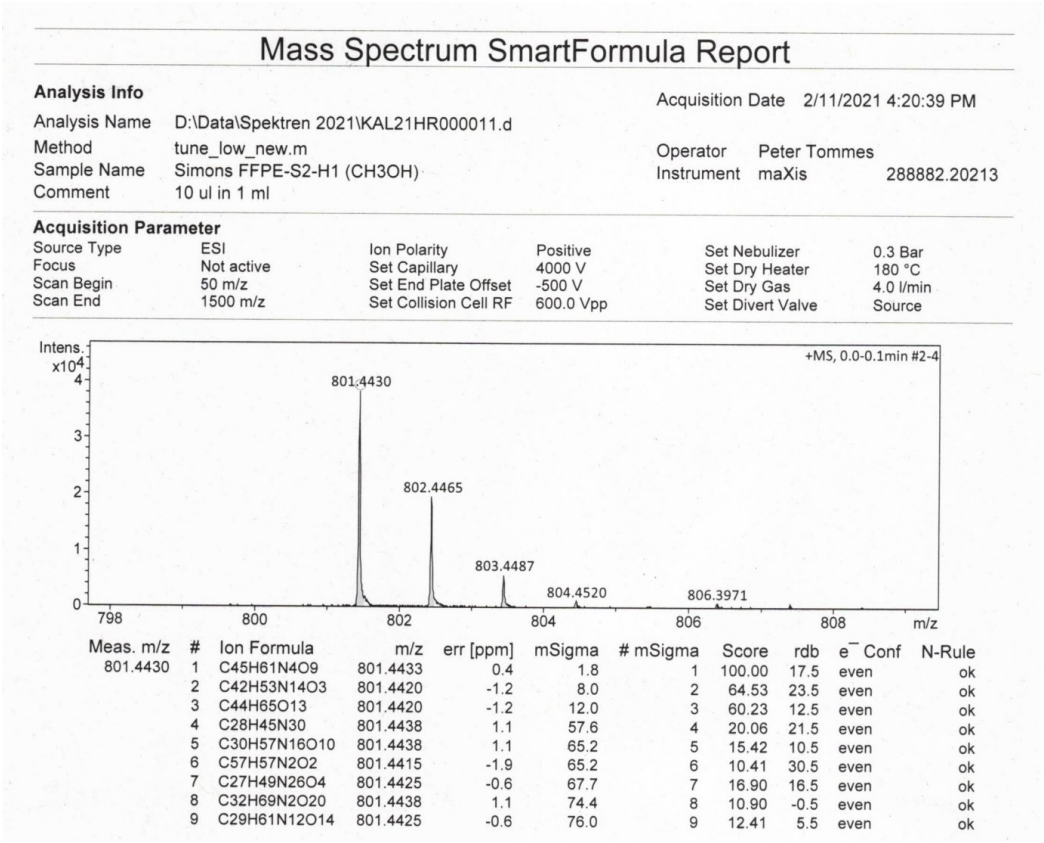


S64. HPLC-DAD UV-Vis Spectrum of Compound 9 (Methanol)





S65. High Resolution ESI(+)MS Spectrum of Compound 9



Mass Spectrum SmartFormula Report

Analysis Info

Analysis Name	D:\Data\Spektren 2021\KAL21HR000011.d	Acquisition Date	2/11/2021 4:20:39 PM
Method	tune_low_new.m	Operator	Peter Tommes
Sample Name	Simons FFPE-S2-H1 (CH3OH)	Instrument	maXis 288882.20213
Comment	10 ul in 1 ml		

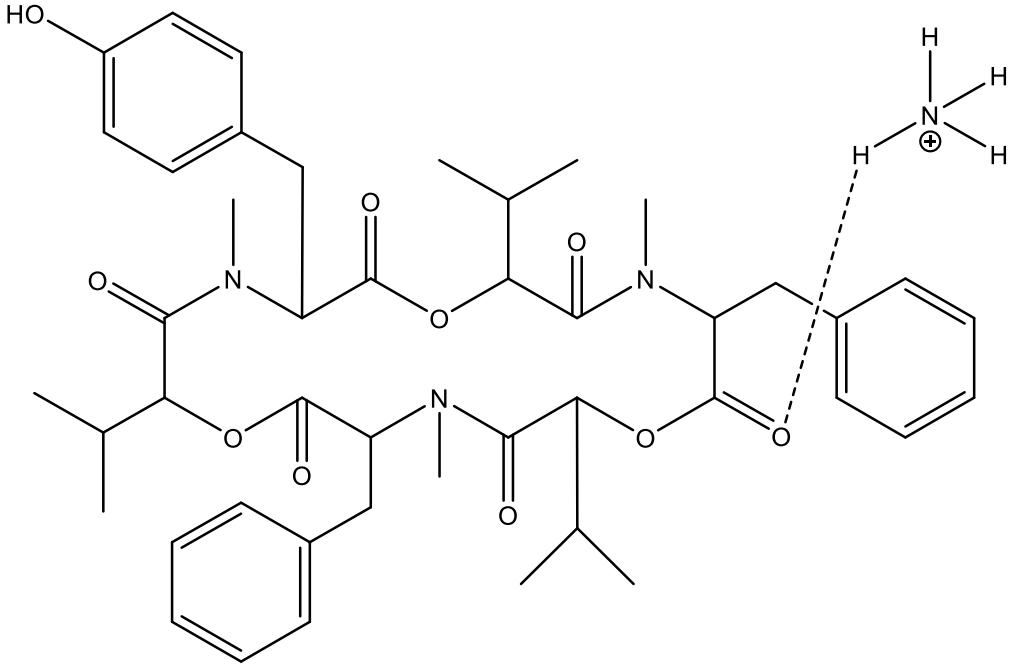
Acquisition Parameter

Source Type	ESI	Ion Polarity	Positive	Set Nebulizer	0.3 Bar
Focus	Not active	Set Capillary	4000 V	Set Dry Heater	180 °C
Scan Begin	50 m/z	Set End Plate Offset	-500 V	Set Dry Gas	4.0 l/min
Scan End	1500 m/z	Set Collision Cell RF	600.0 Vpp	Set Divert Valve	Source

Meas. m/z	#	Ion Formula	m/z	err [ppm]	mSigma	# mSigma	Score	rdb	e¯ Conf	N-Rule
801.4430	1	C45H61N4O9	801.4433	0.4	1.8	1	100.00	17.5	even	ok
	2	C42H53N14O3	801.4420	-1.2	8.0	2	64.53	23.5	even	ok
	3	C44H65O13	801.4420	-1.2	12.0	3	60.23	12.5	even	ok
	4	C28H45N30	801.4438	1.1	57.6	4	20.06	21.5	even	ok
	5	C30H57N16O10	801.4438	1.1	65.2	5	15.42	10.5	even	ok
	6	C57H57N2O2	801.4415	-1.9	65.2	6	10.41	30.5	even	ok
	7	C27H49N26O4	801.4425	-0.6	67.7	7	16.90	16.5	even	ok
	8	C32H69N2O20	801.4438	1.1	74.4	8	10.90	-0.5	even	ok
	9	C29H61N12O14	801.4425	-0.6	76.0	9	12.41	5.5	even	ok

S66. NMR Data of Compound 10 (DMSO-d_6, ^{1}H: 600MHz)

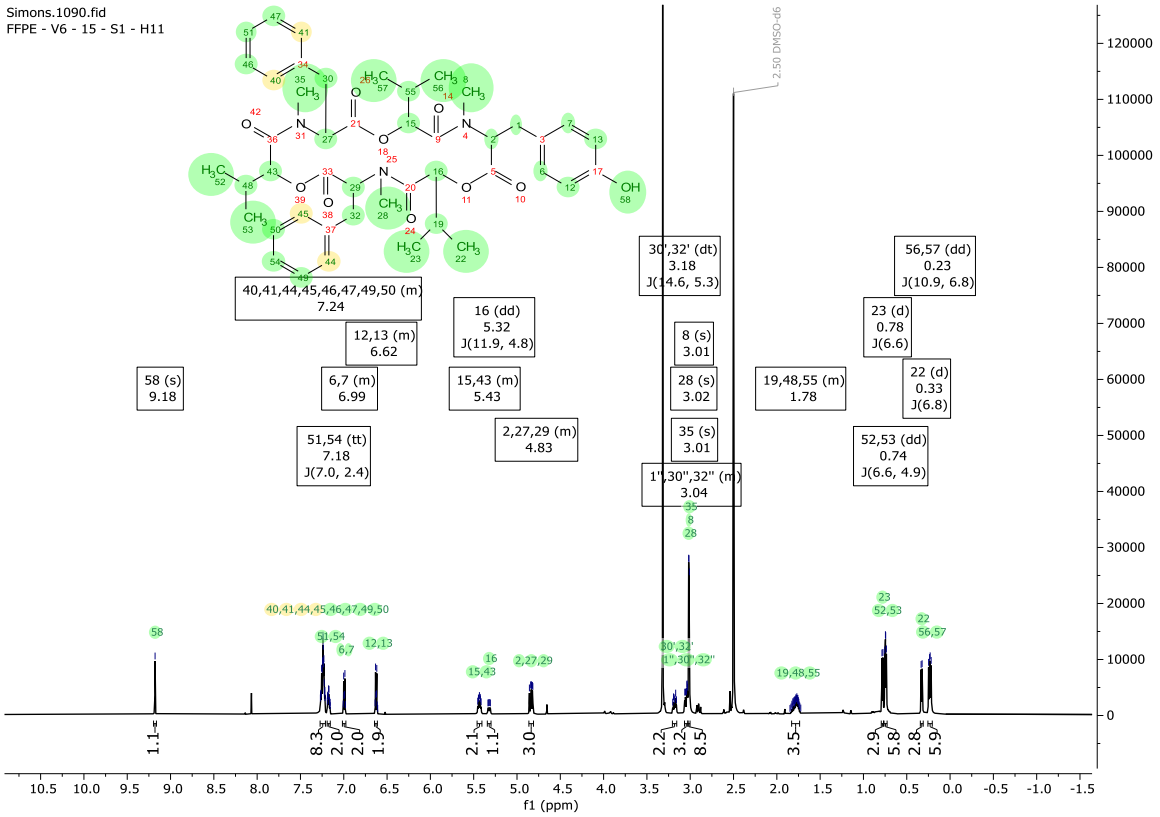
Beauvericin J



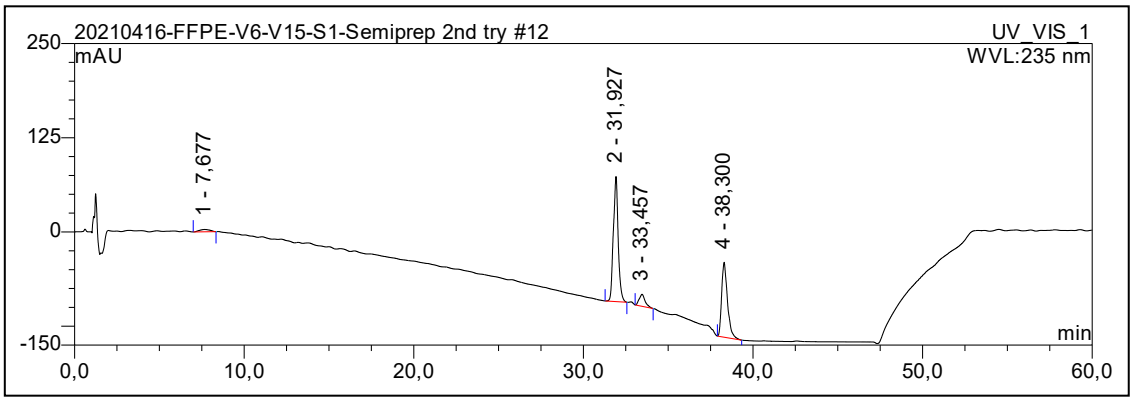
Chemical formula:$C_{45}H_{61}N_4O_{10}^+$
Molecular mass: 817.44 g/mol

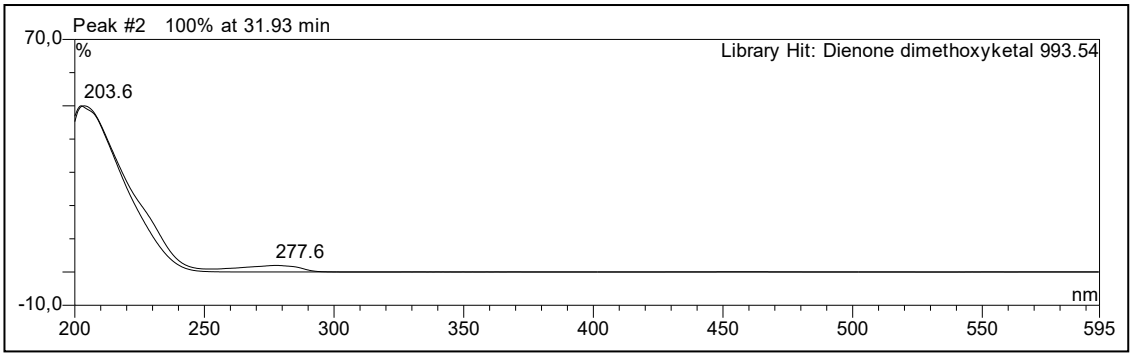
^{1}H-NMR-data: δ 9.18 (1H, s), 7.27-7.21 (8H, m), 7.18 (2H, tt, *J* = 7.0, 2.4), 6.99 (2H, m), 6.62 (2H, m), 5.43 (2H, m), 5.32 (1H, dd, *J* = 11.9, 4.8), 4.83 (3H, m), 3.18 (2H, dt, *J* = 14.6, 5.3), 3.04 (3H, m), 3.02 (3H, s), 3.01, (3H, s), 3.01 (3H, s), 1.78 (3H, m), 0.78 (3H, d, *J* = 6.6), 0.74 (6H, dd, *J* = 6.6, 4.9), 0.33 (3H, d, *J* = 6.8), 0.23 (6H, dd, *J* = 10.9, 6.8)

S67. [1]H-NMR Spectrum of Compound 10 (DMSO-d_6, 600 MHz)

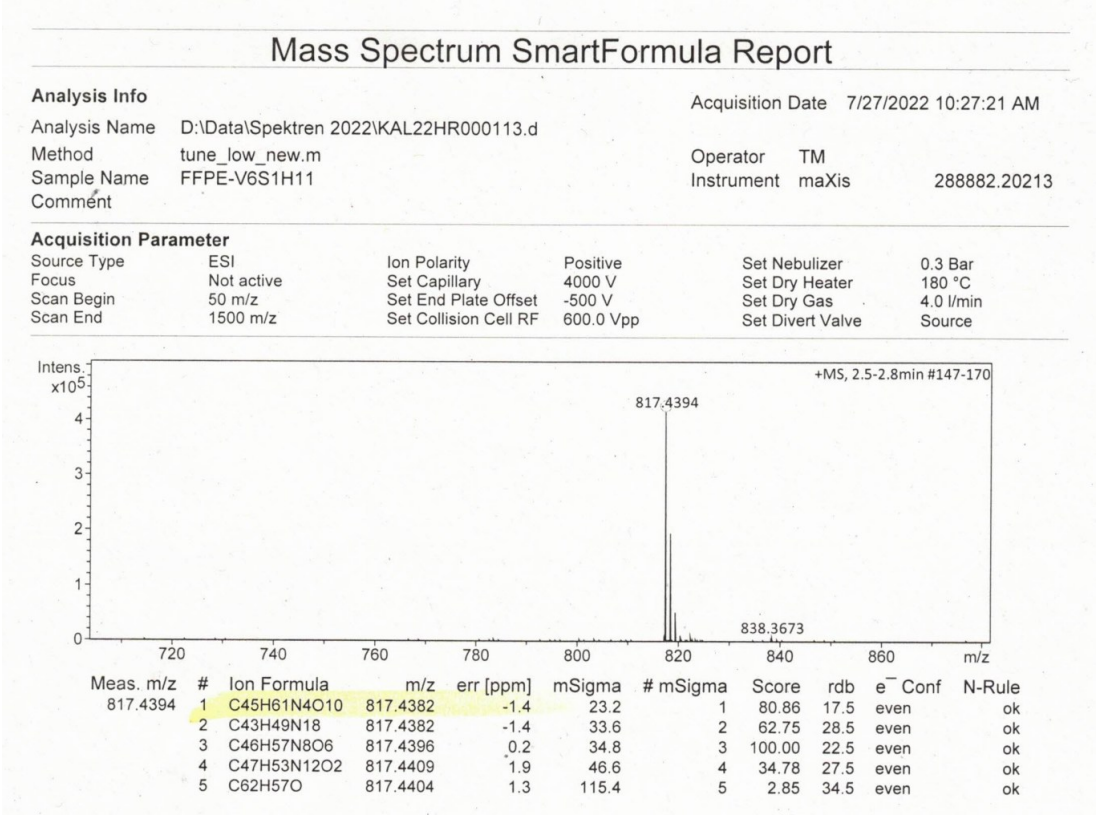


S68. HPLC-DAD UV-Vis Spectrum of Compound 10 (Methanol)





S69. High Resolution ESI(+)MS Spectrum of Compound 10



Mass Spectrum SmartFormula Report

Analysis Info

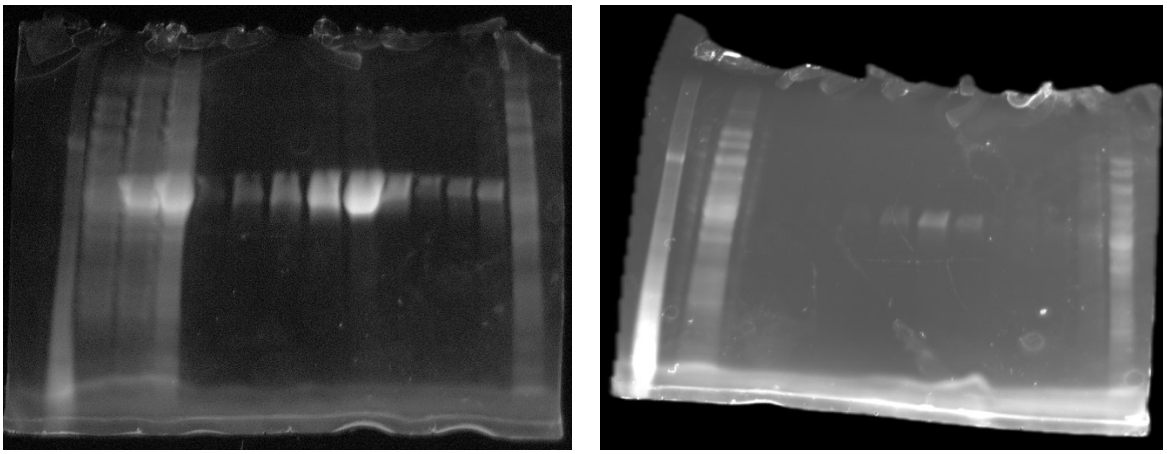
Analysis Name	D:\Data\Spektren 2022\KAL22HR000113.d	Acquisition Date	7/27/2022 10:27:21 AM
Method	tune_low_new.m	Operator	TM
Sample Name	FFPE-V6S1H11	Instrument	maXis 288882.20213
Comment			

Acquisition Parameter

Source Type	ESI	Ion Polarity	Positive	Set Nebulizer	0.3 Bar
Focus	Not active	Set Capillary	4000 V	Set Dry Heater	180 °C
Scan Begin	50 m/z	Set End Plate Offset	-500 V	Set Dry Gas	4.0 l/min
Scan End	1500 m/z	Set Collision Cell RF	600.0 Vpp	Set Divert Valve	Source

Meas. m/z	#	Ion Formula	m/z	err [ppm]	mSigma	# mSigma	Score	rdb	e¯ Conf	N-Rule
817.4394	1	C45H61N4O10	817.4382	-1.4	23.2	1	80.86	17.5	even	ok
	2	C43H49N18	817.4382	-1.4	33.6	2	62.75	28.5	even	ok
	3	C46H57N8O6	817.4396	0.2	34.8	3	100.00	22.5	even	ok
	4	C47H53N12O2	817.4409	1.9	46.6	4	34.78	27.5	even	ok
	5	C62H57O	817.4404	1.3	115.4	5	2.85	34.5	even	ok

S70. SDS-PAGE analysis of recombinant FO-LovD-like protein expression and purification.



SDS-PAGE analysis of the expression and purification of the recombinant LovD-like protein. The right gel shows protein expression after IPTG induction, and the left gel shows the purified protein fractions after Ni-NTA affinity chromatography.

5. Manuscript 3

In this study, I participated as a collaborator and contributed to the determination of the sugar configuration of the glycosylated asperphenalenone derivatives. The sugar moiety of asperphenalenone K (compound 6) was experimentally identified as α-D-mannose, and this assignment supported the proposed sugar configuration of the structurally related asperphenalenones J–M (compounds 5–8).

JOURNAL OF AGRICULTURAL AND FOOD CHEMISTRY

pubs.acs.org/JAFC Article

Asperphenalenones Isolated from the Biocontrol Agent *Clonostachys rosea* and Their Antimicrobial Activities

Lin Wang, Anna-Lene Kiffe-Delf, Philipp Niklas Ostermann, Viktor Emanuel Simons, Di He, Ying Gao, Lasse van Geelen, Hao-Fu Dai, You-Xing Zhao, Heiner Schaal, Attila Mándi, Sándor Balázs Király, Tibor Kurtán,* Zhen Liu,* and Rainer Kalscheuer*

Cite This: *J. Agric. Food Chem.* 2023, 71, 11056−11068 Read Online

ACCESS | Metrics & More | Article Recommendations | Supporting Information

ABSTRACT: *Clonostachys rosea* is a fungus widely distributed on Earth and has a high capacity to adapt to complex environments in soil, plants, or sea. It is an endophyte that can be used as a potential biocontrol agent to protect plants from pathogenic fungi, nematodes, and insects. However, the spectrum of secondary metabolites produced by *C. rosea* has only scarcely been studied. In the present study, eight new phenalenones, asperphenalenones F−M (**1**−**8**), together with two known derivatives, asperphenalenones E and B (**9** and **10**), were isolated from the axenic rice culture of this fungus. The structures of the new compounds were elucidated by nuclear magnetic resonance, high-resolution electrospray ionization mass spectrometry, electronic circular dichroism, and gas chromatography−mass spectrometry analyses. Asperphenalenones J−M (**5**−**8**) are unusual phenalenone adducts that are conjugated to diterpenoid glycosides. Asperphenalenones F and H showed moderate antibacterial activity against methicillin-resistant *Staphylococcus aureus*, with minimal inhibitory concentrations of 12.5 and 25 μM, respectively. Asperphenalenone B exhibited low antiviral activity against the human immunodeficiency virus replication. Furthermore, asperphenalenones F and H exhibited low cytotoxicity against Jurkat cells, while all other compounds were devoid of cytotoxicity.

KEYWORDS: *Clonostachys rosea, asperphenalenones, antibacterial activity, methicillin-resistant Staphylococcus aureus (MRSA), anti-HIV activity*

Downloaded via DUESSELDORF LIBRARIES on May 15, 2026 at 20:51:54 (UTC).
See https://pubs.acs.org/sharingguidelines for options on how to legitimately share published articles.

INTRODUCTION

The ascomycete *Clonostachys rosea* (family Bionectriaceae) shows a wide distribution all over the world. The fungus inhabits subarctic, temperate, subtropical, and tropical regions of the world,[1] owing to its pronounced ability to adapt to complex environments that enables it to withstand a wide range of physical (temperature and ultraviolet light), chemical (pesticides and disinfectant), or biological (bacteria and virus) stressors. *C. rosea* can colonize living plants as an endophyte and, as a result of its mycoparasitic properties, might be usable as a biological control agent because it showed antagonistic effects against a wide variety of plant pathogenic fungi, such as *Fusarium* seed-borne diseases of cereals,[2] *Botrytis cinerea* sporulation on rose debris,[3] strawberry gray mold,[4] and *Fusarium* head blight of wheat.[5] Furthermore, it can detoxify the mycotoxin zearalenone, which is produced by several *Fusarium* species and can affect the health and performance of livestock, through the enzyme zearalenone lactonohydrolase.[6] The emergence time and emergence of carrot seed were consistently improved when *C. rosea* was applied during a commercial drum priming process,[7] and co-inoculation of *C. rosea* together with the fungus *Beauveria bassiana* controlled insect pests and suppressed gray mold in greenhouse tomatoes and sweet peppers when vectored by bumble bees.[8] Strong inhibition to gastrointestinal nematodes in sheep was shown with *Bacillus thuringiensis* and *C. rosea* isolates.[9,10]

Despite its potential beneficial applications in agriculture and livestock, however, the profile of secondary metabolites produced by *C. rosea* is largely unknown, and only a few compounds have been reported. For example, bisorbicillinoids have open-ended cage structures and displayed antibacterial activity.[11] Clonostach acids exhibited phytotoxicity against lettuce and enhanced the production of secondary metabolites.[12] Unique cyclic heptapeptides exhibited significant cytotoxicity against the L5178Y mouse lymphoma cell.[13] The TMC-151 series of compounds, which are reduced polyketide derivatives isolated from *C. rosea*, exhibited antibacterial properties,[14] while eburicol displayed significant antiproliferative activity against MCF-7 cells.[15] Two novel indole alkaloids featuring clonorosins A and B were isolated, and clonorosin A was active against *Fusarium oxysporum*, with a minimum inhibitory concentration (MIC) value of 50 μg/mL.[16] These reports on diverse bioactivities with potential applicability in agriculture or human health motivated us to further study the secondary metabolite profile of *C. rosea*, with a special focus on compounds potentially exhibiting antimicrobial properties.

Methicillin-resistant *Staphylococcus aureus* (MRSA) is a Gram-positive pathogen causing nosocomial infections that

Received: January 23, 2023
Revised: June 26, 2023
Accepted: June 28, 2023
Published: July 12, 2023



ACS Publications © 2023 American Chemical Society

https://doi.org/10.1021/acs.jafc.3c00447
J. Agric. Food Chem. 2023, 71, 11056−11068

Table 1. NMR Data for Compounds 1−4

	1[a]		2[b]		3[b]		4[b]	
number	δ_C, type[c]	δ_H (J in Hz)	δ_C, type[c]	δ_H (J in Hz)	δ_C, type	δ_H (J in Hz)	δ_C, type	δ_H (J in Hz)
1	86.3, C		87.4, C		80.9, C		84.9, C	
2	198.2, C		196.6, C		198.8, C		196.0, C	
3	101.0, C		103.1, C		101.2, C		100.0, C	
4	136.9, C		136.3, C		138.0, C		136.1, C	
5	111.4, C		107.9, C		106.6, C		111.0, C	
6	200.2, C		201.9, C		203.4, C		197.8, C	
7	161.3, C		163.5, C		164.0, C		159.1, C	
8	114.0, CH	7.03, s	117.3, CH	6.70, s	117.1, CH	6.72, s	113.1, CH	6.97, s
9	148.7, C		150.4, C		149.9, C		145.7, C	
10	115.5, C		114.4, C		113.5, C		114.7, C	
11	165.3, C		165.0, C		164.0, C		165.1, C	
12	108.3, C		107.2, C		99.4, CH	6.17, s	106.6, C	
13	167.8, C		165.8, C		167.2, C		165.9, C	
14	7.6, CH_3	2.18, s	8.2, CH_3	2.04, s			8.1, CH_3	2.06, s
15	26.6, CH_3	2.96, s	26.2, CH_3	2.81, s	25.5, CH_3	2.77, s	26.1, CH_3	2.89, s
16	41.8, CH_2	2.60, dd (14.1, 8.0) 2.54, dd (14.1, 8.0)	40.8, CH_2	2.58, d (8.0)	41.4, CH_2	2.54, d (7.9)	40.1, CH_2	2.42, d (8.0)
17	117.2, CH	5.05, t (8.0)	114.8, CH	4.79, t (8.0)	115.4, CH	4.81, t (8.0)	116.9, CH	5.00, t (8.0)
18	141.1, C		140.4, C		139.8, C		138.2, C	
19	40.5, CH_2	1.83, m	39.3, CH_2	1.61, t (7.9)	39.4, CH_2	1.63, t (7.7)	39.4, CH_2	1.78, m
20	27.2, CH_2	1.84, m	25.9, CH_2	1.47, m	26.0, CH_2	1.51, m	26.0, CH_2	1.80, m
21	125.2, CH	5.06, t (7.0)	123.7, CH	4.87, t (7.0)	123.8, CH	4.89, t (6.9)	124.2, CH	5.03, t (6.9)
22	135.6, C		134.5, C		134.4, C		133.9, C	
23	40.6, CH_2	2.01, t (7.5)	39.5, CH_2	1.85, t (7.7)	39.6, CH_2	1.85, t (7.5)	38.7, CH_2	1.99, t (7.5)
24	26.9, CH_2	2.18, m	25.6, CH_2	2.03, m	25.6, CH_2	2.03, m	27.5, CH_2	2.42, m
25	128.6, CH	5.32, t (7.3)	125.1, CH	5.08, t (7.3)	125.1, CH	5.09, t (7.1)	138.7, CH	5.76, t (7.3)
26	139.3, C		139.8, C		139.7, C		138.1, C	
27	33.0, CH_2	2.40, m; 2.10, m	31.9, CH_2	2.27, m; 1.92, m	31.9, CH_2	2.27, m; 1.92, m	31.7, CH_2	2.40, m; 2.07, m
28	30.7, CH_2	1.75, m; 1.37, m	29.7, CH_2	1.61, m; 1.16, m	29.7, CH_2	1.61, m; 1.16, m	30.5, CH_2	1.60, m; 1.17, m
29	78.8, CH	3.26, dd (10.5, 1.7)	77.3, CH	3.04, dd (10.3, 1.5)	77.3, CH	3.04, dd (10.3, 1.6)	76.8, CH	3.04, dd (10.4, 1.8)
30	73.5, C		71.7, C		71.7, C		71.5, C	
31	25.3, CH_3	1.16, s	26.1, CH_3	1.01, s	26.2, CH_3	1.02, s	26.2, CH_3	1.02, s
32	24.7, CH_3	1.13, s	24.7, CH_3	0.96, s	24.7, CH_3	0.97, s	24.5, CH_3	0.96, s
33	59.7, CH_2	4.12, d (12.1) 4.06, d (12.1)	58.2, CH_2	3.90, d (12.0) 3.86, d (12.0)	58.2, CH_2	3.91, d (12.1) 3.86, d (12.1)	169.2, C	
34	15.8, CH_3	1.56, s	15.5, CH_3	1.37, s	15.5, CH_3	1.40, s	15.5, CH_3	1.51, s
35	15.9, CH_3	1.29, s	15.7, CH_3	1.29, s	15.7, CH_3	1.29, s	15.6, CH_3	1.21, s
1-OMe			54.1, CH_3	3.11, s				
7-OMe	56.3, CH_3	3.99, s					55.9, CH_3	3.89, s

[a]Recorded at 600 MHz (^{1}H) and 150 MHz (^{13}C) in CD_3OD. [b]Recorded at 600 MHz (^{1}H) and 150 MHz (^{13}C) in DMSO-d_6. [c]Data were extracted from heteronuclear single quantum correlation (HSQC) and heteronuclear multiple bond correlation (HMBC).

not only has acquired resistance against β-lactam antibiotics but often has become multi-resistant against several classes of antibiotics. Roughly one-third of healthy human individuals carry *S. aureus*, and around 2% of people carry MRSA.[17] Furthermore, MRSA is responsible for several difficult to treat infections in humans, including skin and soft tissue infections, septicemia, endocarditis, pneumonia, enteritis, meningitis, osteomyelitis, and toxic shock syndrome. It represents a significant global health threat, resulting in extensive mortality and a burden on global healthcare systems.[18] Thus, to overcome this increasing threat, new bioactive compounds are urgently needed.

MATERIALS AND METHODS

General Experimental Procedure. Optical rotations were recorded on a PerkinElmer-241 MC polarimeter with compounds dissolved in methanol at the mentioned concentrations given as grams per 100 mL. Electrospray ionization mass spectrometry (ESI−MS) was obtained utilizing a HP1100 Agilent Finnigan LCQ Deca XP Thermoquest mass spectrometer, and high-resolution electrospray ionization mass spectrometry (HRESIMS) was obtained with a UHR-QTOF Maxis 4G mass spectrometer. One-dimensional (1D) and two-dimensional (2D) nuclear magnetic resonance (NMR) spectra were measured on a Bruker Avance III 300 or 600 NMR spectrometer, using tetramethylsilane (TMS) as an internal standard. High-performance liquid chromatography (HPLC) for analysis was performed using a Dionex P580 system with a photodiode array detector (DAD, UVD340S) and an Eurospher II C_{18} column (125 × 4 mm, length × inner diameter, Knauer), while semi-preparative HPLC was performed with a Lachrom-Merck Hitachi system [L7100 pump, L7400 ultraviolet (UV) light detector, and a 300 × 8 mm inner diameter, 10 mm, Eurospher II C_{18} column] employing a mixture of methanol (MeOH)−H_2O or acetonitrile (MeCN)−H_2O. Merck MN silica gel 60M (0.04−0.063 mm) and Sephadex LH-20 were used as stationary phases for column chromatography. Gas chromatography−mass spectrometry (GC−MS) analyses were performed on an Agilent 8890 GC coupled to an Agilent 5977B Inert Plus MSD Turbo EI.

Fungus Material. The fungal strain *C. rosea* was isolated from the plant *Conyza canadensis* collected in April 2018 in Beijing, China, on

https://doi.org/10.1021/acs.jafc.3c00447
J. Agric. Food Chem. 2023, 71, 11056−11068

solid medium containing 7.5 g of Bacto agar, 7.5 g of malt extract, and 0.125 g of chloramphenicol in 500 mL of demineralized water by subpassaging until an axenic culture was obtained. Polymerase chain reaction (PCR) amplification of the internal transcribed spacer region from chromosomal DNA followed by Sanger sequencing was performed according to a previously reported protocol to identify the fungal strain (the DNA sequence was deposited in GenBank under accession number OL597994).[19] The strain was deposited and cryopreserved in an −80 °C freezer in our laboratory.

Fermentation, Extraction, and Isolation. Mycelium of *C. rosea* was grown aerobically on solid rice medium in 20 1 L Erlenmeyer flasks each containing 100 g of autoclaved rice and 110 mL of water at 22 °C and incubated for 24 days. Fermented rice cultures were fragmented to small pieces before being extracted with 500 mL of ethyl acetate (EtOAc) for each flask, which was soaked overnight. Harvested extracts were combined and concentrated by a rotary evaporator to yield a final crude EtOAc extract (39.2 g). The crude extract was fractionated via vacuum liquid chromatography (VLC) on silica gel with a gradient of *n*-hexane/EtOAc (100:0, 80:20, 60:40, 40:60, 20:80, and 0:100) and dichloromethane/methanol (100:0, 60:40, 20:80, and 0:100) as an elution solvent to obtain seven fractions (fractions 1−7). The following purification steps were bioactivity-monitored for antibacterial activity against *S. aureus* MRSA activity (Figure S1 of the Supporting Information). Fraction 6 (2.6 g) was further separated by a Sephadex LH-20 column with MeOH to obtain five subfractions 6.1−6.5. Subfraction 6.1 (1.1 g) was chromatographed by VLC on silica gel using dichloromethane/MeOH (80:20, 70:30, 60:40, 50:50, and 40:60) as the mobile phase, followed by separation using semi-preparative HPLC with a mixture of MeCN and H_2O to yield compounds **1** (1.5 mg), **2** (2.7 mg), **3** (2.1 mg), **4** (7.0 mg), **9** (37.5 mg), and **10** (4.3 mg). Subfraction 6.4 (0.9 g) was eluted on silica gel using dichloromethane/MeOH (60:40, 50:50, 40:60, and 30:70), followed by purification using semi-preparative HPLC with MeOH−H_2O as the mobile phase to obtain compounds **5** (4.2 mg), **6** (10.7 mg), **7** (3.6 mg), and **8** (4.5 mg).

Asperphenalenone F (**1**): brown gum; $[\alpha]_D^{25}$ −48.9 (*c* 0.38, MeOH); UV (MeOH) λ_{max} (nm), 340, 258, 215; electronic circular dichroism (ECD, *c* 3.20 × 10^{-4} M, MeOH) λ_{max} ($\Delta\varepsilon$), 393 (−1.23), 349 (−0.32), 329 (+1.49), 303 sh (+1.18), 278 (+1.73), 255 (+4.37), 236 sh (+3.99), 209 (−5.44) nm; ECD (*c* 1.60 × 10^{-4} M, DMSO) λ_{max} ($\Delta\varepsilon$), 422.5 (−3.39), 368.5 (4.16), 321.5 (−1.85), 298.5 (−2.72), 280 (9.16) nm; HRESIMS, *m*/*z* 625.3371 $[M + H]^+$ (calculated for $C_{36}H_{49}O_9$, 625.3371); ^1H and ^{13}C NMR data, see Table 1.

Asperphenalenone G (**2**): brown gum; $[\alpha]_D^{25}$ +6.4 (*c* 0.68, MeOH); UV (MeOH) λ_{max} (nm), 342, 257, 213; ECD (*c* 3.20 × 10^{-4} M, MeOH) λ_{max} ($\Delta\varepsilon$), 380 (−0.39), 331 (+0.63), 251 (+1.25), 234 sh (+1.07), 225 (+1.23), 207 (−3.39), 196 sh (−1.63) nm; ECD (*c* 1.60 × 10^{-4} M, DMSO) λ_{max} ($\Delta\varepsilon$), 462.5 (−1.74) 391.5 (2.80), 371.5 sh (0.99), 353 (−6.79), 326 sh (−2.14) nm; HRESIMS, *m*/*z* 625.3377 $[M + H]^+$ (calculated for $C_{36}H_{49}O_9$, 625.3371); ^1H and ^{13}C NMR data, see Table 1.

Asperphenalenone H (**3**): brown gum; $[\alpha]_D^{25}$ +98.2 (*c* 0.53, MeOH); UV (MeOH) λ_{max} (nm), 335, 257, 212; ECD (*c* 3.35 × 10^{-4} M, MeOH) λ_{max} ($\Delta\varepsilon$), 419 sh (−0.25), 386 (−0.95), 360 (+0.64), 325 (+2.77), 293 sh (−0.63), 266 (−0.95), 254 sh (+4.28), 248 (+4.84), 228 (+0.71), 219 (+3.28), 206 (−12.28) nm; HRESIMS, *m*/*z* 597.3052 $[M + H]^+$ (calculated for $C_{34}H_{45}O_9$, 597.3058); ^1H and ^{13}C NMR data, see Table 1.

Asperphenalenone I (**4**): brown gum; $[\alpha]_D^{25}$ +46.9 (*c* 1.00, MeOH); UV (MeOH) λ_{max} (nm), 344, 258, 214; ECD (*c* 3.13 × 10^{-4} M, MeOH) λ_{max} ($\Delta\varepsilon$), 389 (−1.09), 328 (+0.65), 302 sh (+0.66), 280 (+0.69), 255 (+2.74), 235 sh (+2.19), 209 (−4.06) nm; ECD (*c* 1.56 × 10^{-4} M, DMSO) λ_{max} ($\Delta\varepsilon$), 426 (−3.56), 385 sh (2.69), 372 (3.67), 330 (−1.76), 309 (0.70), 298 (−1.11), 277.5 (9.80) nm; HRESIMS, *m*/*z* 639.3165 $[M + H]^+$ (calculated for $C_{36}H_{47}O_{10}$, 639.3164); ^1H and ^{13}C NMR data, see Table 1.

Asperphenalenone J (**5**): brown gum; $[\alpha]_D^{25}$ +47.5 (*c* 1.00, MeOH); UV (MeOH) λ_{max} (nm), 344, 258, 212; ECD (*c* 2.54 × 10^{-4} M, MeOH) λ_{max} ($\Delta\varepsilon$), 422 sh (−0.77), 389 (−1.16), 346 (−0.41), 328 (+1.12), 302 sh (+1.28), 282 (+1.53), 254 (+4.16), 236 sh (+3.67), 209 (−4.47) nm; HRESIMS, *m*/*z* 804.4159 $[M + NH_4]^+$ (calculated for $C_{42}H_{62}NO_{14}$, 804.4165); ^1H and ^{13}C NMR data, see Table 2.

Asperphenalenone K (**6**): brown gum; $[\alpha]_D^{25}$ −6.9 (*c* 1.00, MeOH); UV (MeOH) λ_{max} (nm), 343, 258, 214; ECD (*c* 2.59 × 10^{-4} M, MeOH) λ_{max} ($\Delta\varepsilon$), 377 (−1.04), 350 (−1.00), 328 (+3.21), 283 (+0.51), 267 (−0.26), 254 (+4.17), 237 sh (+3.67), 219 (+2.67), 208 (−7.30) nm; HRESIMS, *m*/*z* 790.4006 $[M + NH_4]^+$ (calculated for $C_{41}H_{60}NO_{14}$, 790.4008); ^1H and ^{13}C NMR data, see Table 2.

Asperphenalenone L (**7**): brown gum; $[\alpha]_D^{25}$ +89.6 (*c* 0.90, MeOH); UV (MeOH) λ_{max} (nm), 344, 258, 216; ECD (*c* 8.47 × 10^{-5} M, MeOH) λ_{max} ($\Delta\varepsilon$), 427 (−0.28), 386 (+0.13), 351 (−0.65), 301 (+0.75), 280 sh (+0.71), 257 (+1.20), 241 sh (+0.93), 223 (+1.30), 208 (−1.84), 202 sh (−1.48) nm; HRESIMS, *m*/*z* 804.4159 $[M + NH_4]^+$ (calculated for $C_{42}H_{62}NO_{14}$, 804.4165); ^1H and ^{13}C NMR data, see Table 2.

Asperphenalenone M (**8**): brown gum; $[\alpha]_D^{25}$ +47.5 (*c* 1.00, MeOH); UV (MeOH) λ_{max} (nm), 344, 258, 211; ECD (*c* 2.41 × 10^{-4} M, MeOH) λ_{max} ($\Delta\varepsilon$), 417 sh (−0.90), 399 (−1.03), 328 (+1.25), 307 sh (+1.00), 277 (+0.97), 255 (+2.92), 241 sh (+2.57), 221 (+0.81), 208 (−3.38) nm; HRESIMS, *m*/*z* 846.4278 $[M + NH_4]^+$ (calculated for $C_{44}H_{64}NO_{15}$, 846.4270); ^1H and ^{13}C NMR data, see Table 2.

NMR and HRESIMS spectroscopic data used for structure elucidation of compounds **1**−**8** can be found in Figures S2−S53 of the Supporting Information. HPLC−DAD chromatograms of compounds **1**−**8** are shown in Figures S54−S61 of the Supporting Information to demonstrate purity. Compounds **9** and **10** were identified as asperphenalenones E and B, respectively, by comparison of their NMR and MS data to the literature.[20]

Identification of the Sugar Moiety in Asperphenalenone K (6) by GC−MS Analysis. A total of 2.5 mg of compound **6** was solved in 900 μL of demineralized water and 300 μL of MeOH. A total of 800 μL of 37% HCl were then added to the mixture to a final concentration of 15% HCl (v/v) and volume of 2.0 mL in a 10 mL pointed shape flask. The flask was connected to a Dimroth condenser and placed into a water bath at 100 °C for 3 h under reflux condensation. Afterward, the resulting solution was dried under reduced pressure followed by partition between H_2O and CH_2Cl_2.[21] Then, the aqueous phase was filtrated over glass wool into a 10 mL round-bottom flask. The solvent was evaporated to yield an amorphous, dry solid. To the above dried residue, 400 μL of pyridine and 200 μL of *N*,*O*-bis(trimethylsilyl)trifluoroacetamide (BSTFA) with 1% trimethylchlorosilane (TMCS) were added, and trimethylsilylation was carried out at 60 °C with shaking at 300 rpm for 1 h. The samples were subjected to GC−MS analysis using a program with injection temperature at 260 °C, carrier gas flow at 1 mL/min, temperature profile from 40 to 300 °C with 3 °C/min, split ratio of 1:10, and scan mode from *m*/*z* 45 to 600 in full-scan mode.[22]

The reference sugars (D-mannose, D-glucose, and D-galactopyranose) were heated at 90 °C in water for 1 h and freeze-dried. Afterward, trimethylsilylation and measurement via GC−MS were carried out as described for compound **6**.

Culture of Microorganism and Virus Strains. Mueller Hinton broth was used for cultivation of nosocomial bacterial strains, including *Staphylococcus aureus* ATCC 25923, *Staphylococcus aureus* ATCC 70669 (MRSA/VISA), *Enterococcus faecalis* ATCC 51299, and *Enterococcus faecium* ATCC 35667. All bacteria were grown aerobically at 37 °C. *Candida albicans* strain ATCC 24433 was incubated in YPD medium (10 g/L yeast extract, 20 g/L peptone, and 20 g/L D-glucose) at 37 °C aerobically. *Mycobacterium tuberculosis* strain H37Rv was cultured aerobically at 37 °C in Middlebrook 7H9 broth supplemented with 0.5% glycerol, 0.05% tyloxapol, and 10% (v/v) albumin−dextrose−saline (ADS) enrichment yielding final concentrations of 5% bovine serum albumin fraction V, 2% glucose, and 0.85% sodium chloride, respectively. SARS-CoV-2 was propagated in infected Vero cells maintained in Dulbecco's modified Eagle's medium (DMEM) supplemented with 2% heat-inactivated fetal calf serum (FCS), 4.5 g/L glucose, 0.11 g/L sodium pyruvate, stable glutamine, and 1% penicillin/streptomycin solution. Human

https://doi.org/10.1021/acs.jafc.3c00447
J. Agric. Food Chem. 2023, 71, 11056−11068

Table 2. NMR Data for Compounds 5−8

	5[a]		6[a]		7[a]		8[a]	
number	δ_C, type	δ_H (J in Hz)	δ_C, type	δ_H (J in Hz)	δ_C, type[b]	δ_H (J in Hz)	δ_C, type[b]	δ_H (J in Hz)
1	86.7, C		83.6, C		89.2, C		86.7, C	
2	198.4, C		201.2, C		200.2, C		198.4, C	
3	102.6, C		103.5, C		104.1, C		102.7, C	
4	138.0, C		137.2, C		137.5, C		138.1, C	
5	111.8, C		107.4, C		109.0, C		111.9, C	
6	200.4, C		203.5, C		203.2, C		200.1, C	
7	161.7, C		165.4, C		165.1, C		161.5, C	
8	114.5, CH	7.03, s	114.4, CH	6.72, s	119.0, CH	6.78, s	114.1, CH	7.04, s
9	148.9, C		151.2, C		151.8, C		148.9, C	
10	115.7, C		119.3, C		114.4, C		116.1, C	
11	165.2, C		164.7, C		165.7, C		166.6, C	
12	108.4, C		108.4, C		108.3, C		108.4, C	
13	168.1, C		167.4, C		167.3, C		168.6, C	
14	7.8, CH_3	2.18, s	7.8, CH_3	2.16, s	7.5, CH_3	2.19, s	7.7, CH_3	2.19, s
15	26.9, CH_3	2.96, s	26.8, CH_3	2.85, s	26.6, CH_3	2.88, s	26.7, CH_3	2.97, s
16	42.1, CH_2	2.60, dd (14.0, 8.1) 2.54, dd (14.0, 7.5)	43.8, CH_2	2.63, d (8.0)	42.5, CH_2	2.70, d (8.1)	42.1, CH_2	2.61, dd (14.0, 8.1) 2.55, dd (14.0, 7.5)
17	117.4, CH	5.05, dd (8.1, 7.5)	116.3, CH	4.87, t (8.0)	115.3, CH	4.82, t (8.1)	117.3, CH	5.05, dd (8.1, 7.5)
18	141.3, C		142.2, C		142.5, C		141.2, C	
19	40.9, CH_2	1.83, m	40.7, CH_2	1.68, t (7.9)	40.3, CH_2	1.64, t (7.9)	40.9, CH_2	1.84, m
20	27.5, CH_2	1.84, m	27.4, CH_2	1.58, m	27.1, CH_2	1.48, m	27.3, CH_2	1.84, m
21	125.7, CH	5.06, t (7.0)	125.5, CH	4.94, t (7.0)	125.1, CH	4.90, t (7.1)	125.7, CH	5.07, t (7.0)
22	135.7, C		135.6, C		135.4, C		135.3, C	
23	40.8, CH_2	2.00, t (7.5)	40.8, CH_2	1.95, t (7.6)	40.4, CH_2	1.93, t (7.4)	40.8, CH_2	2.02, t (7.3)
24	27.3, CH_2	2.20, m	27.2, CH_2	2.17, m	26.9, CH_2	2.15, m	27.1, CH_2	2.20, m
25	131.3, CH	5.44, t (7.2)	131.2, CH	5.41, t (7.3)	130.9, CH	5.41, t (7.2)	131.4, CH	5.46, t (7.3)
26	136.5, C		136.5, C		136.3, C		136.4, C	
27	33.6, CH_2	2.37, m; 2.10, m	33.6, CH_2	2.36, m; 2.09, m	33.3, CH_2	2.36, m; 2.08, m	33.3, CH_2	2.37, m; 2.09, m
28	31.2, CH_2	1.78, m; 1.36, m	31.2, CH_2	1.77, m; 1.36, m	30.9, CH_2	1.77, m; 1.34, m	31.0, CH_2	1.78, m; 1.36, m
29	79.2, CH	3.26, dd (10.5, 1.7)	79.2, CH	3.26, dd (10.5, 1.7)	78.9, CH	3.26, dd (10.8, 1.6)	79.2, CH	3.25, dd (10.5, 1.7)
30	73.8, C		73.8, C		73.6, C		73.7, C	
31	25.9, CH_3	1.16, s	25.8, CH_3	1.16, s	25.5, CH_3	1.16, s	25.4, CH_3	1.16, s
32	24.9, CH_3	1.12, s	24.9, CH_3	1.12, s	24.5, CH_3	1.12, s	24.6, CH_3	1.13, s
33	66.7, CH_2	4.30, s	66.7, CH_2	4.29, s	66.3, CH_2	4.29, s	66.3, CH_2	4.31, d (11.7) 4.24, d (11.7)
34	16.1, CH_3	1.56, s	16.0, CH_3	1.47, s	15.6, CH_3	1.43, s	16.0, CH_3	1.57, s
35	16.2, CH_3	1.29, s	16.1, CH_3	1.31, s	15.9, CH_3	1.36, s	16.0, CH_3	1.29, s
1′	100.1, CH	4.47, d (0.8)	100.1, CH	4.47, d (0.8)	99.8, CH	4.47, d (0.7)	99.7, CH	4.46, d (0.8)
2′	72.6, CH	3.83, dd (3.2, 0.8)	72.6, CH	3.83, dd (3.2, 0.8)	72.2, CH	3.83, dd (3.2, 0.8)	72.3, CH	3.84, dd (3.3, 0.8)
3′	75.4, CH	3.43, dd (9.5, 3.2)	75.4, CH	3.44, dd (9.5, 3.2)	75.1, CH	3.43, dd (9.6, 3.2)	75.1, CH	3.44, dd (9.5, 3.3)
4′	68.5, CH	3.59, t (9.5)	68.5, CH	3.59, t (9.5)	68.2, CH	3.59, t (9.6)	68.6, CH	3.57, t (9.5)
5′	78.2, CH	3.17, ddd (9.5, 5.5, 2.4)	78.2, CH	3.18, ddd (9.5, 5.4, 2.4)	77.9, CH	3.18, ddd (9.6, 5.4, 2.3)	75.5, CH	3.35, ddd (9.5, 6.5, 2.1)

https://doi.org/10.1021/acs.jafc.3c00447
J. Agric. Food Chem. 2023, 71, 11056−11068

Table 2. continued

	5[a]		6[a]		7[a]		8[a]	
number	δ_C type	δ_H (J in Hz)	δ_C type	δ_H (J in Hz)	δ_C type[b]	δ_H (J in Hz)	δ_C type[b]	δ_H (J in Hz)
6′	62.8, CH_2	3.86, dd (11.8, 2.4)	62.8, CH_2	3.86, dd (11.9, 2.4)	62.4, CH_2	3.86, dd (11.8, 2.3)	65.0, CH_2	4.41, dd (11.8, 2.1)
		3.73, dd (11.8, 5.5)		3.73, dd (11.9, 5.4)		3.73, dd (11.8, 5.4)		4.22, dd (11.8, 6.5)
1-OMe					54.9, CH_3	3.27, s		
7-OMe	56.6, CH_3	3.99, s					56.5, CH_3	3.99, s
6′-OAc							20.7, CH_3	2.05, s
							172.6, C	

[a]Recorded at 600 MHz (^{1}H) and 150 MHz (^{13}C) in CD_3OD. [b]Data were extracted from HSQC and HMBC.

immunodeficiency virus (HIV) was propagated in Jurkat cells maintained in RPMI 1640 medium supplemented with 5% heat-inactivated FCS.

Determination of MIC. All compounds were tested for their antimicrobial bioactivities against the Gram-positive nosocomial bacterial pathogens *S. aureus*, *E. faecalis*, and *E. faecium*, against *M. tuberculosis* as well as against the pathogenic fungus *C. albicans*. The broth microdilution method was used in each case according to recommendations by the Clinical and Laboratory Standards Institute (CLSI).[23] All tests were repeated twice.

Briefly, nosocomial bacteria were grown aerobically in Mueller Hinton (MH) medium at 37 °C as shaking cultures at 180 rpm until reaching the early log phase. Cell suspensions were then diluted to 1 × 10^6 CFU/mL ($OD_{600\ nm}$ of ∼0.1) and seeded at a density of 5 × 10^5 CFU/well in a total volume of 100 μL in 96-well round-bottom microtiter plates. The tested compounds were 2-fold serially diluted and added to the wells to yield final concentrations ranging from 0.78 to 100 μM. Dimethyl sulfoxide (DMSO) at a maximal concentration of 1% was used as a solvent control, while moxifloxacin served as a positive control. After aerobic incubation at 37 °C for 16−20 h, MICs were determined macroscopically.

Cells of *C. albicans* were incubated at 37 °C in YPD medium while being shaken at 180 rpm overnight to promote growth of the cells in the yeast form. To induce growth in the hyphae form, YP medium containing 5% proline was used and cells were incubated at 30 °C with shaking at 80 rpm. Afterward, cells were seeded in 96-well round-bottom microtiter plates at a density of 1 × 10^6 CFU/mL containing 2-fold serial dilutions of compounds at final concentrations ranging from 0.78 to 100 μM in a total volume of 100 μL. A total of 1% Dimethyl sulfoxide (DMSO) was used as a solvent control, while hygromycin B served as a positive control.[24] The plates were incubated at 37 and 30 °C overnight for the yeast and the hyphae form, respectively, and growth inhibition was evaluated macroscopically.

Cells of *M. tuberculosis* were incubated at 37 °C in Middlebrook 7H9 medium with shaking at 180 rpm for 4 days. Afterward, cells were seeded at a density of 1 × 10^6 CFU/mL in a 96-well round-bottom microplate containing 2-fold serial dilutions of compounds at final concentrations ranging from 0.78 to 100 μM in a total volume of 100 μL. Rifampicin served as a positive control, and DMSO at a maximal concentration of 1% was used as a solvent control. After plates were incubated at 37 °C for 5 days aerobically, resazurin solution (10 μL/well from 100 μg/mL stock, Sigma-Aldrich) was added to the cells and incubated for 16 h at room temperature for reduction of resazurin to resorufin by aerobic respiration of metabolically active cells. Next, *M. tuberculosis* cells were inactivated by incubation with formalin (10%, v/v, final concentration) for 30 min at room temperature. Subsequently, fluorescence was measured using a microplate reader (TECAN, excitation at 560 nm and emission at 590 nm).

Determination of Inhibition of SARS-CoV-2 Cytopathic Effects. Vero cells were grown in a 96-well white flat bottom cell culture plate overnight in DMEM supplemented with 2% heat-inactivated FCS and 1% penicillin/streptomycin solution at 37 °C with 5% CO_2 to a final density of 2 × 10^4 cells/well. Afterward, the medium was removed, and 50 μL of fresh medium containing the tested compounds at a concentration of 100 μM was added to each well and incubated for 1 h. Next, a further 50 μL growth medium containing SARS-CoV-2 was added to yield a tissue culture infectious dose of 50% ($TCID_{50}$) and incubated for another 2 h at 37 °C with 5% CO_2. Subsequently, the inoculum was removed and replaced by 100 μL of fresh medium containing the tested compounds at a concentration of 100 μM. After 72 h of incubation, host cell viability was measured using ViroTiter Glo (Promega) following the manual of the manufacturer. All tests were performed in triplicates.

Cytotoxicity Assay. Compounds **1**−**10** were tested for cytotoxicity against the Jurkat cell line (human T lymphocyte cells). Cells were grown in RPMI 1640 medium supplemented with 10% heat-inactivated FCS at 37 °C with 5% CO_2 before diluted to a concentration of 1 × 10^6 cells/mL. Afterward, cells were seeded into

https://doi.org/10.1021/acs.jafc.3c00447
J. Agric. Food Chem. 2023, 71, 11056−11068

96-well flat bottom microtiter plate containing 2-fold serial dilutions of the tested compounds to yield final concentrations ranging from 0.78 to 100 μM in a total volume of 100 μL and incubated at 37 °C with 5% CO_2 for 48 h. Next, 10 μL of resazurin solution (100 μg/mL) was added to each well and incubated for another 4 h before fluorescence was measured to quantify the survival of cells using a microplate reader (excitation at 540 nm and emission at 590 nm). DMSO was used as a solvent control, and growth was calculated relative to non-inoculated (0% growth) and untreated (100% growth) controls.[25]

HIV-1 Infection and Quantification of Replication by HIV-1 Exon 7 qPCR. In 1 mL of RPMI medium (Thermo Fisher Scientific, Waltham, MA, U.S.A.) supplemented with 5% heat-inactivated FCS (PAN Biotech, Germany), 1×10^6 Jurkat T cells were infected with the HIV-1 molecular clone NL4-3[26] at a multiplicity of infection (MOI) of 0.005 for 6 h in a 15 mL centrifugation tube at 37 °C in a humidified atmosphere. Afterward, the cells were centrifuged at 400*g* for 5 min and washed once with 1 mL of PBS. Cell pellets were resuspended in 1 mL of culture medium containing the tested compounds at the indicated concentrations and transferred to T25 cell culture flasks. At 3 days post-infection, the cells were transferred to 2 mL centrifugation tubes, centrifuged at 20000*g* for 14 s, and washed once in 1 mL of PBS and again centrifuged like before. Cell lysis was performed using 500 μL of solution D (4 M guanidinium thiocyanate, 25 mM sodium citrate, 0.5% sarcosyl, and 100 mM β-mercaptoethanol). RNA isolation was conducted via phenol−chloroform extraction. For this, a master mix containing 7.2 μL of β-mercaptoethanol, 50 μL of 2 M sodium acetate (pH 4), and 500 μL of phenol per sample were added to the lysed cells. The samples were briefly vortexed and mixed with 103 μL of a chloroform/isoamyl alcohol mixture (ratio of 24:1). Afterward, the samples were vortexed for 15 s, incubated on ice for 15 min, and centrifuged for 20 min at approximately 10000*g* at 4 °C. After centrifugation, 400 μL of the aqueous upper phase was mixed with the same amount of 100% isopropanol and incubated at −20 °C for at least 1 h. Thereafter, the samples were centrifuged for 20 min at approximately 10000*g* and 4 °C. The pellets were washed twice with 200 μL of ethanol (70%) for 10 min at 10000*g* and 4 °C and air-dried for 5 min at room temperature. RNA was solubilized by adding 10 μL of H_2O.

For cDNA synthesis, 10 μL samples containing exactly 1 μg of RNA were incubated at 70 °C for 5 min and afterward cooled on ice for a few seconds. A total of 5 μL was mixed with 0.5 μL of oligo-d(T) primer (1:20 dilution, Roche, Switzerland), 0.5 μL of dNTPs (Qiagen, Germany), and 0.5 μL of H_2O. After incubation of this mixture for 5 min at 65 °C, 2 μL of first strand buffer (Thermo Fisher Scientific, Waltham, MA, U.S.A.), 0.5 μL of dithiothreitol (DTT, Thermo Fisher Scientific, MA, U.S.A.), 0.5 μL of RNasin (Promega, Madison, WI, U.S.A.), and 0.5 μL of Superscript III (Thermo Fisher Scientific, Waltham, MA, U.S.A.) were added. The samples were then incubated at 50 °C for 60 min and, subsequently, at 72 °C for 15 min.

The amounts of HIV-1 and cellular glyceraldehyde 3-phosphate dehydrogenase (GAPDH) transcripts were analyzed via quantitative polymerase chain reaction (qPCR). For this, the cDNA samples were diluted 1:10, and 2 μL of these dilutions was mixed with 6 μL of H_2O, 1 μL of forward primer [5′-ACCCTGTTGCTGTAGCCA-3′ (GAPDH) and 5′-TTGCTCAATGCCACAGCCAT-3′ (HIV-1 exon 7)], 1 μL of reverse primer [5′-CCACTCCTCCACCTTTGAC-3′ (GAPDH) and 5′-TTTGACCACTTGCCACCCAT-3′ (HIV-1 exon 7)], and 10 μL of qPCR master mix (Primer Design, U.K.). The qPCR samples were filled into glass capillaries (Roche, Switzerland) via centrifugation at 68*g* for 5 s and analyzed using the LightCycler 1.5 capillary-based qPCR system. The samples were run in triplicate and were subject to the following PCR program: segment 1 (amplification) 1, 95 °C for 10 s; 2, 60 °C for 60 s (42 cycles); segment 2 (melting curve) 1, 95 °C for 0 s; 2, 63 °C for 30 s; 3, 95 °C for 0 s with a slope of 0.1 °C/s (1 cycle). The data were analyzed using the comparative C_T method.[27]

Computational Section. Mixed torsional/low-mode conformational searches were carried out by means of the MacroModel 10.8.011 software using the MMFF with an implicit solvent model for $CHCl_3$ applying a 21 kJ/mol energy window.[28] Geometry reoptimizations of the resultant conformers (ωB97X/TZVP level[29] with PCM solvent model for MeOH) and time-dependent density functional theory electronic circular dichroism (TDDFT−ECD) and optical rotation (OR) calculations (B3LYP/TZVP, BH&HLYP/TZVP, CAM-B3LYP/TZVP, and PBE0/TZVP levels with PCM solvent model for MeOH) were performed with Gaussian 09 package.[30] ECD spectra were generated as sums of Gaussians with 2100 and 1000 cm^{-1} widths at half height, using dipole-velocity-computed rotational strength values.[31] Boltzmann distributions were estimated from the ωB97X energies. Visualization of the results was performed by the MOLEKEL software package.[32]

RESULTS AND DISCUSSION

Compound **1** was obtained as a brown gum. Its molecular formula of $C_{36}H_{48}O_9$ was determined by HRESIMS, indicating 13 degrees of unsaturation. The ^{1}H NMR spectrum of compound **1** displayed an aromatic proton at δ_H 7.03 (s, H-8), three olefinic protons at δ_H 5.32 (t, H-25), 5.06 (t, H-21), and 5.05 (t, H-17), oxygenated methylene at δ_H 4.12 (d, H-33a) and 4.06 (d, H-33b), oxygenated methine at δ_H 3.26 (dd, H-29), and six methyl groups at δ_H 2.96 (s, H-15), 2.18 (s, H-14), 1.56 (s, H-34), 1.29 (s, H-35), 1.16 (s, H-31), and 1.13 (s, H-32). The above NMR data of compound **1** were closely related to those of the co-isolated known phenalenone derivative, asperphenalenone E (**9**),[20] except for the presence of an additional methoxy group in compound **1** at δ_C 56.3 and δ_H 3.99 (s). The location of this methoxy group at C-7 in compound **1** was confirmed by the HMBCs from protons of the methoxy group to C-7 (δ_C 161.3). Detailed analysis of the 2D NMR spectra of compound **1** revealed that its remaining structure was identical with that of compound **9** (Figures 1 and 2). The rotating-frame nuclear Overhauser effect correlation spectroscopy (ROESY) correlations between H-17/H_2-19, H-21/H_2-23, and H-24/H2−33 demonstrated that the double bonds at C-17/C-18, C-21/C-22, and C-25/C-26 were *E*, *E*, and *Z* configurations, respectively. The ECD spectrum of compound **1** (Figure S62 of the Supporting Information) showed good agreement with the ECD spectrum of the known compound asperphenalenone A[20] in the region of 200−400 nm. Furthermore, it was also similar to the experimental ECD of compound **3** (Figure S63 of the Supporting Information), of which the absolute configuration at C-1 was determined as (*S*) by TDDFT−ECD calculations (*vide infra*). In fact, the ECD spectra of all of the new derivatives **1**−**8** showed similar ECD patterns, a high wavelength negative transition around 380−420 nm with weak or average intensity, a positive transition around 325 nm, two or more positive transitions in the range of 220−250 nm, and a negative transition around 205−210 nm (Figure S64 of the Supporting Information), suggesting the same orientation of the components at the C-1 chirality center of the isolated compounds. However, in comparison to compound **3**, the replacement of the hydroxy group by a methoxy group at C-7 in compound **1** changed the priority orders of the substituents at C-1. The OH or OMe substituent at C-1 has priority 1 in all compounds. In compound **3** with a hydroxy group at C-7, the C-2 → C-3 → C-13 → C-12 axis substituent at C-1 has priority 2 because there is CH_3 at C-12 but only H at C-8, while in compound **1** with a methoxy group at C-7, the C-6 → C-5 → C-7 axis substituent at C-1 has priority 2 because there is only OH at C-13 but OMe at C-7. Thus, although the orientation of the substituents at C-1 always remains the same in all of the isolated compounds **1**−**10**, there is a change of the Chan−Ingold−Prelog notation

https://doi.org/10.1021/acs.jafc.3c00447
J. Agric. Food Chem. 2023, 71, 11056−11068

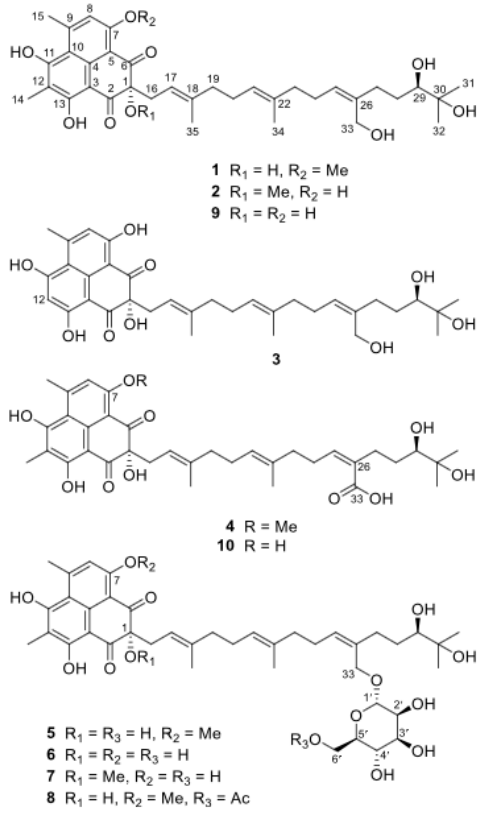


Figure 1. Structure of compounds **1**−**10**.

from (*S*) to (*R*) when the hydroxy group was replaced by a methoxy group at C-7. Thus, the absolute configuration at C-1 of 7-OMe derivatives (**1**, **4**, **5**, and **8**) is (*R*) and opposite to that of 7-OH derivatives (**2**, **3**, **6**, **7**, **9**, and **10**), which is (*S*), simply as a result of change of orders of the components at the C-1 chirality center. While the absolute configuration of C-1 was established as (*R*) in compound **1**, its side chain with a C-29 chirality center was similar to those of known compounds asperphenalenone E,[20] aspergillussanones A,[33] and aspergillussanones K and L,[34] for which the (29*R*) absolute configuration was suggested tentatively. In analogue phenalenone derivatives, the induced ECD spectrum of the Mo_2 $(OAc)_4$ complex[35,36] was frequently used to determine the C-29 chirality center,[37,38] which is part of a *sec*/*tert* vicinal diol moiety. To confirm the (29*R*) absolute configuration, the ECD spectrum of compound **1** was recorded in DMSO, and DMSO solution of $Mo_2(OAc)_4$ was added for complex formation with a 1:30 ligand/metal ratio. Interestingly, the ECD spectrum of compound **1** in DMSO was markedly different from that recorded in MeOH, which was attributed to the strong solvent effect as a result of the coordination of DMSO to the hydroxyl groups. The ECD spectrum of the $Mo_2(OAc)_4$ complex did not show the expected ECD pattern (Figure S65 of the Supporting Information), and only minor wavelength shifts and intensity changes were observed, which could not be used to determine the absolute configuration of the C-29 chirality center. The phenolic hydroxyl groups clearly interfered with the complexation, and the expected induced ECD pattern of the complex did not appear. Thus, the structure of compound **1** was elucidated as drawn in Figure 1, representing a new phenalenone derivative, for which the trivial name asperphenalenone F is given.

The HRESIMS data of compound **2** indicated the same molecular formula of $C_{36}H_{48}O_9$ as that of compound **1**. A comparison of the ^1H and ^{13}C NMR data of compounds **1** and **2** (Table 1) revealed that both compounds differ in the position of the methoxy group. In compound **2**, the methoxy group was attached to C-1 based on the HMBCs from protons of the methoxy group (δ_H 3.11) and H_2-16 (δ_H 2.58) to C-1 (δ_C 87.4) (Figure 2). The positive Cotton effect at around 250 nm in the ECD spectrum of compound **2** (Figure S66 of the Supporting Information) suggested that the absolute configuration of C-1 was identical to that of compound **3** as (*S*). In the ECD spectrum of the Mo_2 $(OAc)_4$ complex of compound **2** in DMSO, the characteristic ECD transitions observed in DMSO disappeared and a near baseline ECD curve was observed (Figure S67 of the Supporting Information). The structure of compound **2**, named asperphenalenone G, was elucidated as drawn in Figure 1.

The molecular formula of asperphenalenone H (**3**) was determined as $C_{34}H_{44}O_9$ by HRESIMS. When the NMR data of compounds **3** and **1** were compared, the obvious differences were the disappearance of the methoxy group and the replacement of the aromatic methyl by an aromatic proton (δ_H 6.17, s, H-12) in compound **3**. The HMBCs from H-12 to C-3 (δ_C 101.2) and C-10 (δ_C 113.5), from Me-15 (δ_H 2.77) to C-8 (δ_C 117.1), C-9 (δ_C 149.9), and C-10, and from H-8 (δ_H 6.72) to C-5 (δ_C 106.6) and C-10 confirmed the location of the additional aromatic methine proton at C-12. Detailed analysis of the 2D NMR spectra of compound **3** (Figure 2) revealed that the remaining substructure and the relative configuration of the double bonds of compound **3** were identical to those of compound **1**. The ECD spectrum of compound **3** (Figure S63 of the Supporting Information) showed intense positive Cotton effects centered around 250 nm, which suggested homochiral (1*S*) absolute configuration with compound **2**. With verification of the related literature on stereochemical analysis, it was found that ECD comparison of related derivatives with different chromophoric systems was performed (e.g., sculezonone A and herqueinone)[39] or the calculated TDDFT−ECD spectra showed only partial agreement with the experimental spectra,[20] which raised some uncertainty in the previous configurational assignments. Therefore, we decided to perform TDDFT−ECD and OR calculations for compound **3**.[40] The Merck molecular force field (MMFF) conformational search of compound (1*S*,29*R*)-**3** resulted in 387 initial conformers in a 21 kJ/mol energy window. These structures were reoptimized at the ωB97X/TZVP[29] PCM/MeOH level yielding 24 low-energy conformers over 1% Boltzmann population (Figure S68 of the Supporting Information). ECD spectra computed at four levels of theory for these conformers gave acceptable to good agreement with the experimental ECD spectrum, and the B3LYP/TZVP PCM/MeOH method provided the best agreement (Figure 3). While the strong positive transitions at 219, 248, and 315 nm and the intense negative transition at 206 nm were rather consistent in the low-energy conformers, allowing for a solid elucidation of the absolute configuration as (1*S*), the low-intensity negative transitions at 386, 293, and 266 nm were present only in some of the low-energy conformers (Figure S69 of the Supporting Information). Although a well-performing DFT functional[41] was chosen for the optimization,

https://doi.org/10.1021/acs.jafc.3c00447
J. Agric. Food Chem. 2023, 71, 11056−11068

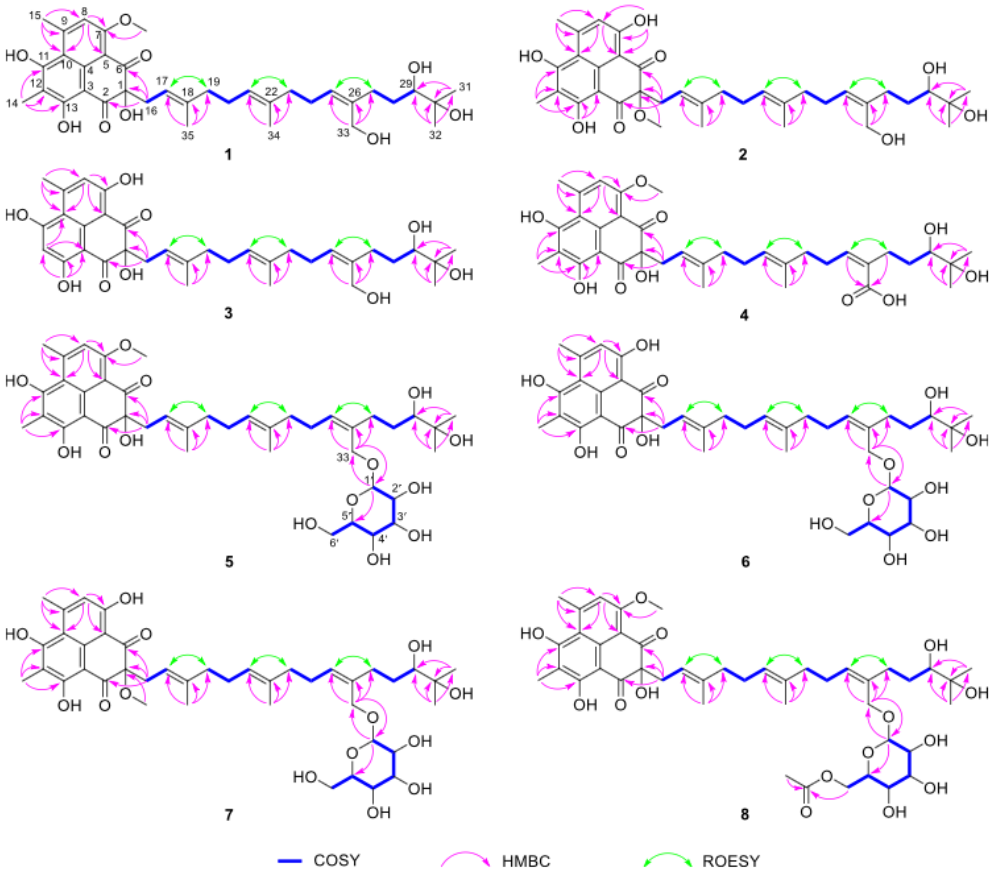


Figure 2. Key correlations of HMBC, COSY, and ROESY of compounds **1**−**8**.

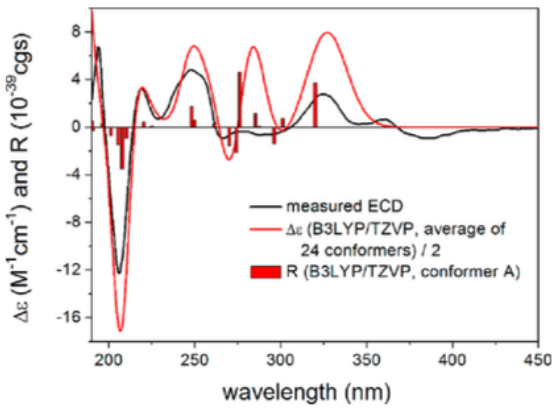


Figure 3. Experimental ECD spectrum of compound **3** in MeOH (black line) compared to the calculated B3LYP/TZVP PCM/MeOH spectrum of compound (1*S*,29R)-**3** (red line). Level of DFT optimization: ωB97X/TZVP PCM/MeOH. Bars represent the rotational strengths of conformer A.

the conformer distribution may show some deviation from the estimated distribution as a result of the high conformational flexibility.[42−44]

Because ECD were expected to be determined by the C-1 chirality center and the side chain implies a large amount of flexibility enhancement, we tested two truncated model systems containing either a methyl (3modMe) or ethyl (3modEt) group attached to the first double bonds of the side chain (Figure 4).[45,46] Previous studies showed that the

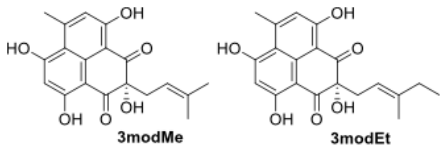


Figure 4. Structure of model compounds (*S*)-3modMe and (*S*)-3modEt.

position of the truncation is important for the result, and in the case of ECD spectroscopy, the first double bond is worth being kept in models of molecules containing more than one isolated double bond in the side chain.[47]

The MMFF conformational search of (*S*)-3modMe and (*S*)-3modEt resulted in only 36 and 94 initial conformers in a 21 kJ/mol energy window. These structures were also reoptimized at the ωB97X/TZVP[29] PCM/MeOH level yielding 9 and 9 low-energy conformers over 1% Boltzmann population, respectively (Figures S70 and S71 of the Supporting Information). ECD spectra computed at various levels of theory for these conformers also gave acceptable to good agreement with the experimental ECD spectrum (Figure 5),

https://doi.org/10.1021/acs.jafc.3c00447
J. Agric. Food Chem. 2023, 71, 11056−11068

suggesting the same (1*S*) absolute configuration as the ECD calculations for the full structure.

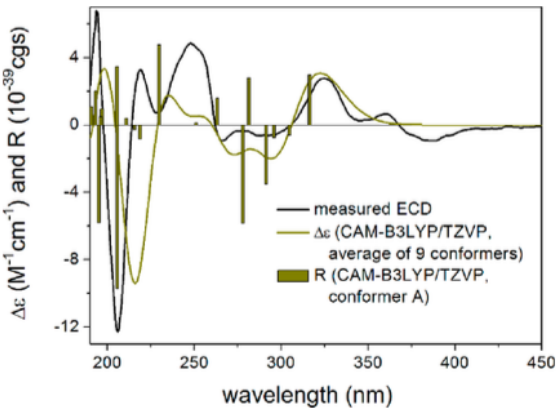


Figure 5. Experimental ECD spectrum of compound **3** in MeOH (black line) compared to the calculated CAM-B3LYP/TZVP PCM/MeOH spectrum of (*S*)-3modEt (dark yellow line). Level of DFT optimization: ωB97X/TZVP PCM/MeOH. Bars represent the rotational strengths of conformer A.

A strong level dependency was found for the applied combinations of methods for the truncated models, underscoring the importance to test several of them; the CAM-B3LYP and BH&HLYP functionals reproduced the position and splitting of the transitions better, while the PBE0 and B3LYP functionals reproduced the relative intensities of the 219 and 248 nm transitions better (Figures S72 and S73 of the Supporting Information). Although the experimental high-wavelength negative transition at 386 nm was not reproduced by the averaged ECD spectra, some low-energy conformers exhibited this transition with a blue shift (Figure S74 of the Supporting Information).

Specific optical rotation calculations of compound (1*S*,29*R*)-**3** were also carried out, which reproduced the experimental $[\alpha]_D$ value very well with Boltzmann-averaged OR values in the range from +62.1 to +96.6 produced with the four applied levels of theory. The B3LYP/TZVP PCM/MeOH//ωB97X/TZVP PCM/MeOH combination gave the best result with +96.6 versus +98.2 of the experimental value (Table S1 of the Supporting Information). Although computed OR values of the individual conformers ranged from −135 to +248, most conformers had positive optical rotation values, verifying the ECD results for the (1*S*) absolute configuration of compound **3**.

For the truncated models, we identified low-energy conformers with OR values ranging from −450 to +430 (Tables S2 and S3 of the Supporting Information). The computed average OR values for 3modEt were around 0, while for 3modMe, they were between +13 and +25. Although the sign of these latter conformers matches the experimental $[\alpha]_D$ value, the deviation of the intensity and especially the large range of the individual conformers did not allow for a solid configurational assignment on the basis of the OR calculations of this truncated model. However, the OR calculation of the truncated models revealed that the side chain and, hence, the C-29 chirality center had a significant effect on the OR value, which can be used to tentatively determine the absolute configuration of C-29.[48,49] To further strengthen this assumption, TDDFT−OR calculations were also performed on the C-29 epimer of compound **3**. The ωB97X/TZVP PCM/MeOH reoptimization of the initial 713 MMFF conformers yielded 21 low-energy conformers over 1% Boltzmann populations (Figure S75 of the Supporting Information). Boltzmann-averaged OR values, computed at the same four levels of theory as for compound (1*S*,29*R*)-**3**, gave specific optical rotation values for compound (1*S*,29*S*)-**3** in the range from +43.2 to +48.9 (Table S4 of the Supporting Information), confirming the above suggested (1*S*,29*R*) absolute configuration for compound **3**. As a conclusion, on the basis of the good agreement of the experimental OR value and the value computed for compound (1*S*,29*R*)-**3**, the (29*R*) absolute configuration was assigned in the side chain, which was also confirmed by the computed OR values of the (1*S*,29*S*) epimer.

On the basis of the HRESIMS data, the molecular formula of compound **4** was determined as $C_{36}H_{46}O_{10}$. The ^1H and ^{13}C NMR data of compound **4** (Table 1) revealed a structural similarity to that of compound **1**, except for the replacement of oxygenated methylene at C-33 (δ_H 4.12 and 4.06 and δ_C 59.7) of compound **1** by a carbonyl group (δ_C 169.2) in compound **4**, which was supported by the HMBCs from H-25 (δ_H 5.76) to C-33. The configurations of the three double bonds in compound **4** were elucidated as 17*E*, 21*E*, and 25*Z*, respectively, on the basis of the nuclear Overhauser effect (NOE) correlations between H-17/H_2-19, H-21/H_2-23 and H-25/H_2-27. The (1*R*) absolute configuration of compound **4** was determined on the basis of an ECD pattern in MeOH similar to that of compounds **1** and **3** (Figure S76 of the Supporting Information), showing positive Cotton effects at around 250 nm. The ECD spectra of compounds **4** and **1** in DMSO were near identical but different from those recorded in MeOH. Although the complexation with $Mo_2(OAc)_4$ showed some distinct changes in the ECD spectrum (Figure S77 of the Supporting Information), it could not be used to determine the absolute configuration of C-29. The failure to utilize the $Mo_2(OAc)_4$ complexation ECD method for the configurational assignment of the C-29 chirality center may raise the question of how reliable the previous assignments in the literature were performed on the side chain of phenalenone derivatives. The structure of compound **4**, named asperphenalenone I, was elucidated as drawn in Figure 1.

Compound **5** was obtained as brown gum with a molecular formula of $C_{42}H_{58}O_{14}$ as determined by HRESIMS. The ^1H and ^{13}C NMR data (Table 1) of compound **5** were similar to those of compound **1**, suggesting that they shared the same structural fragment from C-1 to C-35. The remaining NMR signals in compound **5** included five oxygenated methines and an oxygenated methylene (CH-1′ to 5′ and CH_2-6′), constructing an additional pyranoside unit in compound **5**, which was evident from the correlation spectroscopy (COSY) correlations between H-1′/H-2′/H-3′/H-4′/H-5′/H_2-6′ and the HMBCs from H-1′ to C-5′. Furthermore, the HMBCs from H-1′ (δ_H 4.47) to C-33 (δ_C 66.7) and from H_2-33 (δ_H 4.30) to C-1′ (δ_C 100.1) indicated that the pyranose residue was attached to C-33. By comparison of the experimental ECD spectra (Figure S78 of the Supporting Information), the (*R*) absolute configuration was suggested for C-1 and C-29 in compound **5** on the basis of compounds **1** and **3**. The structure of compound **5** was elucidated as drawn in Figure 1 and named asperphenalenone J.

https://doi.org/10.1021/acs.jafc.3c00447
J. Agric. Food Chem. 2023, 71, 11056−11068

Table 3. Anti-microbial Activities of Compounds 1−10[a]

	MIC (μM)									
strain	1	2	3	4	5	6	7	8	9	10
Staphylococcus aureus ATCC 25923	100	100	>100	>100	>100	>100	>100	>100	>100	>100
Staphylococcus aureus ATCC 700669	12.5	100	25	100	100	>100	50	>100	>100	>100
Enterococcus faecium ATCC 35667	25	50	>100	>100	>100	>100	>100	>100	>100	>100
Enterococcus faecalis ATCC 51299	50	100	>100	>100	>100	>100	>100	>100	>100	>100
Mycobacterium tuberculosis H37Rv	>100	>100	>100	>100	>100	>100	>100	>100	>100	>100
Candia albicans yeast form	>100	>100	>100	>100	>100	>100	>100	>100	>100	>100
Candia albicans hyphae form	>100	>100	>100	>100	>100	>100	>100	>100	>100	>100
SARS-CoV-2	>100	>100	>100	>100	>100	>100	>100	>100	>100	>100

[a]*Staphylococcus aureus* ATCC 700669, methicillin, oxacillin, and vancomycin resistance strains; *Staphylococcus aureus* ATCC 25923, standard strain; *Enterococcus faecium* ATCC 35667, standard strain; *Enterococcus faecalis* ATCC 51299, low-level vancomycin, amikacin, gentamycin, tobramycin, streptomycin resistance strains; *Candia albicans* ATCC 24433, standard strain; *Mycobacterium tuberculosis* H37Rv, standard strain; and SARS-CoV-2, clinical isolate strain.

The molecular formula of asperphenalenone K (**6**) was determined as $C_{41}H_{56}O_{14}$ by the HRESIMS data, missing a CH_2 unit when compared to compound **5**. The obvious difference between the NMR data of compounds **6** and **5** was the disappearance of signals of the methoxy group in compound **6**. Detailed analysis of the 2D NMR spectra indicated that C-7 was attached to a hydroxy group in compound **6** rather than a methoxy group in compound **5** (Figure 2). The ECD spectrum (Figure S79 of the Supporting Information) of compound **6** suggested (*S*) that the absolute configuration for C-1 and C-29 was assigned as (*R*) on the basis of compounds **2** and **3**. We next took advantage of the sufficient compound quantity of compound **6** to further characterize the pyranose constituent of this glycoconjugate. Hydrolysis and GC−MS analysis were carried out, and the pyranose residue was identified as D-mannose by comparison to reference sugars (Figure S80 of the Supporting Information). Furthermore, the coupling constant of H-1′ (0.8 Hz) and an α^D value of +21.7 corroborated identity of the pyranose residue as α-D-mannose.[50]

Asperphenalenone L (**7**) shared the same molecular formula as compound **5**. A comparison of their NMR data (Table 2) suggested that they are structurally similar. As expected, signals for the aromatic rings, the side chain, and the pyranose unit were observed. However, the big differences of the chemical shifts of C-1 and C-7 between compounds **5** and **7** (+2.5 and +3.4 ppm in compound **7**) suggested different locations of the methoxy group. The HMBC of the protons of the methoxy group (δ_H = 3.27) to C-1 (δ_C = 89.2) confirmed the attachment of the methoxy group at C-1 in compound **7** instead of C-7 in compound **5**. The ECD spectrum (Figure S81 of the Supporting Information) of compound **7** suggested that the absolute configuration of C-1 was identical to that of compound **6** and, thus, assigned as (*S*). The absolute configuration of C-29 was assigned as (*R*) on the basis of compound **6**. The structure of compound **7** was elucidated as drawn in Figure 1, and it was named asperphenalenone L.

Compound **8** gave a molecular formula of $C_{44}H_{60}O_{15}$ as determined by HRESIMS, thus differing from that of compound **5** by 42 additional mass units. This difference was accounted for by an additional acetyl group, which was evident from the presence of an additional carbonyl carbon (δ_C 172.6) and an additional methyl group (δ_H 2.05 and δ_C 20.7) in the NMR spectra of compound **8** (Table 2). The location of this acetyl group at C-6′ was confirmed by the HMBCs from the methyl group (δ_H 2.05) and deshielded H_2-6′ (δ_H 4.41 and 4.22) to carbonyl carbon (δ_C 172.6). The remaining structure of compound **8** was identical to that of compound **5**. The ECD spectrum (Figure S82 of the Supporting Information) of compound **8** suggested the (*S*) absolute configuration for C-1, and C-29 was assigned as (*R*) on the basis of compound **1**.

Although we could analyze the pyranose constituent in detail by GC−MS only for compound **6** as a result of restricted compound amounts, the high degree of similarity between compounds **5**−**8** suggests that the pyranose unit in all isolated glycoconjugates is likely D-mannose.

Compounds **1**−**5** and **7** exhibited significant activities against the tested Gram-positive bacteria *S. aureus* ATCC 29213, *S. aureus* ATCC 70669, *E. faecium* ATCC 35667, and *E. faecalis* ATCC 51299 (Table 3). Notably, compounds **1** and **2** showed pronounced activities against all tested strains, with compound **1** resulting in a MIC of 12.5 μM against MRSA. Compounds **1**−**8** did not display growth inhibitory activities against *M. tuberculosis* H37Rv and *C. albicans* as well as no antiviral effects on SARS-CoV-2 up to the maximal tested concentration. When tested for their cytotoxic activity against the human T lymphocyte Jurkat cell line, compounds **1** and **3** showed low cytotoxic potential, with IC_{50} values of 30.8 and 40 μM, respectively, while the other compounds were nearly not cytotoxic, even at the highest tested concentration (Figure 6). Because the known compound asperphenalenone A has been reported to exhibit antiviral activity against HIV,[20] we studied the effect of the compounds on inhibiting replication of HIV in infected Jurkat cells. While most compounds were devoid of any substantial antiviral effects, compound **10** (asperphenale-

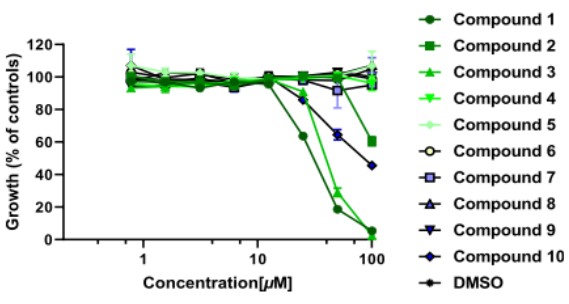


Figure 6. Cytotoxicity of compounds **1**−**10** against human T lymphocyte Jurkat cells. Compounds **1** and **3** showed cytotoxic effects at a high contraction of 50 μM, but the rest of the compounds were virtually devoid of cytotoxicity against Jurkat cells.

https://doi.org/10.1021/acs.jafc.3c00447
J. Agric. Food Chem. 2023, 71, 11056−11068

Table 3. Anti-microbial Activities of Compounds 1−10[a]

	MIC (μM)									
strain	1	2	3	4	5	6	7	8	9	10
Staphylococcus aureus ATCC 25923	100	100	>100	>100	>100	>100	>100	>100	>100	>100
Staphylococcus aureus ATCC 700669	12.5	100	25	100	100	>100	50	>100	>100	>100
Enterococcus faecium ATCC 35667	25	50	>100	>100	>100	>100	>100	>100	>100	>100
Enterococcus faecalis ATCC 51299	50	100	>100	>100	>100	>100	>100	>100	>100	>100
Mycobacterium tuberculosis H37Rv	>100	>100	>100	>100	>100	>100	>100	>100	>100	>100
Candia albicans yeast form	>100	>100	>100	>100	>100	>100	>100	>100	>100	>100
Candia albicans hyphae form	>100	>100	>100	>100	>100	>100	>100	>100	>100	>100
SARS-CoV-2	>100	>100	>100	>100	>100	>100	>100	>100	>100	>100

[a]*Staphylococcus aureus* ATCC 700669, methicillin, oxacillin, and vancomycin resistance strains; *Staphylococcus aureus* ATCC 25923, standard strain; *Enterococcus faecium* ATCC 35667, standard strain; *Enterococcus faecalis* ATCC 51299, low-level vancomycin, amikacin, gentamycin, tobramycin, streptomycin resistance strains; *Candia albicans* ATCC 24433, standard strain; *Mycobacterium tuberculosis* H37Rv, standard strain; and SARS-CoV-2, clinical isolate strain.

The molecular formula of asperphenalenone K (**6**) was determined as $C_{41}H_{56}O_{14}$ by the HRESIMS data, missing a CH_2 unit when compared to compound **5**. The obvious difference between the NMR data of compounds **6** and **5** was the disappearance of signals of the methoxy group in compound **6**. Detailed analysis of the 2D NMR spectra indicated that C-7 was attached to a hydroxy group in compound **6** rather than a methoxy group in compound **5** (Figure 2). The ECD spectrum (Figure S79 of the Supporting Information) of compound **6** suggested (*S*) that the absolute configuration for C-1 and C-29 was assigned as (*R*) on the basis of compounds **2** and **3**. We next took advantage of the sufficient compound quantity of compound **6** to further characterize the pyranose constituent of this glycoconjugate. Hydrolysis and GC−MS analysis were carried out, and the pyranose residue was identified as D-mannose by comparison to reference sugars (Figure S80 of the Supporting Information). Furthermore, the coupling constant of H-1′ (0.8 Hz) and an α^D value of +21.7 corroborated identity of the pyranose residue as α-D-mannose.[50]

Asperphenalenone L (**7**) shared the same molecular formula as compound **5**. A comparison of their NMR data (Table 2) suggested that they are structurally similar. As expected, signals for the aromatic rings, the side chain, and the pyranose unit were observed. However, the big differences of the chemical shifts of C-1 and C-7 between compounds **5** and **7** (+2.5 and +3.4 ppm in compound **7**) suggested different locations of the methoxy group. The HMBC of the protons of the methoxy group (δ_H = 3.27) to C-1 (δ_C = 89.2) confirmed the attachment of the methoxy group at C-1 in compound **7** instead of C-7 in compound **5**. The ECD spectrum (Figure S81 of the Supporting Information) of compound **7** suggested that the absolute configuration of C-1 was identical to that of compound **6** and, thus, assigned as (*S*). The absolute configuration of C-29 was assigned as (*R*) on the basis of compound **6**. The structure of compound **7** was elucidated as drawn in Figure 1, and it was named asperphenalenone L.

Compound **8** gave a molecular formula of $C_{44}H_{60}O_{15}$ as determined by HRESIMS, thus differing from that of compound **5** by 42 additional mass units. This difference was accounted for by an additional acetyl group, which was evident from the presence of an additional carbonyl carbon (δ_C 172.6) and an additional methyl group (δ_H 2.05 and δ_C 20.7) in the NMR spectra of compound **8** (Table 2). The location of this acetyl group at C-6′ was confirmed by the HMBCs from the methyl group (δ_H 2.05) and deshielded H_2-6′ (δ_H 4.41 and 4.22) to carbonyl carbon (δ_C 172.6). The remaining structure of compound **8** was identical to that of compound **5**. The ECD spectrum (Figure S82 of the Supporting Information) of compound **8** suggested the (*S*) absolute configuration for C-1, and C-29 was assigned as (*R*) on the basis of compound **1**.

Although we could analyze the pyranose constituent in detail by GC−MS only for compound **6** as a result of restricted compound amounts, the high degree of similarity between compounds **5**−**8** suggests that the pyranose unit in all isolated glycoconjugates is likely D-mannose.

Compounds **1**−**5** and **7** exhibited significant activities against the tested Gram-positive bacteria *S. aureus* ATCC 29213, *S. aureus* ATCC 70669, *E. faecium* ATCC 35667, and *E. faecalis* ATCC 51299 (Table 3). Notably, compounds **1** and **2** showed pronounced activities against all tested strains, with compound **1** resulting in a MIC of 12.5 μM against MRSA. Compounds **1**−**8** did not display growth inhibitory activities against *M. tuberculosis* H37Rv and *C. albicans* as well as no antiviral effects on SARS-CoV-2 up to the maximal tested concentration. When tested for their cytotoxic activity against the human T lymphocyte Jurkat cell line, compounds **1** and **3** showed low cytotoxic potential, with IC_{50} values of 30.8 and 40 μM, respectively, while the other compounds were nearly not cytotoxic, even at the highest tested concentration (Figure 6). Because the known compound asperphenalenone A has been reported to exhibit antiviral activity against HIV,[20] we studied the effect of the compounds on inhibiting replication of HIV in infected Jurkat cells. While most compounds were devoid of any substantial antiviral effects, compound **10** (asperphenale-

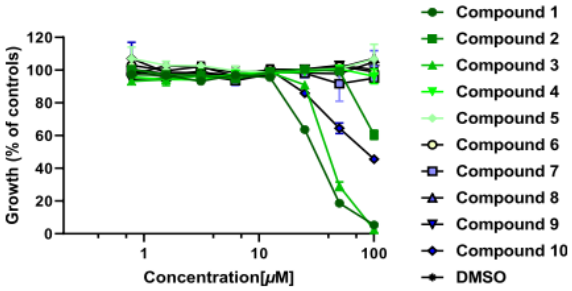


Figure 6. Cytotoxicity of compounds **1**−**10** against human T lymphocyte Jurkat cells. Compounds **1** and **3** showed cytotoxic effects at a high contraction of 50 μM, but the rest of the compounds were virtually devoid of cytotoxicity against Jurkat cells.

https://doi.org/10.1021/acs.jafc.3c00447
J. Agric. Food Chem. 2023, 71, 11056−11068

none B) showed low anti-HIV activity, resulting in ca. 70% decrease in viral transcript in treated HIV-infected Jurkat cells, whereas compound **9** (asperphenalenone E) even seemed to promote viral replication (Figure 7). In comparison to

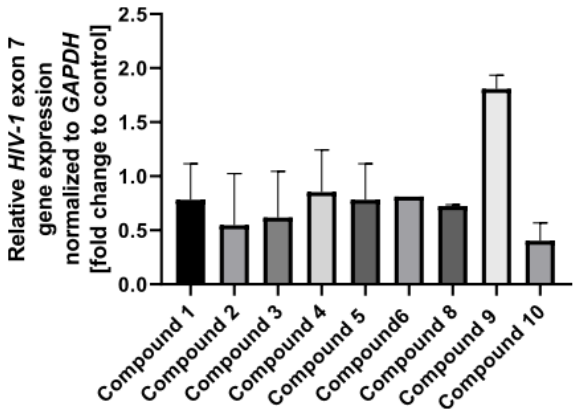


Figure 7. Inhibitory effects of isolated compounds on HIV-1 RNA replication in infected Jurkat cells. Compounds were tested at subcytotoxic concentrations, as estimated from Figure 6. Compound **10** showed inhibitory activity leading to ca. 70% decrease in viral RNA at a concentration of 50 μM.

asperphenalenone A, which displayed an IC_{50} value of 4.5 μM in an assay employing a VSV-G pseudotyped HIV-1,[20] the anti-HIV effect of compound **10** was relatively low (70% inhibition at 50 μM). In comparison to the structure of asperphenalenone A, compound **10** has a carboxylate function at position C-33 instead of a hydroxyl group and an additional hydroxyl group substitution at C-30, suggesting that the increased polarity of compound **10** might impair the anti-HIV activity.

In conclusion, eight new compounds **1**−**8** along with two known derivatives, were obtained from the rice culture of the endophytic fungus *C. rosea*. The sugar constituent of glycosylated compounds **5**−**8** was identified as α-D-mannose by GC−MS analysis of hydrolysis products and optical rotation determination. Remarkably, this is the first report on glycosides being isolated from the rice culture of *C. rosea*, further expanding the diversity of natural compounds produced by this organism. In bioactivity screenings, compounds **1** and **2** showed pronounced antibacterial activities against sensitive and drug-resistant isolates of the Gram-positive pathogens *S. aureus*, *E. faecalis*, and *E. faecium*. In a previous study, structurally related asperphenalenone derivatives isolated from an endophytic *Aspergillus* sp. exhibited not only antibacterial activity against Gram-positive bacteria but also antibacterial activity against Gram-negative bacteria, such as *Pseudomonas aeruginosa* and *Escherichia coli*.[29] However, we could not detect any antibacterial properties of compounds **1**−**8** against these two Gram-negative bacteria. Another asperphenalenone derivative isolated from *Aspergillus* sp., aspergillussanone A, displayed cytotoxic activity against human oral carcinoma (KB) cell lines[28] as well as anti-HIV activity.[20] In our study, however, compounds **1**−**8** were largely devoid of substantial cytotoxic or anti-HIV properties. Concerning antibacterial activities, compounds **1**, **2**, and **3** showed significant activities against MRSA and *E. faecium*, with compound **1** showing the strongest activities, with MICs of 12.5 and 25 μM, respectively. In contrast, compound **9**, which only differs in positions C-1 and C-7 compared to compounds **1** and **2**, was inactive. Thus, from the structure−activity relationship aspect, substitution by a methoxy group at positions C-1 and C-7 is obviously crucial for antibacterial activity. However, also, the side chain plays an indispensable role as well. If position C-33 was glycosylated, the activity against MRSA decreased from 12.5 to 100 μM when comparing compounds **1** and **7**, and the same trend was seen when comparing the activity of compounds **2** and **8**. In summary, asperphenalenone derivatives from the biocontrol agent *C. rosea* might offer structural scaffolds to develop new antibiotics and anti-HIV drugs.

■ ASSOCIATED CONTENT

Supporting Information

The Supporting Information is available free of charge at https://pubs.acs.org/doi/10.1021/acs.jafc.3c00447.

Extraction and isolation, Figures S1−S82, and Tables S1−S5 (PDF)

■ AUTHOR INFORMATION

Corresponding Authors

Tibor Kurtán − *Department of Organic Chemistry, University of Debrecen, 4002 Debrecen, Hungary;* orcid.org/0000-0002-8831-8499; Email: kurtan.tibor@science.unideb.hu

Zhen Liu − *Key Laboratory of Study and Discovery of Small Targeted Molecules of Hunan Province, School of Medicine, Hunan Normal University, Changsha, Hunan 410013, People's Republic of China;* orcid.org/0000-0003-3314-7853; Email: zhenfeizi0@sina.com

Rainer Kalscheuer − *Institute of Pharmaceutical Biology and Biotechnology, Heinrich Heine University Düsseldorf, 40225 Düsseldorf, Germany;* orcid.org/0000-0002-3378-2067; Email: rainer.kalscheuer@hhu.de

Authors

Lin Wang − *Institute of Pharmaceutical Biology and Biotechnology, Heinrich Heine University Düsseldorf, 40225 Düsseldorf, Germany*

Anna-Lene Kiffe-Delf − *Institute of Pharmaceutical Biology and Biotechnology, Heinrich Heine University Düsseldorf, 40225 Düsseldorf, Germany*

Philipp Niklas Ostermann − *Institute of Virology, University Hospital Düsseldorf, Heinrich Heine University Düsseldorf, 40225 Düsseldorf, Germany*

Viktor Emanuel Simons − *Institute of Pharmaceutical Biology and Biotechnology, Heinrich Heine University Düsseldorf, 40225 Düsseldorf, Germany*

Di He − *Institute of Pharmaceutical Biology and Biotechnology, Heinrich Heine University Düsseldorf, 40225 Düsseldorf, Germany*

Ying Gao − *Institute of Pharmaceutical Biology and Biotechnology, Heinrich Heine University Düsseldorf, 40225 Düsseldorf, Germany*

Lasse van Geelen − *Institute of Pharmaceutical Biology and Biotechnology, Heinrich Heine University Düsseldorf, 40225 Düsseldorf, Germany*

Hao-Fu Dai − *Institute of Tropical Bioscience and Biotechnology, Chinese Academy of Tropical Agricultural Sciences, Haikou, Hainan 571101, People's Republic of China*

You-Xing Zhao – *Institute of Tropical Bioscience and Biotechnology, Chinese Academy of Tropical Agricultural Sciences, Haikou, Hainan 571101, People's Republic of China;* orcid.org/0000-0002-8107-2510

Heiner Schaal – *Institute of Virology, University Hospital Düsseldorf, Heinrich Heine University Düsseldorf, 40225 Düsseldorf, Germany*

Attila Mándi – *Department of Organic Chemistry, University of Debrecen, 4002 Debrecen, Hungary;* orcid.org/0000-0002-7867-7084

Sándor Balázs Király – *Department of Organic Chemistry, University of Debrecen, 4002 Debrecen, Hungary*

Complete contact information is available at: https://pubs.acs.org/10.1021/acs.jafc.3c00447

Funding

This work was financially supported by the China Scholarship Council, the Ministry of Education of China, for a doctoral scholarship awarded to Lin Wang. Rainer Kalscheuer acknowledges financial support from the Stiftung zur Erforschung infektiös-immunologischer Erkrankungen. Zhen Liu thanks the Intra Institutional Open Fund of School of Medicine, Hunan Normal University (KF2022001) and the Changsha Municipal Natural Science Foundation (kq2202257) for support. This work was further supported by the Jürgen Manchot Foundation (to Philipp Niklas Ostermann and Heiner Schaal) and the Forschungskommission Düsseldorf (FoKo, to Heiner Schaal). The research work of Tibor Kurtán and Attila Mándi was supported by the National Research, Development and Innovation Office (K138672 and FK134653). The Governmental Information-Technology Development Agency (KIFÜ) is acknowledged for central processing unit (CPU) time. The authors thank the Center for Molecular and Structural Analytics@Heinrich Heine University (CeMSA@HHU) for recording the mass spectrometric and NMR spectroscopic data.

Notes

The authors declare no competing financial interest.

REFERENCES

(1) Toledo, A. V.; Virla, E.; Humber, R. A.; Paradell, S. L.; López Lastra, C. C. First record of *Clonostachys rosea* (Ascomycota: Hypocreales) as an entomopathogenic fungus of *Oncometopia tucumana* and *Sonesimia grossa* (Hemiptera: Cicadellidae) in Argentina. *J. Invertebr. Pathol.* **2006**, *92*, 7–10.

(2) Roberti, R.; Veronesi, A.; Cesari, A.; Cascone, A.; Di Berardino, I.; Bertini, L.; Caruso, C. Induction of PR proteins and resistance by the biocontrol agent *Clonostachys rosea* in wheat plants infected with *Fusarium culmorum*. *Plant Sci.* **2008**, *175*, 339–347.

(3) Morandi, M. A. B.; Mattos, L. P. V.; Santos, E. R.; Bonugli, R. C. Influence of application time on the establishment, survival, and ability of *Clonostachys rosea* to suppress *Botrytis cinerea* sporulation on rose debris. *Crop Prot.* **2008**, *27*, 77–83.

(4) Cota, L. V.; Maffia, L. A.; Mizubuti, E. S. G.; Macedo, P. E. F.; Antunes, R. F. Biological control of strawberry gray mold by *Clonostachys rosea* under field conditions. *Biol. Control* **2008**, *46*, 515–522.

(5) Xue, A. G.; Chen, Y. H.; Voldeng, H. D.; Fedak, G.; Savard, M. E.; Längle, T.; Zhang, J. X.; Harman, G. E. Concentration and cultivar effects on efficacy of CLO-1 biofungicide in controlling *Fusarium* head blight of wheat. *Biol. Control* **2014**, *73*, 2–7.

(6) Kosawang, C.; Karlsson, M.; Vélëz, H.; Rasmussen, P. H.; Collinge, D. B.; Jensen, B.; Jensen, D. F. Zearalenone detoxification by zearalenone hydrolase is important for the antagonistic ability of *Clonostachys rosea* against mycotoxigenic *Fusarium graminearum*. *Fungal Biol.* **2014**, *118*, 364–373.

(7) Bennett, A. J.; Mead, A.; Whipps, J. M. Performance of carrot and onion seed primed with beneficial microorganisms in glasshouse and field trials. *Biol. Control* **2009**, *51*, 417–426.

(8) Kapongo, J. P.; Shipp, L.; Kevan, P.; Sutton, j. C. Co-vectoring of *Beauveria bassiana* and *Clonostachys rosea* by bumble bees (*Bombus impatiens*) for control of insect pests and suppression of grey mould in greenhouse tomato and sweet pepper. *Biol. Control* **2008**, *46*, 508–514.

(9) Baloyi, M. A.; Laing, M. D.; Yobo, K. S. Use of mixed cultures of biocontrol agents to control sheep nematodes. *Vet. Parasitology* **2012**, *184*, 367–370.

(10) Ahmed, M.; Laing, M. D.; Nsahlai, I. V. Use of *Clonostachys rosea* against sheep nematodes developing in pastures. *Biocontrol Sci. Technol.* **2014**, *24*, 389–398.

(11) Zhai, M. M.; Qi, F. M.; Li, J.; Jiang, C. X.; Hou, Y.; Shi, Y. P.; Di, D. L.; Zhang, J. W.; Wu, Q. X. Isolation of secondary metabolites from the soil-derived fungus *Clonostachys rosea* yrs-06, a biological control agent, and evaluation of antibacterial activity. *J. Agric. Food Chem.* **2016**, *64*, 2298–2306.

(12) Supratman, U.; Suzuki, T.; Nakamura, T.; Yokoyama, Y.; Harneti, D.; Maharani, R.; Salam, S.; Abdullah, F. F.; Koseki, T.; Shiono, Y. New metabolites produced by endophyte *Clonostachys rosea* BS–2. *Nat. Prod. Res.* **2021**, *35*, 1525–1531.

(13) Abdel-Wahab, N. M.; Harwoko, H.; Müller, W. E. G.; Hamacher, A.; Kassack, M. U.; Fouad, M. A.; Kamel, M. S.; Lin, W. H.; Ebrahim, W.; Liu, Z.; Proksch, P. Cyclic heptapeptides from the soil-derived fungus *Clonostachys rosea*. *Bioorg. Med. Chem.* **2019**, *27*, 3954–3959.

(14) Okuda, T.; Kohno, J.; Kishi, N.; Asai, Y.; Nishio, M.; Komatsubara, S. Production of TMC-151, TMC-154 and TMC-171, a new class of antibiotics, is specific to 'gliocladium roseum' group. *Mycoscience* **2000**, *41*, 239–253.

(15) Dos Santos Dias, A. C.; Couzinet-Mossion, A.; Ruiz, N.; Lakhdar, F.; Etahiri, S.; Bertrand, S.; Ory, L.; Roussakis, C.; Pouchus, Y. F.; Nazih, E.-H.; Wielgosz-Collin, G. Steroids from marine-derived fungi: Evaluation of antiproliferative and antimicrobial activities of eburicol. *Mar. Drugs* **2019**, *17*, 372.

(16) Jiang, C.-X.; Yu, B.; Miao, Y.-M.; Ren, H.; Xu, Q.; Zhao, C.; Tian, L.-L.; Yu, Z.-Q.; Zhou, P.-P.; Wang, X.; Fang, J.; Zhang, J.; Zhang, J. Z.; Wu, Q.-X. Indole alkaloids from a soil-derived *Clonostachys rosea*. *J. Nat. Prod.* **2021**, *84*, 2468–2474.

(17) Gao, C.; Fan, Y. L.; Zhao, F.; Ren, Q. C.; Wu, X.; Chang, L.; Gao, F. Quinolone derivatives and their activities against methicillin-resistant *Staphylococcus aureus* (MRSA). *Eur. J. Med. Chem.* **2018**, *157*, 1081–1095.

(18) Drougka, E.; Foka, A.; Liakopoulos, A.; Doudoulakakis, A.; Jelastopulu, E.; Chini, V.; Spiliopoulou, A.; Levidiotou, S.; Panagea, T.; Vogiatzi, A.; Lebessi, E.; Petinaki, E.; Spiliopoulou, I. A 12-year survey of methicillin-resistant *Staphylococcus aureus* infections in Greece: ST80-IV Epidemic? *Clin. Microbial. Infect.* **2014**, *20*, O796–O803.

(19) Kjer, J.; Debbab, A.; Aly, A. H.; Proksch, P. Methods for isolation of marine-derived endophytic fungi and their bioactive secondary products. *Nat. Protoc.* **2010**, *5*, 479–490.

(20) Pang, X.; Zhao, J. Y.; Fang, X. M.; Zhang, T.; Zhang, D. W.; Liu, H. Y.; Su, J.; Cen, S.; Yu, L. Y. Metabolites from the plant endophytic fungus *Aspergillus sp.* CPCC 400735 and their anti-HIV activities. *J. Nat. Prod.* **2017**, *80*, 2595–2601.

(21) Elnaggar, M. S.; Ebrahim, W.; Mándi, A.; Kurtán, T.; Müller, W. E. G.; Kalscheuer, R.; Singab, A.; Lin, W. H.; Liu, Z.; Proksch, P. Hydroquinone derivatives from the marine-derived fungus *Gliomastix* sp. *RSC Adv.* **2017**, *7*, 30640–30649.

(22) Kozłowicz, K.; Różyło, R.; Gładyszewska, B.; Matwijczuk, A.; Gładyszewski, G.; Chocyk, D.; Samborska, K.; Piekut, J.; Smolewska, M. Identifcation of sugars and phenolic compounds in honey powders with the use of GC–MS, FTIR spectroscopy, and X-ray diffraction. *Sci. Rep.* **2020**, *10*, 16269.

(23) Clinical and Laboratory Standards Institute (CLSI). Methods for Dilution Antimicrobial Susceptibility Tests for Bacteria That Grow Aerobically. *CLSI Standard M07*, 11th ed.; CLSI: Wayne, PA, 2018.
(24) Gao, Y.; Wang, L.; Kalscheuer, R.; Liu, Z.; Proksch, P. Antifungal polyketide derivatives from the endophytic fungus *Aplosporella javeedii*. *Bioorg. Med. Chem.* **2020**, *28*, 115456.
(25) Rehberg, N.; Sommer, G. A.; Drießen, D.; Kruppa, M.; Adeniyi, E. T.; Chen, S.; Wang, L.; Wolf, K.; Tasch, B. O. A.; Ioerger, T. R.; Zhu, K.; Müller, J. J. T.; Kalscheuer, R. Nature-inspired (di)azine-bridged bisindole alkaloids with potent antibacterial in vitro and in vivo efficacy against methicillin-resistant *Staphylococcus aureus*. *J. Med. Chem.* **2020**, *63*, 12623−12641.
(26) Schmittgen, T. D.; Livak, K. J. Analyzing real-time PCR data by the comparative CT method. *Nat. Prot.* **2008**, *3*, 1101−1108.
(27) Adachi, A.; Gendelman, H. E.; Koenig, S.; Folks, T.; Willey, R.; Rabson, A.; Martin, M. A. Production of acquired immunodeficiency syndrome-associated retrovirus in human and nonhuman cells transfected with an infectious molecular clone. *J. Virol.* **1986**, *59*, 284−291.
(28) Schrödinger, LLC. *MacroModel*; Schrödinger, LLC: New York, 2015; http://www.schrodinger.com/MacroModel.
(29) Chai, J.-D.; Head-Gordon, M. Systematic optimization of long-range corrected hybrid density functionals. *J. Chem. Phys.* **2008**, *128*, 084106.
(30) Frisch, M. J.; Trucks, G. W.; Schlegel, H. B.; Scuseria, G. E.; Robb, M. A.; Cheeseman, J. R.; Scalmani, G.; Barone, V.; Mennucci, B.; Petersson, G. A.; Nakatsuji, H.; Caricato, M.; Li, X.; Hratchian, H. P.; Izmaylov, A. F.; Bloino, J.; Zheng, G.; Sonnenberg, J. L.; Hada, M.; Ehara, M.; Toyota, K.; Fukuda, R.; Hasegawa, J.; Ishida, M.; Nakajima, T.; Honda, Y.; Kitao, O.; Nakai, H.; Vreven, T.; Montgomery, J. A., Jr.; Peralta, J. E.; Ogliaro, F.; Bearpark, M.; Heyd, J. J.; Brothers, E.; Kudin, K. N.; Staroverov, V. N.; Kobayashi, R.; Normand, J.; Raghavachari, K.; Rendell, A.; Burant, J. C.; Iyengar, S. S.; Tomasi, J.; Cossi, M.; Rega, N.; Millam, J. M.; Klene, M.; Knox, J. E.; Cross, J. B.; Bakken, V.; Adamo, C.; Jaramillo, J.; Gomperts, R.; Stratmann, R. E.; Yazyev, O.; Austin, A. J.; Cammi, R.; Pomelli, C.; Ochterski, J. W.; Martin, R. L.; Morokuma, K.; Zakrzewski, V. G.; Voth, G. A.; Salvador, P.; Dannenberg, J. J.; Dapprich, S.; Daniels, A. D.; Farkas, Ö.; Foresman, J. B.; Ortiz, J. V.; Cioslowski, J.; Fox, D. J. *Gaussian 09, Revision E.01*; Gaussian, Inc.: Wallingford, CT, 2013.
(31) Stephens, P. J.; Harada, N. ECD cotton effect approximated by the Gaussian curve and other methods. *Chirality* **2010**, *22*, 229−233.
(32) Varetto, U. *MOLEKEL 5.4*; Swiss National Supercomputing Centre: Manno, Switzerland, 2009.
(33) Rukachaisirikul, V.; Rungsaiwattana, N.; Klaiklay, S.; Phongpaichit, S.; Borwornwiriyapan, K.; Sakayaroj, J. γ-Butyrolactone, cytochalasin, cyclic carbonate, eutypinic acid, and phenalenone derivatives from the soil fungus *Aspergillus sp*. PSURSPG185. *J. Nat. Prod.* **2014**, *77*, 2375−2382.
(34) Gombodorj, S.; Yang, M. H.; Shang, Z. C.; Liu, R. H.; Li, T. X.; Yin, G. P.; Kong, L. Y. New phenalenone derivatives from *Pinellia ternata* tubers derived *Aspergillus* sp. *Fitoterapia* **2017**, *120*, 72−78.
(35) Di Bari, L.; Pescitelli, G.; Pratelli, C.; Pini, D.; Salvadori, P. Determination of Absolute Configuration of Acyclic 1,2-Diols with $Mo_2(OAc)_4$. 1. Snatzke's Method Revisited. *J. Org. Chem.* **2001**, *66* (14), 4819−4825.
(36) Górecki, M.; Jabłońska, E.; Kruszewska, A.; Suszczyńska, A.; Urbańczyk-Lipkowska, Z.; Gerards, M.; Morzycki, J. W.; Szczepek, W. J.; Frelek, J. Practical Method for the Absolute Configuration Assignment of *tert/tert* 1,2-Diols Using Their Complexes with $Mo_2(OAc)_4$. *J. Org. Chem.* **2007**, *72* (8), 2906−2916.
(37) Gombodorj, S.; Yang, M.-H.; Shang, Z.-C.; Liu, R.-H.; Li, T.-X.; Yin, G.-P.; Kong, L.-Y. New phenalenone derivatives from *Pinellia ternata* tubers derived *Aspergillus* sp. *Fitoterapia* **2017**, *120*, 72−78.
(38) Rukachaisirikul, V.; Rungsaiwattana, N.; Klaiklay, S.; Phongpaichit, S.; Borwornwiriyapan, K.; Sakayaroj, J. γ-Butyrolactone, Cytochalasin, Cyclic Carbonate, Eutypinic Acid, and Phenalenone Derivatives from the Soil Fungus *Aspergillus* sp. PSU-RSPG185. *J. Nat. Prod.* **2014**, *77* (11), 2375−2382.
(39) Komatsu, K.; Shigemori, H.; Mikami, Y.; Kobayashi, J. Sculezonones A and B, two metabolites possessing a phenalenone skeleton from a marine-derived fungus *Penicillium Species*. *J. Nat. Prod.* **2000**, *63*, 408−409.
(40) Mándi, A.; Kurtán, T. Applications of OR/ECD/VCD to the structure elucidation of natural products. *Nat. Prod. Rep.* **2019**, *36*, 889−918.
(41) Bremond, E.; Savarese, M.; Su, N. Q.; Perez-Jimenez, A. J.; Xu, X.; Sancho-Garcia, J. C.; Adamo, C. Benchmarking density functionals on structural parameters of small-/medium-sized organic molecules. *J. Chem. Theory Comput.* **2016**, *12*, 459−465.
(42) Zhou, Y.; Mándi, A.; Debbab, A.; Wray, V.; Schulz, B.; Müller, W. E. G.; Lin, W. H.; Proksch, P.; Kurtán, T.; Aly, A. H. *Eur. J. Org. Chem.* **2011**, *2011*, 6009−6019.
(43) Sun, P.; Xu, D. X.; Mándi, A.; Kurtán, T.; Li, T. J.; Schulz, B.; Zhang, W. *J. Org. Chem.* **2013**, *78*, 7030−7047.
(44) Yuan, J. Z.; Yang, Y. L.; Li, W.; Yang, L.; Dai, H. F.; Mándi, A.; Cai, C. H.; Chen, H. Q.; Dong, W. H.; Kurtán, T.; Mei, W. L.; Wang, H. *Molecules* **2022**, *27*, 198.
(45) Hou, X. F.; Yao, S.; Mándi, A.; Kurtán, T.; Tang, C. P.; Ke, C. Q.; Li, X. Q.; Ye, Y. Bicunningines A and B, two new dimeric diterpenes from *Cunninghamia lanceolata*. *Org. Lett.* **2012**, *14*, 460−463.
(46) Gao, Y.; Stuhldreier, F.; Schmitt, L.; Wesselborg, S.; Guo, Z.; Zou, K.; Mándi, A.; Kurtán, T.; Liu, Z.; Proksch, P. Induction of new lactam derivatives from the endophytic fungus *Aplosporella javeedii* Through an OSMAC Approach. *Front. Microbiol.* **2020**, *11*, 600983.
(47) Mándi, A.; Swamy, M. M. M.; Taniguchi, T.; Anetai, M.; Monde, K. Reducing molecular flexibility by cyclization for elucidation of absolute configuration by CD calculations: Daurichromenic acid. *Chirality* **2016**, *28*, 453−459.
(48) Csupor, D.; Kurtán, T.; Vollár, M.; Kúsz, N.; Kövér, K. E.; Mándi, A.; Szűcs, P.; Marschall, M.; Senobar Tahaei, S. A.; Zupkó, I.; Hohmann, J. Pigments of the moss *Paraleucobryum longifolium*: Isolation and Structure Elucidation of prenyl-substituted 8,8′-linked 9,10-Phenanthrenequinone Dimers. *J. Nat. Prod.* **2020**, *83*, 268−276.
(49) Sun, P.; Yu, Q.; Li, J.; Riccio, R.; Lauro, G.; Bifulco, G.; Kurtán, T.; Mándi, A.; Tang, H.; Li, T.-J.; Zhuang, C.-L.; Gerwick, W. H.; Zhang, W. Bissubvilides A and B, cembrane−capnosane heterodimers from the soft coral *Sarcophyton subviride*. *J. Nat. Prod.* **2016**, *79*, 2552−2558.
(50) Steinhardt, R. G., Jr.; Calvin, A. D.; Dodd, E. A. Taste-structure correlation with α-D-mannose and β-D-mannose. *Science* **1962**, *135*, 367−368.

Supporting Information

Lin Wang, [1] Anna-Lene Kiffe-Delf, [1] Philipp Niklas Ostermann, [2] Viktor Emanuel Simons, [1] Di He, [1] Ying Gao, [1] Lasse van Geelen, [1] Hao-Fu Dai, [3] You-Xing Zhao, [3] Heiner Schaal, [2] Attila Mándi, [4] Sándor Balázs Király, [4] Tibor Kurtán, [4,*] Zhen Liu, [5,*] Rainer Kalscheuer[1,*]

[1] Institute of Pharmaceutical Biology and Biotechnology, Heinrich Heine University Düsseldorf, Universitätsstrasse 1, 40225 Düsseldorf, Germany

[2] Institute of Virology, University Hospital Düsseldorf, Heinrich Heine University Düsseldorf, Universitätsstrasse 1, 40225 Düsseldorf, Germany

[3] Institute of Tropical Bioscience and Biotechnology, Chinese Academy of Tropical Agricultural Sciences, Haikou 571101, China

[4] Department of Organic Chemistry, University of Debrecen, Egyetem tér 1, 4002 Debrecen P.O.B. 400, Hungary

[5] Key Laboratory of Study and Discovery of Small Targeted Molecules of Hunan Province, School of Medicine, Hunan Normal University, Changsha 410013, China

[*]Corresponding authors. E-mail address:

Tibor Kurtán: kurtan.tibor@science.unideb.hu; ORCID ID orcid.org/0000-0002-8831-8499

Zhen Liu: zhenfeizi0@sina.com; ORCID ID orcid.org/0000-0003-3314-7853

Rainer Kalscheuer: rainer.kalscheuer@hhu.de; ORCID ID orcid.org/0000-0002-3378-2067

Table of Contents

Extraction and isolation 6

Fig. S1. Dose-response curves against *S. aureus* MRSA with fractions and sub-tractions. Growth (% of control) was quantified by resazurin dye reduction assay. **A**: Activity of VCL fractions from crude extract. **B**: Activity of sub-fractions originating from chromatography of fraction 6 on Sephadex LH-20. **C**: Activity of sub-fractions originating from VCL of subfraction 6.1. 7

Fig. S2. HRESIMS of Compound 1 8

Fig. S3. ^{1}H NMR spectrum of Compound **1** 9

Fig. S4. ^{1}H-^{13}C HSQC of Compound **1** 10

Fig. S5. ^{1}H-^{13}C HMBC of Compound **1** 10

Fig. S6. ^{1}H-^{1}H COSY of Compound **1** 11

Fig. S7. ^{1}H-^{1}H ROESY of Compound **1** 11

Fig. S8. HRESIMS of Compound **2** 12

Fig. S9. ^{1}H NMR spectrum of Compound **2** 13

Fig. S10. ^{1}H-^{13}C HSQC of Compound **2** 14

Fig. S11. ^{1}H-^{13}C HMBC of Compound **2** 14

Fig. S12. ^{1}H-^{1}H COSY of Compound **2** 15

Fig. S13. ^{1}H-^{1}H ROESY of Compound **2** 15

Fig. S14. HRESIMS of Compound **3** 16

Fig. S15. ^{1}H NMR spectrum of Compound **3** 17

Fig. S16. ^{13}C NMR of Compound **3** 17

Fig. S17. ^{1}H-^{13}C HSQC of Compound **3** 18

Fig. S18. ^{1}H-^{13}C HMBC of Compound **3** 18

Fig. S19. ^{1}H-^{1}H COSY of Compound **3** 19

Fig. S20. ^{1}H-^{1}H ROESY of Compound **3** 19

Fig. S21. HRESIMS of Compound **4** 20

Fig. S22. ^{1}H NMR spectrum of Compound **4** 21

Fig. S23. ^{13}C NMR of Compound **4** 21

Fig. S24. ^{1}H-^{13}C HSQC of Compound **4** 22
Fig. S25. ^{1}H-^{13}C HMBC of Compound **4** 22
Fig. S26. ^{1}H-^{1}H COSY of Compound **4** 23
Fig. S27. ^{1}H-^{1}H ROESY of Compound **4** 23
Fig. S28. HRESIMS of Compound **5** 24
Fig. S29. ^{1}H NMR spectrum of Compound **5** 25
Fig. S30. ^{13}C NMR of Compound **5** 25
Fig. S31. ^{1}H-^{13}C HSQC of Compound **5** 26
Fig. S32. ^{1}H-^{13}C HMBC of Compound **5** 26
Fig. S33. ^{1}H-^{1}H COSY of Compound **5** 27
Fig. S34. ^{1}H-^{1}H ROESY of Compound **5** 27
Fig. S35. HRESIMS of Compound **6** 28
Fig. S36. ^{1}H NMR spectrum of Compound **6** 29
Fig. S37. ^{13}C NMR of Compound **6** 29
Fig. S38. ^{1}H-^{13}C HSQC of Compound **6** 30
Fig. S39. ^{1}H-^{13}C HMBC of Compound **6** 30
Fig. S40. ^{1}H-^{1}H COSY of Compound **6** 31
Fig. S41. ^{1}H-^{1}H ROESY of Compound **6** 31
Fig. S42. HRESIMS of Compound **7** 32
Fig. S43. ^{1}H NMR spectrum of Compound **7** 33
Fig. S44. ^{1}H-^{13}C HSQC of Compound **7** 33
Fig. S45. ^{1}H-^{13}C HMBC of Compound **7** 34
Fig. S46. ^{1}H-^{1}H COSY of Compound **7** 34
Fig. S47. ^{1}H-^{1}H ROESY of Compound **7** 35
Fig. S48. HRESIMS of Compound **8**. 36
Fig. S49. ^{1}H NMR spectrum of Compound **8.** 37
Fig. S50. ^{1}H-^{13}C HSQC of Compound **8.** 37
Fig. S51. ^{1}H-^{13}C HMBC of Compound **8.** 38
Fig. S52. ^{1}H-^{1}H COSY of Compound **8.** 38

Fig. S53. ^{1}H-^{1}H ROESY of Compound **8.** 39

Fig. S54. HPLC chromatogram of Compound **1**. 39

Fig. S55. HPLC chromatogram of Compound **2**. 40

Fig. S56. HPLC chromatogram of Compound **3**. 40

Fig. S57. HPLC chromatogram of Compound **4**. 40

Fig. S58. HPLC chromatogram of Compound **5**. 41

Fig. S59. HPLC chromatogram of Compound **6**. 41

Fig. S60. HPLC chromatogram of Compound **7**. 41

Fig. S61. HPLC chromatogram of Compound **8**. 42

Fig. S62. Experimental ECD spectrum of compound **1** in MeOH. 42

Fig. S63. Experimental ECD spectrum of compound **3** in MeOH 43

Fig. S64. Comparison of the experimental ECD spectra of **1**-**8** measured in MeOH. 43

Fig. S65. ECD spectrum of **1** in DMSO (red curve) compared with that of the $Mo_2(OAc)_4$ complex (1.30 ligand/metal ratio) in DMSO (blue). 44

Fig. S66. Experimental ECD spectrum of compound **2** in MeOH. 44

Fig. S67. ECD spectrum of **2** in DMSO (red curve) compared with that of the $Mo_2(OAc)_4$ complex (1.30 ligand/metal ratio) in DMSO (blue). 45

Fig. S68. Low-energy (≥ 1%) ωB97X/TZVP PCM/MeOH conformers of (1*S*,29*R*)-**3**. 45

Fig. S69. Experimental ECD spectrum of **3** in MeOH (black line) compared with the calculated B3LYP/TZVP PCM/MeOH spectra of the five lowest-energy individual conformers of (1*S*,29*R*)-**3** (color lines). Level of DFT optimization: ωB97X/TZVP PCM/MeOH. 46

Fig. S70. Low-energy (≥ 1%) ωB97X/TZVP PCM/MeOH conformers of (*S*)-**3modMe**. 46

Fig. S71. Low-energy (≥ 1%) ωB97X/TZVP PCM/MeOH conformers of (*S*)-**3modEt**. 47

Fig. S72. Experimental ECD spectrum of **3** in MeOH (black line) compared with the calculated PBE0/TZVP PCM/MeOH spectrum of (*S*)-**3modMe** (purple line). Level of DFT optimization: ωB97X/TZVP PCM/MeOH. Bars represent the rotational strengths of conformer A. 47

Fig. S73. Experimental ECD spectrum of **3** in MeOH (black line) compared with the calculated CAM-B3LYP/TZVP PCM/MeOH and PBE0/TZVP PCM/MeOH spectra of (*S*)-**3modEt** (olive and purple lines, respectively). Level of DFT optimization: ωB97X/TZVP PCM/MeOH. 48

Fig. S74. Experimental ECD spectrum of **3** in MeOH (black line) compared with the calculated PBE0/TZVP PCM/MeOH spectra of the individual low-energy conformers of (*S*)-**3modEt** (color lines). Level of DFT optimization: ωB97X/TZVP PCM/MeOH. 48

Fig. S75. Low-energy (≥ 1%) ωB97X/TZVP PCM/MeOH conformers of (1*S*,29*S*)-**3**. 49

Fig. S76. Experimental ECD spectrum of compound **4** in MeOH. 49

Fig. S77. ECD spectrum of **4** in DMSO (red curve) compared with that of the $Mo_2(OAc)_4$ complex (1.30 ligand/metal ratio) in DMSO (blue). 50

Fig. S78. Experimental ECD spectrum of compound **5** in MeOH. 50

Fig. S79. Experimental ECD spectrum of compound **6** in MeOH 51

Fig. S80. GC-MS analysis of the sugar component of asperphenalenone K. 52

Fig. S81. Experimental ECD spectrum of compound **7** in MeOH. 53

Fig. S82. Experimental ECD spectrum of compound **8** in MeOH. 53

Table S1. Boltzmann populations and specific optical rotations of the low-energy conformers of (1*S*,29*R*)-**3** computed at various levels for the ωB97X/TZVP PCM/MeOH optimized MMFF conformers. 54

Table S2. Boltzmann populations and specific optical rotations of the low-energy conformers of (*S*)-**3modMe** computed at various levels for the ωB97X/TZVP PCM/MeOH optimized MMFF conformers. 54

Table S3. Boltzmann populations and specific optical rotations of the low-energy conformers of (*S*)-**3modEt** computed at various levels for the ωB97X/TZVP PCM/MeOH optimized MMFF conformers. 55

Table S4. Boltzmann populations and specific optical rotations of the low-energy conformers of (1*S*,29*S*)-**3** computed at various levels for the ωB97X/TZVP PCM/MeOH optimized MMFF conformers. 55

Table S5. Cartesian coordinates and energies of the low-energy conformers calculated at the ωB97X/TZVP PCM/MeOH level related to Tables S2 – S4. 56

Extraction and isolation

Bioactivity was tracked to guide isolation and purification of compounds. The strain *C. rosea* was cultivated in 1-L Erlenmeyer flasks on solid rice medium containing 100 g rice and 110 ml water for 24 days at 22 °C. Subsequently, culture was extracted by addition of 500 mL EtOAc for each flask and shaking at 145 rpm overnight. The EtOAc crude extract (39.2 g) was subjected to vacuum liquid chromatography (VLC) on silica gel with a gradient of *n*-hexane / EtOAc (100:0, 80:20, 60:40, 40:60, 20:80, 0:100) and dichloromethane / methanol (100:0, 60:40, 20:80, 0:100) as elution solvent to obtain seven fractions on the basis of TLC analysis. Afterwards, seven fractions were tested for anti-MRSA activity following CLSI guidelines (Fig.S1A).

Fraction 6 was further separated by Sephadex LH-20 column with MeOH to obtain five sub-fractions Fr. 6.1- Fr. 6.5. Next, the anti-MRSA activity was determined for all sub-fractions, and weak activity could be observed for fraction 6.1 (Fig.S1B). Further, Fraction.6.1 was subjected to VLC on silica gel using a dichlormethane / methanol step gradient at 80:20, 70:30, 60:40, 50:50 and 40:60 as elution solvent. This yielded three sub-fractions (Fr.6.1.1-Fr.6.1.3), and anti-MRSA activity was tested as well. Interestingly, sub-fraction 6.1.2 exhibited strongest activity against MRSA at 100 mg/L (Fig.S1C), and subsequent semi-preparative HPLC with a mixture of acetonitrile and H_2O yielded compound **2** and **3**. Sub-fraction 6.1.1 and sub-fraction 6.1.3 were separated by semi-preparative HPLC with a mixture of acetonitrile and water to yield compound **1** and **4** as well as **9** and **10**, respectively.

Fraction 6.4 was eluted on silica gel using a dichlormethane / methanol step gradient at 60:40, 50:50 40:60 and 30:70 to achieve four sub-fractions (Fr.6.4.1- Fr.6.4.4). MeOH-H_2O was used as mobile phase to obtain **5** and **6** as well as **7** and **8** by semi-preparative HPLC from

Fr. 6.4.2 and Fr.6.4.4, respectively. All isolated compounds were tested for their activity against MRSA, see Table 1.

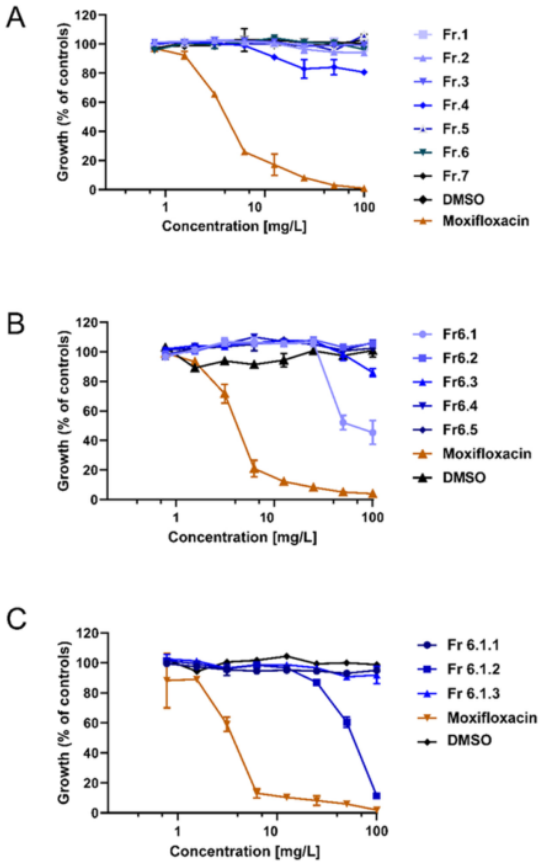
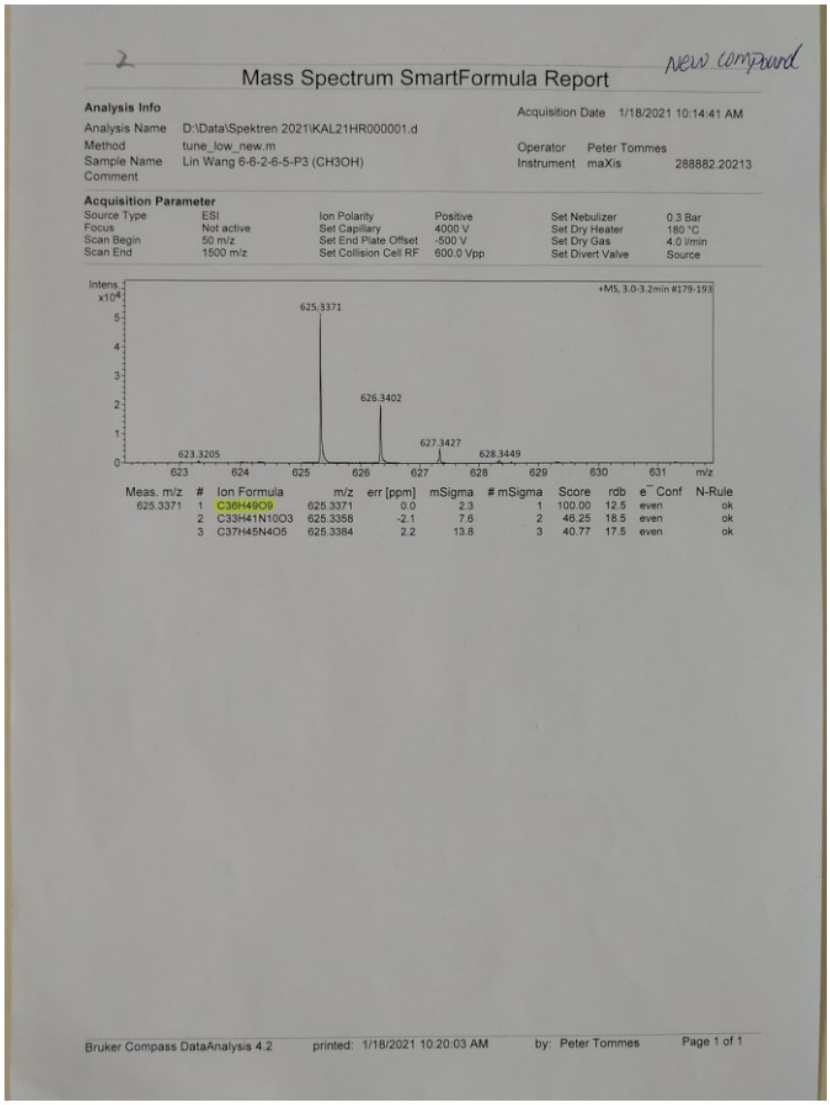


Fig. S1. Dose-response curves against *S. aureus* MRSA with fractions and sub-tractions. Growth (% of control) was quantified by resazurin dye reduction assay. **A**: Activity of VCL fractions from crude extract. **B**: Activity of sub-fractions originating from chromatography of fraction 6 on Sephadex LH-20. **C**: Activity of sub-fractions originating from VCL of subfraction 6.1.



2 new compound

Mass Spectrum SmartFormula Report

Analysis Info

Analysis Name	D:\Data\Spektren 2021\KAL21HR000001.d	Acquisition Date	1/18/2021 10:14:41 AM
Method	tune_low_new.m	Operator	Peter Tommes
Sample Name	Lin Wang 6-6-2-6-5-P3 (CH3OH)	Instrument	maXis 288882.20213
Comment			

Acquisition Parameter

Source Type	ESI	Ion Polarity	Positive	Set Nebulizer	0.3 Bar
Focus	Not active	Set Capillary	4000 V	Set Dry Heater	180 °C
Scan Begin	50 m/z	Set End Plate Offset	-500 V	Set Dry Gas	4.0 l/min
Scan End	1500 m/z	Set Collision Cell RF	600.0 Vpp	Set Divert Valve	Source

Meas. m/z	#	Ion Formula	m/z	err [ppm]	mSigma	# mSigma	Score	rdb	e⁻ Conf	N-Rule
625.3371	1	C36H49O9	625.3371	0.0	2.3	1	100.00	12.5	even	ok
	2	C33H41N10O3	625.3358	-2.1	7.6	2	46.25	18.5	even	ok
	3	C37H45N4O5	625.3384	2.2	13.8	3	40.77	17.5	even	ok

Bruker Compass DataAnalysis 4.2 printed: 1/18/2021 10:20:03 AM by: Peter Tommes Page 1 of 1

Fig. S2. HRESIMS of Compound 1

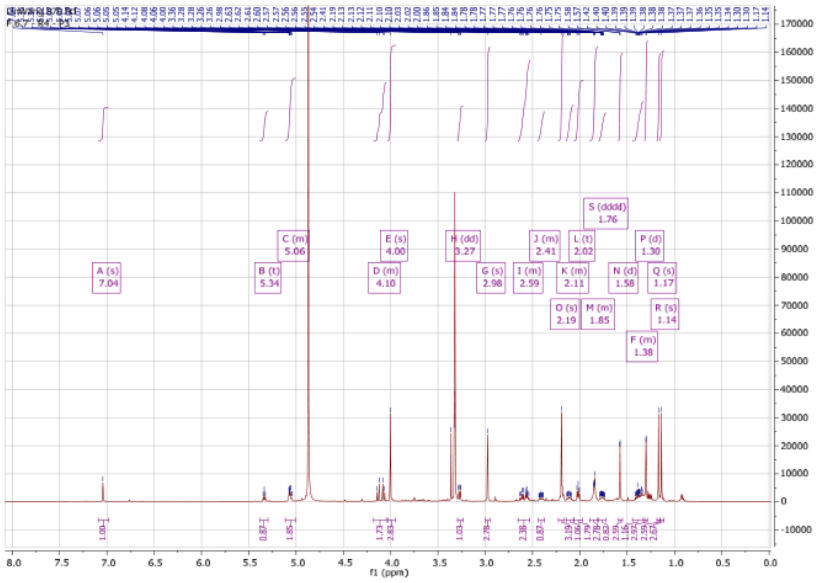


Fig. S3. ^{1}H NMR spectrum of Compound **1**

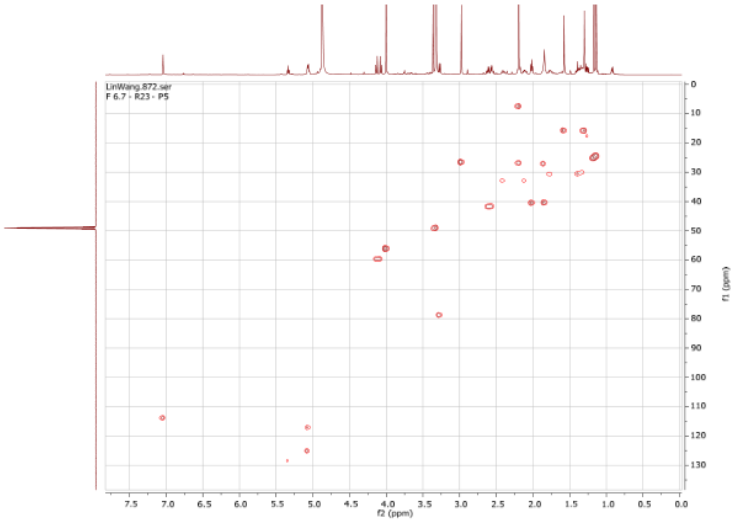


Fig. S4. ^{1}H-^{13}C HSQC of Compound **1**

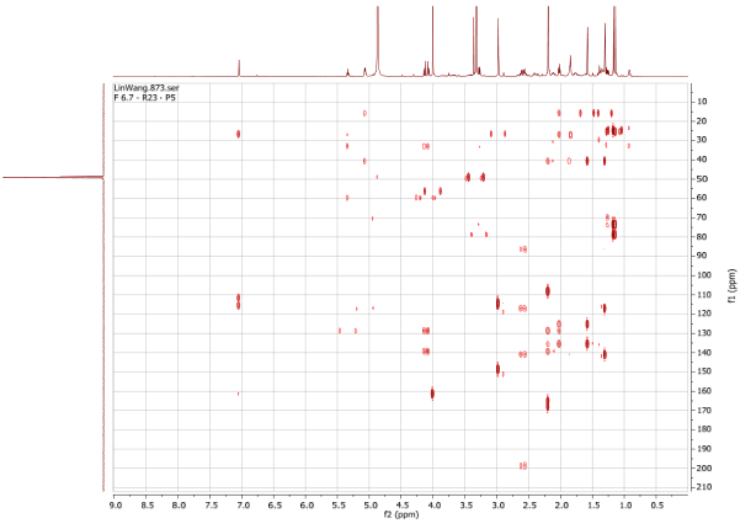


Fig. S5. ^{1}H-^{13}C HMBC of Compound **1**

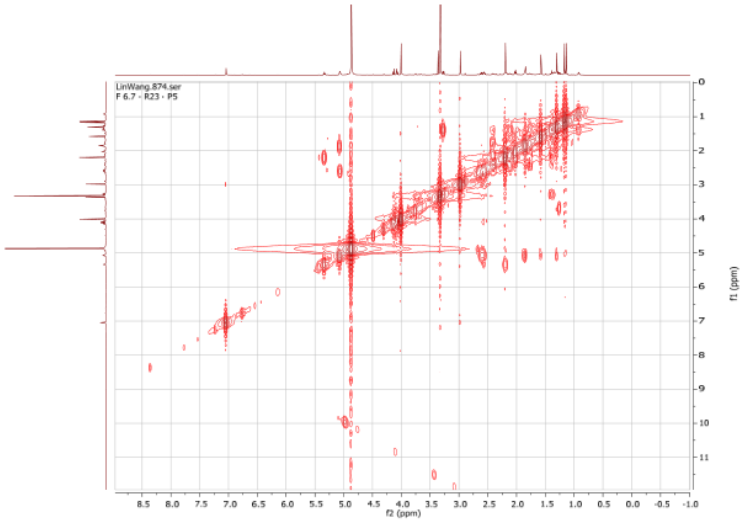


Fig. S6. ^{1}H-^{1}H COSY of Compound **1**

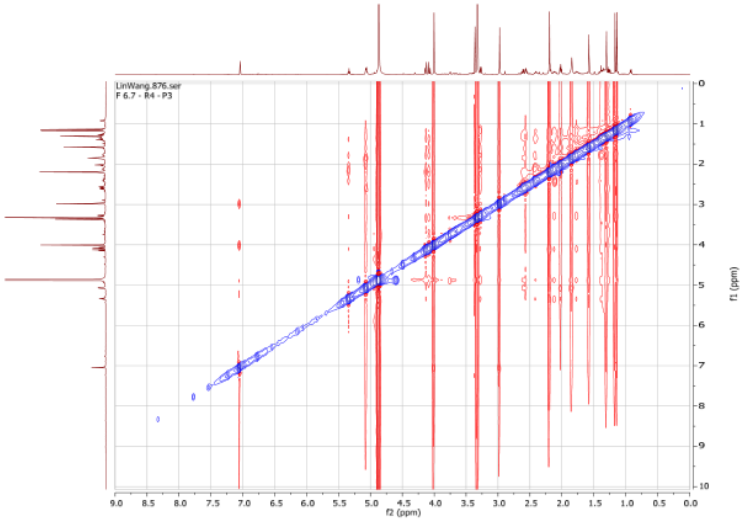
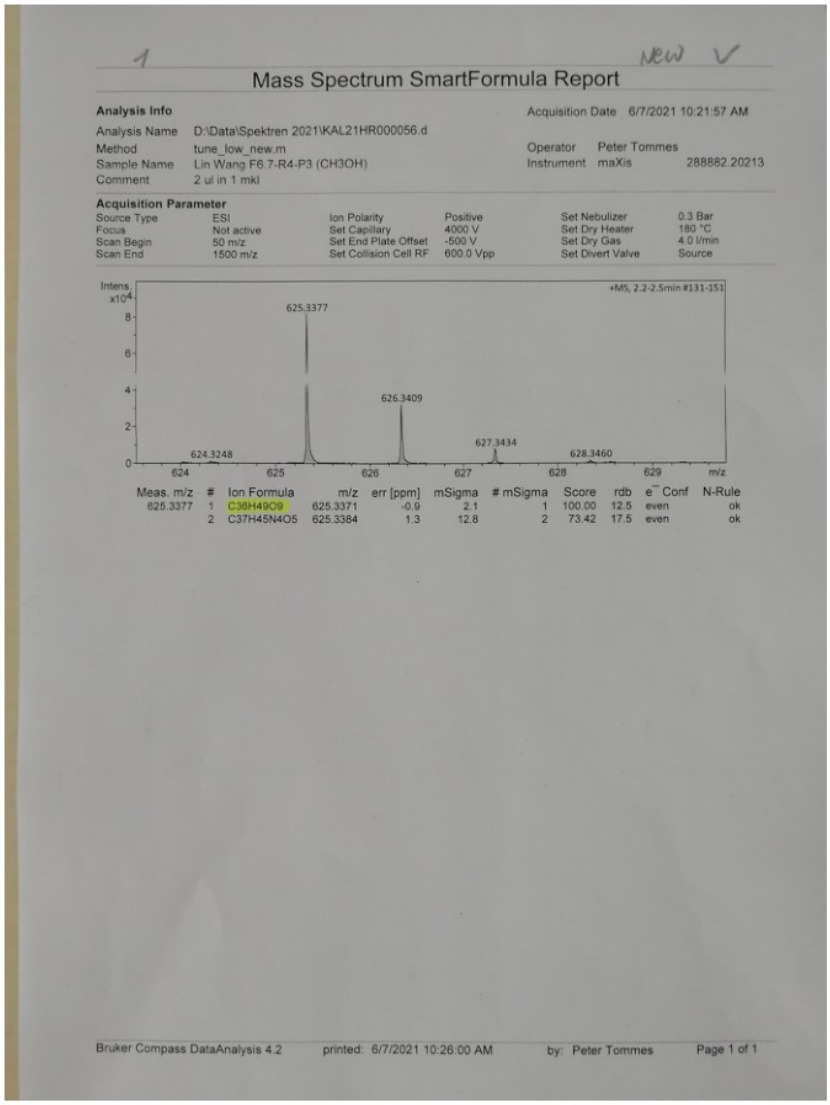


Fig. S7. ^{1}H-^{1}H ROESY of Compound **1**



1 NEW ✓

Mass Spectrum SmartFormula Report

Analysis Info

Analysis Name	D:\Data\Spektren 2021\KAL21HR000056.d	Acquisition Date	6/7/2021 10:21:57 AM
Method	tune_low_new.m	Operator	Peter Tommes
Sample Name	Lin Wang F6.7-R4-P3 (CH3OH)	Instrument	maXis 288882.20213
Comment	2 ul in 1 mkl		

Acquisition Parameter

Source Type	ESI	Ion Polarity	Positive	Set Nebulizer	0.3 Bar
Focus	Not active	Set Capillary	4000 V	Set Dry Heater	180 °C
Scan Begin	50 m/z	Set End Plate Offset	-500 V	Set Dry Gas	4.0 l/min
Scan End	1500 m/z	Set Collision Cell RF	600.0 Vpp	Set Divert Valve	Source

Meas. m/z	#	Ion Formula	m/z	err [ppm]	mSigma	# mSigma	Score	rdb	e⁻ Conf	N-Rule
625.3377	1	C38H49O9	625.3371	-0.9	2.1	1	100.00	12.5	even	ok
	2	C37H45N4O5	625.3384	1.3	12.8	2	73.42	17.5	even	ok

Bruker Compass DataAnalysis 4.2 printed: 6/7/2021 10:26:00 AM by: Peter Tommes Page 1 of 1

Fig. S8. HRESIMS of Compound **2**

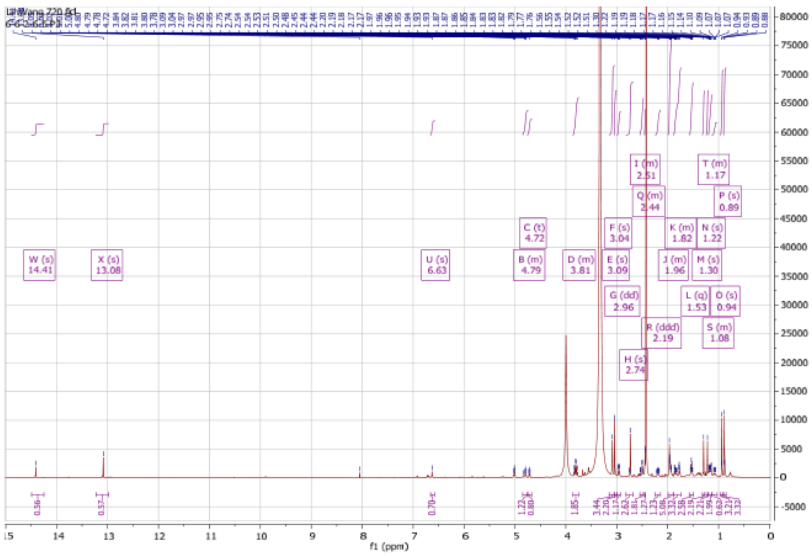


Fig. S9. ^{1}H NMR spectrum of Compound **2**

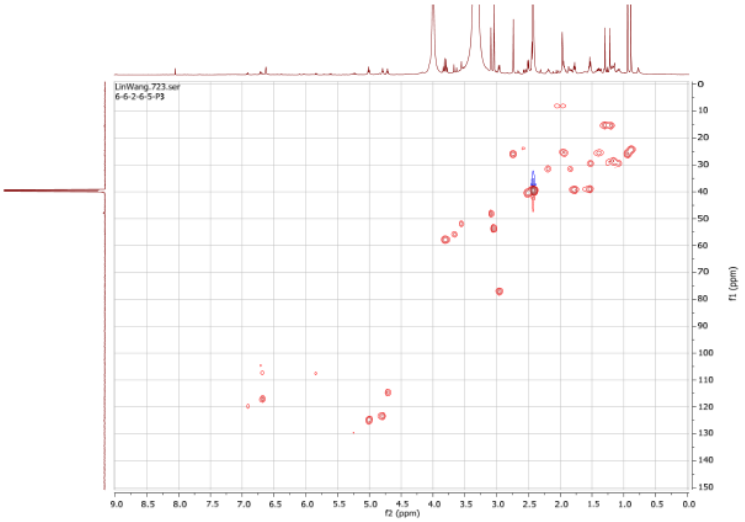


Fig. S10. ^{1}H-^{13}C HSQC of Compound **2**

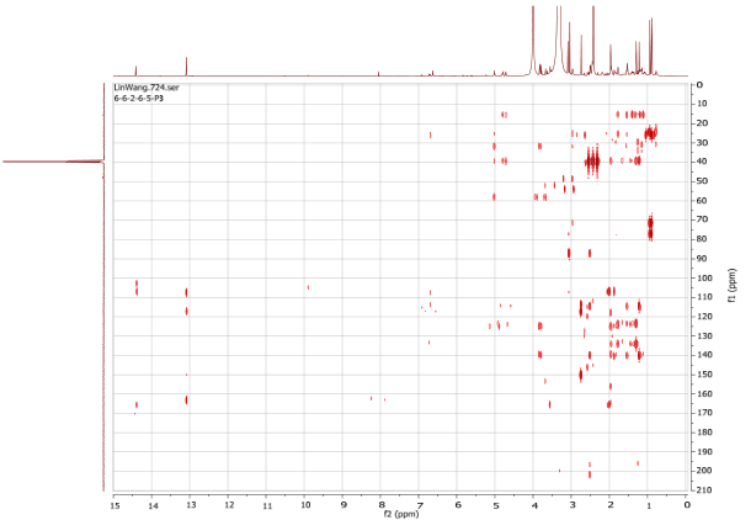


Fig. S11. ^{1}H-^{13}C HMBC of Compound **2**

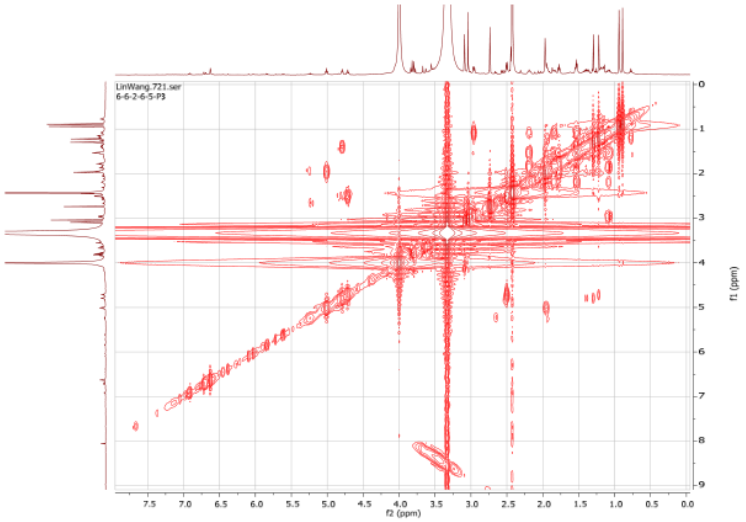


Fig. S12. ^{1}H-^{1}H COSY of Compound **2**

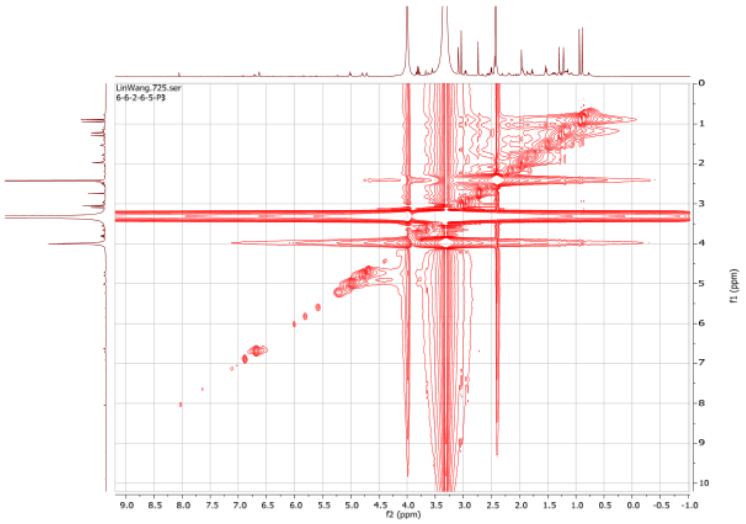
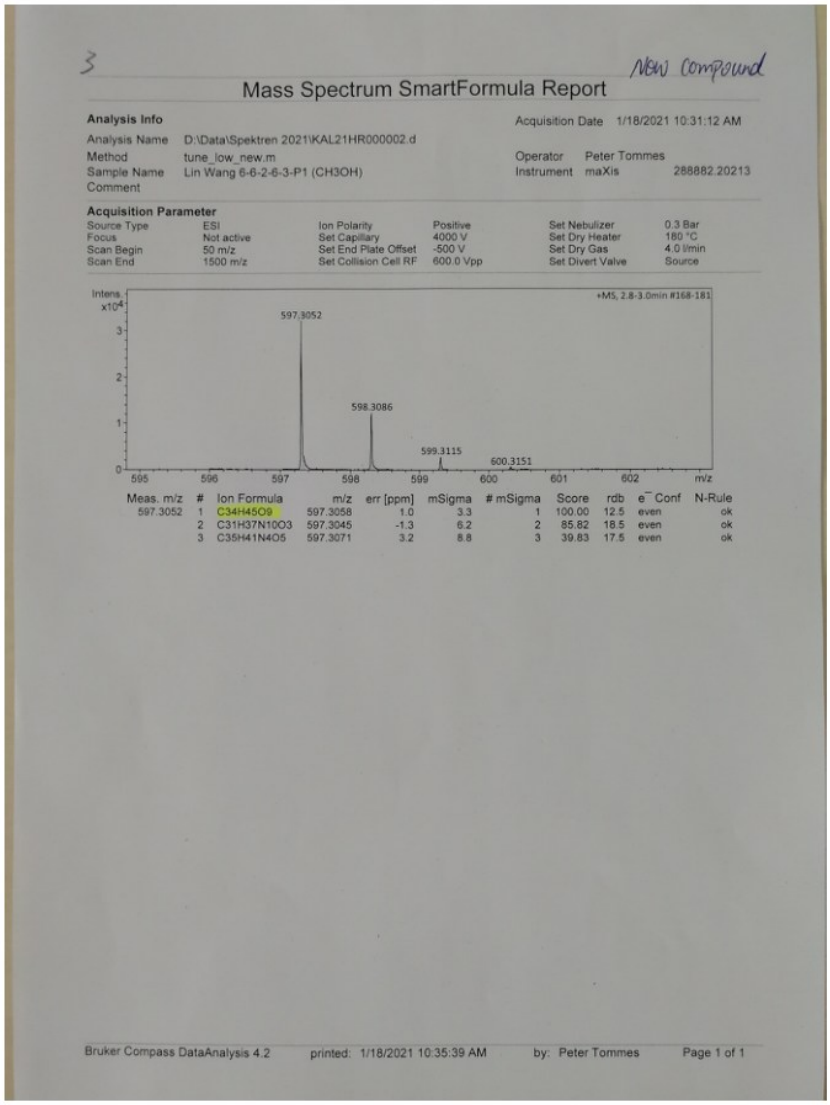


Fig. S13. ^{1}H-^{1}H ROESY of Compound **2**



3 New Compound

Mass Spectrum SmartFormula Report

Analysis Info

Analysis Name	D:\Data\Spektren 2021\KAL21HR000002.d	Acquisition Date	1/18/2021 10:31:12 AM
Method	tune_low_new.m	Operator	Peter Tommes
Sample Name	Lin Wang 6-6-2-6-3-P1 (CH3OH)	Instrument	maXis 288882.20213
Comment			

Acquisition Parameter

Source Type	ESI	Ion Polarity	Positive	Set Nebulizer	0.3 Bar
Focus	Not active	Set Capillary	4000 V	Set Dry Heater	180 °C
Scan Begin	50 m/z	Set End Plate Offset	-500 V	Set Dry Gas	4.0 l/min
Scan End	1500 m/z	Set Collision Cell RF	600.0 Vpp	Set Divert Valve	Source

Meas. m/z	#	Ion Formula	m/z	err [ppm]	mSigma	# mSigma	Score	rdb	e⁻ Conf	N-Rule
597.3052	1	C34H45O9	597.3058	1.0	3.3	1	100.00	12.5	even	ok
	2	C31H37N10O3	597.3045	-1.3	6.2	2	85.82	18.5	even	ok
	3	C35H41N4O5	597.3071	3.2	8.8	3	39.83	17.5	even	ok

Bruker Compass DataAnalysis 4.2 printed: 1/18/2021 10:35:39 AM by: Peter Tommes Page 1 of 1

Fig. S14. HRESIMS of Compound **3**



Fig. S15. ^{1}H NMR spectrum of Compound **3**

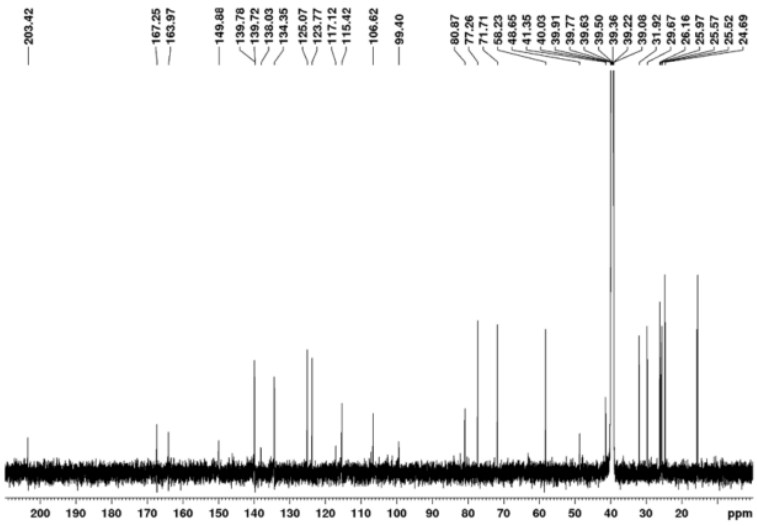


Fig. S16. ^{13}C NMR of Compound **3**

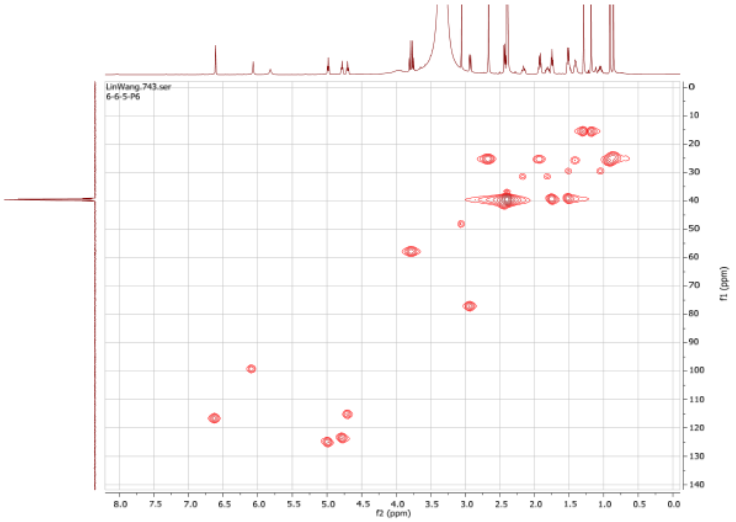


Fig. S17. ^{1}H-^{13}C HSQC of Compound **3**

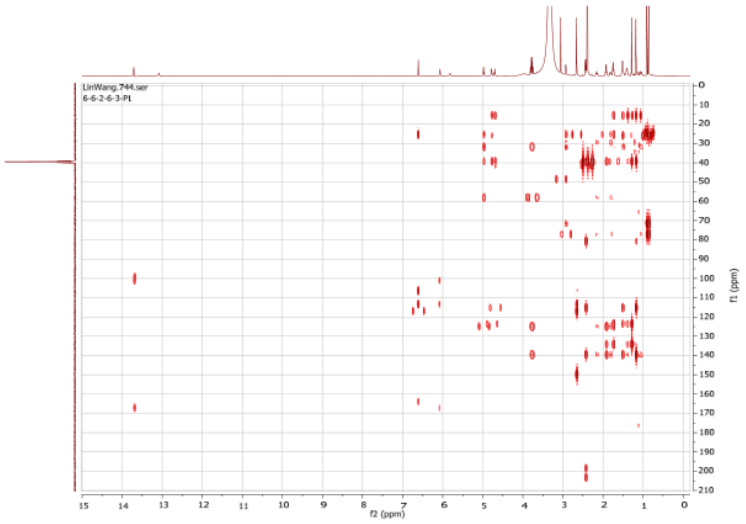


Fig. S18. ^{1}H-^{13}C HMBC of Compound **3**

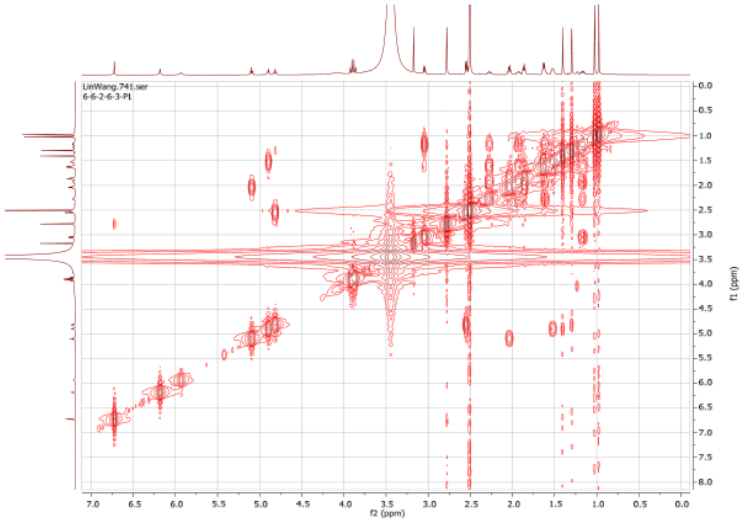


Fig. S19. ^{1}H-^{1}H COSY of Compound **3**

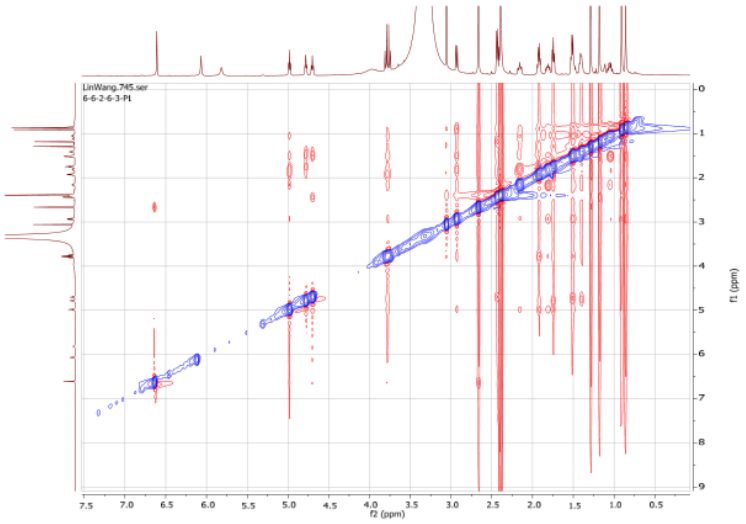
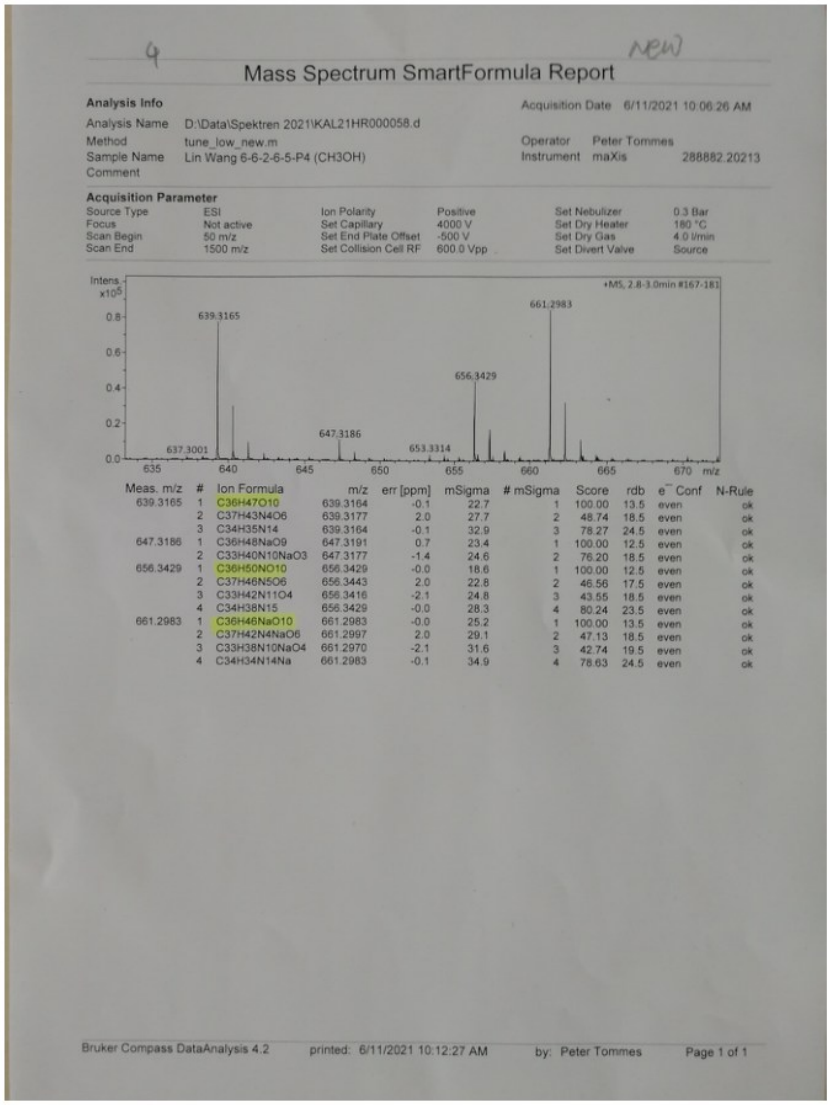


Fig. S20. ^{1}H-^{1}H ROESY of Compound **3**



4 NEW

Mass Spectrum SmartFormula Report

Analysis Info

Analysis Name D:\Data\Spektren 2021\KAL21HR000058.d
Method tune_low_new.m
Sample Name Lin Wang 6-6-2-6-5-P4 (CH3OH)
Comment

Acquisition Date 6/11/2021 10:06:26 AM
Operator Peter Tommes
Instrument maXis 288882.20213

Acquisition Parameter

Source Type	ESI	Ion Polarity	Positive	Set Nebulizer	0.3 Bar
Focus	Not active	Set Capillary	4000 V	Set Dry Heater	180 °C
Scan Begin	50 m/z	Set End Plate Offset	-500 V	Set Dry Gas	4.0 l/min
Scan End	1500 m/z	Set Collision Cell RF	600.0 Vpp	Set Divert Valve	Source

Meas. m/z	#	Ion Formula	m/z	err [ppm]	mSigma	# mSigma	Score	rdb	e⁻ Conf	N-Rule
639.3165	1	C36H47O10	639.3164	-0.1	22.7	1	100.00	13.5	even	ok
	2	C37H43N4O6	639.3177	2.0	27.7	2	48.74	18.5	even	ok
	3	C34H35N14	639.3164	-0.1	32.9	3	78.27	24.5	even	ok
647.3186	1	C36H48NaO9	647.3191	0.7	23.4	1	100.00	12.5	even	ok
	2	C33H40N10NaO3	647.3177	-1.4	24.6	2	76.20	18.5	even	ok
656.3429	1	C36H50NO10	656.3429	-0.0	18.6	1	100.00	12.5	even	ok
	2	C37H46N5O6	656.3443	2.0	22.8	2	46.56	17.5	even	ok
	3	C33H42N11O4	656.3416	-2.1	24.8	3	43.55	18.5	even	ok
	4	C34H38N15	656.3429	-0.0	28.3	4	80.24	23.5	even	ok
661.2983	1	C36H46NaO10	661.2983	-0.0	25.2	1	100.00	13.5	even	ok
	2	C37H42N4NaO6	661.2997	2.0	29.1	2	47.13	18.5	even	ok
	3	C33H38N10NaO4	661.2970	-2.1	31.6	3	42.74	19.5	even	ok
	4	C34H34N14Na	661.2983	-0.1	34.9	4	78.63	24.5	even	ok

Bruker Compass DataAnalysis 4.2 printed: 6/11/2021 10:12:27 AM by: Peter Tommes Page 1 of 1

Fig. S21. HRESIMS of Compound **4**

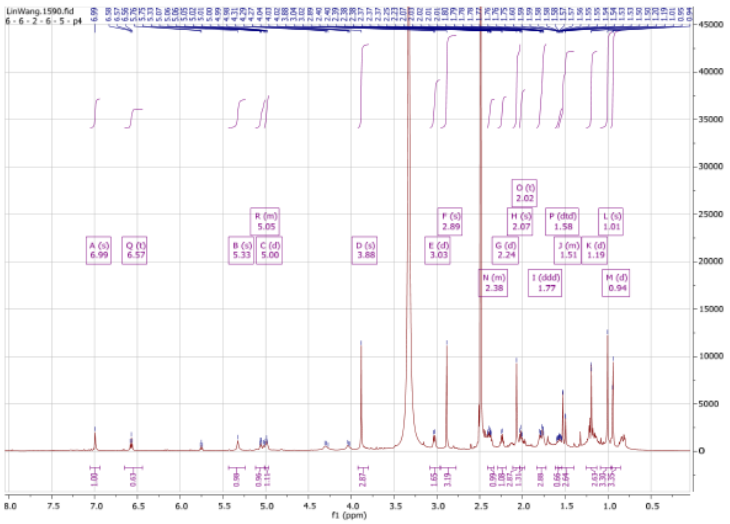


Fig. S22. ^{1}H NMR spectrum of Compound **4**

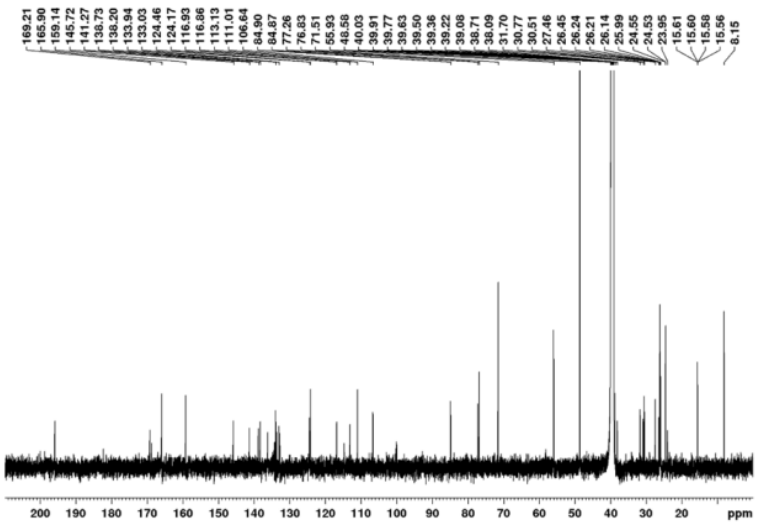


Fig. S23. ^{13}C NMR of Compound **4**

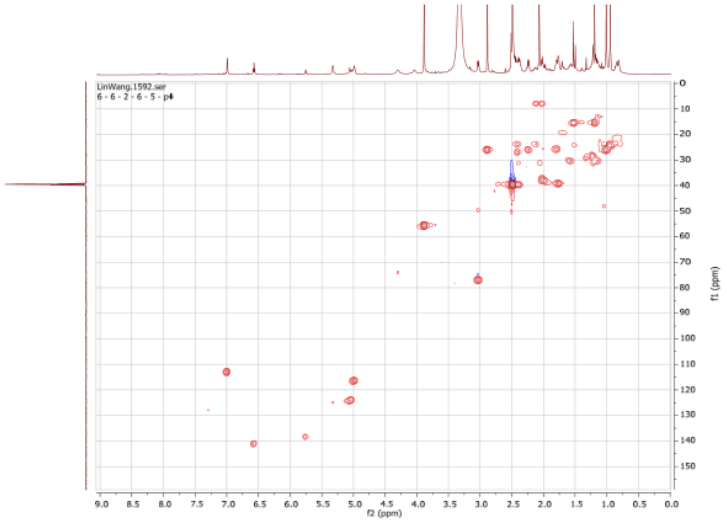


Fig. S24. ^{1}H-^{13}C HSQC of Compound **4**

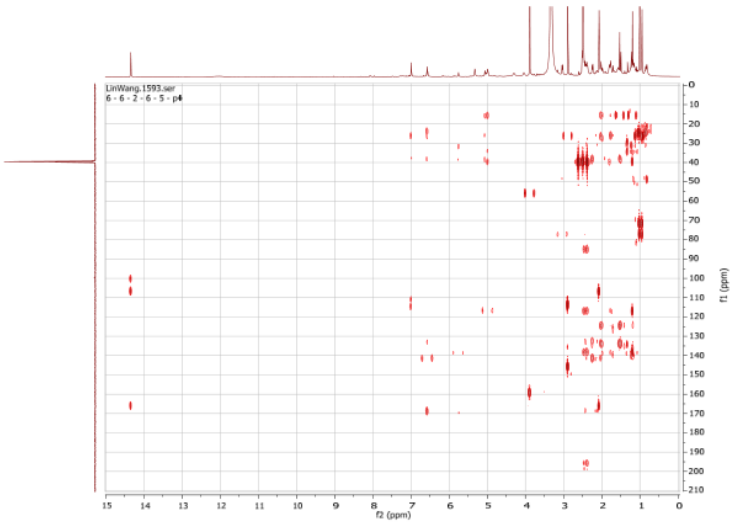


Fig. S25. ^{1}H-^{13}C HMBC of Compound **4**

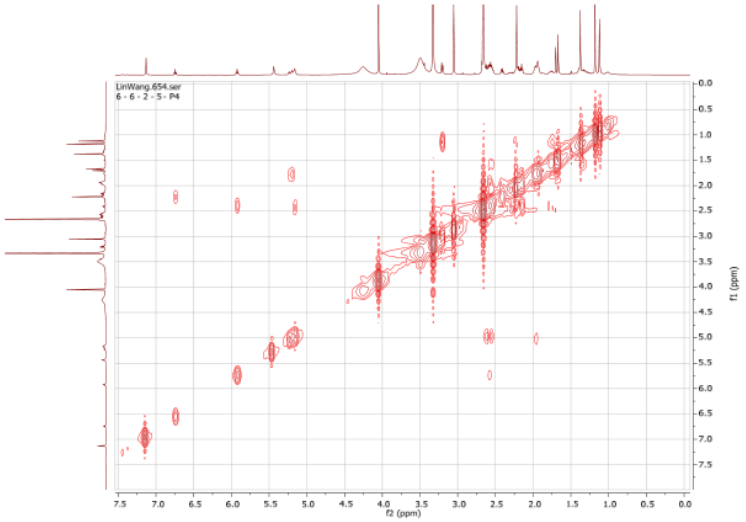


Fig. S26. ^{1}H-^{1}H COSY of Compound **4**

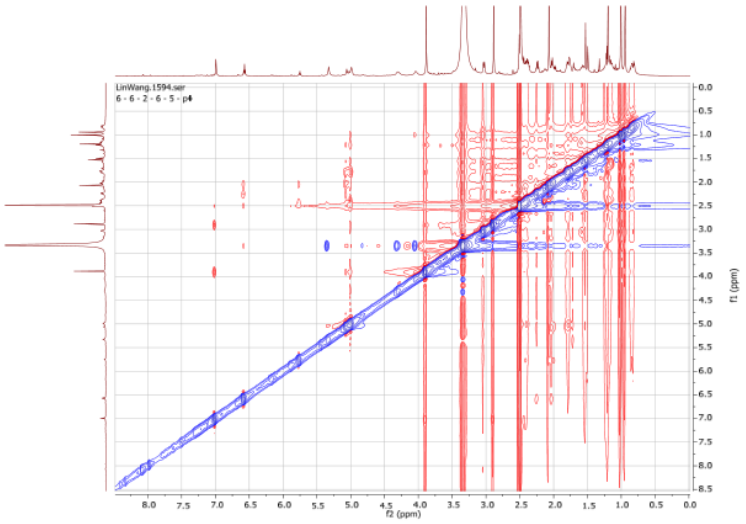
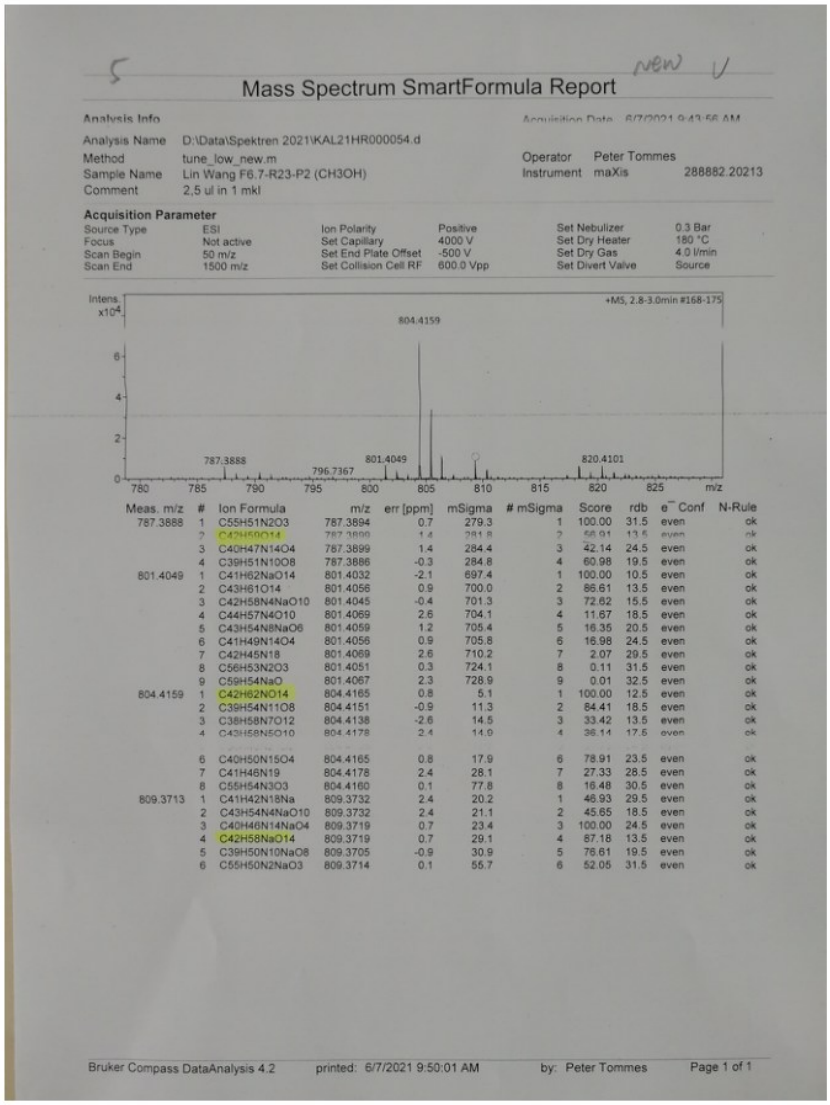


Fig. S27. ^{1}H-^{1}H ROESY of Compound **4**



5 NEW V

Mass Spectrum SmartFormula Report

Analysis Info

Analysis Name D:\Data\Spektren 2021\KAL21HR000054.d
Method tune_low_new.m
Sample Name Lin Wang F6.7-R23-P2 (CH3OH)
Comment 2,5 ul in 1 mkl

Operator Peter Tommes
Instrument maXis 288882.20213

Acquisition Parameter

Source Type	ESI	Ion Polarity	Positive	Set Nebulizer	0.3 Bar
Focus	Not active	Set Capillary	4000 V	Set Dry Heater	180 °C
Scan Begin	50 m/z	Set End Plate Offset	-500 V	Set Dry Gas	4.0 l/min
Scan End	1500 m/z	Set Collision Cell RF	600.0 Vpp	Set Divert Valve	Source

Meas. m/z	#	Ion Formula	m/z	err [ppm]	mSigma	# mSigma	Score	rdb	e⁻ Conf	N-Rule
787.3888	1	C55H51N2O3	787.3894	0.7	279.3	1	100.00	31.5	even	ok
	2	C42H59O14	787.3899	1.4	281.8	2	58.91	13.5	even	ok
	3	C40H47N14O4	787.3899	1.4	284.4	3	42.14	24.5	even	ok
	4	C39H51N10O8	787.3886	-0.3	284.8	4	60.98	19.5	even	ok
801.4049	1	C41H62NaO14	801.4032	-2.1	697.4	1	100.00	10.5	even	ok
	2	C43H61O14	801.4056	0.9	700.0	2	86.61	13.5	even	ok
	3	C42H58N4NaO10	801.4045	-0.4	701.3	3	72.62	15.5	even	ok
	4	C44H57N4O10	801.4069	2.6	704.1	4	11.67	18.5	even	ok
	5	C43H54N8NaO6	801.4059	1.2	705.4	5	16.35	20.5	even	ok
	6	C41H49N14O4	801.4056	0.9	705.8	6	16.98	24.5	even	ok
	7	C42H45N18	801.4069	2.6	710.2	7	2.07	29.5	even	ok
	8	C56H53N2O3	801.4051	0.3	724.1	8	0.11	31.5	even	ok
	9	C59H54NaO	801.4067	2.3	728.9	9	0.01	32.5	even	ok
804.4159	1	C42H62NO14	804.4165	0.8	5.1	1	100.00	12.5	even	ok
	2	C39H54N11O8	804.4151	-0.9	11.3	2	84.41	18.5	even	ok
	3	C38H58N7O12	804.4138	-2.6	14.5	3	33.42	13.5	even	ok
	4	C43H58N5O10	804.4178	2.4	14.9	4	36.14	17.5	even	ok
	6	C40H50N15O4	804.4165	0.8	17.9	6	78.91	23.5	even	ok
	7	C41H46N19	804.4178	2.4	28.1	7	27.33	28.5	even	ok
	8	C55H54N3O3	804.4160	0.1	77.8	8	16.48	30.5	even	ok
809.3713	1	C41H42N18Na	809.3732	2.4	20.2	1	46.93	29.5	even	ok
	2	C43H54N4NaO10	809.3732	2.4	21.1	2	45.65	18.5	even	ok
	3	C40H46N14NaO4	809.3719	0.7	23.4	3	100.00	24.5	even	ok
	4	C42H58NaO14	809.3719	0.7	29.1	4	87.18	13.5	even	ok
	5	C39H50N10NaO8	809.3705	-0.9	30.9	5	76.61	19.5	even	ok
	6	C55H50N2NaO3	809.3714	0.1	55.7	6	52.05	31.5	even	ok

Bruker Compass DataAnalysis 4.2 printed: 6/7/2021 9:50:01 AM by: Peter Tommes Page 1 of 1

Fig. S28. HRESIMS of Compound **5**



Fig. S29. ^{1}H NMR spectrum of Compound **5**

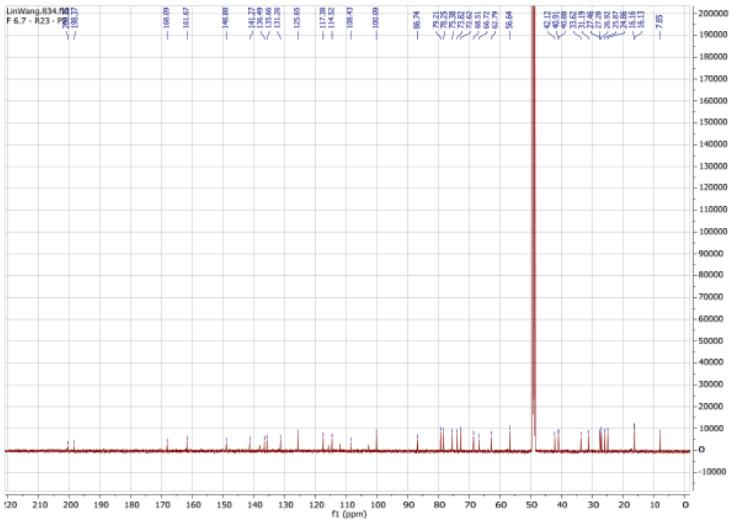


Fig. S30. ^{13}C NMR of Compound **5**

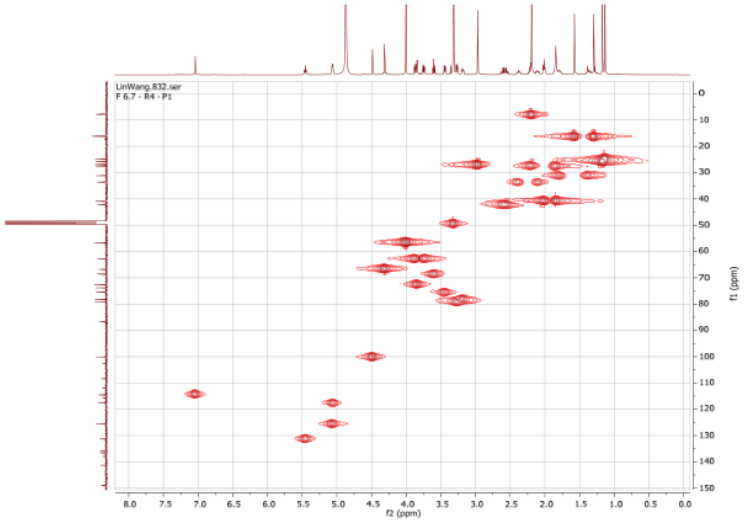


Fig. S31. ^{1}H-^{13}C HSQC of Compound **5**

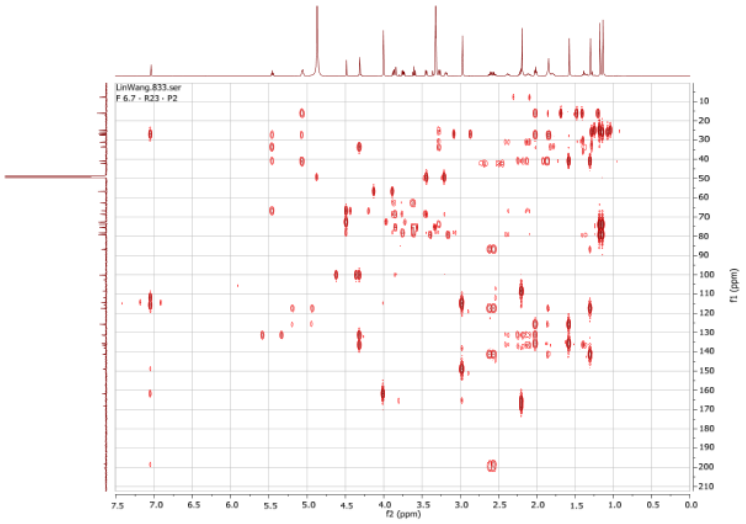


Fig. S32. ^{1}H-^{13}C HMBC of Compound **5**

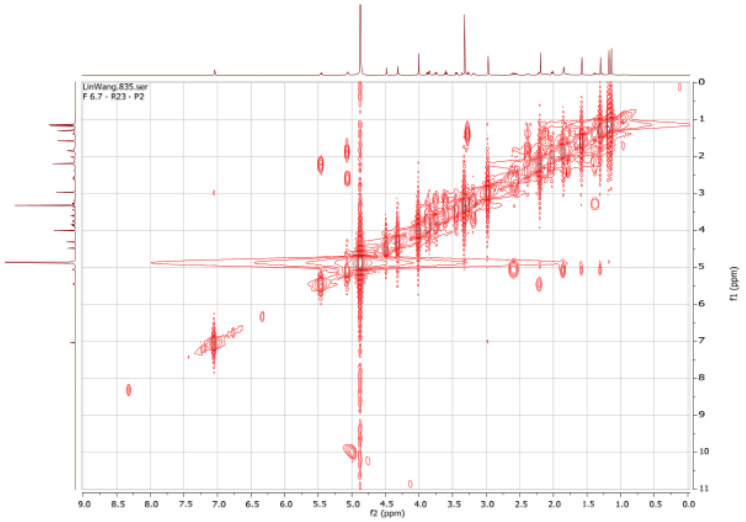


Fig. S33. ^{1}H-^{1}H COSY of Compound **5**

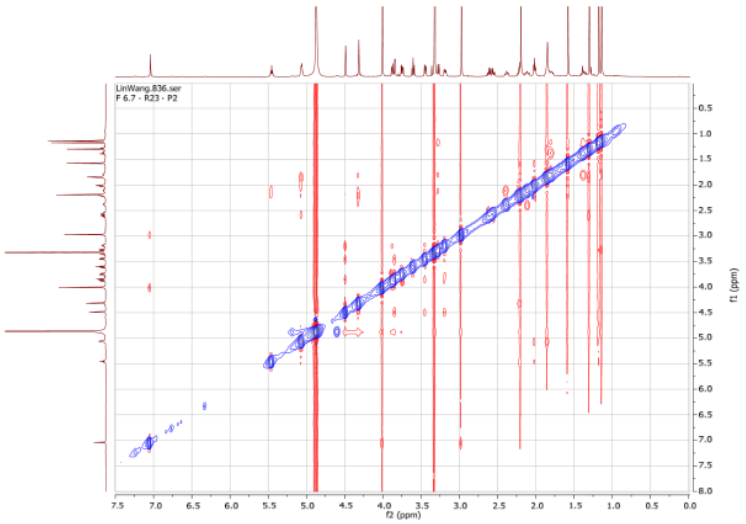
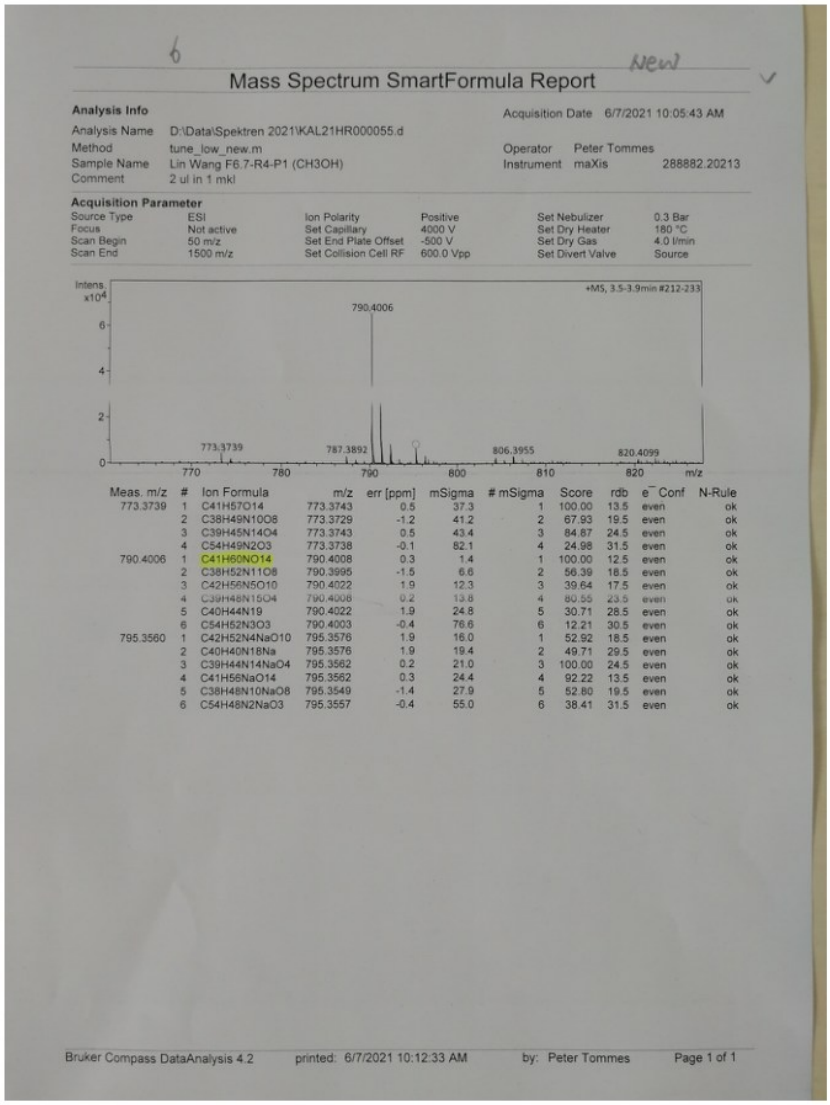


Fig. S34. ^{1}H-^{1}H ROESY of Compound **5**



6 new

Mass Spectrum SmartFormula Report

Analysis Info

Analysis Name	D:\Data\Spektren 2021\KAL21HR000055.d	Acquisition Date	6/7/2021 10:05:43 AM
Method	tune_low_new.m	Operator	Peter Tommes
Sample Name	Lin Wang F6.7-R4-P1 (CH3OH)	Instrument	maXis 288882.20213
Comment	2 ul in 1 mkl		

Acquisition Parameter

Source Type	ESI	Ion Polarity	Positive	Set Nebulizer	0.3 Bar
Focus	Not active	Set Capillary	4000 V	Set Dry Heater	180 °C
Scan Begin	50 m/z	Set End Plate Offset	-500 V	Set Dry Gas	4.0 l/min
Scan End	1500 m/z	Set Collision Cell RF	600.0 Vpp	Set Divert Valve	Source

Meas. m/z	#	Ion Formula	m/z	err [ppm]	mSigma	# mSigma	Score	rdb	e⁻ Conf	N-Rule
773.3739	1	C41H57O14	773.3743	0.5	37.3	1	100.00	13.5	even	ok
	2	C38H49N10O8	773.3729	-1.2	41.2	2	67.93	19.5	even	ok
	3	C39H45N14O4	773.3743	0.5	43.4	3	84.87	24.5	even	ok
	4	C54H49N2O3	773.3738	-0.1	82.1	4	24.98	31.5	even	ok
790.4006	1	C41H60NO14	790.4008	0.3	1.4	1	100.00	12.5	even	ok
	2	C38H52N11O8	790.3995	-1.5	6.6	2	56.39	18.5	even	ok
	3	C42H56N5O10	790.4022	1.9	12.3	3	39.64	17.5	even	ok
	4	C39H48N15O4	790.4006	0.2	13.8	4	80.55	23.5	even	ok
	5	C40H44N19	790.4022	1.9	24.8	5	30.71	28.5	even	ok
	6	C54H52N3O3	790.4003	-0.4	76.6	6	12.21	30.5	even	ok
795.3560	1	C42H52N4NaO10	795.3576	1.9	16.0	1	52.92	18.5	even	ok
	2	C40H40N18Na	795.3576	1.9	19.4	2	49.71	29.5	even	ok
	3	C39H44N14NaO4	795.3562	0.2	21.0	3	100.00	24.5	even	ok
	4	C41H56NaO14	795.3562	0.3	24.4	4	92.22	13.5	even	ok
	5	C38H48N10NaO8	795.3549	-1.4	27.9	5	52.80	19.5	even	ok
	6	C54H48N2NaO3	795.3557	-0.4	55.0	6	38.41	31.5	even	ok

Bruker Compass DataAnalysis 4.2 printed: 6/7/2021 10:12:33 AM by: Peter Tommes Page 1 of 1

Fig. S35. HRESIMS of Compound **6**

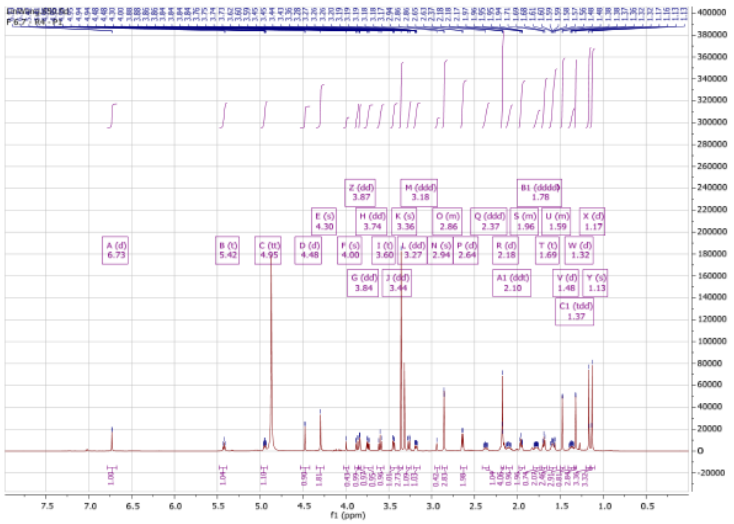


Fig. S36. ^{1}H NMR spectrum of Compound **6**

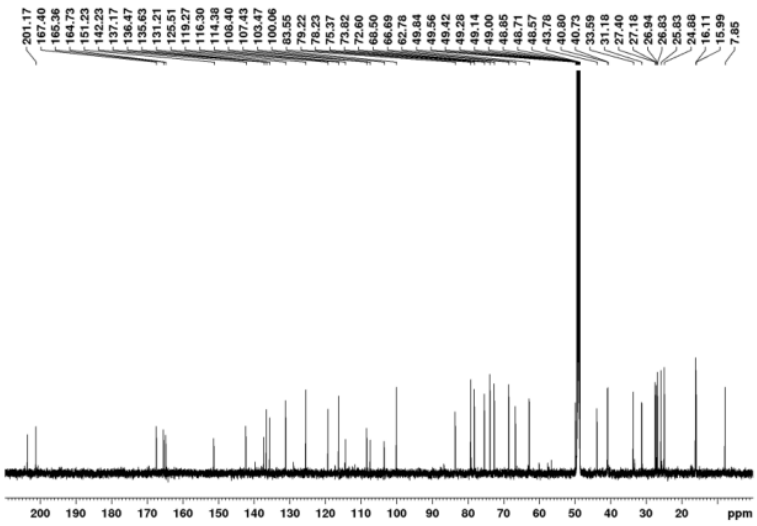


Fig. S37. ^{13}C NMR of Compound **6**

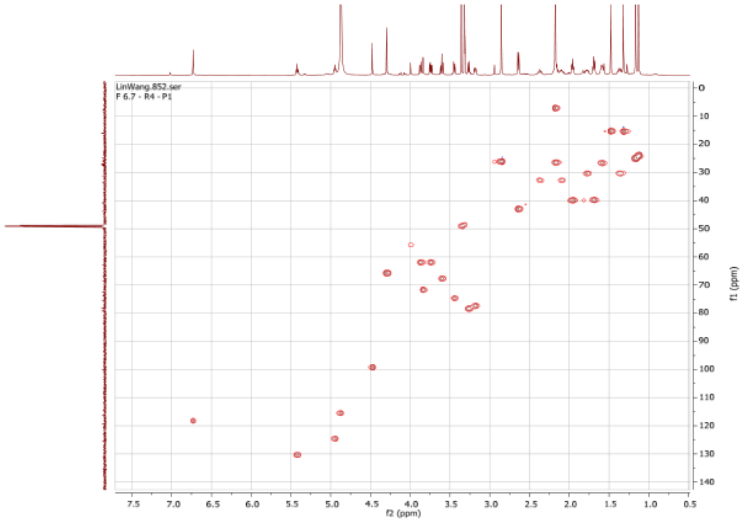


Fig. S38. ^{1}H-^{13}C HSQC of Compound **6**

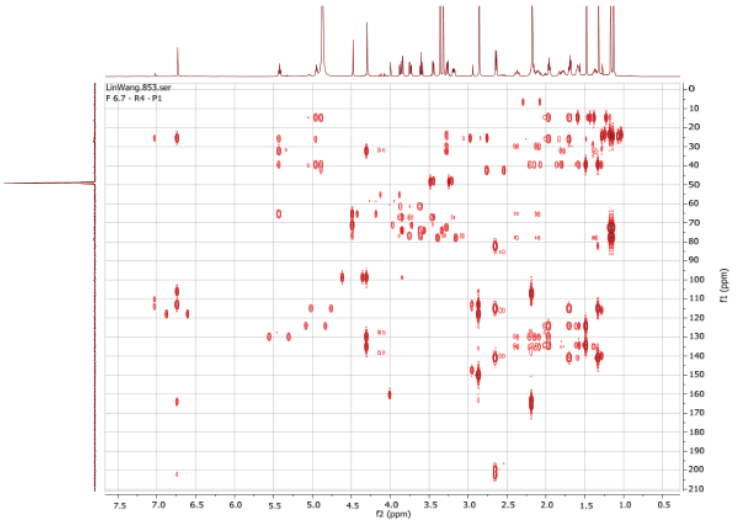


Fig. S39. ^{1}H-^{13}C HMBC of Compound **6**

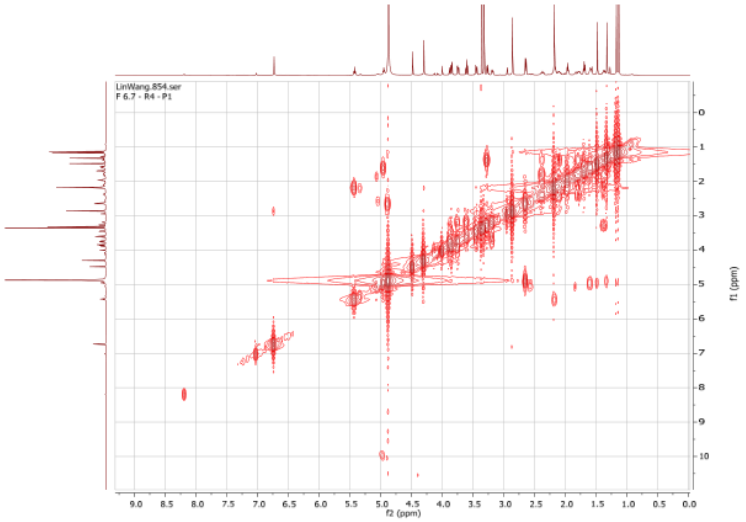


Fig. S40. ^{1}H-^{1}H COSY of Compound **6**

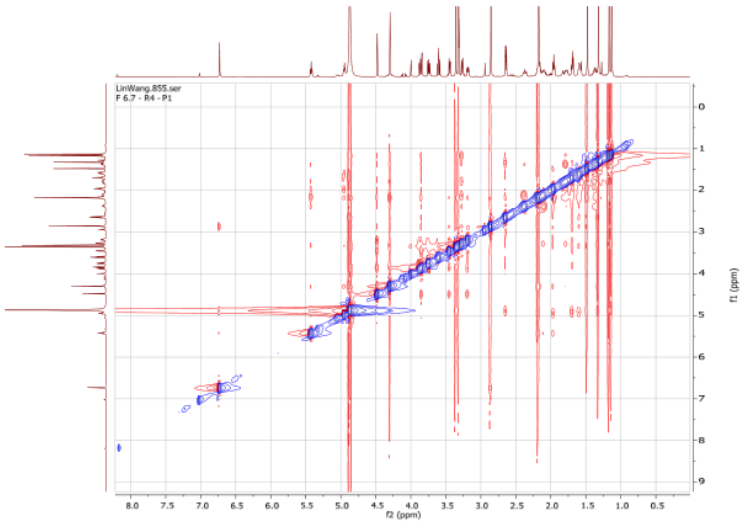
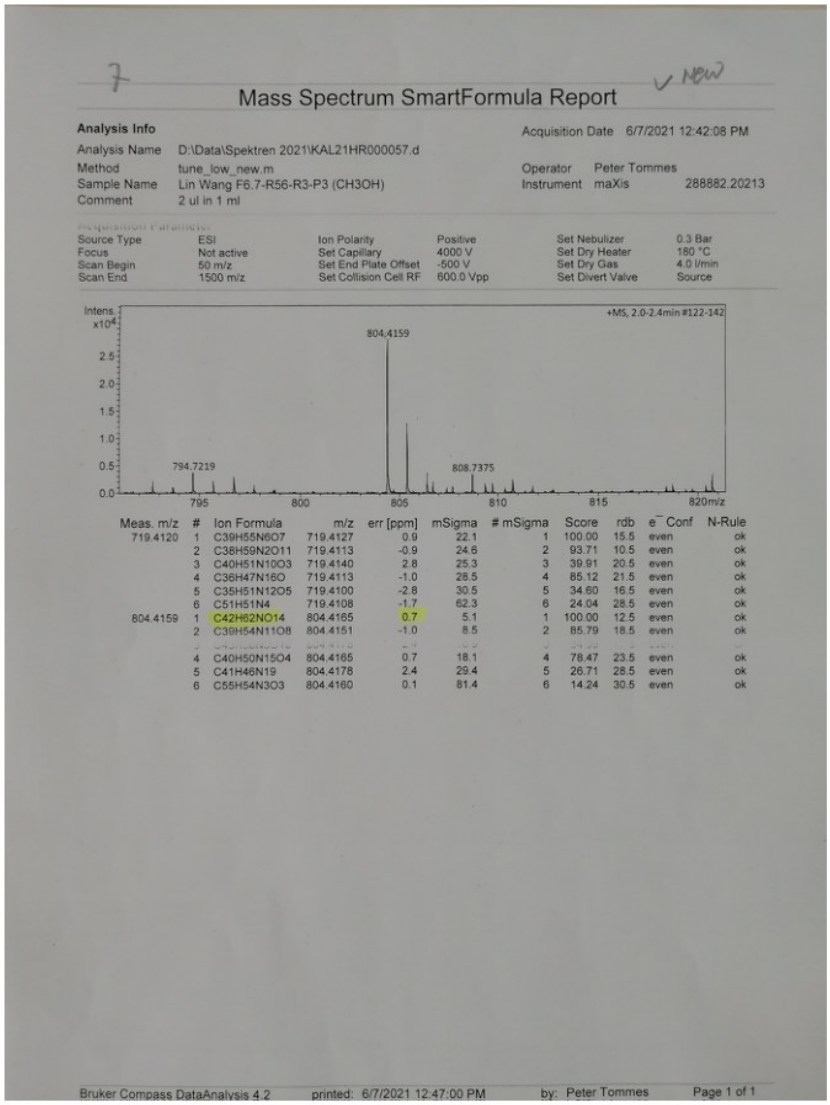


Fig. S41. ^{1}H-^{1}H ROESY of Compound **6**



7 NEW

Mass Spectrum SmartFormula Report

Analysis Info

Acquisition Date 6/7/2021 12:42:08 PM

Analysis Name	D:\Data\Spektren 2021\KAL21HR000057.d		
Method	tune_low_new.m	Operator	Peter Tommes
Sample Name	Lin Wang F6.7-R56-R3-P3 (CH3OH)	Instrument	maXis 288882.20213
Comment	2 ul in 1 ml		

Source Type	ESI	Ion Polarity	Positive	Set Nebulizer	0.3 Bar
Focus	Not active	Set Capillary	4000 V	Set Dry Heater	180 °C
Scan Begin	50 m/z	Set End Plate Offset	-500 V	Set Dry Gas	4.0 l/min
Scan End	1500 m/z	Set Collision Cell RF	600.0 Vpp	Set Divert Valve	Source

Meas. m/z	#	Ion Formula	m/z	err [ppm]	mSigma	# mSigma	Score	rdb	e⁻ Conf	N-Rule
719.4120	1	C39H55N6O7	719.4127	0.9	22.1	1	100.00	15.5	even	ok
	2	C38H59N2O11	719.4113	-0.9	24.6	2	93.71	10.5	even	ok
	3	C40H51N10O3	719.4140	2.8	25.3	3	39.91	20.5	even	ok
	4	C36H47N16O	719.4113	-1.0	26.5	4	85.12	21.5	even	ok
	5	C35H51N12O5	719.4100	-2.8	30.5	5	34.60	16.5	even	ok
	6	C51H51N4	719.4108	-1.7	62.3	6	24.04	28.5	even	ok
804.4159	1	C42H62NO14	804.4165	0.7	5.1	1	100.00	12.5	even	ok
	2	C39H54N11O8	804.4151	-1.0	8.5	2	85.79	18.5	even	ok
	4	C40H50N15O4	804.4165	0.7	18.1	4	78.47	23.5	even	ok
	5	C41H46N19	804.4178	2.4	29.4	5	26.71	28.5	even	ok
	6	C55H54N3O3	804.4160	0.1	81.4	6	14.24	30.5	even	ok

Bruker Compass DataAnalysis 4.2 printed: 6/7/2021 12:47:00 PM by: Peter Tommes Page 1 of 1

Fig. S42. HRESIMS of Compound **7**

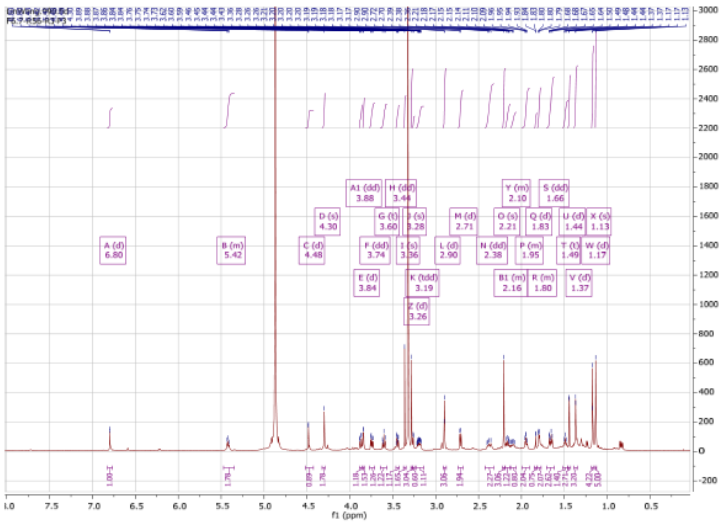


Fig. S43. ^{1}H NMR spectrum of Compound **7**

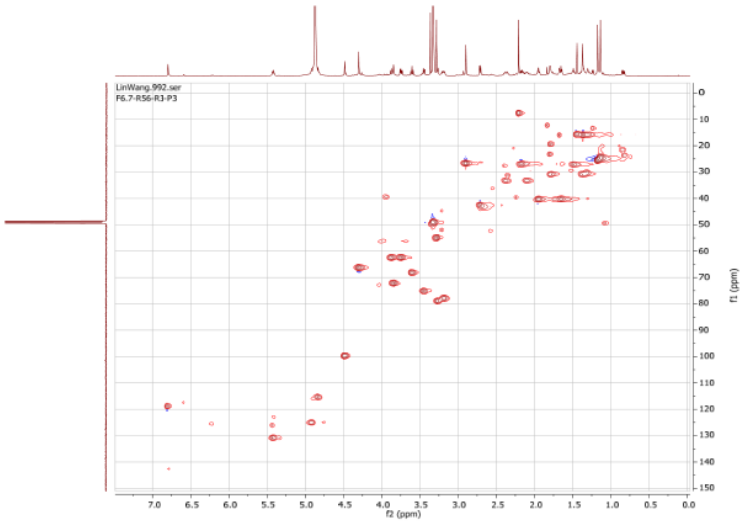


Fig. S44. ^{1}H-^{13}C HSQC of Compound **7**

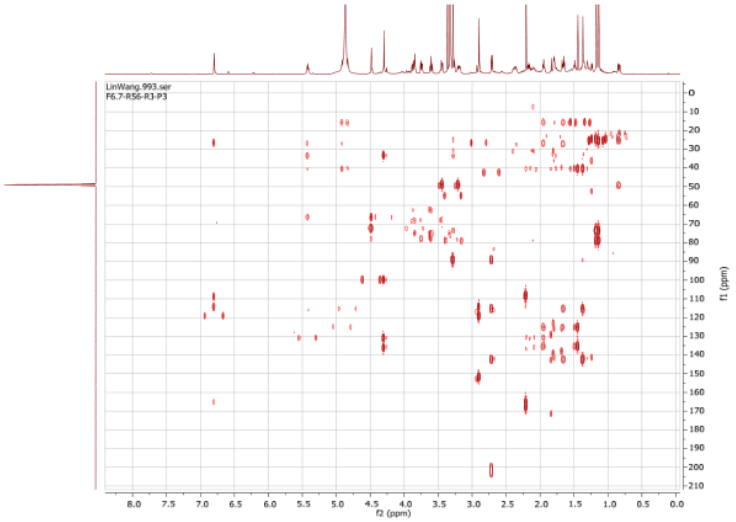


Fig. S45. ^{1}H-^{13}C HMBC of Compound **7**



Fig. S46. ^{1}H-^{1}H COSY of Compound **7**

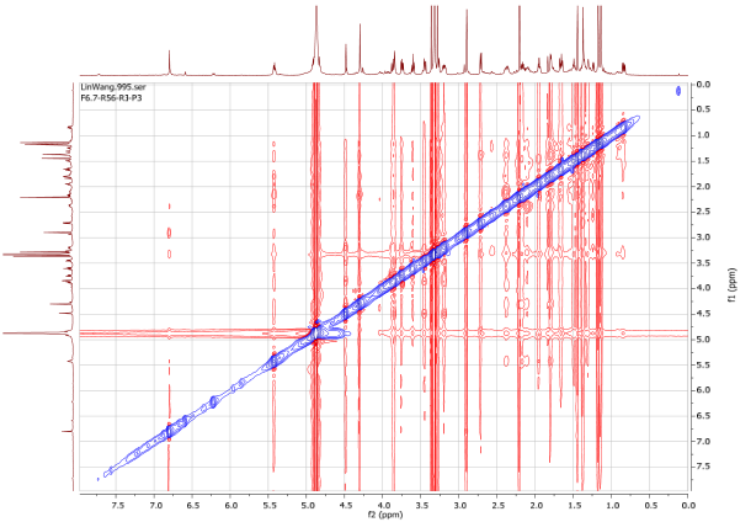
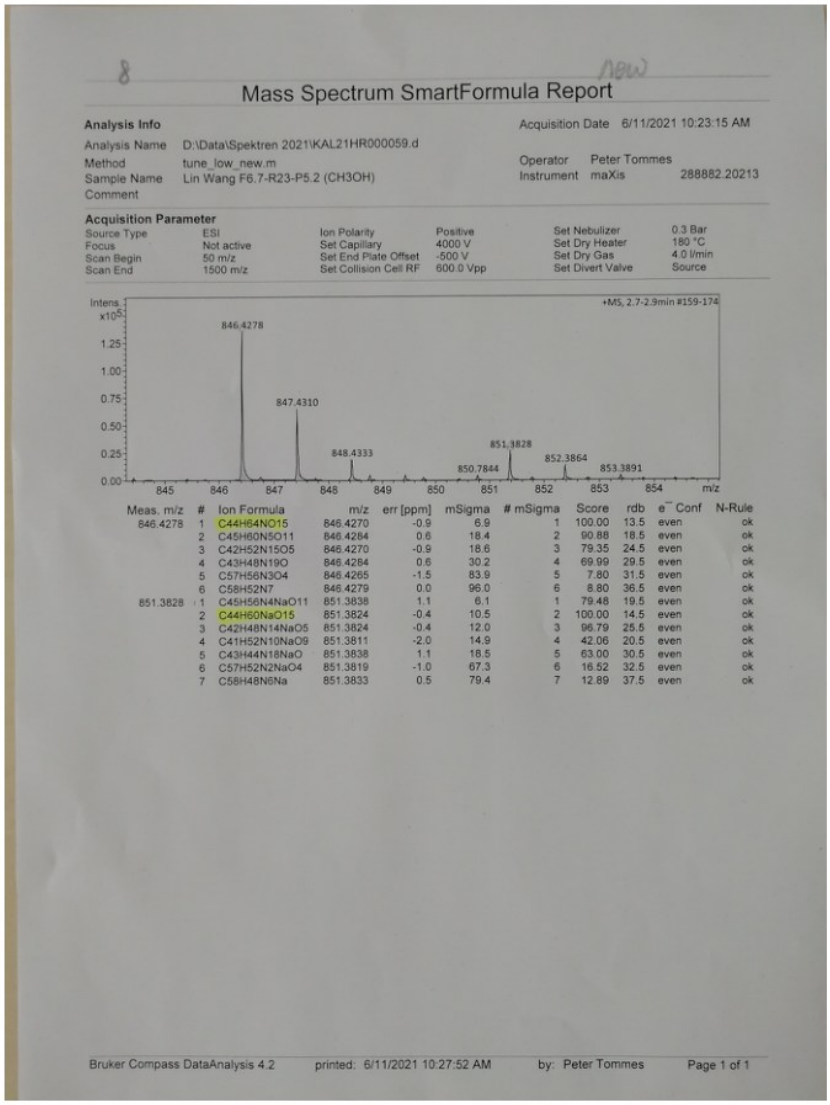


Fig. S47. ^{1}H-^{1}H ROESY of Compound **7**



8 new

Mass Spectrum SmartFormula Report

Analysis Info

Analysis Name D:\Data\Spektren 2021\KAL21HR000059.d
Method tune_low_new.m
Sample Name Lin Wang F6.7-R23-P5.2 (CH3OH)
Comment

Acquisition Date 6/11/2021 10:23:15 AM
Operator Peter Tommes
Instrument maXis 288882.20213

Acquisition Parameter

Source Type	ESI	Ion Polarity	Positive	Set Nebulizer	0.3 Bar
Focus	Not active	Set Capillary	4000 V	Set Dry Heater	180 °C
Scan Begin	50 m/z	Set End Plate Offset	-500 V	Set Dry Gas	4.0 l/min
Scan End	1500 m/z	Set Collision Cell RF	600.0 Vpp	Set Divert Valve	Source

Meas. m/z	#	Ion Formula	m/z	err [ppm]	mSigma	# mSigma	Score	rdb	e⁻ Conf	N-Rule
846.4278	1	C44H64NO15	846.4270	-0.9	6.9	1	100.00	13.5	even	ok
	2	C45H60N5O11	846.4284	0.6	18.4	2	90.88	18.5	even	ok
	3	C42H52N15O5	846.4270	-0.9	18.6	3	79.35	24.5	even	ok
	4	C43H48N19O	846.4284	0.6	30.2	4	69.99	29.5	even	ok
	5	C57H56N3O4	846.4265	-1.5	83.9	5	7.80	31.5	even	ok
	6	C58H52N7	846.4279	0.0	96.0	6	8.80	36.5	even	ok
851.3828	1	C45H56N4NaO11	851.3838	1.1	6.1	1	79.48	19.5	even	ok
	2	C44H60NaO15	851.3824	-0.4	10.5	2	100.00	14.5	even	ok
	3	C42H48N14NaO5	851.3824	-0.4	12.0	3	96.79	25.5	even	ok
	4	C41H52N10NaO9	851.3811	-2.0	14.9	4	42.06	20.5	even	ok
	5	C43H44N18NaO	851.3838	1.1	18.5	5	63.00	30.5	even	ok
	6	C57H52N2NaO4	851.3819	-1.0	67.3	6	16.52	32.5	even	ok
	7	C58H48N6Na	851.3833	0.5	79.4	7	12.89	37.5	even	ok

Bruker Compass DataAnalysis 4.2 printed: 6/11/2021 10:27:52 AM by: Peter Tommes Page 1 of 1

Fig. S48. HRESIMS of Compound **8**.

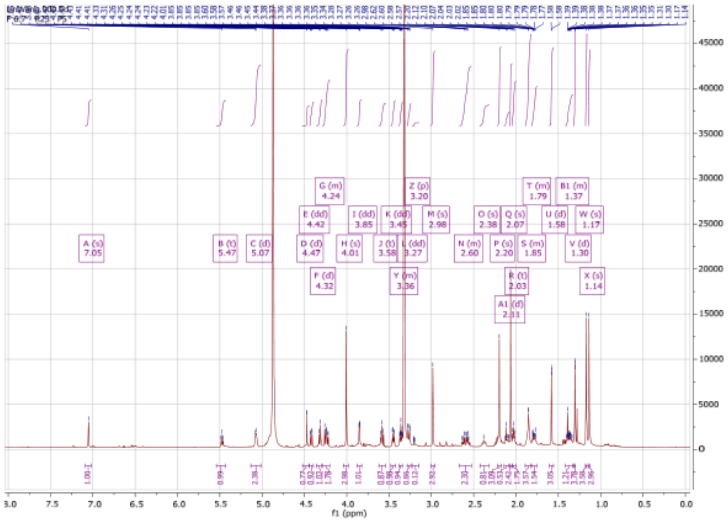


Fig. S49. ^{1}H NMR spectrum of Compound **8.**

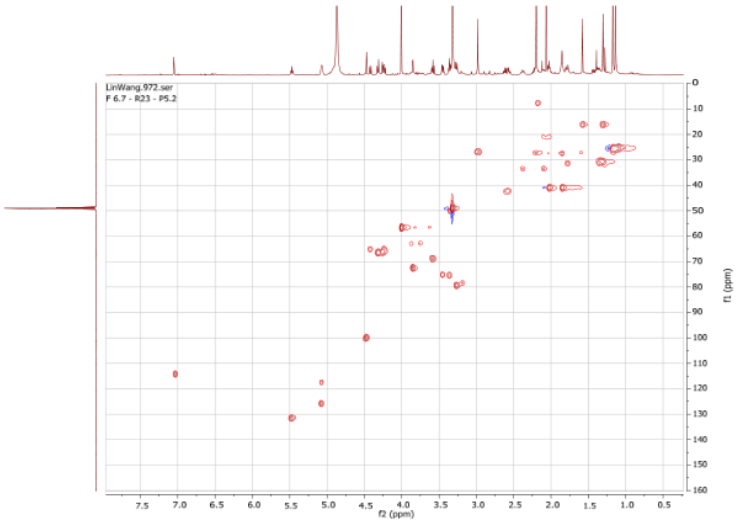


Fig. S50. ^{1}H-^{13}C HSQC of Compound **8.**

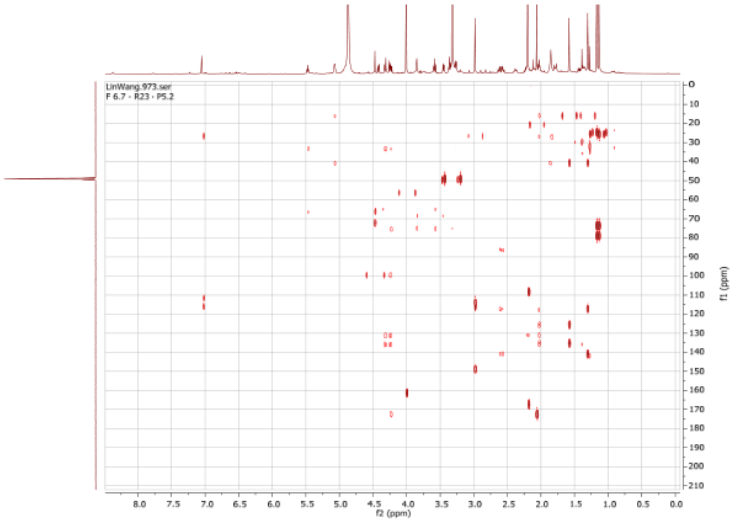


Fig. S51. ^{1}H-^{13}C HMBC of Compound **8.**

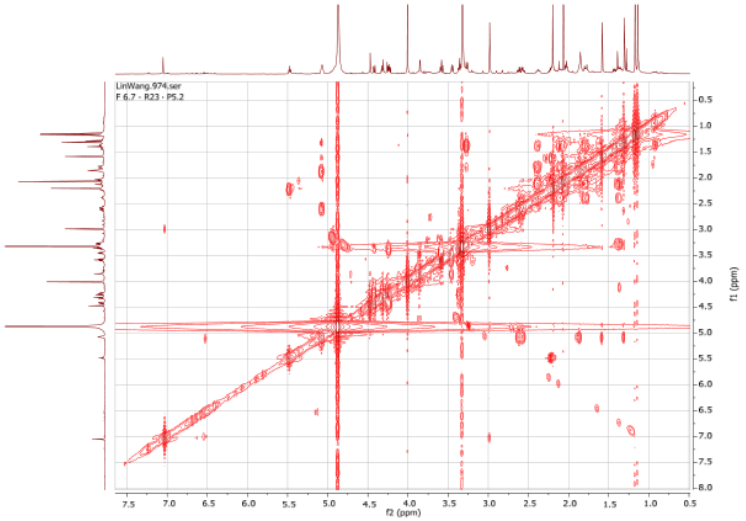


Fig. S52. ^{1}H-^{1}H COSY of Compound **8.**

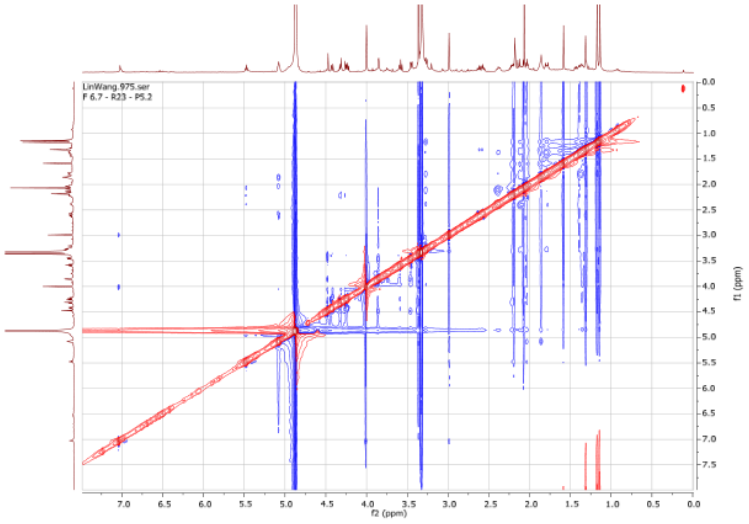


Fig. S53. ^{1}H-^{1}H ROESY of Compound **8.**

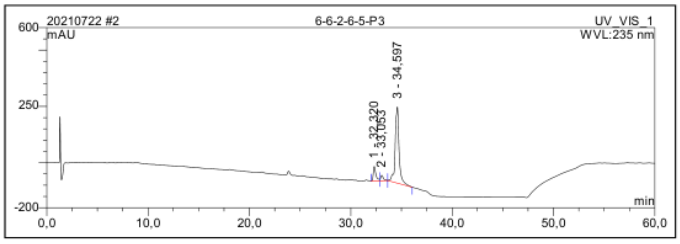


Fig. S54. HPLC chromatogram of Compound **1**.

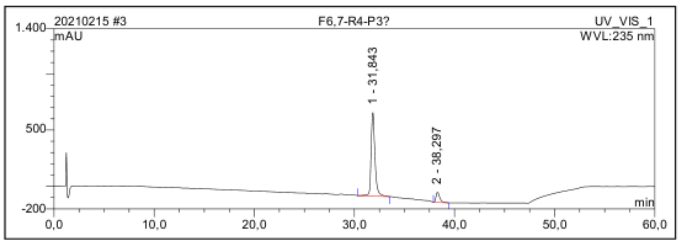


Fig. S55. HPLC chromatogram of Compound **2**.

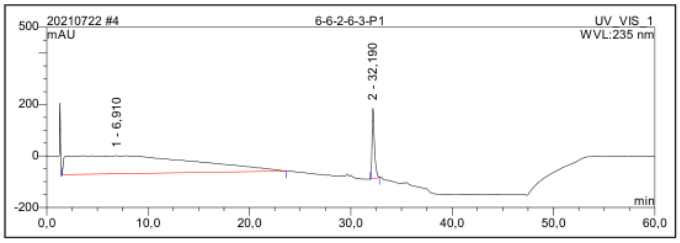


Fig. S56. HPLC chromatogram of Compound **3**.

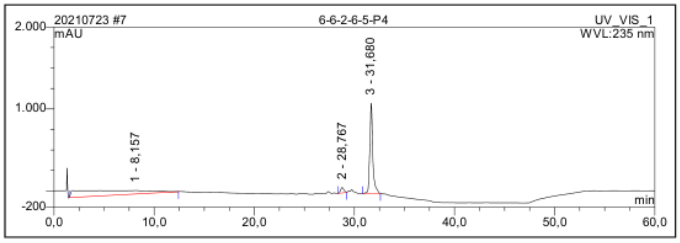


Fig. S57. HPLC chromatogram of Compound **4**.

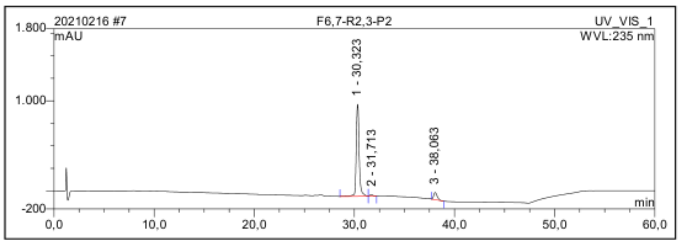


Fig. S58. HPLC chromatogram of Compound **5**.

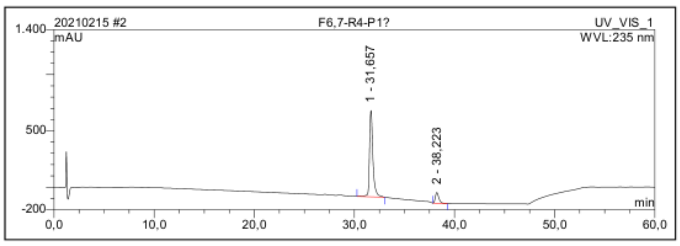


Fig. S59. HPLC chromatogram of Compound **6**.

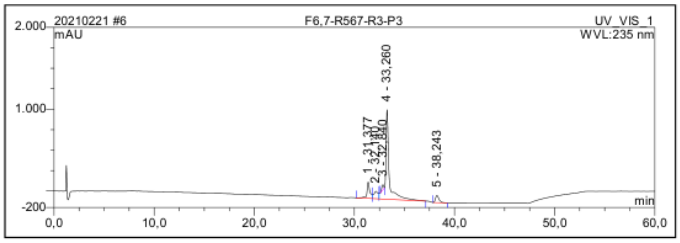


Fig. S60. HPLC chromatogram of Compound **7**.

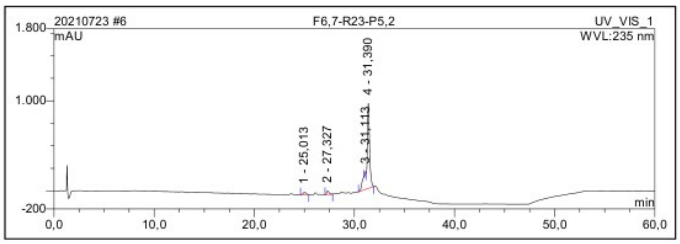


Fig. S61. HPLC chromatogram of Compound **8**.

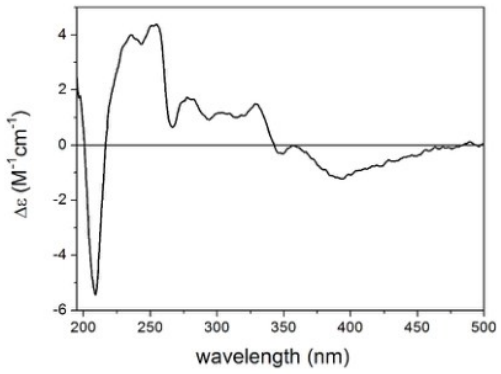


Fig. S62. Experimental ECD spectrum of compound **1** in MeOH.

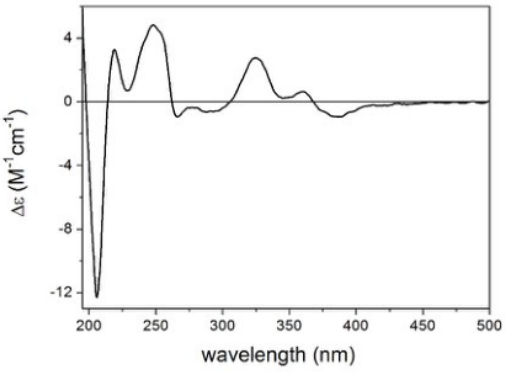


Fig. S63. Experimental ECD spectrum of compound **3** in MeOH

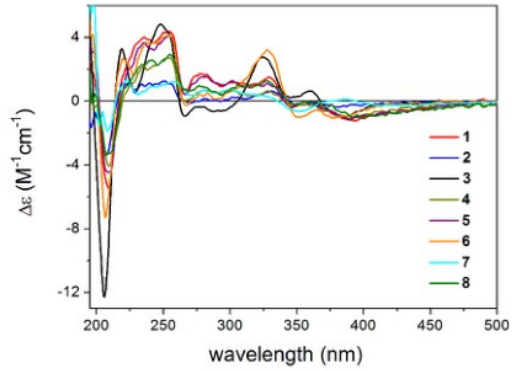


Fig. S64. Comparison of the experimental ECD spectra of **1**-**8** measured in MeOH.

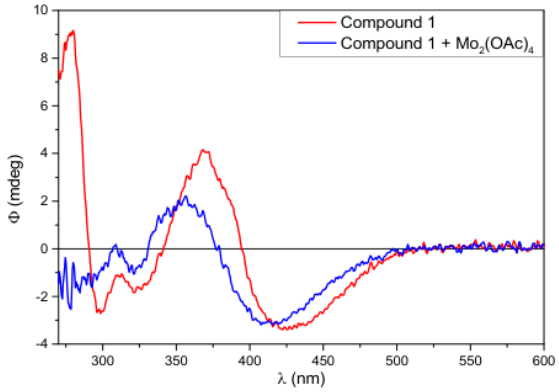


Fig. S65. ECD spectrum of **1** in DMSO (red curve) compared with that of the $Mo_2(OAc)_4$ complex (1.30 ligand/metal ratio) in DMSO (blue).

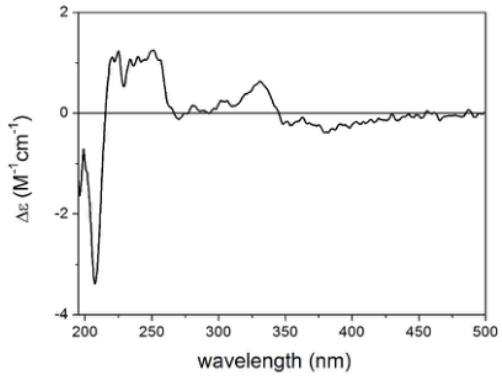


Fig. S66. Experimental ECD spectrum of compound **2** in MeOH.

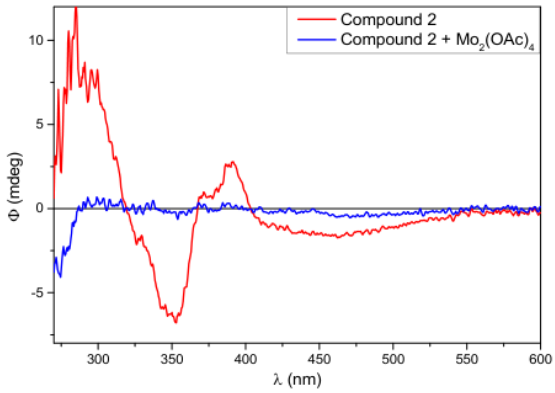


Fig. S67. ECD spectrum of **2** in DMSO (red curve) compared with that of the $Mo_2(OAc)_4$ complex (1.30 ligand/metal ratio) in DMSO (blue).

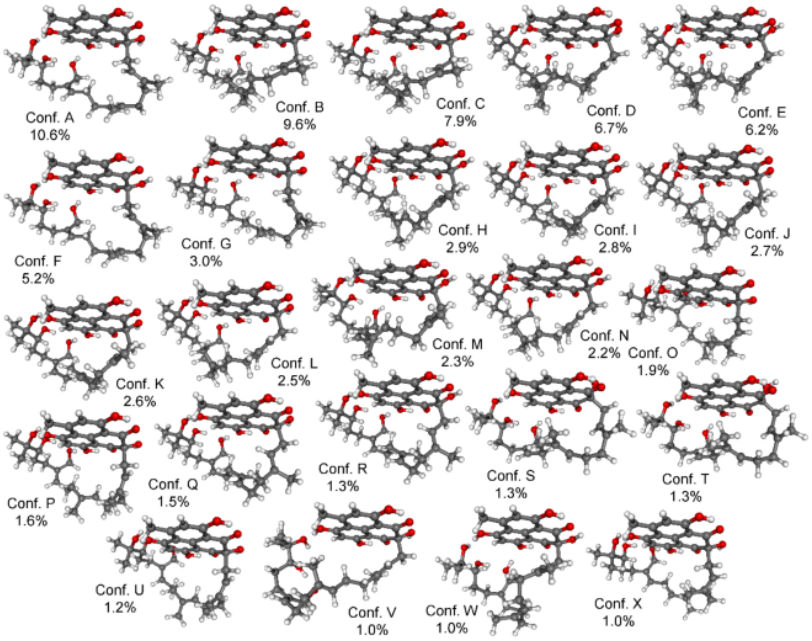


Fig. S68. Low-energy (≥ 1%) ω B97X/TZVP PCM/MeOH conformers of (1*S*,29*R*)-**3**.

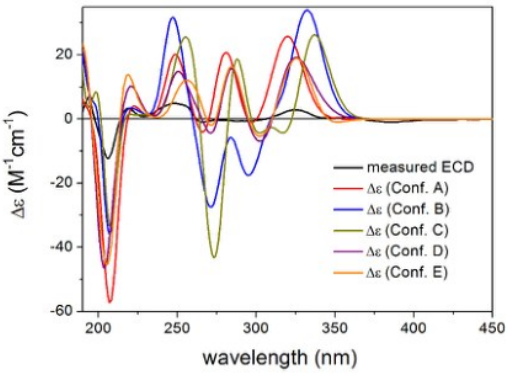


Fig. S69. Experimental ECD spectrum of **3** in MeOH (black line) compared with the calculated B3LYP/TZVP PCM/MeOH spectra of the five lowest-energy individual conformers of (1*S*,29*R*)-**3** (color lines). Level of DFT optimization: ωB97X/TZVP PCM/MeOH.

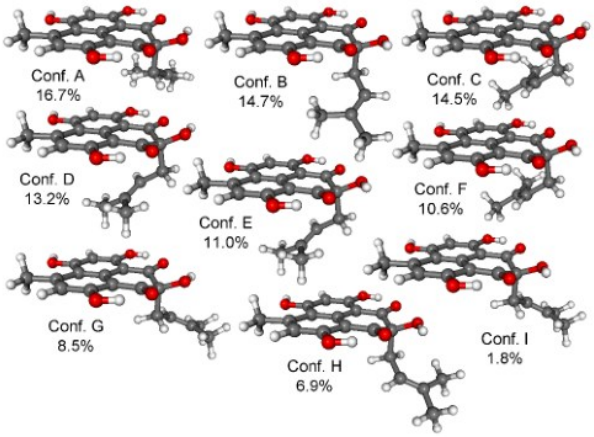


Fig. S70. Low-energy (≥ 1%) ωB97X/TZVP PCM/MeOH conformers of (*S*)-**3modMe**.

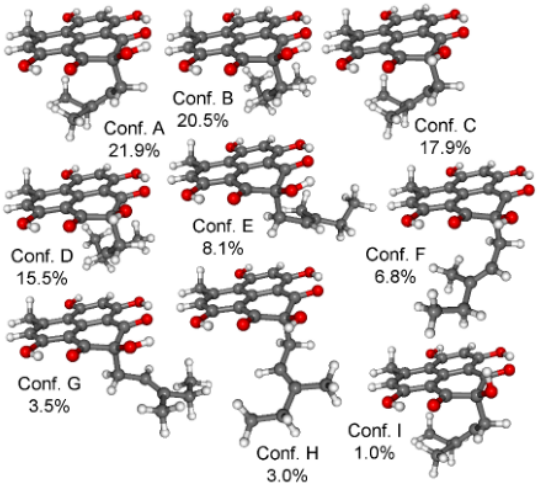


Fig. S71. Low-energy (≥ 1%) ωB97X/TZVP PCM/MeOH conformers of (*S*)-**3modEt**.

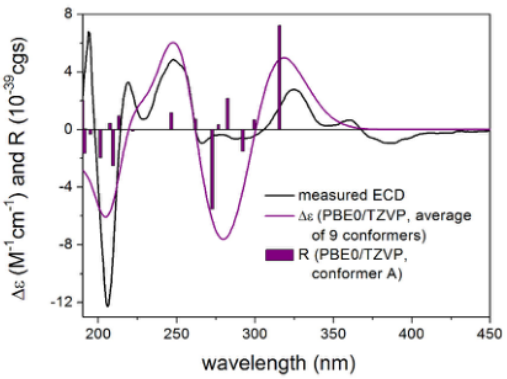


Fig. S72. Experimental ECD spectrum of **3** in MeOH (black line) compared with the calculated PBE0/TZVP PCM/MeOH spectrum of (*S*)-**3modMe** (purple line). Level of DFT optimization: ωB97X/TZVP PCM/MeOH. Bars represent the rotational strengths of conformer A.

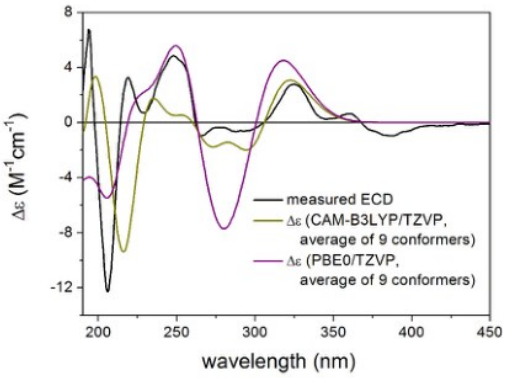


Fig. S73. Experimental ECD spectrum of **3** in MeOH (black line) compared with the calculated CAM-B3LYP/TZVP PCM/MeOH and PBE0/TZVP PCM/MeOH spectra of (*S*)-**3modEt** (olive and purple lines, respectively). Level of DFT optimization: ωB97X/TZVP PCM/MeOH.

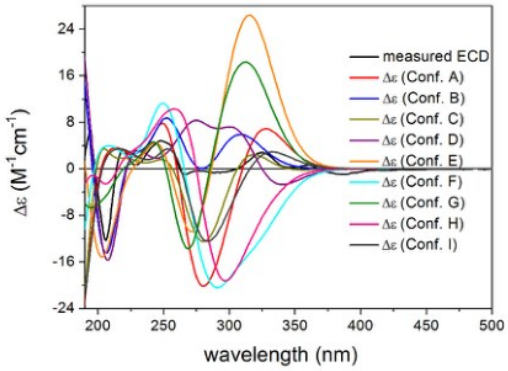


Fig. S74. Experimental ECD spectrum of **3** in MeOH (black line) compared with the calculated PBE0/TZVP PCM/MeOH spectra of the individual low-energy conformers of (*S*)-**3modEt** (color lines). Level of DFT optimization: ωB97X/TZVP PCM/MeOH.

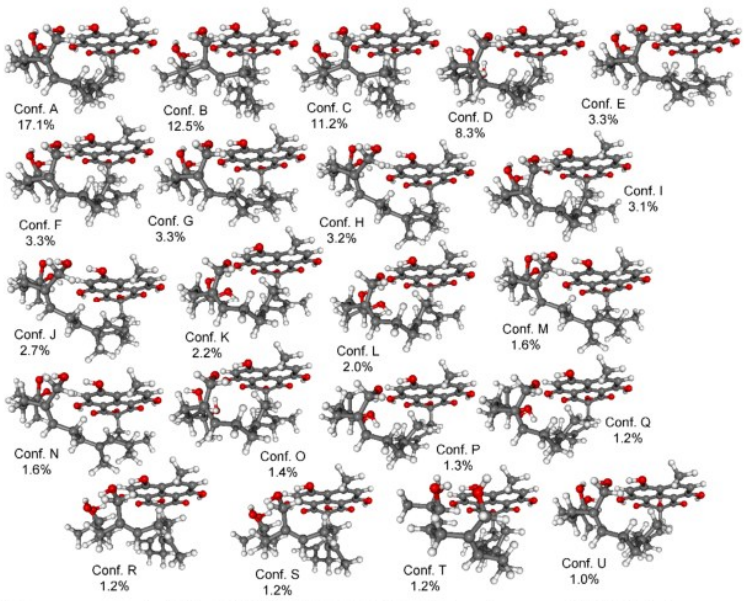


Fig. S75. Low-energy (≥ 1%) ωB97X/TZVP PCM/MeOH conformers of (1*S*,29*S*)-**3**.

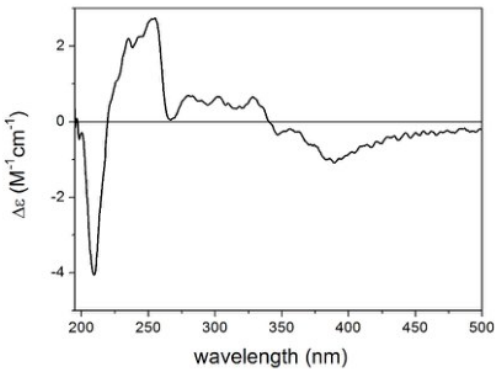


Fig. S76. Experimental ECD spectrum of compound **4** in MeOH.

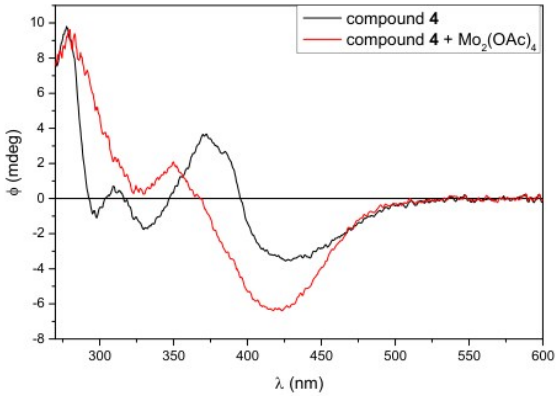


Fig. S77. ECD spectrum of **4** in DMSO (red curve) compared with that of the $Mo_2(OAc)_4$ complex (1.30 ligand/metal ratio) in DMSO (blue).

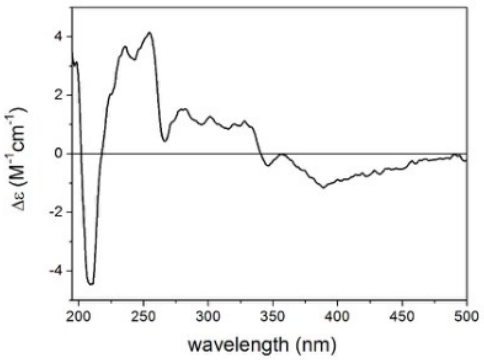


Fig. S78. Experimental ECD spectrum of compound **5** in MeOH.

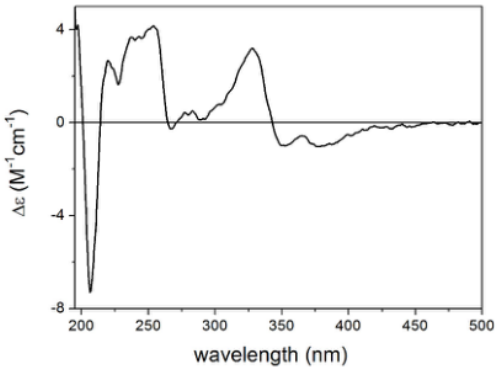


Fig. S79. Experimental ECD spectrum of compound **6** in MeOH

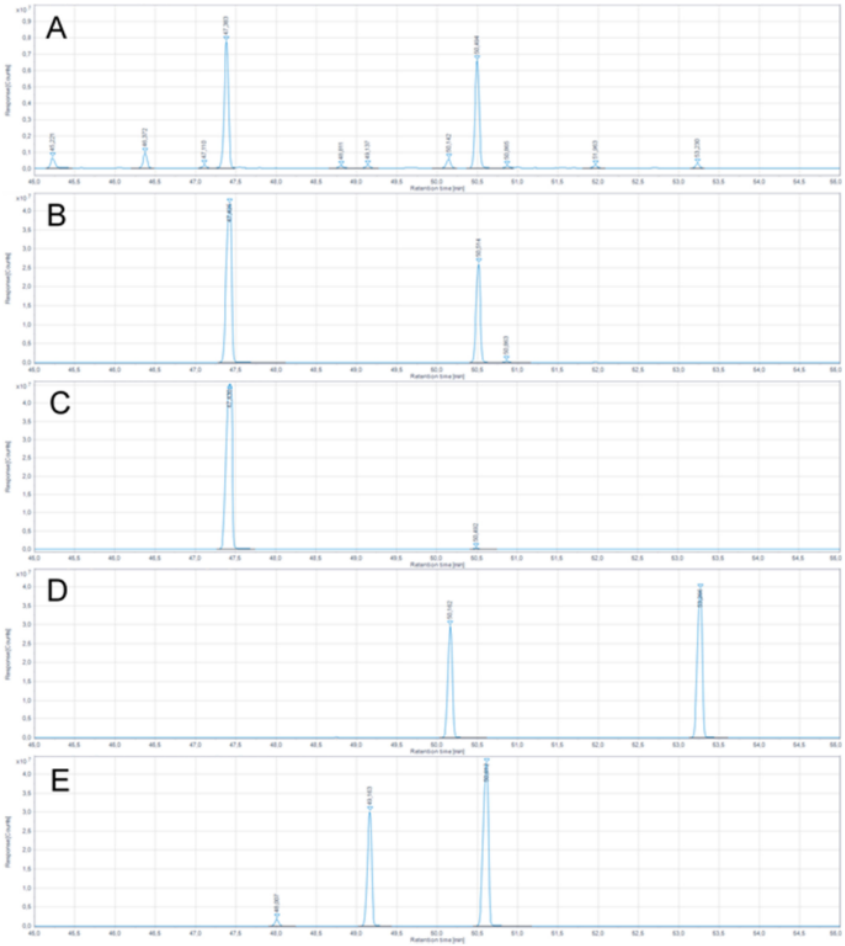


Fig. S80. GC-MS analysis of the sugar component of asperphenalenone K. Total ion chromatograms of the sugar component of asperphenalenone K after hydrolysis (A), D-Mannose with (B) and without heating to 90 °C in water (C), as well as D-Glucose (D) and D-Galactose (E) following heating to 90 °C in water. All samples were analyzed following trimethylsilylation. All reference sugars yielded two peaks after heating likely representing interconversion of α-D- to β-D configuration. The congruence of the sugar profile resulting from hydrolysis of asperphenalenone K (A) with that of the reference α-D-mannose after heating (compare B and C) indicates that the glycoconjugate contains α-D-mannose.

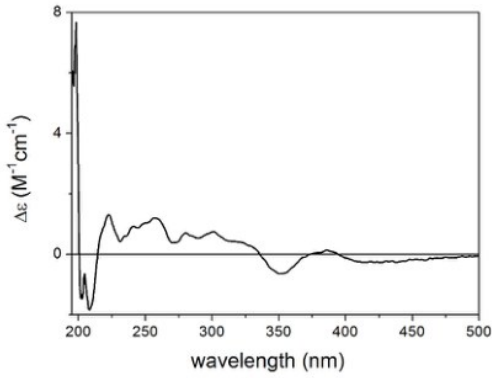


Fig. S81. Experimental ECD spectrum of compound **7** in MeOH.

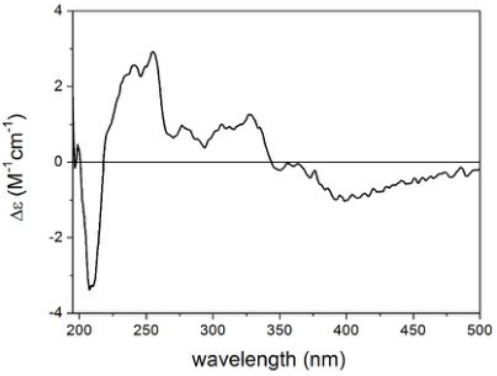


Fig. S82. Experimental ECD spectrum of compound **8** in MeOH.

Table S1. Boltzmann populations and specific optical rotations of the low-energy conformers of (1*S*,29*R*)-**3** computed at various levels for the ωB97X/TZVP PCM/MeOH optimized MMFF conformers.

Conformer	Boltzmann population	B3LYP/TZVP	BH&HLYP/TZVP	CAM-B3LYP/TZVP	PBE0/TZVP
Conf. A	10.59%	151.68	96.71	101.98	142.71
Conf. B	9.61%	-42.39	-56.09	-52.61	-45.04
Conf. C	7.91%	-59.51	-71.50	-68.12	-59.56
Conf. D	6.67%	222.88	168.64	184.43	217.64
Conf. E	6.22%	217.41	160.88	177.67	214.04
Conf. F	5.16%	103.74	62.39	67.21	98.56
Conf. G	2.99%	130.00	92.28	98.72	124.16
Conf. H	2.93%	-13.08	-22.12	-18.52	-15.55
Conf. I	2.82%	92.20	72.44	76.52	89.90
Conf. J	2.70%	5.57	-5.46	-1.44	0.55
Conf. K	2.57%	113.03	90.93	95.74	108.33
Conf. L	2.46%	238.25	194.69	206.75	232.87
Conf. M	2.28%	112.04	77.32	88.48	109.68
Conf. N	2.20%	221.29	180.57	191.80	218.41
Conf. O	1.93%	199.95	135.70	148.99	185.19
Conf. P	1.60%	91.03	56.69	69.65	83.60
Conf. Q	1.46%	192.95	161.31	167.24	189.22
Conf. R	1.32%	178.86	146.02	152.53	177.12
Conf. S	1.26%	-35.84	-47.77	-44.84	-40.46
Conf. T	1.26%	12.45	-25.92	-14.79	5.45
Conf. U	1.16%	157.97	119.26	132.04	152.56
Conf. V	1.00%	71.68	53.08	62.20	69.39
Conf. W	0.97%	-134.99	-130.04	-125.86	-134.05
Conf. X	0.96%	247.68	167.66	179.28	228.22
Average	N/A	96.57	62.08	69.77	91.89

Table S2. Boltzmann populations and specific optical rotations of the low-energy conformers of (*S*)-**3modMe** computed at various levels for the ωB97X/TZVP PCM/MeOH optimized MMFF conformers.

Conformer	Boltzmann population	B3LYP/TZVP	BH&HLYP/TZVP	CAM-B3LYP/TZVP	PBE0/TZVP
Conf. A	16.69%	447.72	320.78	341.74	421.16
Conf. B	14.69%	-429.98	-317.34	-332.75	-402.43
Conf. C	14.54%	180.86	144.88	153.34	176.41
Conf. D	13.17%	-130.51	-116.05	-119.68	-131.27
Conf. E	11.02%	-169.90	-147.47	-152.48	-165.69
Conf. F	10.65%	143.83	114.46	121.54	143.90
Conf. G	8.46%	272.48	169.96	182.52	257.30
Conf. H	6.92%	-283.39	-182.13	-192.93	-266.30
Conf. I	1.81%	217.13	127.75	139.99	207.46
Average	N/A	25.15	13.00	15.78	24.19

Table S3. Boltzmann populations and specific optical rotations of the low-energy conformers of (*S*)-**3modEt** computed at various levels for the ωB97X/TZVP PCM/MeOH optimized MMFF conformers.

Conformer	Boltzmann population	B3LYP/TZVP	BH&HLYP/TZVP	CAM-B3LYP/TZVP	PBE0/TZVP
Conf. A	21.88%	-166.74	-138.59	-144.19	-164.74
Conf. B	20.53%	204.65	160.92	170.06	199.29
Conf. C	17.87%	-186.20	-157.86	-162.86	-181.11
Conf. D	15.46%	179.74	137.26	146.61	177.80
Conf. E	8.07%	442.33	313.88	333.99	418.30
Conf. F	6.77%	-427.42	-312.65	-327.73	-401.92
Conf. G	3.47%	289.76	184.82	198.00	274.55
Conf. H	2.98%	-298.66	-196.20	-207.29	-281.54
Conf. I	0.98%	-180.09	-152.34	-157.65	-176.27
Average	N/A	6.30	-1.08	0.84	6.05

Table S4. Boltzmann populations and specific optical rotations of the low-energy conformers of (1*S*,29*S*)-**3** computed at various levels for the ωB97X/TZVP PCM/MeOH optimized MMFF conformers.

Conformer	Boltzmann population	B3LYP/TZVP	BH&HLYP/TZVP	CAM-B3LYP/TZVP	PBE0/TZVP
Conf. A	17.08 %	21.58	28.79	31.53	18.98
Conf. B	12.52 %	29.56	25.23	28.79	23.08
Conf. C	11.22 %	34.40	22.56	28.55	29.04
Conf. D	8.35 %	83.85	81.20	84.75	81.46
Conf. E	3.33 %	116.46	99.36	98.60	113.18
Conf. F	3.31 %	-143.58	-122.99	-125.58	-143.39
Conf. G	3.29 %	108.12	89.12	89.36	106.67
Conf. H	3.21 %	310.17	257.15	265.62	306.33
Conf. I	3.14 %	-146.39	-127.93	-129.26	-144.70
Conf. J	2.70 %	297.10	244.14	252.85	295.42
Conf. K	2.17 %	-47.51	-42.38	-42.28	-51.56
Conf. L	2.03 %	-50.62	-47.53	-46.17	-52.90
Conf. M	1.65 %	99.87	83.79	85.39	98.97
Conf. N	1.55 %	111.21	95.32	96.65	108.15
Conf. O	1.36 %	-49.79	-44.88	-44.26	-53.39
Conf. P	1.27 %	150.05	134.38	143.48	141.62
Conf. Q	1.20 %	147.77	128.57	139.39	141.27
Conf. R	1.17 %	97.48	97.30	100.45	96.58
Conf. S	1.16 %	96.07	90.12	95.79	96.70
Conf. T	1.16 %	-18.29	-22.48	-21.48	-20.32
Conf. U	1.00 %	26.56	31.52	34.78	24.60
Average	N/A	48.84	43.24	46.48	45.50

Table S5. Cartesian coordinates and energies of the low-energy conformers calculated at the ωB97X/TZVP PCM/MeOH level related to Tables S2 – S4.

(1*S*,29*R*)-**3**, Conf A

O	-4.302243	1.240895	1.899045
O	-2.909514	5.005804	-1.205951
C	1.834012	4.746009	-1.677109
O	2.947987	2.790637	-0.218555
O	0.547492	-0.145368	2.528722
O	-4.198620	3.330030	0.252908
O	-2.004903	0.104726	2.648012
C	1.783234	2.360261	0.252124
C	1.741946	1.314772	1.153709
C	0.524332	0.862257	1.642608
C	-1.820427	4.319664	-0.867959
C	-0.595375	4.772374	-1.378889
C	0.588672	4.161532	-1.066832
C	0.584476	3.027365	-0.181561
C	-3.153918	2.704275	0.415721
C	-1.868095	3.186013	-0.054518
C	-0.649400	2.536421	0.308968
C	-0.681694	1.429826	1.215202
C	-1.925808	0.918236	1.720117
O	2.423312	-2.263597	2.287785
C	-5.935247	-1.311904	-0.860046
C	-2.602244	-2.835000	-2.730279
C	1.817034	-3.245288	1.430830
O	4.812861	-1.123865	1.419627
O	5.082786	1.295687	0.364573
C	4.946183	0.579526	-1.896420
C	6.855921	-0.125488	-0.425983
C	5.362333	0.164268	-0.496664
C	4.504254	-0.996548	0.033139
C	4.673433	-2.314458	-0.709886
C	3.845697	-3.451073	-0.100794
C	2.356111	-3.174510	0.026412
C	1.602714	-2.923625	-1.042695
C	0.123379	-2.669373	-1.097704
C	-0.643837	-3.932901	-1.521833
C	-2.137054	-3.735329	-1.618994
C	-2.945176	-4.331232	-0.742878
C	-4.439387	-4.234420	-0.636426
C	-4.882952	-3.214431	0.433146
C	-4.767199	-1.785476	-0.040369
C	-3.681427	-1.066045	0.241114
C	-3.398376	0.339458	-0.193228
C	-3.216091	1.313010	1.021054
H	-4.155051	0.460684	2.449728
H	-3.674522	4.592406	-0.743849
H	1.565042	5.586691	-2.315480
H	2.526803	5.091456	-0.910857
H	2.367458	4.006137	-2.272698
H	3.704319	2.220995	0.073947
H	-0.380181	-0.303742	2.829153
H	2.657187	0.854007	1.503738
H	-0.612400	5.637368	-2.030610
H	1.800949	-1.527565	2.390408
H	-5.793253	-0.328802	-1.304585
H	-6.836244	-1.277993	-0.240792
H	-6.139012	-2.018953	-1.669864
H	-3.686258	-2.824506	-2.837920
H	-2.283265	-1.803683	-2.552065
H	-2.162947	-3.145574	-3.682943
H	2.058719	-4.222891	1.857562
H	0.732155	-3.133120	1.459493
H	4.051225	-1.557519	1.846926
H	5.162428	0.961191	1.269029
H	5.224253	-0.182838	-2.624364
H	5.452358	1.507765	-2.168183
H	3.867362	0.741550	-1.957820
H	7.411817	0.778682	-0.679494
H	7.141064	-0.443720	0.578274
H	7.139320	-0.908764	-1.130574
H	3.457162	-0.681644	-0.067380
H	4.383490	-2.167896	-1.754307
H	5.725968	-2.610954	-0.704519
H	3.995739	-4.348442	-0.707068
H	4.250238	-3.686211	0.887016
H	2.094725	-2.943682	-2.015717
H	-0.263697	-2.322444	-0.135153
H	-0.066454	-1.867591	-1.817726
H	-0.254835	-4.268042	-2.491137
H	-0.426883	-4.726656	-0.801437
H	-2.476491	-4.945585	0.025783
H	-4.894699	-3.981437	-1.597188
H	-4.834489	-5.215436	-0.358819
H	-5.924398	-3.415092	0.702600
H	-4.282770	-3.363503	1.334773
H	-2.904783	-1.543560	0.834802
H	-4.216812	0.745095	-0.787931
H	-2.493752	0.375215	-0.810543

ωB97X Energy = -1999.37106328 a.u.

(1*S*,29*R*)-**3**, Conf B

O	4.413948	-1.737306	-2.745368
O	5.331899	2.338799	0.144886
C	1.083190	4.277137	1.137304
O	-0.969911	3.004718	-0.030586
O	-0.556585	-0.937373	-2.518309
O	5.526695	0.169112	-1.205415
O	1.765606	-1.934822	-2.857326
C	-0.200469	2.046136	-0.532687
C	-0.760110	1.030451	-1.282234

C	0.040995	0.024763	-1.802631
C	4.015962	2.206582	-0.007594
C	3.203995	3.188646	0.579080
C	1.841143	3.167320	0.459935
C	1.216997	2.109691	-0.289243
C	4.299996	0.085724	-1.211629
C	3.441448	1.135592	-0.694186
C	2.022726	1.085103	-0.841655
C	1.424056	0.010976	-1.574868
C	2.213015	-1.061581	-2.099906
O	-3.309596	-1.565254	-2.356704
C	5.170023	-1.360837	2.115121
C	-1.502172	-0.533746	2.222110
C	-3.431317	-2.724299	-1.517306
O	-4.705534	0.725491	-1.700950
O	-3.583078	2.842224	-0.600168
C	-3.989197	2.204051	1.648059
C	-5.886097	2.731749	0.090281
C	-4.508837	2.095580	0.226302
C	-4.471651	0.647912	-0.295950
C	-5.436691	-0.313406	0.383608
C	-5.392996	-1.727070	-0.208485
C	-4.030468	-2.400908	-0.174182
C	-3.459605	-2.733146	0.981521
C	-2.149338	-3.437765	1.216360
C	-1.471364	-3.079568	2.549718
C	-0.716810	-1.772511	2.556479
C	0.581797	-1.735198	2.851724
C	1.441490	-0.495983	2.916986
C	2.929358	-0.780488	3.093621
C	3.679903	-1.339964	1.906321
C	3.066012	-1.724415	0.788148
C	3.718067	-2.208591	-0.473134
C	3.665544	-1.214313	-1.676368
H	3.818022	-2.329123	-3.224347
H	5.760164	1.592382	-0.334770
H	1.781901	4.923414	1.667157
H	0.525493	4.874589	0.417290
H	0.357786	3.883879	1.848758
H	-1.924480	2.881118	-0.265682
H	0.147363	-1.548870	-2.849890
H	-1.824267	1.018240	-1.481165
H	3.695023	3.982012	1.129387
H	-2.370737	-1.336243	-2.427616
H	5.557361	-0.337203	2.140539
H	5.713054	-1.904554	1.344393
H	5.407823	-1.813102	3.081632
H	-0.968614	0.379378	2.489838
H	-1.721120	-0.490727	1.150051
H	-2.465585	-0.531499	2.740171
H	-4.090778	-3.425075	-2.039242
H	-2.456554	-3.203755	-1.417589
H	-4.297629	-0.067034	-2.095868
H	-3.791732	2.592344	-1.511964
H	-4.663745	1.709450	2.347676
H	-3.917178	3.255630	1.932212
H	-2.999946	1.750581	1.741313
H	-5.817285	3.794821	0.326494
H	-6.266053	2.621818	-0.926977
H	-6.599926	2.274593	0.777347
H	-3.451052	0.278383	-0.130971
H	-5.195251	-0.359832	1.449927
H	-6.457754	0.068640	0.297369
H	-6.112789	-2.343877	0.335945
H	-5.750956	-1.687646	-1.240662
H	-4.018628	-2.509268	1.891593
H	-2.339164	-4.516727	1.224738
H	-1.447926	-3.259623	0.395909
H	-2.240131	-3.057336	3.332420
H	-0.777783	-3.880329	2.816763
H	1.081808	-2.674429	3.086151
H	1.296530	0.122215	2.023512
H	1.117539	0.122335	3.761338
H	3.433510	0.149928	3.378921
H	3.074884	-1.457362	3.945347
H	1.982236	-1.660141	0.750823
H	3.239685	-3.126859	-0.827029
H	4.777769	-2.421579	-0.335449

ωB97X Energy = -1999.37097163 a.u.

(1*S*,29*R*)-**3**, Conf C

O	4.392251	-1.741339	-2.757872
O	5.360149	2.328985	0.137457
C	1.123448	4.284222	1.153075
O	-0.943290	3.023955	-0.003387
O	-0.561133	-0.933200	-2.470531
O	5.522542	0.156100	-1.253598
O	1.720328	-1.969299	-2.792117
C	-0.179417	2.059824	-0.506564
C	-0.744237	1.044989	-1.250340
C	0.049283	0.030253	-1.768820
C	4.041821	2.203089	-0.001513
C	3.238152	3.188726	0.587789
C	1.873859	3.170463	0.474118
C	1.239503	2.116011	-0.271436
C	4.291365	0.084403	-1.207518
C	3.455097	1.131657	-0.676678
C	2.035650	1.084119	-0.824836
C	1.435064	0.012144	-1.558228
C	2.209219	-1.084465	-2.083219
O	-3.321736	-1.510962	-2.388497
C	5.146300	-1.352284	2.126556
C	-1.539509	-0.581577	2.214183
C	-3.470573	-2.685809	-1.576273
O	-4.704481	0.776320	-1.698961
O	-3.560949	2.865475	-0.568673
C	-3.970464	2.198517	1.670466
C	-5.864207	2.766588	0.122708
C	-4.492715	2.115836	0.247959
C	-4.470136	0.675549	-0.295513
C	-5.443943	-0.286606	0.370497

C	-5.418945	-1.690608	-0.245440
C	-4.064943	-2.382092	-0.226329
C	-3.495684	-2.742031	0.921853
C	-2.190314	-3.461012	1.140937
C	-1.510200	-3.135393	2.481452
C	-0.755438	-1.829111	2.518184
C	0.543918	-1.797642	2.811076
C	1.399019	-0.556818	2.901938
C	2.885867	-0.835703	3.095269
C	3.657333	-1.366862	1.908321
C	3.060627	-1.759727	0.783783
C	3.733104	-2.222416	-0.474926
C	3.665385	-1.222044	-1.671747
H	5.317708	-1.515606	-2.593887
H	5.786620	1.590844	-0.351176
H	1.826578	4.928931	1.678876
H	0.564619	4.881930	0.434176
H	0.399468	3.894464	1.867860
H	-1.898528	2.901918	-0.234617
H	0.143027	-1.558498	-2.787074
H	-1.809662	1.034076	-1.442505
H	3.733548	3.982574	1.133290
H	-2.379363	-1.287729	-2.430597
H	5.509397	-0.319700	2.151582
H	5.707380	-1.885953	1.361616
H	5.388414	-1.795851	3.095979
H	-1.013484	0.322425	2.524446
H	-1.737436	-0.499717	1.140303
H	-2.512572	-0.600111	2.713182
H	-4.144119	-3.358887	-2.116125
H	-2.506660	-3.188765	-1.486945
H	-4.300524	-0.011945	-2.106500
H	-3.770805	2.627970	-1.483527
H	-4.646821	1.696902	2.363348
H	-3.891341	3.244934	1.971361
H	-2.983931	1.737377	1.754461
H	-5.785074	3.825871	0.372315
H	-6.246605	2.673139	-0.895281
H	-6.581270	2.307373	0.805032
H	-3.452998	0.294050	-0.136831
H	-5.200115	-0.354039	1.435149
H	-6.460858	0.108405	0.293977
H	-6.145321	-2.307311	0.290351
H	-5.778686	-1.629101	-1.275926
H	-4.051070	-2.530182	1.837017
H	-2.386727	-4.538722	1.126017
H	-1.487958	-3.269100	0.324396
H	-2.278001	-3.131190	3.265404
H	-0.816679	-3.942673	2.728334
H	1.046393	-2.740999	3.022186
H	1.263570	0.070648	2.013235
H	1.060708	0.051029	3.748240
H	3.379078	0.092271	3.406150
H	3.023853	-1.528162	3.935702
H	1.975832	-1.722378	0.738956
H	3.276522	-3.144157	-0.845087
H	4.794716	-2.419782	-0.322134

ωB97X Energy = -1999.37078779 a.u.

(1*S*,29*R*)-**3**, Conf D

O	-4.746482	0.571877	-3.032853
O	-5.263155	-2.648402	0.820661
C	-0.815321	-3.869110	2.046120
O	1.054986	-2.727385	0.497604
O	0.208729	0.801841	-2.455177
O	-5.717405	-0.854699	-0.938970
O	-2.195539	1.422905	-2.957240
C	0.188362	-1.900513	-0.076889
C	0.631603	-0.940331	-0.964101
C	-0.277070	-0.107618	-1.601613
C	-3.974083	-2.391508	0.620089
C	-3.052095	-3.147088	1.358975
C	-1.702041	-3.003765	1.192195
C	-1.208282	-2.043659	0.241654
C	-4.510177	-0.622591	-0.995625
C	-3.531098	-1.404495	-0.265804
C	-2.127032	-1.219788	-0.452914
C	-1.655811	-0.218101	-1.360898
C	-2.561153	0.621636	-2.083551
O	2.933796	1.542630	-2.393705
C	-1.941288	3.257372	0.191757
C	0.550835	2.445136	4.094175
C	3.127024	2.650667	-1.499054
O	4.402445	-0.786141	-2.076569
O	3.518183	-2.788963	-0.583679
C	4.530927	-2.057662	1.429979
C	5.928649	-2.780273	-0.530284
C	4.664941	-2.059865	-0.082385
C	4.548491	-0.643230	-0.664722
C	5.681101	0.311655	-0.316363
C	5.416070	1.741485	-0.814918
C	4.065895	2.287527	-0.379220
C	3.760273	2.384718	0.912408
C	2.440033	2.697060	1.552077
C	1.857390	1.410702	2.163004
C	0.529932	1.598557	2.851120
C	-0.572241	1.042066	2.348996
C	-1.964356	1.142041	2.909251
C	-2.737240	2.398050	2.468839
C	-2.966809	2.486382	0.974814
C	-4.030858	1.885995	0.442964
C	-4.446022	1.859731	-1.000140
C	-4.057663	0.586145	-1.800525
H	-4.284955	1.195830	-3.607994
H	-5.777170	-2.065638	0.213735
H	-1.427737	-4.441894	2.741353
H	-0.231494	-4.558926	1.438251
H	-0.104533	-3.268241	2.612539
H	1.963697	-2.646560	0.112412
H	-0.562920	1.268068	-2.868045
H	1.685989	-0.847018	-1.193444

H	-3.445614	-3.867263	2.065882
H	1.986723	1.350360	-2.457296
H	-2.162561	3.313368	-0.873781
H	-0.955717	2.797140	0.312135
H	-1.860379	4.276313	0.580641
H	1.357897	2.128444	4.761080
H	0.737600	3.494301	3.846310
H	-0.387735	2.401701	4.646160
H	3.562178	3.472446	-2.078152
H	2.160787	2.986574	-1.121084
H	3.926164	0.006393	-2.382922
H	3.495447	-2.613614	-1.535385
H	5.406908	-1.609588	1.899438
H	4.441212	-3.083960	1.790688
H	3.644847	-1.499722	1.744929
H	5.899983	-3.816200	-0.188230
H	6.014144	-2.771603	-1.618452
H	6.817202	-2.305075	-0.110935
H	3.618524	-0.227156	-0.257580
H	5.811135	0.327802	0.769165
H	6.616111	-0.053789	-0.750014
H	6.217755	2.390950	-0.454011
H	5.479172	1.758071	-1.905876
H	4.537379	2.106493	1.625723
H	2.580259	3.447041	2.336392
H	1.722588	3.113209	0.841293
H	1.749978	0.666576	1.366905
H	2.583300	1.007097	2.880375
H	-0.469627	0.471769	1.427192
H	-2.536272	0.260207	2.602030
H	-1.936032	1.128128	4.002202
H	-3.702958	2.399498	2.980673
H	-2.192356	3.284711	2.808254
H	-4.699381	1.359439	1.122912
H	-4.053684	2.712770	-1.557146
H	-5.535637	1.898293	-1.065367

ωB97X Energy = -1999.37062629 a.u.

(1*S*,29*R*)-**3**, Conf E

O	-4.708244	0.566841	-3.053289
O	-5.263053	-2.648339	0.824884
C	-0.815532	-3.855983	2.069807
O	1.057209	-2.734888	0.509022
O	0.217561	0.796925	-2.442079
O	-5.699352	-0.872028	-0.984321
O	-2.163387	1.457018	-2.921113
C	0.191407	-1.906842	-0.067166
C	0.633438	-0.949711	-0.956093
C	-0.274281	-0.114087	-1.594264
C	-3.972465	-2.390987	0.632408
C	-3.052461	-3.141076	1.377408
C	-1.701813	-2.996858	1.209333
C	-1.205324	-2.044323	0.252328
C	-4.488659	-0.629805	-0.992319
C	-3.525013	-1.404271	-0.250969
C	-2.121508	-1.221063	-0.446630
C	-1.654376	-0.225690	-1.362924
C	-2.554473	0.631533	-2.088735
O	2.941344	1.525581	-2.407840
C	-1.952584	3.278192	0.171128
C	0.549728	2.474300	4.069893
C	3.137739	2.640540	-1.522639
O	4.411105	-0.800122	-2.071384
O	3.523184	-2.795051	-0.570910
C	4.528576	-2.052245	1.442301
C	5.933341	-2.785648	-0.508934
C	4.667866	-2.062999	-0.069574
C	4.553273	-0.649515	-0.659957
C	5.685192	0.307010	-0.313854
C	5.422969	1.733342	-0.823621
C	4.071825	2.283976	-0.396664
C	3.761555	2.390008	0.893162
C	2.439606	2.708383	1.526322
C	1.853467	1.426826	2.143897
C	0.526628	1.620975	2.831467
C	-0.576767	1.062938	2.333722
C	-1.967861	1.166688	2.896024
C	-2.740867	2.421115	2.451486
C	-2.972298	2.502843	0.957278
C	-4.032800	1.893423	0.428651
C	-4.447751	1.857245	-1.014557
C	-4.049260	0.581017	-1.804830
H	-5.623620	0.315660	-2.875263
H	-5.777485	-2.081017	0.207447
H	-1.427476	-4.419308	2.773100
H	-0.236235	-4.554163	1.467137
H	-0.100599	-3.251623	2.627093
H	1.965481	-2.654857	0.123528
H	-0.557250	1.276184	-2.840877
H	1.687921	-0.855152	-1.184623
H	-3.444932	-3.858717	2.087368
H	1.994277	1.328054	-2.459359
H	-0.963099	2.827865	0.297344
H	-1.882265	4.300331	0.553685
H	-2.171726	3.323759	-0.895207
H	1.357486	2.160738	4.737435
H	0.736796	3.521992	3.816101
H	-0.388143	2.434489	4.623355
H	3.578420	3.454486	-2.108497
H	2.172043	2.984898	-1.150851
H	3.935054	-0.009549	-2.383320
H	3.502038	-2.622247	-1.523139
H	5.402836	-1.601369	1.912313
H	4.437654	-3.076458	1.808638
H	3.641277	-1.492631	1.750818
H	5.903728	-3.819506	-0.160734
H	6.022415	-2.783611	-1.596850
H	6.820440	-2.307799	-0.089523
H	3.622341	-0.230927	-0.257639
H	5.811250	0.330604	0.772015
H	6.621567	-0.061981	-0.741533

H	6.224039	2.384829	-0.464961
H	5.489704	1.741669	-1.914461
H	4.535663	2.115289	1.611092
H	2.578443	3.463302	2.306155
H	1.724979	3.120750	0.810493
H	1.744438	0.678732	1.351755
H	2.578353	1.025283	2.863498
H	-0.475890	0.487298	1.415064
H	-2.540905	0.283859	2.593744
H	-1.937509	1.157595	3.988982
H	-3.705814	2.425224	2.964796
H	-2.195138	3.309031	2.786131
H	-4.696524	1.364499	1.111618
H	-4.059210	2.703442	-1.582392
H	-5.538868	1.898048	-1.072540

ωB97X Energy = -1999.37056053 a.u.

(1*S*,29*R*)-**3**, Conf F

O	-4.317529	1.166113	1.958000
O	-3.033091	4.973623	-1.156858
C	1.702067	4.760984	-1.737055
O	2.873803	2.832153	-0.290194
O	0.564956	-0.120393	2.517175
O	-4.262547	3.268145	0.364621
O	-1.969099	0.075652	2.685516
C	1.723167	2.385352	0.202136
C	1.710150	1.344671	1.107890
C	0.506917	0.878138	1.623091
C	-1.927317	4.299915	-0.848300
C	-0.720048	4.765013	-1.386507
C	0.476717	4.164696	-1.098974
C	0.506596	3.031147	-0.212981
C	-3.193859	2.660821	0.464020
C	-1.940999	3.161751	-0.040293
C	-0.709703	2.524717	0.304655
C	-0.716289	1.423610	1.217001
C	-1.946483	0.886958	1.758620
O	2.498076	-2.178127	2.330134
C	-5.800841	-1.441713	-1.098176
C	-2.487084	-2.954723	-2.709718
C	1.909050	-3.192488	1.499847
O	4.850152	-0.998673	1.417201
O	5.049126	1.394897	0.299749
C	4.911622	0.621304	-1.941923
C	6.853953	0.004786	-0.474478
C	5.352275	0.251522	-0.536953
C	4.531594	-0.919090	0.029317
C	4.735082	-2.252251	-0.676853
C	3.937383	-3.391937	-0.033826
C	2.442448	-3.145344	0.092397
C	1.681400	-2.934001	-0.979693
C	0.197637	-2.707637	-1.037537
C	-0.547403	-3.995688	-1.424258
C	-2.039850	-3.821190	-1.564328
C	-2.865205	-4.408599	-0.698459
C	-4.363978	-4.337176	-0.647878
C	-4.870122	-3.288321	0.363325
C	-4.730062	-1.869192	-0.132322
C	-3.712744	-1.110158	0.270977
C	-3.418883	0.296827	-0.151927
C	-3.244208	1.265215	1.066872
H	-4.982915	1.795617	1.646497
H	-3.783780	4.561724	-0.676629
H	1.410933	5.594658	-2.374788
H	2.405258	5.118306	-0.985855
H	2.232867	4.023643	-2.338071
H	3.644479	2.281988	0.000854
H	-0.358997	-0.287812	2.832828
H	2.636911	0.897929	1.445739
H	-0.758425	5.630371	-2.036660
H	1.858640	-1.454633	2.419012
H	-5.885783	-2.162212	-1.916924
H	-5.630247	-0.461447	-1.539249
H	-6.772390	-1.424649	-0.595671
H	-1.984473	-3.252259	-3.634693
H	-3.563132	-2.998607	-2.874140
H	-2.228806	-1.907367	-2.526787
H	2.170840	-4.154656	1.949280
H	0.822215	-3.100501	1.528719
H	4.103089	-1.441702	1.860569
H	5.139704	1.081472	1.210903
H	5.198475	-0.152809	-2.653957
H	5.393688	1.553334	-2.242954
H	3.828763	0.757733	-1.994137
H	7.382064	0.916866	-0.757347
H	7.158057	-0.278520	0.534688
H	7.152042	-0.788755	-1.161352
H	3.475253	-0.638227	-0.074089
H	4.440239	-2.142886	-1.724460
H	5.795066	-2.520534	-0.664819
H	4.105943	-4.301537	-0.616576
H	4.351275	-3.591044	0.958051
H	2.171315	-2.967484	-1.953406
H	-0.194198	-2.338955	-0.084968
H	-0.007059	-1.930871	-1.780553
H	-0.134481	-4.364774	-2.371219
H	-0.336930	-4.757968	-0.668725
H	-2.411478	-4.995782	0.099740
H	-4.788125	-4.132353	-1.633950
H	-4.750112	-5.314864	-0.346567
H	-5.926229	-3.485741	0.574049
H	-4.326446	-3.412234	1.303829
H	-3.007030	-1.546644	0.974190
H	-4.227401	0.704968	-0.760016
H	-2.507320	0.334583	-0.759392

ωB97X Energy = -1999.37038461 a.u.

(1*S*,29*R*)-**3**, Conf G

O	4.533686	0.072952	2.142070
O	4.450905	-4.207480	-0.626220

C	-0.123167	-5.089985	-1.682819
O	-1.833414	-3.330249	-0.590087
O	-0.543676	0.196097	2.206747
O	5.119545	-2.170314	0.805972
O	1.973952	0.575477	2.612603
C	-0.867526	-2.633242	-0.002749
C	-1.182745	-1.570995	0.821720
C	-0.176378	-0.818721	1.410412
C	3.200022	-3.771819	-0.490834
C	2.188640	-4.529954	-1.099104
C	0.866978	-4.190911	-0.993277
C	0.497128	-3.030716	-0.227661
C	3.950605	-1.797625	0.768496
C	2.881933	-2.606297	0.206942
C	1.511110	-2.236664	0.358326
C	1.171615	-1.103482	1.163863
C	2.191197	-0.276652	1.742990
O	-3.158152	1.297776	2.551114
C	5.183822	2.777476	-1.495730
C	1.439830	2.596136	-2.863321
C	-3.086294	2.642701	2.050510
O	-5.005243	-0.411108	1.367912
O	-4.308940	-2.446039	-0.124874
C	-4.269826	-1.259948	-2.183059
C	-6.421159	-1.641446	-0.942898
C	-4.932854	-1.340738	-0.819887
C	-4.646021	-0.085759	0.026109
C	-5.340792	1.182932	-0.447079
C	-5.069568	2.386676	0.461221
C	-3.605230	2.754769	0.640619
C	-2.880835	3.185884	-0.390270
C	-1.447587	3.629104	-0.426579
C	-0.655415	2.885428	-1.499265
C	0.753687	3.365333	-1.767003
C	1.319182	4.362616	-1.088428
C	2.705630	4.919815	-1.248474
C	3.689030	4.364049	-0.197006
C	4.092191	2.936628	-0.474324
C	3.457105	1.931513	0.125106
C	3.674480	0.466266	-0.112589
C	3.606720	-0.380612	1.198263
H	4.069291	0.725591	2.684218
H	5.033465	-3.599241	-0.117614
H	0.407815	-5.891933	-2.194157
H	-0.822649	-5.527160	-0.971135
H	-0.718213	-4.538555	-2.409659
H	-2.730596	-2.961291	-0.388473
H	0.272292	0.589611	2.596372
H	-2.217136	-1.321207	1.017956
H	2.487110	-5.411068	-1.653942
H	-2.289645	0.885984	2.428139
H	5.404568	1.739488	-1.738457
H	6.103806	3.250357	-1.140446
H	4.911367	3.284161	-2.426695
H	0.863674	2.650655	-3.791951
H	2.449734	2.949366	-3.065516
H	1.506265	1.537246	-2.593047
H	-3.712131	3.249514	2.710685
H	-2.062731	3.007310	2.140503
H	-4.459597	0.150971	1.947674
H	-4.539334	-2.326912	0.808421
H	-4.733462	-0.485387	-2.794629
H	-4.380302	-2.213452	-2.703085
H	-3.204268	-1.035828	-2.089144
H	-6.554143	-2.615696	-1.415905
H	-6.895262	-1.662130	0.040310
H	-6.926506	-0.892995	-1.555024
H	-3.561698	0.082632	-0.016312
H	-5.009296	1.409026	-1.464962
H	-6.420723	1.017757	-0.486167
H	-5.606991	3.246961	0.053789
H	-5.513777	2.191604	1.440770
H	-3.387567	3.254282	-1.354591
H	-1.428506	4.701406	-0.651719
H	-0.962662	3.506691	0.543839
H	-0.613283	1.819235	-1.238439
H	-1.209714	2.926453	-2.445516
H	0.743706	4.833178	-0.294598
H	3.098912	4.740697	-2.251620
H	2.658938	6.005823	-1.128575
H	4.583423	4.994900	-0.182834
H	3.226344	4.438607	0.790956
H	2.667759	2.190640	0.827140
H	4.658732	0.276163	-0.543260
H	2.930639	0.079097	-0.818537

ωB97X Energy = -1999.36986943 a.u.

(1*S*,29*R*)-**3**, Conf H

O	4.291480	0.866826	3.257614
O	5.341807	-2.627852	-0.268335
C	1.138354	-3.928732	-2.124782
O	-0.956521	-2.813506	-0.868810
O	-0.599058	0.728299	2.166735
O	5.476333	-0.797457	1.547197
O	1.690862	1.481217	2.919165
C	-0.192674	-1.966050	-0.185965
C	-0.769158	-1.019856	0.634036
C	0.023916	-0.164554	1.388056
C	4.033035	-2.386301	-0.276031
C	3.242291	-3.164987	-1.131329
C	1.879677	-3.036476	-1.166603
C	1.236461	-2.072672	-0.314100
C	4.279797	-0.566270	1.345521
C	3.448361	-1.384717	0.502990
C	2.029339	-1.223431	0.495204
C	1.423002	-0.232591	1.330925
C	2.202101	0.670052	2.141006
O	-3.369537	0.943208	2.690722
C	5.198105	0.849252	-1.595166
C	-0.679243	4.136273	-2.897087
C	-3.685947	2.221210	2.111994

O	-4.680512	-1.291260	1.631864
O	-3.525416	-2.925562	-0.092727
C	-4.306289	-1.824175	-2.041082
C	-5.904329	-2.967307	-0.472738
C	-4.632717	-2.138564	-0.592036
C	-4.667887	-0.866821	0.269826
C	-5.803978	0.100741	-0.025424
C	-5.724071	1.369577	0.834647
C	-4.376593	2.072760	0.782623
C	-3.862902	2.478939	-0.375742
C	-2.518036	3.072618	-0.672876
C	-1.752158	2.180140	-1.662768
C	-0.498214	2.801720	-2.222499
C	0.684030	2.190718	-2.147802
C	1.966006	2.717768	-2.747005
C	3.140830	1.744330	-2.727029
C	3.883747	1.561262	-1.423694
C	3.411432	1.997575	-0.256747
C	4.091987	1.902998	1.080511
C	3.713397	0.691197	1.985563
H	5.203411	0.554879	3.183904
H	5.751594	-2.046415	0.410077
H	1.852467	-4.487227	-2.728612
H	0.499487	-4.632797	-1.592959
H	0.491320	-3.351320	-2.783658
H	-1.907623	-2.751685	-0.602657
H	0.103021	1.231464	2.658051
H	-1.845561	-0.960792	0.726472
H	3.742865	-3.892909	-1.758068
H	-2.424270	0.784904	2.546067
H	5.742269	0.700320	-0.663968
H	5.842040	1.410359	-2.278044
H	5.036148	-0.132390	-2.051731
H	-1.634965	4.175824	-3.426677
H	-0.686997	4.948332	-2.163778
H	0.115638	4.350916	-3.611421
H	-4.356776	2.725756	2.813014
H	-2.776859	2.818540	2.034731
H	-4.281465	-0.572983	2.156048
H	-3.611035	-2.911111	0.871737
H	-5.134369	-1.305427	-2.524647
H	-4.125432	-2.753394	-2.584688
H	-3.412917	-1.197993	-2.115213
H	-5.771691	-3.915815	-0.995765
H	-6.133570	-3.173361	0.574438
H	-6.754513	-2.446689	-0.916802
H	-3.725391	-0.341464	0.074028
H	-5.770109	0.372630	-1.084129
H	-6.764843	-0.389721	0.152824
H	-6.513981	2.056198	0.518717
H	-5.949484	1.107495	1.871660
H	-4.471851	2.322081	-1.267812
H	-2.660280	4.062442	-1.118671
H	-1.919140	3.214739	0.229411
H	-1.514901	1.225593	-1.181306
H	-2.423823	1.952290	-2.501108
H	0.739287	1.227427	-1.639330
H	1.780632	2.986279	-3.791565
H	2.264275	3.649593	-2.253302
H	2.806875	0.756879	-3.072911
H	3.874834	2.072360	-3.470550
H	2.443820	2.491848	-0.243876
H	3.836623	2.777570	1.682812
H	5.179708	1.881717	0.985467

ωB97X Energy = -1999.36984899 a.u.

(1*S*,29*R*)-**3**, Conf I

O	4.341762	-1.269886	-2.984452
O	5.296080	2.699829	0.034547
C	1.048516	4.225596	1.592470
O	-1.012061	2.943194	0.451731
O	-0.585556	-0.955033	-2.102431
O	5.474044	0.642211	-1.517854
O	1.727145	-1.823329	-2.646498
C	-0.235123	2.018686	-0.103102
C	-0.792526	0.979139	-0.817439
C	0.019282	0.031243	-1.426831
C	3.987251	2.457342	0.041545
C	3.175285	3.339670	0.765862
C	1.811919	3.214081	0.781015
C	1.190153	2.144512	0.046758
C	4.273509	0.436239	-1.312039
C	3.421668	1.359344	-0.610808
C	2.002879	1.197024	-0.620398
C	1.416883	0.103171	-1.333331
C	2.217136	-0.907180	-1.978659
O	-3.412244	-1.459790	-2.229029
C	5.092124	-0.543595	1.866640
C	0.249199	-3.977478	1.085289
C	-3.772504	-2.611931	-1.445256
O	-4.700738	0.945963	-1.647076
O	-3.568819	2.913643	-0.318645
C	-4.294069	2.221821	1.831121
C	-5.937320	3.001562	0.095138
C	-4.650699	2.229536	0.355557
C	-4.681418	0.806274	-0.227052
C	-5.821417	-0.073719	0.263946
C	-5.784706	-1.478193	-0.351042
C	-4.468265	-2.213723	-0.168779
C	-3.969247	-2.460541	1.040188
C	-2.648588	-3.108522	1.362016
C	-1.481263	-2.119577	1.210651
C	-0.154585	-2.658616	1.688224
C	0.578106	-1.968418	2.562338
C	1.888646	-2.347099	3.192811
C	3.006037	-1.308300	3.047441
C	3.786270	-1.282081	1.750811
C	3.349823	-1.861598	0.633178
C	4.074102	-1.958204	-0.680497
C	3.723547	-0.902749	-1.774094
H	5.249451	-0.941423	-2.932194

H	5.722975	2.035666	-0.550562
H	1.749017	4.863861	2.129590
H	0.419616	4.847858	0.956948
H	0.388653	3.741213	2.310917
H	-1.961116	2.838679	0.188588
H	0.128216	-1.526993	-2.489640
H	-1.866733	0.904408	-0.929064
H	3.659435	4.146754	1.301918
H	-2.455944	-1.318204	-2.164568
H	5.656897	-0.503709	0.936282
H	5.724092	-1.009103	2.628049
H	4.911276	0.485141	2.194699
H	0.148435	-3.935952	-0.004818
H	1.274408	-4.259265	1.319926
H	-0.402410	-4.784164	1.431674
H	-4.451129	-3.209340	-2.060929
H	-2.882700	-3.212876	-1.251912
H	-4.301930	0.136969	-2.016179
H	-3.673509	2.700580	-1.257562
H	-5.097293	1.783410	2.423987
H	-4.137800	3.245340	2.177135
H	-3.379171	1.650648	2.009095
H	-5.804695	4.040751	0.400345
H	-6.193762	2.978080	-0.965756
H	-6.770154	2.581989	0.661535
H	-3.736106	0.331185	0.066244
H	-5.765891	-0.148720	1.353678
H	-6.779668	0.392206	0.019377
H	-6.597833	-2.067176	0.081508
H	-6.005305	-1.399252	-1.418769
H	-4.544423	-2.119794	1.900281
H	-2.672252	-3.480122	2.390132
H	-2.477365	-3.978998	0.724567
H	-1.397766	-1.854966	0.149843
H	-1.716455	-1.194615	1.746058
H	0.174118	-1.016400	2.908787
H	1.707000	-2.473374	4.265519
H	2.243761	-3.315072	2.833324
H	2.602063	-0.303642	3.229377
H	3.731855	-1.472333	3.850865
H	2.379387	-2.345657	0.654185
H	3.842091	-2.916266	-1.151260
H	5.158122	-1.914041	-0.555593

ωB97X Energy = -1999.36981208 a.u.

(1*S*,29*R*)-**3**, Conf J

O	4.310725	0.841910	3.254707
O	5.332671	-2.637653	-0.272194
C	1.123729	-3.941972	-2.110250
O	-0.964208	-2.812897	-0.855525
O	-0.595774	0.728891	2.179281
O	5.495830	-0.801848	1.503707
O	1.719668	1.447689	2.949870
C	-0.198589	-1.966163	-0.175878
C	-0.774998	-1.017555	0.643903
C	0.020443	-0.164264	1.394935
C	4.024602	-2.393994	-0.271270
C	3.229722	-3.174815	-1.122670
C	1.868029	-3.046703	-1.156950
C	1.230199	-2.077687	-0.306611
C	4.296851	-0.571441	1.349998
C	3.445964	-1.393195	0.513708
C	2.027817	-1.229751	0.499041
C	1.419324	-0.233093	1.327638
C	2.205766	0.651014	2.133898
O	-3.374440	0.966794	2.681870
C	5.218730	0.846183	-1.589608
C	-0.659209	4.123829	-2.918040
C	-3.682595	2.241461	2.090978
O	-4.684176	-1.272888	1.630191
O	-3.531406	-2.921695	-0.082858
C	-4.308729	-1.831468	-2.038847
C	-5.910255	-2.959803	-0.463345
C	-4.636565	-2.135089	-0.587866
C	-4.668668	-0.857542	0.265404
C	-5.801380	0.111525	-0.037800
C	-5.719039	1.385445	0.814417
C	-4.369381	2.084341	0.760677
C	-3.851092	2.480371	-0.399142
C	-2.504767	3.070813	-0.696004
C	-1.736242	2.173129	-1.679015
C	-0.480284	2.792200	-2.237066
C	0.702002	2.182205	-2.154905
C	1.986125	2.708224	-2.750333
C	3.161100	1.734931	-2.726149
C	3.902002	1.554248	-1.421185
C	3.424891	1.988116	-0.255271
C	4.100443	1.894190	1.084843
C	3.719403	0.680794	1.986701
H	3.739193	1.450096	3.741814
H	5.743141	-2.043594	0.398656
H	1.836553	-4.503838	-2.712564
H	0.485034	-4.643471	-1.574792
H	0.476619	-3.366914	-2.771085
H	-1.915733	-2.749603	-0.589699
H	0.102089	1.221776	2.680613
H	-1.851232	-0.959971	0.738738
H	3.729915	-3.903463	-1.749013
H	-2.428952	0.803966	2.546009
H	5.765667	0.708870	-0.658495
H	5.857775	1.402890	-2.280596
H	5.059328	-0.140866	-2.035511
H	-0.667180	4.939310	-2.188526
H	0.136834	4.334476	-3.632271
H	-1.614141	4.161794	-3.449136
H	-4.353267	2.755407	2.785272
H	-2.770338	2.833584	2.011563
H	-4.286566	-0.551262	2.150747
H	-3.618860	-2.903526	0.881348
H	-5.135012	-1.313320	-2.526086
H	-4.130770	-2.764892	-2.576142

H	-3.413294	-1.208739	-2.117026
H	-5.780199	-3.911706	-0.980819
H	-6.139834	-3.159048	0.585067
H	-6.759148	-2.439592	-0.910317
H	-3.724326	-0.336373	0.067108
H	-5.764864	0.376530	-1.098153
H	-6.764013	-0.374913	0.141884
H	-6.506210	2.072570	0.492802
H	-5.947245	1.130603	1.852617
H	-4.457407	2.317874	-1.291976
H	-2.645190	4.058379	-1.147378
H	-1.908358	3.217717	0.207179
H	-1.500887	1.220724	-1.192375
H	-2.405144	1.941670	-2.518568
H	0.755814	1.220950	-1.642453
H	1.804121	2.976039	-3.795644
H	2.282968	3.640379	-2.256361
H	2.828162	0.746760	-3.070966
H	3.896260	2.061949	-3.468905
H	2.455349	2.478814	-0.245694
H	3.842130	2.775018	1.678743
H	5.188000	1.869613	1.000404

ωB97X Energy = -1999.36977189 a.u.

(1*S*,29*R*)-**3**, Conf K

O	4.360699	-1.262347	-2.977199
O	5.292575	2.703499	0.029566
C	1.043112	4.241919	1.564949
O	-1.014040	2.940824	0.438295
O	-0.582524	-0.960587	-2.110230
O	5.495814	0.640419	-1.472938
O	1.755936	-1.800961	-2.677694
C	-0.236331	2.017037	-0.114076
C	-0.795247	0.974294	-0.825464
C	0.017260	0.027460	-1.431974
C	3.984295	2.460033	0.029061
C	3.169808	3.347514	0.746405
C	1.807246	3.223945	0.761979
C	1.188911	2.147836	0.034743
C	4.293233	0.431215	-1.315660
C	3.423061	1.360956	-0.625867
C	2.004687	1.199692	-0.627440
C	1.414510	0.100506	-1.330219
C	2.220556	-0.893464	-1.971998
O	-3.413784	-1.479893	-2.215971
C	5.108467	-0.539471	1.866813
C	0.259775	-3.966658	1.106520
C	-3.771614	-2.626581	-1.422708
O	-4.699590	0.931029	-1.644047
O	-3.569232	2.908432	-0.328433
C	-4.293785	2.229672	1.825829
C	-5.937777	2.996698	0.084835
C	-4.650524	2.227501	0.350288
C	-4.679695	0.800474	-0.223146
C	-5.818720	-0.077322	0.273970
C	-5.781559	-1.485493	-0.332417
C	-4.464142	-2.218574	-0.147638
C	-3.961393	-2.455088	1.061831
C	-2.639037	-3.098938	1.385020
C	-1.473004	-2.110410	1.220827
C	-0.145079	-2.644113	1.700750
C	0.587332	-1.947314	2.569847
C	1.897918	-2.321300	3.203042
C	3.016183	-1.284299	3.050588
C	3.797720	-1.269459	1.754353
C	3.356190	-1.850156	0.639361
C	4.076658	-1.956730	-0.675779
C	3.729164	-0.902422	-1.771564
H	3.797847	-1.933883	-3.384806
H	5.718580	2.024772	-0.543953
H	1.743834	4.886411	2.094412
H	0.412149	4.857523	0.925000
H	0.385803	3.763858	2.289944
H	-1.963818	2.834867	0.176674
H	0.126231	-1.524901	-2.509555
H	-1.869465	0.900794	-0.937395
H	3.654978	4.156604	1.278670
H	-2.457302	-1.338908	-2.157822
H	5.677989	-0.517628	0.938922
H	5.732105	-0.998154	2.639097
H	4.933391	0.495534	2.178163
H	0.156528	-3.933050	0.016353
H	1.286015	-4.244880	1.340854
H	-0.389622	-4.772072	1.459960
H	-4.451578	-3.228615	-2.032319
H	-2.881189	-3.225790	-1.226985
H	-4.302177	0.119300	-2.008505
H	-3.674822	2.690944	-1.266221
H	-5.096603	1.794407	2.421551
H	-4.138441	3.255569	2.165133
H	-3.378426	1.660443	2.007563
H	-5.805623	4.038187	0.382268
H	-6.194842	2.965114	-0.975696
H	-6.769937	2.580781	0.654891
H	-3.733749	0.328328	0.072928
H	-5.762473	-0.145499	1.364107
H	-6.777455	0.386458	0.027239
H	-6.593546	-2.072547	0.104894
H	-6.003795	-1.413348	-1.400280
H	-4.534188	-2.107669	1.920815
H	-2.658802	-3.460895	2.416636
H	-2.469084	-3.975231	0.755252
H	-1.392349	-1.856365	0.157166
H	-1.707572	-1.180370	1.747602
H	0.182820	-0.993163	2.909772
H	1.715896	-2.439895	4.276552
H	2.252805	-3.291924	2.850566
H	2.612888	-0.277847	3.224061
H	3.740834	-1.442699	3.856092
H	2.381643	-2.325827	0.663712
H	3.837706	-2.920522	-1.133671

H	5.160905	-1.915283	-0.560783

ωB97X Energy = -1999.36972553 a.u.

(1*S*,29*R*)-**3**, Conf L

O	4.877043	-1.268941	-2.716949
O	5.708454	2.402648	0.675190
C	1.407819	4.047850	1.932035
O	-0.595202	2.924734	0.545540
O	-0.105811	-0.825628	-2.209510
O	5.963359	0.425918	-0.928443
O	2.240558	-1.695791	-2.684719
C	0.190393	2.004990	-0.003890
C	-0.347131	1.039294	-0.830302
C	0.474325	0.094406	-1.427511
C	4.396845	2.228448	0.537194
C	3.559427	3.107727	1.238668
C	2.197213	3.051296	1.126716
C	1.601621	2.058504	0.272880
C	4.741865	0.280410	-0.916298
C	3.851144	1.207648	-0.245781
C	2.432620	1.118943	-0.383369
C	1.860464	0.100672	-1.211532
C	2.678293	-0.873707	-1.865795
O	-2.922278	-1.126173	-2.506669
C	1.686454	-3.269018	0.535361
C	-1.946457	-0.703482	2.031728
C	-3.408324	-2.317127	-1.866758
O	-4.141786	1.301554	-2.042806
O	-3.054711	3.131526	-0.492794
C	-4.091305	2.417313	1.515648
C	-5.450908	3.345660	-0.379814
C	-4.251722	2.490531	0.008445
C	-4.285592	1.094789	-0.639291
C	-5.511522	0.252210	-0.318850
C	-5.504689	-1.108123	-1.026387
C	-4.316232	-2.002833	-0.706554
C	-4.160595	-2.514717	0.512704
C	-3.116636	-3.470833	1.018632
C	-2.587974	-3.150745	2.428657
C	-1.525619	-2.079343	2.471157
C	-0.287974	-2.373279	2.864570
C	0.892650	-1.441374	2.948936
C	2.249953	-2.138705	2.764823
C	2.637797	-2.420705	1.332531
C	3.778916	-1.925558	0.851602
C	4.355415	-2.136432	-0.518164
C	4.161254	-0.976809	-1.540071
H	4.314434	-1.862731	-3.231818
H	6.155622	1.734756	0.104640
H	2.084309	4.619229	2.566430
H	0.864780	4.736610	1.286023
H	0.666786	3.553307	2.558739
H	-1.516048	2.896160	0.182136
H	0.611686	-1.383949	-2.601441
H	-1.410263	1.022679	-1.033949
H	4.029148	3.852149	1.869948
H	-1.961142	-1.074774	-2.400298
H	0.747069	-2.733211	0.368392
H	1.430068	-4.177715	1.086707
H	2.084742	-3.557085	-0.436677
H	-2.935901	-0.463007	2.430935
H	-1.250062	0.071464	2.353806
H	-2.026886	-0.652776	0.941703
H	-3.972460	-2.879446	-2.618288
H	-2.563335	-2.934389	-1.560371
H	-3.740796	0.488455	-2.399679
H	-3.060289	2.975800	-1.448534
H	-4.974488	1.978830	1.981328
H	-3.958844	3.422554	1.920144
H	-3.220643	1.816527	1.788197
H	-5.301110	4.364258	-0.018324
H	-5.574840	3.372132	-1.463953
H	-6.369099	2.957550	0.064036
H	-3.401724	0.558584	-0.271441
H	-5.562440	0.097475	0.763166
H	-6.415756	0.792442	-0.613257
H	-6.426624	-1.631176	-0.759456
H	-5.555045	-0.944284	-2.105989
H	-4.915756	-2.253460	1.256385
H	-3.574600	-4.465397	1.059062
H	-2.272467	-3.553011	0.329087
H	-3.434397	-2.856199	3.061452
H	-2.176046	-4.066117	2.859960
H	-0.088724	-3.398131	3.177614
H	0.805316	-0.627957	2.221234
H	0.897772	-0.967506	3.937090
H	3.029689	-1.523530	3.219231
H	2.233709	-3.084604	3.320427
H	4.383435	-1.314050	1.518621
H	3.954969	-3.031162	-0.998135
H	5.438540	-2.261466	-0.447105

ωB97X Energy = -1999.36968488 a.u.

(1*S*,29*R*)-**3**, Conf M

O	4.412471	-0.245148	3.361998
O	4.923950	-2.425842	-1.191616
C	0.461073	-3.136131	-2.737193
O	-1.387984	-2.502836	-0.896814
O	-0.510972	0.177765	2.839049
O	5.366697	-1.238557	1.056570
O	1.879575	0.700645	3.441710
C	-0.517709	-1.845568	-0.137701
C	-0.948065	-1.139052	0.965865
C	-0.030010	-0.497586	1.788022
C	3.636685	-2.191300	-0.948376
C	2.708501	-2.686733	-1.873921
C	1.359615	-2.566999	-1.672980
C	0.875760	-1.902926	-0.492343
C	4.169490	-0.938036	1.089672
C	3.201755	-1.459215	0.159686

C	1.801716	-1.304351	0.395396
C	1.348083	-0.561196	1.531056
C	2.259273	0.085426	2.440116
O	-3.098573	1.258192	2.631176
C	5.256824	1.335567	-1.208214
C	-0.230086	3.169303	-3.586722
C	-3.049713	2.489016	1.890595
O	-4.690754	-0.832199	1.736364
O	-3.910285	-2.700337	0.013709
C	-4.685349	-1.572036	-1.921353
C	-6.293961	-2.387580	-0.171447
C	-4.927472	-1.771471	-0.435698
C	-4.692676	-0.476162	0.355250
C	-5.667293	0.657062	0.070474
C	-5.308183	1.942753	0.830132
C	-3.868357	2.389054	0.631307
C	-3.396244	2.636338	-0.587850
C	-1.999980	2.967087	-1.025060
C	-1.385588	1.786003	-1.796368
C	-0.099387	2.124387	-2.508463
C	1.047411	1.530158	-2.174546
C	2.397706	1.794123	-2.777270
C	3.262720	2.729602	-1.906055
C	3.992387	2.030891	-0.783677
C	3.527345	2.058130	0.465999
C	4.193381	1.483037	1.686123
C	3.753234	0.067756	2.153331
H	5.308045	-0.514979	3.120008
H	5.441744	-2.077857	-0.431768
H	1.063638	-3.469656	-3.581123
H	-0.113759	-3.980329	-2.358396
H	-0.257887	-2.395249	-3.085247
H	-2.304106	-2.493250	-0.520367
H	0.269149	0.545556	3.333844
H	-1.999647	-1.103202	1.223113
H	3.091777	-3.191464	-2.752251
H	-2.194065	0.939736	2.770645
H	5.920532	2.040876	-1.715471
H	5.030063	0.544110	-1.930353
H	5.804400	0.882108	-0.384031
H	0.590577	3.146608	-4.302218
H	-1.164572	3.032855	-4.137550
H	-0.259399	4.174203	-3.155433
H	-3.462193	3.277118	2.529962
H	-2.011371	2.743783	1.675473
H	-4.189546	-0.139043	2.203668
H	-3.958241	-2.691970	0.980001
H	-5.471607	-0.961639	-2.365979
H	-4.683030	-2.540715	-2.424318
H	-3.723797	-1.083909	-2.101405
H	-6.361190	-3.356472	-0.668926
H	-6.454525	-2.530039	0.898762
H	-7.090155	-1.748487	-0.556922
H	-3.687003	-0.133800	0.079048
H	-5.669809	0.859301	-1.004016
H	-6.680803	0.351610	0.344848
H	-5.990847	2.735713	0.513821
H	-5.494274	1.790397	1.895983
H	-4.097978	2.534890	-1.417122
H	-2.038192	3.845165	-1.677028
H	-1.349788	3.228025	-0.187241
H	-1.224179	0.955863	-1.101277
H	-2.117420	1.441946	-2.538822
H	1.022232	0.802311	-1.364480
H	2.923838	0.845148	-2.927350
H	2.289160	2.244434	-3.764923
H	4.008643	3.211428	-2.545739
H	2.625772	3.522145	-1.505537
H	2.594381	2.588876	0.646410
H	3.998263	2.127667	2.545862
H	5.276849	1.430621	1.559945

ωB97X Energy = -1999.36961462 a.u.

(1*S*,29*R*)-**3**, Conf N

O	4.822730	-1.292322	-2.730116
O	5.734387	2.404200	0.629562
C	1.455038	4.084969	1.915536
O	-0.571224	2.959647	0.564800
O	-0.132163	-0.834492	-2.136507
O	5.944709	0.411055	-0.993865
O	2.175618	-1.750270	-2.605563
C	0.205001	2.027933	0.019308
C	-0.343591	1.054075	-0.787177
C	0.466335	0.094879	-1.380620
C	4.419606	2.235444	0.514420
C	3.595327	3.126943	1.213763
C	2.231058	3.074268	1.115114
C	1.619277	2.075617	0.279458
C	4.719960	0.272795	-0.921641
C	3.856576	1.205489	-0.243558
C	2.436340	1.121803	-0.374394
C	1.856017	0.099187	-1.190296
C	2.655543	-0.904999	-1.843407
O	-2.938258	-1.082466	-2.532825
C	1.708381	-3.336074	0.532494
C	-1.968158	-0.740461	2.032508
C	-3.448673	-2.277921	-1.921039
O	-4.149740	1.344158	-2.026325
O	-3.041987	3.146729	-0.458829
C	-4.066827	2.408256	1.547089
C	-5.435536	3.372920	-0.323972
C	-4.238401	2.505279	0.042454
C	-4.286157	1.119125	-0.624956
C	-5.515715	0.280686	-0.307560
C	-5.526120	-1.067288	-1.037937
C	-4.341884	-1.976995	-0.745778
C	-4.177621	-2.510514	0.463067
C	-3.134241	-3.481189	0.942232
C	-2.604158	-3.199764	2.359882
C	-1.544458	-2.127402	2.432297
C	-0.305802	-2.428291	2.817369

C	0.870282	-1.492624	2.926712
C	2.233635	-2.181979	2.758655
C	2.637176	-2.464159	1.330729
C	3.770536	-1.947760	0.853652
C	4.354937	-2.150102	-0.514295
C	4.141685	-0.993275	-1.534276
H	5.747762	-1.056770	-2.579839
H	6.174708	1.738165	0.055858
H	2.140320	4.660586	2.536471
H	0.909381	4.768264	1.265975
H	0.717379	3.602137	2.555127
H	-1.495285	2.926357	0.211533
H	0.582806	-1.410365	-2.516037
H	-1.409072	1.037605	-0.977583
H	4.073788	3.878721	1.829448
H	-1.982344	-1.031568	-2.383726
H	0.762014	-2.817579	0.350948
H	1.462127	-4.243443	1.090528
H	2.121128	-3.625680	-0.432738
H	-2.954963	-0.510250	2.444319
H	-1.269270	0.025397	2.370331
H	-2.055458	-0.660837	0.944869
H	-4.030968	-2.803491	-2.684882
H	-2.617025	-2.924602	-1.639729
H	-3.752967	0.534879	-2.396648
H	-3.052184	2.998718	-1.415792
H	-4.949508	1.969165	2.013193
H	-3.923950	3.406316	1.965614
H	-3.198508	1.796941	1.803482
H	-5.277738	4.384732	0.052863
H	-5.566046	3.417686	-1.406724
H	-6.353100	2.982884	0.119456
H	-3.404019	0.571465	-0.270123
H	-5.557685	0.108372	0.772204
H	-6.418496	0.832509	-0.584425
H	-6.449630	-1.587712	-0.771183
H	-5.585546	-0.884593	-2.114068
H	-4.923534	-2.256832	1.218641
H	-3.592551	-4.476329	0.956111
H	-2.290635	-3.544761	0.249982
H	-3.450483	-2.925544	3.001914
H	-2.189458	-4.126005	2.764575
H	-0.102883	-3.460672	3.101719
H	0.790513	-0.675344	2.202379
H	0.858078	-1.024153	3.917396
H	3.004205	-1.560160	3.219651
H	2.217732	-3.126667	3.316269
H	4.358637	-1.320823	1.521104
H	3.968262	-3.045226	-1.002444
H	5.439693	-2.264603	-0.433677

ωB97X Energy = -1999.36957820 a.u.

(1*S*,29*R*)-**3**, Conf O

O	4.498767	1.806538	1.973349
O	5.940235	-2.798739	0.264842
C	2.021684	-4.906929	-1.478391
O	-0.229770	-3.494592	-1.058850
O	-0.372374	0.599359	1.200730
O	5.820947	-0.459063	1.358522
O	1.869210	1.701305	1.878060
C	0.418062	-2.495535	-0.467734
C	-0.288412	-1.431392	0.055095
C	0.376362	-0.379403	0.667846
C	4.631937	-2.660874	0.055352
C	3.969097	-3.723811	-0.577052
C	2.619252	-3.703465	-0.801081
C	1.852243	-2.562748	-0.377550
C	4.648730	-0.389548	1.002679
C	3.930466	-1.512265	0.418889
C	2.516625	-1.467798	0.224240
C	1.775274	-0.338264	0.697907
C	2.444764	0.799229	1.258940
O	-2.930661	-0.001736	2.524107
C	1.935790	2.112654	-2.503976
C	-2.006418	5.374691	-1.594908
C	-3.789230	1.150715	2.489810
O	-4.083970	-2.289278	1.434479
O	-2.843487	-3.498608	-0.504662
C	-3.756065	-2.199641	-2.272770
C	-5.189424	-3.774597	-0.939195
C	-4.034270	-2.781736	-0.899019
C	-4.235990	-1.674179	0.155958
C	-5.553266	-0.918479	0.059012
C	-5.733156	0.120962	1.171130
C	-4.656393	1.190890	1.255943
C	-4.531254	2.106551	0.296121
C	-3.535149	3.222451	0.192155
C	-2.505847	2.968009	-0.920130
C	-1.488832	4.078092	-1.033976
C	-0.235980	3.873608	-0.628251
C	0.911540	4.840121	-0.622696
C	1.993817	4.519905	-1.669565
C	2.541857	3.111686	-1.557094
C	3.490163	2.840752	-0.660729
C	4.152976	1.519897	-0.424621
C	3.937061	0.953309	1.017698
H	3.767801	2.338613	2.319351
H	6.250156	-1.999083	0.745823
H	2.810811	-5.617422	-1.721487
H	1.289405	-5.397759	-0.838346
H	1.502503	-4.628485	-2.394592
H	-1.207896	-3.402590	-0.949860
H	0.236542	1.246795	1.627470
H	-1.368884	-1.423939	0.010113
H	4.561951	-4.581003	-0.872292
H	-2.118821	0.207695	2.038628
H	2.231993	1.082849	-2.306686
H	2.214809	2.356849	-3.533388
H	0.845084	2.167232	-2.453436
H	-2.757122	5.817196	-0.933780
H	-1.221216	6.113313	-1.749123

H	-2.497361	5.197665	-2.556261
H	-4.423685	1.073533	3.375836
H	-3.185483	2.052361	2.593749
H	-3.681598	-1.617522	2.013474
H	-2.911722	-3.590853	0.458117
H	-4.632675	-1.678294	-2.659111
H	-3.504659	-3.001148	-2.969961
H	-2.921320	-1.495167	-2.237675
H	-4.919393	-4.613587	-1.582510
H	-5.406572	-4.157528	0.060119
H	-6.094476	-3.315045	-1.339195
H	-3.421309	-0.951598	0.018349
H	-5.610295	-0.426190	-0.916667
H	-6.384999	-1.625592	0.115317
H	-6.703582	0.602662	1.026074
H	-5.796374	-0.402043	2.128863
H	-5.224141	2.042097	-0.544283
H	-4.073177	4.152468	-0.016762
H	-2.999996	3.375800	1.131104
H	-1.994933	2.022976	-0.711678
H	-3.032931	2.848041	-1.874191
H	0.004601	2.878810	-0.255023
H	0.567056	5.864341	-0.777829
H	1.381496	4.813886	0.366438
H	1.573291	4.666063	-2.669265
H	2.806492	5.241600	-1.554688
H	3.854319	3.658956	-0.041889
H	5.237966	1.629049	-0.517736
H	3.839068	0.775354	-1.155947

ωB97X Energy = -1999.36945683 a.u.

(1*S*,29*R*)-**3**, Conf P

O	4.722943	0.822661	2.360477
O	5.417308	-3.438665	-0.380697
C	1.123515	-4.731673	-2.025480
O	-0.886582	-3.273478	-0.998326
O	-0.290367	0.462158	1.758936
O	5.699581	-1.362518	1.123099
O	2.107087	1.092683	2.451912
C	-0.066967	-2.428710	-0.381884
C	-0.581409	-1.380980	0.356117
C	0.267916	-0.515046	1.029173
C	4.124355	-3.121755	-0.411891
C	3.276790	-3.964058	-1.146849
C	1.925063	-3.759241	-1.202843
C	1.350599	-2.649525	-0.490000
C	4.517876	-1.095914	0.925484
C	3.611403	-1.993506	0.228164
C	2.203179	-1.757464	0.202747
C	1.658310	-0.652792	0.932063
C	2.512247	0.265645	1.625829
O	-3.050406	0.750084	2.531732
C	3.252410	2.908804	-2.310872
C	-0.768199	3.720199	-3.038548
C	-3.569392	2.032341	2.138261
O	-4.410618	-1.517571	1.636363
O	-3.415472	-3.133262	-0.160017
C	-4.275779	-1.993506	-2.055285
C	-5.803831	-3.155569	-0.433848
C	-4.534349	-2.329427	-0.597823
C	-4.526496	-1.068887	0.286719
C	-5.722521	-0.145758	0.109103
C	-5.669452	1.074584	1.034423
C	-4.422206	1.931725	0.899900
C	-4.126949	2.545038	-0.243905
C	-2.935596	3.414026	-0.543731
C	-1.690131	2.608326	-0.955815
C	-0.626305	3.498357	-1.556822
C	0.305764	4.060040	-0.787754
C	1.381178	5.023338	-1.202437
C	2.745971	4.707705	-0.576002
C	3.243577	3.311804	-0.862138
C	3.662734	2.532936	0.133440
C	4.201175	1.137319	0.004207
C	3.994886	0.284141	1.292435
H	4.088331	1.316511	2.899057
H	5.869744	-2.784211	0.197810
H	1.798013	-5.424994	-2.526520
H	0.432991	-5.300170	-1.403536
H	0.523759	-4.217787	-2.775323
H	-1.830386	-3.120847	-0.742161
H	0.432260	0.941826	2.228941
H	-1.651753	-1.250717	0.446023
H	3.727577	-4.801922	-1.664685
H	-2.135464	0.673072	2.223098
H	2.230925	2.793775	-2.686261
H	3.785521	1.976312	-2.489872
H	3.726994	3.688150	-2.914121
H	-0.067946	4.452519	-3.436942
H	-0.621116	2.777502	-3.574571
H	-1.779800	4.061591	-3.278139
H	-4.178553	2.386655	2.974468
H	-2.744471	2.734168	2.005688
H	-3.968646	-0.804005	2.130862
H	-3.442438	-3.104659	0.808210
H	-5.108035	-1.430299	-2.478751
H	-4.163392	-2.914820	-2.630006
H	-3.363690	-1.401556	-2.165007
H	-5.684626	-4.106912	-0.954765
H	-6.001201	-3.357092	0.620907
H	-6.668108	-2.640386	-0.855772
H	-3.620750	-0.505428	0.025112
H	-5.765395	0.183792	-0.933178
H	-6.644611	-0.696215	0.313609
H	-6.552541	1.689097	0.840876
H	-5.761560	0.733637	2.068943
H	-4.808894	2.393029	-1.080356
H	-3.202391	4.098808	-1.353476
H	-2.672688	4.042982	0.310387
H	-1.301569	2.081241	-0.078886
H	-1.983100	1.843213	-1.683331

H	0.293335	3.813031	0.275380
H	1.477202	5.054802	-2.289025
H	1.099981	6.036278	-0.893753
H	3.473031	5.431237	-0.962512
H	2.694802	4.856242	0.506391
H	3.642150	2.943073	1.140212
H	5.285583	1.148848	-0.149965
H	3.756932	0.618793	-0.847719

ωB97X Energy = -1999.36927740 a.u.

(1*S*,29*R*)-**3**, Conf Q

O	-4.343258	-0.404559	2.996711
O	-5.039541	3.245374	-0.425463
C	-0.679863	4.525862	-1.882778
O	1.287981	3.156047	-0.683764
O	0.609665	-0.443088	2.224627
O	-5.389818	1.286975	1.179147
O	-1.770257	-1.116127	2.806610
C	0.451590	2.344786	-0.048991
C	0.943889	1.345993	0.767927
C	0.075009	0.502133	1.441223
C	-3.742912	2.962449	-0.346439
C	-2.867388	3.771587	-1.084264
C	-1.511587	3.593803	-1.043614
C	-0.962883	2.546509	-0.223805
C	-4.184312	1.048429	1.126544
C	-3.249698	1.898590	0.415154
C	-1.838107	1.690532	0.486711
C	-1.315425	0.628676	1.294096
C	-2.178298	-0.265335	2.001734
O	3.370940	-1.164628	2.496658
C	-4.765574	-3.378460	-1.324862
C	-0.901067	-3.853498	-0.331160
C	3.551257	-2.481114	1.945885
O	4.887878	0.910066	1.401932
O	3.869860	2.774610	-0.129048
C	4.167801	1.622328	-2.182502
C	6.138641	2.426683	-0.847545
C	4.739827	1.826694	-0.790970
C	4.676899	0.533183	0.041873
C	5.642714	-0.560374	-0.389420
C	5.538253	-1.817233	0.481575
C	4.149180	-2.428174	0.563776
C	3.525745	-2.872350	-0.525245
C	2.147842	-3.463945	-0.631266
C	1.092464	-2.389467	-0.944115
C	-0.245354	-2.960189	-1.348602
C	-0.767260	-2.663959	-2.538813
C	-2.065830	-3.135877	-3.130006
C	-3.221831	-2.135601	-2.917594
C	-3.822986	-2.226006	-1.538712
C	-3.516910	-1.351678	-0.583355
C	-4.054366	-1.412776	0.824731
C	-3.682067	-0.239195	1.761769
H	-3.825521	-1.051337	3.493961
H	-5.515787	2.611190	0.160297
H	-1.335197	5.181151	-2.455154
H	-0.023680	5.136290	-1.263478
H	-0.040938	3.974888	-2.571523
H	2.234514	2.953959	-0.469764
H	-0.135595	-0.931308	2.658533
H	2.010580	1.229579	0.907457
H	-3.300997	4.559798	-1.687489
H	2.442946	-0.909720	2.383900
H	-4.991580	-3.555710	-0.273658
H	-4.351044	-4.301293	-1.740020
H	-5.709124	-3.195389	-1.848130
H	-0.976785	-3.330902	0.629041
H	-1.905364	-4.156806	-0.623360
H	-0.309300	-4.756576	-0.156121
H	4.232958	-3.007018	2.619985
H	2.597269	-3.009954	1.956117
H	4.443108	0.239071	1.951035
H	4.070066	2.694428	0.815356
H	4.814342	0.978216	-2.779214
H	4.086442	2.584621	-2.691527
H	3.174989	1.167812	-2.135409
H	6.091262	3.408002	-1.322324
H	6.553045	2.542928	0.155824
H	6.813491	1.797806	-1.430158
H	3.655483	0.143240	-0.060189
H	5.443763	-0.817327	-1.433866
H	6.668288	-0.185394	-0.337187
H	6.240074	-2.561669	0.096363
H	5.883104	-1.574298	1.490016
H	4.048906	-2.769024	-1.476040
H	2.144267	-4.204905	-1.436355
H	1.873395	-3.998006	0.280473
H	0.973754	-1.759902	-0.053159
H	1.465626	-1.740188	-1.742092
H	-0.201041	-1.981607	-3.172064
H	-1.922544	-3.273110	-4.205011
H	-2.347930	-4.114683	-2.734349
H	-2.856256	-1.122283	-3.104953
H	-4.003730	-2.338307	-3.656702
H	-2.823373	-0.552077	-0.831405
H	-3.710715	-2.320953	1.332764
H	-5.147142	-1.438644	0.826650

ωB97X Energy = -1999.36919118 a.u.

(1*S*,29*R*)-**3**, Conf R

O	-4.323207	-0.380720	3.004885
O	-5.034245	3.266492	-0.441210
C	-0.668761	4.513901	-1.913267
O	1.294758	3.157688	-0.692987
O	0.600987	-0.450926	2.199418
O	-5.373850	1.322383	1.214967
O	-1.758213	-1.152605	2.748480
C	0.454354	2.345139	-0.063005
C	0.939348	1.344144	0.753022

C	0.066266	0.499326	1.422859
C	-3.738441	2.976495	-0.369689
C	-2.860569	3.776817	-1.112209
C	-1.505045	3.591169	-1.068570
C	-0.959142	2.546928	-0.242626
C	-4.169415	1.072422	1.112184
C	-3.247145	1.909237	0.387937
C	-1.836595	1.693824	0.468980
C	-1.324158	0.633063	1.283268
C	-2.186885	-0.276643	1.990079
O	3.359475	-1.157885	2.497825
C	-4.736031	-3.437509	-1.264752
C	-0.879443	-3.859908	-0.301083
C	3.549208	-2.474932	1.951914
O	4.885896	0.914349	1.417021
O	3.874392	2.778823	-0.118990
C	4.188986	1.629389	-2.171509
C	6.148919	2.435149	-0.821353
C	4.750534	1.833166	-0.775651
C	4.683673	0.538706	0.055342
C	5.652744	-0.553804	-0.371208
C	5.544789	-1.810901	0.498987
C	4.156089	-2.423678	0.573494
C	3.540252	-2.871609	-0.518358
C	2.164658	-3.467661	-0.629520
C	1.105619	-2.398111	-0.946099
C	-0.233622	-2.976941	-1.333949
C	-0.765270	-2.697476	-2.523920
C	-2.064552	-3.185924	-3.100241
C	-3.228559	-2.194315	-2.892950
C	-3.821740	-2.268428	-1.509663
C	-3.541923	-1.360603	-0.577673
C	-4.085577	-1.396410	0.829193
C	-3.689253	-0.222250	1.754556
H	-5.233437	-0.079207	2.886484
H	-5.514270	2.649703	0.155772
H	-1.320459	5.164780	-2.494668
H	-0.014078	5.128798	-1.296838
H	-0.027724	3.955044	-2.593629
H	2.239405	2.955698	-0.472412
H	-0.152000	-0.949445	2.615247
H	2.005153	1.221699	0.894435
H	-3.288655	4.565394	-1.718743
H	2.431604	-0.906009	2.375167
H	-4.941235	-3.604302	-0.207514
H	-4.311013	-4.357710	-1.674609
H	-5.691979	-3.279781	-1.773757
H	-0.940623	-3.329641	0.655889
H	-1.888711	-4.161215	-0.577703
H	-0.289351	-4.764252	-0.126894
H	4.228732	-2.995985	2.631960
H	2.597459	-3.007858	1.957481
H	4.435634	0.243843	1.962373
H	4.066755	2.696382	0.826866
H	4.840877	0.987061	-2.764310
H	4.109526	2.592115	-2.680016
H	3.196672	1.173076	-2.132037
H	6.103682	3.416921	-1.295411
H	6.555733	2.550898	0.185168
H	6.828925	1.807862	-1.399694
H	3.663246	0.147926	-0.053290
H	5.459188	-0.810756	-1.416677
H	6.677754	-0.178044	-0.313644
H	6.249613	-2.554471	0.117629
H	5.883575	-1.567589	1.509396
H	4.068833	-2.769688	-1.466302
H	2.166205	-4.209402	-1.433898
H	1.889179	-4.001908	0.281761
H	0.992014	-1.759736	-0.060919
H	1.471622	-1.756810	-1.753771
H	-0.206517	-2.020954	-3.169889
H	-1.927243	-3.334362	-4.174539
H	-2.334644	-4.162761	-2.691737
H	-2.875076	-1.180119	-3.098007
H	-4.013422	-2.416033	-3.623557
H	-2.874820	-0.545412	-0.847401
H	-3.763940	-2.300849	1.354781
H	-5.180009	-1.404328	0.819041

ωB97X Energy = -1999.36909587 a.u.

(1*S*,29*R*)-**3**, Conf S

O	-3.855208	0.753414	3.165502
O	-4.142021	3.194905	-1.008892
C	0.476816	4.203972	-1.615485
O	2.093858	2.788473	-0.027496
O	0.698480	-0.791971	2.640706
O	-4.912243	1.397230	0.613006
O	-1.770609	-1.232325	2.904536
C	1.115728	2.023234	0.439690
C	1.395114	0.980557	1.299231
C	0.363944	0.207761	1.815148
C	-2.906515	2.865601	-0.647762
C	-1.860121	3.594489	-1.229910
C	-0.550847	3.356044	-0.915313
C	-0.231621	2.317255	0.028090
C	-3.738780	1.139547	0.881256
C	-2.634151	1.841453	0.266633
C	-1.275862	1.550678	0.601223
C	-0.977576	0.474313	1.497200
C	-2.010840	-0.296175	2.129201
O	3.039180	-2.278287	2.102771
C	-5.827691	-1.353691	-0.989078
C	-1.482794	0.065543	-2.906475
C	2.677704	-3.229532	1.086776
O	4.977847	-0.374961	1.455840
O	4.602517	2.116315	0.592916
C	4.832644	1.591082	-1.712318
C	6.757525	1.317034	-0.122895
C	5.252255	1.186547	-0.310197
C	4.721109	-0.205874	0.063487
C	5.278606	-1.355749	-0.763252

C	4.739427	-2.718813	-0.315016
C	3.223212	-2.824864	-0.256860
C	2.473121	-2.577951	-1.328432
C	0.980861	-2.629076	-1.479266
C	0.417562	-1.291295	-1.958277
C	-1.038834	-1.268500	-2.368817
C	-1.821048	-2.343680	-2.290259
C	-3.246184	-2.505884	-2.732603
C	-4.133901	-3.121972	-1.637997
C	-4.602969	-2.133105	-0.597016
C	-3.965688	-2.015701	0.568609
C	-4.356593	-1.153349	1.737549
C	-3.482923	0.084551	1.960860
H	-3.729193	0.133770	3.893689
H	-4.759628	2.611111	-0.507343
H	-0.022337	4.869790	-2.318332
H	1.047600	4.802517	-0.906912
H	1.193831	3.589074	-2.158432
H	2.990288	2.491948	0.275222
H	-0.146506	-1.219106	2.942968
H	2.413328	0.774172	1.605439
H	-2.123600	4.365851	-1.943079
H	2.248219	-1.766581	2.331671
H	-6.682343	-2.029502	-1.089584
H	-5.679593	-0.888464	-1.968433
H	-6.082613	-0.566582	-0.283012
H	-2.562215	0.139011	-3.033762
H	-1.166724	0.868021	-2.234037
H	-1.013375	0.262393	-3.875439
H	3.115058	-4.188244	1.380927
H	1.594181	-3.350138	1.070963
H	4.372464	-1.065421	1.784744
H	4.736626	1.755046	1.480287
H	5.377739	1.014861	-2.460229
H	5.055401	2.647963	-1.869796
H	3.762047	1.435348	-1.866678
H	7.055171	2.353536	-0.290169
H	7.048642	1.026394	0.887955
H	7.297752	0.687756	-0.831835
H	3.634721	-0.173481	-0.092985
H	5.026292	-1.186095	-1.813671
H	6.369600	-1.371709	-0.691452
H	5.131552	-3.485018	-0.989355
H	5.150718	-2.949673	0.670835
H	2.996011	-2.302565	-2.245831
H	0.742086	-3.399931	-2.220046
H	0.489031	-2.926962	-0.551033
H	0.572397	-0.536876	-1.175314
H	1.009616	-0.940520	-2.813693
H	-1.390319	-3.259105	-1.889704
H	-3.676155	-1.564454	-3.081285
H	-3.256790	-3.182610	-3.594167
H	-5.015563	-3.567854	-2.108474
H	-3.585389	-3.937588	-1.158390
H	-3.093196	-2.646624	0.730261
H	-4.278938	-1.750265	2.650351
H	-5.384444	-0.802237	1.659707

ωB97X Energy = -1999.36905211 a.u.

(1*S*,29*R*)-**3**, Conf T

O	-3.810462	0.721910	3.193994
O	-4.140449	3.183812	-1.015400
C	0.479365	4.190780	-1.626499
O	2.095876	2.790697	-0.023809
O	0.702879	-0.789732	2.644862
O	-4.907780	1.399077	0.629894
O	-1.761008	-1.247595	2.893154
C	1.117963	2.024387	0.442893
C	1.396540	0.984305	1.305089
C	0.365584	0.210452	1.821059
C	-2.903774	2.855455	-0.656875
C	-1.857779	3.582451	-1.241333
C	-0.548684	3.346116	-0.923026
C	-0.229027	2.313219	0.026844
C	-3.728417	1.127463	0.872827
C	-2.629686	1.830704	0.255830
C	-1.272683	1.546481	0.600974
C	-0.976715	0.478042	1.507164
C	-2.008023	-0.297578	2.142872
O	3.042756	-2.274945	2.105300
C	-5.824529	-1.350887	-0.977650
C	-1.481923	0.063412	-2.908817
C	2.679638	-3.226550	1.090391
O	4.982829	-0.374320	1.457300
O	4.604668	2.117535	0.596122
C	4.830602	1.593183	-1.709741
C	6.758418	1.318730	-0.123988
C	5.252784	1.188215	-0.308494
C	4.722590	-0.204417	0.065681
C	5.278028	-1.353834	-0.763055
C	4.739652	-2.717191	-0.314599
C	3.223509	-2.823304	-0.254364
C	2.472202	-2.578084	-1.325464
C	0.979747	-2.629129	-1.474565
C	0.416839	-1.292132	-1.956153
C	-1.039490	-1.269350	-2.366805
C	-1.822881	-2.343434	-2.285028
C	-3.248093	-2.505108	-2.727470
C	-4.136074	-3.121848	-1.633467
C	-4.601432	-2.134708	-0.589183
C	-3.962308	-2.022253	0.575904
C	-4.346846	-1.162087	1.748528
C	-3.478867	0.081369	1.962205
H	-4.738941	0.979052	3.147464
H	-4.757862	2.608386	-0.504848
H	-0.018927	4.851335	-2.334867
H	1.047966	4.794547	-0.920622
H	1.198300	3.573030	-2.163691
H	2.992010	2.494821	0.279963
H	-0.141616	-1.224872	2.938055
H	2.414562	0.778151	1.612127

H	-2.120392	4.351598	-1.957185
H	2.252517	-1.761849	2.333933
H	-6.680438	-2.024445	-1.082290
H	-5.675050	-0.880403	-1.954302
H	-6.078520	-0.566969	-0.267656
H	-2.561261	0.137819	-3.036282
H	-1.164908	0.867657	-2.239016
H	-1.012362	0.256516	-3.878479
H	3.117002	-4.185284	1.384509
H	1.596040	-3.346862	1.076093
H	4.377326	-1.064151	1.787284
H	4.740181	1.755741	1.483051
H	5.374953	1.017782	-2.458833
H	5.052314	2.650320	-1.866997
H	3.759888	1.436711	-1.862538
H	7.055727	2.355310	-0.291355
H	7.051491	1.027589	0.886149
H	7.297306	0.689798	-0.834273
H	3.635794	-0.171901	-0.087947
H	5.023368	-1.183585	-1.812819
H	6.369188	-1.369998	-0.693711
H	5.130883	-3.482997	-0.989894
H	5.152375	-2.948414	0.670563
H	2.994121	-2.304168	-2.243855
H	0.739809	-3.401600	-2.213290
H	0.488747	-2.924507	-0.545090
H	0.572168	-0.536190	-1.174714
H	1.008978	-0.943312	-2.812329
H	-1.393195	-3.258162	-1.881734
H	-3.677827	-1.563336	-3.075523
H	-3.258979	-3.181232	-3.589532
H	-5.019247	-3.564431	-2.104221
H	-3.588959	-3.940049	-1.156688
H	-3.091404	-2.655972	0.734579
H	-4.254035	-1.745996	2.666272
H	-5.380949	-0.824225	1.673076

ωB97X Energy = -1999.36904938 a.u.

(1*S*,29*R*)-**3**, Conf U

O	4.606291	1.156159	2.390763
O	5.693319	-3.150537	-0.149836
C	1.587166	-4.715602	-2.023451
O	-0.555645	-3.302355	-1.221774
O	-0.335523	0.492589	1.507191
O	5.770306	-1.017911	1.303114
O	1.979389	1.271547	2.327498
C	0.179392	-2.416064	-0.557451
C	-0.435168	-1.382038	0.120134
C	0.321107	-0.465820	0.835482
C	4.390886	-2.902528	-0.275172
C	3.636970	-3.809019	-1.035760
C	2.283865	-3.675124	-1.188821
C	1.609215	-2.574289	-0.554501
C	4.592378	-0.821003	1.020924
C	3.780601	-1.785904	0.295829
C	2.367295	-1.623653	0.169555
C	1.719645	-0.532844	0.832571
C	2.478156	0.447282	1.551686
O	-2.980464	0.234301	2.638154
C	3.079456	2.869278	-2.430267
C	-1.802112	4.785623	-2.417248
C	-3.656032	1.492688	2.470792
O	-4.207462	-2.011410	1.521056
O	-3.121491	-3.288409	-0.474334
C	-4.082498	-1.968755	-2.199653
C	-5.501445	-3.463888	-0.762441
C	-4.302794	-2.524514	-0.804445
C	-4.391161	-1.399416	0.245354
C	-5.668395	-0.573859	0.207935
C	-5.702655	0.511902	1.289565
C	-4.544676	1.495877	1.253821
C	-4.358126	2.293570	0.204455
C	-3.270637	3.302084	-0.030347
C	-2.158992	2.740335	-0.932487
C	-1.215952	3.802452	-1.437858
C	0.047925	3.871757	-1.022452
C	1.058212	4.899131	-1.468904
C	2.434393	4.734460	-0.815741
C	3.052956	3.370422	-1.012605
C	3.551270	2.706389	0.028888
C	4.208376	1.358160	-0.002299
C	3.974413	0.539128	1.304471
H	3.913168	1.626716	2.875457
H	6.072855	-2.457280	0.435523
H	2.324538	-5.402167	-2.437698
H	0.871848	-5.283962	-1.430030
H	1.028645	-4.260384	-2.840214
H	-1.518826	-3.190184	-1.028736
H	0.329840	1.020709	2.008744
H	-1.513773	-1.300156	0.124679
H	4.161755	-4.638848	-1.493223
H	-2.110414	0.299357	2.216726
H	3.478632	3.642003	-3.093653
H	2.067371	2.644971	-2.780006
H	3.687009	1.974737	-2.555989
H	-1.034287	5.299113	-2.996254
H	-2.476419	4.280930	-3.114095
H	-2.390116	5.551537	-1.902138
H	-4.263732	1.632362	3.368564
H	-2.918928	2.295806	2.438753
H	-3.799670	-1.337865	2.094653
H	-3.138086	-3.375852	0.491043
H	-4.960821	-1.421647	-2.544096
H	-3.899212	-2.787388	-2.898220
H	-3.223205	-1.293729	-2.221184
H	-5.312728	-4.318043	-1.414727
H	-5.671597	-3.830018	0.252052
H	-6.408008	-2.964137	-1.107182
H	-3.546760	-0.723830	0.055234
H	-5.766151	-0.112441	-0.779217
H	-6.531980	-1.229493	0.347429

H	-6.644458	1.058424	1.193700
H	-5.734143	0.028324	2.269336
H	-5.063710	2.197699	-0.621821
H	-3.716384	4.178780	-0.509296
H	-2.825027	3.653017	0.902825
H	-1.606249	1.976180	-0.376483
H	-2.624599	2.240024	-1.790685
H	0.395934	3.126855	-0.306381
H	1.169225	4.859085	-2.558125
H	0.693802	5.907454	-1.249314
H	3.104459	5.490085	-1.241409
H	2.360561	4.943320	0.255212
H	3.501719	3.183801	1.004775
H	5.296889	1.454035	-0.076278
H	3.873085	0.773005	-0.860260

ωB97X Energy = -1999.36897625 a.u.

(1*S*,29*R*)-**3**, Conf V

O	-6.304189	0.342557	-1.480766
O	-4.870789	-0.980992	3.193582
C	-0.429832	-2.684536	2.813858
O	0.569472	-2.524989	0.334312
O	-1.761129	-0.860178	-3.356693
O	-6.111490	-0.022100	1.171948
O	-4.147086	0.030659	-3.003651
C	-0.524789	-1.964008	-0.168652
C	-0.596524	-1.671339	-1.513249
C	-1.744883	-1.093847	-2.045694
C	-3.848327	-1.170174	2.362774
C	-2.692733	-1.756136	2.897139
C	-1.594414	-2.023711	2.125312
C	-1.619031	-1.688867	0.726843
C	-5.087413	-0.154910	0.502999
C	-3.894769	-0.800296	1.016015
C	-2.768990	-1.071159	0.179299
C	-2.827794	-0.757843	-1.216867
C	-3.976591	-0.123174	-1.785578
O	3.382395	1.865368	-1.568478
C	-2.056669	2.783809	-2.038818
C	1.780983	0.428539	2.020407
C	4.504349	2.593185	-1.035754
O	4.214406	-0.743025	-2.111023
O	2.673681	-2.732630	-1.287572
C	3.796267	-3.057892	0.788100
C	4.952657	-3.480812	-1.400016
C	3.965620	-2.595817	-0.648190
C	4.319173	-1.099700	-0.733191
C	5.677565	-0.735762	-0.142519
C	6.132523	0.696234	-0.443022
C	5.218996	1.812222	0.037594
C	5.068940	2.067765	1.337046
C	4.225603	3.126064	1.986418
C	2.995743	2.557301	2.711051
C	1.969232	1.902623	1.801537
C	1.285747	2.635176	0.920542
C	0.161163	2.213312	0.016028
C	-1.097730	3.044421	0.305745
C	-2.284107	2.689959	-0.555243
C	-3.437000	2.330567	0.009475
C	-4.717626	1.990085	-0.695464
C	-5.040332	0.473947	-0.877586
H	-6.152082	0.416223	-2.432869
H	-5.609694	-0.595465	2.667324
H	-0.662722	-2.823636	3.868853
H	-0.210255	-3.655395	2.370929
H	0.477486	-2.087681	2.727327
H	1.293432	-2.597263	-0.337826
H	-2.646972	-0.493785	-3.583350
H	0.223085	-1.915010	-2.177074
H	-2.700396	-2.010279	3.950067
H	2.728169	1.811683	-0.858565
H	-1.522889	3.705806	-2.284574
H	-2.980301	2.759230	-2.615474
H	-1.431783	1.954451	-2.385450
H	1.128676	-0.044717	1.286964
H	2.751618	-0.077486	1.992849
H	1.365314	0.248282	3.017131
H	5.168112	2.764203	-1.884392
H	4.162866	3.565216	-0.678316
H	3.906121	0.179622	-2.135096
H	2.732011	-2.189000	-2.087241
H	4.755514	-3.061673	1.306405
H	3.399622	-4.075074	0.803116
H	3.106887	-2.410063	1.334768
H	4.558172	-4.497187	-1.445157
H	5.100547	-3.117298	-2.418351
H	5.920794	-3.514010	-0.898533
H	3.537753	-0.563775	-0.178177
H	5.634162	-0.886285	0.940669
H	6.441903	-1.414899	-0.530047
H	7.118805	0.829200	0.009235
H	6.278553	0.793730	-1.521465
H	5.616748	1.434390	2.036493
H	4.838460	3.652400	2.724519
H	3.897290	3.875777	1.265416
H	3.328409	1.830385	3.457718
H	2.519105	3.371822	3.263046
H	1.513362	3.701841	0.877237
H	0.449900	2.364487	-1.030690
H	-0.071302	1.150899	0.129784
H	-1.363433	2.933551	1.360381
H	-0.854144	4.102322	0.147337
H	-3.474367	2.285998	1.095998
H	-4.756662	2.421595	-1.697351
H	-5.568089	2.388141	-0.136861

ωB97X Energy = -1999.36883805 a.u.

(1*S*,29*R*)-**3**, Conf W

O	4.515228	1.397826	2.693118
O	5.436689	-1.212670	-1.569523

C	1.529542	-3.810333	-2.463236
O	-0.451110	-3.407734	-0.700347
O	-0.024291	-0.799565	3.171291
O	5.535791	0.380513	0.472419
O	2.080158	0.591585	3.481736
C	0.277094	-2.599284	0.062418
C	-0.231678	-2.112303	1.250118
C	0.520863	-1.237909	2.026008
C	4.209825	-1.514654	-1.149086
C	3.479071	-2.438109	-1.909619
C	2.207508	-2.811880	-1.564541
C	1.606001	-2.265244	-0.376573
C	4.355052	0.094443	0.692718
C	3.639563	-0.933900	-0.016101
C	2.330453	-1.329041	0.396897
C	1.784249	-0.803772	1.608752
C	2.464270	0.215422	2.371869
O	-2.610411	0.261569	2.677566
C	3.356423	1.991253	-2.105716
C	-2.814704	2.993286	-2.657331
C	-2.280620	1.217419	1.666428
O	-4.069032	-1.858280	1.609363
O	-3.053434	-3.558001	-0.121874
C	-3.400432	-2.198292	-2.039932
C	-5.337067	-3.129567	-0.740868
C	-3.934032	-2.542085	-0.660930
C	-3.837415	-1.342479	0.300215
C	-4.779209	-0.185639	-0.017324
C	-4.780956	0.952730	1.014849
C	-3.537602	1.813311	1.073601
C	-3.568143	3.058092	0.598851
C	-2.464759	4.075560	0.551610
C	-2.257357	4.699745	-0.839913
C	-1.751992	3.726785	-1.884366
C	-0.439602	3.565334	-2.056878
C	0.255108	2.606770	-2.979347
C	0.883855	1.421621	-2.223414
C	2.065757	1.793997	-1.360469
C	1.933291	1.892956	-0.038484
C	3.013481	2.183491	0.962366
C	3.618668	0.946445	1.713194
H	5.375453	1.468700	2.256551
H	5.828043	-0.577398	-0.930599
H	2.210461	-4.101338	-3.262061
H	1.229318	-4.700585	-1.912263
H	0.624910	-3.392931	-2.904087
H	-1.391100	-3.468898	-0.394046
H	0.643726	-0.206725	3.602553
H	-1.218116	-2.403409	1.590480
H	3.954068	-2.853765	-2.789800
H	-1.774712	-0.091684	3.019497
H	3.225858	2.708320	-2.920611
H	3.668839	1.047318	-2.564490
H	4.172263	2.343714	-1.475734
H	-3.478468	2.453299	-1.976843
H	-3.438128	3.705290	-3.206646
H	-2.409875	2.277164	-3.371064
H	-1.658452	2.001367	2.103886
H	-1.687481	0.731547	0.877746
H	-3.652984	-1.224734	2.218173
H	-3.277611	-3.622596	0.817361
H	-4.058927	-1.489149	-2.542475
H	-3.346981	-3.102321	-2.649443
H	-2.400785	-1.761322	-1.978795
H	-5.303216	-4.064936	-1.301661
H	-5.731320	-3.333220	0.256535
H	-6.021634	-2.451054	-1.251727
H	-2.798647	-0.994491	0.239652
H	-4.530465	0.220508	-1.003010
H	-5.799380	-0.574834	-0.075744
H	-5.622077	1.606721	0.776131
H	-4.989893	0.535157	2.002981
H	-4.513469	3.406194	0.182237
H	-2.716710	4.887252	1.243972
H	-1.513586	3.657445	0.887292
H	-3.201142	5.143520	-1.175303
H	-1.541927	5.518968	-0.734619
H	0.220787	4.167249	-1.433323
H	-0.436173	2.212448	-3.725369
H	1.036350	3.136258	-3.535073
H	0.111176	0.951127	-1.607270
H	1.212593	0.673953	-2.953789
H	0.945540	1.710491	0.381181
H	2.627440	2.821773	1.760696
H	3.862684	2.702662	0.514322

ωB97X Energy = -1999.36880753 a.u.

(1*S*,29*R*)-**3**, Conf X

O	4.575817	1.396076	1.770301
O	5.684021	-3.177488	-0.196862
C	1.527398	-5.241560	-1.324364
O	-0.614309	-3.832494	-0.516340
O	-0.380647	0.352952	1.559295
O	5.759617	-0.845911	0.893406
O	1.932497	1.439066	1.877204
C	0.121409	-2.817951	-0.075303
C	-0.486232	-1.732661	0.522078
C	0.271149	-0.659750	0.970339
C	4.361861	-3.021940	-0.213695
C	3.599815	-4.078687	-0.732456
C	2.231801	-4.043974	-0.746154
C	1.551221	-2.894083	-0.214645
C	4.548702	-0.752342	0.712241
C	3.736084	-1.859229	0.238418
C	2.310236	-1.794846	0.254142
C	1.661190	-0.638492	0.795702
C	2.417534	0.499790	1.234300
O	-3.153724	0.241678	2.492927
C	1.691036	2.376045	-2.353836
C	-1.287092	6.480067	-1.014283
C	-3.737877	1.493473	2.093372

O	-4.570616	-1.886667	1.387071
O	-3.244012	-3.608219	-0.072002
C	-3.586797	-2.519873	-2.152195
C	-5.501940	-3.561076	-0.900541
C	-4.195430	-2.786588	-0.787258
C	-4.342129	-1.491367	0.034894
C	-5.410373	-0.525373	-0.455815
C	-5.537234	0.721576	0.429844
C	-4.238889	1.474124	0.669717
C	-3.586792	2.059892	-0.333163
C	-2.266069	2.767669	-0.278793
C	-2.387646	4.258541	-0.578902
C	-1.096428	5.046105	-0.599312
C	0.077204	4.501707	-0.279318
C	1.430554	5.150861	-0.280506
C	2.339501	4.666348	-1.424935
C	2.577362	3.169175	-1.433820
C	3.537870	2.652011	-0.668170
C	3.971404	1.220766	-0.592785
C	3.882682	0.606911	0.843899
H	3.921355	1.998833	2.150330
H	6.070305	-2.379407	0.229985
H	2.264284	-5.946711	-1.706885
H	0.917585	-5.742733	-0.573472
H	0.857418	-4.954349	-2.133590
H	-1.579748	-3.686374	-0.352460
H	0.291125	1.011070	1.858991
H	-1.558305	-1.722128	0.664029
H	4.131382	-4.942547	-1.112505
H	-2.233976	0.233635	2.187405
H	0.646339	2.662010	-2.208210
H	1.770648	1.298429	-2.213098
H	1.935379	2.602375	-3.396137
H	-1.714095	6.528521	-2.020327
H	-1.997427	6.977233	-0.346882
H	-0.362700	7.054869	-1.013605
H	-4.576908	1.659175	2.771923
H	-3.018906	2.296944	2.259068
H	-4.130718	-1.224498	1.950486
H	-3.493744	-3.537482	0.861529
H	-4.267098	-1.939882	-2.776588
H	-3.387338	-3.466678	-2.657840
H	-2.646830	-1.969490	-2.060329
H	-5.307254	-4.535223	-1.351857
H	-5.948419	-3.714217	0.083994
H	-6.220463	-3.031344	-1.527950
H	-3.376574	-0.974338	-0.020280
H	-5.167283	-0.224637	-1.479323
H	-6.380615	-1.028205	-0.486880
H	-6.268895	1.392050	-0.028854
H	-5.961157	0.423566	1.392047
H	-4.041449	2.015052	-1.323849
H	-1.785443	2.620213	0.689163
H	-1.603672	2.306867	-1.020778
H	-2.884092	4.390782	-1.548349
H	-3.062216	4.717871	0.154576
H	0.093034	3.451638	0.002359
H	1.351014	6.237659	-0.340346
H	1.931300	4.924137	0.667030
H	1.895249	4.966872	-2.379027
H	3.298106	5.184378	-1.340716
H	4.127096	3.338534	-0.063218
H	5.030835	1.157468	-0.861221
H	3.423232	0.586516	-1.290513

ωB97X Energy = -1999.36880059 a.u.

(1*S*,29*S*)-**3**, Conf A

O	5.257031	-2.481826	-0.535961
O	5.497264	2.548397	-0.470303
C	1.156531	4.102507	-1.691812
O	-0.668024	2.145500	-1.897505
O	0.265732	-2.399837	-1.318403
O	5.976445	0.068655	-0.107628
O	2.646211	-3.099598	-0.726982
C	0.205375	1.187663	-1.611736
C	-0.190785	-0.134000	-1.625542
C	0.712684	-1.137645	-1.304326
C	4.244170	2.178943	-0.718025
C	3.334405	3.193559	-1.047466
C	2.025206	2.925090	-1.339304
C	1.563965	1.562233	-1.318297
C	4.783024	-0.174975	-0.283197
C	3.825245	0.846432	-0.656763
C	2.466638	0.528990	-0.966404
C	2.039818	-0.836931	-0.967654
C	2.934000	-1.899588	-0.615555
O	-3.213621	1.451874	-1.893772
C	1.474003	-2.864333	2.546607
C	-0.668127	2.919088	1.497222
C	-4.097382	2.256028	-1.100918
O	-4.051179	-1.163537	-2.088403
O	-2.459564	-3.191258	-1.618380
C	-4.548513	-3.903578	-0.802071
C	-2.749096	-3.179350	0.791669
C	-3.399876	-2.935535	-0.561081
C	-3.823822	-1.452100	-0.703078
C	-5.063594	-1.049485	0.077563
C	-5.591586	0.353444	-0.244858
C	-4.679414	1.526202	0.082021
C	-4.518157	1.914882	1.346159
C	-3.775967	3.092571	1.905807
C	-2.731857	2.693894	2.962290
C	-1.509997	2.032233	2.376495
C	-1.236806	0.752613	2.629454
C	-0.092704	-0.056618	2.097253
C	0.914340	-0.472558	3.180803
C	1.936801	-1.435717	2.628008
C	3.117448	-0.985705	2.203644
C	4.191906	-1.786259	1.527967
C	4.298392	-1.590764	-0.014118

H	4.818713	-3.340458	-0.600833
H	6.014016	1.728856	-0.285544
H	1.755978	5.011962	-1.681403
H	0.706949	3.984653	-2.676542
H	0.336865	4.213527	-0.981972
H	-1.595222	1.796732	-1.953291
H	1.031783	-2.993781	-1.121131
H	-1.212262	-0.393796	-1.873536
H	3.706389	4.210541	-1.072732
H	-3.618034	0.590975	-2.118398
H	2.179730	-3.525963	2.048124
H	0.524974	-2.928150	2.005192
H	1.288143	-3.252345	3.552139
H	-0.559388	3.907638	1.951912
H	0.329882	2.516938	1.323215
H	-1.137762	3.065176	0.519494
H	-3.512385	3.121802	-0.794832
H	-4.912665	2.614261	-1.740193
H	-3.435974	-1.734561	-2.573402
H	-1.569536	-2.904665	-1.362193
H	-5.275931	-3.868620	0.009322
H	-4.150285	-4.917321	-0.861771
H	-5.060245	-3.676895	-1.739504
H	-2.415177	-4.216037	0.864109
H	-1.882794	-2.525443	0.927897
H	-3.449971	-2.987557	1.605835
H	-2.974705	-0.839864	-0.360580
H	-5.867438	-1.757948	-0.136487
H	-4.843753	-1.121243	1.146690
H	-5.862702	0.387785	-1.303494
H	-6.526713	0.480346	0.305724
H	-5.034311	1.325352	2.106392
H	-3.304456	3.689495	1.123337
H	-4.509046	3.748101	2.387430
H	-2.424232	3.599011	3.496812
H	-3.198500	2.030162	3.696117
H	-1.912110	0.213723	3.294283
H	-0.498904	-0.958224	1.624477
H	0.441664	0.478278	1.309668
H	1.405961	0.423591	3.568811
H	0.378058	-0.936376	4.015868
H	3.323827	0.076635	2.325940
H	4.044185	-2.856654	1.676335
H	5.177410	-1.534001	1.926850

ωB97X Energy = -1999.37376033 a.u.

(1*S*,29*S*)-**3**, Conf B

O	4.989584	-2.054843	-1.472851
O	5.034226	2.724496	0.001886
C	0.684377	4.368714	-1.051454
O	-1.014523	2.465237	-1.865589
O	0.026171	-2.083168	-2.106668
O	5.606341	0.249090	-0.171752
O	2.387352	-2.830672	-1.560000
C	-0.130437	1.488807	-1.706305
C	-0.488753	0.185733	-1.984389
C	0.429316	-0.841080	-1.814092
C	3.810080	2.378799	-0.382652
C	2.872813	3.411662	-0.524988
C	1.592192	3.173491	-0.941229
C	1.192298	1.826780	-1.252594
C	4.436781	0.009439	-0.472867
C	3.445625	1.051804	-0.635712
C	2.114290	0.767703	-1.070540
C	1.727940	-0.582903	-1.348177
C	2.650343	-1.669367	-1.214452
O	-3.563830	1.823258	-1.922843
C	1.440256	-3.371291	1.743066
C	-1.018760	1.621652	4.198345
C	-4.135356	2.535615	-0.811627
O	-4.395393	-0.826720	-1.845741
O	-2.731199	-2.863402	-1.936074
C	-4.523654	-3.629275	-0.612541
C	-2.349480	-2.963685	0.459061
C	-3.346888	-2.666580	-0.651050
C	-3.783014	-1.182713	-0.599539
C	-4.734411	-0.820103	0.526972
C	-5.263253	0.616373	0.452078
C	-4.205630	1.708764	0.446028
C	-3.429517	1.906395	1.510511
C	-2.337282	2.915058	1.711378
C	-0.938061	2.276745	1.742774
C	-0.755506	1.195001	2.778942
C	-0.372669	-0.031027	2.417623
C	-0.129350	-1.205911	3.319671
C	1.360345	-1.536885	3.503992
C	2.061478	-2.119360	2.299478
C	3.184363	-1.567221	1.835692
C	4.091580	-2.123029	0.773920
C	4.035733	-1.451922	-0.619383
H	4.631014	-2.917511	-1.717236
H	5.576811	1.900831	0.031357
H	1.227383	5.265286	-0.755244
H	0.316406	4.497486	-2.068386
H	-0.191421	4.258669	-0.411584
H	-1.934148	2.113070	-1.999965
H	0.803668	-2.686255	-1.984484
H	-1.478393	-0.039687	-2.362322
H	3.198544	4.418857	-0.295561
H	-3.965823	0.934925	-2.000910
H	2.098276	-3.914451	1.067151
H	0.531696	-3.129637	1.182542
H	1.142672	-4.043573	2.552348
H	-0.665216	0.900112	4.932741
H	-2.088430	1.777467	4.370239
H	-0.526110	2.577286	4.399295
H	-3.517973	3.422919	-0.682773
H	-5.141821	2.866522	-1.088791
H	-3.944392	-1.364340	-2.514251
H	-1.797987	-2.602593	-1.904881
H	-5.011072	-3.621873	0.362709

H	-4.163936	-4.640295	-0.808318
H	-5.262545	-3.370302	-1.373399
H	-1.975355	-3.984842	0.361233
H	-1.500932	-2.274026	0.410003
H	-2.811627	-2.861004	1.442557
H	-2.865473	-0.585490	-0.488495
H	-5.592849	-1.496008	0.513679
H	-4.216900	-0.971450	1.478578
H	-5.886943	0.711201	-0.440257
H	-5.931708	0.771050	1.302976
H	-3.590695	1.243497	2.361690
H	-2.346910	3.676761	0.930047
H	-2.516281	3.440169	2.655205
H	-0.719998	1.863828	0.756977
H	-0.206533	3.073010	1.928648
H	-0.195071	-0.207441	1.355186
H	-0.563505	-1.028340	4.304358
H	-0.648178	-2.083133	2.918610
H	1.888428	-0.640453	3.840058
H	1.441057	-2.276342	4.309758
H	3.530264	-0.652094	2.313343
H	3.903965	-3.184119	0.603576
H	5.131491	-2.021008	1.093396

ωB97X Energy = -1999.37346717 a.u.

(1*S*,29*S*)-**3**, Conf C

O	4.962368	-2.088963	-1.483984
O	5.042479	2.716050	0.005567
C	0.686234	4.367703	-1.015357
O	-1.011408	2.475098	-1.856235
O	0.022031	-2.073986	-2.111577
O	5.613385	0.229259	-0.234640
O	2.353719	-2.841571	-1.539181
C	-0.128339	1.496063	-1.699996
C	-0.485073	0.195398	-1.985073
C	0.431870	-0.834756	-1.817675
C	3.813640	2.376394	-0.370293
C	2.876157	3.409485	-0.499561
C	1.594724	3.172085	-0.916417
C	1.193603	1.828573	-1.240797
C	4.424049	0.007528	-0.484558
C	3.442760	1.051706	-0.624518
C	2.113752	0.766437	-1.066511
C	1.733768	-0.582570	-1.357890
C	2.650379	-1.684620	-1.223901
O	-3.562199	1.834033	-1.920837
C	1.440506	-3.390037	1.744842
C	-1.030693	1.600944	4.204399
C	-4.135856	2.541348	-0.807661
O	-4.391581	-0.816374	-1.857062
O	-2.730207	-2.853973	-1.952220
C	-4.526148	-3.624414	-0.636308
C	-2.353834	-2.965956	0.443179
C	-3.348436	-2.662561	-0.667818
C	-3.783724	-1.178563	-0.610425
C	-4.738869	-0.820601	0.514434
C	-5.267293	0.616260	0.443688
C	-4.209564	1.708573	0.445908
C	-3.436250	1.900876	1.513383
C	-2.343971	2.907980	1.721612
C	-0.945306	2.268493	1.752356
C	-0.765405	1.181375	2.783261
C	-0.382622	-0.042976	2.416289
C	-0.140058	-1.221868	3.313291
C	1.349982	-1.550471	3.499498
C	2.053482	-2.131677	2.295734
C	3.171533	-1.572534	1.828590
C	4.081825	-2.126854	0.768820
C	4.031603	-1.457917	-0.626185
H	5.837192	-1.788065	-1.207461
H	5.590583	1.897890	0.011075
H	1.227241	5.261434	-0.707292
H	0.321371	4.507215	-2.032001
H	-0.191677	4.249202	-0.380039
H	-1.930701	2.124179	-1.993760
H	0.798344	-2.679892	-1.975252
H	-1.475138	-0.029285	-2.362536
H	3.201016	4.415671	-0.264836
H	-3.963184	0.945606	-2.002978
H	1.151448	-4.062326	2.557225
H	2.100391	-3.928915	1.067489
H	0.527892	-3.157074	1.187209
H	-0.537754	2.555230	4.410993
H	-2.100531	1.756584	4.375383
H	-0.678787	0.875455	4.935680
H	-3.518389	3.427753	-0.673090
H	-5.141577	2.874126	-1.085433
H	-3.938954	-1.351935	-2.526194
H	-1.797550	-2.590453	-1.918766
H	-5.014968	-3.622141	0.338280
H	-4.166921	-4.634618	-0.837167
H	-5.263749	-3.360681	-1.396781
H	-1.983586	-3.988344	0.343495
H	-1.502293	-2.279803	0.396913
H	-2.817122	-2.863740	1.426214
H	-2.866208	-0.582437	-0.493305
H	-5.597372	-1.496276	0.495521
H	-4.224499	-0.976003	1.467088
H	-5.887649	0.714917	-0.450537
H	-5.938883	0.767491	1.292752
H	-3.599702	1.233830	2.360873
H	-2.351564	3.673540	0.944037
H	-2.524415	3.428501	2.667714
H	-0.725692	1.860554	0.764792
H	-0.213589	3.063237	1.943990
H	-0.203235	-0.214182	1.353332
H	-0.576899	-1.049499	4.297719
H	-0.656282	-2.098121	2.906905
H	1.875918	-0.653052	3.836299
H	1.431202	-2.289891	4.305221
H	3.510613	-0.653083	2.302900

H	3.897401	-3.185421	0.587305
H	5.119024	-2.026852	1.102311

ωB97X Energy = -1999.37336378 a.u.

(1*S*,29*S*)-**3**, Conf D

O	5.311532	-2.356739	-0.576524
O	5.437720	2.601930	0.380925
C	1.232517	4.348476	-1.042520
O	-0.522028	2.457858	-1.786798
O	0.484022	-2.094179	-2.076118
O	5.934313	0.097231	0.315594
O	2.791682	-2.899252	-1.282038
C	0.346230	1.466892	-1.609267
C	-0.007010	0.174993	-1.934808
C	0.886580	-0.868330	-1.726814
C	4.230343	2.283378	-0.079186
C	3.340132	3.339583	-0.316835
C	2.080890	3.127294	-0.808866
C	1.655025	1.784795	-1.099300
C	4.771904	-0.109448	-0.032354
C	3.840630	0.962938	-0.320647
C	2.536147	0.705729	-0.844875
C	2.150031	-0.635672	-1.162735
C	3.020506	-1.742176	-0.902247
O	-3.017431	1.602410	-1.982903
C	1.126094	-3.113606	1.902065
C	-1.055429	2.744297	1.573332
C	-4.087091	2.269675	-1.293928
O	-3.165246	-1.168319	-1.940497
O	-1.650686	-2.900949	-0.274798
C	-3.664122	-3.956832	-1.073320
C	-3.390296	-3.137648	1.281616
C	-3.076650	-2.865143	-0.182158
C	-3.549749	-1.453052	-0.582345
C	-5.032555	-1.181393	-0.359207
C	-5.500116	0.187547	-0.864062
C	-4.766260	1.387722	-0.281050
C	-4.788371	1.629980	1.027845
C	-4.178437	2.758215	1.806118
C	-3.184903	2.263808	2.873078
C	-1.901217	1.725967	2.290763
C	-1.584925	0.435860	2.401444
C	-0.394489	-0.272289	1.826990
C	0.540094	-0.855743	2.898608
C	1.599683	-1.738144	2.283379
C	2.826823	-1.262952	2.068556
C	3.960627	-1.980732	1.396648
C	4.278605	-1.545891	-0.067310
H	4.884595	-3.169062	-0.880565
H	5.950679	1.763926	0.463265
H	1.804116	5.241037	-0.790880
H	0.911011	4.415771	-2.080985
H	0.328817	4.324871	-0.433969
H	-1.436936	2.108124	-1.939567
H	1.227274	-2.715797	-1.892283
H	-0.987480	-0.052325	-2.334272
H	3.686761	4.344260	-0.107471
H	-3.197006	0.648381	-2.079121
H	1.892800	-3.721413	1.424202
H	0.274262	-3.050028	1.217622
H	0.776938	-3.643302	2.793631
H	-1.025794	3.679273	2.140047
H	-0.029494	2.408529	1.421222
H	-1.469998	2.979015	0.588336
H	-3.650484	3.157605	-0.839236
H	-4.822486	2.601227	-2.035852
H	-3.725467	-1.667621	-2.544607
H	-1.367710	-2.589489	-1.144960
H	-4.753670	-3.989340	-1.015512
H	-3.278102	-4.925040	-0.750985
H	-3.373228	-3.818249	-2.117706
H	-2.870878	-4.045603	1.592649
H	-3.047446	-2.312472	1.911482
H	-4.458777	-3.282707	1.443286
H	-2.961047	-0.746427	0.011318
H	-5.632833	-1.953664	-0.851533
H	-5.236241	-1.262074	0.710763
H	-5.427256	0.213754	-1.954897
H	-6.566436	0.280226	-0.642514
H	-5.337863	0.920724	1.649377
H	-3.692718	3.487727	1.155981
H	-4.985708	3.292582	2.317291
H	-2.952818	3.102984	3.537727
H	-3.667450	1.494394	3.483043
H	-2.272375	-0.201269	2.959955
H	-0.755174	-1.086552	1.188176
H	0.186342	0.387610	1.178570
H	1.003845	-0.036320	3.454778
H	-0.053273	-1.437946	3.613032
H	3.037432	-0.245311	2.393999
H	3.779636	-3.055149	1.345419
H	4.893180	-1.833363	1.947356

ωB97X Energy = -1999.37308391 a.u.

(1*S*,29*S*)-**3**, Conf E

O	-4.758069	3.192115	-0.023642
O	-5.337810	-1.654079	-1.356024
C	-1.012345	-3.221431	-2.625971
O	0.920812	-1.388106	-2.334014
O	0.230065	2.944539	-0.723667
O	-5.684918	0.708285	-0.441121
O	-2.117111	3.620284	0.019932
C	0.088053	-0.461280	-1.878046
C	0.559916	0.799070	-1.572336
C	-0.292021	1.750857	-1.030977
C	-4.048300	-1.335793	-1.436739
C	-3.180135	-2.315581	-1.939284
C	-1.839465	-2.086326	-2.086084
C	-1.302832	-0.799131	-1.733651
C	-4.466154	0.876592	-0.460399

C	-3.552787	-0.094639	-1.028748
C	-2.159840	0.181542	-1.177915
C	-1.646263	1.463674	-0.802560
C	-2.487020	2.459985	-0.209556
O	3.507937	-0.917869	-2.130734
C	-4.461682	-1.173909	2.354791
C	1.240842	-1.113970	1.441363
C	4.204124	-2.006516	-1.504990
O	4.566206	1.522664	-1.391362
O	3.039910	3.452579	-0.500904
C	5.001759	3.666788	0.786449
C	2.933314	2.649754	1.786578
C	3.785810	2.788387	0.534209
C	4.162112	1.392374	-0.022537
C	5.261078	0.661596	0.728952
C	5.711890	-0.645467	0.065386
C	4.643591	-1.715553	-0.093637
C	4.200022	-2.382257	0.970286
C	3.202873	-3.503069	1.055815
C	2.196930	-3.357352	2.213881
C	0.979603	-2.525863	1.890146
C	-0.244932	-3.040464	2.013062
C	-1.534848	-2.316365	1.732175
C	-1.980191	-1.402320	2.888583
C	-3.123999	-0.502696	2.489266
C	-2.889373	0.783526	2.228989
C	-3.874214	1.816810	1.763775
C	-3.900052	2.105526	0.230566
H	-4.242288	3.988605	0.159971
H	-5.816393	-0.860440	-1.019539
H	-1.656080	-4.077700	-2.823367
H	-0.502615	-2.941717	-3.546770
H	-0.240843	-3.516103	-1.914402
H	1.866955	-1.091271	-2.292508
H	-0.501483	3.515826	-0.382033
H	1.603430	1.043316	-1.728365
H	-3.608465	-3.272102	-2.212889
H	3.996686	-0.077653	-2.026225
H	-5.272078	-0.479760	2.135482
H	-4.707807	-1.710305	3.275143
H	-4.436867	-1.918906	1.553142
H	1.767822	-1.102574	0.483133
H	0.326833	-0.529902	1.330491
H	1.890549	-0.600071	2.157687
H	3.523339	-2.855117	-1.549880
H	5.083147	-2.254618	-2.110614
H	4.059194	2.272690	-1.737803
H	2.100716	3.218770	-0.448221
H	5.584919	3.303501	1.633188
H	4.668828	4.681298	1.009428
H	5.647993	3.699456	-0.093183
H	2.652911	3.637177	2.158107
H	2.019570	2.085466	1.576068
H	3.478252	2.130399	2.576984
H	3.248701	0.779692	0.006866
H	6.134957	1.312129	0.812683
H	4.911114	0.453729	1.744419
H	6.142154	-0.410754	-0.911804
H	6.530977	-1.051510	0.664043
H	4.640302	-2.115328	1.932924
H	2.659566	-3.637855	0.117308
H	3.763865	-4.429084	1.221148
H	1.865387	-4.351549	2.521755
H	2.717399	-2.919550	3.074781
H	-0.331587	-4.066953	2.364354
H	-1.433830	-1.703972	0.832511
H	-2.318810	-3.047321	1.517673
H	-2.265253	-2.017845	3.748698
H	-1.129721	-0.790924	3.200317
H	-1.868713	1.141595	2.354697
H	-3.640595	2.778883	2.227730
H	-4.901089	1.566051	2.034095

ωB97X Energy = -1999.37221739 a.u.

(1*S*,29*S*)-**3**, Conf F

O	-5.040897	2.808916	0.001859
O	-5.241783	-2.164779	-0.861559
C	-0.979113	-3.397778	-2.618252
O	0.856725	-1.438411	-2.453147
O	-0.119311	2.953090	-1.174143
O	-5.715706	0.213089	-0.052230
O	-2.483762	3.505619	-0.381798
C	-0.022339	-0.549369	-2.003952
C	0.364196	0.761619	-1.811425
C	-0.544153	1.691745	-1.324440
C	-4.011205	-1.733041	-1.125049
C	-3.117465	-2.658593	-1.684112
C	-1.828656	-2.322705	-1.996319
C	-1.371986	-0.980427	-1.751384
C	-4.537615	0.502457	-0.257949
C	-3.601610	-0.422886	-0.865759
C	-2.264323	-0.036764	-1.187569
C	-1.851023	1.317723	-0.986245
C	-2.739121	2.294529	-0.428379
O	3.407438	-0.804230	-2.107661
C	-3.902514	-1.151572	2.843671
C	0.693614	-2.932517	0.632653
C	4.219327	-1.811431	-1.487403
O	4.236758	1.773041	-1.484894
O	2.585479	3.611930	-0.676982
C	4.416010	3.948998	0.761394
C	2.359337	2.767511	1.588945
C	3.292651	2.986442	0.407018
C	3.810009	1.623408	-0.125444
C	4.957923	1.013486	0.661614
C	5.574196	-0.233694	0.019016
C	4.677094	-1.455263	-0.096154
C	4.432853	-2.197384	0.983119
C	3.682577	-3.488058	1.121840
C	2.611169	-3.430986	2.222062
C	1.439610	-2.546627	1.880419

C	1.100286	-1.507888	2.643075
C	-0.062752	-0.581646	2.396805
C	-1.383202	-1.161640	2.908875
C	-2.636723	-0.374579	2.606097
C	-2.595738	0.874348	2.145700
C	-3.761909	1.737901	1.762192
C	-4.035510	1.851652	0.229721
H	-4.600874	3.669347	0.020019
H	-5.752850	-1.398600	-0.509336
H	-1.578610	-4.295355	-2.764707
H	-0.578430	-3.079550	-3.579766
H	-0.126003	-3.643358	-1.986456
H	1.784444	-1.094194	-2.399463
H	-0.886271	3.495529	-0.865187
H	1.374081	1.074207	-2.047804
H	-3.485985	-3.659830	-1.871311
H	3.828954	0.075242	-2.059559
H	-4.803364	-0.541218	2.798388
H	-3.869251	-1.639626	3.821318
H	-3.997775	-1.947211	2.097071
H	0.512903	-4.011658	0.615467
H	-0.267701	-2.427667	0.540888
H	1.275986	-2.693100	-0.262141
H	3.618216	-2.719570	-1.494883
H	5.097901	-1.990165	-2.118172
H	3.691712	2.488908	-1.846164
H	1.661303	3.320436	-0.701833
H	4.955133	3.621466	1.650653
H	3.989356	4.932647	0.961613
H	5.126043	4.040369	-0.063304
H	1.983919	3.725214	1.954395
H	1.505804	2.144359	1.303096
H	2.878992	2.268687	2.409491
H	2.957325	0.927504	-0.112126
H	5.753188	1.755640	0.763079
H	4.607491	0.772126	1.669736
H	5.957225	0.035470	-0.968970
H	6.449544	-0.504753	0.614012
H	4.875297	-1.850687	1.919072
H	3.233695	-3.805581	0.179153
H	4.402258	-4.267185	1.393978
H	2.244832	-4.449571	2.392218
H	3.068927	-3.094480	3.156971
H	1.690800	-1.316401	3.537219
H	0.136461	0.375689	2.886098
H	-0.158298	-0.366529	1.326807
H	-1.512565	-2.163993	2.483720
H	-1.320035	-1.318720	3.992584
H	-1.623128	1.335507	1.999455
H	-3.583974	2.765046	2.092850
H	-4.699581	1.407663	2.210005

ωB97X Energy = -1999.37220951 a.u.

(1*S*,29*S*)-**3**, Conf G

O	-4.744308	3.208831	-0.005173
O	-5.348188	-1.642092	-1.365108
C	-1.017764	-3.223934	-2.604030
O	0.914624	-1.385201	-2.340348
O	0.231378	2.937417	-0.701485
O	-5.681899	0.756641	-0.477570
O	-2.082743	3.612776	0.073810
C	0.082938	-0.459765	-1.876528
C	0.553474	0.798123	-1.565499
C	-0.297370	1.749632	-1.018018
C	-4.055815	-1.332191	-1.437822
C	-3.188153	-2.314524	-1.932888
C	-1.846072	-2.084692	-2.075089
C	-1.307501	-0.796562	-1.728220
C	-4.453243	0.881275	-0.466662
C	-3.554463	-0.095890	-1.023335
C	-2.162312	0.186404	-1.172560
C	-1.654366	1.469951	-0.797085
C	-2.488213	2.476447	-0.187830
O	3.503902	-0.915570	-2.134381
C	-4.449624	-1.187432	2.340036
C	1.256755	-1.108395	1.443209
C	4.203747	-2.003117	-1.511212
O	4.563506	1.526782	-1.403662
O	3.036167	3.453245	-0.506362
C	5.006506	3.674633	0.766591
C	2.947666	2.654179	1.783131
C	3.790922	2.792853	0.524498
C	4.166642	1.396984	-0.032662
C	5.270516	0.668428	0.713723
C	5.719210	-0.638759	0.048953
C	4.651172	-1.710251	-0.102697
C	4.214607	-2.376067	0.964680
C	3.219366	-3.497929	1.057690
C	2.216586	-3.349246	2.218184
C	0.997861	-2.520041	1.894131
C	-0.225780	-3.036724	2.017115
C	-1.516729	-2.316115	1.732385
C	-1.970452	-1.405384	2.888101
C	-3.116263	-0.509785	2.485470
C	-2.887728	0.779157	2.233258
C	-3.877347	1.808947	1.770711
C	-3.900292	2.109360	0.239581
H	-5.644266	2.857203	-0.029980
H	-5.831052	-0.847740	-1.044723
H	-1.658842	-4.085718	-2.785173
H	-0.515764	-2.955113	-3.532340
H	-0.239946	-3.504489	-1.893768
H	1.860390	-1.088894	-2.297710
H	-0.502295	3.501357	-0.343126
H	1.597341	1.043151	-1.718352
H	-3.614909	-3.271811	-2.205915
H	3.992934	-0.075110	-2.033618
H	-5.261047	-0.498162	2.108649
H	-4.703851	-1.719984	3.260437
H	-4.413092	-1.936424	1.542673
H	1.777889	-1.097389	0.481744

H	0.342347	-0.524006	1.337608
H	1.910901	-0.594563	2.155473
H	3.522940	-2.851952	-1.551219
H	5.079539	-2.251932	-2.121286
H	4.052149	2.274710	-1.748277
H	2.097986	3.215570	-0.447958
H	5.596709	3.314423	1.609798
H	4.672566	4.688684	0.990151
H	5.646361	3.707505	-0.117684
H	2.667706	3.641542	2.155148
H	2.033696	2.087827	1.579584
H	3.499274	2.137137	2.570401
H	3.254282	0.783034	0.001942
H	6.143970	1.320223	0.792213
H	4.926267	0.461014	1.731222
H	6.143450	-0.404511	-0.930988
H	6.542266	-1.043264	0.643178
H	4.660024	-2.107204	1.924419
H	2.673363	-3.637128	0.121423
H	3.782238	-4.422470	1.224897
H	1.886769	-4.342740	2.530176
H	2.738953	-2.908037	3.076179
H	-0.310859	-4.062741	2.370200
H	-1.413654	-1.701837	0.834308
H	-2.297215	-3.049379	1.513111
H	-2.256673	-2.023161	3.746244
H	-1.123806	-0.790918	3.204195
H	-1.870413	1.143471	2.367108
H	-3.653254	2.773016	2.232737
H	-4.901788	1.546761	2.043271

ωB97X Energy = -1999.37220521 a.u.

(1*S*,29*S*)-**3**, Conf H

O	-4.398444	3.450012	-0.131502
O	-5.538308	-1.070659	-2.128260
C	-1.366200	-3.285469	-2.819408
O	0.754082	-1.753402	-2.216546
O	0.488068	2.343073	0.019372
O	-5.656583	1.230755	-1.014642
O	-1.811364	3.321345	0.514400
C	0.010428	-0.800189	-1.672270
C	0.614208	0.300155	-1.096768
C	-0.154825	1.307659	-0.534076
C	-4.223797	-0.994167	-1.938128
C	-3.450204	-2.072076	-2.391985
C	-2.085099	-2.070582	-2.298410
C	-1.421384	-0.936437	-1.714893
C	-4.449356	1.163095	-0.787760
C	-3.617584	0.089063	-1.295814
C	-2.195185	0.118364	-1.174293
C	-1.557718	1.230927	-0.536121
C	-2.320126	2.291175	0.046380
O	3.367390	-1.388398	-2.153911
C	-1.862229	0.759268	3.357092
C	0.454340	-3.644068	3.243009
C	4.096597	-2.352085	-1.376109
O	4.470188	1.117191	-1.742577
O	3.151614	3.209180	-0.779603
C	5.424928	3.581536	-0.275742
C	3.825799	2.862704	1.524461
C	4.214999	2.724250	0.060063
C	4.415096	1.239332	-0.315163
C	5.637061	0.560093	0.277219
C	5.841240	-0.876327	-0.223767
C	4.628114	-1.782532	-0.086943
C	4.077431	-2.019966	1.101652
C	2.816589	-2.767012	1.416156
C	1.793660	-1.820879	2.064495
C	0.448834	-2.452182	2.324734
C	-0.649157	-1.934116	1.774460
C	-2.068729	-2.387203	1.961919
C	-2.831998	-1.588531	3.035496
C	-2.929976	-0.104871	2.746064
C	-3.927190	0.348956	1.988025
C	-4.212253	1.771416	1.603094
C	-3.836508	2.188757	0.150334
H	-3.801299	4.102001	0.258784
H	-5.933898	-0.234037	-1.789662
H	-2.094848	-4.033437	-3.129370
H	-0.732926	-3.035835	-3.669935
H	-0.716428	-3.716628	-2.058641
H	1.723711	-1.540829	-2.165425
H	-0.196448	2.983282	0.338637
H	1.693294	0.381951	-1.086976
H	-3.970123	-2.911202	-2.837882
H	3.823157	-0.522593	-2.137130
H	-1.910076	0.694524	4.448104
H	-1.939487	1.808715	3.073498
H	-0.872218	0.399121	3.065090
H	1.026562	-3.419639	4.148098
H	-0.547595	-3.946386	3.544911
H	0.936379	-4.504234	2.769451
H	3.411037	-3.180253	-1.205142
H	4.929903	-2.729695	-1.977930
H	3.878262	1.805054	-2.082068
H	2.298369	2.905431	-0.432878
H	6.269874	3.338874	0.369591
H	5.173206	4.632749	-0.128797
H	5.728170	3.438570	-1.314486
H	3.607465	3.908575	1.747815
H	2.936472	2.267152	1.750259
H	4.633252	2.535741	2.181423
H	3.521841	0.705011	0.040999
H	6.534121	1.137168	0.039246
H	5.532034	0.559104	1.365246
H	6.144102	-0.839368	-1.273142
H	6.687437	-1.308733	0.316848
H	4.555379	-1.568112	1.972399
H	2.373924	-3.209278	0.520848
H	3.040407	-3.588751	2.103887
H	2.209790	-1.455388	3.011947

H	1.662058	-0.947505	1.417843
H	-0.522468	-1.057535	1.142009
H	-2.602902	-2.281247	1.010855
H	-2.109818	-3.446050	2.226412
H	-3.838304	-2.006701	3.119856
H	-2.339416	-1.739182	4.001531
H	-4.644750	-0.381818	1.616934
H	-3.721497	2.484782	2.267519
H	-5.287687	1.955529	1.663560

ωB97X Energy = -1999.37218039 a.u.

(1*S*,29*S*)-**3**, Conf I

O	-5.022675	2.839027	0.015177
O	-5.264009	-2.144019	-0.873404
C	-0.993518	-3.402295	-2.595250
O	0.845289	-1.445315	-2.453879
O	-0.111301	2.944107	-1.155865
O	-5.727666	0.270917	-0.100181
O	-2.438644	3.511471	-0.338170
C	-0.030163	-0.554325	-1.998515
C	0.358793	0.753705	-1.801743
C	-0.546323	1.687524	-1.311518
C	-4.027030	-1.723830	-1.126568
C	-3.134697	-2.654387	-1.676415
C	-1.842760	-2.321523	-1.983193
C	-1.380644	-0.980081	-1.742620
C	-4.529317	0.516622	-0.270854
C	-3.606813	-0.418486	-0.861037
C	-2.269216	-0.030733	-1.181805
C	-1.857799	1.323584	-0.980014
C	-2.737104	2.316399	-0.411283
O	3.399849	-0.815059	-2.106378
C	-3.892424	-1.162422	2.827481
C	0.712415	-2.922426	0.638337
C	4.216439	-1.819741	-1.488393
O	4.235880	1.764669	-1.502913
O	2.591256	3.607126	-0.690203
C	4.433002	3.950798	0.731685
C	2.383063	2.773079	1.581228
C	3.306830	2.986631	0.390802
C	3.820026	1.621189	-0.139394
C	4.974085	1.014768	0.641238
C	5.584190	-0.236068	-0.000118
C	4.685083	-1.457307	-0.102339
C	4.447648	-2.193362	0.982573
C	3.697029	-3.482487	1.133146
C	2.626480	-3.416100	2.233591
C	1.454910	-2.533479	1.887195
C	1.111538	-1.494773	2.648075
C	-0.054196	-0.572460	2.399461
C	-1.373731	-1.158597	2.907076
C	-2.629777	-0.376921	2.600883
C	-2.593563	0.874806	2.147726
C	-3.763096	1.734678	1.767019
C	-4.033879	1.863129	0.234806
H	-5.871792	2.395338	0.143225
H	-5.780006	-1.376554	-0.539011
H	-1.592697	-4.301304	-2.733698
H	-0.592464	-3.092379	-3.559284
H	-0.140395	-3.641418	-1.961015
H	1.773569	-1.104048	-2.399741
H	-0.878666	3.484081	-0.832862
H	1.369787	1.064682	-2.035745
H	-3.504606	-3.654889	-1.864193
H	3.822452	0.064238	-2.066202
H	-4.797648	-0.559218	2.772495
H	-3.865713	-1.648395	3.806386
H	-3.974544	-1.960249	2.081750
H	0.530845	-4.001495	0.623737
H	-0.248116	-2.416904	0.542160
H	1.297776	-2.686090	-0.255295
H	3.615065	-2.727746	-1.487166
H	5.090010	-2.001469	-2.125264
H	3.688041	2.479243	-1.862597
H	1.667411	3.312977	-0.708633
H	4.979310	3.627691	1.618195
H	4.007854	4.935389	0.930485
H	5.136351	4.038199	-0.099155
H	2.010900	3.732529	1.945459
H	1.526878	2.149373	1.304729
H	2.909081	2.277574	2.399713
H	2.967496	0.925313	-0.116217
H	5.770544	1.756989	0.732305
H	4.632024	0.778785	1.653487
H	5.959519	0.027937	-0.992429
H	6.464067	-0.505095	0.589101
H	4.896548	-1.841978	1.913675
H	3.247525	-3.808146	0.193569
H	4.416759	-4.259375	1.411423
H	2.259341	-4.433164	2.411188
H	3.085078	-3.073518	3.165878
H	1.699834	-1.300950	3.543170
H	0.140035	0.385048	2.890367
H	-0.147795	-0.356359	1.329525
H	-1.497128	-2.161222	2.480902
H	-1.313255	-1.316077	3.990877
H	-1.623151	1.342970	2.009390
H	-3.595544	2.762250	2.098287
H	-4.697311	1.393394	2.215995

ωB97X Energy = -1999.37215984 a.u.

(1*S*,29*S*)-**3**, Conf J

O	-4.362842	3.456263	-0.144512
O	-5.538699	-1.076796	-2.124063
C	-1.368261	-3.296781	-2.817430
O	0.756380	-1.766557	-2.225925
O	0.496819	2.324541	0.019414
O	-5.632856	1.257484	-1.028011
O	-1.775971	3.289057	0.561377
C	0.013315	-0.811547	-1.681120

C	0.615894	0.288872	-1.108203
C	-0.151821	1.296143	-0.539669
C	-4.223320	-1.006338	-1.935156
C	-3.452108	-2.084571	-2.389057
C	-2.085998	-2.080919	-2.297429
C	-1.418560	-0.945430	-1.720154
C	-4.426874	1.149551	-0.787303
C	-3.612385	0.072629	-1.290910
C	-2.188995	0.110328	-1.175878
C	-1.554840	1.228146	-0.545283
C	-2.309794	2.294912	0.058134
O	3.372114	-1.399730	-2.150602
C	-1.856898	0.784700	3.362438
C	0.460714	-3.608282	3.273250
C	4.099236	-2.357422	-1.363703
O	4.466969	1.112215	-1.751484
O	3.144407	3.205398	-0.796547
C	5.417779	3.586232	-0.298784
C	3.823856	2.872414	1.507929
C	4.210560	2.727650	0.043414
C	4.413609	1.241385	-0.324592
C	5.637801	0.567737	0.269394
C	5.842903	-0.871535	-0.223037
C	4.630564	-1.777728	-0.078977
C	4.080467	-2.006224	1.111620
C	2.819622	-2.750463	1.432617
C	1.796617	-1.797831	2.071367
C	0.452813	-2.427246	2.341048
C	-0.646554	-1.916987	1.786300
C	-2.065101	-2.369992	1.982200
C	-2.824546	-1.566280	3.054662
C	-2.924645	-0.084032	2.758284
C	-3.923508	0.364292	1.999119
C	-4.209553	1.783846	1.602884
C	-3.825446	2.186634	0.148922
H	-5.295077	3.313414	-0.354282
H	-5.934907	-0.238656	-1.797193
H	-2.097115	-4.045852	-3.124057
H	-0.736921	-3.048382	-3.669747
H	-0.716296	-3.725517	-2.057204
H	1.725477	-1.554449	-2.172400
H	-0.192203	2.955040	0.357510
H	1.695071	0.369546	-1.094774
H	-3.971417	-2.924548	-2.833872
H	3.825991	-0.532907	-2.137041
H	-0.867552	0.434941	3.055349
H	-1.890452	0.711315	4.453379
H	-1.946734	1.835122	3.086840
H	-0.540406	-3.906981	3.581448
H	0.941366	-4.473926	2.808341
H	1.035532	-3.373435	4.174055
H	3.412509	-3.183228	-1.185985
H	4.932772	-2.741412	-1.961232
H	3.872442	1.796797	-2.093146
H	2.292842	2.898499	-0.447744
H	6.264900	3.347907	0.345348
H	5.164135	4.637474	-0.155312
H	5.718668	3.439851	-1.337740
H	3.602241	3.918663	1.726219
H	2.937071	2.274943	1.738502
H	4.633822	2.551814	2.164959
H	3.521885	0.707143	0.035436
H	6.533431	1.144771	0.025970
H	5.535041	0.573453	1.357628
H	6.144298	-0.840812	-1.273048
H	6.690211	-1.299863	0.319086
H	4.558626	-1.547414	1.978614
H	2.377344	-3.201236	0.541344
H	3.043029	-3.565454	2.128440
H	2.213764	-1.420937	3.013893
H	1.663322	-0.932234	1.414688
H	-0.521944	-1.048293	1.142679
H	-2.603370	-2.269976	1.032860
H	-2.104213	-3.427418	2.252713
H	-3.830307	-1.984567	3.145053
H	-2.328094	-1.711835	4.019449
H	-4.639738	-0.370167	1.632526
H	-3.721948	2.507043	2.257336
H	-5.286917	1.961600	1.666574

ωB97X Energy = -1999.37201982 a.u.

(1*S*,29*S*)-**3**, Conf K

O	-4.899788	2.828982	-0.163832
O	-5.318213	-2.209708	-0.218129
C	-1.241447	-3.882578	-2.053948
O	0.608775	-1.980950	-2.492148
O	-0.111730	2.582759	-1.818893
O	-5.663111	0.287175	0.210162
O	-2.365753	3.350713	-0.858785
C	-0.208243	-0.999073	-2.109094
C	0.217928	0.308480	-2.186046
C	-0.597605	1.338386	-1.737323
C	-4.105265	-1.875197	-0.652326
C	-3.282372	-2.916140	-1.106526
C	-2.021810	-2.684451	-1.584893
C	-1.525631	-1.335398	-1.638332
C	-4.497076	0.489357	-0.127349
C	-3.643908	-0.556657	-0.654999
C	-2.335328	-0.278129	-1.156346
C	-1.868224	1.073872	-1.208404
C	-2.664072	2.157950	-0.711799
O	3.045722	-1.024583	-1.924401
C	-3.544494	-0.792886	3.041132
C	1.099195	-2.723549	0.781897
C	4.230066	-1.740003	-1.530473
O	2.592821	0.732966	0.087399
O	2.632759	3.365514	-1.115520
C	4.170767	4.135874	0.504728
C	1.942316	3.253747	1.200859
C	3.094000	3.099770	0.210221
C	3.669715	1.668272	0.293583

C	4.766324	1.368979	-0.720987
C	5.595232	0.118422	-0.390664
C	4.847893	-1.192080	-0.265889
C	4.788644	-1.820898	0.908845
C	4.125631	-3.116511	1.269894
C	3.070686	-2.937531	2.374991
C	1.853301	-2.153011	1.950985
C	1.469672	-1.054609	2.606861
C	0.249233	-0.220986	2.305067
C	-1.025559	-0.786659	2.931484
C	-2.307283	-0.046577	2.624404
C	-2.311964	1.138437	2.016546
C	-3.505883	1.956683	1.619330
C	-3.909026	1.869550	0.113381
H	-4.433068	3.663963	-0.302163
H	-5.779833	-1.376238	0.035015
H	-1.847656	-4.780153	-1.938078
H	-0.954811	-3.782818	-3.100240
H	-0.319297	-4.001099	-1.485721
H	1.546866	-1.668720	-2.458493
H	-0.816707	3.201056	-1.511750
H	1.199015	0.545483	-2.577177
H	-3.681587	-3.922482	-1.070655
H	2.826190	-0.378171	-1.220449
H	-3.460545	-1.114821	4.082650
H	-3.653999	-1.700508	2.438433
H	-4.459003	-0.210355	2.937466
H	0.917439	-3.790927	0.939399
H	0.137605	-2.236696	0.620225
H	1.675763	-2.633802	-0.142997
H	3.974077	-2.794897	-1.420449
H	4.949235	-1.657525	-2.350724
H	2.473575	0.187799	0.876274
H	1.773510	2.941113	-1.245824
H	4.674750	3.919060	1.449216
H	3.714282	5.124209	0.578597
H	4.916927	4.169344	-0.289084
H	1.545577	4.269300	1.149163
H	1.137603	2.551646	0.972662
H	2.280043	3.065661	2.223260
H	4.062580	1.529103	1.308076
H	4.310437	1.289448	-1.710769
H	5.457576	2.211966	-0.766666
H	6.357342	0.008798	-1.170223
H	6.130789	0.299631	0.545877
H	5.284782	-1.334949	1.749914
H	3.676682	-3.602049	0.402421
H	4.889432	-3.803582	1.647186
H	2.744241	-3.933160	2.695364
H	3.532876	-2.458972	3.243171
H	2.064163	-0.742550	3.463838
H	0.421582	0.793229	2.675549
H	0.101130	-0.130813	1.223364
H	-1.152137	-1.824246	2.599555
H	-0.906721	-0.846977	4.020051
H	-1.357741	1.581478	1.746645
H	-3.294771	3.015738	1.791061
H	-4.402527	1.706407	2.187373

ωB97X Energy = -1999.37181007 a.u.

(1*S*,29*S*)-**3**, Conf L

O	-4.879479	2.859845	-0.159830
O	-5.337704	-2.190734	-0.230473
C	-1.249813	-3.883557	-2.025966
O	0.601506	-1.988455	-2.487559
O	-0.102453	2.576504	-1.808331
O	-5.675512	0.338324	0.148349
O	-2.313510	3.360243	-0.825429
C	-0.212642	-1.003475	-2.102551
C	0.214908	0.302121	-2.178826
C	-0.597498	1.336223	-1.729286
C	-4.117846	-1.866267	-0.653740
C	-3.295173	-2.910836	-1.096113
C	-2.030978	-2.681402	-1.569026
C	-1.530253	-1.334119	-1.629053
C	-4.487442	0.501500	-0.147855
C	-3.646024	-0.551682	-0.652977
C	-2.337003	-0.271544	-1.153232
C	-1.872650	1.080642	-1.206770
C	-2.658028	2.181999	-0.703065
O	3.044350	-1.034078	-1.922694
C	-3.536746	-0.802536	3.027122
C	1.107617	-2.719240	0.787330
C	4.231654	-1.746148	-1.532089
O	2.600963	0.732850	0.083746
O	2.637377	3.361468	-1.125630
C	4.183359	4.135671	0.485246
C	1.957673	3.257374	1.194461
C	3.104427	3.099542	0.198617
C	3.679269	1.667798	0.283547
C	4.771662	1.364759	-0.734444
C	5.601426	0.115167	-0.402818
C	4.853724	-1.194401	-0.271159
C	4.797029	-1.818782	0.906059
C	4.133747	-3.112495	1.273394
C	3.080516	-2.928749	2.379351
C	1.862448	-2.145702	1.954468
C	1.478482	-1.046115	2.608192
C	0.256769	-0.214526	2.305490
C	-1.017813	-0.784276	2.928736
C	-2.301368	-0.048987	2.617807
C	-2.308985	1.138423	2.014591
C	-3.505152	1.954193	1.619784
C	-3.905273	1.882196	0.111716
H	-5.727601	2.471243	0.093577
H	-5.806293	-1.358809	0.003575
H	-1.855428	-4.780463	-1.902519
H	-0.961785	-3.792930	-3.072680
H	-0.328200	-3.995771	-1.455562
H	1.539846	-1.678493	-2.454728
H	-0.806160	3.193694	-1.485773

H	1.197017	0.537991	-2.568184
H	-3.695509	-3.916614	-1.059614
H	2.827955	-0.384523	-1.220753
H	-4.455446	-0.229286	2.908917
H	-3.461957	-1.114639	4.072370
H	-3.631575	-1.716249	2.431318
H	0.925468	-3.786105	0.947933
H	0.146290	-2.232212	0.624677
H	1.683733	-2.632146	-0.138057
H	3.978207	-2.801324	-1.418807
H	4.947518	-1.664138	-2.355310
H	2.482552	0.191378	0.875258
H	1.777489	2.936360	-1.251180
H	4.691351	3.921341	1.428171
H	3.727940	5.124578	0.558174
H	4.926021	4.166216	-0.311968
H	1.560694	4.272742	1.140812
H	1.151678	2.554587	0.973142
H	2.300719	3.073323	2.215846
H	4.075987	1.530801	1.296861
H	4.311660	1.281609	-1.722045
H	5.462919	2.207390	-0.786110
H	6.360867	0.002586	-1.184562
H	6.140211	0.299350	0.531299
H	5.295690	-1.330167	1.744101
H	3.683246	-3.601171	0.408489
H	4.897708	-3.798520	1.652269
H	2.754301	-3.923034	2.704158
H	3.544149	-2.446991	3.244999
H	2.073573	-0.731542	3.463824
H	0.426211	0.799518	2.677705
H	0.110258	-0.123092	1.223662
H	-1.139721	-1.822435	2.597025
H	-0.901694	-0.843698	4.017663
H	-1.355899	1.587679	1.751028
H	-3.303400	3.013830	1.792756
H	-4.399036	1.693789	2.189399

ωB97X Energy = -1999.37174977 a.u.

(1*S*,29*S*)-**3**, Conf M

O	3.986084	3.755130	-0.111124
O	5.357943	-0.585009	2.136966
C	1.305956	-2.992435	2.915893
O	-0.894851	-1.579040	2.295458
O	-0.835881	2.398960	-0.159536
O	5.323110	1.707258	0.944068
O	1.385598	3.457583	-0.739840
C	-0.198573	-0.625701	1.688012
C	-0.854487	0.408159	1.053772
C	-0.138396	1.428184	0.441906
C	4.041072	-0.595538	1.942012
C	3.326771	-1.691962	2.442031
C	1.962008	-1.762625	2.349744
C	1.237925	-0.688619	1.725986
C	4.130092	1.509942	0.691794
C	3.376377	0.415836	1.243730
C	1.953372	0.377653	1.130466
C	1.265286	1.432347	0.449960
C	1.966012	2.509255	-0.202403
O	-3.529388	-1.353405	2.195728
C	5.226302	-0.788077	-1.559011
C	-0.125809	-3.971211	-2.844756
C	-4.103719	-2.408068	1.404642
O	-4.733166	1.038865	1.442230
O	-3.553448	3.200884	0.448399
C	-5.809412	3.317393	-0.228612
C	-4.022648	2.669351	-1.871093
C	-4.501642	2.568852	-0.430018
C	-4.582534	1.092951	0.017165
C	-5.683596	0.263797	-0.619539
C	-5.808152	-1.144116	-0.022573
C	-4.515542	-1.943184	0.032540
C	-3.802125	-2.185472	-1.064721
C	-2.477071	-2.876708	-1.186329
C	-1.470573	-2.005228	-1.951464
C	-0.117547	-2.653036	-2.113977
C	0.981256	-2.063064	-1.640930
C	2.392503	-2.563988	-1.757807
C	3.224927	-1.748445	-2.772644
C	3.883791	-0.523427	-2.182299
C	3.293177	0.670933	-2.228542
C	3.860857	1.976002	-1.741201
C	3.481067	2.454750	-0.306699
H	4.911540	3.647716	0.146600
H	5.708658	0.261110	1.780722
H	2.071092	-3.695709	3.242134
H	0.668407	-2.745931	3.764061
H	0.671558	-3.477476	2.174580
H	-1.872427	-1.409518	2.239574
H	-0.178715	3.049436	-0.522436
H	-1.936038	0.439340	1.047302
H	3.887632	-2.484008	2.922922
H	-4.018392	-0.519578	2.043543
H	5.133190	-1.539339	-0.767693
H	5.693640	0.095646	-1.127588
H	5.908780	-1.203783	-2.305504
H	-0.462142	-4.782740	-2.192813
H	-0.823895	-3.930764	-3.685475
H	0.853471	-4.243298	-3.235435
H	-3.353634	-3.196330	1.362417
H	-4.975649	-2.808248	1.932311
H	-4.239548	1.799839	1.782417
H	-2.656328	2.929747	0.197751
H	-6.571486	2.972213	-0.928090
H	-5.643432	4.381569	-0.401953
H	-6.184265	3.185244	0.787971
H	-3.889420	3.718967	-2.139477
H	-3.066292	2.155246	-2.001138
H	-4.745876	2.230487	-2.560270
H	-3.617577	0.634586	-0.242941
H	-6.645076	0.770084	-0.502936

H	-5.482945	0.195963	-1.691884
H	-6.215691	-1.056869	0.987472
H	-6.555920	-1.695262	-0.599445
H	-4.199679	-1.815271	-2.011252
H	-2.059580	-3.123798	-0.207225
H	-2.614723	-3.822264	-1.721699
H	-1.885028	-1.790031	-2.944495
H	-1.360752	-1.046639	-1.435092
H	0.862914	-1.099185	-1.147670
H	2.876427	-2.520481	-0.774620
H	2.399074	-3.613799	-2.052990
H	4.008282	-2.392925	-3.181881
H	2.579593	-1.463767	-3.607265
H	2.317149	0.734101	-2.705598
H	3.520840	2.784802	-2.391645
H	4.952722	1.974099	-1.774282

ωB97X Energy = -1999.37155289 a.u.

(1*S*,29*S*)-**3**, Conf N

O	4.006416	3.750297	-0.098315
O	5.358404	-0.585270	2.138397
C	1.307596	-2.989217	2.925727
O	-0.892077	-1.582106	2.286447
O	-0.833959	2.409090	-0.147277
O	5.347391	1.672834	0.930619
O	1.410693	3.482992	-0.691128
C	-0.196306	-0.626189	1.684877
C	-0.855182	0.408832	1.052343
C	-0.139695	1.431217	0.447206
C	4.041557	-0.590184	1.945112
C	3.326426	-1.686534	2.447305
C	1.962735	-1.760413	2.355960
C	1.240423	-0.688085	1.727687
C	4.149589	1.519005	0.694216
C	3.379309	0.426345	1.251492
C	1.957484	0.378672	1.135457
C	1.264258	1.428796	0.451453
C	1.970146	2.500108	-0.183069
O	-3.525019	-1.363559	2.188116
C	5.238557	-0.783106	-1.560857
C	-0.111416	-3.970799	-2.848399
C	-4.097327	-2.418593	1.395871
O	-4.736893	1.025882	1.440267
O	-3.563325	3.194501	0.453729
C	-5.818389	3.304776	-0.226890
C	-4.026473	2.667003	-1.867829
C	-4.507761	2.561142	-0.427924
C	-4.584259	1.083893	0.015582
C	-5.681607	0.252766	-0.625000
C	-5.803540	-1.156604	-0.031039
C	-4.509259	-1.952991	0.024049
C	-3.794725	-2.192831	-1.073044
C	-2.468693	-2.882208	-1.194453
C	-1.461969	-2.008123	-1.956319
C	-0.107436	-2.653503	-2.116067
C	0.989118	-2.062492	-1.639089
C	2.401364	-2.561651	-1.751821
C	3.234634	-1.747897	-2.767436
C	3.893029	-0.521699	-2.178687
C	3.298034	0.670602	-2.220584
C	3.862617	1.977891	-1.735186
C	3.486359	2.456592	-0.299499
H	3.384223	4.357822	-0.519698
H	5.706868	0.259148	1.768653
H	2.073669	-3.687766	3.259962
H	0.664587	-2.740694	3.769151
H	0.679443	-3.481400	2.183740
H	-1.870452	-1.414810	2.230149
H	-0.182937	3.069081	-0.495242
H	-1.936739	0.438447	1.047959
H	3.889446	-2.477158	2.928204
H	-4.016986	-0.531001	2.038297
H	5.149005	-1.531680	-0.766463
H	5.706248	0.102493	-1.134013
H	5.917699	-1.201349	-2.308961
H	-0.807124	-3.930586	-3.691103
H	0.869476	-4.240699	-3.236552
H	-0.448227	-4.783647	-2.198339
H	-3.345855	-3.205484	1.353275
H	-4.968674	-2.820661	1.922987
H	-4.246945	1.787985	1.783234
H	-2.664899	2.928110	0.203608
H	-6.578122	2.958796	-0.928490
H	-5.655629	4.369901	-0.397420
H	-6.194487	3.168936	0.788738
H	-3.896288	3.717746	-2.133253
H	-3.068206	2.156346	-1.997606
H	-4.746938	2.227481	-2.559462
H	-3.617416	0.629196	-0.244084
H	-6.644751	0.756073	-0.509405
H	-5.478547	0.187581	-1.697065
H	-6.212551	-1.072286	0.978659
H	-6.549329	-1.708243	-0.609982
H	-4.192343	-1.822303	-2.019411
H	-2.052205	-3.130985	-0.215368
H	-2.604641	-3.826792	-1.731957
H	-1.874457	-1.792484	-2.950067
H	-1.355054	-1.049920	-1.438600
H	0.867945	-1.099240	-1.145372
H	2.883349	-2.514343	-0.767862
H	2.409923	-3.612348	-2.043827
H	4.018249	-2.393060	-3.174977
H	2.589915	-1.464745	-3.603079
H	2.319566	0.730071	-2.693238
H	3.518396	2.779608	-2.393963
H	4.953548	1.984455	-1.765475

ωB97X Energy = -1999.37149689 a.u.

(1*S*,29*S*)-**3**, Conf O

O	-5.061906	2.657093	-0.190972

O	-5.186920	-2.403855	-0.077070
C	-1.046798	-3.908308	-1.919739
O	0.707441	-1.922526	-2.385829
O	-0.328054	2.618041	-2.024088
O	-5.670882	0.086278	0.258816
O	-2.625451	3.285748	-1.071646
C	-0.167529	-0.973912	-2.059281
C	0.176697	0.352834	-2.203975
C	-0.718295	1.351486	-1.842078
C	-4.002201	-2.017348	-0.546232
C	-3.125519	-3.025555	-0.972739
C	-1.884898	-2.740182	-1.474758
C	-1.466561	-1.368260	-1.580657
C	-4.525483	0.340946	-0.112172
C	-3.622204	-0.675370	-0.614757
C	-2.338952	-0.341296	-1.146799
C	-1.965147	1.032942	-1.286452
C	-2.824794	2.086556	-0.835850
O	3.190139	-0.982700	-2.185802
C	-3.481811	-0.740922	3.114843
C	1.183585	-2.746765	0.851614
C	4.267064	-1.736555	-1.606870
O	3.208825	1.725193	-1.557833
O	1.408876	2.892072	0.302933
C	3.400481	4.219956	0.031857
C	2.971469	2.805350	2.058593
C	2.817185	2.906972	0.548436
C	3.435682	1.672251	-0.137100
C	4.906169	1.426685	0.175217
C	5.516993	0.246011	-0.586409
C	4.831881	-1.095815	-0.366725
C	4.803478	-1.649339	0.843931
C	4.226351	-2.960490	1.287232
C	3.190668	-2.795029	2.412278
C	1.929996	-2.089278	1.979621
C	1.519638	-0.967308	2.570169
C	0.282299	-0.182371	2.219534
C	-0.970098	-0.711766	2.918593
C	-2.270691	-0.006851	2.608348
C	-2.313740	1.139020	1.930425
C	-3.536544	1.917998	1.540689
C	-4.009294	1.759295	0.059297
H	-4.644369	3.499799	-0.415543
H	-5.692350	-1.588665	0.150772
H	-1.611777	-4.831111	-1.793380
H	-0.757808	-3.811123	-2.965556
H	-0.124542	-3.976373	-1.343501
H	1.623393	-1.550030	-2.424450
H	-1.075409	3.201507	-1.754622
H	1.147897	0.638236	-2.586895
H	-3.465806	-4.051150	-0.897049
H	3.332928	-0.023243	-2.083291
H	-4.407739	-0.176226	3.014860
H	-3.353052	-1.001895	4.168810
H	-3.602837	-1.682798	2.569482
H	1.087262	-3.821437	1.034329
H	0.183237	-2.336039	0.714070
H	1.717195	-2.630418	-0.096096
H	3.868994	-2.730904	-1.410615
H	5.062202	-1.837526	-2.354588
H	3.809001	2.365525	-1.955130
H	1.252780	2.846950	-0.649968
H	4.475692	4.287088	0.208191
H	2.919631	5.052477	0.547849
H	3.214174	4.344119	-1.038049
H	2.340522	3.558975	2.532547
H	2.660376	1.819935	2.415295
H	4.002725	2.979815	2.366931
H	2.847157	0.809702	0.192431
H	5.490536	2.324696	-0.051463
H	5.004111	1.252674	1.248956
H	5.534016	0.474179	-1.655736
H	6.565592	0.162729	-0.289774
H	5.276445	-1.087077	1.651251
H	3.786177	-3.512869	0.455642
H	5.041819	-3.582386	1.670222
H	2.929872	-3.794057	2.779459
H	3.646665	-2.256578	3.248398
H	2.117977	-0.579164	3.393385
H	0.443026	0.864194	2.491354
H	0.119599	-0.189308	1.136469
H	-1.095932	-1.771299	2.663848
H	-0.818329	-0.696584	4.005034
H	-1.376145	1.574091	1.597029
H	-3.341084	2.987652	1.657312
H	-4.404847	1.677660	2.155212

ωB97X Energy = -1999.37136945 a.u.

(1*S*,29*S*)-**3**, Conf P

O	5.146982	-2.566071	-0.603554
O	5.706723	2.414720	-0.111883
C	1.516992	4.353313	-1.316641
O	-0.393671	2.549663	-1.856040
O	0.198495	-2.077286	-1.581556
O	6.009190	-0.111921	0.053968
O	2.512322	-2.989981	-0.946743
C	0.407962	1.512455	-1.615127
C	-0.065250	0.228562	-1.768757
C	0.742083	-0.861296	-1.464701
C	4.444986	2.152637	-0.441411
C	3.614417	3.250856	-0.704463
C	2.305800	3.095182	-1.071893
C	1.766575	1.769835	-1.216166
C	4.811599	-0.259451	-0.189209
C	3.940781	0.850666	-0.517949
C	2.581792	0.651183	-0.914395
C	2.067507	-0.678674	-1.043938
C	2.871105	-1.824438	-0.732510
O	-2.938785	1.724231	-1.558684
C	1.348666	-3.167383	2.379399
C	-0.850829	2.281107	1.565900

C	-4.094158	2.391047	-1.018694
O	-2.787967	-0.622287	-0.272436
O	-2.392856	-3.260906	-0.244471
C	-3.214268	-2.705545	-2.442715
C	-4.623326	-3.850180	-0.707928
C	-3.546304	-2.806403	-0.956492
C	-3.968277	-1.440906	-0.364039
C	-5.025070	-0.697869	-1.173253
C	-5.697414	0.461666	-0.425224
C	-4.794896	1.581456	0.049347
C	-4.678004	1.836092	1.352868
C	-3.869669	2.884896	2.055063
C	-2.896616	2.267265	3.074801
C	-1.771512	1.481879	2.447394
C	-1.616965	0.178395	2.694295
C	-0.531307	-0.713723	2.155057
C	0.680587	-0.822060	3.094368
C	1.746828	-1.722500	2.521945
C	2.917188	-1.214745	2.133788
C	4.032254	-1.961884	1.463196
C	4.223545	-1.654798	-0.052471
H	4.656023	-3.384205	-0.756485
H	6.161153	1.549082	0.018876
H	2.154915	5.220250	-1.148979
H	1.129877	4.390395	-2.333934
H	0.656815	4.412794	-0.650015
H	-1.343246	2.272864	-1.862912
H	0.910527	-2.737051	-1.406267
H	-1.079725	0.047858	-2.094587
H	4.045077	4.239792	-0.605480
H	-2.853189	0.855256	-1.113939
H	0.802977	-3.495916	3.267543
H	2.196255	-3.835329	2.236651
H	0.678490	-3.302429	1.524985
H	-0.578737	3.216864	2.062235
H	0.068571	1.749466	1.320737
H	-1.341280	2.552393	0.626130
H	-3.774406	3.359702	-0.632771
H	-4.787596	2.575844	-1.844846
H	-2.631996	-0.371446	0.647499
H	-1.667767	-2.659170	-0.461564
H	-4.098545	-2.470191	-3.037041
H	-2.814315	-3.661076	-2.786626
H	-2.459195	-1.936745	-2.623911
H	-4.294832	-4.813850	-1.100920
H	-4.808761	-3.959363	0.362645
H	-5.560391	-3.584744	-1.199236
H	-4.337066	-1.624202	0.651604
H	-4.567877	-0.337982	-2.099618
H	-5.807927	-1.400388	-1.469199
H	-6.455769	0.887525	-1.091416
H	-6.231648	0.055544	0.438348
H	-5.242553	1.193877	2.029945
H	-3.323434	3.518291	1.354348
H	-4.553182	3.542172	2.601712
H	-2.465800	3.078934	3.670700
H	-3.456109	1.626032	3.761735
H	-2.319656	-0.292603	3.380565
H	-0.949451	-1.711153	1.988008
H	-0.183693	-0.359211	1.180144
H	1.088660	0.177675	3.266699
H	0.347244	-1.209682	4.063783
H	3.082178	-0.149191	2.285757
H	3.871510	-3.039133	1.516105
H	4.993600	-1.748664	1.937499

ωB97X Energy = -1999.37130742 a.u.

(1*S*,29*S*)-**3**, Conf Q

O	5.124188	-2.596153	-0.597025
O	5.718989	2.403487	-0.136167
C	1.514663	4.351113	-1.279826
O	-0.392619	2.553258	-1.852088
O	0.189579	-2.073968	-1.565129
O	6.014881	-0.149820	-0.028738
O	2.467769	-2.999473	-0.908997
C	0.407306	1.514124	-1.607857
C	-0.065395	0.231318	-1.759572
C	0.740606	-0.861133	-1.454538
C	4.451086	2.148488	-0.448729
C	3.618972	3.247845	-0.695534
C	2.306860	3.091706	-1.054022
C	1.765518	1.767900	-1.206298
C	4.799036	-0.264089	-0.215514
C	3.939112	0.849585	-0.518681
C	2.579546	0.646069	-0.912379
C	2.069983	-0.684738	-1.043827
C	2.866167	-1.846223	-0.727310
O	-2.942251	1.728946	-1.554192
C	1.358700	-3.159522	2.411275
C	-0.869164	2.277595	1.565369
C	-4.105854	2.386940	-1.021659
O	-2.791685	-0.622553	-0.278841
O	-2.385308	-3.259584	-0.259166
C	-3.206561	-2.702171	-2.457035
C	-4.612997	-3.856481	-0.726716
C	-3.539508	-2.808047	-0.971302
C	-3.968058	-1.445726	-0.375945
C	-5.025559	-0.703918	-1.185471
C	-5.703759	0.450970	-0.435502
C	-4.806260	1.572856	0.043388
C	-4.692522	1.824842	1.347658
C	-3.888238	2.874505	2.053173
C	-2.915469	2.257580	3.073590
C	-1.787246	1.475827	2.447280
C	-1.627786	0.173115	2.695015
C	-0.537091	-0.714425	2.158076
C	0.677136	-0.809052	3.095960
C	1.746762	-1.709933	2.530338
C	2.911275	-1.198938	2.129059
C	4.029041	-1.947454	1.464697
C	4.218782	-1.661675	-0.056006

H	6.008183	-2.266363	-0.387628
H	6.180734	1.541529	-0.029718
H	2.149738	5.217452	-1.099035
H	1.127250	4.402210	-2.296371
H	0.654243	4.397565	-0.612444
H	-1.342038	2.277782	-1.858669
H	0.902868	-2.733072	-1.375833
H	-1.080585	0.049905	-2.082790
H	4.048814	4.236893	-0.595026
H	-2.857009	0.857880	-1.113442
H	0.825056	-3.480029	3.309671
H	2.210284	-3.822168	2.268229
H	0.680760	-3.311090	1.565894
H	-0.603457	3.216541	2.059152
H	0.053601	1.750108	1.323829
H	-1.359415	2.542573	0.623691
H	-3.795882	3.358438	-0.634872
H	-4.796417	2.565725	-1.851597
H	-2.635132	-0.379212	0.642933
H	-1.659186	-2.660307	-0.480768
H	-4.091453	-2.469723	-3.051599
H	-2.801815	-3.655036	-2.802768
H	-2.454927	-1.929487	-2.635902
H	-4.281724	-4.817461	-1.123947
H	-4.797338	-3.970746	0.343519
H	-5.551325	-3.591974	-1.216172
H	-4.339044	-1.633313	0.638138
H	-4.567416	-0.339575	-2.109664
H	-5.805223	-1.408215	-1.485617
H	-6.462622	0.875658	-1.101872
H	-6.237898	0.040429	0.426059
H	-5.256080	1.179312	2.022399
H	-3.342282	3.510251	1.354339
H	-4.574252	3.529242	2.599753
H	-2.487583	3.069406	3.671422
H	-3.474587	1.614054	3.758701
H	-2.329221	-0.300373	3.380828
H	-0.948536	-1.715522	1.996553
H	-0.193526	-0.362421	1.180821
H	1.080737	0.194159	3.258573
H	0.347259	-1.189282	4.069465
H	3.068973	-0.130202	2.265649
H	3.876905	-3.024830	1.520264
H	4.987705	-1.722939	1.941687

ωB97X Energy = -1999.37125575 a.u.

(1*S*,29*S*)-**3**, Conf R

O	4.874166	-2.255298	-1.131057
O	4.876050	2.634714	-0.079290
C	0.668588	4.247748	-1.645383
O	-1.106333	2.297662	-2.133601
O	-0.034437	-2.251170	-2.229619
O	5.408101	0.144699	-0.009169
O	2.284671	-2.981111	-1.489990
C	-0.211720	1.332674	-1.957313
C	-0.558707	0.020005	-2.203847
C	0.354114	-0.997639	-1.963157
C	3.678720	2.276849	-0.531152
C	2.780252	3.308848	-0.839008
C	1.525736	3.054810	-1.319762
C	1.110238	1.691681	-1.518195
C	4.262711	-0.101328	-0.387526
C	3.309337	0.939289	-0.709231
C	2.006918	0.639251	-1.215234
C	1.627896	-0.721660	-1.444953
C	2.526172	-1.805533	-1.180329
O	-3.642799	1.620591	-1.937361
C	1.347599	-3.738845	2.050893
C	-0.572979	2.576710	4.026447
C	-4.140535	2.406623	-0.841661
O	-4.407734	-1.002847	-1.559559
O	-2.743261	-3.040939	-1.756667
C	-4.364287	-3.712296	-0.187451
C	-2.075596	-3.024450	0.579013
C	-3.194839	-2.767067	-0.418986
C	-3.613499	-1.277776	-0.398122
C	-4.380479	-0.833793	0.836044
C	-4.988218	0.568928	0.729605
C	-4.015941	1.714743	0.492425
C	-3.165479	2.091297	1.447258
C	-2.175116	3.218119	1.437546
C	-0.714317	2.744886	1.488126
C	-0.339219	1.918951	2.693531
C	0.199539	0.708674	2.544536
C	0.649021	-0.220154	3.642432
C	0.539220	-1.694088	3.263128
C	1.564025	-2.270013	2.311664
C	2.583788	-1.567529	1.816576
C	3.707689	-2.118149	0.985190
C	3.843154	-1.563556	-0.455789
H	4.515995	-3.123347	-1.356822
H	5.396882	1.808025	0.059319
H	1.238805	5.161390	-1.482280
H	0.330289	4.221228	-2.680527
H	-0.226391	4.273711	-1.023693
H	-2.029616	1.934371	-2.188655
H	0.732925	-2.848573	-2.038817
H	-1.541834	-0.222925	-2.588406
H	3.118448	4.327481	-0.693275
H	-4.023754	0.719709	-1.903929
H	1.685741	-4.330132	2.907329
H	1.860742	-4.101859	1.161862
H	0.281686	-3.943646	1.926573
H	-0.158419	3.589133	4.023896
H	-1.643030	2.676133	4.234074
H	-0.120223	2.030952	4.852584
H	-3.580911	3.339541	-0.872058
H	-5.192821	2.643668	-1.031469
H	-4.052675	-1.579428	-2.252819
H	-1.816839	-2.772325	-1.856652
H	-4.729773	-3.651188	0.837846

H	-4.036182	-4.735892	-0.372980
H	-5.188660	-3.484510	-0.865820
H	-1.723702	-4.053399	0.479100
H	-1.229953	-2.349780	0.409096
H	-2.424576	-2.881335	1.603494
H	-2.689558	-0.684455	-0.469846
H	-5.195742	-1.534264	1.032295
H	-3.703098	-0.875706	1.694121
H	-5.737057	0.561970	-0.066058
H	-5.535269	0.759582	1.656402
H	-3.189300	1.520927	2.377185
H	-2.295809	3.845746	0.553271
H	-2.376046	3.862869	2.299740
H	-0.499334	2.172974	0.583867
H	-0.073800	3.635561	1.463729
H	0.338536	0.338872	1.527766
H	1.680546	0.005592	3.937387
H	0.042570	-0.058583	4.535735
H	0.581663	-2.301899	4.174692
H	-0.457680	-1.879543	2.843987
H	2.663483	-0.512725	2.069644
H	3.626725	-3.199806	0.877701
H	4.666928	-1.911785	1.468035

ωB97X Energy = -1999.37123005 a.u.

(1*S*,29*S*)-**3**, Conf S

O	4.852990	-2.290969	-1.133360
O	4.884083	2.626933	-0.080421
C	0.669901	4.245047	-1.625655
O	-1.104407	2.298899	-2.130753
O	-0.035391	-2.249617	-2.230230
O	5.421521	0.119606	-0.071509
O	2.252985	-2.994981	-1.469202
C	-0.209679	1.332844	-1.954040
C	-0.553884	0.021332	-2.203026
C	0.359015	-0.998394	-1.963509
C	3.681706	2.274098	-0.523574
C	2.782041	3.306324	-0.822253
C	1.527239	3.051195	-1.304152
C	1.110858	1.689075	-1.509329
C	4.252170	-0.104662	-0.400743
C	3.306125	0.938180	-0.699143
C	2.006951	0.634291	-1.211964
C	1.635744	-0.726886	-1.450112
C	2.529717	-1.825551	-1.184693
O	-3.643144	1.621386	-1.940353
C	1.345385	-3.741953	2.051577
C	-0.583683	2.571948	4.028611
C	-4.143910	2.406174	-0.845302
O	-4.409471	-1.002263	-1.568287
O	-2.741651	-3.037147	-1.765339
C	-4.363675	-3.713395	-0.199248
C	-2.077276	-3.022555	0.571338
C	-3.195498	-2.765898	-0.428060
C	-3.616686	-1.277340	-0.405873
C	-4.386514	-0.835989	0.827436
C	-4.995060	0.566478	0.721968
C	-4.022967	1.713210	0.488603
C	-3.175755	2.089585	1.446386
C	-2.185822	3.216820	1.440400
C	-0.724952	2.743756	1.490541
C	-0.350055	1.916075	2.694753
C	0.188318	0.705854	2.544097
C	0.637472	-0.224281	3.640988
C	0.529523	-1.697811	3.259731
C	1.556707	-2.272073	2.309823
C	2.574059	-1.566841	1.813617
C	3.700535	-2.117185	0.985693
C	3.841493	-1.571065	-0.458603
H	5.695017	-1.956326	-0.799147
H	5.413355	1.804821	0.036388
H	1.239133	5.158412	-1.457887
H	0.333105	4.222316	-2.661359
H	-0.226081	4.267687	-1.005372
H	-2.027049	1.935289	-2.187775
H	0.731141	-2.848085	-2.025981
H	-1.536889	-0.222792	-2.587309
H	3.119151	4.325118	-0.675681
H	-4.024363	0.720558	-1.909143
H	1.680782	-4.330084	2.911295
H	1.863826	-4.105251	1.165864
H	0.280472	-3.949563	1.922885
H	-0.169300	3.584450	4.027442
H	-1.653725	2.670885	4.236523
H	-0.130730	2.025070	4.853905
H	-3.584275	3.339171	-0.873238
H	-5.195742	2.643391	-1.037575
H	-4.052375	-1.577709	-2.261480
H	-1.815351	-2.766669	-1.863829
H	-4.731154	-3.653682	0.825429
H	-4.033373	-4.736260	-0.384928
H	-5.187200	-3.486594	-0.878986
H	-1.722951	-4.050553	0.470235
H	-1.232822	-2.345831	0.403839
H	-2.428330	-2.881948	1.595471
H	-2.693560	-0.682475	-0.475381
H	-5.201644	-1.537425	1.020797
H	-3.710917	-0.878740	1.686884
H	-5.742269	0.560294	-0.075242
H	-5.544088	0.755341	1.647963
H	-3.202010	1.518435	2.375771
H	-2.306254	3.846820	0.557768
H	-2.387440	3.859188	2.304197
H	-0.509856	2.173185	0.585462
H	-0.084544	3.634568	1.467779
H	0.327040	0.337208	1.526862
H	1.668510	0.001919	3.937348
H	0.029909	-0.064428	4.533867
H	0.570936	-2.306504	4.170745
H	-0.466454	-1.883835	2.838671
H	2.649868	-0.511258	2.064505

H	3.625577	-3.197513	0.871776
H	4.655526	-1.907800	1.478557

ωB97X Energy = -1999.37122203 a.u.

(1*S*,29*S*)-**3**, Conf T

O	-6.525759	0.735354	0.253200
O	-4.212001	-3.200434	-1.946700
C	0.175849	-1.706424	-3.096082
O	0.812185	0.666185	-1.995142
O	-2.321657	3.539545	-0.059524
O	-5.838971	-1.695752	-0.664940
O	-4.674842	2.624499	0.447354
C	-0.432134	0.890476	-1.582934
C	-0.773394	2.118337	-1.058625
C	-2.051060	2.332112	-0.552838
C	-3.341166	-2.199584	-1.837887
C	-2.081114	-2.382779	-2.425011
C	-1.115399	-1.413577	-2.379658
C	-1.394562	-0.173358	-1.709169
C	-4.946021	-0.856797	-0.551710
C	-3.646339	-1.006687	-1.177272
C	-2.667006	0.031568	-1.125733
C	-2.996999	1.293826	-0.536582
C	-4.271456	1.514216	0.070713
O	5.246522	-1.054167	-1.951507
C	-2.454750	1.318104	3.038465
C	1.488469	-2.381996	0.306152
C	5.741909	-1.898518	-0.898857
O	4.942714	1.690271	-1.599947
O	2.502291	2.665406	-1.437249
C	3.925359	3.966697	0.000535
C	2.254857	2.321899	0.903927
C	3.254584	2.614303	-0.200516
C	4.263052	1.465110	-0.364907
C	5.249531	1.305555	0.782807
C	6.220941	0.138701	0.576812
C	5.552619	-1.217165	0.426220
C	4.897963	-1.768894	1.446258
C	4.198569	-3.095163	1.512799
C	2.897968	-3.039871	2.322577
C	1.817213	-2.147832	1.754760
C	1.186670	-1.270922	2.536833
C	-0.001459	-0.413240	2.206238
C	-1.252382	-0.925210	2.938279
C	-2.507256	-0.135807	2.659838
C	-3.567163	-0.738419	2.119897
C	-4.908146	-0.129184	1.828612
C	-5.182697	0.332650	0.361889
H	-6.543759	1.664895	0.520279
H	-5.050535	-2.907657	-1.519330
H	0.102340	-2.670841	-3.597236
H	0.397480	-0.939191	-3.837197
H	1.018178	-1.729433	-2.405878
H	1.403577	1.433343	-1.785247
H	-3.262075	3.538426	0.232712
H	-0.042840	2.916006	-1.014242
H	-1.898261	-3.318653	-2.938858
H	5.496882	-1.441642	-2.794245
H	-3.429731	1.803959	3.014052
H	-1.796931	1.868251	2.358193
H	-2.037704	1.434762	4.042505
H	1.369163	-3.451512	0.107868
H	0.575251	-1.876578	-0.006415
H	2.303474	-2.028493	-0.335120
H	5.230101	-2.861484	-0.934933
H	6.812379	-2.076136	-1.055881
H	5.189414	0.810796	-1.929784
H	3.169147	2.617711	-2.138500
H	4.427797	4.016971	0.967765
H	3.170209	4.753638	-0.033463
H	4.662754	4.154712	-0.782239
H	1.479227	3.090083	0.919035
H	1.780336	1.348097	0.755999
H	2.744313	2.319388	1.878518
H	3.674492	0.542547	-0.457314
H	5.827074	2.227366	0.894757
H	4.695424	1.152498	1.713543
H	6.837280	0.340156	-0.302837
H	6.905606	0.110375	1.428344
H	4.877600	-1.206678	2.381461
H	3.998433	-3.491131	0.515401
H	4.861089	-3.820114	1.998114
H	2.498611	-4.059273	2.381369
H	3.121362	-2.731014	3.348028
H	1.515715	-1.201602	3.573859
H	0.202140	0.618218	2.512320
H	-0.197835	-0.385724	1.130757
H	-1.414021	-1.972593	2.669445
H	-1.054168	-0.901685	4.017119
H	-3.474287	-1.795460	1.878967
H	-5.103865	0.743527	2.454992
H	-5.694983	-0.858867	2.033960

ωB97X Energy = -1999.37121865 a.u.

(1*S*,29*S*)-**3**, Conf U

O	5.256342	-2.537257	-0.469558
O	5.492097	2.548884	-0.453253
C	1.157045	4.118481	-1.671134
O	-0.670560	2.169333	-1.898792
O	0.244186	-2.378905	-1.322631
O	5.967045	0.067368	-0.120897
O	2.588812	-3.096523	-0.718663
C	0.200233	1.207030	-1.613674
C	-0.199384	-0.111990	-1.629086
C	0.700942	-1.120634	-1.309744
C	4.238791	2.183009	-0.705937
C	3.331847	3.201534	-1.029731
C	2.023162	2.936597	-1.326802
C	1.559395	1.574570	-1.317082
C	4.771273	-0.174671	-0.289591

C	3.816785	0.850769	-0.654217
C	2.459349	0.535462	-0.971509
C	2.031999	-0.829541	-0.979073
C	2.917730	-1.909532	-0.625864
O	-3.219862	1.477315	-1.881090
C	1.493022	-2.900042	2.550826
C	-0.653699	2.883179	1.513490
C	-4.098345	2.273898	-1.075016
O	-4.058587	-1.135956	-2.092771
O	-2.471308	-3.172316	-1.647624
C	-4.561204	-3.887596	-0.836132
C	-2.756969	-3.187003	0.762547
C	-3.409211	-2.925812	-0.586271
C	-3.829277	-1.439637	-0.711000
C	-5.066275	-1.041940	0.076453
C	-5.591561	0.365382	-0.230751
C	-4.674679	1.532455	0.103514
C	-4.504810	1.906449	1.370957
C	-3.755676	3.075457	1.939479
C	-2.710404	2.661958	2.989016
C	-1.494717	1.996983	2.394299
C	-1.224606	0.715757	2.642486
C	-0.084834	-0.094861	2.102999
C	0.931326	-0.506984	3.179567
C	1.951087	-1.469547	2.620473
C	3.124688	-1.016054	2.180944
C	4.196997	-1.813546	1.498986
C	4.295631	-1.605183	-0.035929
H	5.406975	-2.433790	-1.414492
H	6.007083	1.726467	-0.275962
H	1.758393	5.026602	-1.652964
H	0.708091	4.009356	-2.657094
H	0.336940	4.225779	-0.961226
H	-1.598271	1.822887	-1.950789
H	1.012375	-2.972527	-1.114561
H	-1.222124	-0.368851	-1.875149
H	3.705298	4.218148	-1.046408
H	-3.624819	0.617539	-2.109055
H	2.196574	-3.560580	2.048151
H	0.538796	-2.969674	2.019374
H	1.318870	-3.283329	3.560284
H	-0.541361	3.870903	1.969152
H	0.342826	2.478969	1.335844
H	-1.125993	3.031820	0.537395
H	-3.510947	3.136043	-0.763273
H	-4.917099	2.639484	-1.705701
H	-3.445929	-1.703979	-2.584531
H	-1.581355	-2.884327	-1.391293
H	-5.286136	-3.860882	-0.022209
H	-4.165894	-4.901584	-0.909585
H	-5.075124	-3.648000	-1.769158
H	-2.430035	-4.226637	0.823883
H	-1.885558	-2.540874	0.902578
H	-3.454549	-2.998439	1.580301
H	-2.977734	-0.833461	-0.363696
H	-5.872385	-1.746303	-0.142587
H	-4.844034	-1.124860	1.144262
H	-5.866532	0.410447	-1.287980
H	-6.524289	0.489785	0.324469
H	-5.017955	1.309633	2.127531
H	-3.283564	3.677443	1.161274
H	-4.484141	3.729880	2.429543
H	-2.395001	3.561143	3.529050
H	-3.178633	1.995910	3.719727
H	-1.898280	0.177329	3.309303
H	-0.494332	-0.998137	1.636285
H	0.442659	0.438064	1.309492
H	1.424387	0.390953	3.561638
H	0.402424	-0.969783	4.019845
H	3.327170	0.047701	2.297696
H	4.050853	-2.885376	1.630525
H	5.183143	-1.562836	1.897374

ωB97X Energy = -1999.37108238 a.u.

(*S*)-**3modMe**, Conf A

O	2.388905	2.179924	-1.303141
O	-2.272076	3.403179	0.387187
C	-4.655630	-0.695203	0.971764
O	-3.263694	-2.861269	0.219517
O	1.045668	-2.717468	-1.598672
O	0.151162	3.425611	-0.491323
O	2.207017	-0.403555	-1.813586
C	-2.182177	-2.149079	-0.133931
C	-1.092429	-2.784597	-0.676333
C	0.032145	-2.049656	-1.049003
C	-2.195817	2.077746	0.286103
C	-3.334063	1.342051	0.650069
C	-3.375001	-0.022221	0.556380
C	-2.221722	-0.727672	0.064964
C	0.150793	2.198873	-0.439931
C	-1.041270	1.422079	-0.140504
C	-1.057955	0.000464	-0.279235
C	0.085507	-0.670817	-0.815234
C	1.280058	0.059201	-1.143016
C	4.927063	-1.211476	1.436980
C	2.469369	-1.658263	1.805208
C	3.525526	-0.667991	1.400439
C	3.291694	0.586265	1.014807
C	1.960939	1.268932	0.923368
C	1.464674	1.445714	-0.552755
H	2.951287	1.527548	-1.744621
H	-1.418381	3.774223	0.067952
H	-5.106292	-1.235880	0.140009
H	-4.484222	-1.420238	1.766281
H	-5.362111	0.054646	1.325100
H	-3.123315	-3.795490	0.031971
H	1.732624	-2.063978	-1.855738
H	-1.096281	-3.856175	-0.838737
H	-4.196495	1.894294	1.002944
H	5.657431	-0.472644	1.105596

H	5.189166	-1.529322	2.450320
H	5.010984	-2.094530	0.796549
H	1.476757	-1.221844	1.909487
H	2.407884	-2.459373	1.060793
H	2.736397	-2.130427	2.754256
H	4.144082	1.195807	0.725291
H	1.194320	0.751214	1.501349
H	2.040070	2.284705	1.320499

ωB97X Energy = -1186.35542056 a.u.

(*S*)-**3modMe**, Conf B

O	-2.389604	2.168121	-1.303802
O	-1.005170	-2.729995	-1.583846
C	3.393391	-3.037189	0.261127
O	4.462042	-0.657923	0.889791
O	2.246159	3.430298	0.389080
O	-2.182764	-0.417096	-1.820906
O	-0.178870	3.428167	-0.453156
C	3.355830	0.021645	0.545419
C	3.335290	1.389223	0.644081
C	2.190432	2.104684	0.289031
C	-0.002870	-2.045766	-1.031963
C	1.134289	-2.769457	-0.648136
C	2.232423	-2.153887	-0.108903
C	2.226936	-0.726814	0.068171
C	-1.270342	0.053940	-1.141391
C	-0.067683	-0.672044	-0.804651
C	1.067145	0.010515	-0.270965
C	1.035408	1.434206	-0.132442
C	-0.159428	2.198192	-0.420274
C	-4.955691	-1.231495	1.382875
C	-2.502652	-1.688518	1.769402
C	-3.552492	-0.691477	1.365045
C	-3.311597	0.566237	0.995149
C	-1.978100	1.245890	0.922083
C	-1.468107	1.435453	-0.547855
H	-2.955501	1.517047	-1.741938
H	-1.697973	-2.089925	-1.853320
H	3.646598	-2.934279	1.315640
H	3.139367	-4.076913	0.059613
H	4.286364	-2.777100	-0.306186
H	5.146258	-0.047736	1.185593
H	1.378937	3.784152	0.080972
H	4.207158	1.934142	0.986362
H	1.126992	-3.841059	-0.805537
H	-5.036626	-2.105076	0.729198
H	-5.226750	-1.563160	2.389390
H	-5.681500	-0.486154	1.056103
H	-1.509207	-1.256440	1.883624
H	-2.777513	-2.166083	2.713492
H	-2.439240	-2.485005	1.020301
H	-4.159785	1.181438	0.705298
H	-2.057613	2.258250	1.327501
H	-1.217403	0.721282	1.501795

ωB97X Energy = -1186.35529972 a.u.

(*S*)-**3modMe**, Conf C

O	3.304102	1.189516	-1.401270
O	-0.798964	3.786068	0.076785
C	-4.384432	0.644471	0.337124
O	-3.658395	-1.864273	-0.259180
O	0.651314	-3.122603	-1.565056
O	1.583104	3.049433	-0.511720
O	2.496815	-1.327244	-1.604482
C	-2.379304	-1.531665	-0.490754
C	-1.489487	-2.491200	-0.905478
C	-0.158882	-2.153583	-1.146957
C	-1.128312	2.502433	-0.043289
C	-2.470382	2.164161	0.185485
C	-2.921626	0.877944	0.070999
C	-1.998270	-0.159640	-0.303041
C	1.198875	1.881197	-0.520841
C	-0.196306	1.513746	-0.365015
C	-0.636889	0.163671	-0.515187
C	0.292077	-0.844693	-0.925750
C	1.680529	-0.541908	-1.104102
C	0.308852	-1.102496	3.420440
C	1.941614	-2.268471	1.886255
C	1.375327	-0.963323	2.370292
C	1.736759	0.237136	1.919164
C	2.764234	0.534374	0.865501
C	2.236272	0.775190	-0.587461
H	3.722033	0.378958	-1.723490
H	0.161032	3.864598	-0.131566
H	-4.531339	-0.063673	1.151826
H	-4.860608	1.587987	0.600178
H	-4.884683	0.229830	-0.537325
H	-3.793789	-2.802528	-0.430400
H	1.538540	-2.724523	-1.719807
H	-1.807096	-3.516042	-1.057769
H	-3.150964	2.963359	0.452541
H	-0.535053	-1.678906	3.028059
H	0.688314	-1.647186	4.289697
H	-0.061988	-0.132224	3.753050
H	2.351478	-2.836176	2.726264
H	1.145494	-2.881708	1.451728
H	2.724338	-2.154838	1.137031
H	1.239971	1.106005	2.345570
H	3.296892	1.455007	1.114875
H	3.509735	-0.259171	0.784614

ωB97X Energy = -1186.35529005 a.u.

(*S*)-**3modMe**, Conf D

O	-3.326407	1.112483	-1.395540
O	-0.493947	-3.088512	-1.648196
C	3.907909	-1.858715	-0.265266
O	4.149272	0.732969	0.364832
O	0.650098	3.829130	0.184138
O	-2.414814	-1.393950	-1.646729

O	-1.698123	2.996114	-0.472303
C	2.855098	1.000171	0.131313
C	2.384841	2.281200	0.279216
C	1.041009	2.565529	0.042168
C	0.263691	-2.092068	-1.195202
C	1.612992	-2.380640	-0.942535
C	2.484861	-1.426155	-0.495140
C	2.009601	-0.085397	-0.281094
C	-1.658591	-0.567687	-1.138118
C	-0.242137	-0.814170	-0.950999
C	0.643105	0.211031	-0.498676
C	0.150172	1.541364	-0.309076
C	-1.241001	1.846056	-0.474794
C	-0.329585	-1.347695	3.331313
C	-1.967296	-2.441066	1.749657
C	-1.399848	-1.159926	2.292543
C	-1.759251	0.060467	1.896533
C	-2.783718	0.407238	0.855105
C	-2.251010	0.715028	-0.583311
H	-3.424469	2.064788	-1.258039
H	-1.398282	-2.726048	-1.797562
H	4.597506	-1.305528	-0.901876
H	4.214544	-1.680477	0.764742
H	4.004668	-2.921597	-0.482404
H	4.611515	1.534488	0.633041
H	-0.307403	3.873005	-0.039949
H	3.048196	3.087708	0.568541
H	1.951754	-3.393735	-1.121960
H	0.512998	-1.904365	2.908468
H	0.042361	-0.394111	3.708050
H	-0.705221	-1.933536	4.175072
H	-2.343577	-3.063328	2.566204
H	-2.773643	-2.292354	1.032605
H	-1.178784	-3.016842	1.253802
H	-1.258635	0.907975	2.359789
H	-3.320283	1.311801	1.153803
H	-3.526933	-0.381102	0.726231

ωB97X Energy = -1186.35519674 a.u.

(*S*)-**3modMe**, Conf E

O	-3.336562	1.100657	-1.395016
O	-0.520423	-3.119040	-1.595209
C	3.893398	-1.878246	-0.257579
O	4.150382	0.723055	0.325535
O	0.658490	3.824526	0.112413
O	-2.434127	-1.383132	-1.635843
O	-1.688121	3.006981	-0.474034
C	2.855029	0.989888	0.092466
C	2.387565	2.272862	0.217950
C	1.041619	2.557470	-0.015363
C	0.245927	-2.120386	-1.161725
C	1.594489	-2.408591	-0.911910
C	2.470375	-1.445965	-0.487167
C	2.002925	-0.098785	-0.296321
C	-1.655251	-0.577339	-1.116749
C	-0.251687	-0.836745	-0.931456
C	0.636048	0.200345	-0.510045
C	0.143926	1.533964	-0.350815
C	-1.256845	1.852632	-0.501236
C	-0.286739	-1.200942	3.383974
C	-1.903187	-2.370597	1.835849
C	-1.360379	-1.063388	2.340967
C	-1.745204	0.137729	1.911350
C	-2.779320	0.432959	0.863676
C	-2.256696	0.712100	-0.584228
H	-3.731994	0.282101	-1.724585
H	-1.420755	-2.759695	-1.757887
H	3.987960	-2.943823	-0.461847
H	4.581496	-1.333428	-0.902790
H	4.203587	-1.688030	0.769266
H	4.615070	1.528670	0.576413
H	-0.306155	3.859673	-0.095400
H	3.052471	3.083277	0.492769
H	1.931631	-3.424743	-1.075828
H	0.567032	-1.751854	2.976405
H	0.065591	-0.229902	3.734019
H	-0.650703	-1.770499	4.243850
H	-2.285203	-2.967567	2.668541
H	-2.700736	-2.259279	1.102083
H	-1.099792	-2.953914	1.374189
H	-1.262986	1.008400	2.350427
H	-3.507805	-0.374682	0.768113
H	-3.331775	1.337126	1.129670

ωB97X Energy = -1186.35502812 a.u.

(*S*)-**3modMe**, Conf F

O	3.295578	1.184642	-1.410919
O	-0.779840	3.791332	0.141738
C	-4.380176	0.664160	0.385402
O	-3.681046	-1.836388	-0.271072
O	0.616197	-3.101658	-1.609720
O	1.601224	3.031342	-0.519514
O	2.475316	-1.355278	-1.605478
C	-2.399633	-1.507971	-0.501850
C	-1.517122	-2.462988	-0.937244
C	-0.183382	-2.130496	-1.177417
C	-1.120381	2.511504	0.008899
C	-2.461200	2.177632	0.243838
C	-2.918766	0.894535	0.109954
C	-2.006623	-0.142902	-0.291619
C	1.188667	1.868051	-0.501674
C	-0.198791	1.519162	-0.330270
C	-0.643714	0.172979	-0.506738
C	0.279428	-0.827679	-0.945591
C	1.682829	-0.543211	-1.122682
C	0.353616	-1.225754	3.380062
C	1.995243	-2.332760	1.811763
C	1.414449	-1.047453	2.330015
C	1.756726	0.168389	1.905907
C	2.773581	0.505874	0.853876

C	2.233289	0.768573	-0.590567
H	3.376346	2.139268	-1.280689
H	0.172715	3.875494	-0.084392
H	-4.848897	1.604625	0.671583
H	-4.890553	0.268680	-0.492035
H	-4.522606	-0.059213	1.187433
H	-3.822582	-2.770268	-0.459878
H	1.509530	-2.703166	-1.748121
H	-1.839506	-3.484212	-1.103675
H	-3.136589	2.974798	0.529154
H	-0.032605	-0.268950	3.733559
H	-0.481567	-1.808476	2.978428
H	0.744966	-1.781607	4.236890
H	2.790298	-2.189353	1.081117
H	2.390915	-2.928706	2.638775
H	1.209680	-2.932267	1.340056
H	1.248232	1.019331	2.354201
H	3.294549	1.426792	1.129423
H	3.530014	-0.272589	0.743499

ωB97X Energy = -1186.35499594 a.u.

(*S*)-**3modMe**, Conf G

O	2.565987	0.894160	-1.533261
O	-1.492483	3.649936	-0.178350
C	-4.917530	0.564047	1.068837
O	-4.215636	-2.004928	0.746088
O	-0.084802	-3.410160	-0.942016
O	0.812535	2.833282	-0.982387
O	1.694399	-1.611077	-1.488984
C	-2.985372	-1.701696	0.302733
C	-2.134542	-2.704452	-0.090682
C	-0.852985	-2.397450	-0.546289
C	-1.794673	2.361071	-0.036064
C	-3.085181	2.053845	0.420403
C	-3.510761	0.762379	0.571763
C	-2.616147	-0.315197	0.244802
C	0.471261	1.685474	-0.709380
C	-0.881447	1.341090	-0.304707
C	-1.299989	-0.019272	-0.183946
C	-0.404324	-1.070711	-0.556505
C	0.942617	-0.781613	-0.967905
C	5.337779	-1.404326	1.379902
C	5.069182	1.060377	0.897127
C	4.394535	-0.265773	1.105158
C	3.076984	-0.466468	1.070191
C	2.017972	0.566238	0.827599
C	1.519367	0.589807	-0.658842
H	3.025547	0.060165	-1.700812
H	-0.576964	3.701367	-0.536087
H	-5.520565	0.013307	0.348004
H	-4.932315	-0.006621	1.996811
H	-5.380336	1.533960	1.245694
H	-4.348026	-2.958880	0.731595
H	0.760966	-3.032515	-1.272539
H	-2.446970	-3.741838	-0.063085
H	-3.748077	2.880456	0.645171
H	5.930968	-1.201191	2.276416
H	4.807596	-2.346648	1.522242
H	6.044708	-1.524775	0.553918
H	4.376105	1.866686	0.665999
H	5.641163	1.334503	1.788514
H	5.785101	0.987604	0.073576
H	2.716216	-1.479701	1.233765
H	1.163377	0.385817	1.485152
H	2.381015	1.574395	1.031772

ωB97X Energy = -1186.35477841 a.u.

(*S*)-**3modMe**, Conf H

O	2.569948	0.872451	1.524749
O	-0.138167	-3.408342	0.931704
C	-4.410703	-2.111434	-0.768644
O	-4.716220	0.542492	-0.996448
O	-1.440403	3.672451	0.163165
O	1.664773	-1.626768	1.491220
O	0.855093	2.830707	0.936627
C	-3.474090	0.806813	-0.559067
C	-3.061733	2.106815	-0.415108
C	-1.768876	2.390210	0.027649
C	-0.888513	-2.380196	0.539228
C	-2.183142	-2.666289	0.084526
C	-3.046198	-1.677446	-0.304745
C	-2.623611	-0.304374	-0.237607
C	0.931252	-0.788890	0.964399
C	-0.424933	-1.064723	0.550553
C	-1.304774	-0.002682	0.179699
C	-0.865099	1.353881	0.296302
C	0.489113	1.682756	0.684481
C	5.352982	-1.451865	-1.336181
C	5.080916	1.016866	-0.876702
C	4.407629	-0.310539	-1.081200
C	3.089403	-0.509678	-1.059338
C	2.029660	0.526837	-0.836270
C	1.524265	0.572223	0.647425
H	3.042725	0.042910	1.674918
H	0.712503	-3.050109	1.266864
H	-4.609123	-1.774232	-1.785233
H	-4.476909	-3.198152	-0.738632
H	-5.194588	-1.694694	-0.137191
H	-5.187780	1.363955	-1.171544
H	-0.517126	3.703132	0.508322
H	-3.729490	2.929907	-0.641042
H	-2.490025	-3.704704	0.059712
H	5.955596	-1.256465	-2.228087
H	6.051128	-1.565424	-0.501832
H	4.823807	-2.395114	-1.476036
H	4.385662	1.825962	-0.662498
H	5.785733	0.951207	-0.043037
H	5.665042	1.281822	-1.762952
H	2.729526	-1.523860	-1.218717
H	2.394126	1.531877	-1.052579

H	1.177708	0.338352	-1.494957

ωB97X Energy = -1186.35458962 a.u.

(*S*)-**3modMe**, Conf I

O	-2.567572	0.908656	1.561390
O	1.485232	3.651772	0.153971
C	4.890982	0.552730	-1.117273
O	4.192917	-2.014800	-0.773335
O	0.091713	-3.400772	1.000634
O	-0.824106	2.815952	1.005320
O	-1.672178	-1.619548	1.565271
C	2.969998	-1.706145	-0.311087
C	2.123523	-2.701954	0.104658
C	0.849414	-2.389702	0.581422
C	1.788631	2.362549	0.016044
C	3.072120	2.051352	-0.453881
C	3.491639	0.756573	-0.602433
C	2.601974	-0.319610	-0.256454
C	-0.460122	1.674392	0.714499
C	0.880416	1.342445	0.299503
C	1.291874	-0.021745	0.189296
C	0.398743	-1.063833	0.589550
C	-0.952605	-0.779262	1.028068
C	-5.308479	-1.454769	-1.422765
C	-5.063843	1.021227	-0.990900
C	-4.378356	-0.307123	-1.140526
C	-3.064445	-0.504118	-1.042126
C	-2.015161	0.536344	-0.795914
C	-1.521588	0.587134	0.691583
H	-2.576482	1.874077	1.623920
H	0.577925	3.712702	0.523331
H	5.501605	0.003171	-0.401989
H	4.891395	-0.022652	-2.042447
H	5.354182	1.520368	-1.304873
H	4.323215	-2.968874	-0.753995
H	-0.747005	-3.014329	1.345333
H	2.432563	-3.740547	0.081249
H	3.734645	2.874227	-0.692520
H	-6.047625	-1.555482	-0.622630
H	-5.865524	-1.278138	-2.347710
H	-4.771408	-2.399153	-1.518335
H	-5.614312	1.267164	-1.903785
H	-5.799420	0.969155	-0.183225
H	-4.381290	1.839081	-0.767579
H	-2.695457	-1.520816	-1.160405
H	-1.153716	0.351597	-1.443743
H	-2.379627	1.539457	-1.024197

ωB97X Energy = -1186.35332110 a.u.

(*S*)-**3modEt**, Conf A

O	-3.413904	1.193749	-1.360426
O	-0.363694	-2.771018	-2.146472
C	3.996364	-1.433805	-0.736754
O	4.079645	1.032334	0.302849
O	0.394215	3.893244	0.603441
O	-2.385102	-1.227090	-1.877530
O	-1.907089	3.018694	-0.143083
C	2.768165	1.248757	0.119912
C	2.223107	2.462872	0.455127
C	0.859147	2.690048	0.279711
C	0.342701	-1.794368	-1.581382
C	1.717109	-2.017280	-1.413702
C	2.539754	-1.075461	-0.859489
C	1.984371	0.183465	-0.440586
C	-1.669688	-0.421413	-1.283886
C	-0.236924	-0.599659	-1.149640
C	0.594559	0.412768	-0.581347
C	0.025238	1.670045	-0.201605
C	-1.383957	1.909854	-0.312628
C	-1.942922	-2.657573	1.352720
C	-0.368816	-1.683701	3.100652
C	-1.432349	-1.432417	2.059966
C	-1.837905	-0.189088	1.801802
C	-2.866132	0.239107	0.795161
C	-2.331057	0.750539	-0.580466
C	0.918401	-2.263681	2.512616
H	-3.582266	2.105800	-1.086958
H	-1.294273	-2.454480	-2.223040
H	4.626276	-0.731720	-1.281547
H	4.322227	-1.412989	0.302863
H	4.158555	-2.434279	-1.135483
H	4.496555	1.814594	0.679909
H	-0.568754	3.906415	0.397698
H	2.840703	3.259408	0.853218
H	2.115761	-2.967327	-1.747899
H	-2.863561	-2.479106	0.798332
H	-1.198389	-3.031573	0.642784
H	-2.125581	-3.460744	2.071359
H	-0.143857	-0.748554	3.619427
H	-0.763656	-2.378547	3.850484
H	-1.381405	0.616903	2.372801
H	-3.566949	-0.561172	0.552544
H	-3.449284	1.072221	1.197031
H	1.672643	-2.395936	3.290571
H	0.748055	-3.237178	2.047556
H	1.329633	-1.595080	1.751038

ωB97X Energy = -1225.67227205 a.u.

(*S*)-**3modEt**, Conf B

O	3.397040	1.312234	-1.318431
O	-0.581376	3.861281	0.516824
C	-4.330495	0.920625	0.229704
O	-3.724121	-1.498853	-0.742819
O	0.556781	-2.805816	-2.092366
O	1.770134	3.097281	-0.142991
O	2.491454	-1.130094	-1.835537
C	-2.421666	-1.211071	-0.887810
C	-1.570451	-2.150272	-1.414470

C	-0.215258	-1.860622	-1.562243
C	-0.973110	2.630312	0.199006
C	-2.336395	2.336181	0.348975
C	-2.851148	1.110370	0.027970
C	-1.974034	0.093582	-0.487843
C	1.329333	1.964809	-0.333050
C	-0.084842	1.651370	-0.252280
C	-0.590313	0.365010	-0.611972
C	0.297544	-0.625712	-1.139514
C	1.704333	-0.376027	-1.248349
C	1.947324	-2.516806	1.470610
C	0.356393	-1.516779	3.188374
C	1.417507	-1.279593	2.141663
C	1.807798	-0.038586	1.850752
C	2.839265	0.374642	0.841194
C	2.315972	0.833090	-0.557976
C	-0.932235	-2.107023	2.613931
H	3.793143	0.535071	-1.735846
H	0.386209	3.917770	0.336878
H	-4.831089	0.682039	-0.708018
H	-4.535206	0.100381	0.916876
H	-4.761505	1.834999	0.635142
H	-3.903602	-2.392471	-1.054607
H	1.468687	-2.440795	-2.164971
H	-1.937084	-3.121782	-1.724588
H	-2.980959	3.121124	0.725219
H	1.200311	-2.935525	0.789006
H	2.853276	-2.336740	0.892831
H	2.163761	-3.287936	2.214575
H	0.754513	-2.199351	3.947579
H	0.131334	-0.574304	3.693571
H	1.339620	0.777182	2.398091
H	3.401136	1.233811	1.214934
H	3.558321	-0.422524	0.641662
H	-1.352870	-1.443451	1.853173
H	-0.760773	-3.082082	2.152523
H	-1.679658	-2.238683	3.398503

ωB97X Energy = -1225.67221163 a.u.

(*S*)-**3modEt**, Conf C

O	-3.414253	1.234797	-1.337732
O	-0.420391	-2.786538	-2.121522
C	3.962285	-1.498265	-0.732659
O	4.095992	0.992156	0.239178
O	0.443146	3.891152	0.563981
O	-2.418990	-1.170623	-1.881904
O	-1.868652	3.048168	-0.103114
C	2.783032	1.219098	0.073328
C	2.253167	2.440701	0.400224
C	0.888052	2.680787	0.240498
C	0.304768	-1.817362	-1.566793
C	1.674783	-2.059037	-1.399210
C	2.511650	-1.118947	-0.861074
C	1.978940	0.156074	-0.461335
C	-1.672158	-0.401895	-1.268582
C	-0.253347	-0.611156	-1.139143
C	0.591104	0.403525	-0.592964
C	0.035429	1.670408	-0.228373
C	-1.381556	1.935266	-0.313158
C	-1.924569	-2.609316	1.402997
C	-0.353866	-1.611869	3.140390
C	-1.416524	-1.374621	2.095386
C	-1.825458	-0.135408	1.822929
C	-2.857798	0.277422	0.814188
C	-2.330000	0.776115	-0.568930
C	0.937535	-2.191631	2.561388
H	-3.792316	0.452713	-1.761944
H	-1.342811	-2.458939	-2.212289
H	4.601196	-0.823720	-1.301296
H	4.292591	-1.449451	0.304546
H	4.106609	-2.513206	-1.100416
H	4.525166	1.775100	0.600661
H	-0.527398	3.903162	0.380275
H	2.882200	3.235915	0.782897
H	2.060215	-3.018988	-1.720118
H	-2.121800	-3.398588	2.133135
H	-2.836998	-2.436660	0.833170
H	-1.172543	-3.000264	0.710419
H	-0.134295	-0.671033	3.651067
H	-0.747622	-2.301345	3.895713
H	-1.371964	0.678859	2.384476
H	-3.557563	-0.530646	0.591080
H	-3.441382	1.116367	1.200255
H	0.772629	-3.169401	2.103407
H	1.348947	-1.527329	1.796188
H	1.689494	-2.314787	3.343026

ωB97X Energy = -1225.67208092 a.u.

(*S*)-**3modEt**, Conf D

O	3.383869	1.282984	-1.359859
O	-0.545448	3.860043	0.561266
C	-4.323058	0.953009	0.290133
O	-3.757218	-1.454344	-0.734137
O	0.502264	-2.795368	-2.115535
O	1.797818	3.070370	-0.176931
O	2.456062	-1.184353	-1.835205
C	-2.451145	-1.179520	-0.881041
C	-1.612306	-2.119135	-1.422891
C	-0.253213	-1.843277	-1.574979
C	-0.954874	2.635511	0.239639
C	-2.317621	2.351946	0.403238
C	-2.844850	1.133000	0.072603
C	-1.984647	0.113762	-0.466919
C	1.324074	1.941081	-0.333199
C	-0.082812	1.649386	-0.226883
C	-0.598893	0.370823	-0.601690
C	0.278015	-0.616229	-1.151950
C	1.699095	-0.393113	-1.268282
C	1.980194	-2.556009	1.419605
C	0.396747	-1.575884	3.155934

C	1.452425	-1.326788	2.106635
C	1.837765	-0.082100	1.825318
C	2.857266	0.344882	0.809133
C	2.313272	0.813460	-0.578240
C	-0.891239	-2.166883	2.580819
H	3.530731	2.199711	-1.090781
H	0.415306	3.918729	0.361126
H	-4.740941	1.863386	0.717559
H	-4.837066	0.735818	-0.645524
H	-4.526247	0.121504	0.964059
H	-3.947092	-2.341806	-1.056983
H	1.421518	-2.437929	-2.176149
H	-1.989194	-3.084196	-1.740977
H	-2.952464	3.137104	0.794999
H	2.892927	-2.371603	0.854205
H	2.183305	-3.341338	2.152335
H	1.237171	-2.957051	0.723057
H	0.800123	-2.262800	3.908429
H	0.169685	-0.638139	3.669021
H	1.370812	0.726550	2.384194
H	3.421066	1.199521	1.193144
H	3.575992	-0.444974	0.585568
H	-1.636502	-2.306064	3.366152
H	-1.315813	-1.500192	1.824938
H	-0.717272	-3.138410	2.112940

ωB97X Energy = -1225.67194373 a.u.

(*S*)-**3modEt**, Conf E

O	1.798134	2.598834	-1.307073
O	-2.970080	3.109259	0.445246
C	-4.732704	-1.298800	0.975673
O	-3.036008	-3.231751	0.212110
O	1.185249	-2.439024	-1.646072
O	-0.582438	3.495835	-0.443185
O	1.984645	0.024523	-1.858381
C	-2.076082	-2.364587	-0.146484
C	-0.909882	-2.828237	-0.704185
C	0.089696	-1.932554	-1.080798
C	-2.704180	1.810502	0.322543
C	-3.721637	0.912474	0.680026
C	-3.564391	-0.441882	0.567987
C	-2.323423	-0.966108	0.063822
C	-0.406356	2.280971	-0.416305
C	-1.470585	1.335174	-0.122050
C	-1.281455	-0.071942	-0.279502
C	-0.058296	-0.563171	-0.833851
C	1.011587	0.337708	-1.166886
C	2.450490	-1.228860	1.754383
C	4.833122	-0.440585	1.342059
C	3.361578	-0.104681	1.342243
C	2.950930	1.109944	0.976074
C	1.538045	1.604484	0.910311
C	1.001051	1.727706	-0.557093
C	5.193185	-1.567588	0.373497
H	2.441774	2.041059	-1.766827
H	-2.180700	3.604431	0.128560
H	-4.459408	-1.988182	1.773645
H	-5.545818	-0.662757	1.322890
H	-5.090216	-1.903456	0.142863
H	-2.759397	-4.133638	0.017287
H	1.763578	-1.689263	-1.908043
H	-0.757451	-3.887340	-0.875092
H	-4.653054	1.329102	1.043475
H	2.839613	-1.721666	2.649369
H	1.430795	-0.904872	1.959437
H	2.403257	-1.991206	0.970348
H	5.406563	0.455131	1.091286
H	5.127903	-0.734330	2.356050
H	3.706765	1.834450	0.682923
H	0.858887	0.978335	1.490384
H	1.480813	2.616918	1.319475
H	4.885580	-1.316500	-0.644992
H	6.270921	-1.740483	0.367972
H	4.709420	-2.506922	0.649034

ωB97X Energy = -1225.67133038 a.u.

(*S*)-**3modEt**, Conf F

O	-1.798869	2.591617	-1.309184
O	-1.158652	-2.453739	-1.630333
C	3.132914	-3.432113	0.231131
O	4.529502	-1.246817	0.917546
O	2.955400	3.132635	0.440548
O	-1.968260	0.013067	-1.863412
O	0.566191	3.501141	-0.423437
C	3.543806	-0.404848	0.566402
C	3.726565	0.949408	0.680723
C	2.705105	1.831209	0.322427
C	-0.068999	-1.932189	-1.065627
C	0.944342	-2.820908	-0.682493
C	2.118056	-2.381030	-0.130014
C	2.323182	-0.971284	0.064541
C	-1.005373	0.334277	-1.166330
C	0.071167	-0.566481	-0.825813
C	1.289166	-0.066003	-0.274540
C	1.468773	1.344992	-0.120735
C	0.403358	2.281542	-0.407436
C	-2.469838	-1.241276	1.736248
C	-4.849261	-0.446507	1.317827
C	-3.376999	-0.113903	1.324254
C	-2.962107	1.101334	0.964661
C	-1.547853	1.592988	0.907889
C	-1.002523	1.722286	-0.555930
C	-5.208349	-1.571167	0.346219
H	-2.445402	2.035233	-1.765967
H	-1.743489	-1.714802	-1.902988
H	2.731198	-4.418491	0.003611
H	4.061636	-3.293987	-0.321179
H	3.384508	-3.390731	1.290291
H	5.292799	-0.750879	1.232726
H	2.153632	3.614770	0.128957

H	4.663848	1.356198	1.041856
H	0.779326	-3.877690	-0.852774
H	-1.449466	-0.920662	1.943283
H	-2.861627	-1.733935	2.630137
H	-2.423807	-2.003068	0.951634
H	-5.148371	-0.741205	2.330268
H	-5.419678	0.450969	1.066491
H	-3.715195	1.828784	0.671741
H	-1.490174	2.603598	1.321295
H	-0.872308	0.963516	1.488579
H	-6.286538	-1.740914	0.335759
H	-4.895620	-1.319641	-0.670598
H	-4.728562	-2.512266	0.622629

ωB97X Energy = -1225.67116454 a.u.

(*S*)-**3modEt**, Conf G

O	2.170828	-1.432357	1.599922
O	-2.129596	-3.572014	-0.091800
C	-5.109454	-0.010218	-1.208352
O	-4.119932	2.424491	-0.670650
O	0.077581	3.192003	1.247330
O	0.222506	-3.102811	0.841006
O	1.599323	1.152562	1.726746
C	-2.952975	1.942584	-0.214152
C	-2.004327	2.803963	0.278352
C	-0.789223	2.310902	0.752441
C	-2.270142	-2.249180	-0.145089
C	-3.494910	-1.754807	-0.618594
C	-3.756917	-0.413690	-0.685357
C	-2.754676	0.520802	-0.248748
C	0.030439	-1.904768	0.650579
C	-1.254414	-1.369860	0.231154
C	-1.502258	0.036480	0.199239
C	-0.504158	0.941772	0.679525
C	0.779123	0.461433	1.114931
C	4.756563	-1.598023	-0.706405
C	5.267811	0.842802	-1.057638
C	4.199893	-0.212126	-0.882918
C	2.900337	0.083827	-0.895139
C	1.757854	-0.875308	-0.745560
C	1.202115	-0.943212	0.719086
C	4.798857	2.274885	-1.262800
H	2.709065	-0.670549	1.854749
H	-1.241247	-3.759899	0.288415
H	-5.672832	-0.901283	-1.482123
H	-5.674196	0.546464	-0.461319
H	-5.020872	0.632309	-2.083507
H	-4.138036	3.384102	-0.588935
H	0.855805	2.691733	1.580403
H	-2.188307	3.871092	0.318239
H	-4.241604	-2.476459	-0.926532
H	3.990912	-2.353060	-0.541216
H	5.344381	-1.882934	-1.583970
H	5.436537	-1.619927	0.149883
H	5.925595	0.796240	-0.181856
H	5.898133	0.539691	-1.901950
H	2.611582	1.122702	-1.025807
H	0.945413	-0.588301	-1.418431
H	2.043502	-1.898010	-0.995401
H	5.657359	2.939843	-1.370922
H	4.187336	2.372094	-2.162746
H	4.208566	2.629621	-0.414743

ωB97X Energy = -1225.67053394 a.u.

(*S*)-**3modEt**, Conf H

O	-2.176566	-1.412271	1.593587
O	-0.028919	3.197915	1.232414
C	4.293214	2.560470	-0.700838
O	4.910024	-0.013949	-1.129400
O	2.087137	-3.597531	-0.097563
O	-1.572598	1.169042	1.729161
O	-0.260207	-3.102165	0.805947
C	3.727791	-0.459342	-0.673531
C	3.481726	-1.807030	-0.612862
C	2.252327	-2.278350	-0.149160
C	0.823177	2.299910	0.740420
C	2.052865	2.775163	0.263970
C	3.012382	1.929455	-0.224695
C	2.762644	0.513326	-0.244572
C	-0.768923	0.469036	1.111428
C	0.524060	0.939449	0.671434
C	1.509159	0.022512	0.193812
C	1.242340	-1.382729	0.225766
C	-0.045496	-1.902730	0.631356
C	-4.766555	-1.571315	-0.692417
C	-5.285925	0.870082	-1.026889
C	-4.214361	-0.183058	-0.864585
C	-2.915420	0.115827	-0.884326
C	-1.770445	-0.842949	-0.750607
C	-1.207405	-0.927772	0.710263
C	-4.822047	2.303815	-1.231822
H	-2.724025	-0.653022	1.835159
H	-0.813248	2.715412	1.572746
H	4.228359	3.641831	-0.588694
H	5.149210	2.198831	-0.132374
H	4.484989	2.326288	-1.747329
H	5.471697	-0.757058	-1.374319
H	1.188617	-3.765545	0.272957
H	4.233422	-2.524532	-0.920443
H	2.230813	3.842730	0.306209
H	-5.360274	-1.852105	-1.567312
H	-3.998052	-2.325624	-0.537505
H	-5.440072	-1.599941	0.168765
H	-5.922296	0.567892	-1.866957
H	-5.936479	0.819291	-0.145967
H	-2.629992	1.156090	-1.011242
H	-2.055927	-1.863151	-1.010485
H	-0.961279	-0.547950	-1.423904
H	-5.683050	2.966722	-1.332334
H	-4.226806	2.658245	-0.387130

H	-4.217232	2.404651	-2.135887

ωB97X Energy = -1225.67039109 a.u.

(*S*)-**3modEt**, Conf I

O	-3.469324	1.199850	-1.296566
O	-0.390209	-2.794051	-2.114207
C	3.982399	-1.489582	-0.715237
O	4.099545	0.992804	0.275314
O	0.441402	3.886629	0.576104
O	-2.387971	-1.218883	-1.876805
O	-1.858100	3.044978	-0.123004
C	2.787687	1.218829	0.097981
C	2.254232	2.438956	0.424449
C	0.890329	2.677106	0.254204
C	0.326824	-1.818670	-1.559958
C	1.697997	-2.055549	-1.388099
C	2.530529	-1.114883	-0.846783
C	1.990180	0.156761	-0.447631
C	-1.667985	-0.419031	-1.279030
C	-0.239278	-0.612408	-1.141667
C	0.601736	0.400307	-0.588207
C	0.042944	1.665533	-0.222305
C	-1.371915	1.928374	-0.320078
C	-1.964774	-2.610468	1.384969
C	-0.397228	-1.613907	3.125516
C	-1.454690	-1.375613	2.075625
C	-1.854600	-0.135303	1.795643
C	-2.878680	0.277894	0.779061
C	-2.333097	0.771425	-0.591036
C	0.892285	-2.203113	2.551741
H	-3.210301	1.514121	-2.168510
H	-1.316084	-2.465694	-2.198237
H	4.132034	-2.499953	-1.093507
H	4.621965	-0.806717	-1.273009
H	4.307519	-1.451858	0.324107
H	4.523995	1.775093	0.643620
H	-0.527015	3.897840	0.381114
H	2.879061	3.233699	0.814941
H	2.085999	-3.014954	-1.707841
H	-2.881480	-2.438516	0.822105
H	-1.216767	-2.997618	0.685864
H	-2.154304	-3.401491	2.115189
H	-0.173926	-0.672162	3.632910
H	-0.796895	-2.298229	3.882386
H	-1.399333	0.678671	2.356102
H	-3.576160	-0.527350	0.543579
H	-3.463882	1.118068	1.160230
H	1.308288	-1.544941	1.783701
H	1.642288	-2.326281	3.335251
H	0.722890	-3.182279	2.098368

ωB97X Energy = -1225.66933566 a.u.

6. General Discussion

6.1 Fungal secondary metabolites in anti-infective research

Antimicrobial resistance has become one of the major global public health challenges. The long-term and widespread use of conventional antibiotics has promoted the emergence and dissemination of resistant bacterial strains, whereas the development of new antibacterial agents has not kept pace with the increasing rate of resistance. This is particularly critical for clinically important pathogens such as *S. aureus*. The emergence of MRSA, VISA, and VRSA has introduced greater uncertainty and a higher risk of treatment failure in conventional anti-infective therapy [8]. Against this background, natural products remain an important source for the discovery of novel anti-infective lead compounds. Compared with conventional synthetic small molecules, natural products often possess more complex scaffolds, diverse stereochemical features, and unique combinations of functional groups. Consequently, they can cover broader chemical space and provide a basis for identifying antibacterial molecules, antibiofilm agents, and antibiotic adjuvants with new mechanisms of action [140].

Fungi represent an extremely important but still underexplored resource in natural product research. Many fungal genomes contain numerous biosynthetic gene clusters (BGCs), but these gene clusters are often silent or expressed only at low levels under standard laboratory culture conditions. Therefore, the activation of cryptic metabolic pathways through approaches such as the OSMAC strategy, microbial co-culture, epigenetic regulation, genome mining, and metabolomics-guided isolation has become an important direction for the discovery of new fungal natural products [128]. The two main projects of this thesis were developed within this framework. The first part investigated pestalotic acid derivatives produced by the endophytic fungus *Pestalotiopsis chamaeropis* using the OSMAC strategy and elucidates the antibacterial activity and mode of action of pestalotic acid A against VISA. The second part describes the discovery of fusapurpurins A and B from the co-culture of *Fusarium oxysporum* and *Paenibacillus ehimensis*, and explores their antibiofilm activity and possible biosynthetic pathway. Together, these two projects demonstrate the potential value of fungal secondary metabolites in anti-infective research from two complementary perspectives: the inhibition of resistant bacteria and mechanistic investigation, and the disruption of mature biofilms together with biosynthetic hypothesis generation.

6.2 OSMAC and co-culture strategies for activating fungal cryptic metabolism

In Project 1, induction of *P. chamaeropis* using the OSMAC strategy led to the production of a series of pestalotic acid-related natural products. Among them, pestalotic acid H and pestaloside A were identified as new natural products, and the absolute configuration of pestalotic acid C was determined by single-crystal X-ray diffraction. During the application of the OSMAC approach, we found that the addition of sodium iodide to the culture medium promoted the production of secondary metabolites, but no halogenated compounds were detected. This indicates that, in this system, sodium iodide may act as a metabolic inducing factor rather than directly serving as a halogen donor involved in compound structure formation. This result also suggests that changes in OSMAC conditions are not necessarily reflected by direct modifications of structural elements. Instead, they may influence fungal metabolic regulatory networks and alter the expression levels of specific BGCs, thereby inducing the production of metabolites that are otherwise difficult to detect.

In contrast to the OSMAC strategy based on changes in medium composition used in Project 1, Project 2 employed a microbial co-culture strategy. *F. oxysporum* showed markedly different metabolic responses when co-cultured with different bacteria. In particular, co-culture with *P. ehimensis* induced the production of darker purple metabolites, from which the new compounds fusachinon, fusapurpurin A, and fusapurpurin B were isolated. Compared with simply altering medium composition, co-culture more closely resembles the competition, antagonism, and chemical communication between fungi and other microorganisms in natural environments. Therefore, it is more likely to activate metabolic pathways that remain silent under monoculture conditions [134]. In this study, fusapurpurins A and B, as new fusarubin derivatives with complex bridged structures, demonstrate the value of co-culture strategies in inducing natural products with unusual structural features.

These two projects demonstrate that fungal secondary metabolism is not a constant and constitutive process, but is highly dependent on external environmental conditions and ecological interactions. OSMAC and co-culture are therefore not only screening tools for expanding chemical diversity, but also important experimental strategies for understanding fungal metabolic regulation, discovering ecologically relevant bioactive molecules, and exploring the functions of cryptic BGCs.

6.3 Selective antibacterial activity of PAA against VISA and its significance

In Project 1, PAA and pestalotic acid G showed the strongest antibacterial activity, particularly against VISA, with relatively low MIC_{90} values. At higher concentrations, they also exhibited certain activity against other Gram-positive bacteria, including MSSA and MRSA. In addition, their low cytotoxicity and good hemocompatibility make them worthy of further investigation with regard to their mode of action. The development of VISA is usually accompanied by adaptive changes such as cell wall thickening, cell envelope stress regulation, altered surface charge, and remodeling of cell wall metabolism [61]. The research value of PAA lies not only in its antibacterial activity, but also in its degree of selective sensitivity toward VISA. The stronger inhibitory effect of PAA against VISA may exploit or interfere with the specific cell envelope-adaptive state of VISA.

Reduced vancomycin susceptibility in VISA is not determined by a single resistance gene, but usually involves multilayered cell envelope remodeling and changes in regulatory networks [141, 142]. Therefore, if a natural product shows stronger activity against VISA than against MSSA or conventional MRSA, it may act on certain "fitness-cost-associated vulnerabilities" that VISA develops during adaptation to vancomycin pressure. From this perspective, PAA is not only an anti-VISA active compound, but may also serve as a chemical probe for studying cell envelope homeostasis and stress adaptation mechanisms in VISA.

6.4 Mode of action of PAA

Growth curve and time-kill kinetics analyses showed that PAA markedly inhibited the growth of VISA, but its overall effect was more consistent with bacteriostatic activity. Membrane potential and PI uptake assays further showed that the effect of PAA on the cell membrane was concentration-dependent. At high concentrations, it caused a decrease in membrane potential and an increase in membrane permeability, whereas at concentrations close to the MIC, it did not induce rapid or strong membrane disruption.

These results indicate that PAA may have a concentration-dependent dual mode of action. VISA typically reduces its susceptibility to vancomycin through cell wall thickening, cell envelope stress regulation, surface charge modification, and remodeling of regulatory systems such as GraRS and VraSR [141]. Therefore, the stronger sensitivity of VISA to PAA at low concentrations may reflect interference with the cell envelope homeostasis required to maintain the vancomycin-intermediate phenotype.

The MIC of PAA against most other Gram-positive bacteria, including MSSA and MRSA, was approximately 25 μM, and the MIC values of the PAA susceptibility-reduced mutants derived from VISA increased only to 25 μM and did not rise further. This phenomenon suggests that 25 μM may represent a more general activity threshold for PAA. At this concentration, PAA may inhibit the growth of Gram-positive bacteria through broader cell envelope- or membrane-associated effects. This interpretation is also consistent with the membrane potential and PI uptake assays, which showed that PAA could induce membrane depolarization and increased membrane permeability at higher concentrations. Therefore, high concentrations of PAA may exert a more general membrane perturbation or cell envelope-damaging effect, which could explain its inhibitory activity at approximately 25 μM against multiple Gram-positive bacteria as well as PAA-resistant VISA mutants.

This model may also explain why mutants obtained through continuous liquid pressure selection showed only an increase in the PAA MIC from 6.25 μM to 25 μM, rather than developing higher-level resistance. The mutations may weaken or remodel the VISA-specific envelope regulatory state on which the low-concentration activity of PAA depends, thereby allowing the mutants to escape the selective effect of PAA at low concentrations. However, when the PAA concentration reaches 25 μM, its broader membrane-associated or cell envelope-damaging activity can still inhibit mutant growth. Therefore, the mutants derived from VISA are more appropriately described as exhibiting reduced PAA susceptibility rather than highly resistant. This phenomenon also suggests that the mutation-associated changes may affect the low-concentration selective activity window of PAA, rather than completely abolishing all antibacterial effects of PAA.

6.5 GraRS-associated cell envelope homeostasis in the activity of PAA

In this study, all PAA susceptibility-reduced mutants obtained through continuous liquid pressure selection carried disruptive mutations in *graR*. GraRS is an important two-component regulatory system in *S. aureus*, consisting of the histidine kinase GraS and the response regulator GraR. It is involved in resistance to cationic antimicrobial peptides, regulation of cell surface charge, and cell envelope stress defense. GraRS regulates the expression of genes such as the *dlt* operon, *mprF/fmtC*, and *vraFG*, thereby affecting D-alanylation of cell wall teichoic acids, lysinylation of membrane phospholipids, and resistance to cell envelope-associated antimicrobial stress [66].

The regulatory state of GraRS in VISA differs from that in conventional VSSA. Previous studies have shown that the development of VISA/hVISA is not mediated by a single exogenous resistance gene, but is associated with cumulative mutations and abnormal activation of multiple cell envelope regulatory systems, including the two-component systems VraSR, GraSR, and WalKR [60]. In studies related to Mu50, mutations in *graR* have been shown to participate in the phenotypic conversion from hVISA to VISA. Introduction of Mu50-derived *vraS* and *graR* mutations into a vancomycin-susceptible background progressively increased the level of vancomycin resistance, indicating that GraRS in the Mu50/VISA background is not merely a basal surface charge regulatory system, but an important component of the VISA cell envelope adaptation network [67, 143].

In this study, the presence of disruptive mutations in *graR* in all independent mutants suggests that the anti-VISA activity of PAA may be associated with a VISA-specific GraRS-dependent envelope-adaptive state. PAA may interfere with the cell envelope defense network required by VISA to maintain the vancomycin-intermediate phenotype, whereas disruptive mutations in *graR* may remodel or weaken this regulatory state, allowing the bacteria to escape the low-concentration selective activity of PAA.

This inference is supported by multiple experimental findings. Mu2 showed reduced susceptibility to PAA, but at the same time displayed markedly increased susceptibility to vancomycin, daptomycin, polymyxin B, and colistin. Vancomycin mainly binds to the terminal D-Ala-D-Ala motif of the cell wall precursor lipid II, thereby blocking peptidoglycan synthesis and cell wall construction [144]. Daptomycin is a Ca^{2+}-dependent cyclic lipopeptide antibiotic that inserts into the membrane of Gram-positive bacteria and induces membrane depolarization and disruption of ion homeostasis [145]. Polymyxin B and colistin are cationic membrane-active antibiotics. Although they are mainly used against Gram-negative bacteria, their interactions with bacterial surface negative charge and membrane structures make them useful functional probes for reflecting cell surface charge and susceptibility to cationic antimicrobial molecules [146]. The increased susceptibility of Mu2 to these cell envelope-associated antibiotics indicates that disruptive mutations in *graR* reduce susceptibility to PAA, but simultaneously weaken cell envelope defense capacity. These results suggest that loss of GraRS function does not represent high-level resistance in the strict sense, but rather a reduced susceptibility phenotype achieved at the cost of impaired cell envelope defense.

PAA showed synergistic interactions with vancomycin, polymyxin B, and colistin. This result further supports, at the level of drug interactions, that its activity is closely associated with cell envelope homeostasis. The synergy between PAA and vancomycin suggests that PAA may weaken the adaptive defense of VISA against cell wall-targeting antibiotics, thereby allowing vancomycin to exert its inhibitory activity more effectively. The synergy between PAA and polymyxin B or colistin suggests that PAA may affect cell surface charge regulation or resistance to cationic antimicrobial molecules. Together with the increased susceptibility of the *graR* mutant to these antibiotics, these findings suggest that PAA interferes with the GraRS-associated regulatory network used by VISA to maintain cell envelope stability and tolerance to cationic antimicrobial stress.

The cytochrome c binding assay and RT-qPCR results also support a link between PAA and cell surface charge regulation. Cytochrome c is a positively charged protein that can bind to negatively charged structures on the bacterial surface; therefore, this assay is commonly used to indirectly reflect the net surface charge status of *S. aureus*. In general, increased cytochrome c binding indicates enhanced surface negative charge or reduced positive charge modification [147]. In this study, PAA treatment increased cytochrome c binding in VISA, while Mu2 also showed a higher level of cytochrome c binding under untreated conditions, indicating reduced positive charge modification or increased net negative surface charge.

This phenotype is consistent with changes in the expression of downstream GraRS-regulated cell envelope genes. *mprF/fmtC* encodes phosphatidylglycerol lysyltransferase, which increases the positive charge of the cell membrane by adding lysine to phosphatidylglycerol, thereby reducing the interaction between cationic antimicrobial molecules and the cell membrane. The *dlt* operon participates in D-alanylation of teichoic acids, which similarly reduces the overall negative charge of the cell wall and enhances resistance to cationic antimicrobial peptides [148, 149]. The GraRS/GraXRS–VraFG system regulates genes such as *mprF/fmtC*, the *dlt* operon, and *vraFG*, and participates in the sensing of and resistance to cationic antimicrobial peptides and cell envelope stress in *S. aureus* [66].

In this study, short-term high-concentration treatment with PAA led to downregulation of *fmtC/mprF*, *dltA*, and *vraG*, while Mu2 itself also exhibited a low-expression state of these genes. The cytochrome c binding and RT-qPCR results together indicate that both the activity of PAA and the reduced

susceptibility phenotype of Mu2 are accompanied by changes in the downstream GraRS-regulated cell envelope state.

Taken together, these results suggest that the mode of action of PAA can be understood as interference with GraRS-associated cell envelope homeostasis in VISA. The *graR* mutations indicate that PAA may force VISA to make a trade-off between reducing susceptibility to PAA and maintaining cell envelope stress resistance. This trade-off is important for anti-infective research, as it suggests that PAA and its derivatives may serve not only as direct antibacterial agents, but also as synergistic agents that weaken VISA cell envelope defenses and enhance the efficacy of existing antibiotics.

6.6 Possible significance of *cysK* mutations and current limitations

In addition to *graR*, all three mutants with reduced PAA susceptibility carried mutations in *cysK*. CysK is a key enzyme in the cysteine biosynthetic pathway and may be linked to sulfur metabolism, redox balance, and cellular stress adaptation [150]. The recurrent occurrence of *cysK* mutations suggests that alterations in sulfur metabolism or cysteine metabolism may be part of the bacterial adaptation process under sustained PAA pressure. However, the current evidence is insufficient to demonstrate that *cysK* is a direct determinant of reduced susceptibility to PAA. The sequencing results only show that *cysK* mutations co-occurred with the reduced-susceptibility phenotype, but they cannot distinguish whether these mutations are driver mutations, accompanying mutations, or secondary mutations that improve fitness under specific selective pressure.

Complementation of *cysK* alone failed to restore the sensitivity of Mu2 to PAA, indicating that the *cysK* mutation may not be the major factor independently determining this phenotype. The *cysK* mutation emerged during continuous liquid pressure selection, a process involving prolonged drug exposure and gradually increasing selective pressure. Therefore, changes in *cysK* more likely reflect adaptive mutations that help bacteria maintain growth and metabolic balance under long-term PAA pressure, rather than directly participating in the initial mode of action of PAA. *cysK* may be associated with metabolic remodeling, sulfur metabolism, or redox balance adjustment during the development of tolerance.

Therefore, at the current stage, *cysK* is more appropriately considered a candidate factor that may participate in long-term stress adaptation. In the future, construction of an individual *cysK* mutant,

measurement of total thiol levels, oxidative stress susceptibility assays, and cysteine supplementation experiments could be used to evaluate whether *cysK* participates in metabolic adaptation under PAA pressure, and whether this adaptation indirectly affects cell envelope homeostasis or PAA susceptibility.

6.7 Complementation limitations and GraRS regulatory complexity

In this study, the *graR* complementation strain not only failed to restore sensitivity to PAA, but also failed to restore tolerance to vancomycin and polymyxin B. This result may indicate that the mutants obtained through long-term PAA pressure selection did not undergo only a single loss of *graR* function, but had instead developed a global cell envelope-remodeled state. The formation of VISA or VISA-like phenotypes usually involves coordinated changes in multiple cell envelope regulatory systems, cell wall metabolism, autolytic activity, surface charge, and stress responses, rather than being determined independently by a single gene [141, 151]. In this study, Mu2 simultaneously showed reduced susceptibility to PAA, increased susceptibility to multiple cell envelope-associated antibiotics, increased cytochrome c binding, and low expression of *fmtC/mprF*, *dltA*, and *vraG*, indicating that its cell surface charge and envelope defense state had clearly deviated from that of the VISA strain.

GraRS itself is also part of a broader cell envelope regulatory network. GraRS/GraXRS, together with VraFG, participates in the sensing of and resistance to cationic antimicrobial peptides and cell envelope stress in *S. aureus* [66, 152]. Therefore, expression of *graR* alone from a plasmid may not be sufficient to restore native GraRS signaling, GraX/VraFG cooperation, or the overall balance of downstream envelope modification systems. If the PAA-selected mutants have already formed a stable envelope-remodeled state, complementation with *graR* may provide only a single regulatory component, but may not reconstruct the original cell envelope network state present in VISA.

In addition, plasmid-based complementation may be affected by expression dosage, promoter strength, copy number, antibiotic selection pressure, and growth burden. The output of two-component systems usually depends on an appropriate ratio between the response regulator and sensor kinase, signal input, and the native chromosomal regulatory context. For systems such as GraRS, which are closely coupled to VraFG, surface charge modification, and cell wall stress responses, excessive or non-physiological expression of *graR* may fail to produce the same regulatory outcome as native chromosomal expression.

The plasmid itself may affect bacterial growth, antibiotic susceptibility, and cell envelope status, especially in the VISA background, where cell envelope regulation is already highly adapted. If promoter strength, RBS efficiency, copy number, or antibiotic selection pressure in the complementation system is inappropriate, GraR expression may become too high or too low, or may become imbalanced relative to GraS/GraX/VraFG, thereby failing to restore the wild-type regulatory network. Therefore, more ideal validation strategies in the future may include chromosomal in situ repair of the *graR* mutation, construction of a clean-background *graR* single mutant, or use of a controllable expression system to express GraR/GraRS components at near-physiological levels.

6.8 Proteomic evidence for PAA-induced cell envelope remodeling in VISA

The proteomic results also support the effect of PAA on VISA cell envelope homeostasis and stress adaptation. After treatment with 0.5 × MIC PAA for 24 h, the protein expression profile of VISA was markedly altered. These proteomic data reflect the steady-state changes that occurred after cellular adaptation under low-dose, long-term drug pressure, representing an adaptive remodeling state formed by VISA during sustained PAA exposure.

After PAA treatment, several proteins associated with cell wall metabolism, peptidoglycan hydrolysis, and cell envelope remodeling were upregulated, including SceD, IsaA, LytM, LtaS, VraG, and several autolysin- or cell wall hydrolase-related proteins. SceD and IsaA have been reported as putative lytic transglycosylases in *S. aureus* and are associated with cell wall metabolism, cell separation, and colonization ability [153]. LytM is a glycyl-glycine endopeptidase in *S. aureus* that cleaves glycine-glycine bonds in the peptidoglycan cross-bridge and participates in cell wall degradation and cell separation [154]. LtaS is involved in lipoteichoic acid biosynthesis, and lipoteichoic acid is an important anionic polymer in the Gram-positive cell envelope that is closely associated with cell wall integrity, cell division, and tolerance to antimicrobial stress [155]. VraG is the permease component of the VraFG ABC transporter and, together with GraXRS, participates in the sensing of and resistance to cationic antimicrobial peptides and cell envelope stress in *S. aureus* [66]. The upregulation of these proteins suggests that, under long-term stimulation with low-dose PAA, VISA may activate processes related to cell wall turnover, teichoic acid metabolism, and cell envelope structural remodeling.

Proteins associated with the methicillin resistance module, including MecA, MecI, and MecR1, were also upregulated. MecA encodes the low-affinity penicillin-binding protein PBP2a, which is the core determinant of MRSA resistance to β-lactam antibiotics. MecI and MecR1 function as a repressor and signal transducer, respectively, in the regulation of *mecA* expression [156, 157]. The upregulation of these proteins may reflect that VISA senses cell wall- or cell envelope-associated stress under PAA pressure, thereby activating adaptive modules related to cell wall defense. After low-dose long-term PAA treatment, cells may maintain growth by enhancing certain cell wall synthesis and stress resistance modules.

At the same time, molecular chaperones or protein quality control-related proteins, including ClpB, ClpP, DnaK, and GroES, were upregulated, indicating that PAA treatment may also induce proteostasis stress. The DnaK heat shock system is an important protein folding and stress adaptation system in *S. aureus*, helping cells cope with misfolded or aggregated proteins under heat shock, oxidative stress, and other environmental stresses [158]. The ClpP protease system participates in protein quality control, stress tolerance, and virulence regulation, whereas ClpB is commonly associated with the disaggregation of protein aggregates and stress recovery [159, 160]. The GroES/GroEL chaperonin system is also involved in protein folding and cellular stress adaptation [161]. The upregulation of these proteins indicates that long-term PAA pressure affects not only the cell envelope, but may also induce proteostasis stress and broader stress responses.

The upregulated proteins also included SdrD, SdrE, SraP, Fib, SsaA1/SsaA2, HlgA/HlgB/HlgC, leukocidin-like proteins, IsdE/IsdF, and multiple phage-related proteins, indicating that surface proteins, adhesins, virulence-associated proteins, and iron/heme acquisition systems in VISA were also rearranged after PAA treatment. SdrD and SdrE belong to the serine-aspartate repeat-containing protein family and are members of the *S. aureus* surface-anchored protein family, which are associated with adhesion, immune evasion, and host interaction [162]. SraP is a serine-rich adhesin that mediates the adhesion of *S. aureus* to host cells or platelets [163]. Fib is a fibrinogen-binding protein and belongs to the surface factors involved in interactions between *S. aureus* and the host coagulation system and tissue adhesion [162]. IsdE and IsdF are components of the Isd heme uptake system and participate in iron acquisition from host heme [164, 165]. HlgA/HlgB/HlgC and leukocidin-like proteins belong to bicomponent pore-forming toxins and are associated with *S. aureus* virulence and host cell damage [166].

These changes indicate that bacterial surface structures, host interaction-related proteins, and nutrient acquisition strategies were rearranged after long-term PAA treatment, but these changes most likely represent phenotypic adaptation under sustained stress.

The downregulated proteins are also important. After PAA treatment, multiple proteins related to capsular polysaccharide synthesis were markedly decreased, including CapE, CapI, CapG, CapN, CapD, CapM, CapJ, and CapK. The *S. aureus* capsular polysaccharide is an important surface polysaccharide structure, among which type 5 and type 8 capsules are the most common, and are associated with immune evasion, resistance to phagocytosis, and cell surface properties [167]. Cap5/Cap8 biosynthetic enzymes jointly participate in UDP-sugar precursor synthesis, glycosyl transfer, repeat unit formation, and capsule polymer export. For example, CapE/CapF/CapG are associated with UDP-FucNAc precursor synthesis, whereas CapI, CapJ, CapK, CapM, and CapN participate in capsule repeat unit assembly or transport [167, 168]. Therefore, the overall downregulation of capsule-associated proteins suggests that long-term PAA treatment may weaken or remodel the surface polysaccharide structure of VISA, which is consistent with the altered surface properties observed in the cytochrome c binding assay.

IcaA, IcaB, and IcaC were also among the downregulated proteins. IcaA, IcaB, and IcaC are encoded by the *icaADBC* operon and participate in the synthesis, deacetylation, modification, and transport of polysaccharide intercellular adhesin/poly-*N*-acetylglucosamine (PIA/PNAG). Among them, IcaA is an *N*-acetylglucosaminyltransferase, IcaB participates in PNAG deacetylation, and IcaC is associated with PNAG chain elongation/export [169, 170]. PIA/PNAG is an important component of the *S. aureus* biofilm matrix and contributes to intercellular adhesion, biofilm structural stability, and immune evasion [171]. Therefore, the PAA-induced downregulation of Ica-related proteins suggests that PAA may weaken the intercellular aggregation capacity and biofilm matrix formation ability of VISA.

The downregulated proteins also included VraX, AgrB, TagG, CstR, and several proteins associated with nitrate metabolism, biotin metabolism, and transport. VraX is a protein associated with the cell wall stress stimulon and is often linked to stress responses induced by vancomycin or other cell wall-acting antibiotics [65]. AgrB is a membrane component of the accessory gene regulator system and participates in the processing and secretion of the autoinducing peptide, making it an important component of the *agr* quorum-sensing system [172]. TagG is associated with wall teichoic acid transport, and teichoic

acids are important components of *S. aureus* cell wall surface charge and cell envelope function [173]. CstR is a cysteine persulfide-sensing transcriptional repressor involved in sulfur metabolism and the reactive sulfur species stress response [174]. These protein changes indicate that long-term PAA pressure is also accompanied by rearrangement of quorum sensing, wall teichoic acid transport, cell wall stress responses, and sulfur metabolism regulation.

In summary, the proteomic stress profiling following low-dose long-term PAA treatment revealed a pattern of "cell envelope remodeling + stress adaptation + surface structure adjustment". These findings are consistent with the mechanistic model proposed above: at low concentrations, PAA interferes with the cell envelope homeostasis on which VISA depends, forcing cells to remodel the cell wall, surface structures, and stress response networks under long-term pressure. The proteomic data indicate that the effect of PAA on VISA is not a single-target alteration, but rather induces an adaptive network rearrangement centered on the cell envelope. This network-level perturbation may be a key reason why VISA shows selective hypersensitivity to PAA and why PAA can influence antibiotic susceptibility and biofilm formation.

There is one apparently contradictory point in the results: VraG showed opposite trends in the proteomic and RT-qPCR analyses. In the proteomic results under low-dose long-term PAA treatment, VraG expression was upregulated. In contrast, under high-dose short-term PAA treatment, RT-qPCR showed downregulation of *vraG* transcription, and Mu2 also exhibited a low-expression pattern of *vraG* under untreated conditions. This difference may reflect the time- and dose-dependent nature of the cell envelope response induced by PAA. Under long-term treatment with low-dose PAA, upregulation of VraG at the protein level may represent a compensatory adaptive response of VISA to sustained mild envelope stress, in which cells enhance the VraFG/GraRS-associated defense module to maintain cell envelope homeostasis. In contrast, under short-term high-dose treatment, PAA may rapidly disrupt the GraRS-associated regulatory state, leading to inhibition of *vraG* transcription or failure to effectively activate it. Thus, VraG upregulation in the proteomic data is more likely an adaptive outcome formed under long-term subinhibitory pressure, whereas *vraG* downregulation in the qPCR results more likely reflects an early inhibitory effect under high-intensity PAA challenge.

6.9 Inhibition of VISA biofilm formation by PAA

In the proteomic results, several proteins associated with biofilm matrix synthesis and intercellular adhesion were downregulated after PAA treatment. Based on this proteomic clue, this study examined the effect of PAA on VISA biofilm formation. The results showed that PAA clearly inhibited VISA biofilm formation at sub-MIC concentrations, thereby validating the functional changes suggested by the proteomic data.

This result indicates that the activity of PAA is not limited to the inhibition of planktonic growth in VISA, but also weakens its ability to establish early biofilms. Biofilm formation is an important basis for chronic and recurrent *S. aureus* infections. It can enhance bacterial tolerance to antibiotics, host immune responses, and environmental stresses, and is closely associated with medical device-related infections [175]. Therefore, the biofilm formation-inhibitory activity of PAA increases its research value as an anti-infective natural product lead compound. Particularly in VISA strains, which already possess cell envelope adaptation and reduced antibiotic susceptibility, simultaneous weakening of bacterial growth and biofilm formation may help reduce the risk of infection establishment, persistence, and recurrence.

6.10 Fusapurpurins as mature biofilm-disrupting molecules

In contrast to PAA in Project 1, which mainly exhibited anti-VISA activity and inhibition of biofilm formation, fusapurpurins A and B in Project 2 were more prominently characterized by their ability to disrupt mature biofilms. In this project, co-culture of *F. oxysporum* with *P. ehimensis* led to the isolation of one new anthraquinone and two new naphthoquinone derivatives, among which fusapurpurins A and B were structurally unique bridged fusarubin derivatives. Their structures were confirmed by NMR and single-crystal X-ray diffraction, and they were shown to be racemates.

The activity results showed that fusapurpurins A and B exhibited clear disruptive activity against preformed biofilms of *S. aureus* Mu50 and *Pseudomonas aeruginosa* PAO1, with IC_{90} values of 6.25 μM against Mu50 and 12.5 μM against PAO1. Fusapurpurin B also showed moderate disruptive activity against mature biofilms of *Mycobacterium tuberculosis* H37Rv. However, these compounds displayed relatively weak direct antibacterial activity against planktonic cells.

Mature biofilms differ markedly from planktonic cells in cellular metabolic state, matrix composition, redox environment, local pH, nutrient availability, and cell-cell interactions. A compound that disrupts mature biofilms without significantly inhibiting planktonic growth or early biofilm formation may preferentially act on mature biofilm architecture, extracellular matrix stability, or the specific physiological state of biofilm-embedded cells. In biofilm-associated infections, the extracellular polymeric matrix and low metabolic activity often restrict antibiotic penetration and increase bacterial tolerance. Therefore, natural products capable of disrupting mature biofilm structures have potential value as adjunctive therapeutic agents [176].

6.11 PAA and fusapurpurins represent two distinct antibiofilm modes

Both main projects of this thesis involve antibiofilm activity, but they act at clearly different stages. PAA mainly inhibits VISA biofilm formation, suggesting that it may affect early adhesion, cell envelope status, surface charge, or early matrix formation. Biofilm formation in *S. aureus* involves sequential processes including surface attachment, intercellular aggregation, extracellular matrix production, and biofilm maturation, and these steps are influenced by cell surface properties and matrix components such as PIA/PNAG [170, 175]. In contrast, fusapurpurins A and B mainly disrupt already established mature biofilms, suggesting that they may act on mature biofilm architecture, matrix stability, or a biofilm-specific physiological state. Mature biofilms possess a structured extracellular matrix and embedded cells with distinct physiological states, which contribute to antibiotic tolerance and persistence [176, 177]. Together, these findings demonstrate that fungal natural products can act at different stages of the biofilm life cycle.

Compounds that inhibit biofilm formation are more suitable for preventing early colonization or reducing the ability of bacteria to establish stable biofilms, whereas compounds that disrupt preformed biofilms may be more suitable for combination with antibiotics to weaken mature biofilm barriers and improve the penetration and killing activity of antibacterial agents against biofilm-embedded bacteria [175, 178]. Since chronic clinical infections and implant-associated infections often involve already established mature biofilms, biofilm-disrupting compounds such as fusapurpurins have research value distinct from that of conventional bacteriostatic compounds [177, 179]. Together, the two projects highlight the diversity of fungal natural products in antibiofilm strategies.

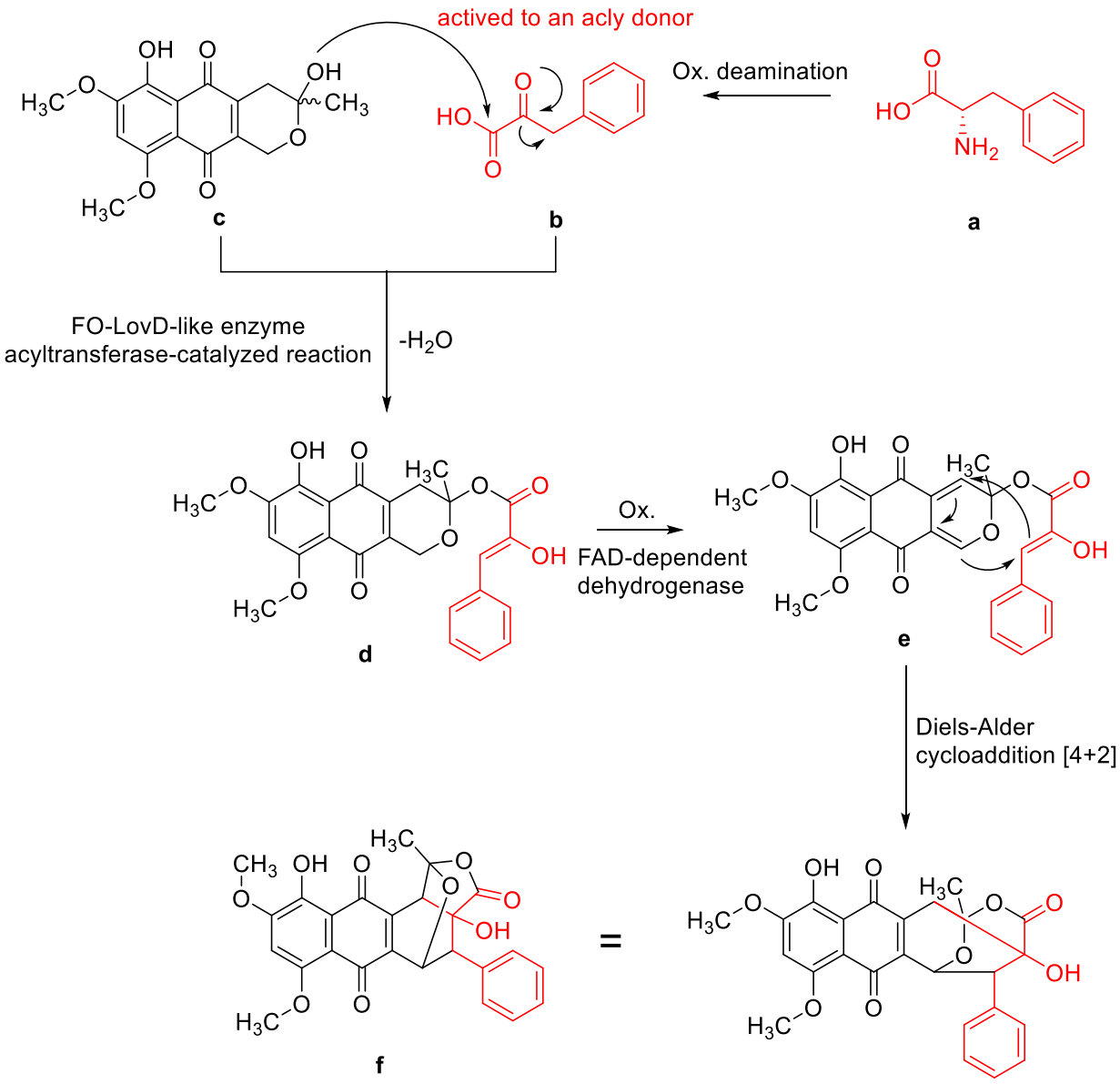


Figure 6.1. Proposed biosynthetic pathway for formation of compounds **3** and **4**. The amino acid L-phenylalanine (a) is oxidized via oxidative deamination to build phenylpyruvic acid (b). 9-O-Methylfusarubin (c) reacts with phenyl pyruvic acid (b) in a nucleophilic substitution to form intermediate d. After an oxidative step to build intermediate e, structure f (compounds **3** and **4**) is built via a Diels-Alder cycloaddition [4+2] as the final step to build the proposed racemic products.

6.12 Biosynthetic hypothesis of fusapurpurins

Fusapurpurins A and B contain a 9-*O*-methylfusarubin core and an additional phenylpyruvate-derived moiety, forming a complex bridged ring structure (**Fig. 6.1**). Genome sequencing and antiSMASH analysis showed that this *F. oxysporum* strain contains a type I PKS gene cluster associated with

fusarubin/oxyjavanicin biosynthesis, supporting its genetic capacity to synthesize the 9-*O*-methylfusarubin core structure. According to the reported fusarubin biosynthetic pathway, the fusarubin-type naphthoquinone core is mainly generated through a PKS pathway and subsequently converted into different derivatives through oxidative modification, *O*-methylation, and related tailoring steps [180]. In this study, 9-*O*-methylfusarubin could be stably detected, whereas fusapurpurins A and B could not be consistently reproduced in subsequent fermentation experiments. This suggests that the late-stage conjugation or cyclization steps may depend on the expression state of a key enzyme or on specific culture conditions.

According to the currently proposed biosynthetic pathway, phenylalanine may first undergo oxidative deamination to generate phenylpyruvic acid, which is then further converted into an activated phenylpyruvate-derived acyl donor, such as phenylpyruvate-CoA or a phenylpyruvate-SNAC-like thioester donor. This activated acyl donor subsequently conjugates with 9-*O*-methylfusarubin to generate an intermediate. We propose that the FO-LovD-like protein may participate in this acyl transfer/conjugation step. We further hypothesize that intermediate d is converted into intermediate e through oxidative dehydrogenation. Based on the reaction type, this step may be catalyzed by an FAD-dependent oxidoreductase or dehydrogenase-like enzyme. Intermediate e may then undergo a Diels–Alder-like [4+2] cycloaddition to form the complex bridged ring structure of fusapurpurins A and B. Since both fusapurpurins A and B are racemates, we consider that the final cyclization reaction is more likely to be a non-stereoselective spontaneous process. In this model, the enzyme-catalyzed steps are mainly responsible for generating the reactive precursor e, whereas the final [4+2] cyclization occurs without clear chiral control, thereby producing racemic products.

However, LC-MS analysis of the fermentation extracts did not detect the proposed reaction intermediates or free phenylpyruvic acid. This result suggests that the formation of fusapurpurins A and B may not be accompanied by substantial accumulation of intermediates. Phenylpyruvic acid may exist only as a transient metabolic intermediate after oxidative deamination of phenylalanine and may be rapidly converted into an activated acyl donor, such as phenylpyruvate-CoA or a related thioester form. The proposed intermediates d and e may also be highly reactive or poorly stable. In particular, after oxidative dehydrogenation of d to e, intermediate e may possess higher conjugated reactivity and further undergo Diels–Alder-like [4+2] cycloaddition to form the final products fusapurpurins A and B. If this

cyclization can proceed spontaneously, e may not accumulate substantially in the fermentation system or during extraction, but may instead be rapidly converted into the final bridged products. This could also explain why fusapurpurins A and B were isolated, whereas clear linear or uncyclized intermediates were not observed in the extract.

The failure to detect intermediates may also be related to the unstable production of fusapurpurins themselves. In this study, the production of fusapurpurins A and B was strongly condition-dependent and could not be consistently reproduced in every subsequent co-culture or extraction experiment. This suggests that their formation may require a specific co-culture state, metabolic time window, or local microenvironment. If the relevant intermediates are generated only transiently, or only within specific hyphal regions, fungus–bacterium contact interfaces, or local microenvironments, conventional bulk extraction and LC-MS analysis may fail to capture these low-abundance intermediates.

6.13 Computational support for the fusapurpurin biosynthetic hypothesis

In the biosynthetic study of fusapurpurins A and B, one important limitation is that the key intermediates in the proposed pathway may be present at low abundance, have short lifetimes, or show high reactivity. This feature increases the difficulty of reconstructing the enzymatic reactions *in vitro*, because experimental validation requires not only the candidate enzymes, but also stable and accessible substrates as well as detectable reaction products.

Under these circumstances, genome mining, protein structure prediction, structural comparison, and protein–ligand complex prediction provide important supporting evidence for the construction of the biosynthetic hypothesis. First, antiSMASH was used to analyze the secondary metabolite biosynthetic gene clusters in the *F. oxysporum* genome. antiSMASH is a widely used tool in natural product genome mining and can identify, annotate, and preliminarily predict the functions of BGCs in bacterial and fungal genomes based on conserved biosynthetic enzymes and gene cluster features [181]. The updated version of antiSMASH further expands the supported BGC types and improves chemical structure prediction, regulatory element identification, and biosynthetic assembly-line visualization [182]. In this study, antiSMASH analysis helped identify a candidate BGC that may be responsible for fusarubin/oxyjavanicin-like naphthoquinone core biosynthesis and provided a basis for subsequent screening of candidate enzymes potentially involved in late-stage tailoring reactions.

After the candidate gene was identified, AlphaFold was used to predict the three-dimensional structure of the FO-LovD-like protein. The development of AlphaFold2 has greatly improved the accuracy of protein structure prediction from amino acid sequences, often reaching near-experimental accuracy in many cases, especially for proteins lacking crystal structures or close homologous structural information [183]. For fungal candidate tailoring enzymes with limited functional annotation, AlphaFold-predicted structures can help determine whether the overall fold is consistent with a known enzyme family and can assist in locating potential active pockets and catalytic residues. Similarly, deep-learning-based structure prediction methods such as RoseTTAFold have also demonstrated that high-quality protein structure models can be rapidly generated from sequence information and used to develop hypotheses regarding protein complexes or functions [184]. Therefore, in the absence of an experimental structure of FO-LovD-like, the AlphaFold-predicted model provided a structural basis for analyzing its potential enzymatic function.

US-align was used to compare the structural similarity between the FO-LovD-like protein and the reported LovD protein. US-align is a universal structural alignment tool that can be used to compare proteins, nucleic acids, and macromolecular complexes, and evaluates overall structural similarity using parameters such as the TM-score [185]. In natural product biosynthesis research, structural similarity can sometimes better reflect the potential function of distantly related enzymes than primary sequence similarity, because many tailoring enzymes differ substantially in sequence but may still retain similar overall folds and catalytic architectures. Structural comparison using US-align showed that FO-LovD-like is similar to LovD in overall structure, active pocket position, and the potential Ser–Lys–Tyr catalytic core, supporting the possibility that it participates in the *c* + activated *b* → *d* acyl transfer/conjugation step in fusapurpurin biosynthesis (Fig. x).

In addition to individual protein structure prediction and structural comparison, this study further used Chai-1 for protein–ligand complex prediction to evaluate the spatial compatibility between the FO-LovD-like protein and the proposed substrates. Chai-1 is a next-generation multicomponent biomolecular structure prediction model that can predict the structures of complexes containing proteins, small molecules, nucleic acids, and other biomolecules based on protein sequences and small-molecule chemical inputs [186]. In this study, Chai-1 was used to predict the complex structures of FO-LovD-like with the 9-*O*-methylfusarubin-like acceptor *c* and an activated phenylpyruvate-derived thioester donor.

The purpose of this analysis was to assess whether the proposed substrates could enter the binding pocket of FO-LovD-like and whether the potential reaction sites showed a reasonable spatial relationship with the Ser–Lys–Tyr catalytic core. The prediction results showed that the binding pocket of FO-LovD-like could accommodate the naphthoquinone acceptor and the activated phenylpyruvate-derived thioester donor, thereby providing further structural plausibility for its involvement in the *c* + activated *b* → *d* acyl transfer/conjugation step (Fig x).

These computational tools helped identify candidate enzymes from genomic and BGC information that matched the proposed biosynthetic step. They provided structural support for the functional hypothesis of FO-LovD-like, including its overall fold, catalytic core, and substrate-binding pocket. They also guided subsequent experimental design, for example by prioritizing phenylpyruvate-CoA or phenylpyruvate-SNAC as donors for *in vitro* reactions. For natural product biosynthetic studies in which intermediates are difficult to capture and the activated substrate forms remain unclear, such *in silico* analyses can effectively narrow the experimental scope and improve the specificity of subsequent *in vitro* enzymatic validation.

However, these computational models have important limitations. AlphaFold2 is highly useful for predicting the overall fold of FO-LovD-like and locating putative catalytic regions, but it mainly provides a static structural model and cannot fully capture enzyme dynamics, substrate-induced conformational changes, cofactor-dependent states, or reaction pathways [187, 188]. US-align can support structural similarity between FO-LovD-like and known LovD-like enzymes, but structural similarity alone does not prove identical catalytic function [185]. Chai-1 allows protein–ligand complex prediction with custom small molecules and was therefore useful for evaluating whether the proposed acceptor and activated acyl donor could be accommodated in the predicted binding pocket [186]. Nevertheless, recent analyses of protein–ligand pose prediction show that predicted poses may not reliably recover key molecular interactions, and such models cannot demonstrate binding affinity, catalytic efficiency, covalent intermediate formation, or product generation [189]. Therefore, the computational results in this study provide structural plausibility for FO-LovD-like as a candidate enzyme, but they remain hypothesis-generating evidence and require validation by in vitro enzyme assays, targeted LC-MS/MS, substrate supplementation, and genetic experiments.

In summary, antiSMASH, AlphaFold, US-align, and Chai-1 prediction together constitute an important computational support framework for the fusapurpurin biosynthetic hypothesis in this study. They connect genomic information, candidate enzyme screening, structural similarity analysis, and substrate spatial compatibility, allowing a more evidence-based hypothesis to be proposed for the potential function of the FO-LovD-like protein in the absence of stable intermediates and a complete *in vitro* enzymatic system. Nevertheless, final confirmation still requires *in vitro* enzymatic experiments and genetic validation. In the future, only by combining computational predictions with substrate feeding, time-course LC-MS, *in vitro* enzymatic reactions, and gene functional validation will it be possible to clearly define each reaction step in the biosynthesis of fusapurpurins A and B.

6.14 Future perspectives and limitations

The two main projects of this thesis revealed the anti-VISA activity of PAA and the mature biofilm-disrupting activity of fusapurpurins, respectively. However, these findings still require further mechanistic investigation and functional validation. For PAA, the current results support a close association with GraRS-related cell envelope homeostasis, but its direct molecular target remains unknown. In the future, transcriptomics, proteomics, cell envelope component analysis, target identification, and genetic validation could be used to further clarify its initial site of action. Meanwhile, the current *graR* complementation system failed to restore the phenotype, indicating that subsequent studies require genetic systems that more closely mimic chromosomal native expression, such as chromosomal repair of the *graR* mutation, construction of single *graR* or *graRS* deletion/complementation strains, and verification of whether the expression of downstream GraRS-regulated genes is truly restored.

For fusapurpurins, the main limitations are their unstable production and the fact that the FO-LovD-like protein currently remains only a candidate enzyme. Its function still needs to be validated through gene knockout, gene silencing, heterologous expression, and *in vitro* enzymatic reactions. In addition, the antibiofilm mechanism of fusapurpurins remains unclear and requires analysis of their effects on extracellular polysaccharides, extracellular DNA, proteinaceous matrix components, cell viability, and the three-dimensional structure of biofilms. The biofilm matrix is usually composed of multiple components, including polysaccharides, proteins, lipids, and extracellular DNA, which together determine biofilm structural stability, antibiotic tolerance, and immune evasion [190, 191]. In future

studies, confocal laser scanning microscopy (CLSM) combined with fluorescent staining could be used to observe the three-dimensional structure, thickness, biovolume, and live/dead cell distribution of biofilms. CLSM has been widely used for analyzing biofilm spatial structure and cell viability distribution, and is particularly suitable for reconstructing three-dimensional biofilm architecture through z-stack imaging [192, 193].

At the same time, matrix composition assays could be combined to analyze changes in matrix components such as extracellular polysaccharides, extracellular DNA, and proteins, because these extracellular polymeric substances are core components that maintain biofilm structural stability and drug tolerance [190, 194]. In addition, time-dependent biofilm disruption assays could be used to compare the disruption kinetics of fusapurpurins against preformed biofilms at different treatment times, thereby determining whether they rapidly disrupt matrix architecture or gradually affect biofilm-embedded bacteria. Such time-dependent analyses are commonly used to evaluate the activity profiles of biofilm-dispersing agents or natural antibiofilm compounds [195, 196]. Therefore, the combination of these methods would help distinguish whether fusapurpurins mainly act on biofilm matrix architecture or on biofilm-embedded bacteria.

Furthermore, since fusapurpurins A and B are both racemates, the influence of stereochemistry on their antibiofilm activity also requires further investigation. The biological activity of natural products is often closely related to their stereochemistry, because different enantiomers may interact differently with biological macromolecules, cell surface structures, or biofilm matrix components [197, 198]. Therefore, single enantiomers could be obtained through chiral separation or asymmetric synthesis and then compared for their biofilm-disrupting activity, cytotoxicity, and direct antibacterial activity. This would clarify the structure–activity relationship of fusapurpurins and provide a basis for further structural optimization and mechanistic studies.

The active compounds from both projects also require further structural optimization and *in vivo* validation. Although PAA shows promising anti-VISA activity and synergistic potential, its selectivity, stability, and *in vivo* safety still require systematic evaluation. Fusapurpurins show clear mature biofilm-disrupting activity, but their weak direct antibacterial activity, cytotoxicity, and production issues may limit further development. Therefore, future studies should combine synthetic modification,

semisynthetic derivatization, fermentation optimization, and mechanistic validation to improve the application potential of these fungal natural products as anti-infective lead structures.

7. Other structural identification work

In addition to the two main projects described above, this thesis also includes a partial contribution to the study of asperphenalenone derivatives from *Clonostachys rosea*. In that study, eight new phenalenones, asperphenalenones F–M, together with two known derivatives, were isolated from the rice culture of *C. rosea*. Some of these compounds showed moderate antibacterial activity against MRSA [199]. My main contribution to this study was participation in determining the configuration of the sugar moiety in glycosylated asperphenalenone derivatives, particularly confirming the sugar as α-D-mannose through hydrolysis product analysis and optical rotation data. This work highlights the importance of structural identification of fungal secondary metabolites in natural product research.

8. Contribution to the three manuscripts

Contribution to the manuscript 1:

- Drafted the second version of manuscript.
- Re-fermented *P. chamaeropis* and performed extraction and chromatographic isolation to obtain PAA.
- Generated and screened spontaneous PAA-resistant mutants of VISA.
- Extracted genomic DNA from the resistant mutants for whole-genome sequencing.
- Treated VISA cells with PAA and extracted cellular proteins for proteomic analysis.
- Performed propidium iodide uptake assays to evaluate the effect of PAA on VISA cell membrane permeability.
- Determined the MICs of different antibiotics against the resistant mutants.
- Conducted checkerboard assays to evaluate the interactions between PAA and different antibiotics.
- Performed cytochrome c binding assays on VISA cells following PAA treatment.
- Extracted RNA from PAA-treated VISA cells, performed reverse transcription, and conducted RT-qPCR analyses. RNA was also extracted from the resistant mutants for RT-qPCR analysis.
- Evaluated the inhibitory effect of PAA on VISA biofilm formation.

- Introduced plasmids expressing the wild-type *cysK* and *graR* gene into the resistant mutants for genetic complementation and subsequently determined their MICs.

Contribution to the manuscript 2:

- Drafted the second version of manuscript.
- Re-fermented *F. oxysporum* and applied an OSMAC strategy to investigate its secondary metabolite production under different culture conditions.
- Analyzed the whole-genome sequencing data and the proposed fusapurpurin biosynthetic pathway to identify FO-LovD-like as a candidate key enzyme involved in fusapurpurin biosynthesis.
- Cloned the gene encoding FO-LovD-like from *F. oxysporum* and heterologously expressed it in *E. coli.*
- Extracted and purified the recombinant FO-LovD-like protein expressed in *E. coli*.
- Predicted the three-dimensional structure of FO-LovD-like using AlphaFold.
- Compared the predicted structure of FO-LovD-like with that of the functionally characterized LovD enzyme from Aspergillus terreus using US-align.
- Used Chai-1 to predict the binding modes of the putative substrates within the FO-LovD-like structure.
- Further refined the proposed biosynthetic pathway of fusapurpurin based on the genomic, structural, and substrate-docking analyses.

Contribution to the manuscript 3:

Contributed to determining the configuration of the sugar moiety in glycosylated asperphenalenone derivatives through hydrolysis product analysis and optical rotation measurements, which confirmed the sugar as α-D-mannose.

Reference

1. Charlotte S Ho, et al. Antimicrobial resistance: a concise update. *The Lancet Microbe*, 2025, 6(1): 100947.

2. Joshua B. Parsons, et al. Methicillin-resistant and susceptible *Staphylococcus aureus*: tolerance, immune evasion and treatment. *Nature Reviews Microbiology*, 2026, 24(2): 127-145.

3. Mark S Butler, et al. Natural product inspired antibiotics approved for human use – 1943 to 2025. *Natural Product Reports*, 2026, 43(5): 813–896.

4. Katarzyna Kala. Advances in Fungal Natural Products: Insights into Bioactivity and Therapeutic Potential. *Pharmaceuticals*, 2025, 18(9), 1313.

5. Fadiah Ammar Almutairi, et al. Marine Fungal Metabolites: A Promising Source for Antibiofilm Compounds. *Molecules*, 2025, 30(21): 4266.

6. Shefali Bansal, et al. Endophytic fungi as a source of antimicrobial compounds against emerging methicillin-resistant *Staphylococcus aureus*. *Mycology*, 2026, 17(1): 1–28.

7. Hedda Schrey, et al. Fungi: pioneers of chemical creativity—techniques and strategies to uncover fungal chemistry. *IMA Fungus*, 2025, 16: e142462.

8. Antimicrobial Resistance Collaborators. Global burden of bacterial antimicrobial resistance in 2019: a systematic analysis. *Lancet*, 2022, 399(10325): 629–655.

9. WHO. Antimicrobial resistance. World Health Organization, 2023.

10. Iruka N Okeke, et al. The scope of the antimicrobial resistance challenge. *The Lancet*, 2024, 403(10442): 2426–2438.

11. WHO. *WHO bacterial priority pathogens list*, 2024: bacterial pathogens of public health importance to guide research, development and strategies to prevent and control antimicrobial resistance. World Health Organization, 2024.

12. Abubakar Nazir, et al. The global challenge of antimicrobial resistance: mechanisms, case studies, and mitigation approaches. *Health Science Reports*, 2025, 8(7): e71077.

13. Gerard D Wright. Bacterial resistance to antibiotics: enzymatic degradation and modification. *Advanced Drug Delivery Reviews*, 2005, 57(10): 1451–1470.

14. Jose M Munita, et al. Mechanisms of antibiotic resistance. *In: Virulence Mechanisms of Bacterial Pathogens*, 2016: 481–511.

15. Xian-Zhi Li, et al. The challenge of efflux-mediated antibiotic resistance in Gram-negative bacteria. *Clinical Microbiology Reviews*, 2015, 28(2): 337–418.

16. Francesca Micoli, et al. The role of vaccines in combatting antimicrobial resistance. *Nature Reviews Microbiology*, 2021, 19(5): 287–302.

17. GBD 2021 Antimicrobial Resistance Collaborators. Global burden of bacterial antimicrobial resistance 1990–2021: a systematic analysis with forecasts to 2050. *The Lancet*, 2024, 404(10459): 1199–1226.

18. Marc Mendelson, et al. Ensuring progress on sustainable access to effective antibiotics at the 2024 UN General Assembly: a target-based approach. *The Lancet*, 2024, 403(10443): 2551–2564.

19. WHO. Global antimicrobial resistance and use surveillance system (GLASS) report: 2022. World Health Organization, 2022.

20. Marco Cavaco, et al. The use of antibody-antibiotic conjugates to fight bacterial infections. *Frontiers in Microbiology*, 2022, 13: 835677.

21. Sophie M Lehar, et al. Novel antibody-antibiotic conjugate eliminates intracellular *S. aureus*. *Nature*, 2015, 527(7578): 323–328.

22. Neeloffer Mookherjee, et al. Antimicrobial host defence peptides: functions and clinical potential. *Nature Reviews Drug Discovery*, 2020, 19(5): 311–332.

23. Robert E W Hancock, et al. Antibiofilm activity of host defence peptides: complexity provides opportunities. *Nature Reviews Microbiology*, 2021, 19(12): 786–797.

24. George P C Salmond, et al. A century of the phage: past, present and future. *Nature Reviews Microbiology*, 2015, 13(12): 777–786.

25. Saartje Uyttebroek, et al. Safety and efficacy of phage therapy in difficult-to-treat infections: a systematic review. *The Lancet Infectious Diseases*, 2022, 22(8): e208–e220.

26. David Bikard, et al. Exploiting CRISPR-Cas nucleases to produce sequence-specific antimicrobials. *Nature Biotechnology*, 2014, 32(11): 1146–1150.

27. Robert J Citorik, et al. Sequence-specific antimicrobials using efficiently delivered RNA-guided nucleases. *Nature Biotechnology*, 2014, 32(11): 1141–1145.

28. Haodi Ma, et al. Antibiotic Mechanisms and Resistance: Molecular Insights and Therapeutic Strategies. *Antibiotics*, 2026, 15(4): 351.

29. Hongbaek Cho, et al. β-Lactam antibiotics induce a lethal malfunctioning of the bacterial cell wall synthesis machinery. *Cell*, 2014, 159(6): 1300–1311.

30. Rúben Fernandes, et al. β-Lactams: chemical structure, mode of action and mechanisms of resistance. *Reviews in Medical Microbiology*, 2013, 24(1): 7–17.

31. Hee-Kyoung Kang, et al. Glycopeptide antibiotics: structure and mechanisms of action. *Journal of Bacteriology and Virology*, 2015, 45(2): 67–78.

32. Esraa M Halawa, et al. Antibiotic action and resistance: updated review of mechanisms, spread, influencing factors, and alternative approaches for combating resistance. *Frontiers in Pharmacology*, 2024, 14: 1305294.

33. Anna Fàbrega, et al. Mechanism of action of and resistance to quinolones. *Microbial Biotechnology*, 2009, 2(1): 40–61.

34. Thu D M Pham, et al. Quinolone antibiotics. *MedChemComm*, 2019, 10(10): 1719–1739.

35. Joseph M Blondeau. Fluoroquinolones: mechanism of action, classification, and development of resistance. *Survey of Ophthalmology*, 2004, 49(Suppl 2): S73–S78.

36. Magnus Johansson, et al. Rate and accuracy of bacterial protein synthesis revisited. *Current Opinion in Microbiology*, 2008, 11(2): 141–147.

37. Suman Jana, et al. Molecular understanding of aminoglycoside action and resistance. *Applied Microbiology and Biotechnology*, 2006, 70(2): 140–150.

38. Quentin Vicens, et al. RNA as a drug target: the case of aminoglycosides. *ChemBioChem*, 2003, 4(10): 1018–1023.

39. Ditlev E Brodersen, et al. The structural basis for the action of the antibiotics tetracycline, pactamycin, and hygromycin B on the 30S ribosomal subunit. *Cell*, 2000, 103(7): 1143–1154.

40. Tanel Tenson, et al. The mechanism of action of macrolides, lincosamides and streptogramin B reveals the nascent peptide exit path in the ribosome. *Journal of Molecular Biology*, 2003, 330(5): 1005–1014.

41. Egor A Syroegin, et al. Structural basis for the inability of chloramphenicol to inhibit peptide bond formation in the presence of A-site glycine. *Nucleic Acids Research*, 2022, 50(13): 7669–7679.

42. Claudia Foti, et al. Oxazolidinone antibiotics: chemical, biological and analytical aspects. *Molecules*, 2021, 26(14): 4280.

43. Declan Alan Gray, et al. More than a pore: a current perspective on the *in vivo* mode of action of the lipopeptide antibiotic daptomycin. *Antibiotics*, 2020, 9(1): 17.

44. Clemente Capasso, et al. Sulfa and trimethoprim-like drugs—antimetabolites acting as carbonic anhydrase, dihydropteroate synthase and dihydrofolate reductase inhibitors. *Journal of Enzyme Inhibition and Medicinal Chemistry*, 2014, 29(3): 379–387.

45. WHO. Analysis of antibacterial agents in clinical and preclinical development: overview and analysis 2025. World Health Organization, 2025.

46. Mark A. T. Blaskovich, et al. Antibiotics re-booted—time to kick back against drug resistance. *npj Antimicrobials and Resistance*, 2025, 3(1): 47.

47. Margherita Sartori, et al. Molecular resistance mechanisms to newly approved antibiotics (2017–2025) in WHO priority pathogens. *Frontiers in Microbiology*, 2026, 16: 1719798.

48. Michael W McCarthy. Cefiderocol to treat complicated urinary tract infection. *Drugs of Today*, 2020, 56(3): 177–184.

49. Shubham Adhikary, et al. Lefamulin: a new hope in the field of community-acquired bacterial

pneumonia. *Current Pharmacology Reports*, 2022, 8(6): 418–426.

50. Pipat Piewngam, et al. *Staphylococcus aureus* colonisation and strategies for decolonisation. *The Lancet Microbe*, 2024, 5(6): e606–e618.

51. Nicholas A Turner, et al. Methicillin-resistant *Staphylococcus aureus*: an overview of basic and clinical research. *Nature Reviews Microbiology*, 2019, 17(4): 203–218.

52. Stefano Di Bella, et al. The virulence toolkit of *Staphylococcus aureus*: a comprehensive review of toxin diversity, molecular mechanisms, and clinical implications. *European Journal of Clinical Microbiology & Infectious Diseases*, 2025, 44(8): 1797–1816.

53. Yanguang Cong, et al. Vancomycin resistant *Staphylococcus aureus* infections: a review of case updating and clinical features. *Journal of Advanced Research*, 2020, 21: 169–176.

54. Henry F Chambers, et al. Waves of resistance: *Staphylococcus aureus* in the antibiotic era. *Nature Reviews Microbiology*, 2009, 7(9): 629–641.

55. Catriona P Harkins, et al. Methicillin-resistant *Staphylococcus aureus* emerged long before the introduction of methicillin into clinical practice. *Genome Biology*, 2017, 18(1): 130.

56. Yukiko Katayama, et al. A new class of genetic element, staphylococcus cassette chromosome mec, encodes methicillin resistance in *Staphylococcus aureus*. *Antimicrobial Agents and Chemotherapy*, 2000, 44(6): 1549–1555.

57. Barry J Hartman, et al. Low-affinity penicillin-binding protein associated with beta-lactam resistance in *Staphylococcus aureus*. *Journal of Bacteriology*, 1984, 158(2): 513–516.

58. Michael Z David, et al. Community-associated methicillin-resistant *Staphylococcus aureus*: epidemiology and clinical consequences of an emerging epidemic. *Clinical Microbiology Reviews*, 2010, 23(3): 616–687.

59. Natalia Malachowa, et al. Mobile genetic elements of *Staphylococcus aureus*. *Cellular and Molecular Life Sciences*, 2010, 67(18): 3057–3071.

60. Keiichi Hiramatsu, et al. Vancomycin-intermediate resistance in *Staphylococcus aureus*. *Journal of Global Antimicrobial Resistance*, 2014, 2(4): 213–224.

61. Longzhu Cui, et al. Cell wall thickening is a common feature of vancomycin resistance in *Staphylococcus aureus*. *Journal of Clinical Microbiology*, 2003, 41(1): 5–14.

62. Longzhu Cui, et al. Contribution of a thickened cell wall and its glutamine nonamidated component to the vancomycin resistance expressed by *Staphylococcus aureus* Mu50. *Antimicrobial Agents and Chemotherapy*, 2000, 44(9): 2276–2285.

63. Mary M Mwangi, et al. Tracking the *in vivo* evolution of multidrug resistance in *Staphylococcus aureus* by whole-genome sequencing. *Proceedings of the National Academy of Sciences of the United States of America*, 2007, 104(22): 9451–9456.

64. Benjamin P Howden, et al. Genomic analysis reveals a point mutation in the two-component sensor gene *graS* that leads to intermediate vancomycin resistance in clinical *Staphylococcus aureus*. *Antimicrobial Agents and Chemotherapy*, 2008, 52(10): 3755–3762.

65. Makoto Kuroda, et al. Two-component system VraSR positively modulates the regulation of cell-wall biosynthesis pathway in *Staphylococcus aureus*. *Molecular Microbiology*, 2003, 49(3): 807–821.

66. Mélanie Falord, et al. GraXSR proteins interact with the *VraFG* ABC transporter to form a five-component system required for cationic antimicrobial peptide sensing and resistance in *Staphylococcus aureus*. *Antimicrobial Agents and Chemotherapy*, 2012, 56(2): 1047–1058.

67. Hui-min Neoh, et al. Mutated response regulator *graR* is responsible for phenotypic conversion of *Staphylococcus aureus* from heterogeneous vancomycin-intermediate resistance to vancomycin-intermediate resistance. *Antimicrobial Agents and Chemotherapy*, 2008, 52(1): 45–53.

68. Miki Matsuo, et al. Mutation of RNA polymerase β subunit (*rpoB*) promotes hVISA-to-VISA phenotypic conversion of strain Mu3. *Antimicrobial Agents and Chemotherapy*, 2011, 55(9): 4188–4195.

69. Linda M Weigel, et al. Genetic analysis of a high-level vancomycin-resistant isolate of *Staphylococcus aureus*. *Science*, 2003, 302(5650): 1569–1571.

70. Guido Werner, et al. Acquired vancomycin resistance in clinically relevant pathogens. *Future Microbiology*, 2008, 3(5): 547–562.

71. Cesar A Arias, et al. The rise of the *Enterococcus*: beyond vancomycin resistance. *Nature Reviews Microbiology*, 2012, 10(4): 266–278.

72. Flavia Rossi, et al. Transferable vancomycin resistance in a community-associated MRSA lineage. *The New England Journal of Medicine*, 2014, 370(16): 1524–1531.

73. David K Warren, et al. Occurrence of co-colonization or co-infection with vancomycin-resistant enterococci and methicillin-resistant *Staphylococcus aureus* in a medical intensive care unit. *Infection Control & Hospital Epidemiology*, 2004, 25(2): 99–104.

74. J. William Costerton, et al. Bacterial biofilms in nature and disease. *Annual Review of Microbiology*, 1987, 41: 435–464.

75. Oana Ciofu, et al. Tolerance and resistance of microbial biofilms. *Nature Reviews Microbiology*, 2022, 20(10): 621–635.

76. Pranay Amruth Maroju, et al. Detection to disruption: a comprehensive review of bacterial biofilms and therapeutic advances. *Antibiotics*, 2026, 15(4): 396.

77. José L Del Pozo. Biofilm-related disease. *Expert Review of Anti-infective Therapy*, 2018, 16(1): 51–65.

78. Philip S Stewart, et al. Physiological heterogeneity in biofilms. *Nature Reviews Microbiology*, 2008,

6(3): 199–210.

79. Niels Høiby, et al. ESCMID guideline for the diagnosis and treatment of biofilm infections 2014. *Clinical Microbiology and Infection*, 2015, 21(Suppl. 1): S1–S25.

80. Anne Brauner, et al. Distinguishing between resistance, tolerance and persistence to antibiotic treatment. *Nature Reviews Microbiology*, 2016, 14(5): 320–330.

81. Nathalie Q Balaban, et al. Definitions and guidelines for research on antibiotic persistence. *Nature Reviews Microbiology*, 2019, 17(7): 441–448.

82. Thien-Fah C Mah, et al. Mechanisms of biofilm resistance to antimicrobial agents. *Trends in Microbiology*, 2001, 9(1): 34–39.

83. Suriani Abdul Rani, et al. Spatial patterns of DNA replication, protein synthesis, and oxygen concentration within bacterial biofilms reveal diverse physiological states. *Journal of Bacteriology*, 2007, 189(11): 4223–4233.

84. Elaine Tuomanen, et al. The rate of killing of *Escherichia coli* by beta-lactam antibiotics is strictly proportional to the rate of bacterial growth. *Journal of General Microbiology*, 1986, 132(5): 1297–1304.

85. Jesús Blázquez, et al. Antibiotic-induced genetic variation: how it arises and how it can be prevented. *Annual Review of Microbiology*, 2018, 72: 209–230.

86. Victoria J Savage, et al. *Staphylococcus aureus* biofilms promote horizontal transfer of antibiotic resistance. *Antimicrobial Agents and Chemotherapy*, 2013, 57(4): 1968–1970.

87. Hong Wu, et al. Strategies for combating bacterial biofilm infections. *International Journal of Oral Science*, 2015, 7(1): 1–7.

88. Alessandra Oliva, et al. Biofilm-related infections in gram-positive bacteria and the potential role of the long-acting agent dalbavancin. *Frontiers in Microbiology*, 2021, 12: 749685.

89. Megan R Kiedrowski, et al. New approaches for treating staphylococcal biofilm infections. *Annals of the New York Academy of Sciences*, 2011, 1241(1): 104–121.

90. Cynthia B Whitchurch, et al. Extracellular DNA required for bacterial biofilm formation. *Science*, 2002, 295(5559): 1487.

91. Jeffrey B Kaplan, et al. Detachment of Actinobacillus actinomycetemcomitans biofilm cells by an endogenous beta-hexosaminidase activity. *Journal of Bacteriology*, 2003, 185(16): 4693–4698.

92. Zhifen Wang, et al. Repurposing DNase I and alginate lyase to degrade the biofilm matrix of dual-species biofilms of *Staphylococcus aureus* and *Pseudomonas aeruginosa* grown in artificial sputum medium: in-vitro assessment of their activity in combination with broad-spectrum antibiotics. *Journal of Cystic Fibrosis*, 2024, 23(6): 1146–1152.

93. Pamela Hindieh, et al. Emerging Multimodal Strategies for Bacterial Biofilm Eradication: A

Comprehensive Review. *Microorganisms*, 2025, 13(12): 2796.

94. C. N. Ugwu, et al. Biofilms: structure, resistance mechanism, emerging control strategies, and applications. *RSC Pharmaceutics*, 2025, 2(6): 1376–1407.

95. M Pitton, et al. Targeting chronic biofilm infections with patient-derived phages: an *in vitro* and *ex vivo* proof-of-concept study in patients with left ventricular assist devices. *Open Forum Infectious Diseases*, 2025, 12: ofaf158.

96. Gerard D Wright. Opportunities for natural products in 21st century antibiotic discovery. *Natural Product Reports*, 2017, 34(7): 694–701.

97. Franz von Nussbaum, et al. *Antibacterial natural products in medicinal chemistry—exodus or revival? Angewandte Chemie International Edition*, 2006, 45(31): 5072–5129.

98. Joana Araújo, et al. Chiral derivatives of xanthones with antimicrobial activity. *Molecules*, 2019, 24(2): 314.

99. Alexander Fleming. On the antibacterial action of cultures of a Penicillium, with special reference to their use in the isolation of B. influenzae. *British Journal of Experimental Pathology*, 1929, 10: 226–236.

100. E L Miller. The penicillins: a review and update. *Journal of Midwifery & Women's Health*, 2002, 47(6): 426–434.

101. Michael P Veve, et al. Lefamulin: review of a promising novel pleuromutilin antibiotic. *Pharmacotherapy*, 2018, 38(9): 935–946.

102. David W Green. The bacterial cell wall as a source of antibacterial targets. *Expert Opinion on Therapeutic Targets*, 2002, 6(1): 1–19.

103. David G Allison, et al. Modes of action of antibacterial agents. In: Molecular Medical Microbiology. 2nd ed. *Amsterdam: Elsevier*, 2015: 583–598.

104. Ramona Barbieri, et al. Phytochemicals for human disease: an update on plant-derived compounds antibacterial activity. *Microbiological Research*, 2017, 196: 44–68.

105. World Health Organization. At UN, global leaders commit to act on antimicrobial resistance. WHO, 2016.

106. SeyedAhmad SeyedAlinaghi, et al. A systematic review on natural products with antimicrobial potential against WHO's priority pathogens. *European Journal of Medical Research*, 2025, 30: 525.

107. Mathew Gideon. Novel strategy for optimizing the antibacterial activity of *Psidium guajava* against clinical isolates of *Escherichia coli*, *Staphylococcus aureus*, *Salmonella* spp., and *Streptococcus* spp. INNOSC Theranostics and Pharmacological Sciences, 2022, 5(1): 27–34.

108. Mark S Butler, et al. The role of natural product chemistry in drug discovery: two decades of progress and perspectives. *Journal of Natural Products*, 2026, 89(1): 3–28.

109. A G Atanasov, et al. Natural products in drug discovery: advances and opportunities. *Nature Reviews Drug Discovery*, 2021, 20(3): 200–216.

110. V Bell, et al. Mushrooms as future generation healthy foods. *Frontiers in Nutrition*, 2022, 9: 1050099.

111. K Wadhwa, et al. A comprehensive review of the diversity of fungal secondary metabolites and their emerging applications in healthcare and environment. *Mycobiology*, 2024, 52(6): 335–387.

112. Vimalah Vallavan, et al. A review on antistaphylococcal secondary metabolites from basidiomycetes. *Molecules*, 2020, 25(24): 5848.

113. Sandip Chowdhury, et al. Anti-MRSA and clot lysis activities of *Pestalotiopsis microspora* isolated from Dillenia pentagyna Roxb. *Journal of Basic Microbiology*, 2023, 63(3–4): 340–358.

114. H Wang, et al. Isolation, identification, and antibacterial evaluation of endophytic fungi from Gannan navel orange. *Frontiers in Microbiology*, 2023, 14: 1172629.

115. Saif Aldeen Mohammad Fayiz Jaber. Metabolomic profiling of antibiofilm compounds from fungal endophytes derived from Scottish seaweeds. Ph.D. *Thesis, University of Strathclyde, Glasgow, UK*, 2021.

116. S Scopel, et al. Dipeptide cis-cyclo (Leucyl-Tyrosyl) produced by sponge associated Penicillium sp. F37 inhibits biofilm formation of the pathogenic *Staphylococcus epidermidis*. *Bioorganic & Medicinal Chemistry Letters*, 2013, 23(3): 624–626.

117. C P Parlet, et al. Apicidin attenuates MRSA virulence through quorum-sensing inhibition and enhanced host defense. *Cell Reports*, 2019, 27(1): 187–198.e6.

118. O P Martínez-Rodríguez, et al. Antimicrobial and antibiofilm activity of fungal metabolites on methicillin-resistant *Staphylococcus aureus* (ATCC 43300) mediated by SarA and AgrA. *Biofouling*, 2023, 39(8): 830–837.

119. Ying Shi, et al. New bioactive secondary metabolites from fungi: 2023. *Mycology*, 2024, 15(3): 283–321.

120. Meiyan Bao, et al. New bioactive secondary metabolites from fungi: 2024. *Mycology*, 2025, 16(3): 961–987.

121. Axel A Brakhage, et al. Evolution of β-lactam biosynthesis genes and recruitment of trans-acting factors. *Phytochemistry*, 2005, 66(11): 1200–1210.

122. Jonathan Kennedy, et al. Modulation of polyketide synthase activity by accessory proteins during lovastatin biosynthesis. *Science*, 1999, 284(5418): 1368–1372.

123. Christopher L Schardl, et al. Ergot alkaloids—biology and molecular biology. *Alkaloids: Chemistry and Biology*, 2006, 63: 45–86.

124. Gregory C A Amos, et al. Comparative transcriptomics as a guide to natural product discovery and biosynthetic gene cluster functionality. *Proceedings of the National Academy of Sciences of the*

United States of America, 2017, 114(52): E11121–E11130.

125. Matthew T Robey, et al. An interpreted atlas of biosynthetic gene clusters from 1,000 fungal genomes. *Proceedings of the National Academy of Sciences of the United States of America*, 2021, 118(19): e2020230118.

126. Yi Wang, et al. Mining silent biosynthetic gene clusters for natural products in filamentous fungi. *Chemistry & Biodiversity*, 2025, 22(6): e202402715.

127. Rahmat Folashade Zakariyah, et al. Progress in endophytic fungi secondary metabolites: biosynthetic gene cluster reactivation and advances in metabolomics. *Bulletin of the National Research Centre*, 2024, 48(1): 44.

128. Helge B Bode, et al. Big effects from small changes: possible ways to explore nature's chemical diversity. *ChemBioChem*, 2002, 3(7): 619–627.

129. Mohammad R Seyedsayamdost. High-throughput platform for the discovery of elicitors of silent bacterial gene clusters. *Proceedings of the National Academy of Sciences of the United States of America*, 2014, 111(20): 7266–7271.

130. Yu Zhang, et al. OSMAC strategy: a promising way to explore microbial cyclic peptides. *European Journal of Medicinal Chemistry*, 2024, 268: 116175.

131. Wangjie Zhu, et al. Enhancing chemical diversity of fungal secondary metabolite by OSMAC strategy. In: Fungi Bioactive Metabolites. *Singapore: Springer Nature Singapore*, 2024: 567–604.

132. Song Huang, et al. Two new cyclopeptides from the co-culture broth of two marine mangrove fungi and their antifungal activity. *Pharmacognosy Magazine*, 2014, 10(40): 410–414.

133. Andrea A Stierle, et al. The berkeleylactones, antibiotic macrolides from fungal coculture. *Journal of Natural Products*, 2017, 80(4): 1150–1160.

134. Samuel Bertrand, et al. Metabolite induction via microorganism co-culture: a potential way to enhance chemical diversity for drug discovery. *Biotechnology Advances*, 2014, 32(6): 1180–1204.

135. Felix Mittermeier, et al. Artificial microbial consortia for bioproduction processes. *Engineering in Life Sciences*, 2023, 23(1): e2100152.

136. Yu-Zhen Li, et al. Harnessing microbial co-culture to increase the production of known secondary metabolites. *Natural Product Reports*, 2025, 42(3): 623–637.

137. Sonja L Knowles, et al. Fungal–fungal co-culture: a primer for generating chemical diversity. *Natural Product Reports*, 2022, 39(8): 1557–1573.

138. David J Gonzalez, et al. Microbial competition between Bacillus subtilis and *Staphylococcus aureus* monitored by imaging mass spectrometry. *Microbiology*, 2011, 157(9): 2485–2492.

139. Kyuho Moon, et al. Cebulantin, a cryptic lanthipeptide antibiotic uncovered using bioactivity-coupled HiTES. *Angewandte Chemie International Edition*, 2019, 58(18): 5973–5977.

140. David J Newman, et al. Natural products as sources of new drugs over the nearly four decades from 01/1981 to 09/2019. *Journal of Natural Products*, 2020, 83(3): 770–803.

141. Benjamin P Howden, et al. Reduced vancomycin susceptibility in *Staphylococcus aureus*, including vancomycin-intermediate and heterogeneous vancomycin-intermediate strains: resistance mechanisms, laboratory detection, and clinical implications. *Clinical Microbiology Reviews*, 2010, 23(1): 99–139.

142. Qiwen Hu, et al. Molecular events for promotion of vancomycin resistance in vancomycin intermediate *Staphylococcus aureus*. *Frontiers in Microbiology*, 2016, 7: 1601.

143. Longzhu Cui, et al. Contribution of *vraSR* and *graSR* point mutations to vancomycin resistance in vancomycin-intermediate *Staphylococcus aureus*. *Antimicrobial Agents and Chemotherapy*, 2009, 53(3): 1231–1234.

144. Susana Gardete, et al. Mechanisms of vancomycin resistance in *Staphylococcus aureus*. *Journal of Clinical Investigation*, 2014, 124(7): 2836–2840.

145. Scott D Taylor, et al. The action mechanism of daptomycin. *Bioorganic & Medicinal Chemistry*, 2016, 24(24): 6253–6268.

146. Tony Velkov, et al. Pharmacology of polymyxins: new insights into an 'old' class of antibiotics. *Future Microbiology*, 2013, 8(6): 711–724.

147. Nagendra N Mishra, et al. Phenotypic and genotypic characterization of daptomycin-resistant methicillin-resistant *Staphylococcus aureus* strains: relative roles of *mprF* and *dlt* operons. *PLOS ONE*, 2014, 9(9): e107426.

148. Andreas Peschel, et al. Inactivation of the *dlt* operon in *Staphylococcus aureus* confers sensitivity to defensins, protegrins, and other antimicrobial peptides. *Journal of Biological Chemistry*, 1999, 274(13): 8405–8410.

149. Christoph M Ernst, et al. The bacterial defensin resistance protein MprF consists of separable domains for lipid lysinylation and antimicrobial peptide repulsion. *PLoS Pathogens*, 2009, 5(11): e1000660.

150. James K Lithgow, et al. Role of a cysteine synthase in *Staphylococcus aureus*. *Journal of Bacteriology*, 2004, 186(6): 1579–1590.

151. Christopher R E McEvoy, et al. Decreased vancomycin susceptibility in *Staphylococcus aureus* caused by IS256 tempering of WalKR expression. *Antimicrobial Agents and Chemotherapy*, 2013, 57(7): 3240–3249.

152. Soo-Jin Yang, et al. The *Staphylococcus aureus* two-component regulatory system, GraRS, senses and confers resistance to selected cationic antimicrobial peptides. *Infection and Immunity*, 2012, 80(1): 74–81.

153. Melanie R Stapleton, et al. Characterization of IsaA and SceD, two putative lytic transglycosylases

of *Staphylococcus aureus*. *Journal of Bacteriology*, 2007, 189(20): 7316–7325.

154. Lakshmanan Ramadurai, et al. A bacteriolytic enzyme from *Staphylococcus aureus* that cleaves the cell wall glycopeptide bridge. *Journal of Bacteriology*, 1999, 181(12): 3627–3633.

155. Angelika Gründling, et al. Genes required for glycolipid synthesis and lipoteichoic acid anchoring in *Staphylococcus aureus*. *Journal of Bacteriology*, 2007, 189(6): 2521–2530.

156. Sharon J Peacock, et al. *Staphylococcus aureus*: genetic variation and the emergence of successful lineages. *Nature Reviews Microbiology*, 2015, 13(10): 638–652.

157. Sahreena Lakhundi, et al. Methicillin-resistant *Staphylococcus aureus*: molecular characterization, evolution, and epidemiology. *Clinical Microbiology Reviews*, 2018, 31(4): e00020-18.

158. Vineet K Singh, et al. An insight into the significance of the DnaK heat shock system in *Staphylococcus aureus*. *International Journal of Medical Microbiology*, 2012, 302(6): 242–252.

159. Dorte Frees, et al. Clp ATPases are required for stress tolerance, intracellular replication and biofilm formation in *Staphylococcus aureus*. *Molecular Microbiology*, 2004, 54(5): 1445–1462.

160. Dorte Frees, et al. New insights into *Staphylococcus aureus* stress tolerance and virulence regulation from an analysis of the role of the ClpP protease in the strains Newman, COL and SA564. *Journal of Proteome Research*, 2012, 11(1): 95–108.

161. Xinyu Liao, et al. Pre-exposure of foodborne *Staphylococcus aureus* isolates to organic acids induces cross-adaptation to mild heat. *Microbiology Spectrum*, 2023, 11(2): e03832-22.

162. Timothy J Foster, et al. Surface protein adhesins of *Staphylococcus aureus*. *Trends in Microbiology*, 1998, 6(12): 484–488.

163. Ian R Siboo, et al. Role of SraP, a serine-rich surface protein of *Staphylococcus aureus*, in binding to human platelets. *Infection and Immunity*, 2005, 73(4): 2273–2280.

164. Sarkis K Mazmanian, et al. An iron-regulated sortase anchors a class of surface protein during *Staphylococcus aureus* pathogenesis. *Proceedings of the National Academy of Sciences of the United States of America*, 2002, 99(4): 2293–2298.

165. Neal D Hammer, et al. Molecular mechanisms of *Staphylococcus aureus* iron acquisition. *Annual Review of Microbiology*, 2011, 65: 129–147.

166. Andras N Spaan, et al. The staphylococcal toxin Panton-Valentine Leukocidin targets human C5a receptors. *Cell Host & Microbe*, 2013, 13(5): 584–594.

167. Karen O'Riordan, et al. *Staphylococcus aureus* capsular polysaccharides. *Clinical Microbiology Reviews*, 2004, 17(1): 218–234.

168. Yvonne G Y Chan, et al. The capsular polysaccharide of *Staphylococcus aureus* is attached to peptidoglycan by the LytR-CpsA-Psr family of enzymes. *Journal of Biological Chemistry*, 2014, 289(22): 15680–15690.

169. Kate E Atkin, et al. A different path: revealing the function of staphylococcal proteins in biofilm formation. *FEBS Letters*, 2014, 588(10): 1869–1872.

170. Hoai T. T. Nguyen, et al. The staphylococcal exopolysaccharide PIA—biosynthesis and role in biofilm formation, colonization, and infection. *Computational and Structural Biotechnology Journal*, 2020, 18: 3324–3334.

171. Jamie L Brooks, et al. Phase variation of poly-N-acetylglucosamine expression in *Staphylococcus aureus*. *PLoS Pathogens*, 2014, 10(7): e1004292.

172. Richard P Novick, et al. The *agr* P2 operon: an autocatalytic sensory transduction system in *Staphylococcus aureus*. *Molecular and General Genetics*, 1995, 248(4): 446–458.

173. Jonathan G Swoboda, et al. Wall teichoic acid function, biosynthesis, and inhibition in *Staphylococcus aureus*. *ChemBioChem*, 2010, 11(1): 35–45.

174. Justin L Luebke, et al. The CsoR-like sulfurtransferase repressor (CstR) is a persulfide sensor in *Staphylococcus aureus*. *Molecular Microbiology*, 2014, 94(6): 1343–1360.

175. Michael Otto. Staphylococcal biofilms. *Microbiology Spectrum*, 2018, 6(4): 10.1128/microbiolspec.GPP3-0023-2018.

176. Hans-Curt Flemming, et al. Biofilms: an emergent form of bacterial life. *Nature Reviews Microbiology*, 2016, 14(9): 563–575.

177. J William Costerton, et al. Bacterial biofilms: a common cause of persistent infections. *Science*, 1999, 284(5418): 1318–1322.

178. Sophia Hawas, et al. Combination therapies for biofilm inhibition and eradication: a comparative review of laboratory and preclinical studies. *Frontiers in Cellular and Infection Microbiology*, 2022, 12: 850030.

179. Thomas Bjarnsholt. The role of bacterial biofilms in chronic infections. *APMIS*, 2013, 121(Suppl. 136): 1–51.

180. Lena Studt, et al. Biosynthesis of fusarubins accounts for pigmentation of *Fusarium fujikuroi* perithecia. *Applied and Environmental Microbiology*, 2012, 78(12): 4468–4480.

181. Marnix H Medema, et al. antiSMASH: rapid identification, annotation and analysis of secondary metabolite biosynthesis gene clusters in bacterial and fungal genome sequences. *Nucleic Acids Research*, 2011, 39(Suppl. 2): W339–W346.

182. Kai Blin, et al. antiSMASH 7.0: new and improved predictions for detection, regulation, chemical structures and visualisation. *Nucleic Acids Research*, 2023, 51(W1): W46–W50.

183. John Jumper, et al. Highly accurate protein structure prediction with AlphaFold. *Nature*, 2021, 596(7873): 583–589.

184. Minkyung Baek, et al. Accurate prediction of protein structures and interactions using a three-track

neural network. *Science*, 2021, 373(6557): 871–876.

185. Chengxin Zhang, et al. US-align: universal structure alignments of proteins, nucleic acids and macromolecular complexes. *Nature Methods*, 2022, 19(9): 1109–1115.

186. Jacques Boitreaud, et al. Chai-1: decoding the molecular interactions of life. *bioRxiv*, 2024: 2024.10.10.615955.

187. Patrick Bryant, et al. Structure prediction of alternative protein conformations. *Nature Communications*, 2024, 15(1): 7328.

188. Mandarina Q C Li, et al. Advantages and limitations of AlphaFold in structural biology: insights from recent studies. *The Protein Journal*, 2026, 45(1): 22–38.

189. David Errington, et al. Assessing interaction recovery of predicted protein-ligand poses. *Journal of Cheminformatics*, 2025, 17(1): 76.

190. Patrick Di Martino. Extracellular polymeric substances, a key element in understanding biofilm phenotype. *AIMS Microbiology*, 2018, 4(2): 274–288.

191. Lucy C Bowden, et al. Beyond the double helix: the multifaceted landscape of extracellular DNA in *Staphylococcus aureus* biofilms. *Frontiers in Cellular and Infection Microbiology*, 2024, 14: 1400648.

192. Joe J Harrison, et al. The use of microscopy and three-dimensional visualization to evaluate the structure of microbial biofilms cultivated in the Calgary Biofilm Device. *Biological Procedures Online*, 2006, 8(1): 194–215.

193. Sophie E Mountcastle, et al. Biofilm viability checker: an open-source tool for automated biofilm viability analysis from confocal microscopy images. *npj Biofilms and Microbiomes*, 2021, 7(1): 44.

194. Courtney Reichhardt, et al. Confocal laser scanning microscopy for analysis of *Pseudomonas aeruginosa* biofilm architecture and matrix localization. *Frontiers in Microbiology*, 2019, 10: 677.

195. Shaochi Wang, et al. Strategy to combat biofilms: a focus on biofilm dispersal enzymes. *npj Biofilms and Microbiomes*, 2023, 9(1): 63.

196. Rojita Mishra, et al. Natural anti-biofilm agents: strategies to control biofilm-forming pathogens. *Frontiers in Microbiology*, 2020, 11: 566325.

197. Jennifer M Finefield, et al. Enantiomeric natural products: occurrence and biogenesis. *Angewandte Chemie International Edition*, 2012, 51(20): 4802–4836.

198. Gabin Thierry M. Bitchagno, et al. Demystifying racemic natural products in the homochiral world. *Nature Reviews Chemistry*, 2022, 6(11): 806–822.

199. Lin Wang, et al. Asperphenalenones isolated from the biocontrol agent *Clonostachys rosea* and their antimicrobial activities. *Journal of Agricultural and Food Chemistry*, 2023, 71(29): 11056–11068.

Acknowledgements

The pursuit of my doctoral degree has been a journey filled with challenges, growth, and rewarding experiences. The completion of this dissertation would not have been possible without the guidance, support, and companionship of many supervisors, colleagues, friends, and family members. I would therefore like to express my sincere gratitude to everyone who has supported and helped me along the way.

First and foremost, I would like to express my deepest gratitude to my supervisor, Prof. Dr. Rainer Kalscheuer. I am sincerely grateful to him for giving me the valuable opportunity to pursue my doctoral studies at the Institute of Pharmaceutical Biology and Biotechnology, Heinrich Heine University Düsseldorf, and to work on meaningful and challenging research projects. Throughout my doctoral research, he provided me with trust, academic freedom, and continuous support. His professional guidance, constructive suggestions, and rigorous scientific attitude not only helped me improve my research but also taught me to approach scientific questions in a more independent, critical, and thoughtful manner.

I would also like to thank my co-supervisor, Prof. Dr. Julia Frunzke, for her valuable guidance, advice, and support throughout my doctoral studies. Her professional insights and inspiring discussions enabled me to examine my research from different perspectives and greatly broadened my academic horizons.

My special thanks go to Prof. Dr. Haofu Dai from the Institute of Tropical Bioscience and Biotechnology, Chinese Academy of Tropical Agricultural Sciences, Haikou, China. I am deeply grateful to him for introducing me to Prof. Dr. Rainer Kalscheuer, which gave me the valuable opportunity to pursue my doctoral degree and conduct research at Heinrich Heine University Düsseldorf.

I would like to sincerely thank Dr. Viktor Simons and Dr. Lin Wang. Their previous work laid an important foundation for my research project and provided valuable references and inspiration for the design and development of my subsequent studies.

I am grateful to all members of our research group, including Dr. Lasse van Geelen, Dr. Viktor Simons, Dr. Emmanuel Adeniyi, Dr. Anna-Lene Kiffe-Delf, Dr. Kristin Vill (née Schwechel), Violetta Krisilia, MengYun Zhang, Chengmin Yang, Aron Trucksess, Kira Schichel, Eveline Derr, Swapna Swapna, and Oliver Eberle. I sincerely appreciate their help, support, and companionship in experimental work, scientific discussions, and daily life. The experience of working and spending time together made my doctoral journey more fulfilling and left me with many precious memories. I would especially like to thank the two technicians in our research group, Heike Goldbach-Gecke and Nicole Teßendorf. Their professional assistance and patient support in experimental techniques, instrument operation, material preparation, and daily laboratory affairs provided an important basis for the smooth progress of my research.

I am grateful to the DFG-funded Research Training Group GRK 2158 and to Dr. Martina Holz. The

programme provided me with a valuable research platform, opportunities for academic exchange, and space for personal and professional development. Through participating in its academic activities and training programmes, I broadened my scientific perspective and strengthened both my professional skills and general competencies. These experiences were highly valuable for both my doctoral research and personal growth.

I am also deeply grateful to Dr. Hao Wang from the Institute of Tropical Bioscience and Biotechnology, Chinese Academy of Tropical Agricultural Sciences, Haikou, China, for his help and support throughout my research. His patient explanations and valuable advice helped me address many questions and contributed to the successful progress of my work.

My sincere thanks also go to Yuxi Gao from the School of Life Science and Technology, ShanghaiTech University, Shanghai, China, for providing extensive professional support throughout my doctoral research. Her expertise and thoughtful explanations helped me resolve many scientific questions and contributed greatly to the progress of my work.

I gratefully acknowledge the financial support provided by the China Scholarship Council (CSC) during my doctoral studies in Germany. This support enabled me to focus on my research and provided an important foundation for my studies, scientific work, and academic exchange.

I would like to thank my parents, Liming He and Yan Lin, for their unconditional love, understanding, and support. They have always been the strongest source of support throughout my journey.

I would also like to express my special gratitude to my girlfriend, Jiaqi Pan, for her understanding, companionship, and continuous support. Her encouragement gave me great strength throughout the completion of my doctoral studies.

Statutory Declaration

I hereby declare under oath that I prepared this dissertation independently and without any unauthorized assistance from third parties, in accordance with the “Principles for Safeguarding Good Scientific Practice at Heinrich Heine University Düsseldorf.”

Düsseldorf, _____

Di He